Ph.D. Thesis

Detailed Three-Dimensional Nonlinear Hybrid Simulation for the Analysis of Large-Scale Reinforced Concrete Structures

George Markou

National Technical University of Athens

School of Civil Engineering

Institute of Structural Analysis and Seismic Research

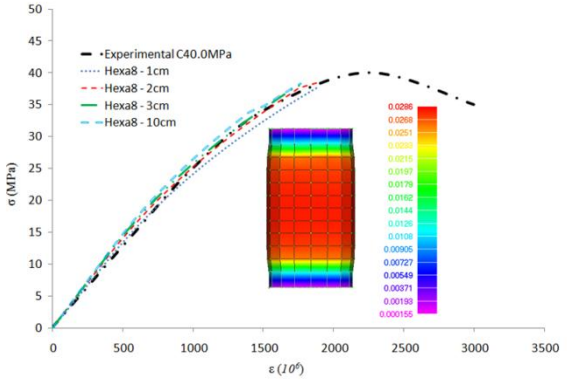

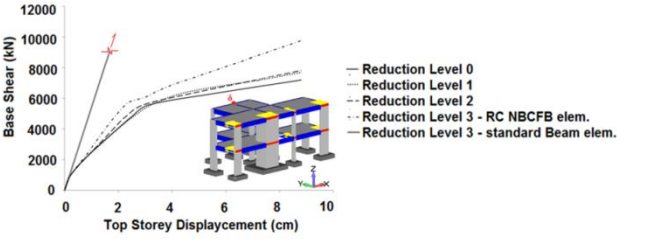

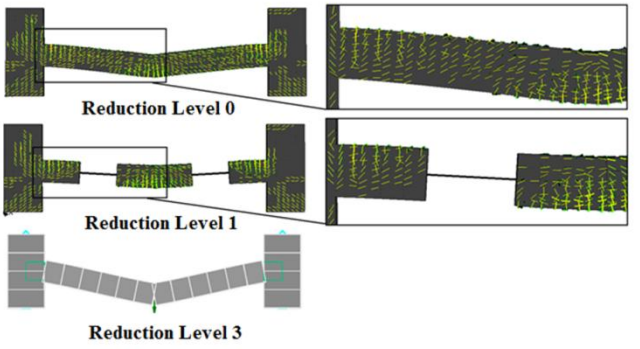

Supervising Professor

Manolis Papadrakakis

Athens, Jan 2011

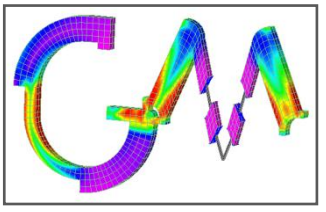

Ph.D. Thesis

Διδακτορική Διατριβή

Detailed Three-Dimensional Nonlinear Hybrid Simulation for the Analysis of Large-Scale Reinforced Concrete Structures

---

Τριδιάστατα Μη-Γραμμικά Υβριδικά Προσομοιώματα για την Ανάλυση Μεγάλης Κλίμακας Κατασκευών από Οπλισμένο Σκυρόδεμα

---

by George Markou

Supervising Professor: Manolis Papadrakakis

Αφιερωμένο με όλη την δύναμη της ψυχής, αγάπης και αφοσίωσης, στους

Μαρίνα, Αλέξανδρο και Στέφανο-Ιβάν

Μάρκου.

Dedicated with all the strength of my soul, love and devotion to

Marina, Alexandros and Stefanos-Ivan

Markou.

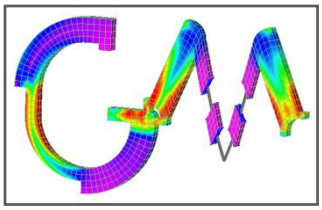

Ph.D. Examination Committee

_____

Professor Manolis Papadrakakis
(Supervisor and Principal Advisor of the Committee)
National Technical University of Athens
School of Civil Engineering

_____

Professor Michail Kotsovos
(Member Advisor of the Committee)
National Technical University of Athens
School of Civil Engineering

_____

Assistant Professor Christos Zeris
(Member Advisor of the Committee)
National Technical University of Athens
School of Civil Engineering

Professor Andreas Kappos
(Member of the Examination Committee)
Aristotle University of Thessaloniki
Department of Civil Engineering

Professor Vintzilaiou Elisavet
(Member of the Examination Committee)
National Technical University of Athens
School of Civil Engineering

Professor Syrmakezis Konstantinos
(Member of the Examination Committee)
National Technical University of Athens
School of Civil Engineering

Associate Professor Spiliopoulos Konstantinos
(Member of the Examination Committee)
National Technical University of Athens
School of Civil Engineering

Ευχαριστίες

Πρωτίστως θα ήθελα να ευχαριστήσω τον επιβλέποντά μου, Καθηγητή Μανόλη Παπαδρακάκη, για την ευκαιρία που μου έδωσε να ασχοληθώ με ερευνητικά θέματα αιχμής, τα οποία έχουν άμεση εφαρμογή μέσω της Μεθόδου των Πεπερασμένων Στοιχείων και αφορούν την επίλυση πρακτικών προβλημάτων Πολιτικού και Αεροναυπηγού Μηχανικού. Μέσω της παραγωγικής μας συνεργασίας και της επιστημονικής του καθοδήγησης, κατάφερε να μου υποδείξει το απεριόριστο των δυνατοτήτων μου και να θέσει ψιλούς ερευνητικούς στόχους στα πλαίσια της παρούσας Διατριβής. Για όλα αυτά που μου έχει προσφέρει, θα ήθελα να εκφράσω την βαθιά μου ευγνωμοσύνη.

Θα ήθελα να εκφράσω ένα μεγάλο ευχαριστώ στον συνάδελφο αλλά και φίλο, Υποψήφιο Διδάκτορα Μέτση Παναγιώτη με τον οποίο περάσαμε αμέτρητες ώρες συζητώντας εποικοδομητικά για διάφορα επιστημονικά θέματα. Επιπλέον ένα μεγάλο ευχαριστώ για την ανιδιοτελή βοήθειά του η οποία ήταν πραγματικά ανεκτίμητης αξίας.

Εν συνεχεία, θα ήθελα να ευχαριστήσω τα άλλα δύο μέλη της Τριμελούς Επιτροπής, Καθηγητή Μιχαήλ Κοτσοβό και Επίκουρο Καθηγητή Χρίστο Ζέρη, για τις ενδιαφέρουσες συζητήσεις που είχαμε σε θέματα της Διδακτορικής Διατριβής αλλά και την παροχή βοήθειας σε ερευνητικό επίπεδο, όποτε αυτή είχε ζητηθεί. Οι συμβουλές και τα σχόλιά τους βοήθησαν σημαντικά στη βελτίωση της παρούσας εργασίας.

Θα ήθελα να εκφράσω την βαθιά μου εκτίμηση στους Καθηγητή Βλάση Κουμούση και Αναπληρωτή Καθηγητή Κωνσταντίνο Σπηλιόπουλο, οι οποίοι ήταν πάντα διαθέσιμοι για εποικοδομητικά σχόλια και συμβουλές επί του ερευνητικού μου έργου.

Ευχαριστώ όλα τα μέλη της 7-μελούς επιτροπής και ειδικότερα τον καθ. Κάππο, για τα εποικοδομητικά τους σχόλια και παρατηρήσεις οι οποίες βοήθησαν στην βελτίωση της παρούσας Διατριβής.

Θα ήθελα επίσης να ευχαριστήσω τον Δρ Γιώργο Σταυρουλάκη για την συνεργασία που είχαμε στα πλαίσια της ερευνητικής ομάδας του Καθηγητή Μανόλη Παπαδρακάκη και η οποία ήταν πάντοτε ευχάριστη και εποικοδομητική. Επίσης θα ήθελα να εκφράσω την εκτίμησή μου στους Δρ. Μιχάλη Φραγκιαδάκη, Δρ. Γεώργιο Λυκίδη, Δρ. Αριστείδη Παπαχρηστίδη και Υποψήφιο Διδάκτορα Κωνσταντίνο Παπανικολόπουλο για τις πολύτιμες συμβουλές τους επί του ερευνητικού μου έργου.

Στα πλαίσια της Διδακτορικής Διατριβής εκπονήθηκαν δύο Διπλωματικές και μία Μεταπτυχιακή Εργασία από την Στεφανία Βασιλομιχελάκη και τον Παναγιώτη Καρακίτσιο, οι οποίοι μέσα από την σχολαστική τους δουλειά συντέλεσαν σημαντικά στην εκτενή παραμετρική διερεύνηση του κώδικα πεπερασμένων στοιχείων που αναπτύχθηκε στα πλαίσια

του ερευνητικού αυτού έργου. Θα ήθελα να τους ευχαριστήσω για την άριστη και συνάμα εποικοδομητική συνεργασία μας.

Θα ήθελα να ευχαριστήσω τον Καθηγητή Κυριάκο Γιαννάκογλου, τον Λέκτορα Δήμο Χαρμπή, τον Δρ. Δημήτρη Κουμπογιάννη και τον Δρ. Ζαχαρία Μουρούτη για την παραγωγική συνεργασία μας στα πλαίσια του ερευνητικού έργου που εκτελέστηκε στο προπτυχιακό, μεταπτυχιακό αλλά και στο αρχικό στάδιο της Διδακτορικής Διατριβής μου, σε θέματα αλληλεπίδρασης ρευστού-κατασκευής.

Ευχαριστώ όλα τα παιδιά της Ερευνητικής ομάδας του Καθηγητή Μανόλη Παπαδρακάκη για την άψογη συνεργασία και την παραγωγική διάθεση που επέδειξαν.

Τέλος θα ήθελα να ευχαριστήσω την γυναίκα μου Μαρίνα για την υπομονή και επιμονή που επέδειξε κατά τη διάρκεια της εκτέλεσης του ερευνητικού αυτού έργου, καθώς επίσης και για την αμέριστη στήριξή της. Την ευχαριστώ για το γεγονός ότι ποτέ δεν έπαψε να πιστεύει στις δυνατότητές μου και γι' αυτό θα της είμαι παντοτινά ευγνώμων.

Ευχαριστώ!

Γεώργιος Μάρκου, Αθήνα, Ιαν 2011.

Acknowledgements

First of all, I would like to begin by expressing my gratitude to my supervisor Professor Manolis Papadrakakis for providing me with the opportunity to work with state of the art research subjects on engineering problems that use the Finite Element Method. Through our productive collaboration and his scientific guidance, he managed to set high research standards in the framework of this Ph.D. Dissertation. I consider myself privileged working with him and I would like to express my deepest appreciation.

I also gratefully acknowledge my colleague and friend Ph.D. Candidate Metsis Panagiotis, with whom I've spend countless hours discussing constructively several scientific subjects. Moreover, I would like to thank him for his great support and altruistic help which was priceless.

Following, I would like to thank the other members of my thesis committee, Professor Michail Cotsovos and Assistant Professor Christos Zeris, for their helpful discussions and scientific comments. Their valuable comments and suggestions contributed to the improvement of the quality of this Dissertation .

My research has been stimulated through the contractive comments of Professor Vlasis Koumousis and Associated Professor Konstantinos Spiliopoulos to whom I would like to express my appreciation.

The comments and suggestions of the 7-member committee and especially those made by Prof Kappos, were very constructive. Their contribution is greatly acknowledged.

I would also like to thank the Dr George Stavroulakis for the constructive and interesting collaboration that we had at the framework of the research team of prof. M.Papadrakakis. In addition, I would like to acknowledge Dr Michalis Fragiadakis, Dr George Lykidis, Dr Aristidis Papachristidis and Ph.D. Candidate Konstantinos Papanikolopoulos for their helpful suggestions during the Ph.D. Dissertation .

During this research, two Diplomas and a Master Thesis were performed by Stefania Vasilomichelaki and Panayiotis Karakitsios whose rigorous work managed to provide significant conclusions through the parametric investigation of the finite element analysis code that was developed in the framework of the present Dissertation. I would like to acknowledge their contribution and thank them for the enjoyable and constructive collaboration.

Furthermore, I would like to thank Professor Kyriakos Giannakoglou, Lecturer Dimos Charmpis, Dr Dimitris Koumpogiannis and Dr Zacharias Mouroutis for the excellent collaboration that we had during my Diploma, Master and Ph.D. research work on fluid-structure interaction problems.

I would like to thank all my colleagues that worked in the research team of Professor Manolis Papadrakakis for their useful suggestions and comments thus maintaining a productive and pleasant environment.

Finally, I would like to thank my wife Marina for her unfailing support during this Dissertation. She always encouraged me and never stopped believing in me, for which I will always be grateful.

Thank You!

George Markou, Athens, Jan 2011.

Χρηματοδότηση - Financial Support

Η ερευνητική αυτή εργασία χρηματοδοτήθηκε από δύο βασικούς οργανισμούς, το Ίδρυμα Ιωάννη Αργύρη και τον Ειδικό Λογαριασμό Έρευνας (ΕΛΕ) του Εθνικού Μετσόβιου Πολυτεχνείου.

Ο Γεώργιος Μάρκου ήταν ο πρώτος Υποψήφιος Διδάκτορας υπότροφος του Ιδρύματος Ιωάννη Αργύρη με σκοπό την εκπόνηση Διδακτορικής Διατριβής στην επιστημονική περιοχή των Πεπερασμένων Στοιχείων.

This research work was mainly funded by the *John Argyris Foundation* (JAF http://argyrisfoundation.org/) and the Research Funding Department (ΕΛΕ) of the National Technical University of Athens.

In January 2005, the JAF was established. The foundation was created in memory of the great Greek scientist and engineer, John Argyris, who invented the "Finite Element Method". This method is said to be one of the greatest discoveries of the 20th century in the fields of Engineering and Applied Sciences. The Chairman of the foundation is his son Holger Argyris, to whom the author would like to personally express his gratitude.

George Markou was the first Ph.D. candidate who received the JAF scholarship, which is awarded to Ph.D. students for the completion of their Ph.D. Dissertation .

Research Funding Department (ΕΛΕ)
of the National Technical University of Athens

Special Reference to the Life of J. Argyris

This article was first published in 2004 in Computer Methods in Applied Mechanics and Engineering, Vol. 193, pp. 3763-3766.
With the permission of the authors and CMAME, I share it with you here.

A person with great vision, class and persuasion, who dramatically influenced Computational Engineering and Science and who will be long remembered as one of the great pioneers of the discipline in its formative years.

John H. Argyris passed away quietly on 2 April 2004 after respiratory complications. John rests in peace in Sankt Jorgens Cemetery in the city of Varberg, 60 km south of Goteborg, Sweden, near Argyris' summer house.

John was born on 19 August 1913 in the city of Volos, 300 km north of Athens, Greece into a Greek Orthodox family. His father was a direct descendant of a Greek Independence War hero, while his mother came from an old Byzantine family of politicians, poets and scientists, which included the famous mathematician Constantine Karatheodori, Professor at the University of Munich.

Volos, as it was during his childhood, remained very much alive in his memory, especially the house he grew up in. He vividly remembered, until the end, details of the room where, at the age two, he almost died from typhoid fever. In 1919 his family moved to Athens where he received his initial education at a Classical Gymnasium in Athens. After studying Civil Engineering for four years at the National Technical University of Athens, he continued his studies at the Technical University of Munich where he obtained his Engineering Diploma in 1936. Just after graduation he was employed by a private consulting organization working on the leading-edge technical design of highly complex structures. One of these early engineering accomplishments was that of designing a 320 m high radio transmitter mast with a heavy mass concentrated at the top.

With the outbreak of World War II, John was in Berlin continuing his studies at the Technical University of Berlin. Just after the German invasion of Greece, John was arrested and led to a concentration camp, on the accusation of transferring research secrets to the Allies. His savior turned out to be the eminent German Admiral Kanaris, of Greek descent, who arranged his escape by informing the guards that the prisoner would be executed outside the camp. In 1944, Kanaris himself was tragically executed as one of the leaders of the assassination attempt against Hitler. Following his escape from prison, John managed to leave Germany soon thereafter in a very dramatic manner. He swam across the Rhine River during a midnight air raid, holding his passport in his teeth. He managed to reach Switzerland where he completed his Doctoral degree at ETH of Zurich in 1942 in Aeronautics. In 1943 he moved to England and worked as a technical officer at the Engineering Department of the Royal Aeronautical Society of London.

John could never derive any pleasure in ordinary day-to-day work and was only attracted to problems that seemed unsolvable. Even when working in industry, his directors soon realized that the best policy towards John Argyris was to entrust him with intractable problems. At the same time he was fascinated by the properties of triangular and tetrahedral components that appeared to him as ideal elements to build up an engineering system. He could never sympathize with Cartesian analytical geometry that he found most inelegant. During the war, he wrote three classic papers in Reports and Memoranda of the then Aeronautical Research Council. These were concerned with the diffusion of loads into stringer-reinforced stressed skin structures of wings and fuselages. He developed a theory using his intuition that combined differential equations and finite difference calculus that was immediately successful and later confirmed by experiments and applied with great success to British fighter and bomber aircraft during the war. However, the real break-through in his way of thinking and approach to technical problems of solid mechanics was achieved when the first electro-mechanical computing devices emerged in 1944 in Britain at the National Physical Laboratory and in the United States at Harvard University.

In those days aeronautical engineers were trying to build the first combat jet aircraft whose speed required swept-back wings. One such example was the flawed German fighter ME262, proof of its designers' failure to develop a reliable method of analyzing the non-orthogonal geometry of wings. In August of 1943 John spent three whole days and nights in a bold attempt to solve that particular problem. His only help was a rudimentary computing device capable of solving a system of up to 64 unknowns. It took one sudden moment of clarity, on the third evening of his brainstorming session for him to realize that the answer could be the application of triangular elements. Here his dislike of orthogonal Cartesian geometry found an ideal field. Astonishingly enough the deviation from preceding experimental test results proved less than 8%. This was the birth of the matrix force and displacement methods, the finite element method, as later named. Immediately, all publications on this method were declared secret. Within the triangular element philosophy, John did not use Cartesian direct and shear stresses and strains, but a novel definition of stresses, expressed in terms of these direct stresses and strains, measured parallel to the three sides of each triangle. This new definition of stresses and strains led to the formulation of the Natural Approach which possessed great computational advantages and allowed a simple and elegant generalization to large displacements.

In 1949 John joined the Imperial College of the University of London as a Senior Lecturer and in 1955 became a Full Professor and Director of the Sub-department of Aeronautical Studies until 1975. After becoming an Emeritus Professor he continued his collaboration with Imperial College as a Visiting Professor until 1980. In 1959 he accepted an offer from the University of Stuttgart and became Director of the Institute for Statics and Dynamics of Aerospace Structures. He created the Aeronautical and Astronautical Campus of the University of Stuttgart, a focal point for applications of digital computers and electronics. After becoming an Emeritus Professor at the University of Stuttgart he continued to work until the age of 88 with the same vigor, writing books and scientific papers with a compelling vitality and creative thinking.

In 1956 John addressed the problem of stress analysis of aircraft fuselages with many cut-outs, openings and severe irregularities. Computers then were not capable of enabling a global application of the finite element method. John, again following his intuition, realized that the problem could be solved by a new physical device involving the application of initial stresses and strains and an extension of matrix methods to a higher level. This was presented at the IUTAM Congress in Brussels in 1956 and created a great upheaval, because the whole derivation involved only 20 lines of physical argument and four lines of advanced matrix algebra. Most experts in the United States and Europe said that the theory must be wrong on the grounds of its simple derivation and they did not even accept the evidence of the computational results obtained by John that proved the correctness of this derivation. Somewhat later, however, a Ph.D. Thesis from Sydney, Australia was sent to John in which the candidate proved in 124 pages of close mathematical argument that the formula of John Argyris was indeed correct. This approach was also extensively applied to the design of the Boeing 747 as early as 1960. In the 1960s and 1970s John had applied the finite element method with great success in Aerodynamics, Optimization, Combustion Problems, Nonlinear Mechanics and other fields of research and industrial interest, among them the suspension roof of the Munich Olympic Stadium in the late 1960s. Around that period NASA sought his knowledge on the thermal shielding of the Apollo spacecraft. He suggested covering the fuselage with specially formulated substances that, upon reentry into the atmosphere, would evaporate and cool its surface. In 1976 John was concerned with the theory of Chaos and introduced these theories in studying the turbulence flow around the European Space Vehicle Hermis.

It is difficult to summarize the impressive accomplishments of John Argyris. Among his writings were over 10 books, including three important textbooks: Introduction to the Finite Element Method, Vols. I, II and III, 1986–88; Dynamics of Structures, 1991; An Explanation of Chaos, 1994. The latter was printed in English and German and in Germany alone was published three times in one year, a rare achievement for a scientific publication of this kind. In addition to these writings, he published over 500 extended scientific articles in major international journals and lectured extensively both within Europe and abroad. His textbooks and extensive journal publications are essential reading material for students, practicing engineers and researchers around the world and have become benchmarks for later treatises on Computational Mechanics. One of his most important contributions in the engineering community was the founding and editorship of the journal Computer Methods in Applied Mechanics and Engineering, a publication that has provided much of the lifeblood of Computational Methods in Applied Mechanics and Engineering for more than three decades. John Argyris took great interest and pride in this venture and insisted on running the journal meticulously and diligently, thus succeeding in making it one of the leading journals in Computational Mechanics available today.

John received many honors including 18 Doctorate Degrees, "Honoris Causa", three honorary professorships and six academy memberships from universities and academies all over the world, and more than 25 other awards and distinctions, among them the Gauss–Newton Award from IACM, the von Karman Medal from ASCE, the Timoshenko Medal from ASME, the Laskowitz

Gold Medal from the Academy of Science of New York for "the invention of the Finite Element Method", the Prince Philip Gold Medal of the Royal Academy of Engineering, the Grand Cross of Merit of the Federal Republic of Germany and the Einstein Award from the Einstein Foundation for his "momentous work on the Finite Element Method and Chaos Theory". He was also Fellow of the Royal Society of London, Honorary Member of the Executive Council of IACM and Honorary President of GACM.

John was blessed with many talents, making him a true modern Renaissance man; he was a scholar, a thinker, a teacher, a visionary, an orator, an elegant writer, a linguist. Deeply cultivated, a man with rare principles and a passionate patriot, he was also unique in blending his Mediterranean temperament with Western European rationalism.

In the paper which coined the name "Finite Element Method", published in 1960, the world-renowned author Ray Clough refers to the finite element method as "the Argyris Method". Von Karman's prophetic statement that Argyris' invention of the Finite Element Method entailed one of the greatest discoveries in Engineering Mechanics and revolutionized our thinking processes more than 50 years ago was proven to be absolutely true. Indeed, the Finite Element Method, based on John Argyris' fundamental and far-reaching contribution, has truly revolutionized today's engineering and scientific environments. He had the vision and intellectual capacity to develop the basic steps of the Finite Element Method and to make numerous contributions in the development of the method. His early work "Energy Theorems of Structural Analysis", published in 1954, is considered to be the most important series of papers ever published in the field of Structural Mechanics.

During the early years at Imperial College he met his wife Inga-Lisa who provided him with unshakable support throughout all the difficult moments of his life. John was also fortunate to see his son Holger follow a successful career in engineering and bring into the world, with his wife Carina, two adorable grandchildren who brightened his final years.

John, in accordance with Herakleitos' aphorism of "τὰ πάντα ῥεῖ", has joined the Pantheon of those enlightening personalities who, with their revolutionary ideas and contributions, have changed the scientific world in the 20th Century. His geometrical spirit, the elegance of his writings, his deep appreciation and understanding of classical ideas, his creativity and his epochal vision of the future initiated and defined the modern era of Engineering Analysis and set us all on life's path of discovery. Our Computational Mechanics Community has lost the most eminent member and for many of us, a devoted friend. He will be deeply missed, but his legacy will empower generations.

By *Thomas J. R. Hughes, J. Tinsely Oden, and Manolis Papadrakakis*

Table of Contents

List of Figures

Introduction

Chapter 1

Chapter 2

Chapter 3

Chapter 4

Chapter 5

Chapter 6

Chapter 7

Chapter 8

Appendices

List of Tables

Chapter 2

Chapter 3

Chapter 4

Chapter 5

Chapter 6

Chapter 7

Chapter 8

Abbreviations

Abbreviation	*Description*
1D	One-Dimensional
2D	Two-Dimensional
3D	Three-Dimensional
AR	Aspect Ratio
CG	Conjugated Gradient
CPU	Central Processing Unit
DE	Discrete Element(s)
DOF	Degree(s) Of Freedom
FE	Finite Element
FEA	Finite Element Analysis
FEM	Finite Element Method
FSI	Fluid-Structure Interaction
HEXA8	8-noded HEXAhedral element
HEXA20	20-noded HEXAhedral element
HEXA27	27-noded HEXAhedral element
HYMOD	HYbrid MODeling method
LFI	Local Fracture Initiation
NR	Newton-Raphson
OOP	Object-Oriented Programming
ΟΣ	Οπλισμένο Σκυρόδεμα

OSFP	Onset of Stable Fracture Propagation
OUFP	Onset of Unstable Fracture Propagation
PDE	Partial Differential Equations
pp.	Page(s)
RC	Reinforced Concrete
ReConAn	Reinforced Concrete Analysis
RL	Reduction Level
US	Ultimate Surface
UTCA	Unified Total Crack Approach
ΕΑΚ	Ελληνικός Αντισεισμικός Κανονισμός
ΠΣ	Πεπερασμένων Στοιχείων

Πρόλογος

Μέσω της ραγδαίας ανάπτυξης των υπολογιστών τις τελευταίες δεκαετίες, υπήρξε μία γεωμετρικά αυξανόμενη πρόοδος στην ανάπτυξη λογισμικών τα οποία δίνουν στους χρήστες τη δυνατότητα ανάλυσης και σχεδιασμού κατασκευών από οπλισμένο σκυρόδεμα με τη χρήση διαφόρων αριθμητικών προσομοιωμάτων. Τα λογισμικά αυτά πακέτα (εμπορικά και ερευνητικά) χρησιμοποιούν τη δημοφιλή αριθμητική μέθοδο των πεπερασμένων στοιχείων (ΠΣ), προκειμένου να διαφοροποιήσουν το μαθηματικό μοντέλο που διέπει τη συμπεριφορά του εκάστοτε προσομοιώματος και μέσω της εφαρμογής συγκεκριμένων αριθμητικών μεθόδων επίλυσης να υπολογίσουν τα εντατικά μεγέθη που αναπτύσσονται σε μία κατασκευή, με απώτερο σκοπό την αποτίμηση της συμπεριφοράς της υπό δεδομένους συνδυασμούς φόρτισης και την οικονομική και ασφαλή διαστασιολόγησή της.

Μετά από την ανακάλυψη και διάδοση της μεθόδου των ΠΣ από τους γνωστούς «πατέρες» της μεθόδου: Argyris J. H.[1], Clough R. W.[2], Turner M. J.[3] και Zienkiewicz O. C.[4], οι οποίοι αναφέρονται με αλφαβητική σειρά με σκοπό την αποφυγή ιεράρχησης της σπουδαιότητας του έργου τους, η χρήση της μεθόδου έγινε ευρέως αποδεκτή από την ερευνητική κοινότητα καθώς επίσης και τους συγγραφείς επαγγελματικών κωδίκων ανάλυσης και σχεδιασμού κατασκευών πολιτικού μηχανικού καθώς και πληθώρας άλλων προβλημάτων στις επιστήμες του μηχανικού. Δεδομένης της μακράς ιστορίας, της λεπτομερούς διατύπωσης αλλά και της παραμετρικής διερεύνησης της μεθόδου των ΠΣ που έχει πραγματοποιηθεί από την ερευνητική ομάδα στην οποία εντάχθηκε ο συγγραφέας της παρούσας Διατριβής, επιλέχθηκε η μέθοδος αυτή για την ανάπτυξη βελτιωμένου λογισμικού προσομοίωσης και εφαρμογών μεγάλης κλίμακας που θα παρουσιαστούν στην παρούσα Διατριβή.

Παρά τις αλματώδεις εξελίξεις των λογισμικών πακέτων πολιτικού μηχανικού, η ανάγκη δημιουργίας ενός λογισμικού προσομοίωσης κατασκευών από οπλισμένο σκυρόδεμα το οποίο να είναι αριθμητικά στιβαρό και να μπορεί να προσομοιώνει με αποδεκτή ακρίβεια τη μη-γραμμική απόκριση οποιασδήποτε τριδιάστατης κατασκευής οπλισμένου σκυροδέματος αποτιμώντας με ρεαλιστικό τρόπο την αντοχή της σε οριακές φορτίσεις, είναι ακόμη υπαρκτή. Το γεγονός αυτό αναδύεται μέσω των υπεραπλουστευμένων προσομοιωμάτων ΠΣ που χρησιμοποιούνται στην πράξη για την ανάλυση κατασκευών από οπλισμένο σκυρόδεμα καθώς επίσης κι από την αδυναμία των πιο λεπτομερών μοντέλων που έχουν αναπτυχθεί ερευνητικά για την προσομοίωση πραγματικών κατασκευών εξαιτίας της αριθμητικής πολυπλοκότητάς τους. Πέραν αυτού, τα σχετικά λίγα εμπορικά προγράμματα που υπάρχουν παρουσιάζουν αδυναμίες καθιστώντας τα μη πρακτικά εργαλεία κατά τον σχεδιασμό πολύπλοκων κατασκευών.

Τα τρία βασικά προβλήματα που παρουσιάζουν τα εμπορικά προγράμματα ΠΣ ανάλυσης κατασκευών από οπλισμένο σκυρόδεμα είναι:

i. Η έλλειψη αντικειμενικότητας των αποτελεσμάτων,
ii. Η έλλειψη αριθμητικής ευστάθειας κατά τη μη-γραμμική ανάλυση
iii. Το υπερβολικό υπολογιστικό κόστος ανάλυσης κατά τη διάρκεια επίλυσης του αριθμητικού προβλήματος.

Το πρώτο πρόβλημα απαντάται σε κώδικες ΠΣ (κυρίως εμπορικών λογισμικών πακέτων) οι οποίοι χρησιμοποιούν στοιχεία δοκού ή κελύφους για την ελαστική προσομοίωση των κατασκευαστικών μελών ενός κτηρίου από οπλισμένο σκυρόδεμα (ΟΣ), η οποία αγνοεί βασικά χαρακτηριστικά του υλικού (όπως τη ρηγμάτωση του σκυροδέματος, την επίδραση των διατμητικών τάσεων, τη διαρροή των οπλισμών κλπ), καταλήγοντας σε προσεγγιστικά αποτελέσματα τα οποία δεν αντικατοπτρίζουν την πραγματική απόκριση των κατασκευών αυτών σε οριακές καταστάσεις φόρτισης. Η χρήση αυτών των υπεραπλουστευμένων προσομοιωμάτων γίνεται ευρέως από πολλά εμπορικά πακέτα πολιτικού μηχανικού στις χώρες μας (Ελλάδα και Κύπρο) αλλά και στο εξωτερικό. Στην αντίπερα όχθη, κάποια ερευνητικά, καθώς επίσης και ορισμένα εμπορικά λογισμικά πακέτα, χρησιμοποιούν τριδιάστατα λεπτομερή προσομοιώματα ανάλυσης κατασκευών από ΟΣ, τα οποία λαμβάνουν υπόψη τα βασικά χαρακτηριστικά των δύο υλικών. Τα κύρια προβλήματα αυτών των λογισμικών πακέτων εντοπίζονται στην αριθμητική ευστάθειά τους (ιδίως όταν παρατηρείται ρηγμάτωση κατά τη διάρκεια της μη-γραμμικής ανάλυσης) και στο υπερβολικό υπολογιστικό κόστος που απαιτείται για την ανάλυση ρεαλιστικού μεγέθους κατασκευών, προβλήματα αλληλένδετα μεταξύ τους, τα οποία οδηγούν στους γνωστούς περιορισμούς ως προς το μέγεθος των μοντέλων τα οποία μπορούν να αναλυθούν εντός αποδεκτών υπολογιστικών χρόνων.

Δεδομένων των πιο πάνω προβλημάτων και με βάση τις τρέχουσες ανάγκες του σύγχρονου πολιτικού μηχανικού, η βασική προσπάθεια της ερευνητικής εργασίας που αναλύθηκε στο πλαίσιο αυτής της Διδακτορικής Διατριβής, είναι η δημιουργία ενός υπολογιστικού εργαλείου το οποίο θα αντιμετωπίζει αποτελεσματικά τις βασικές αυτές δυσκολίες, με απώτερο σκοπό τη δημιουργία ενός λογισμικού προσομοίωσης και ανάλυσης κατασκευών από ΟΣ, το οποίο να έχει τη δυνατότητα μέσω της χρήσης ενός κοινού υπολογιστή, να αναλύει με αποδεκτή ακρίβεια, σχετική αντικειμενικότητα, υπολογιστική ευστάθεια και εντός εύλογου χρονικού διαστήματος, μη-γραμμικά τριδιάστατα προσομοιώματα κατασκευών από ΟΣ σε οριακές φορτίσεις (στατικές και στο προσεχές μέλλον δυναμικές). Η επίτευξη ενός τέτοιου στόχου θα δημιουργήσει όλες τις προϋποθέσεις, που λείπουν στο παρόν στάδιο, ούτως ώστε να μπορέσει η τριδιάστατη μη-γραμμική ανάλυση με τη χρήση λεπτομερών προσομοιωμάτων να αποτελέσει βασικό εργαλείο στη διαδικασία σχεδιασμού αλλά κυρίως σεισμικής αποτίμησης των κατασκευών από ΟΣ.

Preface

During the last decades a significant increase in the number of available commercial and research software was observed, for modeling, analysis and design of reinforced concrete structures. Several type of models were presented in the international literature concerning the prediction of the nonlinear behavior of reinforced concrete structures which have been incorporated in civil engineering commercial and research codes. These software packages (commercial and research), are based on Finite Element Method (FEM), in order to numerically discretize the mathematical models that are used for the simulation of their structural behavior. Through the use of this numerical method, the stress state and deformed shape of any given structure can be computed, providing the analyst with the ability of assessing the structural behavior for any given load combination.

Following the discovery and dissemination of the Finite Element Method by its known "forefathers": Argyris J. H.[1], Clough R. W.[2], Turner M. J.[3] και Zienkiewicz O. C.[4], which are mentioned alphabetically in order to avoid establishing any sense of priority amongst them, the use of the FEM for the development of research and commercial software, in order to solve any type of physical problem which is governed by partial differential equations, becomes a necessity. Given the long term involvement of the author's supervisor research team with this numerical method, it was chosen as the main tool for the development of an enhanced software package which to be used for the large-scale numerical implementations presented in this research work.

Despite the fact that civil engineering software packages have increased in number significantly, the need of a software package that will be able to predict, with an acceptable accuracy, the realistic nonlinear behavior of reinforced concrete structures, in an affordable computational time and with numerical stability, computational efficiency and robustness, is still a task that has not been fully accomplished. This is due to the fact that software developers (especially commercial software companies) use simple finite element formulations for the analysis of reinforced concrete structures that provide numerical robustness during the analysis procedure without the requirement for advanced numerical simulations to cope with the nonlinear behavior under static and dynamic loading. On the other hand, existing software that uses complex or advanced numerical models for the analysis of the nonlinear response of reinforced concrete structures, faces serious problems regarding the numerical robustness and computational efficiency even for relatively small-scale models. This is the main reason which hindered 3D detailed models from being used in the design procedure of full-scale structures.

According to the author's experience, the three main problems that the analysts encounter when using the available commercial civil engineering software, in order to realistically predict the behavior of reinforced concrete structures, are the following:

i. The lack of objectivity in the numerical results,
ii. The lack of numerical stability and robustness during the nonlinear analysis procedure
iii. The excessive computational demand required for the nonlinear solution of large-scale detailed models.

The first problem derives from the fact that most finite element analysis software (mainly commercial packages) use structural type finite elements (beam-column and shell elements) to analyze elastically the behavior of reinforced concrete (RC) structures. This type of modeling does not account for nonlinear material features that affect the overall behavior, thus the predicted structural response deviates from reality. The use of such models has been adopted in many software packages used by civil engineers all over the world. On the other hand, software that incorporate detailed models for the three-dimensional analysis of RC structures are hampered by numerical problems mainly attributed to the numerical complexity and the excessive computational demand of these models. These numerical phenomena inhibit the designers from using this type of modeling in the analysis of full-scale structures and restrict their application to structural members or small parts of RC structures.

Taking into account the above numerical problems and given the modern needs of civil engineers, the main task of the research work conducted in this Dissertation is the development of a software which will alleviate most of the difficulties described above, in order to predict the nonlinear behavior of full-scale RC structures with the use of widely available CPU systems. The accomplishment of such a task requires the development of the necessary tools in order to analyze RC structures with an acceptable accuracy but at the same time with computational robustness and efficiency. In order to make this task feasible, the main drawbacks when implementing 3D detailed models has to be deled with thus making this kind of modeling approach practical even when addressing the seismic nonlinear response of full-scale RC structures.

Introduction

I. General

The realistic prediction of the nonlinear behavior of RC structures has been the subject of intensive research by many researchers thus numerous methods can be found in the literature that describe several numerical and theoretical approaches for the 3D detailed nonlinear modeling of RC structures. Nevertheless, the use of 3D detailed nonlinear analysis for assessing the structural response of real RC structures still remains a numerically and computationally complicated task. Since the present needs of the civil engineering profession require tools that will provide the designer with numerical "confidence" and "reliability" during the simulation procedure, these numerically cumbersome methods are considered to be in a developmental stage thus are not as widely used as they should be. The incremental static nonlinear analysis, also called push over analysis, is used in several cases for the seismic assessment of RC structures but the finite elements that are used for modeling the structural members are beam-column or shell elements with a number of limitations in capturing the realistic nonlinear response of RC structures.

When a civil engineer is called to design seismically resistant structures following the current code provisions (EC8, EAK etc.), the use of a commercial civil engineering software is the only choice available. These software tools attempt to predict the overall nonlinear behavior of the structure when it is excited by a strong seismic wave (design earthquake) by performing linear analyses with simplified finite element formulations and by following the semi-empirical building design codes.

Many researchers have realized the presence of the above problems and have attempted to overcome these difficulties through the development of reliable software. During the last two decades, serious attempts were made, through the development of several finite element analysis (FEA) software that use nonlinear models and solution processes, by a number of research and commercial software development teams. The better-known research software packages are the following:

a) OpenSees (http://opensees.berkeley.edu),
b) Fedeas (http://www.ce.berkeley.edu/~filippou/Research/fedeas.htm),
c) Feap (http://www.ce.berkeley.edu/projects/feap/),
d) Zeus NL (http://www.ideals.illinois.edu/handle/2142/9271),
e) BEFE-Concrete (G. Beer[5], integrated by H. Hartl[6])
f) FINEL (Hitchings[7], integrated by M.D. Kotsovos & M.N. Pavlovic[8])
g) FE77 (integrated by G. Lykidis[9]).
h) ANSR (Maison, Bruce F., http://nisee.berkeley.edu/elibrary/getpkg?id=PCANSR)
i) ReConAn Academic (G. Markou, http://users.ntua.gr/markgeo)

At international level numerous commercial software packages were developed the last decade which incorporate different types of finite elements and material constitutive models. Nonetheless, only a few incorporate nonlinear constitutive models which account for cracking and 3D stress-strain states, albeit they have limitations when addressing full-scale RC structure simulations. The most widely used commercial software packages are the following:

a) ATENA (http://www.Červenka.cz/),
b) TNO DIANA (http://tnodiana.com/),
c) ABAQUS (http://www.simulia.com/products/abaqus_fea.html),
d) ANSYS (http://www.ansys.com/),
e) FEMAP with NXNastran (http://www.plm.automation.siemens.com/en_us/products/velocity/femap/femap.shtml),
f) ADINA (http://www.adina.com/index.shtml),
g) GT STRUDL (http://www.gtstrudl.gatech.edu/)
h) SAP2000 – ETABS (http://www.csiberkeley.com/),
i) STAAD Pro (http://www.bentley.com/en-US/Products/STAAD.Pro/).
j) LS-DYNA (http://www.lstc.com/lsdyna.htm)
k) SEISMOSTRUCT (http://www.seismosoft.com/en/HomePage.aspx)

Considering that the above list of software represents a small portion of the available finite element packages, since the list becomes much larger when accounting for the more general finite element oriented software codes, it is indisputable that the finite element method is the most frequently used numerical method worldwide when dealing with the prediction of a large number of physical phenomena. A second observation which derives from the above presentation is that, regardless of the development of powerful analysis software tools from several software development teams, there is no software available that is able to predict realistically the nonlinear behavior of full-scale RC structures with the use of standard CPU systems.

Based on personal experience of the author, in order for civil engineering software to be able to provide the user with the ability to analyze and design RC structures with the use of advanced numerical methods and sophisticated material constitutive models, it has to combine the following features:

i. Reliable numerical results through the use of advanced FE modeling.
ii. Incorporation of advanced material models that take into account basic material characteristics that control their nonlinear response. In addition to that, the corresponding material models should preferably be described through a small number of material parameters (i.e. compressive strength, steel yielding stress).
iii. Automation of the modeling and discretization procedure.
iv. Automation of the nonlinear solution procedure (i.e. Newton-Raphson load steps).
v. Numerical robustness and computational efficiency.

It is indisputable that the automation tools provided by a software code during the pre-processing phase of the creation of a model, the analysis procedure and the post-processing

phase of presenting the results, characterizes the software commercial advantages (1. Portability 2. Parallel processing 3. Inter-operability with other software 4. Error checking 5. Regularity etc.). The expression "user friendly" derives from the above software features, which play a significant role in decreasing and mainly controlling potential user-induced mistakes. This was, and still is, the reason why software companies invest most of their resources in the development of high quality pre- and post-processing environments. The previously described restrictions when dealing with numerically cumbersome methods, is the reason why the development of 3D detailed FE models addressing the design procedure of RC structures is limited compared to other FE models.

In an effort to overcome the above diachronic problems, the main task of this Dissertation is an attempt to prove that it is feasible to use advanced nonlinear numerical methods combined with sophisticated material modeling for the seismic assessment of full-scale RC structures through advanced programming techniques and development of state-of-the-art modeling methods. In addition to that, this task will require the creation of a software package which will overcome the five limiting features described above and, through the use of standard CPU systems, to predict within an acceptable computational time the nonlinear response of full-scale RC buildings. By fulfilling such a task, the design of safer structures will be accomplished avoiding potential failures which may derive from the use of simplified models for the design procedure of RC buildings (Fig. I.1). Moreover the validity of the numerous code provisions regarding the design of earthquake resistant RC structures can be assessed.

(A) (B)

FIGURE I.1 RC FAILURES DUE TO EARTHQUAKES. (A) FAILURE OF COLUMN, DUE TO SHORT COLUMN EFFECT, OF A 5-STOREY BUILDING IN ANO LIOSIA, WHICH WAS BUILT IN 1997 ACCORDING TO THE NEW GREEK SEISMIC CODE AND (B) BRIDGE COLLAPSE AFTER THE KOBE EARTHQUAKE IN JAPAN 1995.

For the accomplishment of the above task, an extensive literature investigation on 3D concrete material constitutive models was conducted, in order to choose the most feasible and accurate modeling techniques, and advanced numerical methods for the modeling and analysis of RC structures. In addition to that, an object-oriented software code was developed which incorporates the above features in an attempt to accommodate the numerical methods used for the 3D detailed analysis of RC structures. The *ReConAn* FEA software (Reinforced Concrete Analysis) was developed from scratch during this Dissertation so as to provide a controlled programming environment that is based on a unified programming technique. *ReConAn* FEA software is a sophisticated numerical tool which provides the user with the ability of advanced

finite element (FE) analysis options combining different types of finite elements and material models for an accurate, numerically robust and computationally efficient prediction of the nonlinear response of RC structures.

II. Dissertation Objectives

Modeling of RC structures with beam-column type finite elements was proven to be insufficient and inaccurate, especially when dealing with shear dominated structural members and structures with complex geometries. Nevertheless, this type of finite element is used widely for the analysis and design of RC structures due to its computational efficiency which is attributed to the resulting reduced-size numerical finite element models. Based on these limitations, an extensive literature survey was conducted, with the intention to allocate the most promising beam-column FE formulation for modeling RC structures. It was concluded that one of the most numerically advanced beam FE type was the Natural Beam-Column Flexibility-Based (NBCFB) element, which was incorporated in *ReConAn* software code following an extensive parametric investigation regarding its nonlinear numerical behavior.

The second objective of this Dissertation was the literature investigation of 2D and 3D nonlinear modeling methods for RC structures with the purpose of acquiring a general idea about the trends on more sophisticated FE models. Furthermore, the selection of the numerically most promising 3D modeling method was a primary objective, in order to develop a sophisticated software tool capable of predicting the nonlinear response of full-scale RC structures in an acceptable computational time. After this literature review, it was concluded that the existing three-dimensional modeling techniques exhibit a number of limitations for capturing the nonlinear behavior of RC structures and that the corresponding software with sophisticated models for the simulation of nonlinear phenomena, such as cracking and detailed rebar modeling, are very sparse. This is attributed to the numerical restrictions and difficulties described above, whereas the required CPU resources become excessive when dealing with such numerical models even for the case of small-scale FE models.

It is well known that the analysis of multistory RC buildings is performed through the use of beam-column elements which allow fast simulation times without serious numerical instabilities. In order to be able to analyze this type of structures with three-dimensional constitutive material models incorporated into 3D finite elements and the use of standard CPU systems, the availability of a powerful software tool is not enough. This constraint derives from the fact that CPU processors are bounded from an upper limit which is determined from the hardware itself. Processing power was not and will never be enough since the demand for the solution of larger numerical models constantly increases. In general, this is attributed to the necessity of large-scale simulations with detailed models for the purpose of capturing, as realistically as possible, the nonlinear behavior of structural systems. Therefore, the third objective of this Dissertation was to determine numerical techniques which will overcome these limitations when dealing with full-scale RC structures. A well-known approach that is used widely in computational mechanics is the use of parallel solvers which in this case will become a subject of future work. A second approach for overcoming this numerical restriction is to use

models which combine different types of FE models and which will be called "hybrid models". This type of modeling assumes that shear dominated structural members with an expected highly nonlinear behavior are modeled with 3D detailed finite elements and the rest of the structure is modeled with simpler beam-column finite elements. This technique leads to a reduction in the complexity of the model and of the required computational demand for the solution of the discretized model, retaining at the same time an acceptable accuracy during the analysis procedure.

Finally, the last objective of this research work, was the development of an object-oriented FEA code, capable of easily incorporating advanced numerical techniques and modeling methods for the analysis of RC structures. In addition, it will have the ability to incorporate easily future work and simulation enhancements, which will result into a more general FEA code that will provide the ability of realistic and reliable predictions of the nonlinear response of any type of structure. For the purpose of developing an extendable and sustainable program code, modern programming techniques are used and new numerical methods are developed to create the necessary program structure which will incorporate these state of-the-art features. It is the author's personal opinion that this task is of great importance, especially when dealing with the solution of computationally complex numerical problems.

III. Layout of the Thesis

Each Chapter is constructed through a specific format which can be considered as self-contained from the rest of the Thesis, but is indirectly connected with the other Chapters through the general objective that characterizes this work.

The content of each Chapter is described as follows:

Chapter 1: In this Chapter a literature survey on several beam like element models that are used for the RC structure simulation are presented, along with several nonlinear solution techniques.

Chapter 2: The second Chapter deals with the theoretical and numerical aspects of the NBCFB element where the numerical investigation of its nonlinear behavior is performed. In addition, the computational robustness and efficiency between *ReConAn* FEA and OpenSees is presented.

Chapter 3: In the third Chapter a literature survey of 2D and 3D available nonlinear concrete material models is presented and subsequently, the selected constitutive material model for concrete is presented. The smeared crack approach is discussed in detail, since it is the approach adopted for modeling crack formation and propagation, as well as the modifications proposed for the numerically improved concrete material model.

Chapter 4: The fourth Chapter presents the proposed mesh generation method for the case of the allocation of the embedded rebar elements (reinforcement of concrete) inside hexahedral concrete elements. As it will be illustrated, the proposed method

allows the arbitrary positioning of rebar elements inside the concrete volume and moreover can be applied in large-scale models with many thousands of rebar elements.

Chapter 5: In this Chapter the proposed modeling method for RC structures is presented. The concrete domain is modeled with 8-nodded hexahedral elements which treat cracking with the smeared crack approach and the reinforcement is considered to be embedded and modeled with the proposed embedded beam element. An extended parametric investigation is presented of the numerical behavior of the proposed modeling method. The accuracy of the resulting output data are correlated between existing experimental data. The computational performance of the developed code is compared with the commercial code ATENA, which is considered one of the most widely accepted software packages for RC structures incorporating 3D models.

Chapter 6: In this Chapter, the rationale behind the use of hybrid models is explained and the proposed reduction level concept is presented leading to the Hybrid Modeling Method (HYMOD) which is tested through several numerical tests.

Chapter 7: This Chapter describes the basic programming features of *ReConAn* FEA and discusses some automation issues which are required in order to make the use of 3D geometrically complex models more "user friendly".

Chapter 8: The final conclusions derived from this research work are presented in this Chapter and the proposed future work is discussed.

Chapter 1 Modeling of RC Structures with Beam Elements

Contents of Chapter 1

1.1 The Finite Element Method

The FEM is the most widely used numerical technique for the modeling of structures. Many scientists tried to present their own version about the creation of the method, involving Egyptian mathematicians as well as Archimedes and other great scientists as inspirers of the method. It is the authors' belief that the method evolved with time reaching its final form when the CPU systems began to mark their appearance, thus numerical methods that were used prior to the generation of computer systems using some concepts of FEM cannot be baptized as FEM as it is known in its current form. It has to be made clear that FEM is a worthless numerical technique without the existence of CPU systems. Therefore, a substantial acknowledge has to be attributed to those who have contributed to the evolution of CPU systems and of course the scientists and engineers that, through their work, managed to evolve and make this method one of the most important discoveries of the 20th century in engineering science.

Mathematically speaking, FEM involves the approximate solution of partial differential equations (PDE) as well as of integral equations. The solution approach is based either on eliminating the differential equation completely, or rendering the PDE into an approximating system of ordinary differential equations, which are then numerically integrated using standard techniques such as the Euler's method, Gauss, Runge-Kutta, etc. The FEM is the most appropriate choice for solving partial differential equations over complicated domains (like civil engineering structures, airplanes, cars, ships, oil pipelines, fluid flow, weather pattern on Earth, etc.). It's worth mentioning that one of the characteristics that gave the main impulse for its vast development is that symmetric matrices are produced when applying this numerical technique, making its numerical implementation through programming, much easier. This numerical characteristic gave also the ability of using several solution algorithms that can be applied only when the system of equations is symmetric, thus saving substantial computational effort during the analysis process.

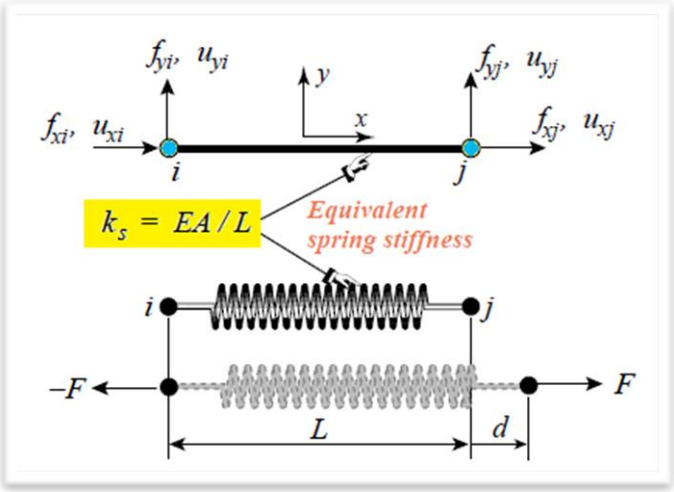

FIGURE 1.1 TWO DIMENSIONAL TRUSS FINITE ELEMENTS.

When modeling 3D structures, the simplest finite element that can be used is the truss element which consists of 2 nodes. The truss element actually acts as a spring that can only be compressed or tensioned and in 3D space it has 3 degrees of freedom (dof) per node. Fig. 1.1

illustrates the 2D formulation, which can easily be integrated to the 3D formulation by introducing an additional dof per node along the z direction.

A more complex rod element is the Euler-Bernoulli beam element (Fig. 1.2b), which also consists of two nodes and has 6 dof per node (three translational and three rotational along the *X*, *Y* and *Z* axis). Mathematically, the main difference of beams with respect to trusses is the increased order of continuity required for the assumed displacement functions. These functions must be continuous and possess continuous first derivatives along the longitudinal direction. To meet this requirement both deflections and slopes must be compatible at nodal points.

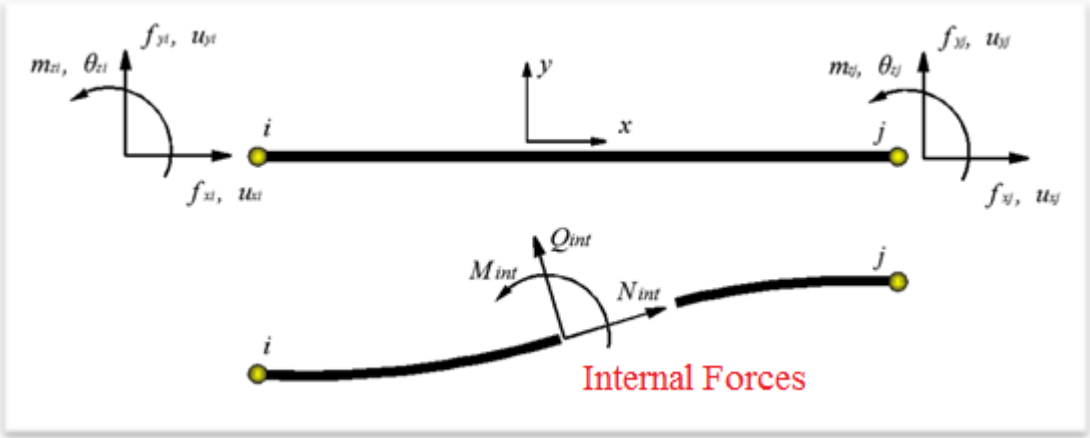

(A)

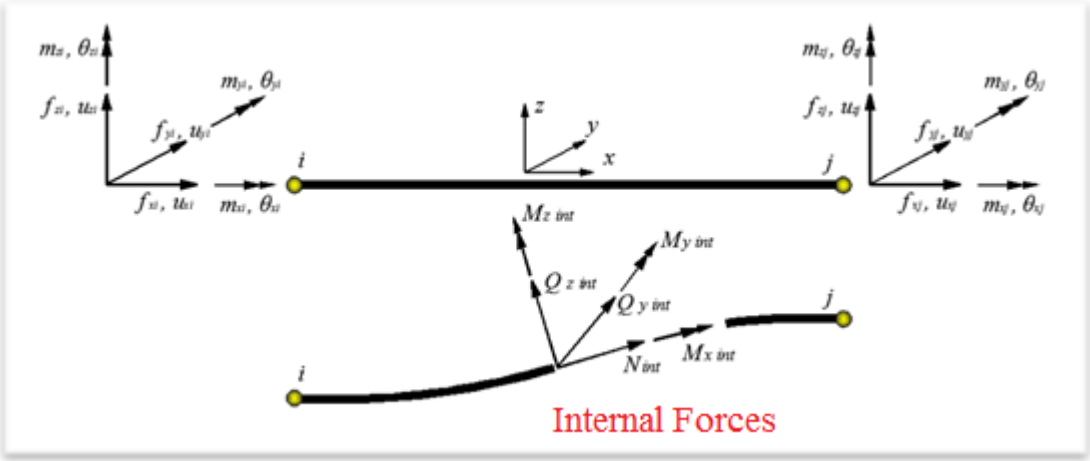

(B)

FIGURE 1.2 DOF AND FORCES OF THE (A) TWO AND (B) THREE DIMENSIONAL BEAM FINITE ELEMENTS.

By far the most popular FE for modeling RC structures is the beam element which takes into account the axial, the bending, torsional and the shear forces providing the ability of modeling structural members whose main deformation is flexure-dominated. What made this element so popular for modeling RC structural members was the simplicity of its formulation providing the engineering software developers with a "computationally light" numerical tool that was also able to capture some of the main characteristics of any beam-like RC structural member, especially when the structure was assumed to behave elastically. The element stiffness matrix is

assumed to be constant throughout the solution procedure thus the stiffness matrix of Eq. 1.1 remains fixed since the material nonlinearities are neglected.

$$\boldsymbol{K} = \begin{bmatrix}
\frac{EA}{l} & & & & & & & & & & & \\
0 & \frac{12EI_{zz}}{l^3} & & & & & & & & & & \\
0 & 0 & \frac{12EI_{yy}}{l^3} & & & & & & & & & \\
0 & 0 & 0 & \frac{GJ}{l} & & & & & & & & \\
0 & 0 & -\frac{6EI_{yy}}{l^2} & 0 & \frac{4EI_{yy}}{l} & & & & & & & \\
0 & \frac{6EI_{zz}}{l^2} & 0 & 0 & 0 & \frac{4EI_{zz}}{l} & & & & & & \\
-\frac{EA}{l} & 0 & 0 & 0 & 0 & 0 & \frac{EA}{l} & & & & & \\
0 & -\frac{12EI_{zz}}{l^3} & 0 & 0 & 0 & -\frac{6EI_{zz}}{l^2} & 0 & \frac{12EI_{zz}}{l^3} & & & & \\
0 & 0 & -\frac{12EI_{yy}}{l^3} & 0 & -\frac{6EI_{yy}}{l^2} & 0 & 0 & 0 & \frac{12EI_{yy}}{l^3} & & & \\
0 & 0 & 0 & -\frac{GJ}{l} & 0 & 0 & 0 & 0 & 0 & \frac{GJ}{l} & & \\
0 & 0 & -\frac{6EI_{yy}}{l^2} & 0 & \frac{2EI_{yy}}{l} & 0 & 0 & 0 & \frac{6EI_{yy}}{l^2} & 0 & \frac{4EI_{yy}}{l} & \\
0 & \frac{6EI_{zz}}{l^2} & 0 & 0 & 0 & \frac{2EI_{zz}}{l} & 0 & -\frac{6EI_{zz}}{l^2} & 0 & 0 & 0 & \frac{4EI_{zz}}{l}
\end{bmatrix} \quad \text{symmetric} \qquad 1.1$$

where A, E,G, I, J and l are the area of the section, modulus of elasticity, shear modulus, moment of inertia, torsional moment of inertia and the length of the beam, respectively.

In RC frame structures designed according to current specifications of earthquake resistant design, forces and displacements induced by earthquakes are expected to exceed those assumed by the design equivalent static lateral loads specified by the codes. When these structures are subjected to severe earthquake excitations, they are expected to enter the inelastic range and dissipate the large seismic energy input into the structure through large but controllable inelastic deformations at critical regions. In order to predict the distribution of forces and deformations in these structures under the maximum possible earthquake that can occur at the site, accurate models of the nonlinear behavior of the structural elements are necessary, thus the elastic response assumption does not apply.

A basic assumption adopted by the design codes for the design of structures is the transformation of the earthquake excitation inertial loads into equivalent static lateral loads. Therefore, it is expected that during a severe earthquake excitation the forces and displacements of the structures will exceed those produced by the equivalent static lateral loads which are prescribed by codes, due to the dissipation of the seismic energy through large but controllable inelastic deformations at structural regions that are assumed as critical (joints, shear walls, short

columns etc.). Thus, the prediction of the distribution of forces and deformations in RC structures under earthquake excitations requires arithmetically accurate models of the nonlinear behavior of the critical regions of the structure.

In the following, a historical representation of previous work will be described, regarding the different attempts presented in the literature in order to create a nonlinear beam element that will incorporate the necessary properties for the nonlinear analysis of RC structures.

1.2 Review of Nonlinear Beam Element Models

Many models were presented the last fifty years for the prediction of the inelastic response of RC elements subjected to large displacements. The majority of these models incorporate information from experimental investigations and on-field observations of the hysteretic behavior of RC structural members, ranging from the simple two-component models with bilinear hysteretic laws to refined fiber or layer models based on more accurate descriptions of the cyclic stress-strain behavior of concrete and reinforcing steel. Some of the presented models take also into account shear strain through the Timoshenko beam theory and relatively advanced material models, as it is going to be presented through this literature overview.

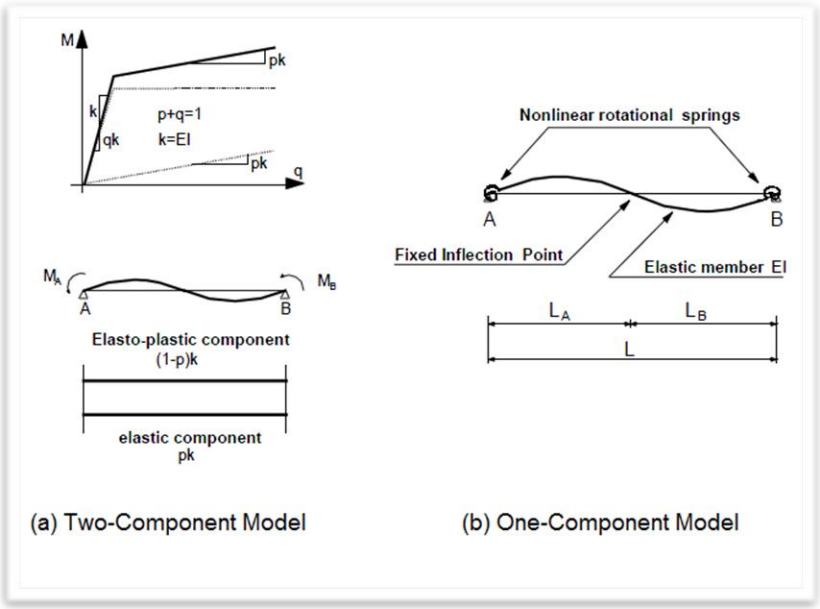

FIGURE 1.3 SIMPLE LUMPED PLASTICITY MODELS. (A) THE CLOUGH & JOHNSON MODEL AND (B) THE GIBERSON MODEL.

The very first inelastic girder model was proposed by Clough et al.[10]. This model consisted of a bilinear elastic-strain hardening moment-curvature relationship, known as the two-component model, which is assumed along the element (Fig. 1.3a). One of the shortcomings of this model is the difficulty of taking into account the stiffness deterioration of RC elements during cyclic load reversals. In addition to that this model is applicable only to flexure-dominated structural members. To overcome the problem of stiffness deterioration Giberson[11] proposed another model in 1967 known as the one-component model (Fig. 1.3b). This model consists of two nonlinear rotational springs which are attached at the ends of a perfectly elastic element. The

elemental nonlinear deformations are lumped in these two rotational springs which endows the model with the advantage that any kind of hysteretic law can be assigned independently to the nonlinear springs.

Otani[12] in 1974 proposed a different approach to the problem of modeling the seismic behavior of RC beams and columns (Fig. 1.4a), by dividing each into two line elements, one linearly elastic and one inelastic, which act in parallel. In addition, an inelastic rotational spring was attached at each end of the element which represented the fixed-end rotation at the beam-column interface due to slip of the reinforcement in the joint. The main disadvantage of this approach was the result of a non-symmetric flexibility matrix, unless one of the following assumptions was made: (a) the inelastic deformations are concentrated at the beam ends, or (b) the contraflexure point is assumed fixed at the midspan of the member. Nevertheless, Otani's study recognizes for the first time the significance of fixed-end rotations in predicting the nonlinear seismic response of RC frame structures.

Mahin and Bertero[13] in 1976, after reviewing the various definitions of ductility factors in earthquake resistant design, pointed out how ductility factors for a beam represented by a two-component model must be modified to match those for a beam in which inelastic deformations spread along the member. In 1977, Anderson and Townsend[14] studied the effect of different hysteretic models on the nonlinear response of RC frames by implementing four different models. The study showed that the degradation of the stiffness played a significant role in the interstory displacements, a numerical phenomenon that affects significantly the P-δ effect.

Soleimani[15] in 1979, introduced the first model which accounts for the spread of inelastic deformations into the element. An inelastic deformation zone was assumed that gradually enters the nonlinear range through the beam-column interface into the element as a function of loading history. It is assumed that the rest of the element behaves elastically throughout the loading history. Furthermore, the fixed-end rotations at the beam-column interface are modeled through point hinges which are placed at the ends of the element. The connection between the point hinges and the curvature at the corresponding end section is implemented through an effective intervention length factor which remains constant during the entire loading history.

The effect of axial force on the flexural stiffness of a member was first taken into account in the model presented by Takayanagi and Schnobrich[16] in 1979 (Fig. 1.4b). Their study was focused on the seismic response of coupled wall systems where the walls and coupling beams were represented by one-dimensional beam elements. Otani's model was selected for modeling the coupling beams where the effect of shear in the coupling beams was also taken into account. The pinching effect was pointed out for during reloading as well as the strength degradation due to loss of shear resistance after cracking initiation and yielding of the reinforcement.

Emori and Schnobrich[17] studied in 1981, the seismic response of a plane frame coupled with a shear wall where they conducted nonlinear static analyses under cyclic loading and compared their results by using three different beam models. The first model was identical to Otani's[12] model, the second was an element composed of several springs acting in series and interconnected by rigid links and the third model, which was a modification of the concentrated spring model, was based on a layered element. The layered approach was applied at a length L_p

at the ends of the beam and was set equal to the length of the region where major inelastic action was expected. The authors concluded that if a detailed study of the nonlinear response of plastic regions in columns was desired, the layer model is the most appropriate choice.

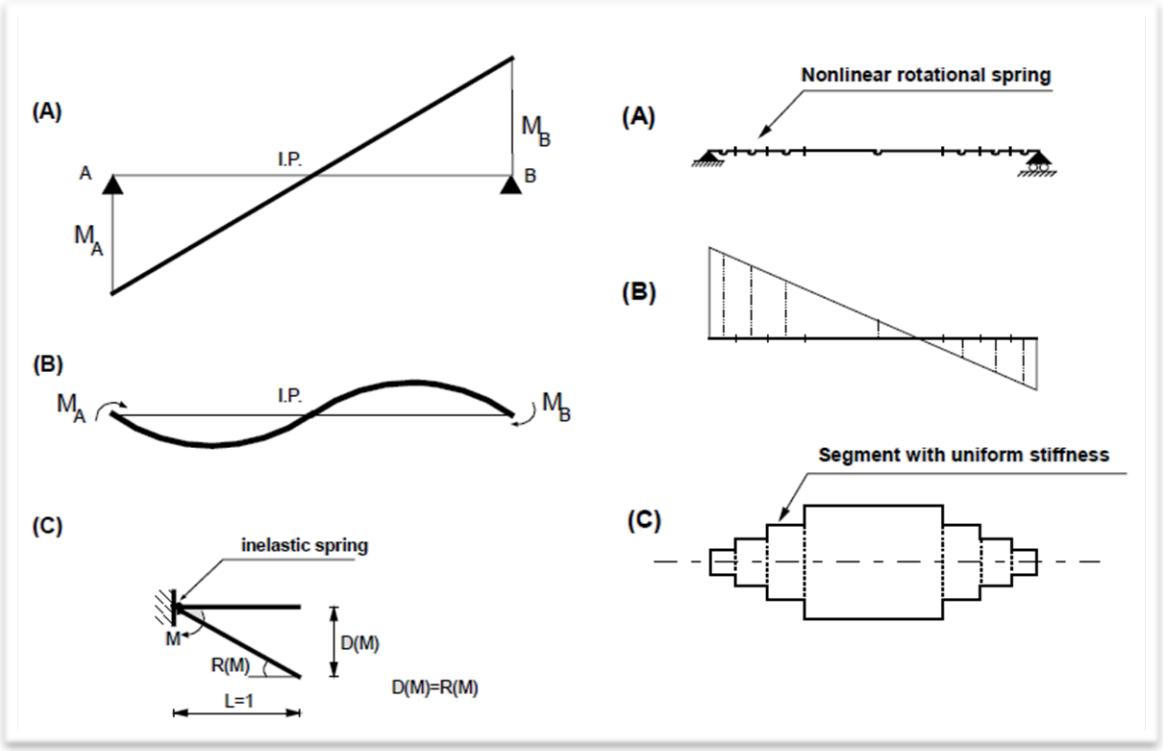

(A) (B)

FIGURE 1.4 MODELS PROPOSED BY (A) OTANI[12] AND (B) TAKAYANAGI AND SCHNOBRICH[16].

Another researcher that investigated the applicability of point hinge models in studying the seismic response of structures was Anagnostopoulos[18]. His study, which was published in 1981, was mainly focused on flexural members subjected to end moments and uniformly distributed gravity loads. Through this investigation, it was concluded that a section hinge model is incapable of reproducing the gradual degradation of stiffness of a member in the post-yielding range. It was also proven that setting the strain hardening ratio equal to the ratio of the moment-curvature relation is incorrect, since this underestimates the post-yield stiffness of flexural members. This study proposed an iterative solution for determining the strain-hardening ratio of the moment-rotation relation of section hinge models.

Banon et al.[19] proposed another model for the analysis of seismic response of RC structures which combined nonlinear rotational springs at the ends of the element with the hysteretic moment-rotation relation based on a modified Takeda[20] model. Moreover, several damage indicators were proposed in order to quantify the performance of a structure during an earthquake. The main conclusions were that the one-component model is sufficiently accurate in modeling the inelastic response of RC members subjected to severe deformation reversals and that the model could predict the damage of RC members.

Park and Ang[21] in 1985 proposed a model where damage was expressed as a linear function of the maximum deformation and the hysteretic energy absorbed during cyclic load reversals. The same year, in their study of plane rectangular frames and coupled shear walls, Keshavarzian and

Schnobrich[22] extended the spread plasticity model proposed by Soleimani[15] to column elements. For the determination of the strength and stiffness of the column element, the interaction between bending moment and axial force was considered. Their numerical implementations showed that the one-component model is suitable and accurate enough for describing the inelastic behavior of RC beams and columns yielding similar results with the two-component model. It was also stated that the layered model was found to be computationally expensive.

It is well known that the main limitation of layered or fiber elements is that they are incapable of simulating the nonlinear response of structural members that undergo high shear deformations. One of the early attempts to overcome this limitation was that of Vecchio and Collins[23] in 1986 who proposed a model with a dual-section analysis procedure discretizing the element into layers where iterations are performed for each layer until the internal equilibrium between adjacent sections is satisfied. Nevertheless, the proposed method was applied only for 2D cases. Another similar attempt was introduced by Ozcebe and Saatcioglu[24] in 1989. This model was based on the experimentally observed stiffness degradation and the associated pinching of hysteretic loops proposing empirically derived expressions that account for the effect of axial load on the hysteretic behavior.

In the 1987 study of Roufaiel and Meyer[25] an extension of the spread plasticity model developed earlier by Meyer et al.[26] (1983) was proposed. This new model, took into account the effect of shear and axial forces on the flexural hysteretic behavior modulated on a set of empirical rules. The same year, Pantazopoulou[27] proposed a formulation for the prediction of the behavior of T beams.

After this extensive investigation and research work with the use of displacement-based finite elements, researchers began to show a great interest at the force (flexibility) method of analysis for the formulation of beam finite elements. The Beam-Column Flexibility-Based Beam element is known for its numerical robustness due to its nonlinear internal state determination procedure which assures that the internal forces equilibrate with the nodal displacements. Mahasuverachai and Powell[28] (1982), Kaba and Mahin[29] (1984), Zeris[30] (1986), Zeris and Mahin[31, 32] (1988, 1991) suggested different formulations and identified the advantages of the force method in the formulation of nonlinear frame elements. The latter introduced material softening in the solution procedure.

Spacone et al.[33-35] presented a beam element for seismic damage analysis which was integrated with the flexibility-based formulation where interpolation of both displacement and force fields was applied and an iterative nonlinear algorithm was implemented for the determination of the resisting forces during the element state determination. The element was integrated with the fiber approach and material models that accounted the pinching phenomenon and stiffness degradation due to cycling loading. The effects of shear and bond-slip were neglected. These studies proved that the flexibility-based formulation utilizes the beam-column element with numerical robustness and computational efficiency. It was also concluded that the comparisons between the results of the proposed model and experimental data were in a good agreement for cases that had average damage of flexural form. This was attributed to the inability of the model

to account for shear deformations. It is imperative to note, that this research work gave the flexibility-based method the required momentum in order to be recognized and used by many researchers, including the author of this Dissertation .

Petrangeli and Ciampi[36] (1997), Petrangeli et al.[37] (1999) and Petrangeli[38] (1999) presented a flexibility-based, fiber element which incorporated through its formulation, shear deformations. The element basic concept was to model the shear mechanism at each concrete fiber of the cross sections, assuming the strain field of the section as given by the superposition of the classical plane section hypothesis for the longitudinal strain field with a predetermined distribution over the cross section for the shear strain field. Transverse strains are determined by imposing the equilibrium between the concrete and the transverse steel reinforcement. As the authors mention, the resulting model, although computationally more demanding than the conventional fiber element, has proved to be very efficient in the analysis of shear sensitive RC structures under cyclic loading where the full 2D and 3D models are too time-consuming.

Mohammad and Spacone[39] presented in 2001, two general formulations of one-dimensional structural elements with deformable interfaces. The interface accounted for the bond-slip between the elemental components. The first formulation was the classical displacement-based formulation and the second one used the flexibility-based approach. The two formulations were derived from the equilibrium and compatibility differential equations of the problem and a special force recovery procedure, based on residual deformations, was presented for the second formulation. The numerical tests selected for illustrating the performance of the two formulations were a reinforcing bar with bond slip and a steel–concrete composite beam with partial interaction between the steel beam and the concrete slab.

After performing a comparison between different beam formulations[40], Neuenhofer and Filippou[41] (1998) presented a geometrically nonlinear flexibility-based element, which accounted for geometrical nonlinearities. Ayoub and Filippou[42] (1999) presented a mixed formulation for problems that account for bond-slip phenomena in the cases of cyclic loading. Schulz and Filippou[43] (2001) presented a spatial Timoshenko beam element with a total Lagrangian formulation, which was based on curvature interpolation that was independent of the rigid-body motion of the beam element in order to simulate members with hyperelastic materials. The section response derived from plane section kinematics, taking into account nonlinear material behavior. The authors stated that the proposed numerical method exhibited accuracy and superior numerical performance.

Limkatanyu and Spacone[44, 45] (2002) continued the work of Mohammad and Spacone[39] and presented the theory and applications of three different formulations of RC frame elements accounting for bond slip in the reinforcing bars. The first was the displacement-based formulation, derived from the principle of stationary potential energy. The second was the flexibility-based formulation, which was derived from the principle of stationary complementary energy and the third was the two-field mixed formulation, derived from the principle of stationary Hellinger–Reissner potential. The final conclusion of this study was that the flexibility-based element is slightly more precise than the mixed element, but it is numerically less stable.

Battini and Pacoste[46, 47] (2002) presented a 3D co-rotational elastic beam element including warping effects and through its formulation incorporated elasto-plastic deformations. In order to achieve this, it was assumed that the element had seven degrees of freedom at each node. The main purpose of this element was to model elasto-plastic instability problems. The performance of the element was tested through several numerical tests. The same year, Klinkel and Govindjee[48] presented their work using finite strain 3D-material models in beam and shell elements, illustrating the importance of using a three-dimensional formulation in modeling material nonlinearities.

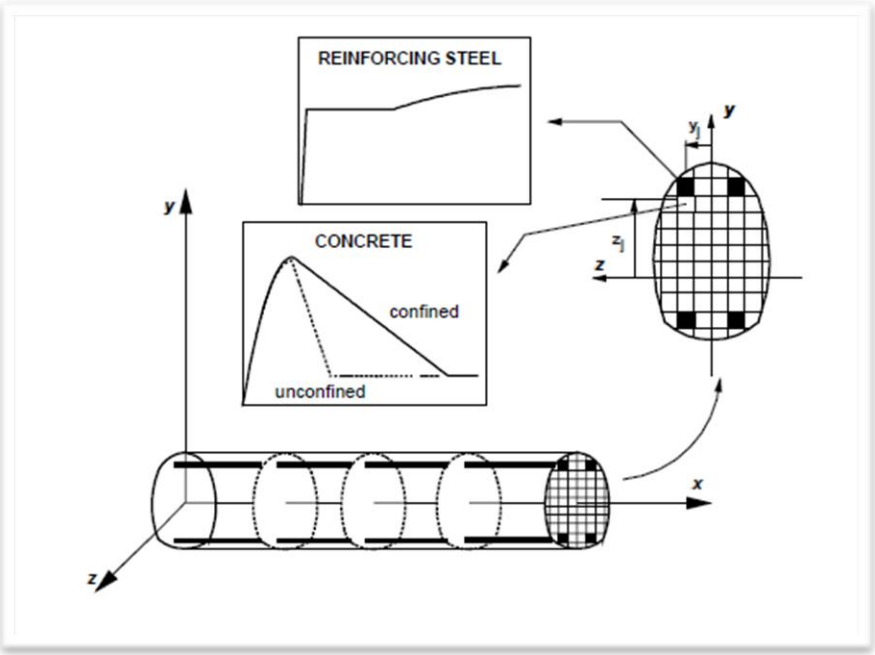

FIGURE 1.5 FIBER ELEMENT. CONTROL SECTIONS AND DISCRETIZATION WITH FIBERS[33].

Klinkel and Govindjee[48] (2002) suggested that, a J_2 three-dimensional plasticity law could be used with the aim of assessing the inelastic response of shear-deformable steel structures and a 3D material law was employed under the assumption of "plane-stress" conditions. The term "plane-stress" in a beam element is loosely adopted to denote a situation where out-of-plane conditions are imposed at the integration points. The verification of the computational efficiency of the proposed element formulation with regard to displacement-based and conventional force-based beam-column elements, was carried out through experimental data available in the literature and numerical results obtained by using detailed discretization with shell finite elements.

Saritas and Filippou[49] (2004) presented a force-based formulation for the seismic assessment of steel structures using a multi-dimensional law, where their study was limited to the two-dimensional case of a single section type and has been numerically examined on simple academic examples.

Papaioannou et al.[50] (2005) presented a fiber flexibility-based beam, which incorporated the natural mode method proposed by Argyris et al.[51]. The numerical results of this study showed that when the flexibility-based method is combined with the natural mode method and the fiber

approach which accounts for material nonlinearities, an elegant formulation is derived which produces numerically efficient and accurate results. This element is also incorporated in *ReConAn* and will be presented in the next Chapter of this Dissertation .

In the research work presented by Mazars et al.[52] in 2006, the solutions for an enhanced multifiber beam element accounting for shear and torsion through the Timoshenko beam theory was investigated. Higher order interpolation functions were used to avoid any shear locking phenomena and the cross section warping kinematics was extended to nonlinear behavior using advanced constitutive laws. The authors reported that the numerical results were in good correlation with corresponding experimental data for T-shaped RC sections.

Marini and Spacone[53] (2006) presented a flexibility-based, shear-deformable beam element where a separate phenomenological constitutive law for the shear component was adopted. This was a simplifying assumption but maintains all the advantages of fiber beam elements in terms of robustness and simplicity of the material laws. Following, Navarro et al.[54] (2007) presented a model for the analysis of reinforced and prestressed concrete frame elements under combined loading conditions, including axial force, biaxial bending, torsion and biaxial shear force. The proposed model was based on the simple kinematic assumptions of the Timoshenko beam theory and was implemented through the FEDEASLab[55], a Matlab-based toolbox developed at the University of California, Berkeley. The control sections of the frame element were subdivided into regions with 1D, 2D and 3D material response. The validity of the model was illustrated through the numerical comparisons to flexure dominated well-known tests.

Another resent attempt to present a flexibility-based beam element with a damage-plastic section constitutive law was that of Addessi and Ciampi[56] (2007). In their work, both displacement-based and flexibility-based approaches were used and compared. With the intension of overcoming the analytical problems and the pathological mesh dependency of the numerical response in the presence of strain-softening post-peak behavior, a classical non-local regularization procedure was adopted. The regularization technique was based on a selected integration procedure along the element length, which predefines the location of the Gauss points in the beam region, where the localization phenomena take place.

Mata et al.[57] (2007) in continuation of the work of Simo and Vu-Quoc[58, 59], presented a beam model for static analysis under nonlinear geometric and material behavior. The displacement-based method was used for the solution of the resulting nonlinear equations and thermodynamically consistent three-dimensional constitutive laws were used for describing the material behavior where the simple mixing rule was applied. For describing the residual strength and the load carrying capacity of the beam element, they proposed a method defining the global damage state of a structure based on a scalar damage index. Through the numerical example conducted in their work on a RC cantilever beam, it was clear that the displacement formulation lacked the robustness and accuracy, requiring the discretization of the structural member with a large number of beam elements.

Ghosh and Roy[60] in 2008, investigated an isoparametric interpolation of total quaternion for geometrically consistent, strain-objective and path-independent finite element solutions of the geometrically exact beam. This interpolation was a variant of the broader class known as slerp.

The interpolation of rotations uses a standard finite element discretization, as adopted by Simo and Vu-Quoc[58].

Fardis[61] (2008) presented a numerical investigation on the nonlinear response of fiber models when used for the nonlinear analysis of RC structures. Moreover he used a phenomenological model which was based on the Otani[12] model to perform dynamic analysis on real RC buildings. The main conclusions of this research work were that the fiber approach was prohibitive for the analysis of real RC structures where their use is adequate as a research tool and the concentrated plasticity models reproduce acceptable results when used for the seismic assessment of real RC buildings.

Papachristidis et al.[62, 63] extended the element presented by Papaioannou et al.[50] incorporating the Klinkel and Govindjee[48] three-dimensional plasticity law to assess the inelastic response of shear-deformable steel and RC structures. The Timoshenko beam theory was incorporated and the interaction between axial, bending and shear behavior was accounted for through their corresponding material models. The numerical results of the proposed model were in a good correlation with experimental data and numerical examples.

Kwak and Kim[64] (2010), proposed a simple analytical procedure to analyze RC beams with a cracked section on the basis of the simplified moment-curvature relations of RC sections. The proposed model also considered fixed-end rotation caused by anchorage and was tested through numerical correlation with experimental data.

Through his paper, Landesmann[65] (2010) presented an application of a computational tool, named SAAFE Program, developed to analyze nonlinear inelastic steel and composite 2D framed structures. The proposed plastic-hinge model was formulated based on three characteristics which controlled the beam stiffness, the residual stresses and the structural member instability. The validity of the proposed formulation was refined through numerical examples and available experimental data. As the author stated, based on the obtained results, the proposed model can be used to perform inelastic analysis for 2D isolated or full frame members, incorporating geometric and material nonlinearity.

Valipour and Foster[66] (2010) presented an element for nonlinear analysis of RC framed structures subjected to torsion, using the flexibility formulation. The interaction between the axial force and bending moment was considered by adopting the Navier-Bernoulli assumption and using the fiber element approach. The torsional dofs were formulated independently and the effect of normal and tangential forces on the torsional stiffness of section was accounted for by modifying the torque-twist curve of a section under pure torsion. The authors conclude by stating that the model requires further development in order to be used for full-scale simulation of RC structures subjected to torsional deformations.

It is very clear that a lot of effort has been devoted to create a robust, efficient, rational and objective beam-column model, which will be able to analyze the three-dimensional nonlinear response of steel and RC framed structures. It is indisputable that none of the above research-works managed to fully succeed in this task and it is the author's belief that, it will be difficult to accomplish such a task in the future, especially when dealing with shear dominated RC

structures. This conclusion derives from the fact that when three-dimensional nonlinear phenomena occur (3D shear stains, cracking, warping, increase of concrete strength due to 3D confinement, etc.), the beam element formulation is incapable of capturing deformations and, therefore, these can only be modeled with the use of 3D finite elements. As it will be presented in Chapter 5, the most accurate and objective numerical way of predicting the nonlinear response of RC structures, is by using detailed simulation with 3D solid finite elements, which account for most of the nonlinear phenomena, through their 3D formulation. It is inevitable that when 3D nonlinear FE models will become computationally efficient and the use of 3D models completely automatic, they will be the optimum numerical tool for the prediction of the inelastic response of RC structures. Until then, beam-column elements will be the main analytical tool for the analysis and design of full-scale RC structures.

Through this literature review, it is easy to conclude that the flexibility-based formulation of beam-column elements appears to be the most accurate and efficient method when large amplitude nonlinearities occur, establishing equilibrium between the internal resisting forces and external nodal deformations. In addition to that, when combined with the fiber approach, it provides a numerical tool which can model with relative accuracy the inelastic response of RC structural members. Given that this numerical method is computationally demanding, the use of the natural mode method is essential for the decrease of the computational cost, as it will be demonstrated in the next Chapter through the presentation of the relevant algorithmic implementation.

1.3 Solution Algorithms for Systems of Nonlinear Equations

One of the most important numerical features of the FEM is that after the stiffness formulation and regardless of the nature of the problem at hand, the system of equations required to be solved has the simple form of

$$K_s \cdot u_s = f_s \tag{1.2}$$

where K_s is the global stiffness matrix of the structure, u_s is the array which contains the unknown nodal displacements and f_s is the corresponding array with the external loads. In addition to that, the stiffness of the structure is always symmetric, which permits the implementation of advanced solution algorithms combined with memory and storage saving programming techniques, optimizing the computational performance during analysis.

It is obvious that, when dealing with nonlinearities, Eq. 1.2 cannot be solved explicitly, requiring iterative solution algorithms like the well-known family of Newton-Raphson type of methods. Early work presented by several researchers[67-71] highlighted the advantages of the Newton-Raphson method for solving nonlinear systems of equations resulting from the finite element method, making it perhaps the best known incremental step method for finding successively better approximations to the roots of a nonlinear set of equations. Many alternative versions of the method were proposed in the literature for handling the incremental steps. Three basic Newton-Raphson (NR) iterative algorithms will be presented in this section: (1) Force-Control, (2) Displacement-Control and (3) Arc-Length.

1.3.1 Force-Control Newton-Raphson

If in the FE formulation, it is assumed that the boundary conditions remain constant during the solution of Eq. 1.2, then the displacements for a given load combination $\Delta t \cdot f_s$ are equal to $\Delta t \cdot u_s$ for a linear static problem. If the structural problem at hand contains nonlinearities (material and/or geometrical) then this is not the case. In order to find the equilibrium state between the internal forces of the structure and the external loads, it is assumed that the applied loads can be expressed as a function of pseudo-time *t*, for static problems, and the equilibrium at each step can be expressed as:

$$F_s^t - R_s^t = 0 \qquad 1.3$$

where $F_s^t$are the externally applied nodal forces of the structure at time *t* and R_s^t are the nodal forces that correspond to the internal stresses of the structure. The relation of Eq. 1.3 expresses the equilibrium of the system in the current deformed geometry accounting for all nonlinearities. It is important to note that, this relation is general and applies also for dynamic problems where the forces due to inertia and damping are included in the F_s^t array.

Therefore, by dividing the external forces into *n* load steps and by using a specific load increment ($\Delta t = {}^1/_n$), the external loads are applied incrementally and at each time step a new load increment is added to the structure external loading. This requires the satisfaction of Eq. 1.3 through the whole loading time history. For the case of static loads, the definition of time is only a convenient variable which specifies different load levels and, correspondingly, different structural configurations.

Assuming that *i* is the current load step of the analysis, then the accepted solution can be stated as

$$u_s^t, \qquad t = i \cdot \Delta t \qquad 1.4$$

therefore, the solution of the next load increment at time $t + \Delta t$ will be

$$u_s^{t+\Delta t} = u_s^t + u_s^{\Delta t}, \qquad \Delta u_s = u_s^{\Delta t}, \qquad t_{i+1} = (i+1) \cdot \Delta t \qquad 1.5$$

For the computation of the unknown displacements at load increment t_{i+1} a prediction of the solution is obtained by using the stiffness matrix of the previous load increment.

$$K_s^t \cdot \Delta u_s^{t+\Delta t} = \Delta f_s^{t+\Delta t} \qquad 1.6$$

The next stage of the nonlinear algorithm is to compute the resisting forces at each node of the structure and assemble the R_s^t array in order to verify if Eq. 1.3 is satisfied. In nonlinear solution algorithms, Eq. 1.3 is never equal to zero thus a convergence criterion is applied which specifies if convergence is achieved. The result of Eq. 1.3 is the vector of the residual forces r_s^j (Eq. 1.8). This vector is used in order to compute the error of the iterative procedure according to the adopted convergence criterion (Eqs. 1.7).

$$e_{er} = \frac{\left\|\Delta u_s^j\right\|}{\left\|u_s^{t+\Delta t}\right\|} \leq e_D \qquad 1.7a$$

$$e_{er} = \frac{\left\|F_s^{t+\Delta t} - R_s^{t+\Delta t}\right\|}{\left\|F_s^{t+\Delta t} - R_s^t\right\|} \leq e_F \qquad 1.7b$$

$$e_{er} = \frac{\Delta u_s^j \| F_s^{t+\Delta t} - R_s^{t+\Delta t} \|}{\Delta u_s^1 \| F_s^{t+\Delta t} - R_s^t \|} \leq e_E \qquad 1.7c$$

$$r_s^j = F_s^{t+\Delta t} - R_s^{t+\Delta t} \qquad 1.8$$

where j is the corresponding internal iteration, e_D is the displacement, e_F is the force and e_E is the energy convergence tolerance criterion, respectively. For each internal iteration j, the stiffness matrix of the structure is updated by using the new material properties which are implemented through the material constitutive matrix $\boldsymbol{C}$ of the finite element formulation. If the numerical problem at hand accounts for geometrical nonlinearities, then the stiffness matrix of the FE model is also affected by the current configuration. The updated global stiffness matrix is known as the tangent stiffness matrix. In the event that the convergence criterion is not satisfied, the residual forces are applied as external forces through Eq. 1.6 and the nonlinear solution algorithm proceeds with the *j+1* internal iteration.

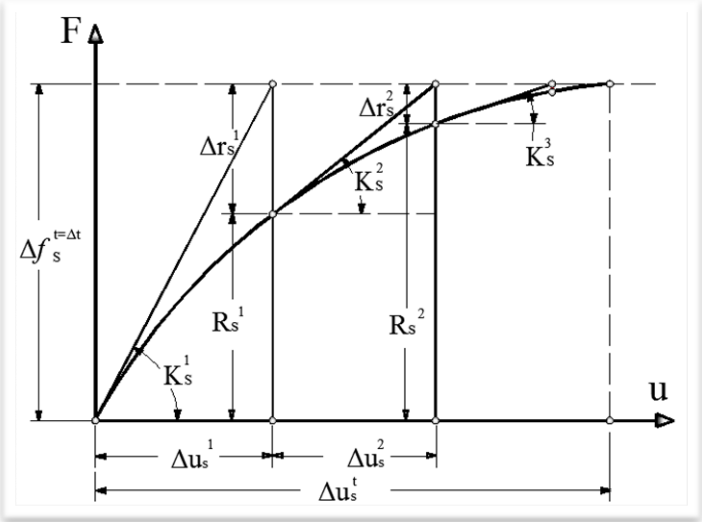

FIGURE 1.6 FULL NEWTON-RAPHSON ITERATIVE SCHEME.

When the global stiffness matrix of the structure is updated for each internal iteration, then we have the full NR scheme (Fig. 1.6). This is computationally demanding with respect to the computational effort required for the factorization and back substitution procedures of the stiffness matrix at each iteration, but at the same time this effort is counter balanced by the increased convergence properties of the method. Most researchers also state that the assemblage of the stiffness matrix is time consuming, a statement that is not verified in this research work. A reduction of the computational cost per iteration may be achieved with alternative NR algorithms like the "Modified" scheme or quasi-Newton scheme, where the stiffness matrix is updated after a specific number of internal iterations or implicitly after each iteration, respectively, during the solution procedure. The disadvantage of these methods is the slow convergence rate for cases with strong nonlinearities requiring larger number of iterations until convergence. This is illustrated in Figs. 1.7a and 1.7b where two NR schemes are presented.

It is worth mentioning that the force-control NR schemes appear to be numerically less stable than the corresponding displacement-control schemes which are presented below. In this work

the full NR scheme with the force-control approach is used, which exhibited numerical robustness and efficiency in the numerical tests considered.

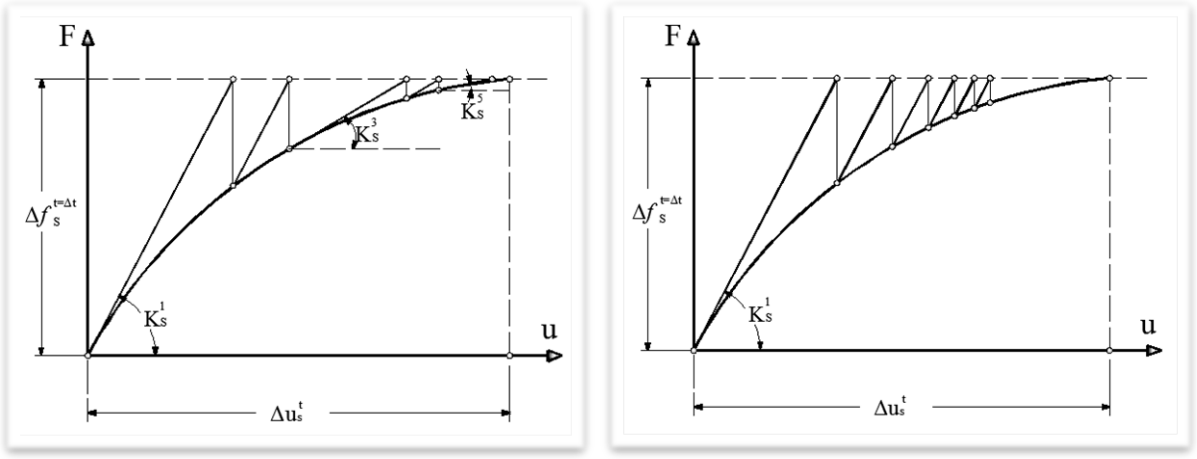

(A) (B)

FIGURE 1.7 (A) MODIFIED NEWTON-RAPHSON AND (B) QUASI-NEWTON SCHEMES. STIFFNESS MATRIX UPDATES EVERY TWO INTERNAL ITERATIONS.

1.3.2 Displacement-Control Newton-Raphson

When the inelastic branch of the *P-δ* curve is descending (Fig. 1.8 case: B) then it is evident that the force-control approach fails to converge regardless the number of internal iterations performed. In Fig. 1.8, two possible unstable branches (A and B) are shown. Branch A is followed by a stable branch until it reaches the equilibrium point P_{eq}, while branch B is an unstable descending branch until failure. In both cases the force-control approach fails to capture the descending branch of the *P-δ* curve. When ultimate load analysis is performed, the main task is to predict the maximum carrying capacity of the structure (ultimate load). In this case the force-control approach still has some difficulties in computing the exact ultimate load.

For the case where one needs to compute the unstable descending branch of a structure during a nonlinear analysis, the displacement-control approach has to be used. This approach, assumes that instead of a load incrementation, a specific displacement is imposed on a structural node and the corresponding nonlinear response of the structure is predicted by computing the internal resisting forces. Solving this kind of problems, the conversion of the Dirichlet problem into an equivalent Neumann through the use of Eqs. 1.9 & 1.10 is required. Fig. 1.9 illustrates the graphical representation of such a transformation for the case of a cantilever beam, which is discretized with three beam elements.

The corresponding equation is transformed as follows:

$$\boldsymbol{u}_S = \begin{Bmatrix} \boldsymbol{u}_U \\ \boldsymbol{u}_I \end{Bmatrix}, \quad \boldsymbol{f}_S = \begin{Bmatrix} \boldsymbol{f}_U \\ \boldsymbol{f}_I \end{Bmatrix} \tag{1.9a}$$

$$\boldsymbol{K}_S = \begin{bmatrix} \boldsymbol{K}_{U,U} & \boldsymbol{K}_{U,I} \\ \boldsymbol{K}_{I,U} & \boldsymbol{K}_{I,I} \end{bmatrix} \text{ therefore,} \tag{1.9b}$$

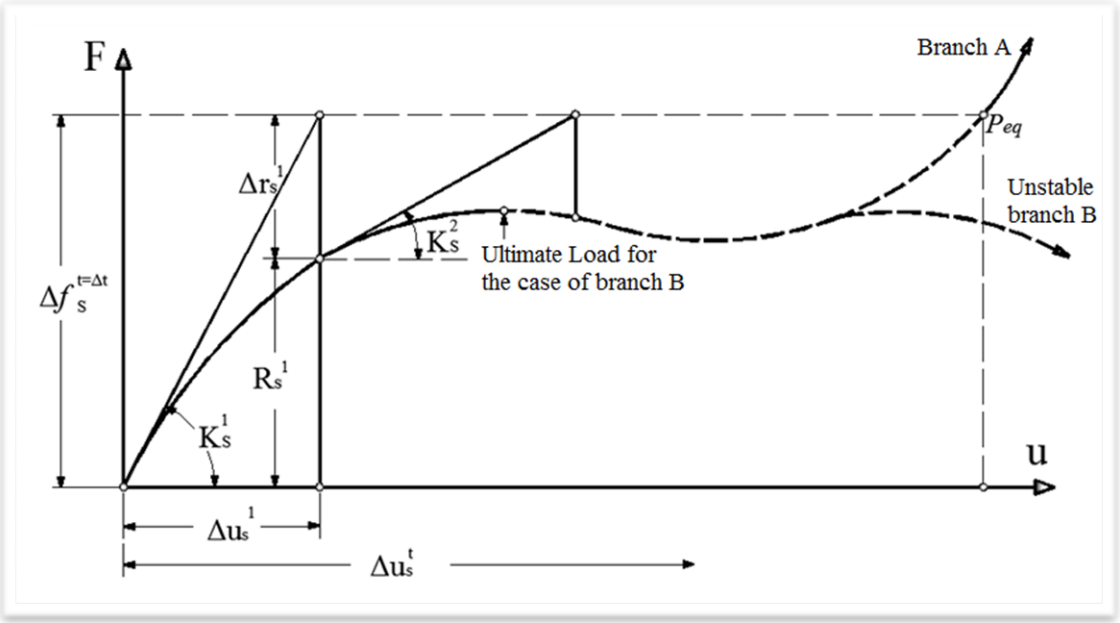

FIGURE 1.8 FORCE-CONTROL NEWTON-RAPHSON. POSSIBLE SOLUTION DIVERGENCE.

Transforming the Dirichlet problem into an equivalent Neumann problem requires the separation of the dof of the unknown displacements ($\boldsymbol{u}_U$) from the dof where the displacements are imposed ($\boldsymbol{u}_I$), rearranging the rows and columns of the displacement, force and stiffness matrices (Eqs. 1.9a-1.9b). After the rearrangement of the dof and with the use of Eq. 1.2, the transformation is carried out where Eq. 1.10 is formed, which explicitly computes the unknown displacements.

$$\boldsymbol{K}_s \cdot \boldsymbol{u}_s = \boldsymbol{f}_s \Rightarrow \begin{bmatrix} \boldsymbol{K}_{U,U} & \boldsymbol{K}_{U,I} \\ \boldsymbol{K}_{I,U} & \boldsymbol{K}_{I,I} \end{bmatrix} \begin{Bmatrix} \boldsymbol{u}_U \\ \boldsymbol{u}_I \end{Bmatrix} = \begin{Bmatrix} \boldsymbol{f}_U \\ \boldsymbol{f}_I \end{Bmatrix} \Rightarrow \boldsymbol{K}_{U,U} \cdot \boldsymbol{u}_U + \boldsymbol{K}_{U,I} \cdot \boldsymbol{u}_I = \boldsymbol{f}_U \Rightarrow$$

$$\boldsymbol{u}_U = \boldsymbol{K}_{U,U}^{-1} \cdot \left(\boldsymbol{f}_U - \boldsymbol{K}_{U,I} \cdot \boldsymbol{u}_I \right) = \boldsymbol{K}_{U,U}^{-1} \cdot \tilde{\boldsymbol{f}}_U \qquad 1.10$$

The displacement-control method does not introduce any significant modification to the NR formulation since the equations remain unaltered. Assuming that the total imposed displacements are divided into *n* steps, then the implementation is straightforward, as it was illustrated previously. What changes here is that the imposed displacements are known and must remain unaltered during any internal iteration inside each load step. This requires the solution of the system of equations by using Eq. 1.10 predicting the unknown displacements due to the imposed displacement increment by setting $\boldsymbol{u}_I = \Delta \boldsymbol{u}_I^t$, thus Eq. 1.6 takes the form

$$\boldsymbol{K}_{U,U}^t \cdot \Delta \boldsymbol{u}_U^{t+\Delta t} = \Delta \tilde{\boldsymbol{f}}_s^{t+\Delta t} \qquad 1.11$$

Following the computation of the unknown displacements (Eq. 1.11), the state determination is carried out for the computation of the nodal resisting forces for each uknown dof ($\Delta \boldsymbol{r}_U^{j=1}$). At this point, the first internal iteration has been completed and the error criteria are implemented in order to check if the algorithm has converged. If this is not the case, the computed residual forces are applied as external forces through Eq. 1.12, in order to correct the solution and achieve convergence.

$$\boldsymbol{K}_{U,U}^{t} \cdot \Delta \boldsymbol{u}_{U}^{j+1} = -\Delta \boldsymbol{r}_{U}^{j} \qquad 1.12$$

It is important to note, that the force resulting from the multiplication of $-\boldsymbol{K}_{U,I} \cdot \boldsymbol{u}_{I}$ in Eq. 1.10, is set to zero after the *1st* internal iteration, therefore the $\Delta \boldsymbol{u}_{I}^{t}$ displacement array is applied only once at the beginning of each incremental NR step.

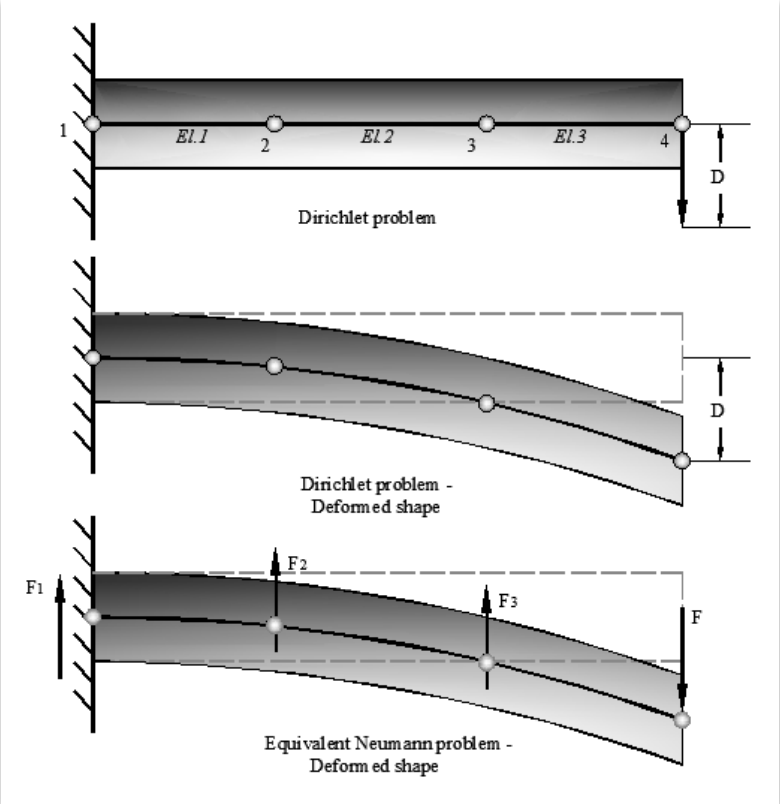

FIGURE 1.9 GRAPHICAL REPRESENTATION OF THE TRANSFORMATION OF A DIRICHLET PROBLEM INTO THE EQUIVALENT NEUMANN PROBLEM.

1.3.3 The Arc-Length Method

To obtain a more general technique, for capturing any type of unstable branches, the arc-length method for structural analysis, originally developed by Wempner[72] in 1971 and Riks[73, 74] (1972, 1979) and later modified by several researchers, has been proposed. Various forms of the arc-length method followed the original work of Wempner and Riks making the method widely acceptable[75-82].

As it was mentioned above, in the load-control method the load increment remains constant during a load step, a strategy used also for the displacement-control method in which the displacement is kept constant during the increment. Unlike the load- and displacement-control methods, the arc-length method considers a load-factor at each iteration which is modified so that the iterations follow some specified path until convergence is achieved.

Treating the load-factor as a separate variable, an additional unknown is introduced in the system of equations which results from the finite element procedure. If *N* is the number of unknown dof then the solution of *N+1* equations is required, thus an additional constraint

equation expressed in terms of current displacement, load-factor and arc-length is necessary. For the achievement of this task, two approaches can be used, the fixed arc-length and the varying arc-length. For the first approach the arc-length is kept constant for the current increment, whereas in the second approach, a new arc-length is evaluated at the beginning of each load step to achieve convergence. Simplifying the constraint equation leads to a quadratic equation, whose roots are used for the determination of the load-factor, a procedure which is concerned to be a key issue of the method since the proper selection of the root is crucial.

Concerning the initialization of the method, for the first increment a trial value is assumed for the load-factor, usually equal to $^1/_{10}$ of the total applied external load. For the following increments, the load-factor is computed according to the rate of convergence of the solution process. If the procedure fails to converge, the arc-length is reduced and computations are repeated. Another major issue, when dealing with this method, is the computation time of the solution process during the FEA process, thus a maximum number of internal iterations is set and if the solution fails to converge in the specified number then the load step is reduced and the process restarts.

In order to describe the technique used in the Arc-Length method, the following equilibrium of nonlinear system of equations is assumed:

$$\boldsymbol{g}_j(\lambda_j) = \boldsymbol{f}_j - \boldsymbol{q}\lambda_j \tag{1.13}$$

where $\boldsymbol{f}_j$ is the vector of resisting nodal forces, $\boldsymbol{q}$ is the external applied load vector, λ is the load-level parameter, and $\boldsymbol{g}_j$ is the residual force vector. The arc-length method is aiming at finding the intersection of Eq. 1.13 with the arc-length constant $\bar{s}$ which can be written as:

$$\bar{s} = \int \sqrt{d\boldsymbol{u}^T d\boldsymbol{u} + d\lambda^2 \psi^2 \boldsymbol{q}^T \boldsymbol{q}} \tag{1.14}$$

or in incremental form

$$s = \boldsymbol{\Delta u}^T \boldsymbol{\Delta u} + \Delta\lambda^2 \psi^2 \boldsymbol{q}^T \boldsymbol{q} - \Delta l^2 = 0 \tag{1.15}$$

where $\boldsymbol{\Delta u}$ is the vector of incremental displacements, $\Delta\lambda$ is the incremental load-factor, Δl is the fixed radius, and ψ is the scaling parameter of the loading terms. Eqs. 1.13 and 1.15 can be used to compute the iterative change of the displacement vector and the load-factor, through the following equation which is written in matrix form as:

$$\begin{Bmatrix} \delta\boldsymbol{u} \\ \delta\lambda \end{Bmatrix} = -\begin{bmatrix} \boldsymbol{K}_T & -\boldsymbol{q} \\ 2\boldsymbol{\Delta u}^T & 2\boldsymbol{\Delta}\lambda\psi^2 \boldsymbol{q}^T \boldsymbol{q} \end{bmatrix}^{-1} \begin{Bmatrix} \boldsymbol{g}_{old} \\ s_{old} \end{Bmatrix} \tag{1.16}$$

where $\delta\boldsymbol{u}$ is the iterative change of the displacement vector, $\delta\lambda$ is the iterative change of the load-factor, $\boldsymbol{K}_T$ is the tangential stiffness matrix and $\boldsymbol{g}_{old}$ and s_{old} are the previous values of the unbalanced loads and arc-length, respectively. After the computations of the iterative change $\delta\boldsymbol{u}$ and $\delta\lambda$, the displacement vector and the corresponding load-factor are updated.

A different technique, is to introduce the constraint proposed by Baltoz and Dhatt[75] for the displacement-control at a single point (Crisfield[76]). According to this study, the iterative

change of the displacements for the new unknown load level $\Delta\lambda_{j+1} = \Delta\lambda_j + \delta\lambda$ can be written as:

$$\delta\boldsymbol{u} = -\boldsymbol{K}_T^{-1}\boldsymbol{g} + \delta\lambda\boldsymbol{K}_T^{-1}\boldsymbol{q} = \delta\boldsymbol{g} + \delta\lambda\delta\boldsymbol{u}_T \quad 1.17$$

thus the corresponding iterative displacement increment for the next increment is written as:

$$\Delta\boldsymbol{u}_{i+1} = \Delta\boldsymbol{u}_i + \delta\boldsymbol{u} \quad 1.18$$

and by substituting Eqs.1.17 and 1.18 into the constraint Eq. 1.16, the following expression is dimmed

$$c_1\delta\lambda^2 + c_2\delta\lambda \quad + c_3 = 0 \quad 1.19$$

where,

$$c_1 = \delta\boldsymbol{u}^T\delta\boldsymbol{u} \quad + \psi^2\boldsymbol{q}^T\boldsymbol{q} \quad 1.20a$$

$$c_2 = 2\delta\boldsymbol{u} \quad (\Delta\boldsymbol{u} + \delta\boldsymbol{g}) + 2\Delta\psi^2\boldsymbol{q}^T\boldsymbol{q} \quad 1.20b$$

$$c_3 = (\Delta\boldsymbol{u} + \delta\boldsymbol{g})^T(\Delta\boldsymbol{u} + \delta\boldsymbol{g}) - \Delta l^2 + \Delta\psi^2\boldsymbol{q}^T\boldsymbol{q} \quad 1.20c$$

The solution of Eq. 1.19 is performed for the evaluation of $\delta\lambda$ and the definition of the iterative change. This equation leads to two results (roots) of $\delta\lambda$ but only one of them is selected[79]. Fig.1.10 represents graphically the described method.

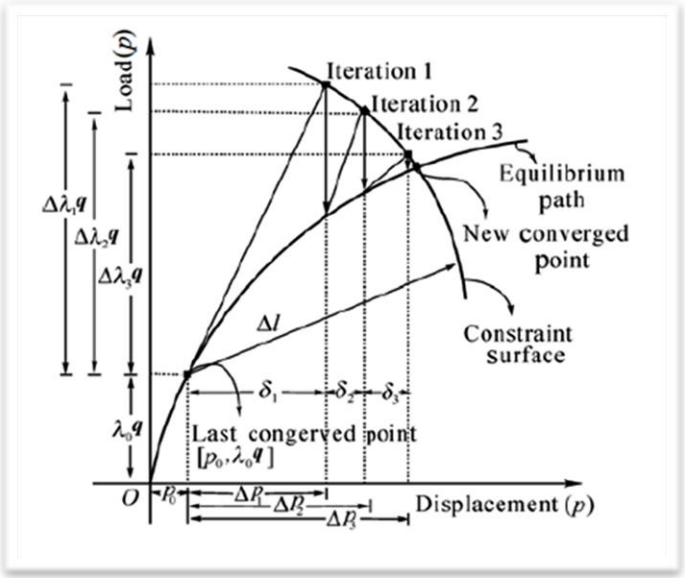

FIGURE 1.10 THE ARC-LENGTH METHOD FOR A SPECIFIC ITERATION[79].

Chapter 2 The Natural Beam-Column Flexibility-Based Element

Contents of Chapter 2

2.1 General Characteristics of the Element

The NBCFB element is a 2-noded three-dimensional beam FE which is shown in Fig. 2.1. The element has *12* dof (*6* per node) and assuming that *xyz* represent the global coordinate system, they are grouped in the vector

$$\boldsymbol{\rho} = \begin{bmatrix} u_1 & v_1 & w_1 & \theta_1 & \varphi_1 & \psi_1 & u_2 & v_2 & w_2 & \theta_2 & \varphi_2 & \psi_2 \end{bmatrix} \tag{2.1}$$

were *u*, *v* and *w* represent the translational dof, whereas θ, φ and ψ denote the rotational dof. These dof can refer either to a global or to a local Cartesian coordinate system that are related through transformation matrices which contain directional cosines.

A local Cartesian coordinate system *x'y'z'* is assigned to the element with the corresponding Cartesian dof:

$$\bar{\boldsymbol{\rho}} = \begin{bmatrix} \bar{u}_1 & \bar{v}_1 & \bar{w}_1 & \bar{\theta}_1 & \bar{\varphi}_1 & \bar{\psi}_1 & \bar{u}_2 & \bar{v}_2 & \bar{w}_2 & \bar{\theta}_2 & \bar{\varphi}_2 & \bar{\psi}_2 \end{bmatrix} \tag{2.2}$$

A natural coordinate α is adopted spanning the beam's axis which coincides with the local Cartesian axis *x'*. The local Cartesian dof are transformed into natural invariant rigid body and straining modes ρ_0 and ρ_N, respectively, so that a unique and reversible relation exists between the natural modes and the local and global dof:

$$\underset{(12x1)}{\boldsymbol{\rho}} \Leftrightarrow \underset{(12x1)}{\bar{\boldsymbol{\rho}}} \Leftrightarrow \underset{(6x1)}{\boldsymbol{\rho}_0}, \underset{(6x1)}{\boldsymbol{\rho}_N} \qquad \underset{(6x1)}{\boldsymbol{\rho}_N} = \underset{(12x1)}{\bar{\boldsymbol{\rho}}} - \underset{(6x1)}{\boldsymbol{\rho}_0} \tag{2.3}$$

In case of a fiber consideration along the cross section of the beam, an additional coordinate system is defined for every fiber (*k*), namely the *123* coordinate system with axis *1* along the principal reinforcement direction and axis *2* perpendicular to it. Note that material axis *3* is parallel to the local Cartesian axis *z'*. Then, for every fiber *k*, axis *1* forms an angle θ_k with the local axis *x'* (see Fig. 1.2). Therefore, the NBCFB element comprises *12* Cartesian dof but the actual number of straining modes is *6* (Eq. 2.4).

$$12\,Cartesian\ d.o.f\ -\ 6\ rigid\ body\ d.o.f\ =\ 6\ straining\ modes \tag{2.4}$$

It is worth noting, that the number of natural modes are always the difference of the nodal dof and the rigid body modes[83].

2.2 Kinematics

2.2.1 Natural Rigid Body Modes

Fig. 2.2 illustrates the rigid body modes that were selected for the beam element. The first three modes correspond to the translations and the last three to the rotations in space

$$\boldsymbol{\rho}_0 = \begin{bmatrix} \rho_{01} & \rho_{02} & \rho_{03} & \rho_{04} & \rho_{05} & \rho_{06} \end{bmatrix} \tag{2.5}$$

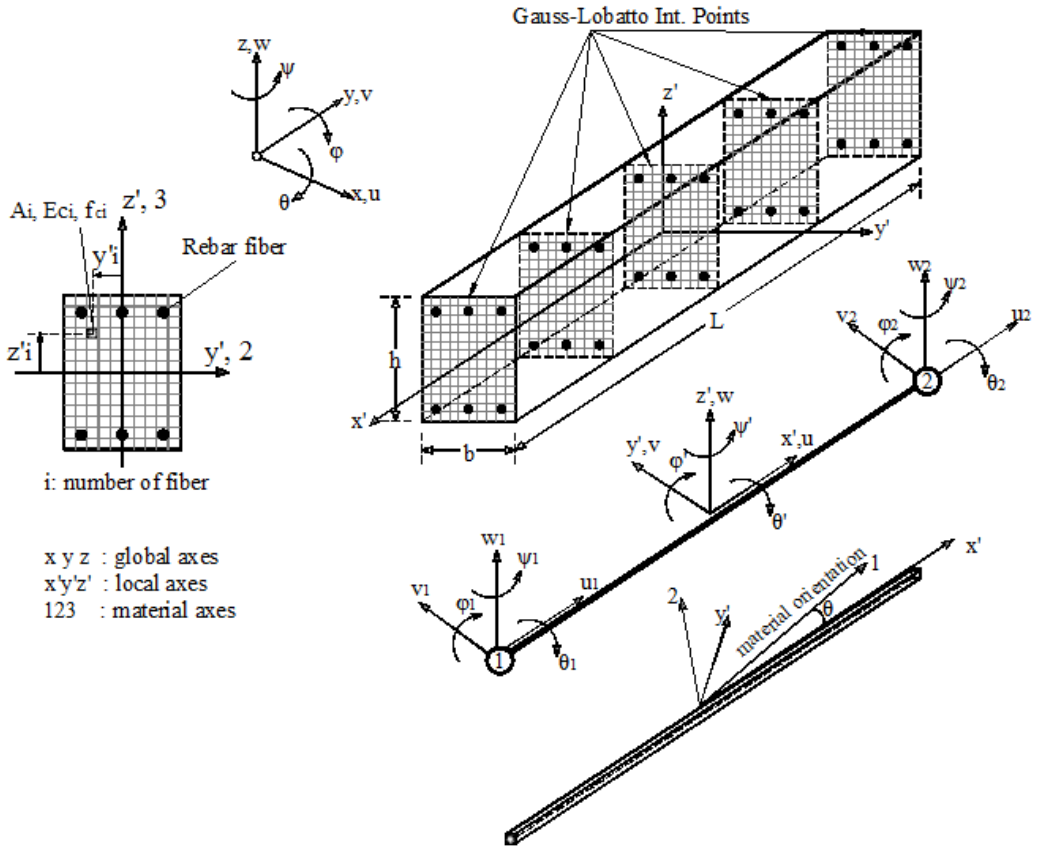

FIGURE 2.1 RC FIBER BEAM IN SPACE.

Rigid body modes do not create any strains and therefore they only produce body forces and moments which can be written in vector form

$$\boldsymbol{P}_0 = \begin{bmatrix} P_{01} & P_{02} & P_{03} & P_{04} & P_{05} & P_{06} \end{bmatrix} \tag{2.6}$$

The three translational modes can be deduced from Fig. 2.2 and are equal to

$$u_1 = \rho_{01},\ \ u_2 = \rho_{01},\ \ v_1 = \rho_{02} - \frac{1}{2}\rho_{06},\ \ v_2 = \rho_{02} + \frac{1}{2}\rho_{06},\ \ w_1 = \rho_{03} + \frac{1}{2}\rho_{05},\ \ w_2 = \rho_{03} - \frac{1}{2}\rho_{05} \tag{2.7a}$$

from which we obtain

$$\rho_{01} = \frac{1}{2}(u_1 + u_2),\quad \rho_{02} = \frac{1}{2}(v_1 + v_2),\quad \rho_{03} = \frac{1}{2}(w_1 + w_2)$$
$$\rho_{05} = \frac{1}{L}(w_1 - w_2),\ \ \rho_{06} = \frac{1}{L}(v_2 - v_1),\quad \text{L : beam's length} \tag{2.7b}$$

The fourth rigid body mode is a rotation with respect to the *x* axis, which is equal

$$\rho_{04} = \frac{1}{2}(\theta_1 + \theta_2) \tag{2.8}$$

The above relations can be expressed in compact matrix notation format as

$$\underset{(6x1)}{\boldsymbol{\rho}_0} = \underset{(6x12)}{\bar{\boldsymbol{\alpha}}_0}\ \underset{(12x1)}{\bar{\boldsymbol{\rho}}} \tag{2.9}$$

where $\bar{\rho}$ is the vector of the local Cartesian dof.

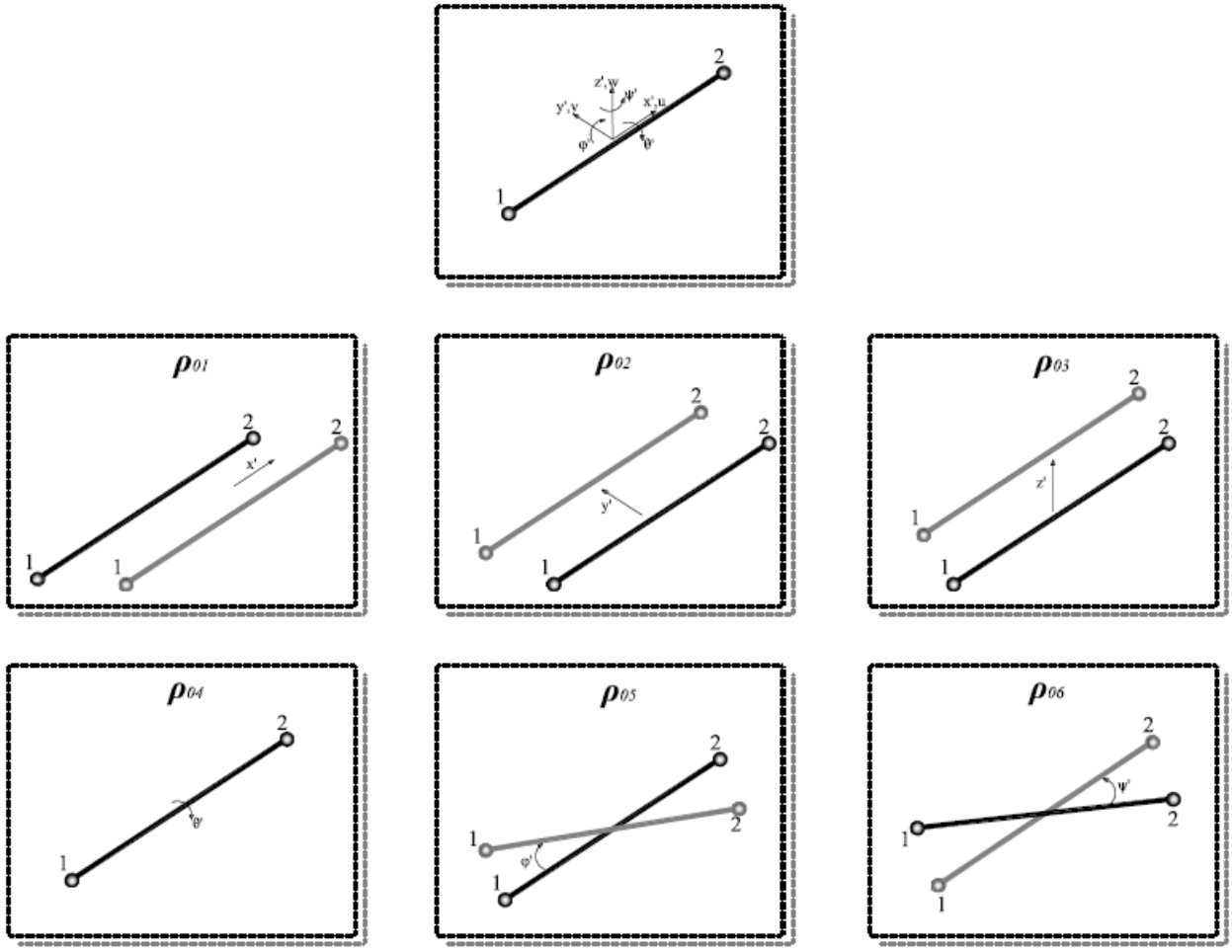

FIGURE 2.2 NATURAL RIGID BODY MODES.

The matrix $\bar{\alpha}_0$ which extracts the natural rigid body modes from the local Cartesian dof is given by

$$\underset{(6x12)}{\bar{\boldsymbol{\alpha}}_0} = \begin{bmatrix} \frac{1}{2} & . & . & . & . & . & \frac{1}{2} & . & . & . & . & . \\ . & \frac{1}{2} & . & . & . & . & . & \frac{1}{2} & . & . & . & . \\ . & . & \frac{1}{2} & . & . & . & . & . & \frac{1}{2} & . & . & . \\ . & . & . & \frac{1}{2} & . & . & . & . & . & \frac{1}{2} & . & . \\ . & . & \frac{1}{L} & . & . & . & . & . & -\frac{1}{L} & . & . & . \\ . & -\frac{1}{L} & . & . & . & . & . & \frac{1}{L} & . & . & . & . \end{bmatrix} \qquad 2.10$$

In order to reduce the required matrix calculations, the rigid body motions are not extracted when the local dof are available (they are deduced from the global displacements and rotations); instead the element's rigid body motions are calculated from the global dof

$$\underset{(12x1)}{\bar{\boldsymbol{\rho}}} = \underset{(12x12)}{\boldsymbol{T}_{04}} \underset{(12x1)}{\boldsymbol{\rho}} \tag{2.11}$$

where $\boldsymbol{\rho}$, $\boldsymbol{T}_{04}$ represent the vector of global nodal displacements and matrix of direction cosines respectively. Therefore, Eq. 2.9 becomes

$$\underset{(6x1)}{\boldsymbol{\rho}_0} = \underset{(6x12)}{\bar{\boldsymbol{\alpha}}_0} \underset{(12x1)}{\bar{\boldsymbol{\rho}}} = \underset{(6x12)}{\bar{\boldsymbol{\alpha}}_0} \underset{(12x12)}{\boldsymbol{T}_{04}} \underset{(12x1)}{\boldsymbol{\rho}} \tag{2.12}$$

In this work, the extraction of the rigid body motion is done through the global dof.

2.2.2 Natural Strain Modes

The natural strain modes are those that create internal stresses and strains which are used in order to calculate the beam internal forces. Fig. 2.3 illustrates the natural modes that were selected for the beam element and Fig. 2.4 depicts the corresponding generalized forces and moments. The vector that contains the 6 natural strain modes is

$$\boldsymbol{\rho}_N = \begin{bmatrix} \rho_{N1} & \rho_{N2} & \rho_{N3} & \rho_{N4} & \rho_{N5} & \rho_{N6} \end{bmatrix} \tag{2.13}$$

while the corresponding work conjugate natural forces are grouped in the vector

$$\boldsymbol{P}_N = \begin{bmatrix} P_{N1} & P_{N2} & P_{N3} & P_{N4} & P_{N5} & P_{N6} \end{bmatrix} \tag{2.14}$$

The natural straining modes and forces are related via the natural stiffness matrix

$$\boldsymbol{P}_N = \boldsymbol{k}_N \boldsymbol{\rho}_{\mathrm{N}} \tag{2.15}$$

The operations are performed on a non-dimensional coordinate ζ with origin being the center of the beam.

$$-1 \le \zeta \le 1, \qquad \zeta = \frac{2x}{L}, \qquad -\frac{L}{2} \le x \le \frac{L}{2} \tag{2.16}$$

And also

$$\frac{\partial(.)}{\partial x} = \frac{\partial(.)}{\partial \zeta}\frac{\partial \zeta}{\partial x} \Rightarrow \frac{\partial}{\partial x} = \frac{\partial}{\partial \zeta}\frac{2}{L} \tag{2.17}$$

The natural stiffness matrix of the beam element is extracted from the natural deformations without considering the rigid body motions.

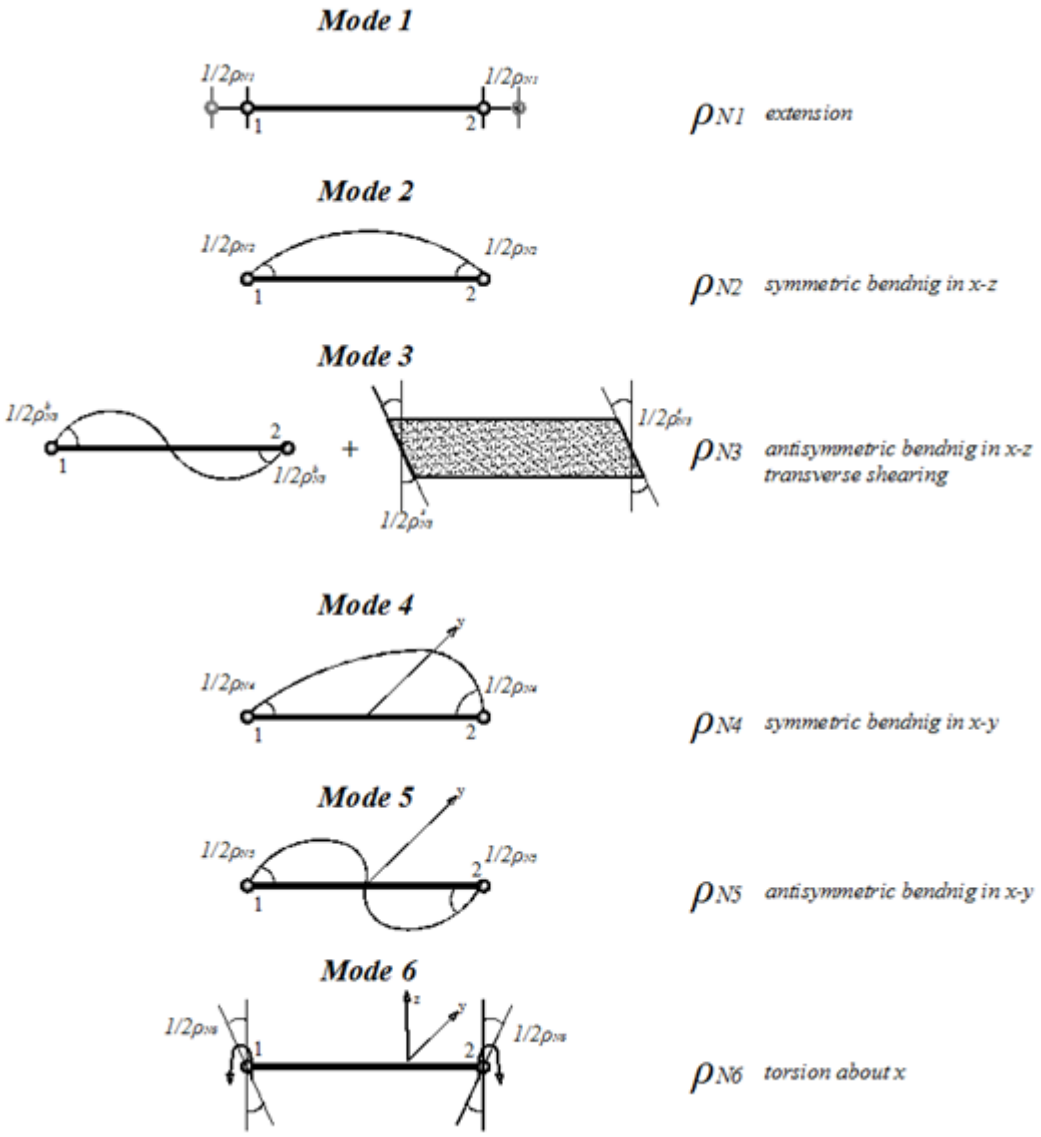

FIGURE 2.3 NATURAL STRAINING MODES.

2.2.2.1 Mode 1: Extension

The first natural strain mode is a unit extension ρ_{N1}. Half of this extension is assigned to the left beam end and the other half to the right, as shown in Fig. 2.3. Consequently, the displacement along the beam is written as a linear function of the coordinate ζ as

$$u(\zeta) = \frac{1}{2}\zeta\rho_{\mathrm{N1}} \qquad 2.18$$

The displacement u gives rise to the axial strain

$$\gamma_{xx}^{\epsilon} = \frac{\partial u}{\partial x} = \frac{\partial u}{\partial \zeta}\frac{\partial \zeta}{\partial x} = \frac{\rho_{\mathrm{N1}}}{L} = a^{\epsilon}\rho_{\mathrm{N1}}, \qquad a^{\epsilon} = \frac{1}{L} \qquad 2.19$$

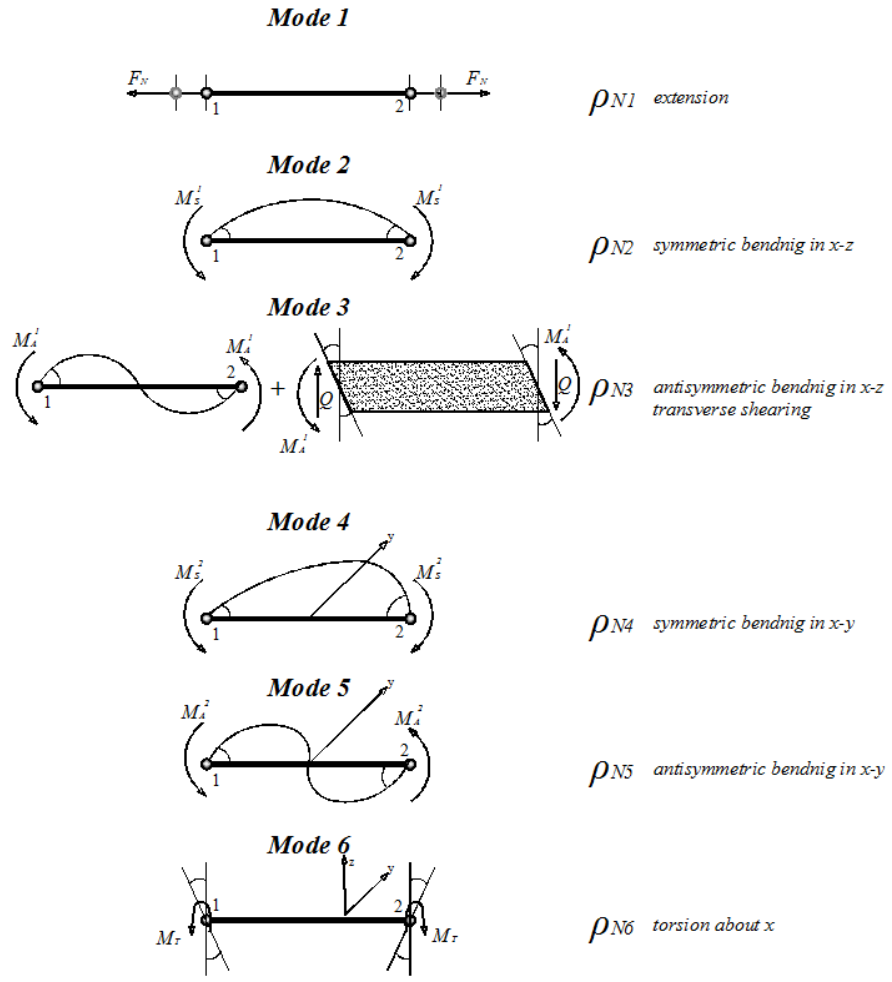

FIGURE 2.4 GENERALIZED NATURAL FORCES.

2.2.2.2 Mode 2: Symmetric Bending in the X-Z Plane

The second natural straining mode is a symmetrical bending mode in the *x-z* plane and is denoted as ρ_{N2}. This mode comprises a unit rotation equal to $1/2\rho_{N2}$ at the left and at the right node, respectively. These node rotations deform the elastic curve into a quadratic polynomial

$$w(x)=\alpha x^2+bx+c, \quad x:-\frac{L}{2}\to\frac{L}{2} \tag{2.20}$$

and by implementing the set of boundary conditions

$$\begin{aligned} &w\left(-\frac{L}{2}\right)=0, \qquad w\left(\frac{L}{2}\right)=0\,, \\ &w'\left(-\frac{L}{2}\right)=\frac{1}{2}\rho_{N2}, \quad w'\left(\frac{L}{2}\right)=-\frac{1}{2}\rho_{N2} \end{aligned} \tag{2.21}$$

we get

$$w(y)=-\frac{1}{2}x^2\rho_{N2}+\frac{L}{8}\rho_{N2} \tag{2.22}$$

but

$$x = \frac{L}{2}\zeta \tag{2.23}$$

and therefore

$$w(\zeta) = \frac{L}{8}\left(1-\zeta^2\right)\rho_{N2} \tag{2.24}$$

2.2.2.3 Mode 3: Antisymmetrical Bending and Transverse in the X-Z Plane

The third mode consists of two different kinds of deformation, the bending and transverse shearing deformation

$$\rho_{N3} = \rho_{N3}^{b} + \rho_{N3}^{S} \tag{2.25}$$

2.2.2.3.1 Solely Antisymmetrical Bending

For the case of antisymmetrical bending mode in the *x*-*z* plane denoted as ρ^{b}_{N3}, the equation of the displacement curve takes the form of a cubic polynomial

$$w(x) = \alpha x^3 + bx^2 + cx + d \tag{2.26}$$

and using the boundary conditions

$$\begin{aligned} &w\left(-\frac{L}{2}\right) = 0, \qquad w\left(\frac{L}{2}\right) = 0\ , \\ &w'\left(-\frac{L}{2}\right) = \frac{1}{2}\rho_{N3}, \quad w'\left(\frac{L}{2}\right) = -\frac{1}{2}\rho_{N3}, \quad \rho_{N3}^{b} = \rho_{N3} \end{aligned} \tag{2.27}$$

we get

$$w(\zeta) = \frac{L}{8}\left(\zeta^3 - \zeta^2\right)\rho_{N3} \tag{2.28}$$

Superimposing the elastic displacement curves originated from the second and third modes we obtain

$$w(\zeta) = \frac{L}{8}\left(1-\zeta^2\right)\rho_{N2} + \frac{L}{8}\left(\zeta^3 - \zeta^2\right)\rho_{N3} \tag{2.29}$$

The axial direct strain is equal to

$$\gamma_{xx} = -z\frac{d^2 w(x)}{dx^2} \tag{2.30}$$

therefore

$$\gamma_{xx} = \frac{z}{L}\rho_{N2} - 3\frac{z}{L}\zeta\rho_{N3} \tag{2.31}$$

2.2.2.3.2 Antisymmetric Bending and Transverse Shearing

The transverse shear strains are generated via the antisymmetric natural straining mode ρ^{S}_{N3}. In fact, equilibrium arguments substantiate the existence of the transverse shear force in order to equilibrate the antisymmetrical bending moments (Fig. 2.5).

Thus

$$Q = \frac{2M_A}{L} \tag{2.32}$$

The angle on the left beam node, due to the action of the moment M_A on the same node is

$$\theta_b^1 = \frac{M_A L}{3EI} \tag{2.33}$$

where E, I and L are the Young modulus, moment of inertia and length of the beam, respectively. When the same moment M_A is applied to the right edge on the left node then

$$\theta_b^2 = -\frac{M_A L}{6EI} \tag{2.34}$$

Superposing the two angles, the antisymmetric bending is obtained

$$\theta_b = \theta_b^1 + \theta_b^2 = \frac{M_A L}{6EI} \tag{2.35}$$

For the case of transverse shear, the angle of straining is

$$\rho_{N3} = \rho_{N3}^b + \rho_{N3}^S = 2\left(\theta_b + \theta_S\right) = 2\left(\frac{M_A L}{6EI} + \frac{2M_A}{LGA}\right) \tag{2.36}$$

And if we want to express M_A in terms of ρ_{N3} we deduce from Eq. 2.36 the expression

$$M_A = \left(\frac{\frac{3EI}{L}}{1+\frac{12EI}{L^2GA}}\right)\rho_{N3} \tag{2.37}$$

or

$$M_A = \left(\frac{\frac{3EI}{L}}{1+\frac{12EI}{L^2GA}}\right)\rho_{N3} = \left(\frac{3EI}{L\left(1+\lambda\right)}\right)\rho_{N3}, \qquad \lambda = \frac{12EI}{L^2GA} \tag{2.38}$$

where λ is the beam's shearing coefficient. From Eq. 2.38 it can be easily observed that if

$$GA \to \infty \Rightarrow \lambda \to 0, \qquad M_A = \frac{3EI}{L} \tag{2.39}$$

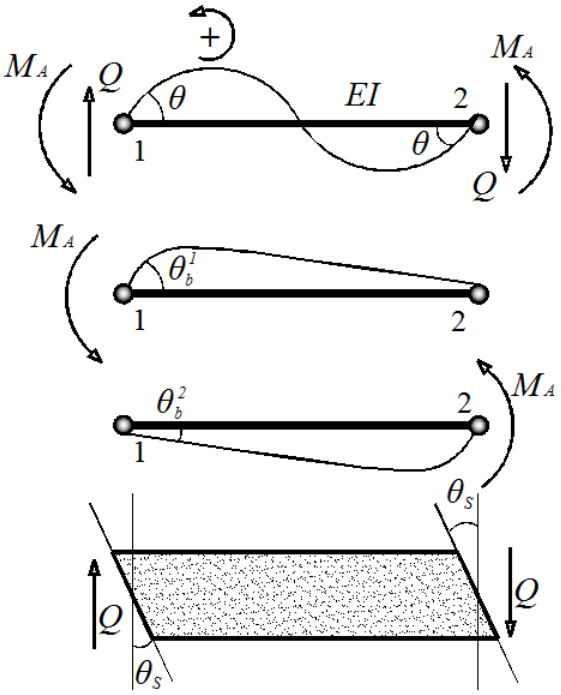

FIGURE 2.5 BENDING AND SHEAR DEFORMATIONS INDUCED BY THE ANTISYMMETRICAL MODE.

This is an important mechanical feature of the beam element that naturally leads to the circumvention of the transverse shear locking phenomenon that is frequently encountered in classical finite element methods.

2.2.2.4 Mode 4: Symmetrical Bending in the X-Y Plane

The fourth natural straining mode ρ_{N4} is the same to the symmetrical bending mode ρ_{N2} with the difference that it is assigned to the *x-y* plane. Therefore, the equation of the elastic curve due to this natural straining mode is

$$v(\zeta)=\frac{L}{8}\left(1-\zeta^2\right)\rho_{N4} \tag{2.40}$$

2.2.2.5 Mode 5: Antisymmetrical Bending in the X-Y Plane

The fifth natural straining mode is also similar to mode ρ_{N3} with the difference that it occurs in the *x-y* plane and includes only bending. This means that shear deformation is not accounted for which raises an equilibrium problem due to the absence of the transverse shear. The moment M_A^2 is not equilibrated; however for a laminated beam M_A^2 is small and its contribution to the overall deformation is negligible. Therefore, by superpositioning the displacement curves stemming from the fourth and fifth modes, we obtain

$$v(\zeta)=\frac{L}{8}\left(1-\zeta^2\right)\rho_{N4}+\frac{L}{8}\left(\zeta^3-\zeta\right)\rho_{N5} \tag{2.41}$$

and the strain field is equal to

$$\gamma_{xx}=\frac{y}{L}\rho_{N4}-3\frac{y}{L}\zeta\rho_{N5} \tag{2.42}$$

2.2.2.6 Mode 6: Torsion about the X Axis

The last straining mode (sixth natural straining mode) is a unit twisting angle ρ_{N6} which is illustrated in Fig. 2.4. Half of the angle is assigned to the left beam node and the other half to the right. Its linear variation with respect to the non-dimensional coordinate ζ is

$$\theta(\zeta)=\frac{1}{2}\zeta\rho_{N6} \tag{2.43}$$

The displacement field due to this twisting angle is (Fig. 2.6)

$$\begin{aligned} u(x,y,z)&=\theta(x)\Psi(y,z),\\ v(x,z)&=-\theta(x)z,\\ w(x,y)&=\theta(x)y \end{aligned} \tag{2.44}$$

where $\Psi(y,z)$ is the warping function. By substituting Eq. 2.43 in Eq. 2.44 we get

$$\begin{aligned} u(\zeta,y,z)&=\theta\,\Psi(y,z)=\frac{1}{L}\Psi(y,z)\rho_{N6},\\ v(\zeta,z)&=-\theta\,z=-\frac{1}{2}\zeta z\rho_{N6},\\ w(\zeta,y)&=\theta\,y=\frac{1}{2}\zeta y\rho_{N6} \end{aligned} \tag{2.45}$$

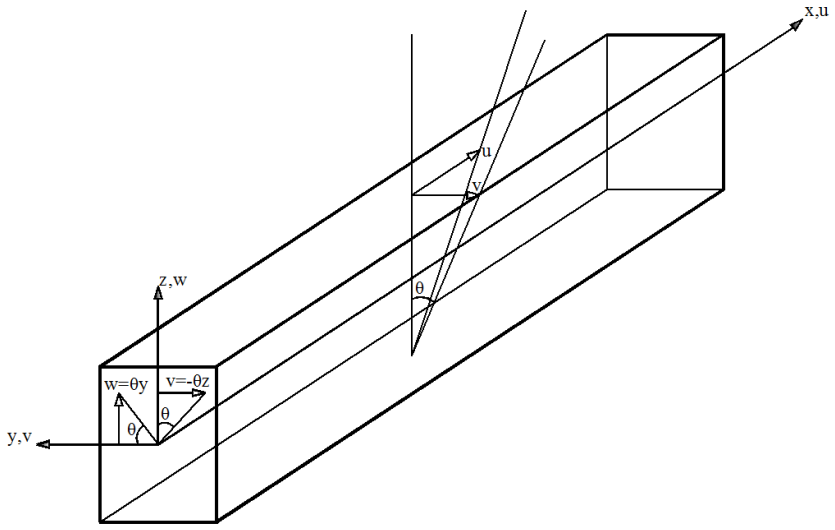

FIGURE 2.6 DISPLACEMENT FIELD DUE TO TORSION.

Finally, the derivation of the strain field that arises from this mode in terms of the x coordinate is accomplished by using Eqs. 2.16 and 2.45:

$$\begin{aligned} u(x,y,z)&=\frac{1}{L}\Psi(y,z)\rho_{N6},\\ v(x,z)&=-\frac{x}{L}z\rho_{N6},\\ w(x,y)&=\frac{x}{L}y\rho_{N6} \end{aligned} \tag{2.46}$$

As for the derivation of the strain field, we proceed the same way as before. Thus

$$\gamma_{ij} = \frac{1}{2}\left(\frac{\partial u_i}{\partial x_j} + \frac{\partial u_j}{\partial x_i} \right), \quad i, j = x, y, z \tag{2.47}$$

Being consistent with the definition of strain energy, all shear strains and stresses must be multiplied by $\sqrt{2}$. Therefore

$$U = \frac{1}{2}\sigma_{ij}\gamma_{ij} = \frac{1}{2}\left[\sqrt{2}\sigma_{ij}\right]\left[\sqrt{2}\gamma_{ij}\right] = \frac{1}{2}\sigma_{ij}\left(\frac{\partial u_i}{\partial x_j} + \frac{\partial u_j}{\partial x_i} \right) \tag{2.48}$$

The strain field is therefore the following

$$\begin{aligned}
&\gamma_{xx} = \frac{\partial u}{\partial x} = 0, \quad \gamma_{yy} = \frac{\partial v}{\partial y} = 0, \quad \gamma_{zz} = \frac{\partial w}{\partial z} = 0, \\
&\sqrt{2}\gamma_{xy} = \frac{1}{\sqrt{2}}\left(\frac{\partial u}{\partial y} + \frac{\partial v}{\partial x} \right) = \frac{1}{\sqrt{2}}\left(\frac{1}{L}\frac{\partial \Psi}{\partial y} - \frac{z}{L} \right)\rho_{\mathrm{N6}}, \\
&\sqrt{2}\gamma_{yz} = \frac{1}{\sqrt{2}}\left(\frac{\partial u}{\partial z} + \frac{\partial w}{\partial x} \right) = \frac{1}{\sqrt{2}}\left(\frac{1}{L}\frac{\partial \Psi}{\partial z} + \frac{y}{L} \right)\rho_{\mathrm{N6}}, \\
&\sqrt{2}\gamma_{yz} = \frac{1}{\sqrt{2}}\left(\frac{\partial v}{\partial z} + \frac{\partial w}{\partial y} \right) = \frac{1}{\sqrt{2}}\left(-\frac{x}{L} + \frac{x}{L} \right)\rho_{\mathrm{N6}} = 0
\end{aligned} \tag{2.49}$$

By grouping the non-zero strains due to the torsional natural mode we get

$$\gamma_{xx} = 0, \quad \sqrt{2}\gamma_{xy} = \frac{1}{L\sqrt{2}}\left(\frac{\partial \Psi}{\partial y} - z \right)\rho_{\mathrm{N6}}, \quad \sqrt{2}\gamma_{yz} = \frac{1}{L\sqrt{2}}\left(\frac{\partial \Psi}{\partial z} + y \right)\rho_{\mathrm{N6}} \tag{2.50}$$

and in matrix form

$$\begin{bmatrix} \gamma_{xx} \\ \sqrt{2}\gamma_{xy} \\ \sqrt{2}\gamma_{yz} \end{bmatrix} = \frac{1}{L}\begin{bmatrix} 0 \\ \frac{1}{\sqrt{2}}\left(\frac{\partial \Psi}{\partial y} - z \right) \\ \frac{1}{\sqrt{2}}\left(\frac{\partial \Psi}{\partial z} + y \right) \end{bmatrix}\rho_{\mathrm{N6}} \qquad \text{or} \qquad \underset{(3x1)}{\boldsymbol{\gamma}_{\mathrm{T}}} = \underset{(3x1)}{\boldsymbol{\alpha}^{\mathrm{T}}}\underset{(1x1)}{\boldsymbol{\rho}_{\mathrm{N6}}} \tag{2.51}$$

2.3 Natural Stiffness Matrix

To compute the natural stiffness matrix we must have the strain operator matrix and the constitutive relations referred to the material coordinate system *123* (Fig. 2.1). Subsequent to that, by using the strain energy expression, the natural stiffness matrix is derived.

2.3.1 Strain Operator Matrix

By superposing all the natural straining modes the complete strain field is arranged in the vector

$$\begin{bmatrix} \gamma_{xx} \\ \sqrt{2}\gamma_{xy} \\ \sqrt{2}\gamma_{yz} \end{bmatrix} = \begin{bmatrix} \gamma_{xx}^{\in} + \gamma_{xx}^{Sb} + \gamma_{xx}^{Ab} + \gamma_{xx}^{T} \\ \sqrt{2}\gamma_{xy} \\ \sqrt{2}\gamma_{yz} \end{bmatrix} \tag{2.52}$$

where $\gamma_{xx}^{\in}, \gamma_{xx}^{Sb}, \gamma_{xx}^{Ab}, \gamma_{xx}^{T}$ are the strains due to the axial straining, symmetrical bending, antisymmetrical bending and torsional modes, respectively.

By collecting all derived expressions for the axial strain γ_{xx} we have

$$\gamma_{xx} = \gamma_{xx}^{\in} + \gamma_{xx}^{Sb} + \gamma_{xx}^{Ab} + \gamma_{xx}^{T} = \frac{1}{L}\left(\rho_{N1} + z\rho_{N2} - 3z\zeta\rho_{N3} + y\rho_{N4} - 3y\zeta\rho_{N5}\right) \tag{2.53}$$

or in matrix form

$$\begin{bmatrix} \gamma_{xx} \\ \sqrt{2}\gamma_{xy} \\ \sqrt{2}\gamma_{yz} \end{bmatrix} = \frac{1}{L}\begin{bmatrix} 1 & z & -3z\zeta & y & -3y\zeta & . \\ . & . & . & . & . & \frac{1}{\sqrt{2}}\left(\frac{\partial\Psi(y,z)}{\partial y} - z\right) \\ . & . & . & . & . & \frac{1}{\sqrt{2}}\left(\frac{\partial\Psi(y,z)}{\partial z} + y\right) \end{bmatrix}\begin{bmatrix} \rho_{N1} \\ \rho_{N2} \\ \rho_{N3} \\ \rho_{N4} \\ \rho_{N5} \\ \rho_{N6} \end{bmatrix} \tag{2.54}$$

and by using vector notation

$$\underset{(3x1)}{\boldsymbol{\gamma}} = \underset{(3x6)}{\boldsymbol{\alpha}_{N}} \underset{(6x1)}{\boldsymbol{\rho}_{N}} \tag{2.55}$$

where $\boldsymbol{\alpha}_N$ is a strain operator matrix which connects the Cartesian strains with the natural straining modes and is defined as

$$\boldsymbol{\alpha}_N = \frac{1}{L}\begin{bmatrix} 1 & z & -3z\zeta & y & -3y\zeta & . \\ . & . & . & . & . & \frac{1}{\sqrt{2}}\left(\frac{\partial\Psi(y,z)}{\partial y} - z\right) \\ . & . & . & . & . & \frac{1}{\sqrt{2}}\left(\frac{\partial\Psi(y,z)}{\partial z} + y\right) \end{bmatrix} \tag{2.56}$$

2.3.2 Constitutive Relation

The material constitutive relations that refer to the material coordinate *123* (Fig. 2.1) for every fiber *i* read

$$\boldsymbol{\sigma} = \boldsymbol{\kappa}_{12}\boldsymbol{\gamma}, \qquad \boldsymbol{\sigma}_S = \boldsymbol{\kappa}_S\boldsymbol{\gamma}_S \tag{2.57}$$

and for an orthotropic material

$$\begin{bmatrix} \sigma_{11} \\ \sigma_{22} \\ \sqrt{2}\sigma_{12} \end{bmatrix}_i = \frac{1}{1-\nu_{12}^2 \frac{E_2}{E_1}} \begin{bmatrix} E_1 & \nu_{12}E_2 & . \\ \nu_{12}E_2 & E_2 & . \\ . & . & 2G_{12}\left(1-\nu_{12}^2 \frac{E_2}{E_1}\right) \end{bmatrix}_i \begin{bmatrix} \gamma_{11} \\ \gamma_{22} \\ \sqrt{2}\gamma_{12} \end{bmatrix}_i, \qquad 2.58$$

$$\begin{bmatrix} \sqrt{2}\sigma_{13} \\ \sqrt{2}\sigma_{23} \end{bmatrix}_i = \begin{bmatrix} 2G & . \\ . & 2G \end{bmatrix}_i \begin{bmatrix} \sqrt{2}\gamma_{13} \\ \sqrt{2}\gamma_{23} \end{bmatrix}_i$$

For complete isotropy $\nu_{12} = \nu_{21} = \nu, E_1 = E_2 = E, G_{12} = G$, Eq. 2.58 reduces to

$$\begin{bmatrix} \sigma_{11} \\ \sigma_{22} \\ \sqrt{2}\sigma_{12} \end{bmatrix}_i = \begin{bmatrix} \frac{E}{1-\nu^2} & \nu\frac{E}{1-\nu^2} & . \\ \nu\frac{E}{1-\nu^2} & \frac{E}{1-\nu^2} & . \\ . & . & 2G \end{bmatrix}_i \begin{bmatrix} \gamma_{11} \\ \gamma_{22} \\ \sqrt{2}\gamma_{12} \end{bmatrix}_i, \qquad 2.59$$

$$\begin{bmatrix} \sqrt{2}\sigma_{13} \\ \sqrt{2}\sigma_{23} \end{bmatrix}_i = \begin{bmatrix} 2G & . \\ . & 2G \end{bmatrix}_i \begin{bmatrix} \sqrt{2}\gamma_{13} \\ \sqrt{2}\gamma_{23} \end{bmatrix}_i$$

The material stiffnesses are transformed from the material coordinate *123* to the local Cartesian coordinate system *x'y'z'* by using the following transformations

$$\boldsymbol{\kappa}' = \left[A_1^T \kappa_{12} \mathrm{A}_1 \right]_i, \qquad 2.60$$
$$\boldsymbol{G}' = \left[A_S^T G_{12} \mathrm{A}_S \right]$$

where

$$\boldsymbol{A} = \begin{bmatrix} c_\theta^2 & s_\theta^2 & \sqrt{2}s_\theta c_\theta \\ s_\theta^2 & c_\theta^2 & -\sqrt{2}s_\theta c_\theta \\ -\sqrt{2}s_\theta c_\theta & \sqrt{2}s_\theta c_\theta & 2G \end{bmatrix}_i, \qquad 2.61$$

$$\boldsymbol{A}_S = \begin{bmatrix} c_\theta & s_\theta \\ -s_\theta & c_\theta \end{bmatrix}_i, \quad c_\theta = \cos\theta, \quad s_\theta = \sin\theta$$

The angle θ represents the angle formed between the fiber axis *1* and the local axis *x'* (Fig. 2.1). Since in this work we take into account only the strains γ_{xx}, γ_{xy} and γ_{xz} the transformed Cartesian constitutive relation becomes

$$\begin{bmatrix} \sigma_{xx} \\ \sqrt{2}\sigma_{xy} \\ \sqrt{2}\sigma_{xz} \end{bmatrix}_i = \begin{bmatrix} E_{xx} & E_{xy} & . \\ E_{xy} & 2G_{xy} & . \\ . & . & 2G_{xz} \end{bmatrix}_i \begin{bmatrix} \gamma_{xx} \\ \sqrt{2}\gamma_{xy} \\ \sqrt{2}\gamma_{xz} \end{bmatrix} \quad \Rightarrow \quad \boldsymbol{\sigma} = \boldsymbol{\kappa}\,\boldsymbol{\gamma} \tag{2.62}$$

2.3.3 Strain Energy and the Natural Stiffness Matrix

For the derivation of the natural stiffness matrix the utilization of the expression of the strain energy is required.

$$U = \int_V \boldsymbol{\sigma}^t \boldsymbol{\gamma} dV \tag{2.63}$$

By using Eqs. 2.54 and 2.62 we get

$$\boldsymbol{\gamma} = \boldsymbol{\alpha}_{\mathrm{N}} \boldsymbol{\rho}_{\mathrm{N}}, \qquad \boldsymbol{\sigma} = \boldsymbol{\kappa}\,\boldsymbol{\gamma} \tag{2.64}$$

therefore

$$U = \underset{(1x6)}{\boldsymbol{\rho}_{\mathrm{N}}^t} \underbrace{\left[\int \underset{(6x3)}{\boldsymbol{\alpha}_N^t} \underset{(3x3)}{\boldsymbol{\kappa}} \underset{(3x6)}{\boldsymbol{\alpha}_N}\, dV \right]}_{natural\ \text{stiffness}\ matrix} \underset{(6x1)}{\boldsymbol{\rho}_{\mathrm{N}}} \tag{2.65}$$

It's easy to conclude that the final natural stiffness matrix is a *6*x*6* matrix and its expression is

$$\underset{(6x6)}{\boldsymbol{k}_N} = \frac{1}{L^2}\int_V \begin{bmatrix} E_{xx} & zE_{xx} & -3z\zeta E_{xx} & yE_{xx} & -3y\zeta E_{xx} & \frac{E_{xy}}{\sqrt{2}}\left(\Psi_{,y} - z\right) \\ & z^2E_{xx} & -3z^2\zeta E_{xx} & zyE_{xx} & -3zy\zeta E_{xx} & \frac{zE_{xy}}{\sqrt{2}}\left(\Psi_{,y} - z\right) \\ & & 9z^2\zeta^2E_{xx} & -zyE_{xx} & 9zy\zeta^2E_{xx} & -3zy\zeta E_{xy}\left(\Psi_{,y} - z\right) \\ & & & y^2E_{xx} & -3y^2\zeta^2E_{xx} & \frac{yE_{xy}}{\sqrt{2}}\left(\Psi_{,y} - z\right) \\ & \textit{symm.} & & & 9y^2\zeta^2E_{xx} & -\frac{3y\zeta E_{xy}}{\sqrt{2}}\left(\Psi_{,y} - z\right) \\ & & & & & G_{xy}\left(\Psi_{,y} - z\right)^2 + G_{xz}\left(\Psi_{,y} + y\right)^2 \end{bmatrix} \tag{2.66}$$

The above matrix corresponds to the full natural stiffness matrix of a beam element for the most general stiffness formulation with an anisotropic material. Some of the entries in the above full stiffness matrix represent a very small to negligible contribution and therefore they can be eliminated. In particular, the coupling term E_{xy} is very small and equal to zero for isotropic materials. In addition, we assume that some of the natural straining modes are not coupled.

$$
\begin{aligned}
&E_{xy} \approx 0, \\
&\rho_{N1} \rhd\lhd \rho_{N3}, \quad \rho_{N1} \rhd\lhd \rho_{N5} \\
&\rho_{N2} \rhd\lhd \rho_{N3}, \quad \rho_{N2} \rhd\lhd \rho_{N5} \\
&\rho_{N3} \rhd\lhd \rho_{N4}, \quad \rho_{N3} \rhd\lhd \rho_{N5} \\
&\rho_{N4} \rhd\lhd \rho_{N5}, \quad \rhd\lhd\text{: no interaction}
\end{aligned}
\qquad 2.67
$$

Thus a simplified form of the natural stiffness matrix is given by

$$
\underset{(6x6)}{\boldsymbol{k}_N} = \frac{1}{L^2}\int_V \begin{bmatrix}
E_{xx} & zE_{xx} & . & yE_{xx} & . & . \\
 & z^2E_{xx} & . & zyE_{xx} & . & . \\
 & & 9z^2\zeta^2E_{xx} & . & . & . \\
 & & & y^2E_{xx} & . & . \\
 & \textit{symm.} & & & 9y^2\zeta^2E_{xx} & . \\
 & & & & & G_{xy}\left(\Psi_{,y}-z\right)^2 + G_{xz}\left(\Psi_{,y}+y\right)^2
\end{bmatrix} \qquad 2.68
$$

Eq. 2.68 represents the *6*x*6* simplified natural stiffness matrix of the NBCFB element. With this formulation we reduce the required stiffness data for the solution procedure from *78* double precision variables to *21*. In *ReConAn* FEA, all symmetrical matrices are stored in arrays therefore, if we have a *n*x*n* matrix the required array size is equal to *n(n+1)/2*. For instance, if we have a *12*x*12* matrix the required array size is *78* which represents the *78* upper triangular values of the matrix. This storage type reduces significantly the required memory of our models and speeds up the CPU time required by the processor when performing calculations related to this type of arrays. In order to be able to conduct matrix operations with array type variables, we have developed special subroutines that perform several matrix operations such as matrix multiplication etc. This means that it is not required to transform the array variable into a square matrix, perform the required calculation and then store it again in an array format. Everything is done explicitly.

As we are going to see in the numerical implementation section, software architecture, variable manipulation, data flow control, dynamic memory redistribution and smart programming gives us the ability to solve fast and accurate large-scale RC structures.

The final step in order to compute the natural stiffness matrix is to evaluate the integrals of Eq. 2.68[83]. By doing so and by taking into consideration that the material is isotropic, the above stiffness matrix takes its final form

$$\underset{(6x6)}{\boldsymbol{k}_N} = \frac{1}{L}\begin{bmatrix} EA & . & . & . & . & . \\ & EI_{yy} & . & . & . & . \\ & & \dfrac{3EI_{yy}}{\left(L+\dfrac{12EI_{yy}}{L(GA)}\right)} & . & . & . \\ & & & EI_{zz} & . & . \\ & symm. & & & 3EI_{zz} & . \\ & & & & & GJ_p \end{bmatrix} \tag{2.69}$$

where E, G, A, I_{yy}, I_{zz} and J_p are the Young Modulus, the shear Modulus, the area of the section, the bending moment of inertia with respect to the y axis, the bending moment of inertia with respect to the z axis and the polar moment of inertia, respectively.

2.4 Local and Global Stiffness Matrix

In this section the transformation matrices will be presented in order to transform the natural stiffness matrix k_N to the local and ultimately to the global Cartesian coordinates. This requires the connection between the natural straining modes and the local dof. The relevant matrix equation is

$$\underset{(6x1)}{\boldsymbol{\rho}_N} = \underset{(6x12)}{\bar{\boldsymbol{\alpha}}_N}\ \underset{(12x1)}{\bar{\boldsymbol{\rho}}} \tag{2.70}$$

The connection matrix $\bar{\boldsymbol{\alpha}}_N$ contains only geometrical parameters and this is established from the fact that most natural straining modes are generated simply by addition or subtraction of the local nodal dof. The contribution of the vertical nodal displacements to the antisymmetrical mode is illustrated in Fig. 2.7.

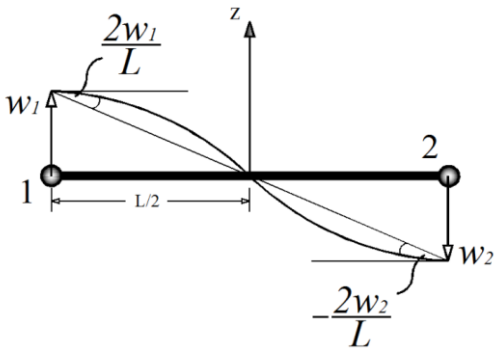

FIGURE 2.7 ANTISYMMETRICAL ROTATION DUE TO VERTICAL NODAL DISPLACEMENTS.

The explicit expressions for the natural modes are

$$\begin{aligned} &\rho_{N1} = u_2 - u_1, \quad \rho_{N2} = \varphi_2 - \varphi_1, \quad \rho_{N3} = -(\varphi_1 + \varphi_2) + \frac{2(w_1 - w_2)}{L}, \\ &\rho_{N4} = \psi_1 - \psi_2, \quad \rho_{N5} = (\psi_1 + \psi_2) + \frac{2(v_1 - v_2)}{L}, \quad \rho_{N6} = \theta_2 - \theta_1 \end{aligned} \tag{2.71}$$

from which the matrix relation is deduced

$$\underset{(6x12)}{\bar{\boldsymbol{\alpha}}_N} = \begin{bmatrix} -1 & . & . & . & . & . & 1 & . & . & . & . & . \\ . & . & . & . & -1 & . & . & . & . & . & 1 & . \\ . & . & \frac{2}{L} & . & -1 & . & . & . & -\frac{2}{L} & . & -1 & . \\ . & . & . & . & . & 1 & . & . & . & . & . & -1 \\ . & \frac{2}{L} & . & . & . & 1 & . & -\frac{2}{L} & . & . & . & 1 \\ . & . & . & -1 & . & . & . & . & . & 1 & . & . \end{bmatrix} \qquad 2.72$$

We are now in position to connect the natural rigid body modes and the natural straining modes with the local Cartesian dof through the two matrices:

$$\begin{bmatrix} \underset{(6x12)}{\bar{\boldsymbol{\alpha}}_0} \\ ..... \\ \underset{(6x12)}{\bar{\boldsymbol{\alpha}}_N} \end{bmatrix} = \begin{bmatrix} \frac{1}{2} & . & . & . & . & . & \frac{1}{2} & . & . & . & . & . \\ . & \frac{1}{2} & . & . & . & . & . & \frac{1}{2} & . & . & . & . \\ . & . & \frac{1}{2} & . & . & . & . & . & \frac{1}{2} & . & . & . \\ . & . & . & \frac{1}{2} & . & . & . & . & . & \frac{1}{2} & . & . \\ . & . & \frac{1}{L} & . & . & . & . & . & -\frac{1}{L} & . & . & . \\ . & -\frac{1}{L} & . & . & . & . & . & \frac{1}{L} & . & . & . & . \\ \hline -1 & . & . & . & . & . & 1 & . & . & . & . & . \\ . & . & . & . & -1 & . & . & . & . & . & 1 & . \\ . & . & \frac{2}{L} & . & -1 & . & . & . & -\frac{2}{L} & . & -1 & . \\ . & . & . & . & . & 1 & . & . & . & . & . & -1 \\ . & \frac{2}{L} & . & . & . & 1 & . & -\frac{2}{L} & . & . & . & 1 \\ . & . & . & -1 & . & . & . & . & . & 1 & . & . \end{bmatrix} \qquad 2.73$$

From Eq. 2.12, Eq. 2.70 and Eq. 2.73 we have

$$\begin{bmatrix} \underset{(6x1)}{\boldsymbol{\rho}_0} \\ ..... \\ \underset{(6x1)}{\boldsymbol{\rho}_N} \end{bmatrix} = \begin{bmatrix} \underset{(6x12)}{\bar{\boldsymbol{\alpha}}_0} \\ ..... \\ \underset{(6x12)}{\bar{\boldsymbol{\alpha}}_N} \end{bmatrix} \underset{(12x1)}{\bar{\boldsymbol{\rho}}_N} = \begin{bmatrix} \underset{(6x12)}{\bar{\boldsymbol{\alpha}}_0} \\ ..... \\ \underset{(6x12)}{\bar{\boldsymbol{\alpha}}_N} \end{bmatrix} \underset{(12x12)}{\boldsymbol{T}_{04}} \underset{(12x1)}{\boldsymbol{\rho}} \qquad 2.74$$

Conversely,

$$\underset{(12x1)}{\boldsymbol{\rho}} = \underset{(12x12)}{\boldsymbol{T}_{04}^{-1}} \left[\underset{(12x6)}{\bar{\boldsymbol{A}}_0} \;\middle|\; \underset{(12x6)}{\bar{\boldsymbol{A}}_N} \right] \begin{bmatrix} \underset{(6x1)}{\bar{\boldsymbol{\rho}}_0} \\ ..... \\ \underset{(6x1)}{\bar{\boldsymbol{\rho}}_N} \end{bmatrix} \tag{2.75}$$

and therefore

$$\left[\bar{\boldsymbol{\alpha}}\right]^{-1} = \bar{\boldsymbol{A}} \tag{2.76}$$

Once more, the expression for the strain energy takes the form

$$\begin{aligned} U &= \int_V \boldsymbol{\sigma}^t \boldsymbol{\gamma} dV \\ &= \underset{(1x6)}{\boldsymbol{\rho}_{\mathrm{N}}^t} \underbrace{\left[\int \underset{(6x3)}{\boldsymbol{\alpha}_N^t} \underset{(3x3)}{\boldsymbol{\kappa}} \underset{(3x6)}{\boldsymbol{\alpha}_N} dV \right]}_{\textit{natural}\ \text{stiffness}\ \textit{matrix}} \underset{(6x1)}{\boldsymbol{\rho}_{\mathrm{N}}} \\ &= \underset{(1x12)}{\bar{\boldsymbol{\rho}}^t} \underbrace{\left[\underset{(12x6)}{\bar{\boldsymbol{\alpha}}_{\mathrm{N}}^t} \underbrace{\left[\int \underset{(6x3)}{\boldsymbol{\alpha}_N^t} \underset{(3x3)}{\boldsymbol{\kappa}} \underset{(3x6)}{\boldsymbol{\alpha}_N} dV \right]}_{\textit{natural}\ \text{stiffness}\ \textit{matrix}} \underset{(6x12)}{\bar{\boldsymbol{\alpha}}_{\mathrm{N}}} \right]}_{\text{local Cartesian stiffness matrix}} \underset{(12x1)}{\bar{\boldsymbol{\rho}}} \end{aligned} \tag{2.77}$$

The local elemental vector $\bar{\rho}$ is related to the global elemental vector ρ via

$$\bar{\boldsymbol{\rho}} = \boldsymbol{T}_{04} \boldsymbol{\rho} \tag{2.78}$$

where $\boldsymbol{T}_{04}$ is a matrix that contains submatrices of direction cosines

$$\underset{(12x12)}{\boldsymbol{T}_{04}} = \begin{bmatrix} \boldsymbol{T}_0 & . & . & . \\ . & \boldsymbol{T}_0 & . & . \\ . & . & \boldsymbol{T}_0 & . \\ . & . & . & \boldsymbol{T}_0 \end{bmatrix} \tag{2.79}$$

with

$$\underset{(3x3)}{\boldsymbol{T}_0} = \begin{bmatrix} c_{x'x} & c_{x'y} & c_{x'z} \\ c_{y'x} & c_{y'y} & c_{y'z} \\ c_{z'x} & c_{z'y} & c_{z'z} \end{bmatrix} \tag{2.80}$$

where $c_{x'x}$ denotes the cosine of the angle formed between the local Cartesian axis x' and the global Cartesian axis x. the same convention is used for all other entries.

Using

$$\boldsymbol{\rho}_N = \bar{\boldsymbol{\alpha}}_N \bar{\boldsymbol{\rho}} = \bar{\boldsymbol{\alpha}}_N \boldsymbol{T}_{04} \boldsymbol{\rho} = \boldsymbol{\alpha}_N \boldsymbol{\rho} \tag{2.81}$$

the strain energy expression becomes

$$U = \underset{(1x12)}{\boldsymbol{\rho}^t} \Bigg[\underbrace{\underset{(12x12)}{\boldsymbol{T}_{04}^t} \Bigg[\underbrace{\underset{(12x6)}{\bar{\boldsymbol{\alpha}}_{\mathrm{N}}^t} \Bigg[\underbrace{\int \underset{(6x3)}{\boldsymbol{\alpha}_N^t} \underset{(3x3)}{\boldsymbol{\kappa}} \underset{(3x6)}{\boldsymbol{\alpha}_N} dV}_{\textit{natural stiffness matrix } k_N} \Bigg] \underset{(6x12)}{\bar{\boldsymbol{\alpha}}_{\mathrm{N}}}}_{\text{local Cartesian stiffness matrix } \bar{\mathrm{k}}} \Bigg] \underset{(12x12)}{\boldsymbol{T}_{04}}}_{\text{global Cartesian stiffness matrix k}} \Bigg] \underset{(12x1)}{\boldsymbol{\rho}} \tag{2.82}$$

From which we deduce the equilibrium equations in natural, local and global coordinate systems as follows:

$$\begin{aligned} &\boldsymbol{P}_N = \boldsymbol{k}_N \boldsymbol{\rho}_N, && \text{natural coordinate system,} \\ &\bar{\boldsymbol{P}} = \bar{\boldsymbol{k}}\bar{\boldsymbol{\rho}}, && \text{local coordinate system,} \\ &\boldsymbol{P} = \boldsymbol{k}\boldsymbol{\rho}, && \text{global coordinate system} \end{aligned} \tag{2.83}$$

We must note at this point that from the numerical implementation view, the most "sensitive" matrices are the cosine matrix $\boldsymbol{T}_{04}$ and the connection matrix $\bar{\boldsymbol{a}}_N$. Due to their numerical role and arithmetical nature they must be given special attention in order to reassure that they obey the same coordinate system rules (either left hand side or right hand side orientation).

2.5 Flexibility-Based Formulation and Element's State Determination Procedure

In this section we will describe the NBCFB formulation concerning the procedure for the calculation of its internal forces and the modifications that are required in order to incorporate the natural mode method. As it was mentioned in Chapter 1, Spacone et al[33] proposed a Fibre Beam-Column model for the nonlinear analysis of RC frames with a flexibility-based formulation which relied on force interpolation functions that strictly satisfy the equilibrium of bending moments and axial force along the element. This flexibility-based formulation requires an iterative procedure for calculating the internal forces during the elements state determination.

2.5.1 Generalized Forces and Deformations

As it was mentioned above (Fig. 2.1), the natural beam element has *12* dof (*6* dof per node) and therefore *12* nodal forces when we refer to the global system. These work conjugate nodal forces and displacements when referred to the global system can be written in the following vectors

$$\begin{aligned} \boldsymbol{P} &= \begin{bmatrix} P_1 & P_2 & \dots & \dots & P_{11} & P_{12} \end{bmatrix}^T \\ \boldsymbol{\rho} &= \begin{bmatrix} \rho_1 & \rho_2 & \dots & \dots & \rho_{11} & \rho_{12} \end{bmatrix}^T \end{aligned} \tag{2.84}$$

The connection between these nodal forces and displacements with the natural rigid body and straining modes is done with the use of the connecting matrices of Eqs. 2.72 and 2.79. It was assumed that the torsion response is linear elastic and uncoupled from the other dof. Therefore,

the element has five general dof: one axial extension ρ_1 and two rotations relative to the cord at each node, (ρ_2, ρ_3) at node *1* and (ρ_4, ρ_5) at node *2*. These five deformations (Fig. 2.8) are called element generalized deformations $\boldsymbol{q}$ and the corresponding generalized forces $\boldsymbol{Q}$ (Fig. 2.8): Q_1 is the axial force and the two bending moments at each end node, (Q_2, Q_3) at node *1* and (Q_4, Q_5) at node *2*.

$$\boldsymbol{Q} = \begin{bmatrix} Q_1 & Q_2 & Q_3 & Q_4 & Q_5 \end{bmatrix}^T$$
$$\boldsymbol{q} = \begin{bmatrix} q_1 & q_2 & q_3 & q_4 & q_5 \end{bmatrix}^T \qquad 2.85$$

The transformation of $\boldsymbol{\rho}$ into $\boldsymbol{q}$ writes as follows

$$\underset{(6x1)}{\boldsymbol{q}} = \underset{(6x12)}{\boldsymbol{\alpha}_N} \underset{(12x12)}{\boldsymbol{T}_{04}} \underset{(12x1)}{\boldsymbol{\rho}}, \quad \boldsymbol{q}(6) = 0 \qquad 2.86$$

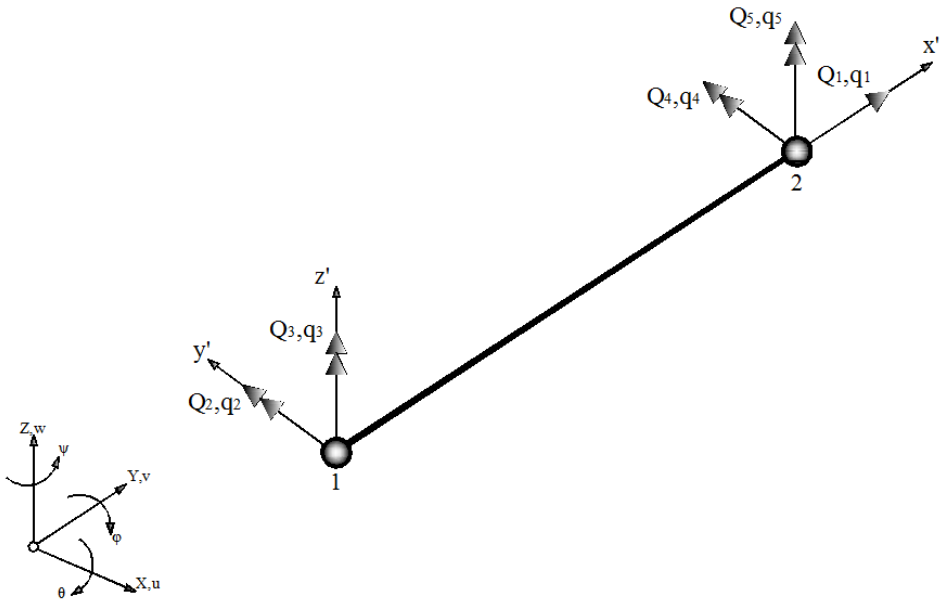

FIGURE 2.8 GENERALIZED DISPLACEMENTS AND FORCES OF NBCFB ELEMENT.

The section's force and deformation vectors have the form

$$\boldsymbol{D}(\xi) = \begin{Bmatrix} N(\xi) \\ M_y(\xi) \\ M_z(\xi) \end{Bmatrix} \qquad 2.87$$

$$\boldsymbol{d}(\xi) = \begin{Bmatrix} \varepsilon(\xi) \\ \chi_y(\xi) \\ \chi_z(\xi) \end{Bmatrix} \qquad 2.88$$

ReConAn FEA is appropriately constructed with the intention of minimizing the computational cost during the solution procedure. In order to accomplish this task, several parameters were selected to be available throughout the solution procedure. These constant and non-constant variables are stored dynamically in array type matrices and are reachable at any time and any

module of the code. In the fiber formulation, the geometrical and material inputs for each type of section are stored including fiber strain and stress vectors

$$\boldsymbol{e}(\xi)=\begin{Bmatrix}\varepsilon_1(\xi,y_1,z_1)\\ \vdots\\ \varepsilon_{ifiber}(\xi,y_{ifiber},z_{ifiber1})\\ \vdots\\ \varepsilon_n(\xi,y_n,z_n)\end{Bmatrix} \tag{2.89}$$

$$\boldsymbol{E}(\xi)=\begin{Bmatrix}\sigma_1(\xi,y_1,z_1)\\ \vdots\\ \sigma_{ifiber}(\xi,y_{ifiber},z_{ifiber1})\\ \vdots\\ \sigma_n(\xi,y_n,z_n)\end{Bmatrix} \tag{2.90}$$

where ξ describes the natural coordinate position of the section along the beam longitudinal axis and y_{ifiber}, z_{ifiber} are the fiber coordinates in the section's local coordinate system. The fiber strain vector $\boldsymbol{e}(\xi)$ and the section deformation vector $\boldsymbol{d}(\xi)$ are related by the matrix relation

$$\boldsymbol{e}(\xi)=\boldsymbol{l}(\xi).\boldsymbol{d}(\xi) \tag{2.91}$$

where $\boldsymbol{l}(\xi)$ is a linear geometric matrix

$$\boldsymbol{l}(\xi)=\begin{Bmatrix}1 & -z_1 & y_1\\ & \vdots & \\ 1 & -z_{ifiber} & y_{ifiber}\\ & \vdots & \\ 1 & -z_n & y_n\end{Bmatrix} \tag{2.92}$$

The Bernoulli hypothesis that the plane of the section remains plane and normal to the longitudinal axis gives us the ability to assume this linear connection between the two strain matrices, something that is rather unrealistic for RC structures especially when the structural members are shear dominated. More complex forms of the compatibility matrix $\boldsymbol{l}(\xi)$ can be used to account for the effects of shear.

2.5.2 Beam-Column Element Formulation

In the two-field mixed formulation of Zienkiewicz and Taylor[84-85] independent shape functions were used for approximating the force and deformation fields. In this work, we adopt the simplified mixed finite element method which is known as the flexibility or force method of Spacone et al.[33] who proposed a deformation shape function that simplifies the standard two-field mixed method into the flexibility method. Denoting with Δ the increments of the corresponding quantities, the two fields are expressed as follows:

$$\Delta \boldsymbol{d}^i(\xi) = \boldsymbol{a}(\xi).\Delta \boldsymbol{q} \tag{2.93}$$

$$\boldsymbol{D}^i(\xi) = \boldsymbol{b}(\xi).\boldsymbol{Q}^i \quad \text{and} \quad \Delta \boldsymbol{D}^i(\xi) = \boldsymbol{b}(\xi).\Delta \boldsymbol{Q}^i \tag{2.94}$$

where matrices $\boldsymbol{a}(\xi)$ and $\boldsymbol{b}(\xi)$ are the deformation and force interpolation matrices respectively. Parameter ξ represents the natural position of the Gauss-Lobato integration point (control-section). Superscript i denotes the i-th iteration of the NR scheme, until equilibrium is satisfied[84-85].

The integral forms of equilibrium and section force-deformation relations are combined to obtain the relation between element force and deformation increments. The weighted integral form of the linearized section force-deformation relation is given by

$$\int_0^L \delta \boldsymbol{D}^T(\xi).\left[\Delta \boldsymbol{d}^i(\xi) - \boldsymbol{f}^{i-1}(\xi).\Delta \boldsymbol{D}^i(\xi)\right] d\xi = 0 \tag{2.95}$$

and the flexibility form of the section force-deformation relation writes

$$\Delta \boldsymbol{d}^i(\xi) = \boldsymbol{f}^{i-1}(\xi).\Delta \boldsymbol{D}^i(\xi) \tag{2.96}$$

in order for the resulting element flexibility matrix $\boldsymbol{f}$ to be symmetric[84-85]. The superscript *i-1* indicates that the section flexibility matrix of the previous NR iteration is used. Substituting Eqs. 2.94 and 2.96 in Eq. 2.95 we get

$$\delta \boldsymbol{Q}^T \int_0^L \boldsymbol{b}^T(\xi).\left[\boldsymbol{a}(\xi).\Delta \boldsymbol{q}^i - \boldsymbol{f}^{i-1}(\xi).\boldsymbol{b}(\xi).\Delta \boldsymbol{Q}^i\right] d\xi = 0 \tag{2.97}$$

and since Eq. 2.97 must hold for any $\delta \boldsymbol{Q}^T$, it follows that

$$\left[\int_0^L \boldsymbol{b}^T(\xi).\boldsymbol{a}(\xi)\, d\xi\right].\Delta \boldsymbol{q}^i - \left[\int_0^L \boldsymbol{b}^T(\xi).\boldsymbol{f}^{i-1}(\xi).\boldsymbol{b}(\xi) d\xi\right].\Delta \boldsymbol{Q}^i = 0 \tag{2.98}$$

where

$$\boldsymbol{F}^{i-1} = \left[\int_0^L \boldsymbol{b}^T(\xi).\boldsymbol{f}^{i-1}(\xi).\boldsymbol{b}(\xi) d\xi\right] \tag{2.99}$$

$$\boldsymbol{T} = \left[\int_0^L \boldsymbol{b}^T(\xi).\boldsymbol{a}(\xi)\, d\xi\right] \tag{2.100}$$

$\boldsymbol{F}$ is the element flexibility matrix and $\boldsymbol{T}$ is a matrix that depends on the interpolation functions. Using Eq. 2.99 and Eq. 2.100, Eq. 2.98 can be written as

$$\boldsymbol{T}.\Delta \boldsymbol{q}^i = \boldsymbol{F}^{i-1}.\Delta \boldsymbol{Q}^i \tag{2.101}$$

which is the linearized section force-deformation relation in matrix format.

Next, the equilibrium of the beam element must be satisfied. The classical two-field mixed method requires that the integral form of the equilibrium equation is derived from the virtual displacement principle

$$\int_0^L \delta \boldsymbol{d}^T(\xi).\left[\boldsymbol{D}^i(\xi)+\Delta\boldsymbol{D}^i(\xi)\right]d\xi = \delta\boldsymbol{q}^T.\boldsymbol{P}^i \tag{2.102}$$

where $\boldsymbol{P}^i$ is the vector of the applied forces that have to be in equilibrium with the internal forces $\boldsymbol{D}^i(\xi)+\Delta\boldsymbol{D}^i(\xi)$. By substituting Eqs. 2.93 and 2.94 in Eq. 2.102 results in

$$\begin{gathered}\delta\boldsymbol{q}^T\left[\int_0^L \boldsymbol{a}^T(\xi).\left[\boldsymbol{b}(\xi)\boldsymbol{Q}^{i-1}+\boldsymbol{b}(\xi)\Delta\boldsymbol{Q}^i\right]d\xi\right]=\delta\boldsymbol{q}^T.\boldsymbol{P}^i \Rightarrow \\ \left[\int_0^L \boldsymbol{a}^T(\xi).\boldsymbol{b}(\xi)d\xi\right].\boldsymbol{Q}^{i-1}+\left[\int_0^L \boldsymbol{a}^T(\xi).\boldsymbol{b}(\xi)d\xi\right].\Delta\boldsymbol{Q}^i=\boldsymbol{P}^i\end{gathered} \tag{2.103}$$

and by using Eq. 2.100 we get in matrix notation the relation

$$\boldsymbol{T}^T.\boldsymbol{Q}^{i-1}+\boldsymbol{T}^T.\Delta\boldsymbol{Q}^i=\boldsymbol{P}^i \tag{2.104}$$

which is the matrix expression of the integral form of the element equilibrium equations. The rearrangement and combination of Eq. 2.101 and Eq. 2.104 results in

$$\begin{bmatrix}-\boldsymbol{F}^{i-1} & \boldsymbol{T}\\ \boldsymbol{T}^T & 0\end{bmatrix}.\begin{Bmatrix}\Delta\boldsymbol{Q}^i\\ \Delta\boldsymbol{q}^i\end{Bmatrix}=\begin{Bmatrix}0\\ \boldsymbol{P}^i-\boldsymbol{T}^T.\boldsymbol{Q}^{i-1}\end{Bmatrix} \tag{2.105}$$

Solving the above equation system in terms of $\Delta\boldsymbol{Q}^i$, the following expression is derived

$$\boldsymbol{T}^T.\left[\boldsymbol{F}^{i-1}\right]^{-1}.\boldsymbol{T}.\Delta\boldsymbol{q}^i=\boldsymbol{P}^i-\boldsymbol{T}^T.\boldsymbol{Q}^{i-1} \tag{2.106}$$

At this point the selection of force and deformation interpolation functions $\boldsymbol{\alpha}$ and $\boldsymbol{b}$ must be performed. Although, in the mixed FEM the deformation interpolation functions $\boldsymbol{\alpha}(x)$ are completely independent of $\boldsymbol{b}(x)$ (x represents the longitudinal axis of the beam), Mahasuverachai and Mahasuverachai and Powell[28] proposed a choice of the deformation shape functions $\boldsymbol{\alpha}(x)$ which simplifies considerably (Eq. 2.106). Replacing the parameter x with the ξ we get

$$\boldsymbol{a}(\xi)=\boldsymbol{f}^{i-1}(\xi).\boldsymbol{b}(\xi).\left[\boldsymbol{F}^{i-1}\right]^{-1} \tag{2.107}$$

These interpolation functions relate the section deformations with the corresponding element deformations according to

$$\Delta\boldsymbol{d}^i(\xi)=\boldsymbol{f}^{i-1}(\xi).\boldsymbol{b}(\xi).\left[\boldsymbol{F}^{i-1}\right]^{-1}.\Delta\boldsymbol{q}^i \tag{2.108}$$

where $\boldsymbol{F}^{i-1}$ is the tangent element flexibility matrix at the end of the *i-1* NR iteration. This special selection of deformation shape functions reduces matrix $\boldsymbol{T}$ in Eq. 2.106 to *3*x*3* identity matrix $\boldsymbol{I}$. To prove this statement we proceed with the following relation:

$$\boldsymbol{T} = \left[\int_0^L \boldsymbol{b}^T(\xi).\boldsymbol{a}(\xi)\,d\xi\right] = \left[\int_0^L \boldsymbol{b}^T(\xi).\boldsymbol{f}^{i-1}(\xi).\boldsymbol{b}(\xi).d\xi\right]\left[\boldsymbol{F}^{i-1}\right]^{-1} = \left[\boldsymbol{F}^{i-1}\right].\left[\boldsymbol{F}^{i-1}\right]^{-1} = \boldsymbol{I} \qquad 2.109$$

The above choice of the deformation shape functions $\boldsymbol{\alpha}(\xi)$ simplifies Eq. 2.106 into

$$\left[\boldsymbol{F}^{i-1}\right]^{-1}.\Delta\boldsymbol{q}^i = \boldsymbol{P}^i - \boldsymbol{Q}^{i-1} \qquad 2.110$$

and at the same time the two-field mixed finite element method reduces into the classical flexibility method. Eq. 2.110 expresses the linearized relation between the applied unbalanced forces $\boldsymbol{P}^i - \boldsymbol{Q}^{i-1}$ and the corresponding incremental displacements $\Delta\boldsymbol{q}^i$ at the element level.

The four main differences between the flexibility-based method and the classical stiffness method are a) the elements stiffness matrix is calculated by inverting the flexibility matrix, b) the element's state determination begins from the elements internal forces equilibrium, c) the section flexibility needs to be evaluated, which involves an inversion of the section stiffness obtained in the classical stiffness approach and d) codes that use the direct stiffness approach treat deformations as the primary unknown. The flexibility formulation provides numerical robustness to the nonlinear solution algorithm, which is attributed to the fact that the internal nonlinear state determination procedure computes the exact solution of the equilibrium between the resisting forces and the nodal displacements of each element, inducing numerical stability in the nonlinear NR solution procedure of the structure.

In order to extract the force distribution $\boldsymbol{D}(\xi)$ along the element from the generalized force vector $\boldsymbol{Q}$, a selection of the interpolation functions $\boldsymbol{b}(\xi)$ is required. If we take under consideration that the force field was selected so that the two bending moment fields $M_y(\xi)$ and $M_z(\xi)$ in Eq. 2.87 are linear and the axial force $N(x)$ is constant, the interpolation function becomes

$$\boldsymbol{b}(\xi) = \begin{Bmatrix} 1 & . & . & . & . & . \\ . & -1 & \xi & . & . & . \\ . & . & . & -1 & \xi & . \end{Bmatrix} \qquad 2.111$$

where ξ is the natural position coordinate of the Gauss-Lobato point (corresponding control-section) which is the integration method adopted in this work.

When one of the sections enters for the first time into the nonlinear strain-stress field, the update of the sections stiffness matrix is necessary. As it was indicated above, *ReConAn* stores the geometric and material data for each type of section and therefore all area and Young modulus for each fiber are stored in array type matrices. By denoting the array type matrix $\boldsymbol{A}$, with entries the areas A_{ifiber} of the fibers and the array type matrix $\boldsymbol{E}$ with entries the Young modulus E_{ifiber} of the fibers for each section type, then the section tangent stiffness matrix becomes

$$\boldsymbol{k}^j(\xi) = \boldsymbol{l}^T(\xi)\left(\boldsymbol{E}^j_{ifiber}\boldsymbol{A}_{ifiber}\right)\boldsymbol{l}(\xi) \qquad 2.112$$

which results in

$$\boldsymbol{k}^{j}(\xi)=\begin{bmatrix} \sum_{ifiber=1}^{nfibers} E_{ifiber}^{j}.A_{ifiber} & -\sum_{ifiber=1}^{nfibers} E_{ifiber}^{j}.A_{ifiber}.z_{ifiber} & \sum_{ifiber=1}^{nfibers} E_{ifiber}^{j}.A_{ifiber}.y_{ifiber} \\ -\sum_{ifiber=1}^{nfibers} E_{ifiber}^{j}.A_{ifiber}.z_{ifiber} & \sum_{ifiber=1}^{nfibers} E_{ifiber}^{j}.A_{ifiber}.z_{ifiber}^{2} & -\sum_{ifiber=1}^{nfibers} E_{ifiber}^{j}.A_{ifiber}.z_{ifiber}.y_{ifiber} \\ \sum_{ifiber=1}^{nfibers} E_{ifiber}^{j}.A_{ifiber}.y_{ifiber} & -\sum_{ifiber=1}^{nfibers} E_{ifiber}^{j}.A_{ifiber}.z_{ifiber}.y_{ifiber} & \sum_{ifiber=1}^{nfibers} E_{ifiber}^{j}.A_{ifiber}.y_{ifiber}^{2} \end{bmatrix} \quad 2.113$$

When the beam's section is located in the elastic range, the above formulation leads to the classical beam's stiffness matrix. It must be noted at this point, that when a section enters the nonlinear range, its fibers do not necessarily enter the plastic range, all at the same time. Therefore, some of the fibers can be in the nonlinear stress-strain state and the rest of them can still respond elastically capturing the phenomenon of the spreading plasticity.

To obtain the updated natural stiffness matrix of the NBCFB element, we have to calculate for each beam section its stiffness matrix and then invert each one of them to obtain the tangent flexibility matrix $\boldsymbol{f}^{j}(\xi)$ and then add their contribution (Eq. 2.114) to compute the beam flexibility matrix $\boldsymbol{F}$:

$$\underset{(6x6)}{\boldsymbol{F}} = \sum_{iSection}^{nSections} \underset{(6x3)}{b^{T}(\xi)}.\underset{(3x3)}{f^{iSection}(\xi)}.\underset{(3x6)}{b(\xi)}.w^{iSection} \quad 2.114$$

where the *w* parameter represents the sections integration weight factor. Finally, by inverting the beams natural flexibility matrix $\boldsymbol{F}$ we get the tangential (or elastic) natural stiffness matrix

$$\left[\underset{(6x6)}{\boldsymbol{K}_{Natural}^{beam}}\right]=[\underset{(6x6)}{\boldsymbol{F}_{beam}}]^{-1} \quad 2.115$$

Similarly, the section internal resisting forces $\boldsymbol{D}_{R}^{j}(\xi)$ cannot be obtained directly from the section force-deformation relation (Eq. 2.88), but are determined by summation of the axial force and biaxial bending contribution of the fibers as shown below

$$\boldsymbol{D}_{R}^{j}(\xi)=\boldsymbol{l}^{T}(\xi).\boldsymbol{E}^{j}.\boldsymbol{A} \quad 2.116$$

and after carrying the multiplications

$$\boldsymbol{D}_{R}^{j}(\xi)=\begin{Bmatrix} \sum_{ifiber=1}^{nfibers} \sigma_{ifiber}^{j}.A_{ifiber} \\ -\sum_{ifiber=1}^{nfibers} \sigma_{ifiber}^{j}.A_{ifiber}.z_{ifiber} \\ \sum_{ifiber=1}^{nfibers} \sigma_{ifiber}^{j}.A_{ifiber}.y_{ifiber} \end{Bmatrix} \quad 2.117$$

The relation that connects the section internal resisting forces $\boldsymbol{D}_{R}^{j}(\xi)$ with the general forces $\boldsymbol{Q}$ is

$$\underset{(6x1)}{\boldsymbol{Q}} = \sum_{iSection=1}^{nSections} \underset{(6x3)}{\boldsymbol{b}^T(\xi)} . \underset{(3x1)}{\boldsymbol{D}_R^{iSection}(\xi)} . w^{iSection} \quad 2.118$$

where *w* is the parameter that represents the sections Gauss-Lobato integration weight factor.

The relation that provides the element's internal forces in the Global Cartesian system is

$$\underset{(12x1)}{\boldsymbol{P}_{internal}} = \underset{(12x12)}{\boldsymbol{T}_{04}^T} . \underset{(12x6)}{\boldsymbol{a}_n^T} . \underset{(6x1)}{\boldsymbol{Q}} \quad 2.119$$

At this point, we are ready to move to the description of the modified nonlinear flexibility-based element's state determination procedure which is integrated with the natural mode method.

2.5.3 Integrated Beam-Column Flexibility-Based Element with the Natural Mode Method

In this section we are going to describe the NBCFB element's state determination integrated with the natural mode method. In order to be able to describe the state determination process, a few words on the nonlinear solution algorithm implemented in this study are necessary. *ReConAn* code architecture is based on a general in-core object-oriented structure which gives the ability to use any kind of material model or solution strategy. One of the nonlinear solution algorithms incorporated in our code, is the standard NR scheme (Fig. 1.6) which performs the update of the structures stiffness matrix whenever nonlinearities occur. Therefore, the total load is divided into *n* load increments and the external load vector $\boldsymbol{P}_{external}$ is varied in an incremental fashion at each NR load step.

Assuming that *k* stands for the *k*-th NR load step and *i* denotes the *i*-th NR internal iteration, then the incremental-iterative NR procedure can be described as follows:

1) ***Initialization.***
   Initialize all required variables including *k = 1, i = 1*.
2) ***Solve the global equation system and update the structural displacement increments.***

$$\Delta \boldsymbol{P}_{\mathrm{E}}^k = \left(\boldsymbol{K}_{structure}^k\right)^{i-1} . \left(\delta \Delta \boldsymbol{\rho}^k\right)^i \Rightarrow \left(\delta \Delta \boldsymbol{\rho}^k\right)^i = \left[\left(\boldsymbol{K}_{structure}^k\right)^{i-1}\right]^{-1} . \Delta \boldsymbol{P}_{\mathrm{E}}^k \quad 2.120$$

   If the internal iteration is greater than 1, then $\Delta \boldsymbol{P}_{\mathrm{E}}^{\boldsymbol{k}} = \left(\boldsymbol{P}_{\boldsymbol{U}}^{\boldsymbol{k}}\right)^{\boldsymbol{i-1}}$ where $\left(\boldsymbol{P}_{\boldsymbol{U}}^{\boldsymbol{k}}\right)^{\boldsymbol{i-1}}$ is the unbalanced load vector from the previous NR iteration. The unbalanced force vector is obtained as the difference between the total applied loads and the internal resisting forces at the end of the *i-1* NR iteration in step ***(18)***. A check is performed for the need to update the stiffness matrix before proceeding to the displacement calculation. The calculated structural incremental displacements $(\delta \Delta \boldsymbol{\rho}^k)^i$ are added to the displacement increments $(\Delta \boldsymbol{\rho}^k)^{i-1}$ which were calculated at the previous NR iteration *i-1* to obtain the new displacement increment $(\Delta \boldsymbol{\rho}^k)^i$ for iteration *i* inside the *k-th* load step.

$$\left(\Delta \boldsymbol{\rho}^k\right)^i = \left(\Delta \boldsymbol{\rho}^k\right)^{i-1} + \left(\delta \Delta \boldsymbol{\rho}^k\right)^i \quad 2.121$$

3) Compute the element's deformation increments.

By using the connection matrix $\boldsymbol{\alpha}_N$ and the direction cosine matrix $\boldsymbol{T}_{04}$ the change in the element deformation increments is computed from the structural displacement increments.

$$\underset{(6x1)}{\left(\delta\Delta\boldsymbol{q}^k\right)^i} = \underset{(6x12)}{\boldsymbol{a}_N} \cdot \underset{(12x12)}{\boldsymbol{T}_{04}} \cdot \underset{(12x1)}{\left(\delta\Delta\boldsymbol{p}^k\right)^i} \qquad 2.122$$

It must be noted here that the element displacement increments do not change during the element iteration loop *j*.

4) Start the element state determination.

Set $j = 1$.

5) Compute the change in the element force increment.

For $j = 1$, $\left((\delta\Delta\boldsymbol{Q}^k)^i\right)^1$ is *obtained* from the element displacement increments $(\delta\Delta\boldsymbol{q}^k)^i$ for the current NR iteration *i* using the element natural stiffness matrix.

$$\underset{(6x1)}{\left(\left(\delta\Delta\boldsymbol{Q}^k\right)^i\right)^1} = \underset{(6x6)}{\left(\boldsymbol{K}_N^k\right)^{i-1}} \cdot \underset{(6x1)}{\left(\delta\Delta\boldsymbol{q}^k\right)^i} \qquad 2.123$$

For $j > 1$, $\left((\delta\Delta\boldsymbol{Q}^k)^i\right)^j$ is obtained from the residual element deformation $\left((\boldsymbol{s}^k)^i\right)^{j-1}$ at the end *of* the previous element iteration *j-1* and the corresponding element natural stiffness matrix.

$$\underset{(6x1)}{\left(\left(\delta\Delta\boldsymbol{Q}^k\right)^i\right)^j} = \underset{(6x6)}{\left(\left(\boldsymbol{K}_N^k\right)^i\right)^{j-1}} \cdot \underset{(6x1)}{\left(\left(\boldsymbol{s}^k\right)^i\right)^{j-1}} \qquad 2.124$$

6) Update the element force increments and element resisting forces

With the change in the elements force increments $\left((\delta\Delta\boldsymbol{Q}^k)^i\right)^j$, an update of the previous vector is obtained by

$$\underset{(6x1)}{\left(\left(\Delta\boldsymbol{Q}^k\right)^i\right)^j} = \underset{(6x1)}{\left(\left(\Delta\boldsymbol{Q}^k\right)^i\right)^{j-1}} + \underset{(6x1)}{\left(\left(\delta\Delta\boldsymbol{Q}^k\right)^i\right)^j} \qquad 2.125$$

The current element resisting forces are calculated by adding the element force increments to the resisting force vector $\boldsymbol{Q}^{k-1}$ of the previous element iteration *k-1*:

$$\underset{(6x1)}{\left(\left(\boldsymbol{Q}^k\right)^i\right)^j} = \underset{(6x1)}{\boldsymbol{Q}^{k-1}} + \underset{(6x1)}{\left(\left(\Delta\boldsymbol{Q}^k\right)^i\right)^j} \qquad 2.126$$

7) Compute the section force increments.

In order to compute the element section force increments we must know the total number of Gauss-Lobato integration points. By using the interpolation functions $\boldsymbol{b}(\xi)$ the following equation gives the section force increments:

$$\underset{(3x1)}{\left(\left(\delta\Delta\boldsymbol{D}^k(\xi)\right)^i\right)^j} = \underset{(3x6)}{\boldsymbol{b}(\xi)} \cdot \underset{(6x1)}{\left(\left(\delta\Delta\boldsymbol{Q}^k\right)^i\right)^j} \qquad 2.127$$

$$\underset{(3x1)}{\left(\left(\Delta\boldsymbol{D}^k(\xi)\right)^i\right)^j} = \underset{(3x1)}{\left(\left(\Delta\boldsymbol{D}^k(\xi)\right)^i\right)^{j-1}} + \underset{(3x1)}{\left(\left(\delta\Delta\boldsymbol{D}^k(\xi)\right)^i\right)^j} \qquad 2.128$$

and the total section forces are computed by

$$\underset{(3x1)}{\left(\left(\boldsymbol{D}^{k}\left(\xi\right)\right)^{i}\right)^{j}}=\underset{(3x1)}{\boldsymbol{D}^{k-1}\left(\xi\right)}+\underset{(3x1)}{\left(\left(\Delta\boldsymbol{D}^{k}\left(\xi\right)\right)^{i}\right)^{j}} \qquad 2.129$$

8) Compute the change in section deformation increments.

The change in the section deformation increments $\left((\delta\Delta\boldsymbol{d}^{k}(\xi))^{i}\right)^{j}$ is computed from:

$$\underset{(3x1)}{\left(\left(\delta\Delta\boldsymbol{d}^{k}\left(\xi\right)\right)^{i}\right)^{j}}=\underset{(3x1)}{\left(\left(\boldsymbol{r}^{k}\left(\xi\right)\right)^{i}\right)^{j-1}}+\underset{(3x3)}{\left(\left(\boldsymbol{f}^{k}\left(\xi\right)\right)^{i}\right)^{j-1}}\underset{(3x6)}{\left(\boldsymbol{b}\left(\xi\right)\right)}.\underset{(6x6)}{\left(\left(\boldsymbol{K}_{N}^{k}\right)^{i}\right)^{j-1}}\underset{(6x1)}{\left(\left(\boldsymbol{s}^{k}\right)^{i}\right)^{j-1}} \qquad 2.130$$

then

$$\underset{(3x1)}{\left(\left(\Delta\boldsymbol{d}^{k}\left(\xi\right)\right)^{i}\right)^{j}}=\underset{(3x1)}{\left(\left(\Delta\boldsymbol{d}^{k}\left(\xi\right)\right)^{i}\right)^{j-1}}+\underset{(3x1)}{\left(\left(\delta\Delta\boldsymbol{d}^{k}\left(\xi\right)\right)^{i}\right)^{j}} \qquad 2.131$$

9) Compute the fiber deformation increments.

The fiber deformation increments are computed by using the section compatibility matrix ***l(x)*** of Eq. 2.92 and the fiber deformation increments are updated as follows:

$$\underset{(1x1)}{\left(\left(\delta\Delta\boldsymbol{e}^{k}\left(\xi\right)\right)^{i}\right)^{j}}=\underset{(1x3)}{\boldsymbol{l}\left(x\right)}.\underset{(3x1)}{\left(\left(\delta\Delta\boldsymbol{d}^{k}\left(\xi\right)\right)^{i}\right)^{j}} \qquad 2.132$$

then

$$\underset{(1x1)}{\left(\left(\Delta\boldsymbol{e}^{k}\left(\xi\right)\right)^{i}\right)^{j}}=\underset{(1x1)}{\left(\left(\Delta\boldsymbol{e}^{k}\left(\xi\right)\right)^{i}\right)^{j-1}}+\underset{(1x1)}{\left(\left(\delta\Delta\boldsymbol{e}^{k}\left(\xi\right)\right)^{i}\right)^{j}} \qquad 2.133$$

and the fiber deformations are updated by

$$\underset{(1x1)}{\left(\left(\boldsymbol{e}^{k}\left(\xi\right)\right)^{i}\right)^{j}}=\underset{(1x1)}{\boldsymbol{e}^{k-1}\left(\xi\right)}+\underset{(1x1)}{\left(\left(\Delta\boldsymbol{e}^{k}\left(\xi\right)\right)^{i}\right)^{j}} \qquad 2.134$$

10) Compute fiber stresses and update the tangent modulus of the fibers.

By using the current fiber deformation of Eq. 2.134, the fiber material subroutine will compute the fiber normal stresses and the updated Young's modulus of each fiber.

11) Compute the section tangent stiffness and flexibility matrices.

From step ***(10)*** we obtain the updated Young's modulus for each fiber and with the help of Eq. 2.113 the calculation of the current section tangent (or elastic) stiffness matrix $\left(\left(k^{k}(\xi)\right)^{i}\right)^{j}$ is carried out. By inverting the computed stiffness matrix, the flexibility matrix is obtained.

$$\underset{(3x3)}{\left(\left(\boldsymbol{f}^{k}\left(\xi\right)\right)^{i}\right)^{j}}=\left[\underset{(3x3)}{\left(\left(\boldsymbol{k}^{k}\left(\xi\right)\right)^{i}\right)^{j}}\right]^{-1} \qquad 2.135$$

12) Compute the section resisting forces.

Eq. 2.117 determines the section internal forces which are derived explicitly from the fiber stresses.

13) Compute the sections unbalanced forces.

The difference between applied loads and resisting forces results in the section unbalanced forces:

$$\underset{(3x1)}{\left(\left(\boldsymbol{D}_U^k(\xi)\right)^i\right)^j} = \underset{(3x1)}{\left(\left(\boldsymbol{D}^k(\xi)\right)^i\right)^j} - \underset{(3x1)}{\left(\left(\boldsymbol{D}_R^k(\xi)\right)^i\right)^j} \qquad 2.136$$

14) Compute the residual section deformations.

$$\underset{(3x1)}{\left(\left(\boldsymbol{r}^k(\xi)\right)^i\right)^j} = \underset{(3x3)}{\left(\left(\boldsymbol{f}^k(\xi)\right)^i\right)^j} \cdot \underset{(3x1)}{\left(\left(\boldsymbol{D}_U^k(\xi)\right)^i\right)^j} \qquad 2.137$$

15) Compute the element flexibility matrices.

The element flexibility matrix is computed by numerical integration and more precisely by the Gauss-Lobato integration rule, of section flexibilities

$$\underset{(6x6)}{\left(\left(\boldsymbol{F}^k\right)^i\right)^j} = \sum_{i\text{sec}=1}^{tot.num.\text{sec}} \left[w_{i\text{sec}} \cdot \underset{(6x3)}{\boldsymbol{b}^T(\xi_{i\text{sec}})} \cdot \underset{(3x3)}{\left(\left(\boldsymbol{f}^k(\xi_{i\text{sec}})\right)^i\right)^j} \cdot \underset{(3x6)}{\boldsymbol{b}(\xi_{i\text{sec}})} \right] \qquad 2.138$$

where *tot.num.sec* is the total number of Gauss-Lobato integration points (total number of control sections), ξ_{isec} is the natural position coordinate of the section along the beam length and w_{isec} is the corresponding weight factor. We must state here that in the case of natural modes all elements of the 6^{th} row and column of the flexibility matrix are equal to zero. This is attributed to the values of the 6^{th} column of the matrix $\boldsymbol{b}(\xi)$ which are equal to zero and therefore the corresponding values of the flexibility matrix $\left(\left(\boldsymbol{F}^k\right)^i\right)^j$ become equal to zero. Finally, the element's stiffness matrix is obtained by inverting the flexibility matrix $\underset{(5x5)}{\left(\left(\boldsymbol{F}^k\right)^i\right)^j}$ and the main diagonal stiffness coefficient $\left(\left(\boldsymbol{K}(6,6)^k\right)^i\right)^j$ corresponds to the torsional stiffness:

$$\underset{(5x5)}{\left(\left(\boldsymbol{K}^k\right)^i\right)^j} = \left[\underset{(5x5)}{\left(\left(\boldsymbol{F}^k\right)^i\right)^j}\right]^{-1}, \qquad \left(\left(\boldsymbol{K}^k(6,6)\right)^i\right)^j = \frac{GJ_P}{L} \qquad 2.139$$

16) Check for element convergence.

The convergence criterion that was implemented in this work was an energy-based criterion given by Eq. 2.140 and its tolerance was set to 10^{-16}.

if $(tolerance > error)$ ***then*** $\rightarrow$ *exit*

$$error = \frac{\left[\left(\left(\boldsymbol{s}^k\right)^i\right)^j\right]^T \cdot \left(\left(\boldsymbol{K}^k\right)^i\right)^j \cdot \left(\left(\boldsymbol{s}^k\right)^i\right)^j}{\left(\Delta\boldsymbol{q}^k\right)^T \cdot \left(\left(\boldsymbol{K}^k\right)^i\right)^1 \cdot \left(\Delta\boldsymbol{q}^k\right)} \qquad 2.140$$

where $\boldsymbol{s}^k$ is the residual element deformation

$$\underset{(6x1)}{\left(\left(\boldsymbol{s}^k\right)^i\right)^j} = \sum_{i\text{sec}=1}^{tot.num.\text{sec}} \left[weight_{i\text{sec}} \cdot \underset{(6x3)}{\boldsymbol{b}^T(\xi_{i\text{sec}})} \cdot \underset{(3x1)}{\left(\left(\boldsymbol{r}^k(\xi_{i\text{sec}})\right)^i\right)^j} \right] \qquad 2.141$$

If the convergence criterion is satisfied then we proceed to the next step, otherwise we return to step ***(5)*** and increase *j* by *1*.

17) Compute the resisting forces of each element and the internal forces of the structure - Update the stiffness matrix of the structure.

When all NBCFB elements manage to converge, the *i*-th NR iteration is completed regarding the calculation of the internal forces at structural level. The internal forces of the structure $\left(\boldsymbol{P}_R^k\right)^i$ are calculated by assembling all element internal forces $\left(\boldsymbol{Q}_{ele}^k\right)^i$ according to the expression

$$\underset{(12x1)}{\left(\boldsymbol{P}_{ele}^k\right)^i} = \underset{(12x12)}{\boldsymbol{T}_{04}^T} \cdot \underset{(12x6)}{\boldsymbol{a}_n^T} \cdot \underset{(6x1)}{\left(\boldsymbol{Q}_{ele}^k\right)^i}, \qquad 2.142a$$

then

$$\left(\boldsymbol{P}_R^k\right)^i = \sum_{iele=1}^{num.ele} \left(\boldsymbol{P}_{iele}^k\right)^i \qquad 2.142b$$

The structural stiffness matrix is updated by assembling the element stiffness matrices

$$\underset{(12x12)}{\left(\boldsymbol{K}_{ele}^k\right)^i} = \underset{(12x12)}{\boldsymbol{T}_{04}^T} \cdot \underset{(12x6)}{\boldsymbol{a}_n^T} \cdot \underset{(6x6)}{\left(\boldsymbol{K}_N^k\right)^i} \cdot \underset{(6x12)}{\boldsymbol{a}_n} \cdot \underset{(12x12)}{\boldsymbol{T}_{04}}, \qquad 2.143a$$

then

$$\left(\boldsymbol{K}_S^k\right)^i = \sum_{iele=1}^{num.ele} \left(\boldsymbol{K}_{ele}^k\right)^i \qquad 2.143b$$

18) Compute the unbalanced forces of the structure.

$$\left(\boldsymbol{P}_U^k\right)^i = \boldsymbol{P}_E^k - \left(\boldsymbol{P}_R^k\right)^i \qquad 2.144$$

where $\boldsymbol{P}_E^k$ is computed from the total applied load at the current NR load step *k*.

$$\boldsymbol{P}_E^k = \boldsymbol{P}_E^{k-1} + \Delta\boldsymbol{P}_E^k \qquad 2.145$$

19) Check for global convergence.

If the convergence criterion at structural level is achieved, then we can proceed to the next load step, otherwise we increase *i* by *1* and return to step ***(2)*** for the *i+1* NR iteration. In this work, an energy based convergence criterion was used to check if the solution converged. The convergence tolerance selected for all numerical applications was 10^{-4}.

20) Check if the prescribed load is achieved.

If the entire external load was applied the analysis is complete, otherwise we increase *k* by *1* and proceed to the computation of the new external load vector and return to step ***(2)***. Spacone et al[33] proposed that in this step all force and deformation vectors are updated by adding the vector increments of the previous load step *k* to the corresponding total forces and deformations. The proposed nonlinear state determination algorithm does not require something similar because the update and storage of all current variables is done in-core during the element's state determination process.

2.5.4 Fiber Constitutive Material Models

ReConAn material library contains several 1D material models, among them the Menegotto-Pinto[86] for the reinforcing steel bars and the Kent-Park[87] for confined and unconfined concrete. As it was mentioned above, the NBCFB element uses the fiber approach which means that the nonlinear behavior of the proposed finite element derives entirely from the nonlinear behavior of the fibers. Consequently the accuracy of the arithmetical results depends on the numerical reliability of the fiber material models. It is important to note here that both material stress-strain models are explicit functions of strain. This means that in order to determine the stress field the only necessary variable is that of the strain increment which are determined from the section increment deformations.

2.5.4.1 Steel Stress-Strain Relation

The Menegotto-Pinto[86] material model is presented in this sub-section. The steel stress-strain model has the form[88]

$$\sigma^* = b \cdot \varepsilon^* + \frac{(1-b)\cdot \varepsilon^*}{\left(1-\varepsilon^{*R}\right)^{1/R}} \qquad 2.146$$

where

$$\varepsilon^* = \frac{\varepsilon - \varepsilon_r}{\varepsilon_0 - \varepsilon_r} \qquad 2.147$$

and

$$\sigma^* = \frac{\sigma - \sigma_r}{\sigma_0 - \sigma_r} \qquad 2.148$$

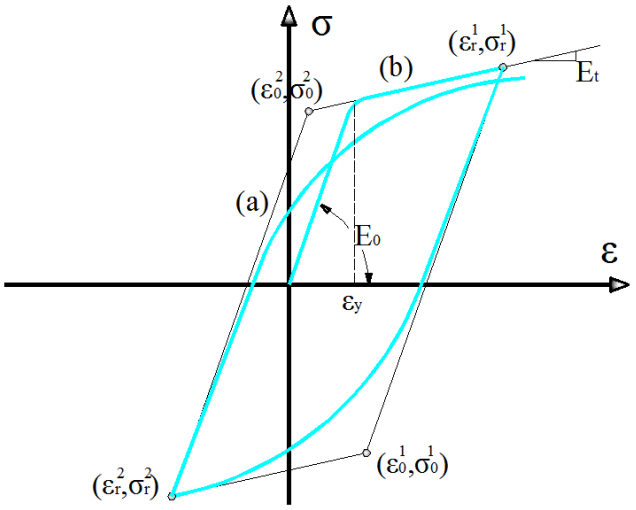

FIGURE 2.9 MENEGOTTO – PINTO STEEL MODEL.

Fig. 2.9 illustrates the theoretical curve of the Menegotto-Pinto[86] material model and Fig. 2.10 represents the curve for the specific values of the characteristic parameters used in this work. R_0 is the value of the parameter R during the first loading and a_1, a_2 are experimentally determined

parameters together with R_0. This particular material model was also integrated with the Filippou et al.[88] isotropic hardening

$$R = R_0 - \frac{a_1 \cdot \xi}{a_2 + \xi} \qquad 2.149$$

where ξ is updated following a strain reversal. The definition of ξ remains valid in case that reloading occurs after partial unloading.

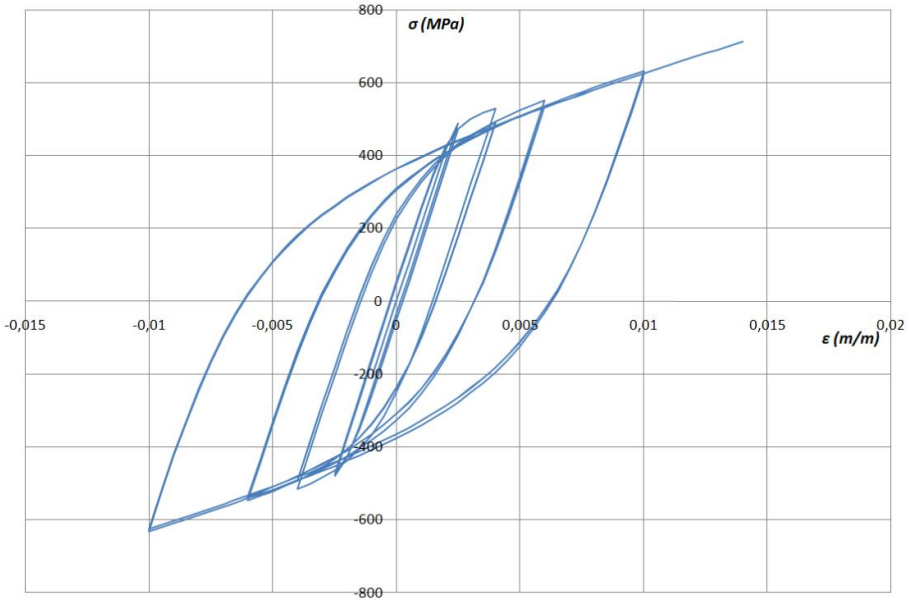

FIGURE 2.10 MENEGOTTO – PINTO STEEL MODEL FOR THE SPECIFIC PARAMETERS USED IN THIS WORK ($R_0 = 20$, $a_1 = 18.5$, $a_2 = 0.15$, $f_y = 500MPa$).

Regarding the simplicity of the formulation, its major drawback stems from its failure to allow for isotropic hardening. To account for this effect Filippou et al.[88] proposed a stress shift in the linear yield asymptote as a function of the maximum plastic strain as follows:

$$\frac{\sigma_{st}}{\sigma_y} = \alpha_3 \left(\frac{\varepsilon_{\max}}{\varepsilon_y} - \alpha_4 \right) \qquad 2.150$$

where ε_{max} is the absolute maximum strain at the instant of strain reversal, ε_y, σ_y are, the strain and stress at yield, respectively, and α_3, α_4 are experimentally determined parameters which are set to zero in this study.

2.5.4.2 Concrete Stress-Strain Relation

The monotonic envelope curve of concrete material in compression is modeled with the use of a Kent-Park[87] concrete material model that was later extended by Scott et al.[89]. The so-called modified Kent-Park model offers simplicity and accuracy at the same time and it is considered to be arithmetically one of the most efficient and convenient 1D material models. In the modified Kent-Park model the monotonic stress-strain relation in compression is divided into three regions.

$$\varepsilon_c \le \varepsilon_0 \qquad \sigma_c = K \cdot f_c' \left[2\left(\frac{\varepsilon_c}{\varepsilon_0}\right) - \left(\frac{\varepsilon_c}{\varepsilon_0}\right)^2 \right] \tag{2.151}$$

$$\varepsilon_0 \le \varepsilon_c \le \varepsilon_u \qquad \sigma_c = K \cdot f_c' \left[1 - Z\left(\varepsilon_c - \varepsilon_0\right) \right] \ge 0.2K \cdot f_c' \tag{2.152}$$

where

$$\varepsilon_0 = 0.002 \cdot K \tag{2.153}$$

$$K = 1 + \frac{\rho_s f_{y\,hoop}}{f_c'}, \qquad Z = \frac{0.5}{\frac{3 + 0.29 f_c'}{145 f' - 1000} + 0.75\rho_s \sqrt{\frac{h'}{s_h}} - 0.002 \cdot K} \tag{2.154}$$

ε_0 is the concrete strain at maximum stress, K is a factor which takes account for the strength increase due to confinement, Z is the strain softening slope, f_c' is the concrete compressive cylinder strength in *MPa*, $f_{y\,hoop}$ is the yield strength of stirrups in *MPa*, ρ_s is the ratio of the volume of hoop reinforcement to the volume of concrete core measured outside of stirrups, h' is the width of concrete core measured outside the stirrups and s_h is the center to center spacing of stirrups or hoop sets.

When concrete is assumed to be inside the confinement area of the beam's section (concrete located inside stirrups), Scott et al.[89] suggest that ε_u can be computed conservatively from

$$\varepsilon_u = 0.004 + 0.9 \cdot \rho_s \cdot \left(f_{s\,hoop} / 300 \right) \tag{2.155}$$

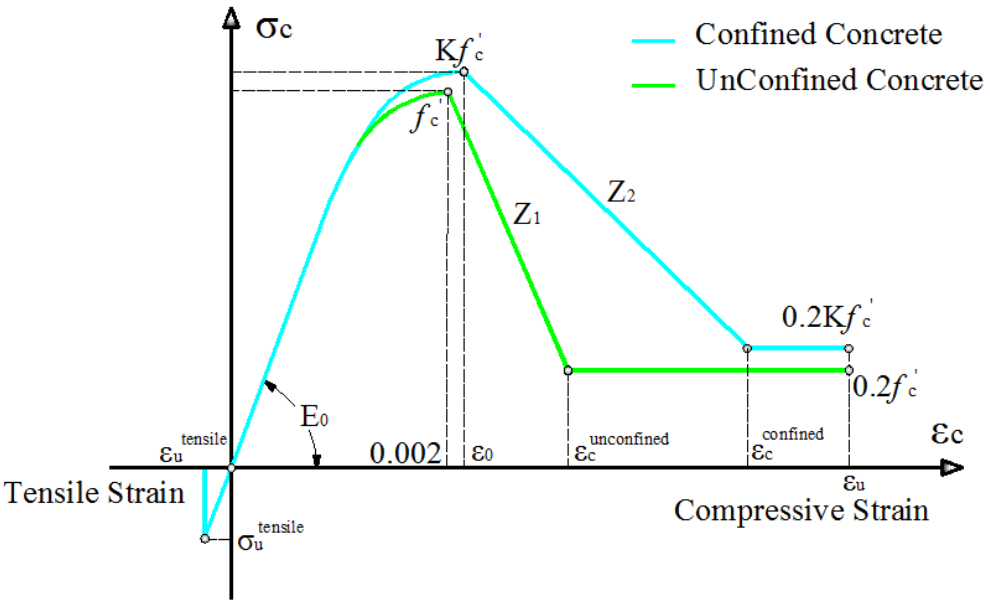

FIGURE 2.11 KENT – PARK CONCRETE MODEL WITH TENSILE STRENGTH FOR MONOTONIC LOADING.

In order to take into consideration the crushing of concrete, the strength is reduced to $0.2f_c'$ and $0.2Kf_c'$ once the compressive strain exceeds the value of ε_c. We must note that in the Kent-Park model, the tensile strength is neglected. In our model the tensile strength is accounted through the use of a simple linear relationship that requires only one percentile parameter.

$$\sigma_u^{tensile} = p_t \cdot f_c' \qquad 2.156$$

where p_t is the tensile strength percentile parameter. Fig. 2.12 shows the arithmetical data retrieved from a numerical simulation that was performed from *ReConAn* and illustrates the stress-strain relationship for a single fiber during the analysis. Fig. 2.13 shows the corresponding fiber normal strain history. We must note here that compression is assumed to have a positive sign in both graphs.

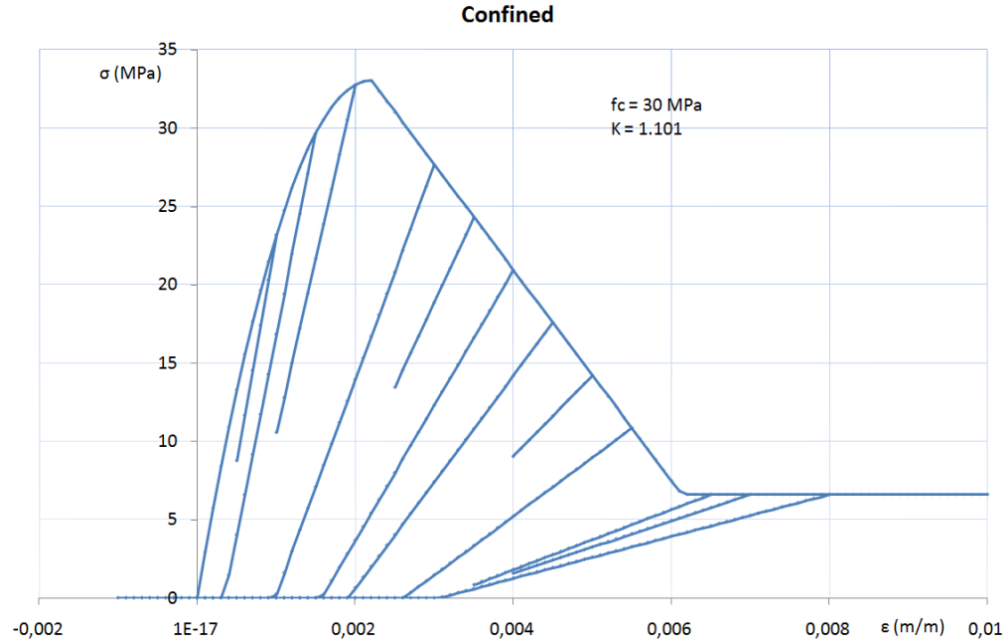

FIGURE 2.12 KENT – PARK CONCRETE MODEL FROM ANALYSIS DATA ($f_c = 30MPa$, $K = 1.101$).

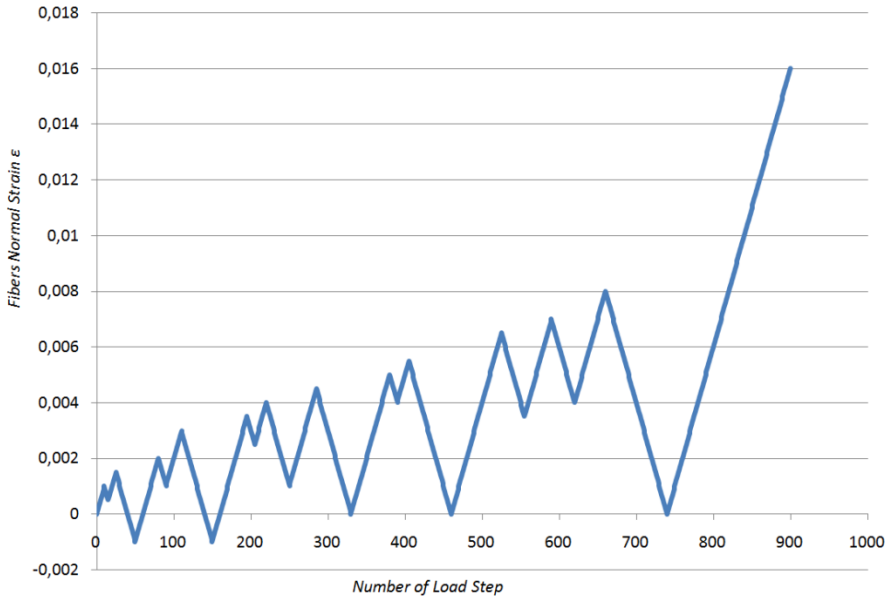

FIGURE 2.13 SCHEMATIC REPRESENTATION OF THE NORMAL STRAIN HISTORY OF A CONCRETE FIBER.

2.6 Computational Experiments

Many researchers use software packages such as OpenSees[90] and Fedeas[55] in order to perform several numerical simulations by using various element types and material models. OpenSees seems to be the most popular thanks to its simplicity, the existence of a variety of FEM models, its computational efficiency and numerical robustness. OpenSees, is written in C++ programming language and uses Tcl scripting language in order to interpret the input data into FEM analysis data. In addition to that it is one of the few software packages that contain the flexibility-based element, therefore it was chosen for the comparison tests that will be presented in the following sub-sections.

We proceed with the numerical experiments by using specific models that were chosen in order to illustrate the numerical robustness and efficiency of the NBCFB element and consequently the computational superiority of *ReConAn* FEA. All FEM models that will be presented were analyzed by using the nonlinear incremental-iterative force-control NR algorithm. For the numerical simulations a *1.9GHz* processor was used (personal laptop) with *2GB* DDR2 Ram.

2.6.1 Cantilever I Beam

The first tests example is the cantilever steel I beam shown in Fig. 2.14 with a vertical load on its right end (*P = 600 kN*). Its length is equal to *3 m* and the I section dimensions are illustrated in Fig. 2.14. The FEM model is shown in Fig. 2.15 which consists of *10* elements. The material model used in this numerical experiment is the Menegotto – Pinto with Young modulus, tangent modulus and yield stress equal to: $E = 200\ GPa$, $E_t = 2\ GPa$ and $f_y = 500\ MPa$, respectively. In order to make this problem computationally demanding we set the number of Gauss-Lobato points equal to *10* for each element, the number of fibers to *400* for each section and the number of loading steps equal to *1000*.

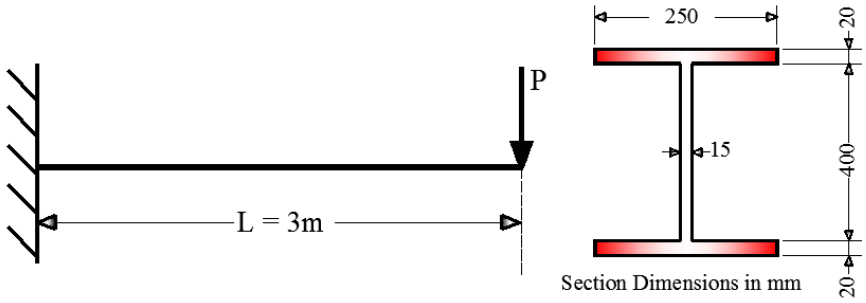

FIGURE 2.14 CANTILEVER I BEAM.

As it was stated previously, OpenSees uses a Tcl scripting language so as to interpret input data into FEM analysis data, meaning that a txt style input file is required. For rather simple FEM models this type of input generation is adequate. When the FEM models become large, txt type input files become difficult to manipulate and especially to control. For this reason, *ReConAn* was given the ability to read and write neutral type files of the pre- and post- processing FEA program Femap[91]. Furthermore, an external program ("SMAD Custom Properties" by G.Stavroulakis) is used for assigning customized parameters to the required FEM properties for the purpose of introducing extra parameters like the number of fibers, rebar elements etc. that Femap does not include in its basic property types.

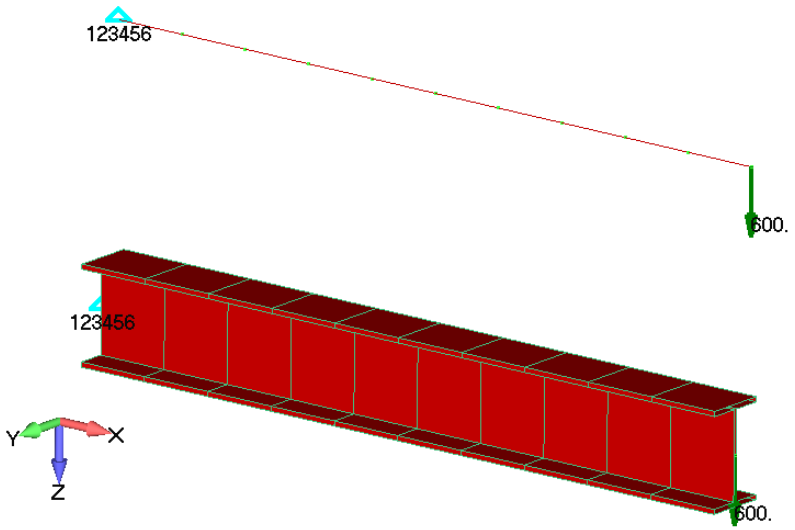

FIGURE 2.15 CANTILEVER I BEAM. FE MESH.

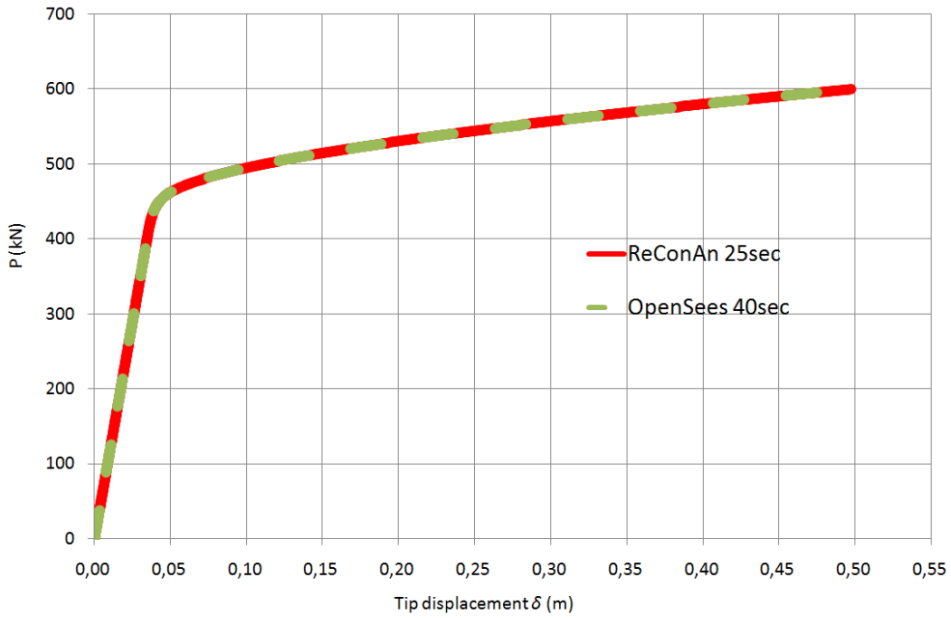

FIGURE 2.16 CANTILEVER I BEAM. *P-δ* CURVE.

Fig. 2.16 shows the *P-δ* curves for both software packages and as it can be seen they are identical. On the other hand, if we compare the required computational time *ReConAn* is *1.5* times faster than OpenSees. This shows the computational efficiency of the developed code which results from the formulation of the natural mode method that the NBCFB element is integrated with. It is also clear that the *P-δ* curves match without any variations even after the cantilever beam enters the inelastic range.

It is important to point out at this point, that an extensive sensitivity investigation was conducted with *ReConAn* (Vasilomichelaki[92-93]) in order to examine the numerical behavior of the NBCFB element. The main conclusions of this research work were the following:

1. The results are not sensitive to load increment deviations, meaning that when the load increment is increased the predicted *P-δ* curve is not affected. This is attributed to the

nonlinear state determination procedure and the numerical robustness of the developed FEA code.

2. The element is not affected from the degree of discretization, maintaining its accuracy even for the case where only a single element is used for the simulation of a structural member. This numerical phenomenon is attributed to the use of the nonlinear state determination procedure integrated with the natural mode method, Gauss-Lobato integration scheme and the fiber approach, utilizes the element in predicting the stiffness matrix degradation of the structural member accurately capturing the plasticity distribution during the loading history.
3. The computational robustness and efficiency of the developed nonlinear code is very satisfactory.

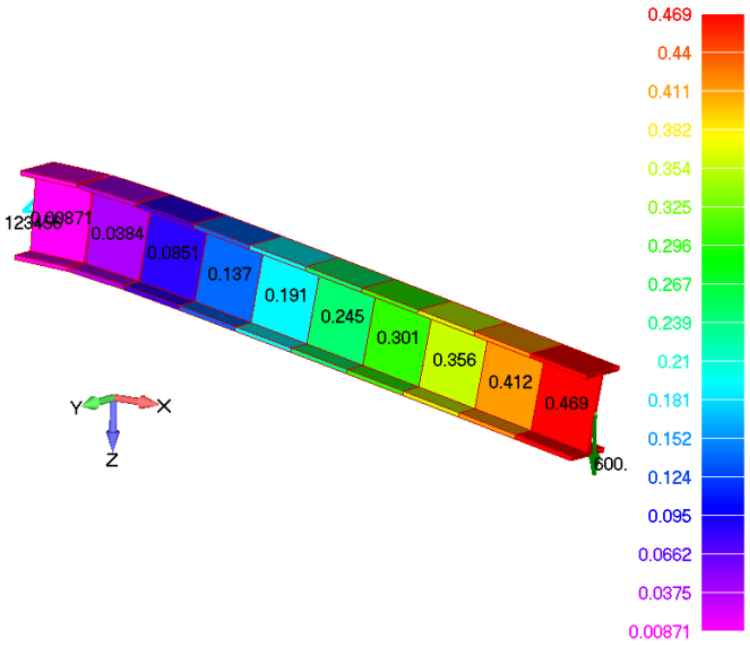

FIGURE 2.17 CANTILEVER I BEAM. DEFORMED SHAPE AT THE FINAL LOAD STEP.

Before moving to the next test example, it is worth mentioning that, the speed of the developed code with regards to Fedeas[55] code is obvious since the latter is a matlab code which is much slower.

2.6.2 Cantilever RC Beam

The second numerical test is a RC cantilever beam depicted in Fig. 2.18. The discretization and boundary conditions that were used in this case are the same with that of the previous test example. The vertical load applied to the edge of the cantilever is equal to *120 kN* and the FEM model and analysis parameters the same as before (number of fibers, NR load steps, Gauss-Lobato points).

The material characteristics that were used for the concrete material model were: $E_c = 30\ GPa$ and $f_c = 30\ MPa$, (Young modulus and compressive strength, respectively). The corresponding material characteristics of the reinforcing steel bars were: $E_s = 210\ GPa$, $E_t = 2.1\ GPa$, $f_y = 500$

MPa and h_c = *30 mm*, where E, E_t, f_y and h_c are the Young modulus, the tangent modulus, the yielding stress and the concrete cover width, respectively.

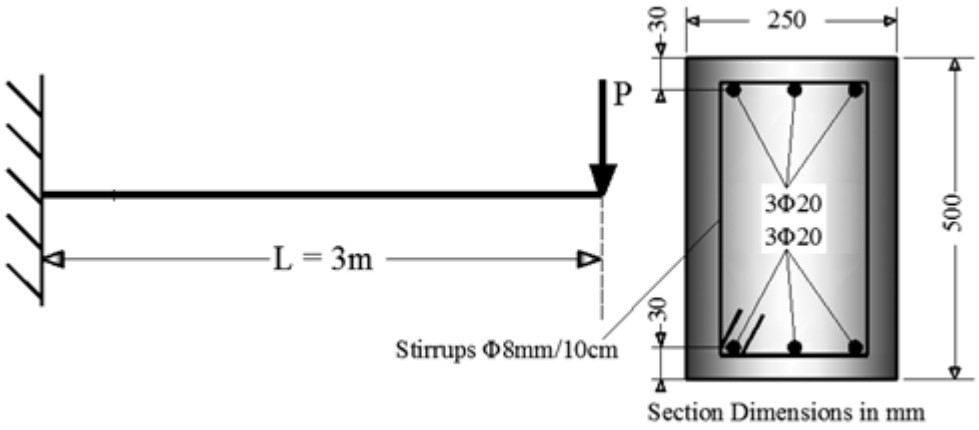

FIGURE 2.18 CANTILEVER RC BEAM. GEOMETRIC AND REINFORCEMENT DETAILS.

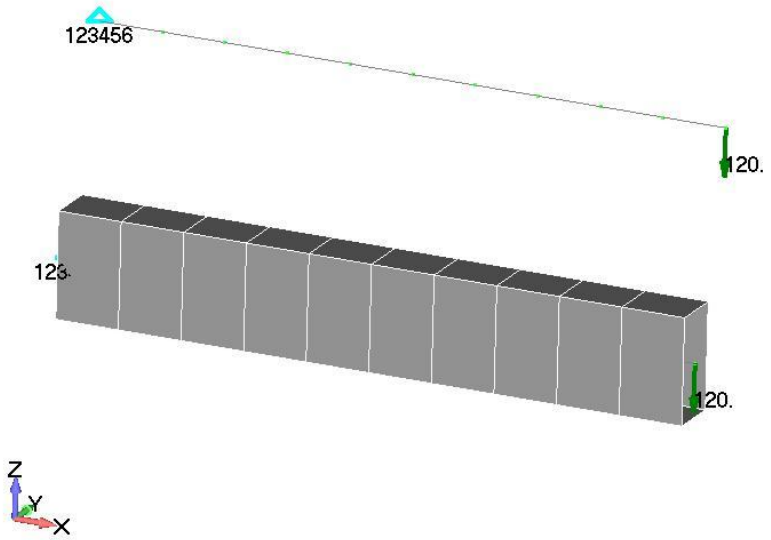

FIGURE 2.19 CANTILEVER RC BEAM. DISCRETIZATION WITH RC BEAMS.

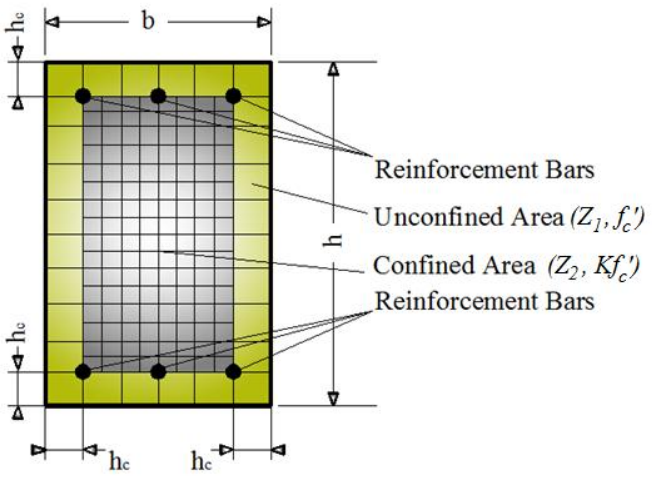

FIGURE 2.20 DISCRETIZATION OF THE RECTANGULAR RC SECTION WITH FIBERS.

The discretization of the rectangular section with fibers is performed by dividing the section into two main regions. The first region is the unconfined area corresponding to the concrete cover width as it can be seen in Fig. 2.20 and the second region is the confined concrete area, which is discretized by using a finer grid as illustrated in Fig. 2.20. When the fiber discretization procedure is performed, the appropriate material model is assigned to each fiber and the geometric characteristics are properly stored, providing the required information during the analysis procedure.

From the obtained results it can be seen that the NBCFB element of the *ReConAn* code manages to solve *843* load steps in *1 min* with a total tip displacement of *37 cm*. On the other hand, OpenSees ends its solution procedure at load step *733* as it was unable to converge beyond the load level of *88 kN*. The numerical robustness of the developed code is attributed to the same reasons previously discussed and the improved code architectural structure which will be described at a later stage in this Dissertation . The incorporation of advanced numerical techniques, equipped *ReConAn* with the ability to reduce the necessary computational effort and converge faster in predicting the nonlinear response with accuracy and computational efficiency. Concerning the computational time, this can be approximately estimated and is in favor of *ReConAn*.

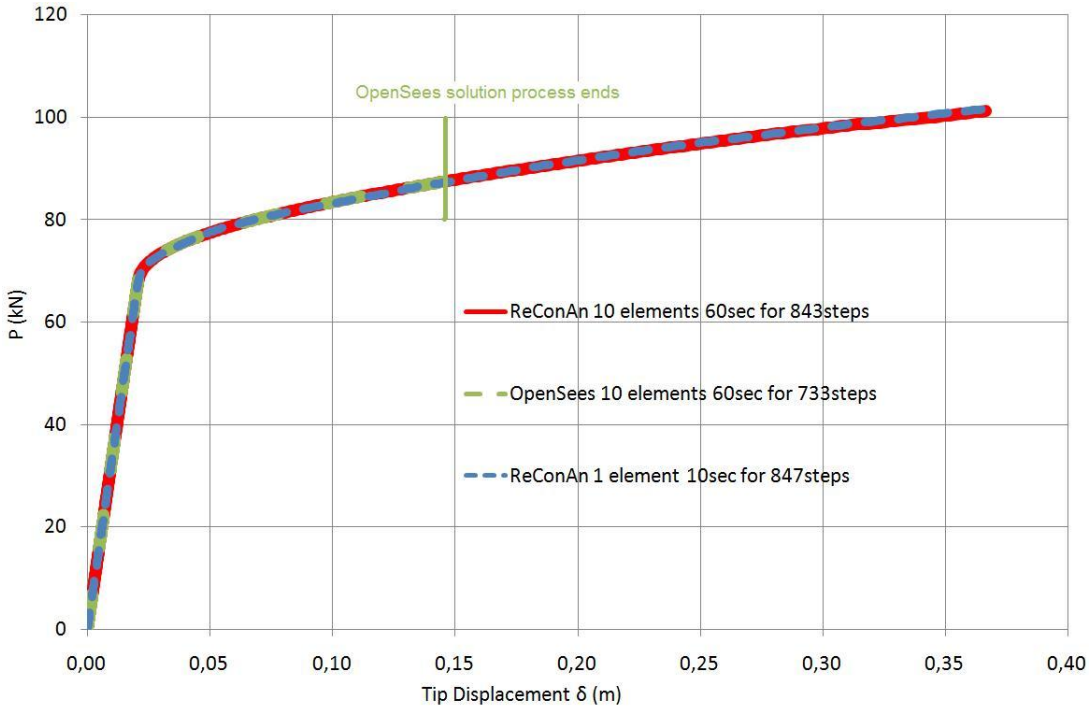

FIGURE 2.21 CANTILEVER RC BEAM. *P-δ* CURVE.

To conclude with this numerical test and illustrate the robustness of the NBCFB element, the same problem was solved with only a single NBCFB element. The *P-δ* curve can be seen in Fig. 2.21 and it is clear that the reproduced numerical results were the same with those obtained when discretizing the cantilever beam with *10* NBCFB elements. This shows that as a result of the element's formulation, it is feasible to discretize structural members with one element per structural member and reduce significantly the computational effort without losing the required accuracy.

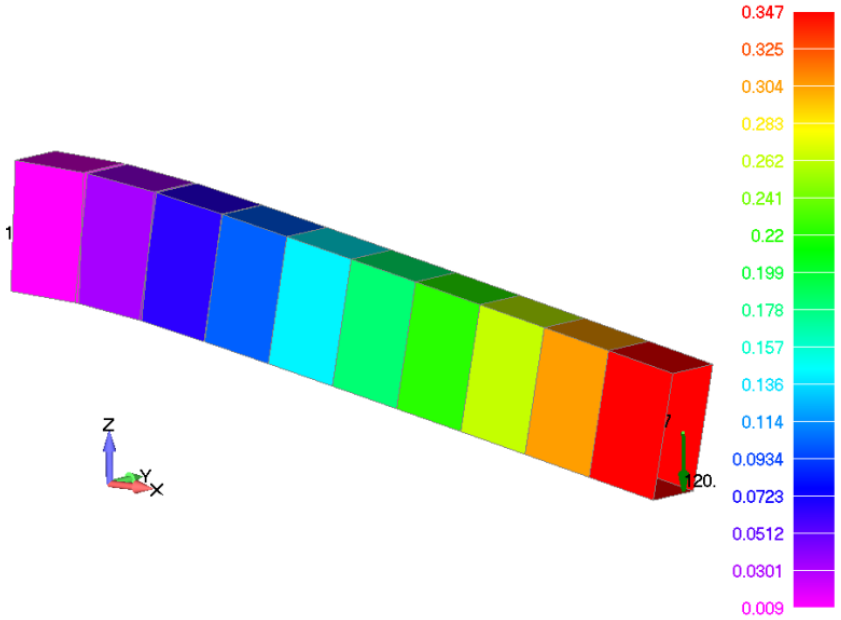

FIGURE 2.22 CANTILEVER RC BEAM. DEFORMED SHAPE AT THE FINAL NR LOAD STEP. DISPLACEMENT CONTOUR.

As it was mentioned in the previous section, an extended parametric investigation on the behavior of the steel and RC NBCFB element can be found in the Diploma and M.Sc. Theses conducted by Vasilomichelaki[92-93]. One of the most interesting result of this work, was obtained for a similar cantilever RC beam modeled with *10* elements, *10* Gauss-Lobato per element, *1000* fibers per control section and the collapse load was divided into *5* and *1000* load increments, respectively. For both load increment scenarios *ReConAn* managed to predict the maximum capacity load (*166 kN*) without any numerical instabilities. Furthermore, the corresponding CPU times illustrate the computational superiority of the developed code (Table 2.1).

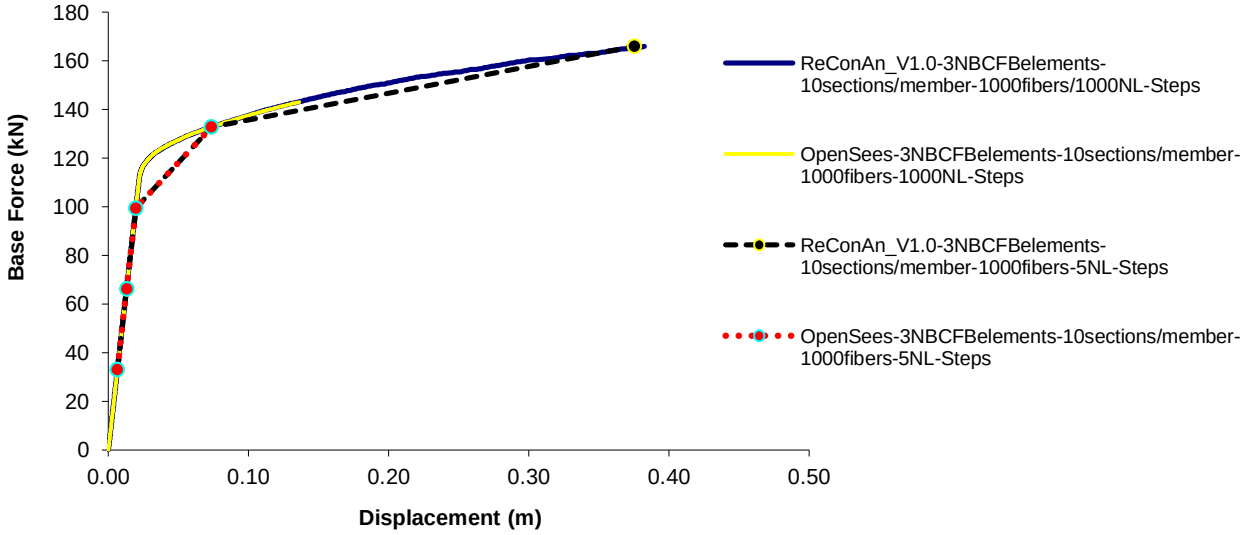

FIGURE 2.23 RC CANTILEVER BEAM[93]. *P-δ* CURVES OBTAINED BY *RECONAN* AND OPENSEES FOR *5* AND *1000* LOAD STEPS.

Program	*Load steps analyzed*	*Required CPU time (sec)*
ReConAn	1000	23.8
Opensees	862	23.9

TABLE 2.1 RC CANTILEVER BEAM[93]. CPU TIME FOR THE NONLINEAR ANALYSIS PROCEDURE.

2.6.3 RC Frame

In continuation to the above parametric investigation, a single-span RC frame is considered with the geometrical features illustrated in Fig. 2.24. It is assumed that the structural members of the frame are reinforced identically and the corresponding material properties are provided in Table 2.2. As can be seen from Fig. 2.24, the sections have the same rectangular geometry (*20x40 cm*) with *5Φ14* longitudinal rebar on the upper and lower sectional regions (concrete cover *3 cm*). The RC frame span is *4.60 m*, its height measures *2.80 m* and is considered to be fixed on its base.

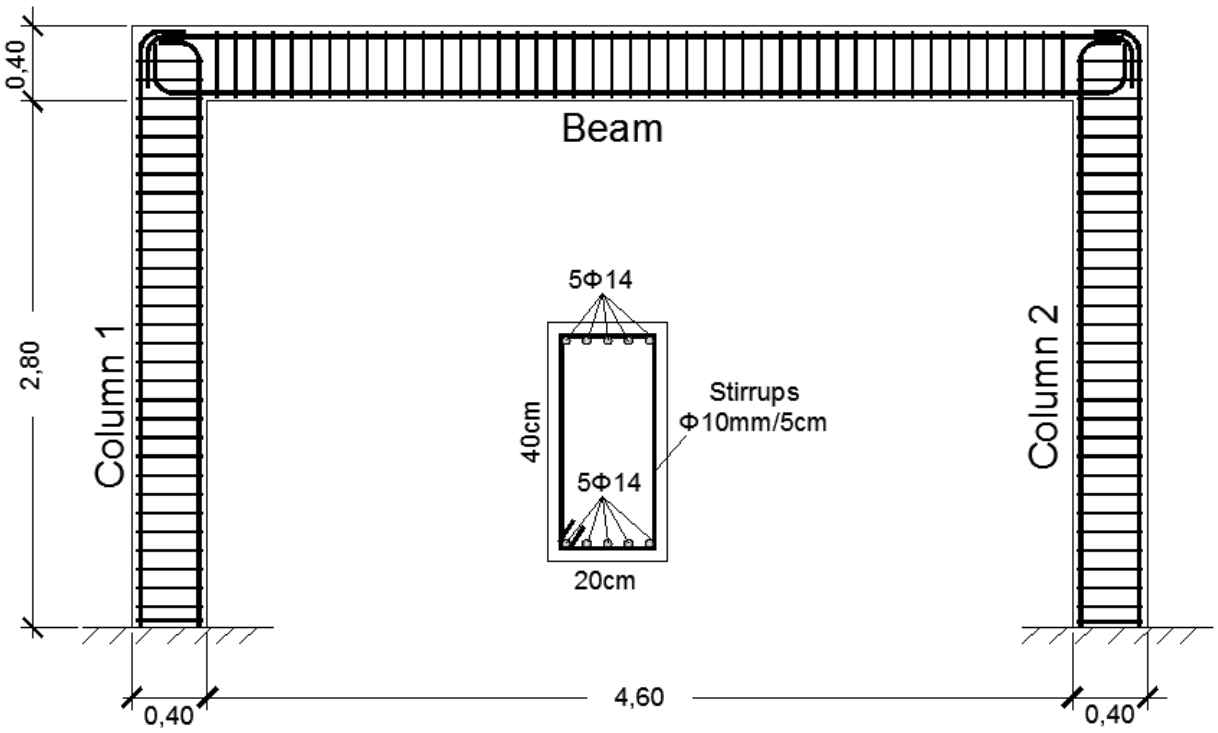

FIGURE 2.24 RC FRAME. GEOMETRIC CHARACTERISTICS AND REINFORCING DETAILS.

Material	*Yielding Stress (MPa)*	*Compressive Strength (MPa)*	*Young Modulus E_0 (GPa)*	*Hardening Parameter $b = E_T / E_0$*
Concrete	-	35	28	-
Steel	500	-	210	0.0085

TABLE 2.2 RC FRAME. MATERIAL DETAILS.

Two FE models were created in order to analyze this RC frame, by discretizing each structural member with *1* and *5* NBCFB elements, respectively. The first FE model can be seen in Fig. 2.25, where *4* Gauss-Lobato points were applied for each element and their corresponding control-sections were discretized with *400* fibers. A horizontal load was applied on the upper

left node of the frame and the number of load increments was set to *25*. The NR energy tolerance criterion was set to 10^{-4} and the corresponding tolerance of the state determination procedure was set to 10^{-16}.

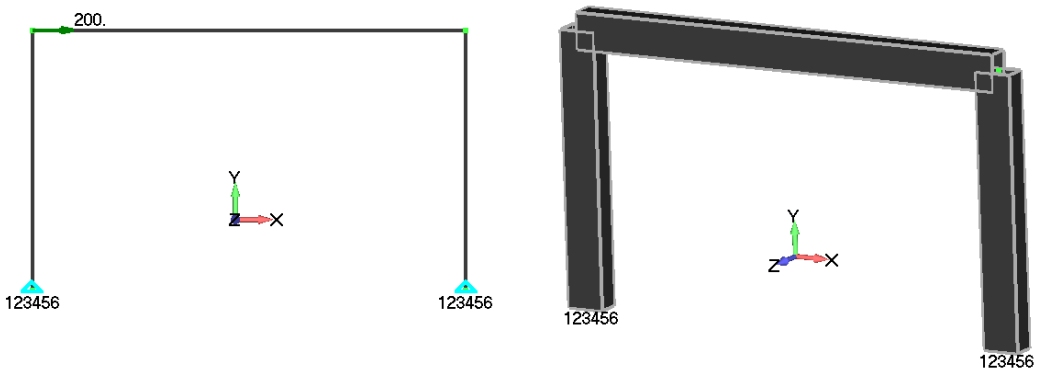

FIGURE 2.25 RC FRAME. FE MODEL WHEN DISCRETIZING WITH *1* ELEMENT PER STRUCTURAL MEMBER.

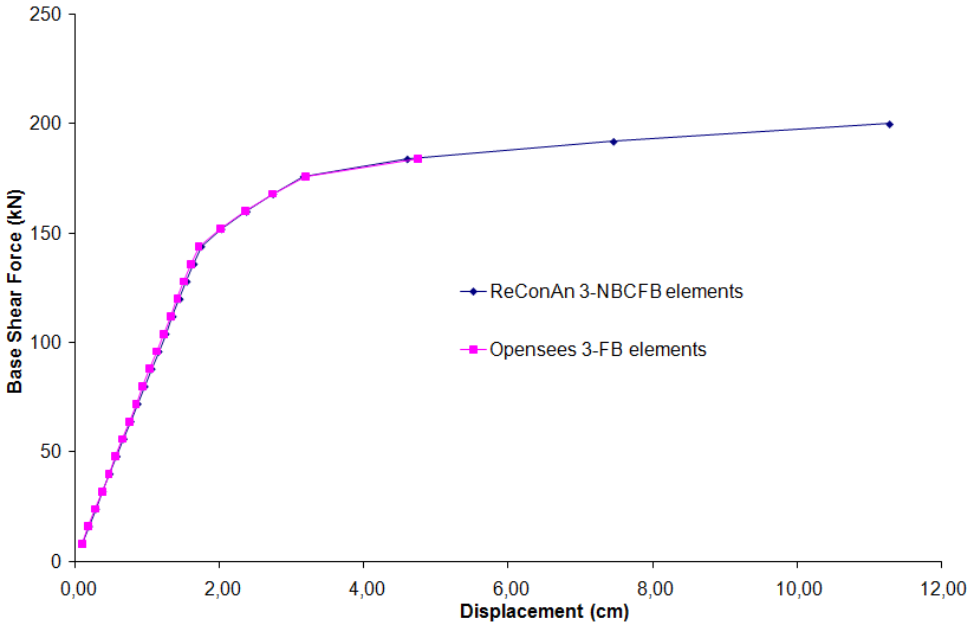

FIGURE 2.26 RC FRAME. *P-δ* CURVE FOR THE CASE OF DISCRETIZING WITH *1* ELEMENT PER STRUCTURAL MEMBER.

Fig. 2.26 illustrates the base shear force vs. horizontal displacement of the upper left node for the first FE model, where it can be seen that the two curves are identical when the frame is in the elastic region and in the first inelastic branch of the inelastic region. When the total horizontal load reaches a value of *144 kN* the reinforcement of the beam yields and when the total horizontal load reaches *176 kN* the reinforcement of the columns also yields deteriorating even more the stiffness of the RC frame (second reduction of the slope of the *P-δ* curve). The second characteristic point is also the point where OpenSees fails to converge on elemental level due to high nonlinearities. On the other hand *ReConAn* manages to continue with the nonlinear steps predicting the inelastic branch of the *P-δ* curve without any significant convergence problems. Once again, the previous conclusions are confirmed through this test example illustrating the computational robustness of the developed FEA code.

As it was presented previously, the natural mode method leads to a *6x6* decreased elemental stiffness matrix (natural matrix) which is used during the nonlinear state determination procedure. This has the advantage of reducing the numerical error induced due to the precision of the numerical computations regarding the natural stiffness matrix during the state determination procedure and makes the process more stable. Additionally, the NBCFB element is shear lock free and computations during the state determination stage are not affected by this numerical phenomenon.

The second FE model is produced by discretizing each structural member with *5* beam elements, considering *4* Gauss-Lobato points for each finite element and *400* fibers per control-section (Fig. 2.27).

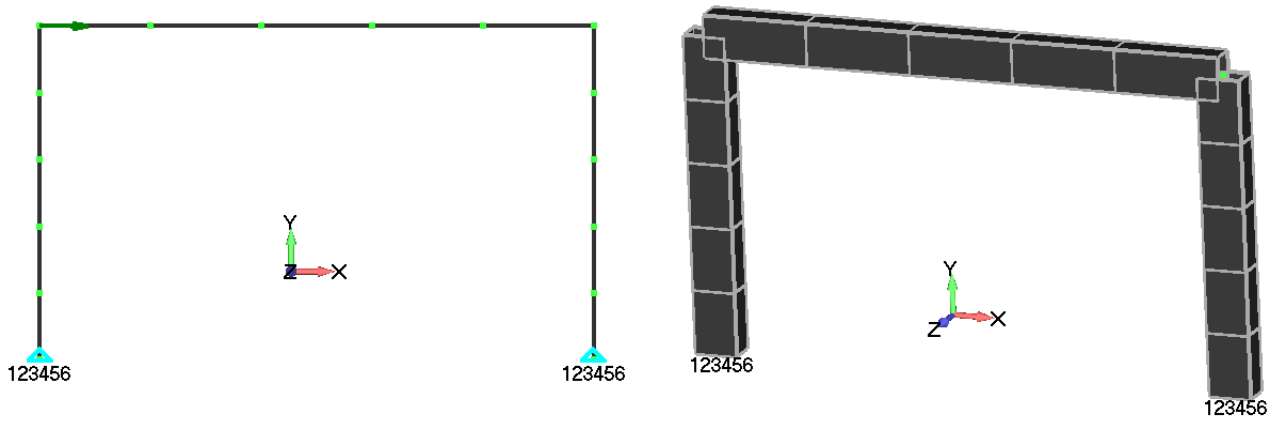

FIGURE 2.27 RC FRAME. FE MODEL WHEN DISCRETIZING WITH *5* ELEMENTS PER STRUCTURAL MEMBER.

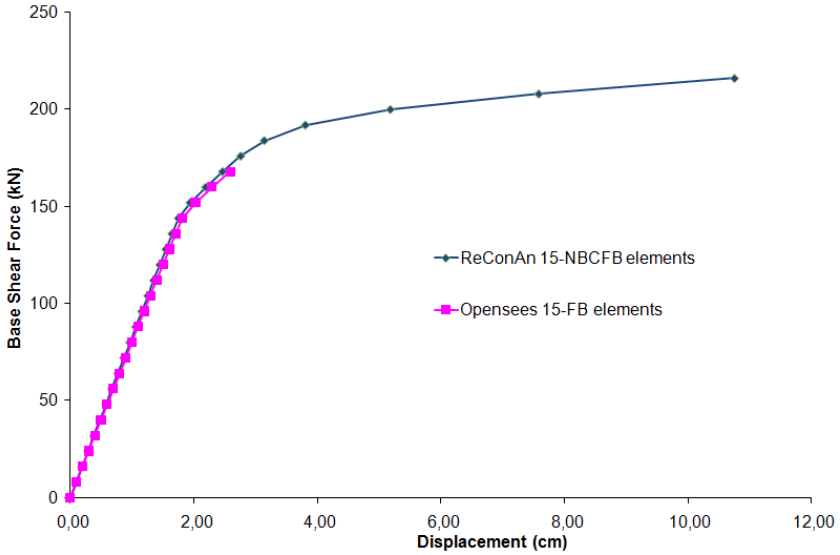

FIGURE 2.28 RC FRAME. *P-δ* CURVE FOR THE CASE OF DISCRETIZING WITH *5* ELEMENTS PER STRUCTURAL MEMBER.

From Fig 2.28 it can be seen that the two curves are the same when the reinforcement response is at the elastic range. After yielding occurs and the nonlinearities become excessive (point where the second reduction of the slope Fig. 2.28), OpenSees fails to converge terminating the analysis procedure prematurely. Despite the large nonlinearities *ReConAn* continues the numerical procedure managing to predict the entire inelastic branch without any numerical

instabilities. The deformed shapes of the frame are depicted in Fig. 2.29. The ZY view illustrates that the FE model manages to predict the in-plane deformation without producing out-of-plane displacements.

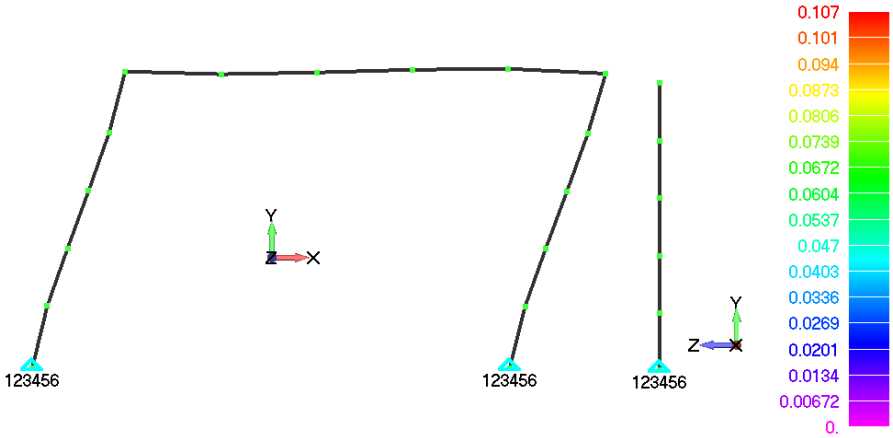

FIGURE 2.29 RC FRAME. DEFORMED SHAPES. XY AND YZ VIEWS.

2.6.4 High Rise RC Building

A full scale 37-storey RC building with I beam shear braces was designed (Figs. 2.30 and 2.31) specifically for this numerical test in order to illustrate the computational capabilities of the proposed FEA code and how the earthquake resistant design of this structure can be improved.

Structural Member Type	*Levels applied*	*Concrete Compr./ Tensile Strength (MPa)*	*Concrete Young Modulus (GPa)*	*Steel Yield Stress (MPa)*	*Steel Young and Hardening Modulus (GPa)*	*Steel Failure Strain (m/m)*	*Number of Gauss-Lobato Points and Fibers/Section*
Column100x100	-	60.0/3.0	50.0	555.0	210.0 / 2.1	0.10	5 / 400
Column75x75	1-19	60.0/3.0	50.0	555.0	210.0 / 2.1	0.10	5 / 300
Column60x60	19-37	60.0/3.0	50.0	555.0	210.0 / 2.1	0.10	5 / 300
Beam40x80	1-30	60.0/3.0	50.0	555.0	210.0 / 2.1	0.10	5 / 200
Beam35/70	31-37	60.0/3.0	50.0	555.0	210.0 / 2.1	0.10	5 / 200
IPE600	-	-	-	355.0	210.0 / 2.1	0.10	5 / 200

TABLE 2.3 RC HIGH RISE BUILDING. MATERIAL CHARACTERISTICS AND FIBER DATA FOR INITIAL CARCASS.

Fig. 2.30 illustrates the initial plan views of the building carcass and as it can be seen its base has a total area of *1298.88 m*^{2} (*45.40*x*28.60 m*). Each storey has a height of *3.50 m* and the total height of the building is *129.50 m* (*37-stories* x *3.50 m*). At the *15*th and *30*th floors, a change in geometry occurs as is depicted in Fig. 2.31 where inclined steel I beam-column elements are placed (IPE600) for structural reasons in order to strengthen the transition areas. The same steel sections were used for the shear braces located at the sides and at the center of the building (Fig. 2.31). In Table 2.3 material characteristics and fiber data for each section used in the FE models can be found.

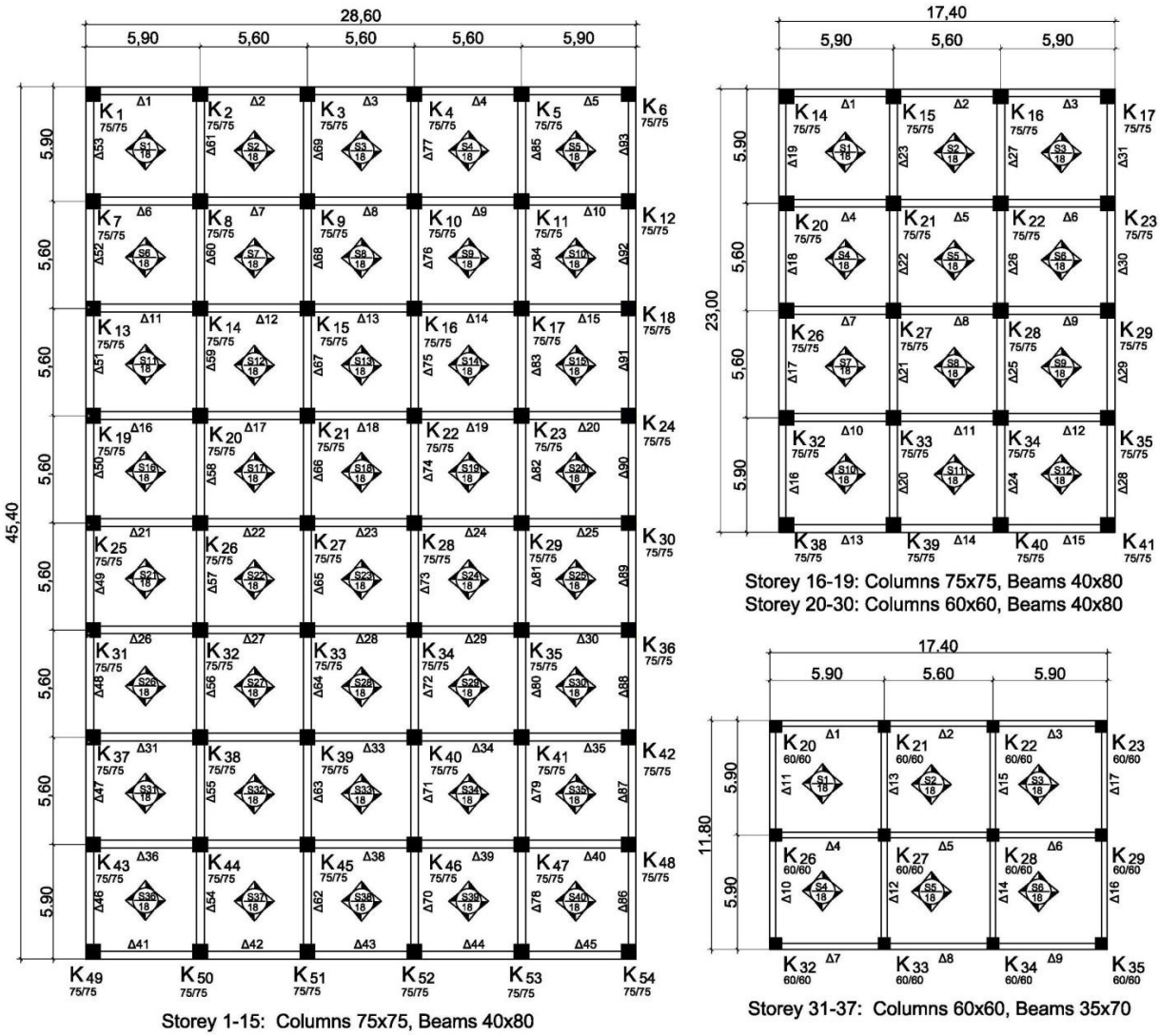

FIGURE 2.30 RC HIGH RISE BUILDING. PLAN VIEWS AT DIFFERENT LEVELS.

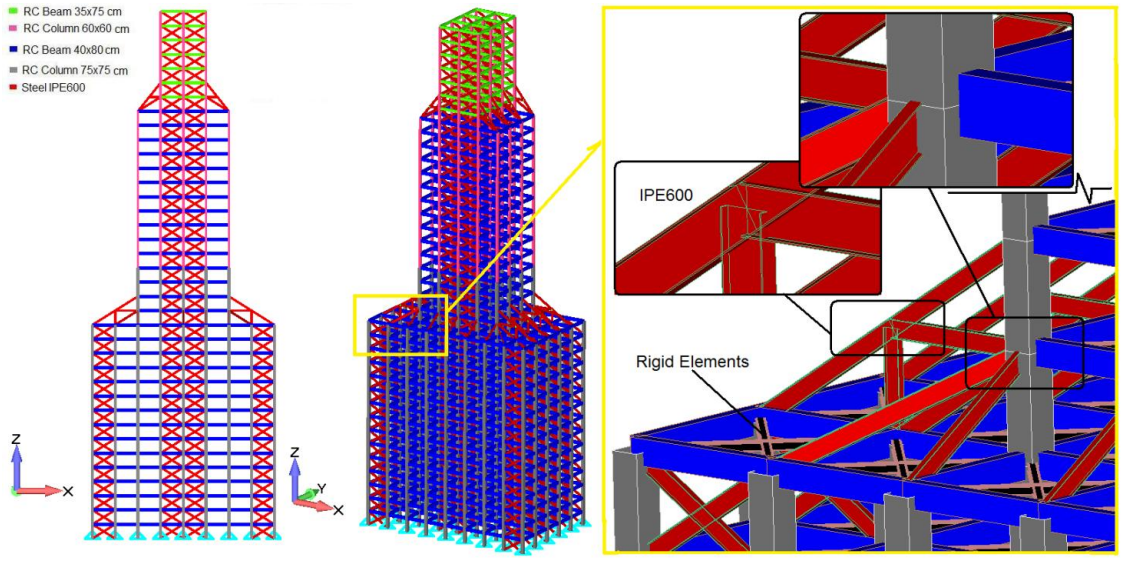

(A) (B)

FIGURE 2.31 RC HIGH RISE BUILDING. INITIAL FEM MODEL (A) FRONT AND (B) 3D VIEW.

As it was mentioned previously, NBCFB element has the advantage of using one element per structural member without losing the desired accuracy of the nonlinear analysis decreasing this way the total dof of the FE model. By applying this discretization rule (one finite element per structural member) a FE model for this building is created which consists of *5,855* NBCFB elements and *1,264* nodes. It is also assumed that each slab acts as a diaphragm which is modeled with rigid elements. Regarding the boundary conditions, all nodes that are located on the base of the structure are considered to be fixed (Fig. 2.31) and the horizontal loads are computed by using the EC8 earthquake design code (Design Spectrum).

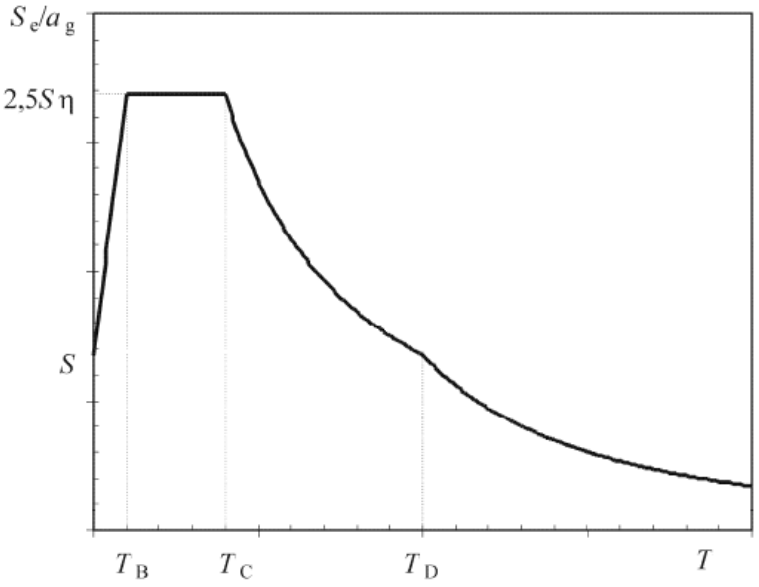

FIGURE 2.32 SHAPE OF THE ELASTIC RESPONSE SPECTRUM (EC8).

$$P_{base\ shear}^{total} = M \cdot S_d(T) \tag{2.157}$$

$$S_d(T) = \gamma_I \cdot a_g \cdot S \cdot \frac{2.5}{q} \cdot \frac{T_C \cdot T_D}{T^2}, \quad \text{for } T_D \le T \le 4s \tag{2.158}$$

where M and $S_d(T)$ are the effective mass of the structure and the response spectrum acceleration, respectively, while γ_I is the importance building factor, T is the vibration period, a_g is the design ground acceleration, S is the soil factor, q is the behavior factor, T_C is the upper limit of the period of the constant spectral acceleration branch and T_D is the value defining the beginning of the constant acceleration response range of the spectrum (Fig. 2.32) where the fundamental period of this structure is located.

According to EC8, the distribution of the base shear force is computed as follows

$$P_{horizontal}^{i} = P_{base\ shear}^{total} \frac{m_i z_i}{\sum_{j=1}^{n} m_j z_j} \tag{2.159}$$

where m_i, m_j are the storey masses computed and z_i, z_j are the heights of the masses above the level of application of the seismic action (foundation or top of a rigid basement). The assumptions made regarding the several parameters of Eqs. 2.157 and 2.158 are given in Table 2.4.

Given that the computed fundamental period of the structure in the load direction (x axis) is *3.25 sec*, the normalized horizontal load distribution was computed according to EC8 and is given in Table 2.5. We must point out here that the dead loads caused from the structure's self-

weight of the beams and columns were also accounted for during the base shear force computations of the building and were applied in the FE model by activating the body load command. The vertical load that is depicted at the end of Table 2.5 was distributed to each storey nodes according to the structural mass distribution.

Parameters of EC8	*Value*
Ground Type	A
T_C	0.4 sec
T_D	2.0 sec
S	1
q	1
Acceleration a_g	0.24g
Importance Class	IV
Importance Factor γ_I	1.4

TABLE 2.4 RC HIGH RISE BUILDING. EC8 PARAMETERS.

Four different analyses were performed using *50*, *20*, *10* and *6* load steps, respectively. The *P-δ* curves can be seen in Fig. 2.34, the deformed shape prior to failure for the *10* NR load steps case, in Fig. 2.35 and Table 2.6 contains the computational times required for the solution of the four analysis cases. Regarding the size of this numerical problem, the required skyline storage for the stiffness matrix was *1,888,662* double precision variables and the required RAM for the solution procedure was approximately *800 Mb*. Since the required computational times are affordable (Table 2.6), it is clear that the limitation when solving this kind of problems with *ReConAn*, becomes the *2 Gb* maximum size (*32bit* system) for allocating the stiffness matrix of the structure, which is always the largest array of the numerical problem. This limitation can be alleviated by using a *64bit* system or multicore computing environment.

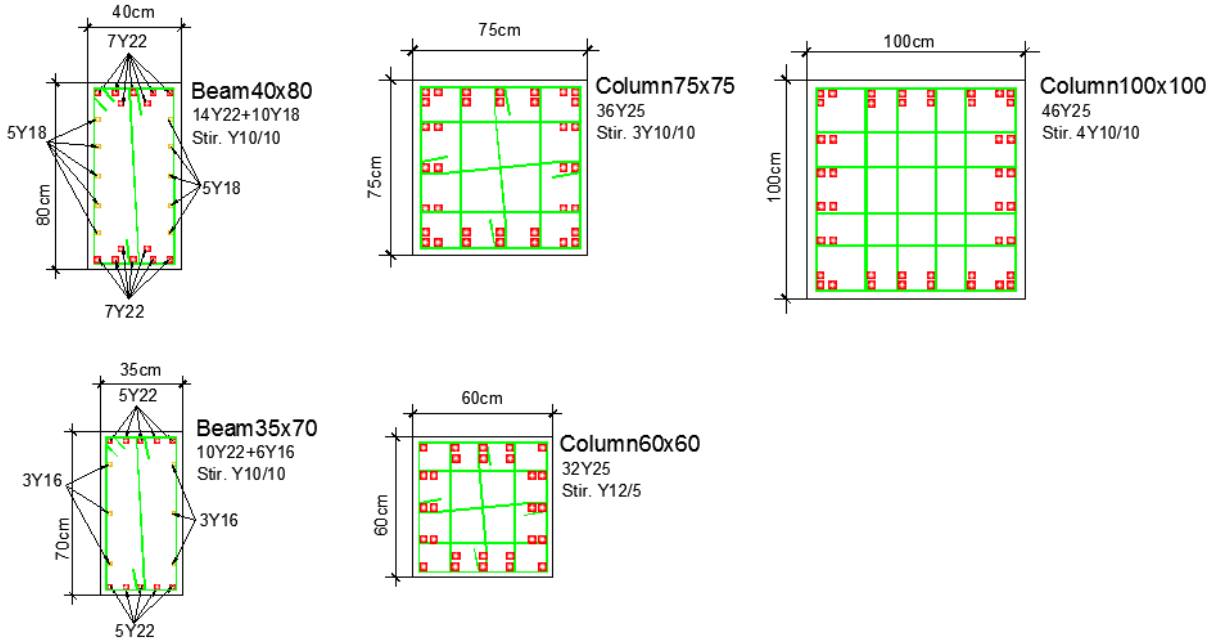

FIGURE 2.33 RC HIGH RISE BUILDING. RC SECTIONS REINFORCEMENT DETAILS.

Storey	*Normalized Horizontal Load*		*Storey*	*Normalized Horizontal Load*
1	0.0667		20	0.4110
2	0.1333		21	0.4315
3	0.2000		22	0.4521
4	0.2667		23	0.4726
5	0.3333		24	0.4931
6	0.4000		25	0.5137
7	0.4667		26	0.5342
8	0.5333		27	0.5548
9	0.6000		28	0.5753
10	0.6667		29	0.5959
11	0.7333		30	0.6164
12	0.8000		31	0.3268
13	0.8667		32	0.3373
14	0.9333		33	0.3479
15	1.0000		34	0.3584
16	0.3288		35	0.3690
17	0.3493		36	0.3795
18	0.3699		37	0.3900
19	0.3904			
	Total Horizontal Load		*130.35 MN*	
	Total Vertical Load		*208.63 MN*	

TABLE 2.5 RC HIGH RISE BUILDING. LOAD DISTRIBUTION ACCORDING TO EC8.

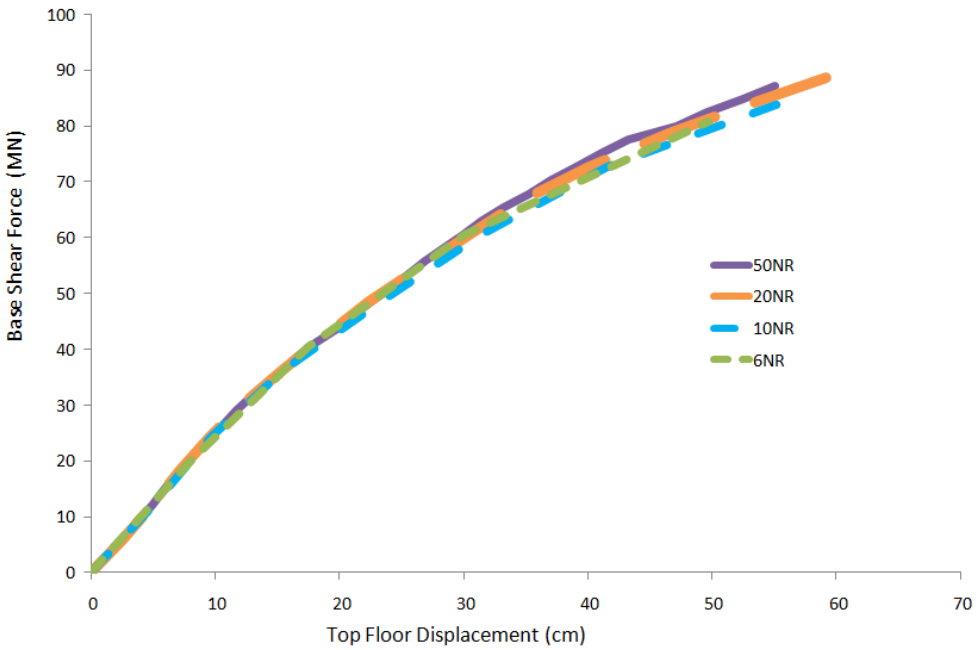

FIGURE 2.34 RC HIGH RISE BUILDING. *P-δ* CURVES OF HIGH RISE RC BUILDING.

As it can be seen from the *P-δ* curves in Fig. 2.34, the numerical procedure of the solution terminates for a horizontal load of *85 MN* (*55 cm top floor horizontal displacement*) which is the ultimate limit state of the structure. The failure mechanism that resulted from the loading

history was due to rebar failure at the base of the structure (columns and beams) and therefore the numerical procedure could not continue due to zero diagonal values of the global stiffness matrix of the structure. When a NBCFB element section looses completely its bearing strength, *ReConAn* sets the natural stiffness matrix of that element to zero and proceeds with the computations. Thus, the solution procedure continues and a redistribution of the internal forces is accomplished. The solution procedure terminates when the global stiffness matrix of the structure becomes singular thus it is not possible to solve the system of equations.

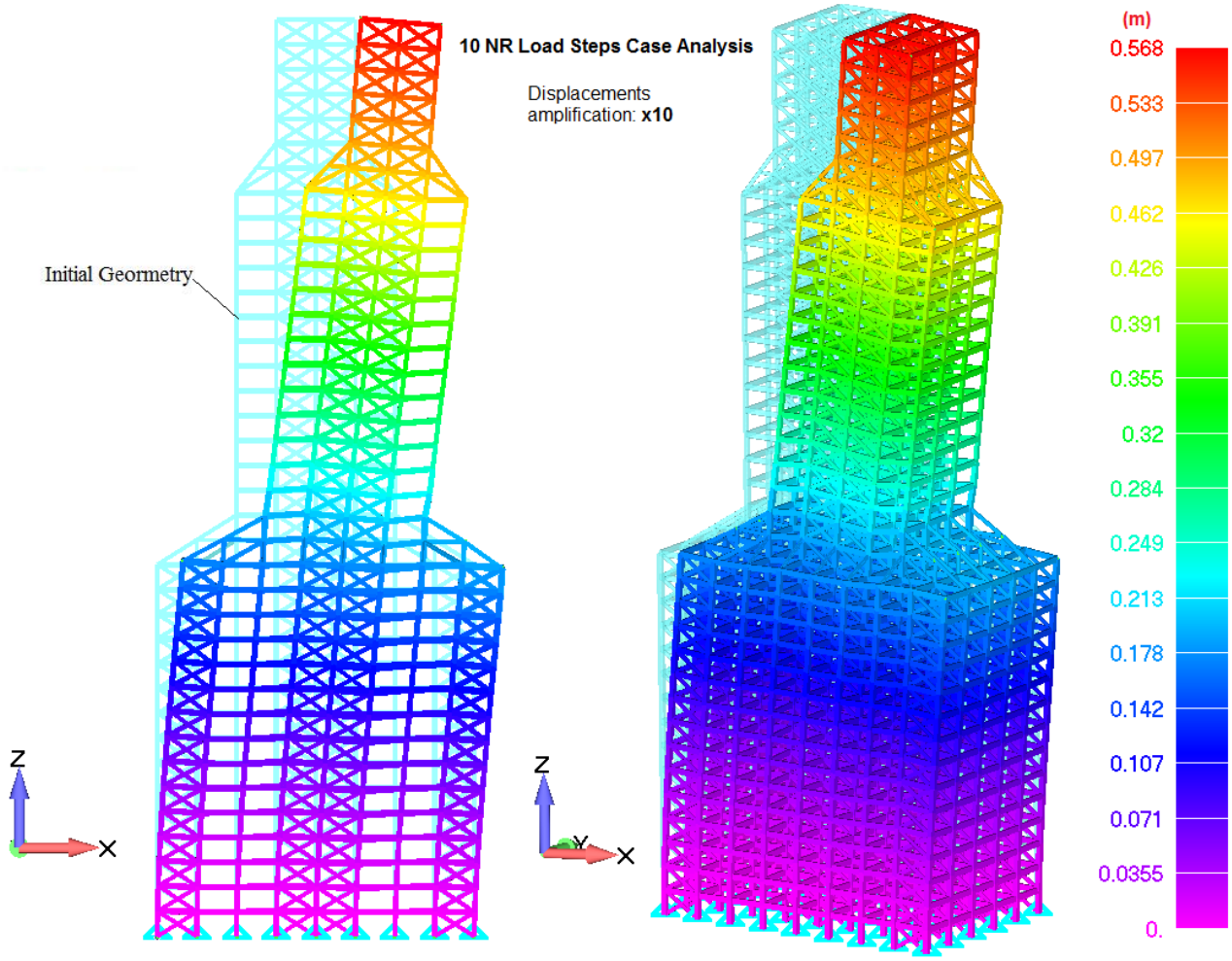

FIGURE 2.35 RC HIGH RISE BUILDING. INITIAL AND DEFORMED SHAPES PRIOR TO FAILURE – INITIAL CARCASS.

Fig. 2.34 shows that the initial design of the carcass is unable to bear the seismic load computed according to EC8 (*130.35 MN*) failing prematurely for a total base shear load of *85 MN*. Therefore, a redesign was implemented in order to reinforce the carcass of the building by assigning to the columns, which had the section type Column *75x75 cm*, a larger section type (Column*100x100 cm* as shown in Fig. 2.33). Correspondingly the section type Column*75x75 cm* was assigned to the columns that were initially discretized with the section type Column *60x60 cm*. Following the strengthening of the members, the four analyses were performed and the new predicted *P-δ* curves can be seen in Fig. 2.36. As it was expected, the predicted *P-δ* curves illustrate an increased structural capacity with a mean ultimate base shear force of *135 MN*.

Newton-Raphson Load Steps	*Computational Time (minutes)*
50	45
20	25
10	15
6	8

TABLE 2.6 RC HIGH RISE BUILDING. COMPUTATIONAL TIMES FOR DIFFERENT LOAD INCREMENTS.

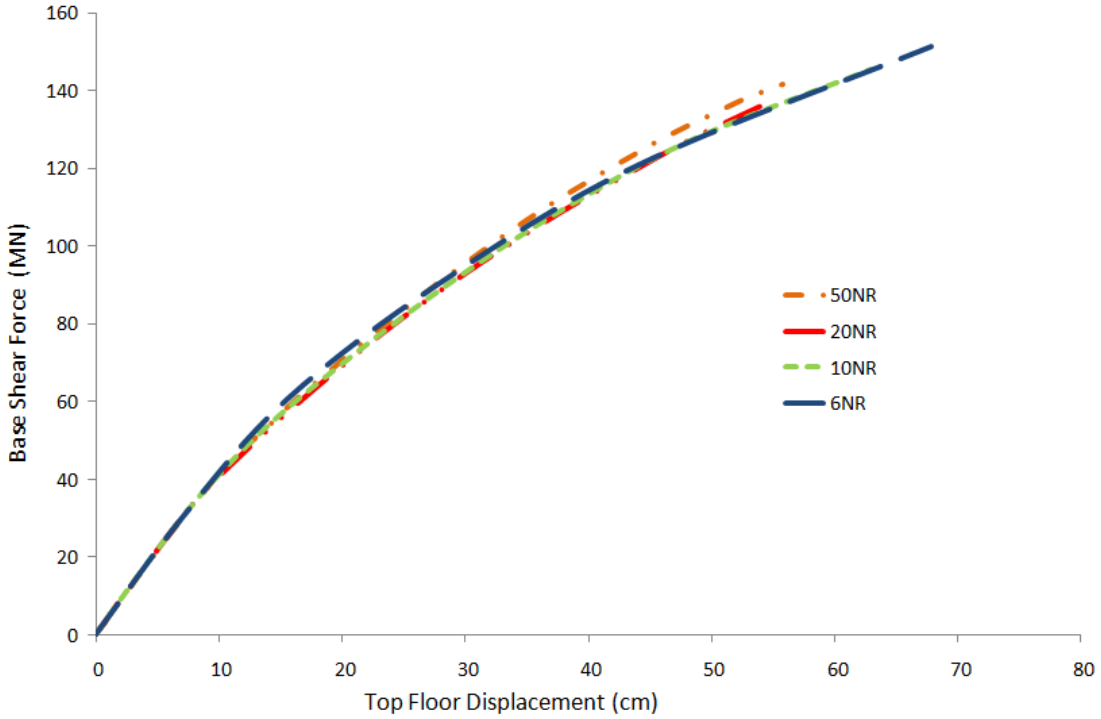

FIGURE 2.36 RC HIGH RISE BUILDING. *P-δ* CURVES FOR THE REDESIGNED CARCASS.

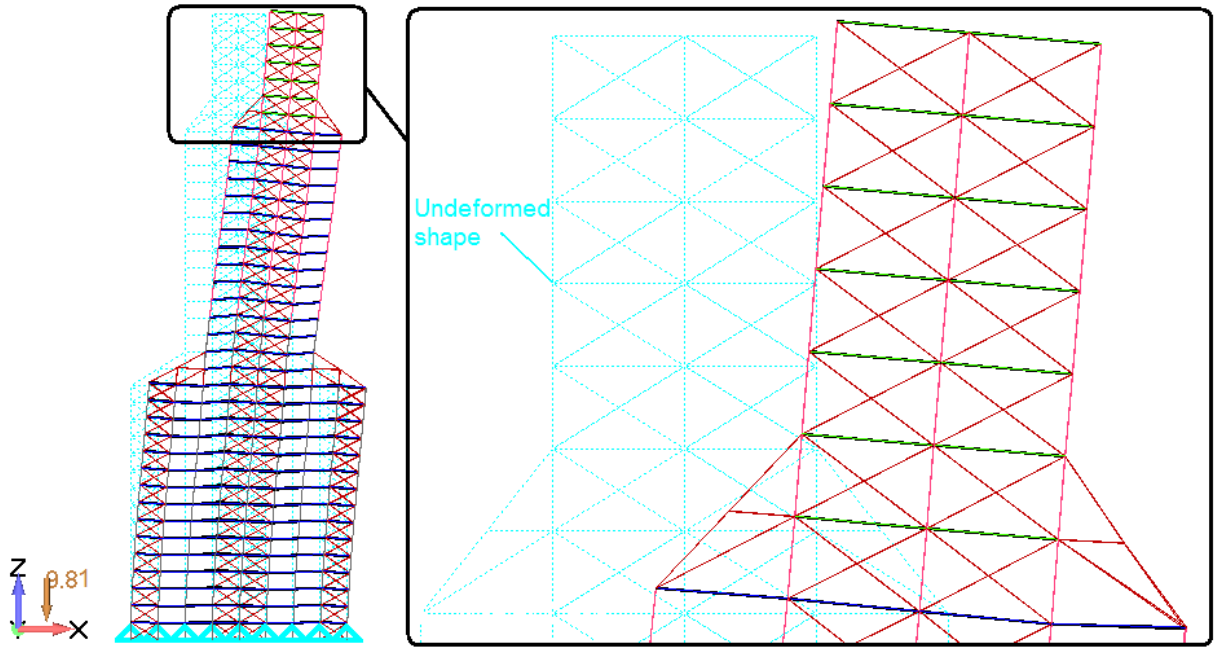

FIGURE 2.37 RC HIGH RISE BUILDING. DEFORMED SHAPE PRIOR TO FAILURE.

An intention grabbing observation can be depicted in Fig. 2.37, where the initial and deformed shapes of the structure are shown. As it can be seen, the deformed shape maintains its initial geometry regarding the out-of-plane deformations, thus no abnormal distortion of the mesh can be observed. Since the loading was applied horizontally along the positive X direction and given the structure's symmetry about the Z and Y axes, then no rotations of the structure should be produced which would have been translated through abnormal deformation of the lines when viewing the deformed shape in the XZ view (Fig. 2.37). Even though the predicted deformations are scaled by X*20* in Fig. 2.37, the deformed shapes of the lines retain their initial thickness illustrating the numerical robustness of the developed FEA code.

Before moving to the next Chapter, it is important to note at this time, that this numerical test was basically created in order to illustrate the computational robustness and efficiency of the developed FEA code and in no case represents a complete design procedure for this kind of structures, where the *P-δ* effect, wind loading, structure-soil interaction, time history analysis and other response features should be considered during the design process. Nevertheless, it is obvious that *ReConAn* is able to analyze large-scale RC and steel structures at an affordable computational time which is a good indicator that it can equally well be applied to the design of this type of structures under earthquake loading.

Chapter 3 3D Modeling of Concrete Materials

Contents of Chapter 3

3.1 Brief Overview of the Material

It is indisputable that concrete has been established as the most significant structural material of the last century. Concrete material has been used in many areas of civil engineering structures, especially for the construction of residential buildings, bridges, offshore platforms, containment structures, arc dams, nuclear power plants, high-rise buildings (Figs. 3.1), irrigation systems etc.

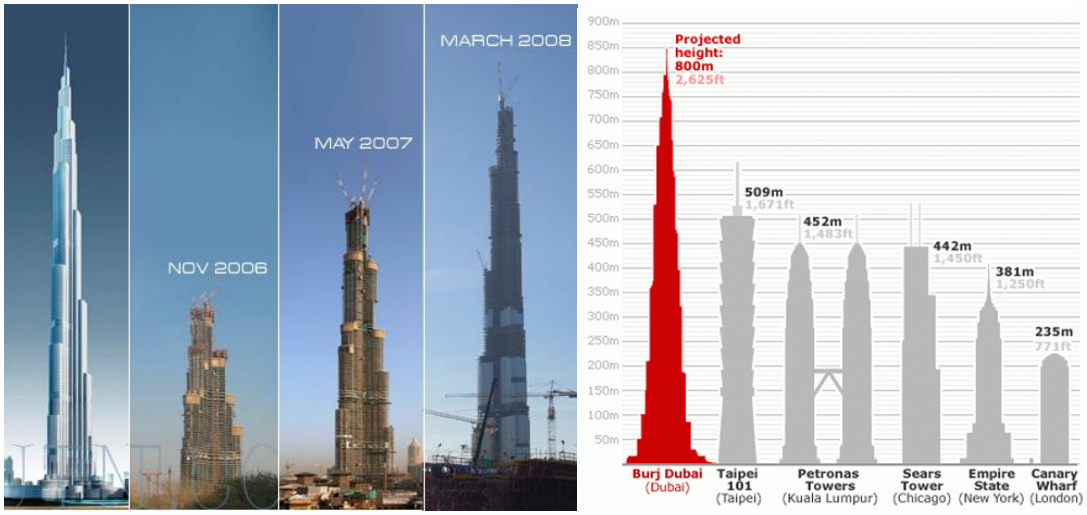

(A) (B)

FIGURE 3.1 BURJ KHALIFA. (A) CONSTRUCTION PROGRESS AND (B) COMPARISON WITH OTHER PROJECTS.

Being a heterogeneous material, concrete consists of hardened cement paste in which aggregates are embedded making the numerical prediction of its behavior complex. In addition to that, the nonlinear stress-strain behavior and anisotropic elastic degradation during loading makes this task even more complex. Nevertheless, material behavior has been one of the most important parameters for modeling RC structures predicting the overall response. It is clear that, idealizing this behavior into an elasto-plastic material model is not a proper description of the material's behavior that turns to be a key factor for the successful prediction of the nonlinear behavior of RC structures.

The main "nonlinear" material characteristics of concrete behavior are:

i. Elastic degradation.
ii. Stress-strain constitutive relation.
iii. Micro- and macro-cracking.
iv. Fracture mechanisms.
v. Ultimate strength and behavior at failure.
vi. Shrinkage and Creep.
vii. Rate of loading.

Taking into consideration these characteristics, an extensive research work has been made in recent years in the area of 3D constitutive modeling, aiming at the formulation of plasticity and crack models that will predict objectively the response of the material. Despite the fact that

several material models were presented, none of them managed to combine computational robustness and efficiency.

In this Chapter, the concrete material behavior will be discussed, illustrating the main parameters that affect its mechanical characteristics. A discussion on whether concrete should be modeled with the use of a brittle or a softening branch model will be performed and the proposed material model adopted will be presented. In the final section of this Chapter a numerical investigation will be presented regarding the modeling of cylindrical concrete specimens under uniaxial loading.

3.2 Mechanical Parameters of Concrete – Physical Interpretation and Idealization

Several effects which alter the mechanical behavior of concrete, as observed in experiments, are presented in this section. The performance of concrete is dependent on numerous factors which will be discussed thoroughly.

3.2.1 Experimental Data and Test Methods

Over the past decades, numerous experimental results were presented in the literature, for the prediction of the behavior of plain concrete, producing a considerable data-base of experimental data. Studying these stress-strain curves, the main conclusion that has been reached is that none of them has the same quantitative or qualitative features especially when referring to the inelastic braches of these curves. Taking into consideration that most material models proposed in the literature are calibrated (and their parameters defined) through experimental data, a significant question arises: "Which material model formulation will provide realistic approximation of the behavior of concrete when combined with the FEM?" It is the author's belief that the answer to this question lies in the numerical aspect of the problem, meaning that the proper selection of the corresponding material parameters accounted for in the numerical model, will postulate on the objectivity of its results. In search of an objective modeling method of RC structures, the proper concrete material model should be selected and therefore, a discussion on the corresponding model selected in this work is analyzed.

It is well known that conducting and obtaining triaxial material data for the realistic modeling of concrete through experimental setups, is rather expensive and difficult to attain. This conclusion is justified through the scatter of available experimental data which proves that concrete material properties are not easy to obtain, especially when referring to its inelastic range. Numerically speaking, an inelastic branch is ideal for establishing numerical stability and robustness when high nonlinearities occur (Fig. 2.12). On the other hand, when considering the actual concrete behavior in simple compressive experiments, it is evident that this inelastic softening branch is clearly an outcome of the interaction between the loading system and the concrete specimen.

An extensive discussion on strength, constitutive response and interaction between loading mechanisms and concrete specimens can be found in several articles[94-98]. More specifically, Gerstle et al.[94, 95] presented the differences among test methods which vary depending on the

loading system type used (Fig. 3.2). The main characteristic variables of the different loading systems are as follows:

i. Degree of normal boundary constraint in the direction of the applied load.
ii. Degree of lateral boundary constraint on the plane of the boundary.

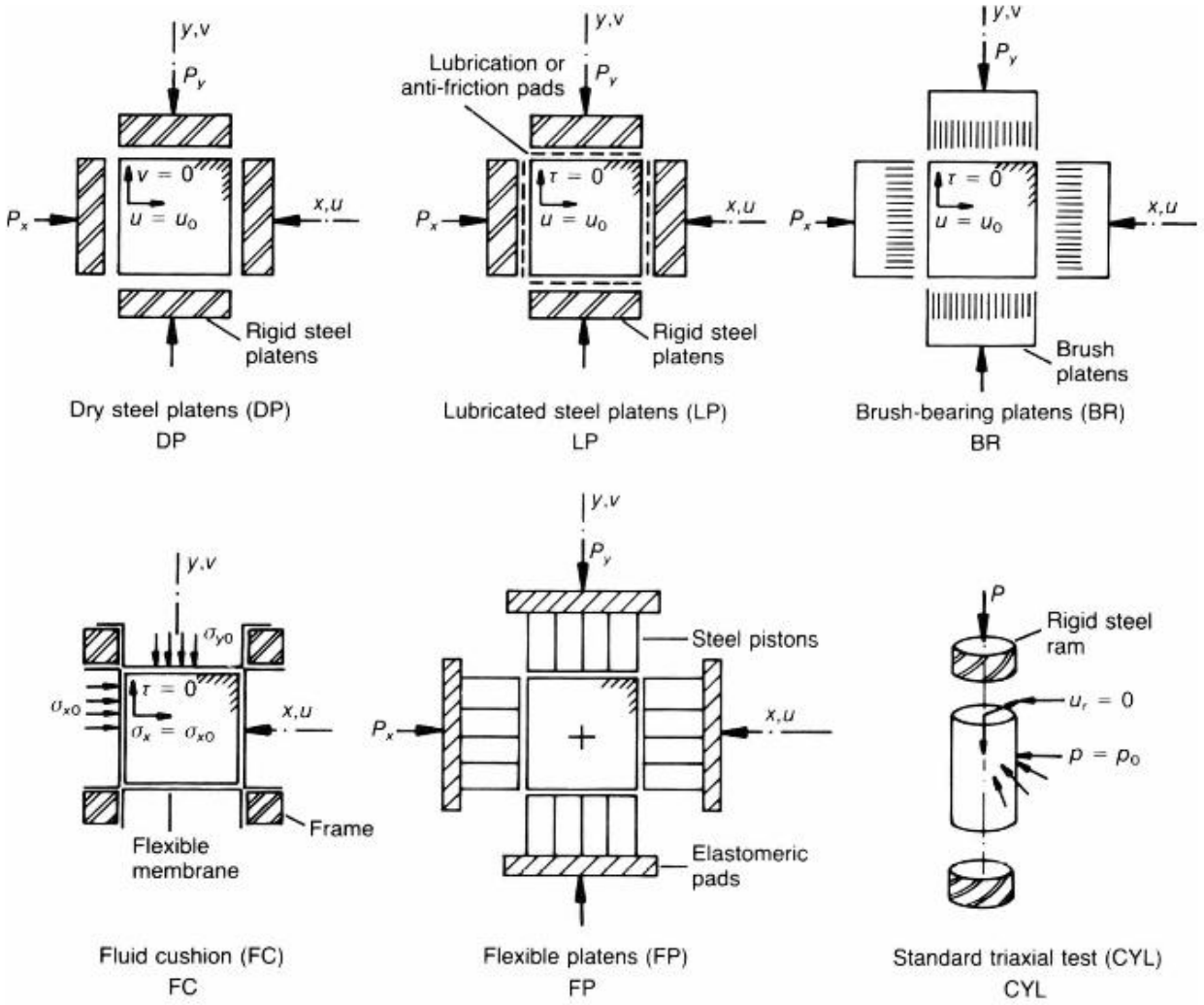

FIGURE 3.2 MULTIAXIAL TEST METHODS[94, 95].

In Fig. 3.2, different types of loading systems for applying compression to concrete specimens are shown. As discussed in Gerstle et al.[94, 95], devices with rigid steel plates are most common and permit the application of uniform normal displacements in the direction of loading. These types of devices create normal stresses which are non-uniformly distributed because of the friction between the concrete and the steel plates. Alternatively, a fluid cushion assures uniform normal stress free of lateral displacements thus the shear stress on the boundary conditions is zero. Consequently, the behavior of the other loading system types usually ranges between the behaviors of these two devices. Gerstle et al.[94, 95] presented their results which showed a large scatter which can be depicted from Fig. 3.3.

In resolving this problem and giving an answer to the question whether concrete has an inelastic branch and in what ways the loading mechanisms affect the specimen's behavior, van Mier et al.[96] (1997) presented the results of an international experimental program where *10* different

research labs participated in order to study the behavior of concrete during uniaxial compression. One of the most characteristic results of this research program is given in Fig. 3.4, which illustrates different stress-strain curves for the same specimens that were tested by using different loading mechanisms. Through this work, Zisopoulos et al.[97] showed that when the shear stresses due to friction between the loading device and the concrete specimen tend to zero, then the concrete material behavior is brittle thus the inelastic branch becomes vertical (Fig. 3.4). Similar results were obtained by Schickert's[98] (1981) research where the slenderness ratio for two different loading systems was investigated (Fig. 3.5).

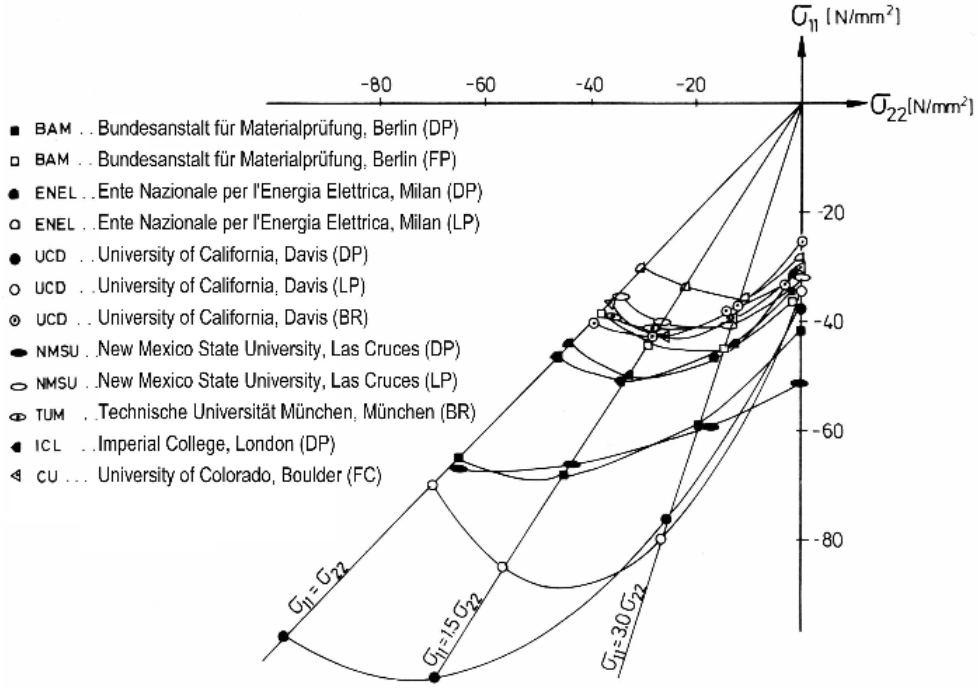

FIGURE 3.3 FAILURE ENVELOPE FOR BIAXIAL LOADING CONDITIONS[94, 95].

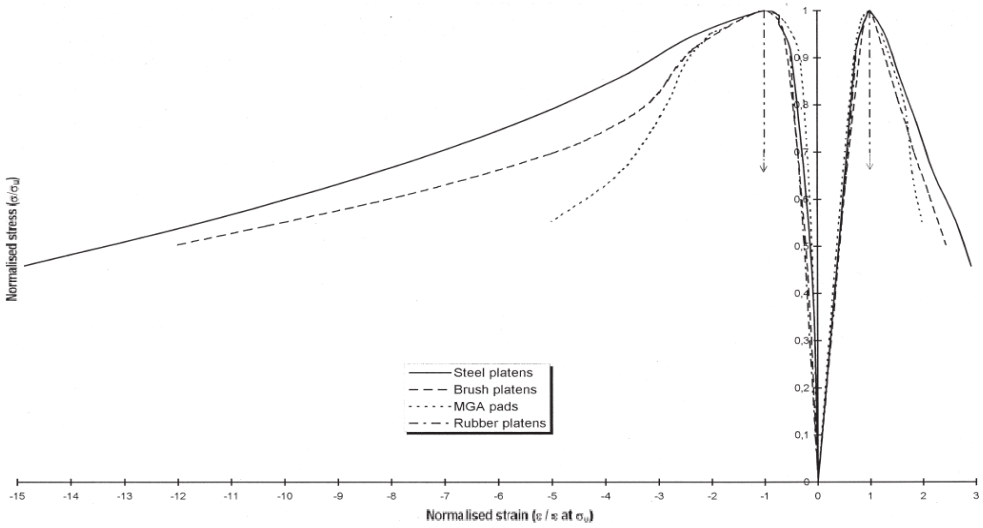

FIGURE 3.4 STRESS-STRAIN CURVES FOR DIFFERENT TYPES OF LOADING TYPES[97].

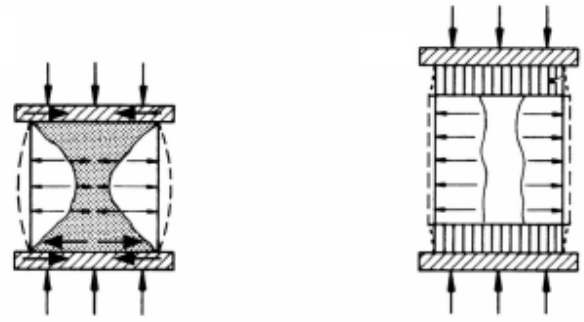

(A) (B)

FIGURE 3.5 TEST DEVICES WITH (A) HIGH AND (B) NEGLIGIBLE FRICTION ON THE LOADING DEVICE-SPECIMEN INTERFACE[6].

Extensive analysis and discussions on the effects of loading devices influencing the material behavior can be found also in Kotsovos and Pavlovic[8] (1995), Wesche[99] (1996) and Grübl et al.[100] (2001). In continuations to the description of the concrete material behavior, the findings in Kotsovos and Newman[101-103] will be discussed in section 3.3.2 and the numerically modified Kotsovos and Pavlovic concrete material model will be presented in section 3.3.5.

3.2.2 Size and Shape of Specimen

An important issue when testing the strength of concrete is the size of the specimen, which affects the ultimate strength. The smaller a specimen is, it appears to develop greater strength than larger specimens (Fig. 3.6) of the same age (usually *28* days). Different reasons may cause this effect where one of them is the core moisture obtained in relation to the size at *28* days, as it was described in the Schickert[98] (1981) and Wesche[99] (1996) research works. The influence of moist core may decrease when the specimen becomes older and moreover, the initial stresses are larger for larger specimen.

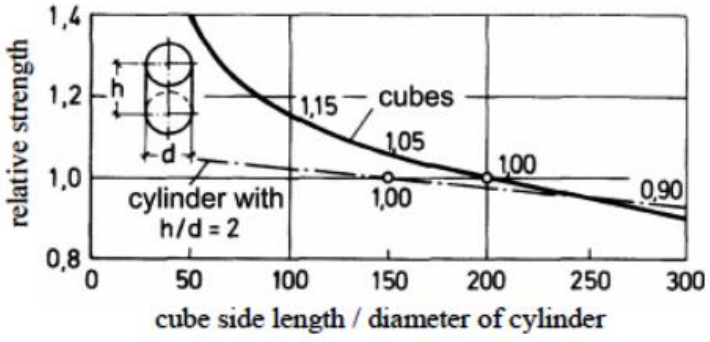

FIGURE 3.6 DEPENDENCE OF THE COMPRESSIVE STRENGTH ON THE SPECIMEN SIZE[6].

A second reason for obtaining higher ultimate strengths in uniaxial compression tests when specimens are smaller, is related to the triaxial stress field that is created from the loading device-concrete specimen interaction thus an additional strength is induced to the specimen due to triaxial stress state phenomena. This is the main reason why the cube specimens appear to have larger ultimate strength than the corresponding cylindrical ones. Fig. 3.7a illustrates the schematic representation of the effect of the boundary friction restraint τ on the state of stress within cylindrical specimens under uniaxial compression σ_o[104], a figure which also shows the

triaxial stress state created by the loading device-specimen interaction at the ends of the specimen. Moreover, Fig. 3.7b shows the stress paths induced in the central and at the end zones of cylinders under increasing uniaxial compression as presented by Kotsovos[104].

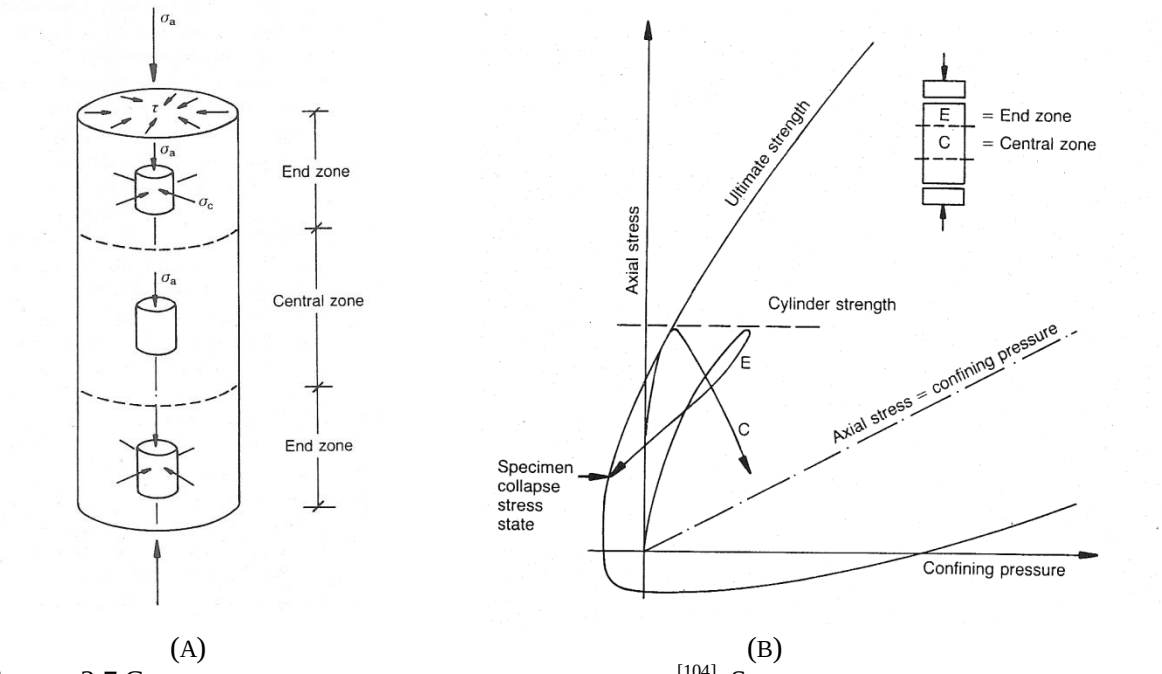

(A) (B)

FIGURE 3.7 CYLINDERS UNDER UNIAXIAL COMPRESSION σ_o[104]. SCHEMATIC REPRESENTATION OF THE (A) EFFECT BOUNDARY FRICTIONAL RESTRAINT (τ) ON THE STATE STRESS WITHIN AND (B) STRESS PATHS INDUCED IN THE CENTRAL AND END ZONES OF THE CYLINDERS.

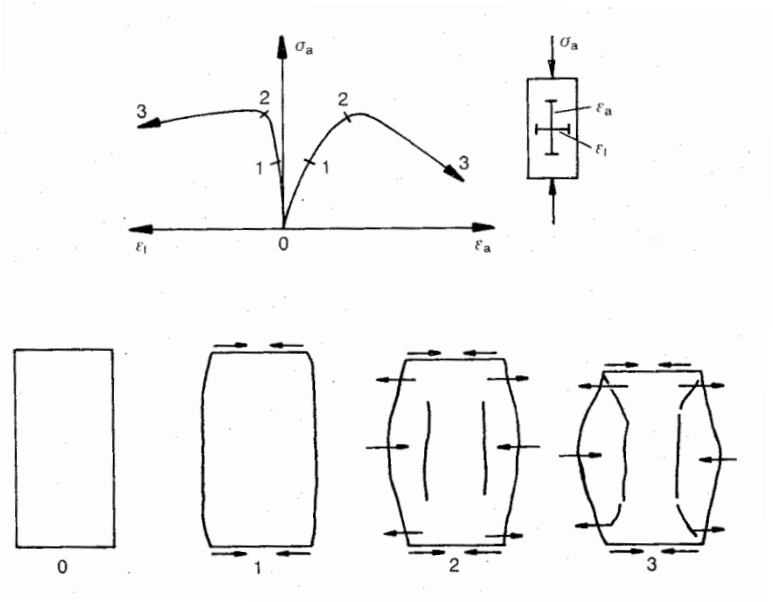

FIGURE 3.8 CYLINDERS UNDER UNIAXIAL COMPRESSION σ_o[104]. DEFORMED SHAPES AND CORRESPONDING CRACK PATTERNS

In Fig. 3.8, the deformed shapes and corresponding crack patterns of a cylindrical specimen under uniaxial compression are illustrated. It can be seen that the end zones of the cylindrical specimen at a load level close to the maximum load-carrying capacity of the specimen, are inclined due to the restrain of the boundary conditions. If the height of the cylindrical specimen

is decreased, then the central zone of the specimen will be diminished and the stress state within the specimen will be governed from triaxial phenomena overestimating the ultimate strength of concrete. This is a third size related effect which plays a significant role on the mechanical behavior of concrete specimens, thus it is evident that when a cubic specimen is tested the compressive strength is governed by triaxial state phenomena.

3.2.3 Concrete in Tension

The tensile behavior of concrete was studied extensively by several researchers in an attempt to create an objective formulation for the constitutive tensile behavior of concrete. In CEB 1996[105] it is assumed that tensile stress can be transferred even after the crack initiation. However, this phenomenon is attributed to the stiff experimental setup[8, 106]. Bažant and Celodin[106] stated that the inelastic branch in tension is just a numerical manifestation in order to induce stability when tensile failure occurs.

As it can be seen in Figs. 3.9, the tensile behavior is linear up to about two thirds of the tensile strength and near the ultimate tensile strength a nonlinear behavior is observed. The inelastic softening branch represents the remaining tensile strength after cracking[107-109].

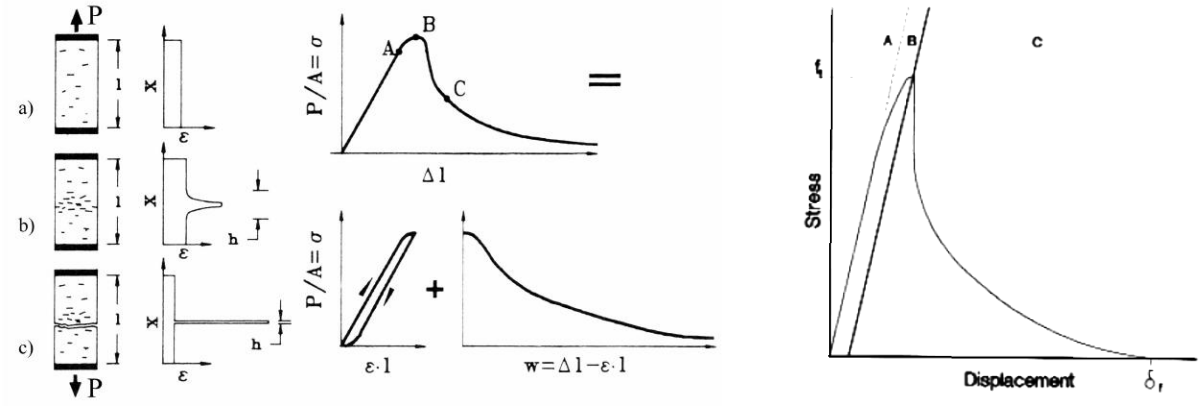

(A) (B)

FIGURE 3.9 TENSILE BEHAVIOR OF CONCRETE BY (A) DUBA[107] AND (B) COTTEREL AND MAI[108].

Taking into consideration the extensive experimental work conducted for the investigation of the fragile behavior of concrete, it is the author's belief that a simple linear formulation, which has a vertical softening branch, is the most realistic numerical model for the description of the tensile behavior of concrete. Despite the fact that near the maximum tensile failure stress f_t the behavior is inelastic, the linearization of the branch is acceptable given the magnitude of the corresponding ultimate tensile stress, which is assumed approximately equal to *5%* of the compressive strength. Therefore, the error induced by making such an assumption is negligible.

3.2.4 Shrinkage and Creep

3.2.4.1 Shrinkage

Shrinkage of concrete material is the time-dependent volume change of concrete without any external loading. The shrinkage deformations can be separated into four different components:

1. ***Plastic shrinkage***, which is also known as capillary shrinkage and occurs when water is lost from concrete while it is still in its plastic state.
2. ***Carbonation shrinkage***, which is caused by the reaction of hydrated cement paste with carbon dioxide in the air when moisture is present. Carbonation of shrinkage is limited to the outer zones thus its contribution is not significant in most cases.
3. ***Drying shrinkage*** which is caused by the water reduction in concrete to the level of moisture that the surrounding air contains. The rate of drying shrinkage is dependent on the member size[110] since small sections lose moisture at much higher rate than thick sections. Although a thick section may reach the final shrinkage value only after a considerable time, the final value of drying shrinkage is considered independent of member size. Fig. 3.10 shows different stages of a section cured at *100%* moisture content and then exposed to *50%* moisture content in the surrounding environment.

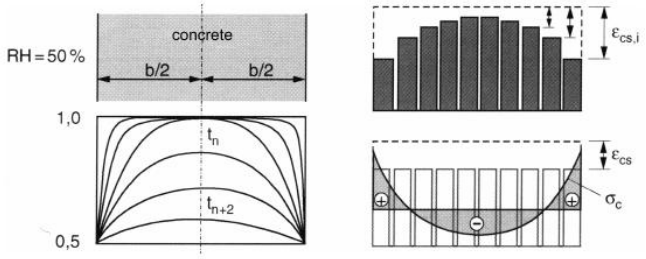

FIGURE 3.10 MOISTURE, STRAIN AND STRESS DISTRIBUTION ATTRIBUTED TO DRYING SHRINKAGE[110].

4. ***Autogenous shrinkage***, which is also known as self-desiccation shrinkage or chemical shrinkage. This type of shrinkage is associated with the continual hydration of cement where the volume of the hardened cement paste is less than the volume of water and the volume of cement. Member size and the moisture content in the surrounding environment do not affect autogenous shrinkage, which is small compared to drying shrinkage for normal strength concrete. However, the phenomenon of shrinkage is governed from this component when dealing with high-strength concrete (Fig. 3.11).

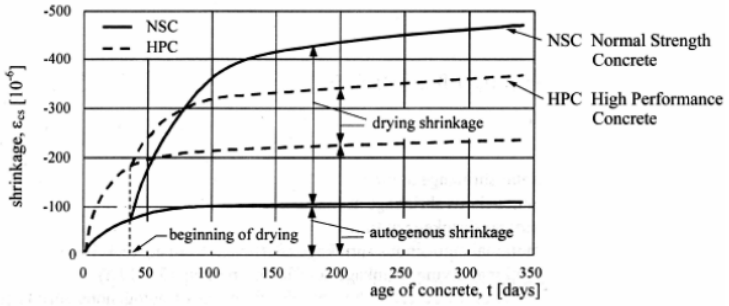

FIGURE 3.11 AUTOGENOUS AND DRYING SHRINKAGE COMPONENTS[111].

3.2.4.1 Creep

Creep is the physical phenomenon for the time-dependent increase of strain at constant stress and it is considered to be directly related to the stress state and temperature of concrete. The chemical activity which occurs during the creep phenomenon is that of the re-arrangement of water particles in consequence of internal stresses and temperature deviations, thus the creep behavior is mainly governed by the consistency of the cement paste. Strains due to creep also

increase if the ratio of cement paste is high compared to the aggregates or if the corresponding stiffness of the aggregate is relatively small. In addition to that, a large water/cement ratio will increase significantly the creep strains.

The total creep strains ε_{cc} can be separated into different components depending on the phenomenological properties considered by researchers. One way is to split creep into a reversible component that may be recovered when unloading occurs and into an irreversible component as shown in Fig. 3.12, (Grübl et al.[100]). The reversible component is referred to as delayed elastic strain ε_{cd} and the irreversible component as flow ε_{cf}.

Fig. 3.12 assumes that for a constant internal stress state and temperature around a concrete specimen, the rate of strains attributed to creep, decreases geometrically converging to a steady state which is constant (Ross et al.[112], England[113], Browne[114], Lykidis[115], Grübl et al.[100]).

A second way to separate the creep strains into components is to assume that creep has a short-time and a long-time component. Short-time creep is explained by stress-induced redistribution of water and long-time creep is caused by displacements of particles in the hardened cement paste, (Wittmann[116]).

Given that in this work, we are going to study RC structures under static loadings, the phenomenon of creep may affect, in some cases, the accuracy of the resulting displacements, since this phenomenon is not accounted for in the proposed modeling method.

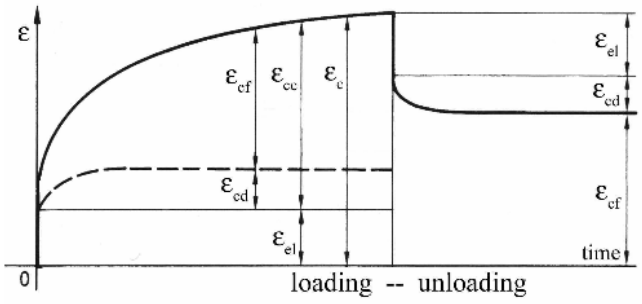

FIGURE 3.12 CREEP STRAIN COMPONENT DEFINITIONS[100].

3.2.5 Rate of Loading

Another significant effect that should be taken into consideration when modeling RC structures is the rate of loading which affects the material behavior. Mahin et al.[117] (1972) conducted an experimental research on RC specimens where it was found that the effect of the rate of loading on strains is relatively small (*0.001* and *0.25 strain/sec* for high seismic excitations). In addition to that, when many loading cycles are applied, the behavior is similar to that of static loading and the phenomenon does not play a significant role[117].

Lowes[118] (1999) presents a literature review of experimental tests conducted in order to study if the rate of loading affects the response of strain rate in concrete. As it was presented through Fig. 3.13, the compressive strength of concrete obtained with dynamically imposed loads, does not deviate from the corresponding compressive strength when the loading is performed statically. Therefore, when analyzing concrete material it is acceptable to assume that the

response can be modeled by using material characteristics obtained through statically imposed loads.

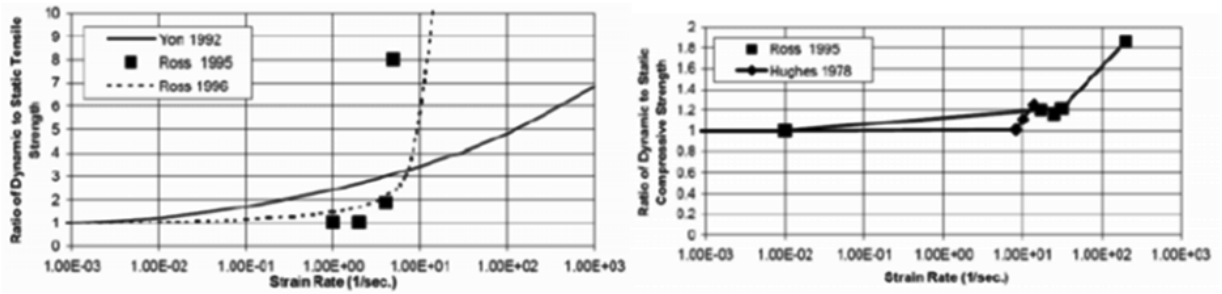

FIGURE 3.13 INFLUENCE OF CONCRETE STRENGTH DUE TO STRAIN RATE[118].

3.3 Constitutive Relations of Concrete

3.3.1 Review

As it was presented in Chapter 1, concrete was initially modeled with the use of 1D constitutive relations, which were described through simple strain-stress curves. These constitutive relations for concrete were unable to capture the response of shear dominated structural members even when the new code provisions were implemented during the design process (Kotsovos and Pavlovic[119]). Researchers tried to improve the constitutive relations of concrete by combining them with advanced beam elements formulations in order to capture the nonlinear response of RC structures without any significant success. Even in cases where shear strains were accounted for, the modeling of three-dimensional geometries (3D RC Joints, Shear Walls, Slabs, etc.) with beam elements is inadequate (Fig. 3.14).

FIGURE 3.14 LEFT: SHEAR WALL FAILURE (VIÑA DEL MAR) CHILE, FEB 2010. RIGHT: TYPICAL JOINT FAILURE.

According to the above statements, it is obvious that for such models, a three-dimensional constitutive relation for the concrete material behavior is necessary, combined with the use of solid finite elements that discretize the exact geometry of the structure. For accomplishing such a task, a three-dimensional constitutive law has to be implemented according to the literature findings on concrete material behavior. This material law has to incorporate the basic concrete material characteristics thus being numerically robust and computationally efficient.

As it was mentioned previously, the experimental data on concrete behavior used for the development of constitutive laws are obtained from tests on specimens such as cylinders, prisms, cubes etc. Such specimens are subjected to various load combinations, usually applied through rigid steel plates (pure compression or triaxial test). The obtained results are expressed in the form of stress-strain curves which consist of a branch of positive stiffness, gradually reducing, followed by a strain softening one. After an extensive research work that started at the early 80's (Kotsovos[104], van Mier[120]) and confirmed in late 90's (van Mier et al.[96]), it was found that only strain hardening may describe material behavior under a definable state of stress. This means that the strain softening branch basically reflects the interaction between specimens and loading platens (Figs. 3.15), which is affected through the development of uncontrolled frictional stresses at the faces between the specimen and the loading device.

For proving the above theory through experimental evidence, Kotsovos and Newman[101-103] conducted an experimental program, which involved the testing of two different types of specimens with two different concrete mixes:

1. *250 mm* height x *100 mm* diameter cylinders with *50* and *29 N/mm*^{2}.
2. *100 mm* cubes with *60* and *37.7 N/mm*^{2}.

The specimens were subjected to varying degrees of frictional restraint across their loaded surfaces. This was achieved by placing various types of anti-friction media at the specimen-loading device interface. The antifriction media used were:

a. a layer of synthetic rubber *0.45 mm* thickness,
b. a MGA pad,
c. a brush platen,
d. no anti-friction medium (plain steel plates),
e. an active restraint induced by Hi-Torque hose clamps.

During these test experiments, the strength was measured for both cubic and cylindrical specimens and the complete deformational behavior was recorded within the central zone of the cylinders. The results can be depicted in Figs. 3.15, where the diversification of the inelastic branches for each boundary condition type is obvious. The less friction induced on the interface of the specimen the more vertical softening branches occur, verifying the brittle nature of concrete material. It is also interesting to note here that the nonlinear behavior of the stresses depicted in Figs. 3.15 approximately begin between *60-80%* of the ultimate strength[8].

In his Ph.D. thesis, Hartl[6] (2000) used these experimental evidence and is also based on the research study conducted by Newman[121] (1973). Hartl[6] assumed that concrete behaved linearly elastic and isotropic up to failure which was described by the Ottosen[122] (1977) surface. In addition to that, Hartl referred to a comment made by Gerstle et al.[94] saying: "Concrete response to multiaxial stress states at working load level can be considered elastic for engineering purposes".

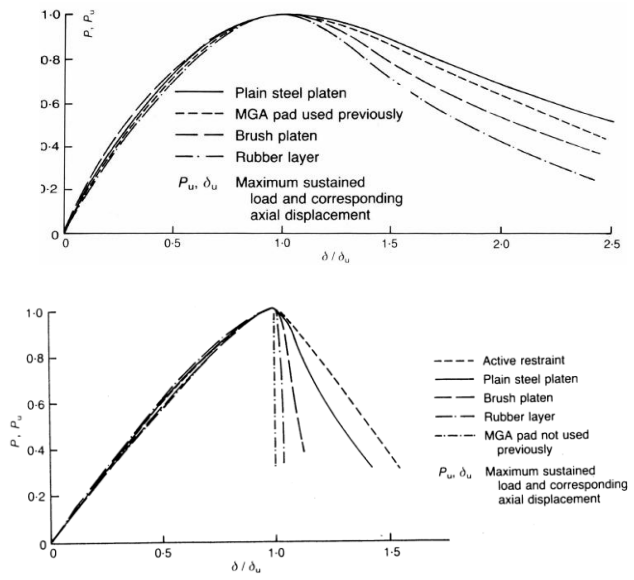

(A) (B)

FIGURE 3.15 STRESS-STRAIN CURVES FOR DIFFERENT BOUNDARY CONDITIONS[104]. (A) $f_c = 29\ N/mm^2$ AND (B) $f_c = 50\ N/mm^2$.

It is indisputable that concrete behaves as an elastic medium up to a certain level, but consequently a nonlinear branch will always evolve prior to cracking thus with the intention of predicting accurately the nonlinear response of RC structures a more advanced material law is required. Nevertheless, linear elastic behavior of concrete materials is used by several software codes for the analysis and design of concrete structures.

Many papers have been published on plasticity models, smeared crack approach or combination of these models, specifically implemented on concrete structures (Rashid[123] (1968), Červenka and Gerstle[124] (1971), Owen et al.[125] (1983), Bažant and Oh[126] (1983), De Borst[127] (1986), Simo and Ju[128] (1987), Rots[129] (1989), Pramono and Willam[130] (1989), Kotsovos and Pavlovic[8] (1995), Etse[131] (1992), Feenstra[132] (1993), Feenstra et al.[133] (1998), Menetrey et al.[134] (1997), Bažant et al.[135] (2000), Bažant and Caner[136, 137] (2005), Spiliopoulos and Lykidis[138] (2006), Sato and Naganuma[139] (2007), Červenka et al.[140] (2008)), but a few researchers stated that their algorithms showed computational accuracy and numerical robustness. Furthermore, concerning the combination of plasticity with smeared crack models, none of them succeeded in providing a computationally efficient code even when dealing with relatively small-scale FE models. This is attributed to the increased demands of the numerical problem that results from a 3D FE formulation and the numerical instabilities induced from the smeared crack formulation when cracking occurs.

Since many studies have been conducted on 3D concrete material laws, a brief presentation will follow of the different types of material formulation that have been proposed in the literature and following the Kotsovos and Newman[101-103] experimental findings will be presented. Moreover, the Kotsovos and Pavlovic[8] material constitutive model will be presented, together with the proposed numerical modifications for improving its numerical behavior during the nonlinear analysis of RC structures.

Observed material behaviour under increasing stress	Deduced changes in internal structure	Deduced changes in deformational behaviour	Approximate stress level	Influencing characteristics
Presence of cracks detected microscopically and from X-rays	Pre-existing cracks		Prior to load	Shrinkage, thermal effects, etc.
From structural investigations: Bond cracking and matrix cracking increases depending on spacing of particles of aggregate, with cracking aligned in direction of maximum compressive stress as load increases	Start of localized stable cracking	Quasi-elastic behaviour	30–40% ultimate	Spacing of particles for a given mix, etc.
From phenomenological investigations: Decrease in ultrasonic pulse velocity, start of significant acoustic emissions, measurable void formation		Plastic behaviour	45–90% ultimate	Method of detection, type of aggregate, type of specimen, state of stress, rate of loading, curing conditions, and level decreases with: increase with *w/c* ratio; increase in volume fraction of aggregate; decrease in age; decreasing roughness and angularity of aggregate
From structural investigations: Formation of continuous crack patterns through matrix and around aggregate particles	Start of continuous cracking		70–90% ultimate	Spacing of aggregate particles for a given mix
From phenomenological investigations: Increase in volume, marked increase in acoustic emission, and change in stress–strain relationship	Unstable behaviour caused by reduction in number of load paths due to cracking (leading to complete disruption)		70–90% ultimate	As for localized stable cracking (detected phenomenologically)

FIGURE 3.16 FAILURE PROCESS OCCURRING WHEN CONCRETE IS SUBJECTED TO INCREASED LOADING[121, 141].

3.3.1.1 Models Based on Elasticity

In this category five main models are encountered:

1. Isotropic Linear Elastic
2. Cauchy Elastic
3. Hyper Elastic or Green Elastic
4. Hypo Elastic
5. Variable Moduli

The first two types are the simplest to use requiring only a few parameters for their implementation (usually the Young Modulus E and the Poisson Ratio ν). As it was discussed previously, this type of material models is used extensively, as a result of its simplicity, by most commercial software for the analysis and design of RC structures.

The Cauchy Elastic Model is usually of the form

$$\sigma = f(\varepsilon) \tag{3.1}$$

and its main drawback is the generation of energy under certain loading-unloading cycles, which is inadmissible since it violates the laws of thermodynamics.

In Hyper and Hypo Elastic models, the energy can be generated through any load cycle and thermodynamic laws are always satisfied. Their main difference is that for the Hyper Elastic model stresses are expressed in terms of a strain-energy density function independent from the loading path leading to the current state. On the other hand, Hypo Elastic models are described in terms of increments of stresses and strains. Such models are dependent on the deformation history and conceptually, such models are capable of accounting for the material anisotropy at high loads. The main drawback of this model is the complexity of their formulation since their aim is to predict the nonlinear behavior of concrete at moderately high load levels.

The last model type is the Variable Moduli where the employment of a loading surface is adopted in order to make a distinction between loading and unloading. Unloading and loading are performed when the new stress increment gives a stress state within or outside the loading surface, respectively. Nevertheless, this type of models is not based on solid mechanical foundations.

3.3.1.2 Models Based on Plasticity

Plasticity models usually rely on the classical plasticity theory assuming that the strains can be separated into an elastic and a plastic component, according to Eq. 3.2.

$$d\boldsymbol{\varepsilon}_{ij} = d\boldsymbol{\varepsilon}_{ij}^{e} + d\boldsymbol{\varepsilon}_{ij}^{p} \qquad 3.2$$

When the yield criterion is satisfied (von Mises, Mohr-Coulomb, Drucker-Prager, Tresca-Guest, Huber–Mises–Hencky, Mroz multi-surface plasticity) a decrease of the elastic modulus is assumed (hardening modulus) resulting to the degradation of stiffness. This formula may be suitable for steel materials, however for concrete is not suitable since hardening is a phenomenon that does not occur in concrete materials as it was explained previously. In Figs. 3.17 different yield surfaces can be seen. Lubliner et al.[142] (1989) and Lubliner[143] (1990) suggested that the yield surfaces should be readjusted according to the stress state with multiple criteria.

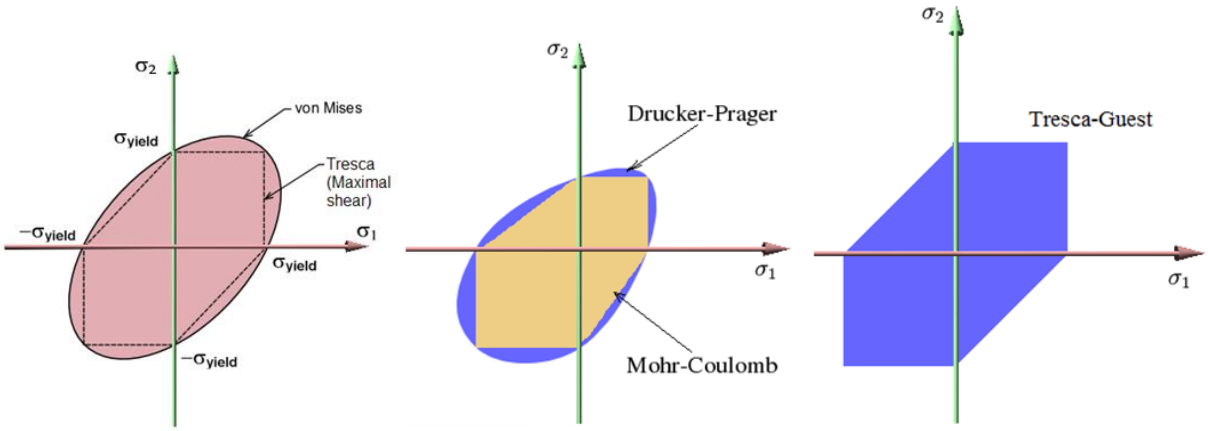

(A) (B) (C)

FIGURE 3.17 DIFFERENT YIELD CRITERIA.

In order to capture the elastic degradation of concrete, the plastic fracturing theory is used which is an extension of the classical plasticity theory. It accounts for the degradation of the elastic material modulus with respect to the increase of deformation according to:

$$\dot{\boldsymbol{\sigma}} = \boldsymbol{C}\dot{\boldsymbol{\varepsilon}}_{ij}^{el} + \dot{\boldsymbol{C}}\boldsymbol{\varepsilon}_{ij}^{el} \quad 3.3$$

where $\boldsymbol{C}$ is the elastic constitutive matrix, $\dot{\boldsymbol{C}}$ denotes the rate of degradation of the elastic constitutive matrix and $\dot{\boldsymbol{\varepsilon}}_{ij}^{el} = \dot{\boldsymbol{\varepsilon}}_{ij} - \dot{\boldsymbol{\varepsilon}}_{ij}^{p}$. This formulation is more accurate when modeling concrete materials since it accounts for the elastic degradation of the elastic branch caused by micro-cracking.

A more complex plasticity-based type of model is called Endochronic (Valanis[144] (1971)) and can be regarded as a more sophisticated type of a visco-plasticity model, which is characterized by the dependence of the viscosity on the strain rate. Through the endochronic theory the prediction of material behavior under non-proportional loading is achieved accounting for pronounced rotations of the principal stresses. Given its complex formulation, there are very few experimental data existing for such loading paths. Moreover, it is difficult to obtain the large number of material parameters required through experimental tests.

3.3.1.3 Damage Models

Damage models are based on the thermodynamic law and can model the internal mechanism of progressive propagation and concentration of micro-cracks in brittle materials like concrete. The damage of the material is induced through the use of a damage index $0 < d < 1$ which causes the degree of the degradation in the stiffness matrix.

Several studies on damage models can be found in the literature (Bažant and Kim[145] (1979), Mazars, J.[146] (1986), Lemaitre[147] (1986), Chaboche[148, 149] (1988), Lubliner et al.[142] (1989), Lemaitre[150] (1996), Meschke et al.[151] (1998), Ragueneau et al.[152] (2000), Kattan and Voyiadjis[153] (2002), Cusatis et al.[154] (2008), Benzarti et al.[155] (2009), Yu et al.[156] (2010)).

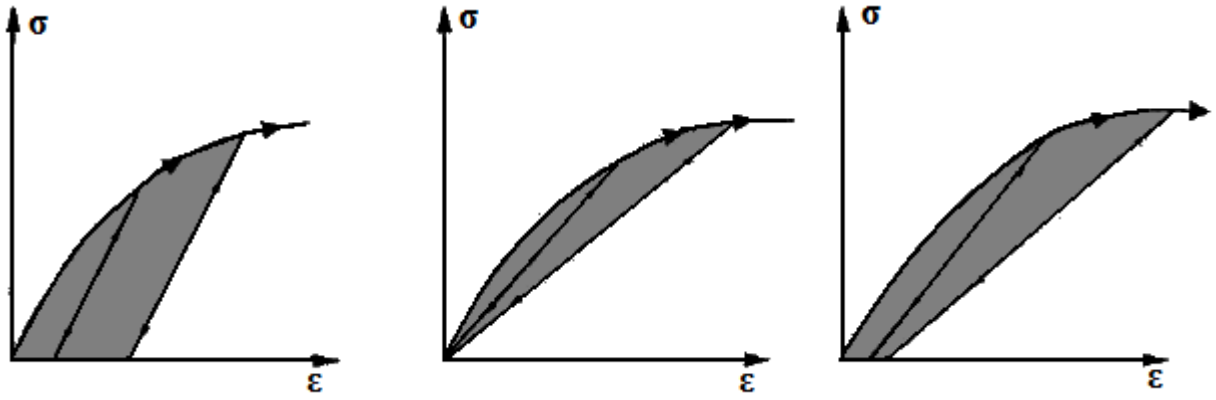

(A) (B) (C)

FIGURE 3.18 (A) ELASTOPLASTIC MODEL WITH HARDENING, (B) ELASTIC MODEL WITH DAMAGE AND (C) COMBINATION OF (A) AND (B).

It is evident that damage models are widely used, due to the simplicity of their formulation and ability of combining them with other methods like elasticity, elastoplasticity or even debonding

behavior models in order to capture the nonlinear behavior of brittle materials. A schematic illustration of the resulted model when combining a damage model with the elastoplastic model with hardening is given in Fig. 3.18.

3.3.1.4 Microplane Models

This type of models, project the strain tensor of a material point to numerous spatially oriented planes which this point contains. The constitutive relations are formulated for each one of these planes where the stresses acting on them are obtained. The initial idea behind these models was presented by Bažant and Gambarova[157] (1984), Bažant and Prat[158] (1988) and in continuation of the latter the models were extended in Bažant et al.[135, 159] (2000, 2001), Bažant and Caner[136, 137] (2005). In Bažant and Ozbolt[160] (1990) it was shown that microplane models are suitable for modeling brittle material in monotonic and cyclic loadings. Fig. 3.19 shows schematically the coupling of kinematically and statically constrained microplane systems for hardening and softening responses and the components of strain or stress vectors on microplane proposed by Bažant and Caner[136, 137].

These models have also the advantage of being able to account for time-depending material phenomena. According to CEB[105] 1996 this type of models can predict objectively the behavior of plain concrete for any type of loading.

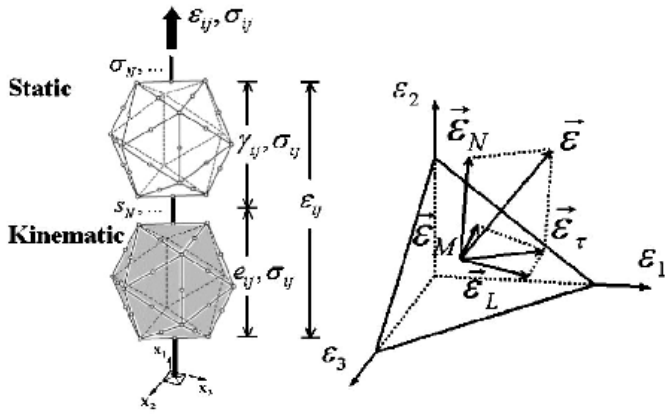

FIGURE 3.19 LEFT: COUPLING OF KINEMATICALLY AND STATICALLY CONSTRAINED MICROPLANE SYSTEMS FOR HARDENING AND SOFTENING RESPONSES. RIGHT: COMPONENTS OF STRAIN OR STRESS VECTORS ON MICROPLANE[136].

3.3.1.5 Crack Models

All the previously mentioned models have a significant disadvantage when it comes to the objective and realistic modeling of brittle materials. Since brittle materials do not appear to have softening branches and for a specific level of loading the ultimate tensile stress is reached, the opening of cracks occurs initiating a significant redistribution of the internal stresses. In order to account for cracking and to predict the redistribution of internal stresses and strains, the use of crack models is necessary. Four main categories can be found in the literature for modeling the crack phenomena:

A. Discrete Crack Models
B. Smeared Crack Models
C. Discrete Element Methods
D. Meshless or Meshfree Methods

The first two models are widely used by several researchers with satisfactory results in terms of accuracy and experimental verification. The other two models are relatively new and appeared the last two decades illustrating very good characteristics but with many numerical and computational problems to be solved.

A brief presentation of these four crack modeling methods will follow and a more extensive discussion on the smeared crack approach will be presented, since this is the method adopted in this research work.

3.3.1.5.1 Discrete Crack Models

The main idea behind this type of models is to create the discrete crack occurring within the FE mesh and separate the nodes between the two adjacent crack faces (Fig. 3.20). This way a discrete representation of the crack is achieved (Fig. 3.21) and the stiffness of the structure is regenerated accordingly. This method was used in the first FE analysis conducted by Ngo and Scordelis[161] (1967), but the method did not become as popular as the smeared crack approach. This is attributed to the numerous computational issues that arise when crack opening occurs.

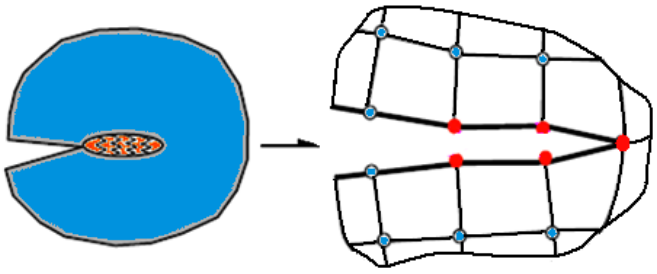

FIGURE 3.20 SCHEMATIC REPRESENTATION OF CRACK OPENING IN 2D.

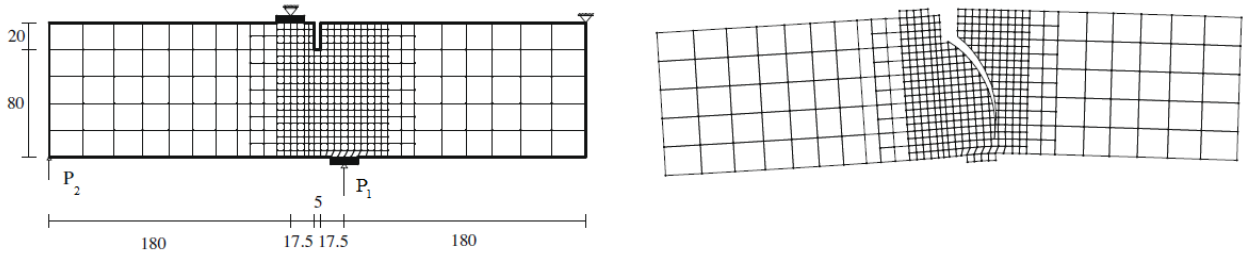

FIGURE 3.21 DISCRETE CRACK MODELS. CRACK PATTERN OF A SINGLE EDGE NOTCHED BEAM[172].

Several researchers tried to improve this type of methods (Nilson[162] (1968), Grootenboer et al.[163] (1981), Feenstra et al.[164] (1991), Rots[165] (1991), Xie and Gerstle[166] (1995), Bittencourt and Ingraffea[167] (1995), Riddell et al.[168] (1997), Ruiz et al.[169] (2001), Galvez et al.[170] (2002), Prasad and Krishnamoorthy[171] (2002), Dias-da-Costa[172] (2009)). Nevertheless, all numerical tests that are encountered in the literature are strictly limited to simple structural

member implementations pointing the major disadvantage of this approach when it comes to multi-member RC structures.

3.3.1.5.2 Smeared Crack Models

The basic idea of smeared crack models is to introduce cracked areas by modifying the stiffness properties and stresses at relevant integration points. This approach gives the ability of simulating individual cracks without the need of mesh alterations like in the case of the discrete-crack approach described in the previous sub-section. As it was mentioned, the first discrete-crack model appears to have been used by Ngo and Scordelis[161]. The main disadvantage of the discrete-crack approach is that it requires intricate programming techniques and even then it is restricted in use since complicated mesh refinements become necessary to accommodate the propagation of only a few cracks. Then again, the main advantage of the discrete-crack approach is the ability of modeling the crack's tip. Even so, the heterogeneous nature of concrete at such microscopic scale can no longer be ignored, thus this kind of modeling introduces formidable problems even to the powerful analytical tools afforded by present-day. This is the main reason why discrete-crack approach cannot yet be used to simulate and analyze full-scale RC structures.

Other methods were developed in order to model discontinuities like the discrete finite element method, the particle finite element method, the extended finite element method etc. The basic problem in implementing these methods is the computational cost due to the necessity of mesh refinements required when cracks open.

Since material properties are computed and evaluated only at specific points in an element, such as the integration points or the nodes, the change of material properties due to cracking affects the contributing region from which these properties are evaluated. Hence smearing the effect of cracking over a greater region manages to utilize the method with the ability of modeling cracks without the need of remeshing. In fact, a single crack represents an infinite number of parallel fissures throughout that part of the element related to an integration point or a node. Therefore, the essence of smeared modeling is the setting up of cracked areas by modifying the stiffness matrix and stresses at the relevant Gauss points. In this work, an 8-noded hexahedral element with *8* Gauss points is used and when a crack is created, it affects only the stiffness properties of that specific Gauss point, thus one eighth of the element is affected. The smeared crack method implemented in this work is based on the Rashid[123] (1968) work as described by Gonzalez-Vidosa et al.[173] (1991).

The non-linear analysis process considers that the external load is applied incrementally and the computation of the global equilibrium at each load increment is performed. At each load increment, the stress-increments at any Gauss point are found from the corresponding stress-strain increments through the constitutive matrix $\boldsymbol{C}$.

$$\Delta\boldsymbol{\sigma} = \boldsymbol{C} \cdot \Delta\boldsymbol{\varepsilon} \qquad 3.4$$

$$\begin{Bmatrix}\Delta\sigma_x\\ \Delta\sigma_y\\ \Delta\sigma_z\\ \Delta\tau_{xy}\\ \Delta\tau_{yz}\\ \Delta\tau_{zx}\end{Bmatrix}=\begin{bmatrix}2G+\mu & \mu & \mu & . & . & .\\ \mu & 2G+\mu & \mu & . & . & .\\ \mu & \mu & 2G+\mu & . & . & .\\ . & . & . & G & . & .\\ . & . & . & . & G & .\\ . & . & . & . & . & G\end{bmatrix}\cdot\begin{Bmatrix}\Delta\varepsilon_x\\ \Delta\varepsilon_y\\ \Delta\varepsilon_z\\ \Delta\gamma_{xy}\\ \Delta\gamma_{yz}\\ \Delta\gamma_{zx}\end{Bmatrix} \quad 3.5$$

where

$$\mu=\frac{\nu\cdot E}{(1-\nu)(1-2\nu)},\ \text{Lame constant or}\ \ \mu=K-\frac{2G}{3} \quad 3.6$$

Eqs. 3.4 and 3.5 refer to an uncracked Gauss point where we assume that the concrete has no discontinuities. Since the relations are in incremental form, the above material constants are the tangent ones. They may be evaluated[8] by differentiation from the secant material constants and are functions of σ_0 and τ_0 as they are described in the Kotsovos and Pavlovic[8] constitutive concrete law (section 3.3.3).

A crack occurs when the ultimate deviatoric stress τ_{0u} at a Gauss point has been exceeded (usually in tension or tension-compression combinations) where a plane is formed (crack's plane) which is perpendicular to the direction of the maximum tensile stress that existed before the cracking. This tensile stress is set to zero and transformed into unbalanced forces which are going to be distributed throughout the surrounding Gauss points.

The relations between stress-strain increments, in local axes, subsequently become such that the third local axis is perpendicular to the plane of the crack (*axis z΄*), implying zero stress along this axis (Fig. 3.22). The shear rigidity is G in the uncracked plane and a residual shear rigidity βG is assumed in the other two planes (Eq. 3.7). The stress-strain incremental relationship takes the following form:

$$\begin{Bmatrix}\Delta\sigma'_x\\ \Delta\sigma'_y\\ \Delta\sigma'_z\\ \Delta\tau'_{xy}\\ \Delta\tau'_{yz}\\ \Delta\tau'_{zx}\end{Bmatrix}=\begin{bmatrix}2G+\mu & \mu & . & . & . & .\\ \mu & 2G+\mu & . & . & . & .\\ . & . & . & . & . & .\\ . & . & . & G & . & .\\ . & . & . & . & \beta G & .\\ . & . & . & . & . & \beta G\end{bmatrix}\cdot\begin{Bmatrix}\Delta\varepsilon'_x\\ \Delta\varepsilon'_y\\ \Delta\varepsilon'_z\\ \Delta\gamma'_{xy}\\ \Delta\gamma'_{yz}\\ \Delta\gamma'_{zx}\end{Bmatrix} \quad 3.7$$

If a tensile state of stress is reached for the second time, then a second crack opens and its plane is perpendicular to the direction of the new maximum principal tensile stress which together with the previous plane leaves only stiffness along the intersection of the two planes (Fig. 3.22). Therefore, the incremental-stresses in terms of the incremental-strains along these Cartesian axes (x΄΄, y΄΄, z΄΄) are given by

$$\begin{Bmatrix} \Delta\sigma''_x \\ \Delta\sigma''_y \\ \Delta\sigma''_z \\ \Delta\tau''_{xy} \\ \Delta\tau''_{yz} \\ \Delta\tau''_{zx} \end{Bmatrix} = \begin{bmatrix} . & . & . & . & . & . \\ . & 2G+\mu & . & . & . & . \\ . & . & . & . & . & . \\ . & . & . & \beta G & . & . \\ . & . & . & . & \beta G & . \\ . & . & . & . & . & \beta G \end{bmatrix} \cdot \begin{Bmatrix} \Delta\varepsilon''_x \\ \Delta\varepsilon''_y \\ \Delta\varepsilon''_z \\ \Delta\gamma''_{xy} \\ \Delta\gamma''_{yz} \\ \Delta\gamma''_{zx} \end{Bmatrix} \quad 3.8$$

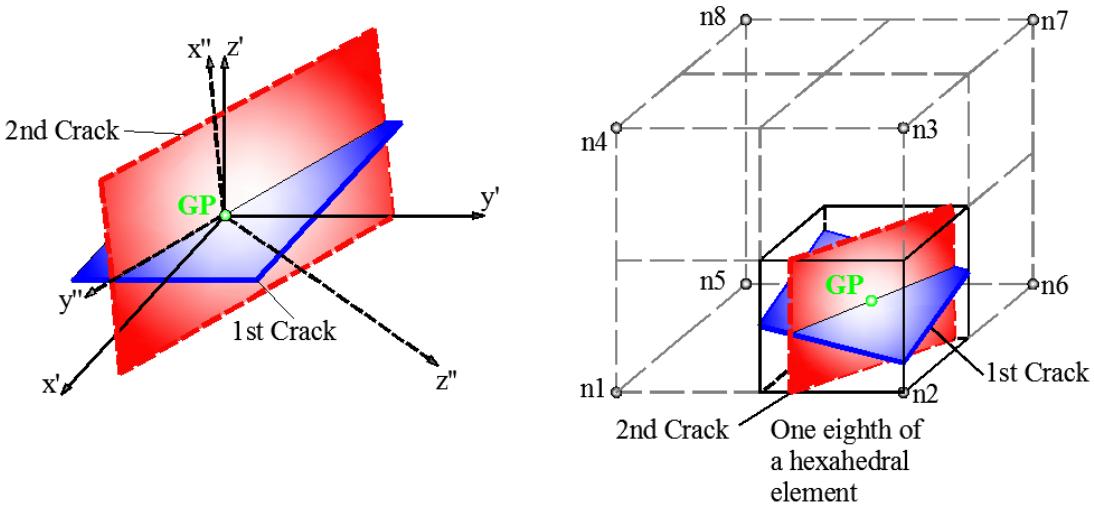

FIGURE 3.22 LOCAL AXES FOR THE CASE OF TWO CRACKS AT A SPECIFIC GAUSS POINT.

Because of the anisotropy induced from the crack openings, the expression of the stress–strain matrix in local axes is transformed to global axes using the standard coordinate system transformation laws. If a third tensile stress occurs at the same Gauss point, then we assume a complete loss of the carrying capacity at that specific Gauss point. This is performed by setting to zero the constitutive matrix ***C***.

Parameter β

The main arithmetical problem of the smeared crack method are the ill-posed stiffness matrices that are produced when crack openings occur, which may result in numerical difficulties during the solution of the nonlinear incremental equations. For this reason, parameter β is vital when using the smeared crack approach due to its numerical contribution when one or more cracks open. This parameter is correlated to the remaining stiffness due to aggregate interlocking along the crack's surface. If this parameter is neglected and set to zero, then an instability of the numerical solution procedure may be observed and it would have been unable to proceed after the opening of the first cracks. The most commonly used value for this variable is that of β = *0.05-0.1* which was extracted through experimental data[174]. It is therefore assumed that *5-10%* of the initial shear stiffness remains after the crack opening and is applied along the crack's plane. In the numerical tests that will be presented in this work, the value assumed for this parameter was set equal to *5%*.

3.3.1.5.3 Discrete Finite Element Methods

The Discrete Element (DE) Methods (also called smooth Particle Hydrodynamics) are rapidly evolving methods that have demonstrated satisfactory results especially for impact problems and problems that produce high nonlinearities attributed to high deformations. The main idea of DE methods is to discretize the continuum media with relatively small discrete elements (tetrahedral, hexahedral, spheres) which are connected to each other through special boundary conditions. Usually these boundary conditions obey material rules that are governed by a yielding surface, as shown in Fig. 3.17. When for the case of two neighboring elements this criterion is satisfied, then the rigid connection ceases and the two elements are not connected to each other and a discontinuity is introduced (crack). The material can be modeled at a meso- or macro-scale, with the size of the DE being small enough in order for the model to be predictive. Nevertheless, the DE size is always restricted from the computational cost due to the large number of elements required when very small sizes during discretization are implemented. Finally, the identification process used, plays a significant role for the predictiveness of a model as described by Hentz et al.[175]. In their work, an extensive presentation of the DE model is attempted.

Because of the computational demands of these models, multi-domain finite and DE method (Fig. 3.23) was proposed by Rousseau et al.[176] (2009). Despite the decrease in the number of dof, this method is unable to overcome the excessive computational effort, thus implementations are restricted to single structural element problems. More literature and details about discrete models can be found in Rousseau et al.[177] (2007) and Hentz et al.[175] (2004).

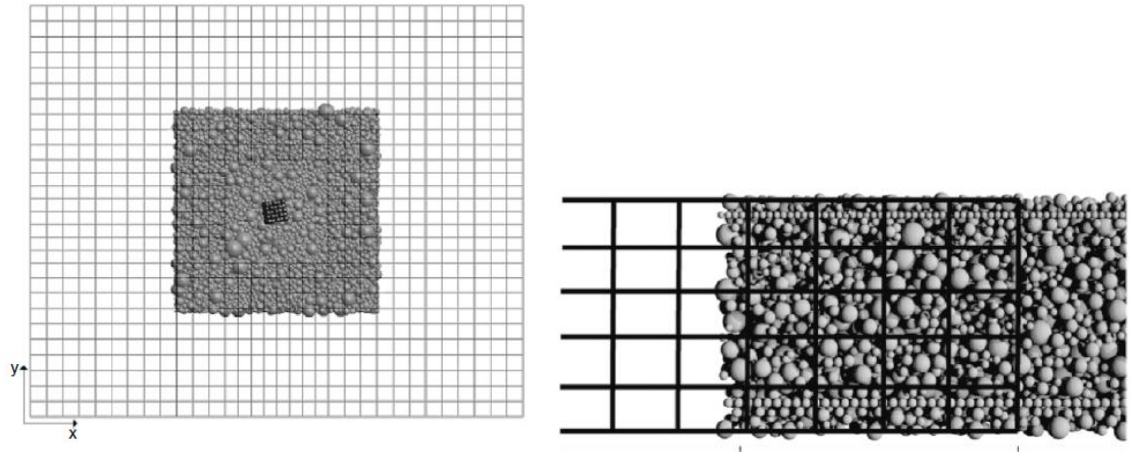

FIGURE 3.23 COMBINED FINITE AND DISCRETE ELEMENT METHODS FOR MODELING AN IMPACT PROBLEM[176]. LEFT: FULL MODEL. RIGHT: TRANSACTION AREA.

3.3.1.5.4 Meshless or Meshfree Methods

These methods are mesh free in terms of the discretization of the media and a particle-based concept is applied, which is particularly suitable for the analysis of fracture, due to its capacity to model large deformation and track the free surfaces generated. Continuum damage models are usually used to predict the fracture within the model and the evolution of damage can be predicted by using the strain history of each particle. For the case of brittle materials, damage

usually inhibits the transmission of tensile stress between particles and once the stress reaches unity it is unable to transmit tensile deformations, resulting in a macro-crack. Connected macro-cracks lead to complete fragmentation.

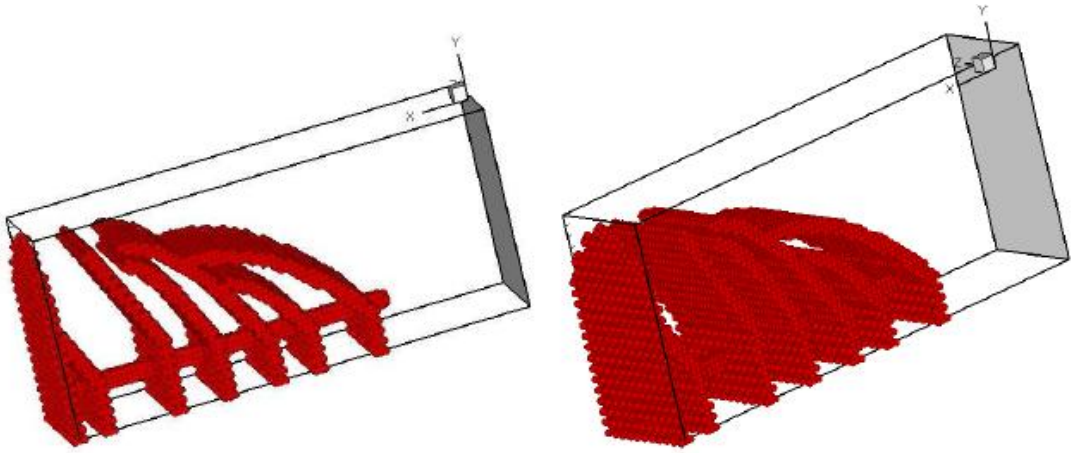

FIGURE 3.24 CRACK PATTERN OF THE REINFORCED CONCRETE BEAM AT FAILURE FROM TWO DIFFERENT VIEWING POINTS[179].

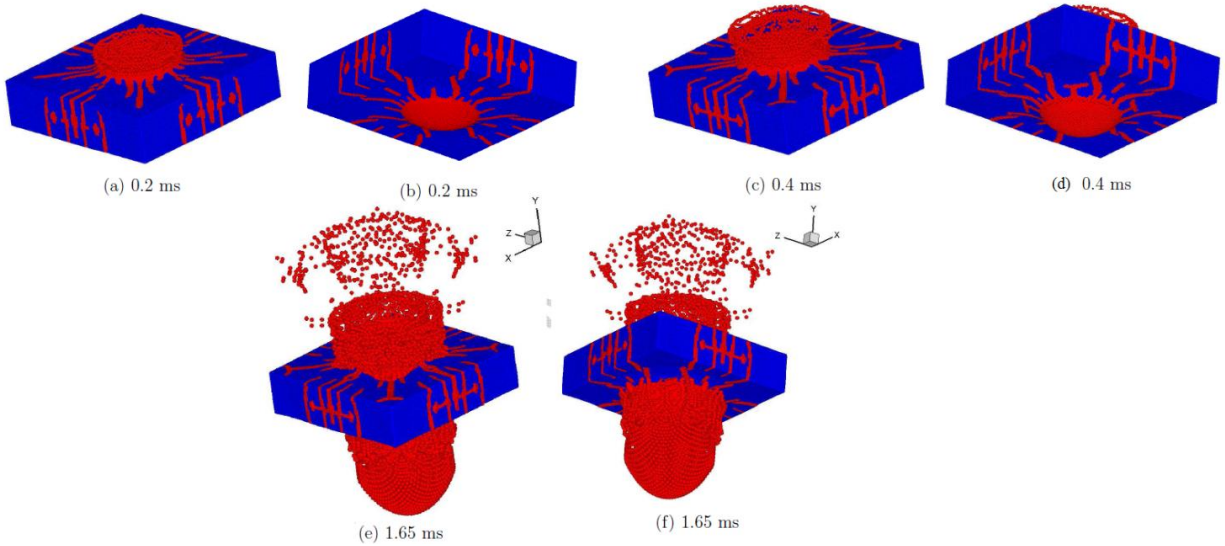

FIGURE 3.25 CONCRETE SLAB O1 UNDER EXPLOSIVE LOADING USING APPROXIMATELY *265,000* PARTICLES, IN RED: CRACKED PARTICLES, IN BLUE: UNCRACKED PARTICLES[178].

As it can be seen in Figs. 3.24 and 3.25, due to the nature of the method, the cracks can be arbitrarily oriented and as it is stated in Rabczuk and Belytschko[178] (2007) their growth is represented discretely by activation of crack surfaces at individual particles.

The method also appears to be less complex than the interelement separation models[179-181] and significantly less complex than the extended finite element method[182]. In the latter, the cracks can be modeled only along element interfaces in the mesh (Camacho and Ortiz[179] (1996), Ortiz and Pandolfi[180] (1999) and Zhou and Molinari[181] (2004), Belytschko and Gracie[182] (2007)).

It is the author's opinion that, despite the fact of the necessity for further improvement, concerning the assumptions made for the particle interactions and the computational excessive demands, which are attributed to the nature of this type of methods, they will eventually dominate the scientific field of crack modeling. Given the large interest shown in the detailed

simulation of heterogeneous materials, it is one of the most promising modeling methods, for the analysis of brittle heterogeneous materials. More references on meshless and meshfree methods can be found in Belytschko and Lu[183] (1995) and Liu[184] (2003).

3.3.2 Kotsovos and Newman Experimental Findings

After the review on the available material models for concrete analysis and the methods for modeling cracks, the Kotsovos and Pavlovic[8] material model will be presented together with the numerical modifications performed for the purposes of this research work. The presentation and discussion of the experimental findings of Kotsovos and Newman[101-103] (1977-1979) will proceed, followed by the proposed modifications.

The experimental program conducted by Kotsovos and Newman[101-103] concerned a range of concrete specimens with uniaxial cylinder compressive strength varying in the range $15\ MPa \leq f_c \leq 65\ MPa$. The specimens were tested under different stress state (compression, tension, triaxial compression, triaxial tension) and the stress-strain relationships were expressed in terms of normal stresses $(\sigma_1, \sigma_2, \sigma_3)$ and normal strains $(\varepsilon_1, \varepsilon_2, \varepsilon_3)$. Typical experimental stress-strain curves obtained for cylindrical specimens under uniaxial compression can be seen in Fig. 3.29a for different concrete types and in Fig. 3.26b the case of concrete with compressive strength $f_c = 31.7\ MPa$, which was tested for different types of triaxial compression for various values of hydrostatic stress σ_o .

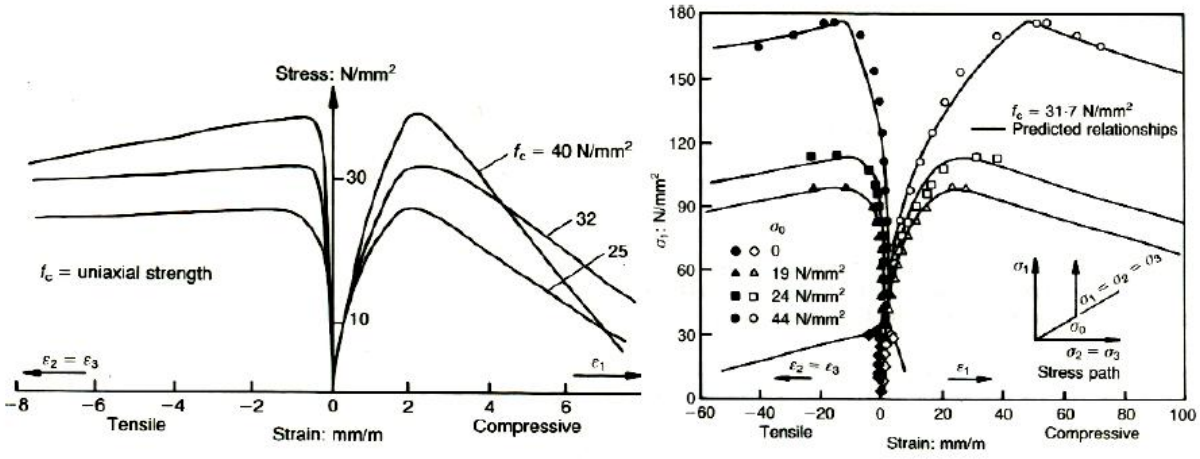

(A) (B)

FIGURE 3.26 TYPICAL STRESS-STRAIN CURVES FOR CONCRETES OBTAINED FROM TESTS ON CYLINDERS[104]. (A) VARIOUS CONCRETES UNDER UNIAXIAL COMPRESSION AND (B) CONCRETE WITH $f_c = 31.7\ MPa$ UNDER TRIAXIAL COMPRESSION FOR VARIOUS VALUES OF HYDROSTATIC STRESSES σ_0.

For the analysis of the experimental data (both uniaxial and multiaxial), use is made of the assumption that the nonlinear material behavior is governed mainly by changes in the structure. These structural changes occur in the form of fracture initiation and propagation processes which have the following two opposing effects on the material deformation:

Effect A. Cracking causes a reduction of the high, predominantly tensile stress concentrations existing near the crack tips. This reduction in tensile stress can be

assumed to be equivalent to the application of a compressive stress that tends to reduce the volume of concrete.

Effect B. Cracking produces voids, which tend to increase the volume of material.

It is assumed that the deformation history and crack pattern evolution until complete failure can be divided into three main stages. These stages are illustrated schematically in Fig. 3.27 and can be described as follows:

Stage I

The elastic deformation is dominant from the onset of loading up to *30 ÷ 70%* of f_c. The lower limiting value applies for low strength concrete and the higher value applies for high strength concrete. There is only a small increase of microcracks and the material behavior is approximately linear. At this stage effect A is significant while effect B is relatively insignificant since cracking is localized. This has the result of the specimen's volume decrease.

During this stage, the microcracks remain stable and do not propagate. With increasing load tensile strains start to concentrate near the crack tips and the initially stable microcracks start to branch in the direction of the maximum principle compressive stress. This branching process tends to relief strain concentrations. Once strain redistribution has occurred, the individual crack configurations remain stable during further increase of the applied stress. The start of such deformational behavior is termed LFI (Local Fracture Initiation) by Kotsovos and Newman[185], see Fig. 3.27. The beginning of this local fracture initiation is shown by a dotted line in the stress and the strain space for the triaxial loading in Fig. 3.28.

Stage II

In this stage, effects A and B are both significant, but effect A is greater than the effect B thus the volume continues to decrease. Analyzing this behavior, it means that the existing cracks propagate in the direction of the compressive load in a relatively stable manner. If the applied load is held constant, crack propagation does not continue. This behavior is termed as OSFP (Onset of Stable Fracture Propagation) which is given in Fig. 3.27.

Stage III

This is the final stage where for the first time effect B is more significant than effect A, causing a volume increase of the specimen. The degree of cracking can reach a level, at which the crack system becomes unstable and failure occurs even if the load remains constant over a relatively long time. The start of this stage is termed as OUFP (Onset of Unstable Fracture Propagation) in Fig. 3.27 and it is characterized from the fact that the volume becomes minimum. The load can still be increased beyond this point to the Ultimate Surface (US), but the amount of increase depends on the rate at which the load is applied and the loading device.

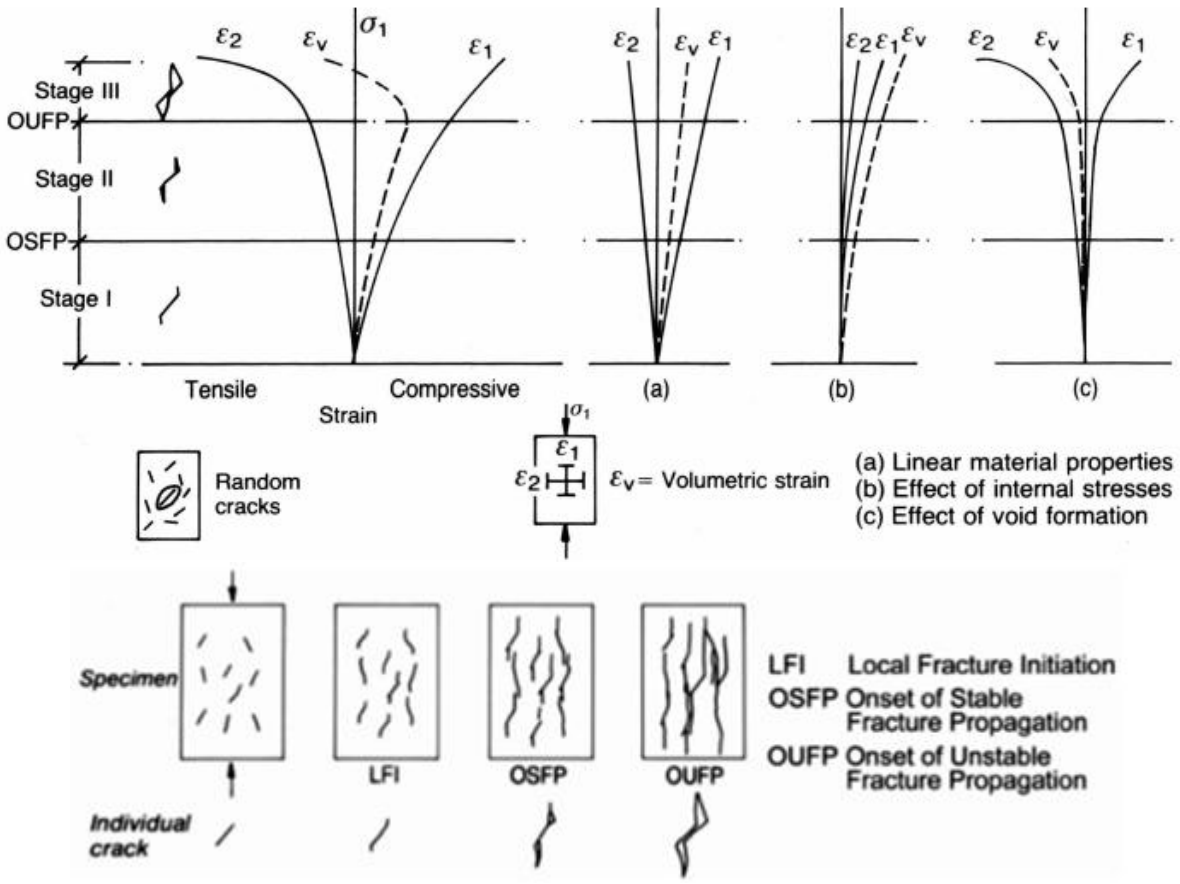

FIGURE 3.27 STAGES IN THE PROGRESS OF CRACK DEVELOPMENT UNDER COMPRESSIVE LOAD[185].

Based on the above description, the deformation behavior of concrete was decomposed into the following three components:

1. A linear component throughout, governed by the material characteristics which is unaffected by the fracture process.
2. A nonlinear component expressing the effect of the internal stresses caused by the fracture processes.
3. A nonlinear component expressing the effect of void formation.

After the gathering of the experimental results (Fig. 3.29), the analysis of the experimental data was performed by transforming the stress-strain curves into corresponding hydrostatic and deviatoric stress and strains components, i.e. in the form of normal and shear octahedral stresses ($\sigma_o - \tau_o$) and strains ($\varepsilon_o - \gamma_o$), respectively (Eqs. 3.9-3.12). For the definition of these octahedral parameters see Appendix A.

$$\sigma_o = \frac{1}{3}(\sigma_1 + \sigma_2 + \sigma_3) \quad 3.9$$

$$\varepsilon_o = \frac{1}{3}(\varepsilon_1 + \varepsilon_2 + \varepsilon_3) \quad 3.10$$

$$\tau_o = \frac{1}{3}\sqrt{(\sigma_1 - \sigma_2)^2 + (\sigma_2 - \sigma_3)^2 + (\sigma_3 - \sigma_1)^2} \quad 3.11$$

$$\gamma_o = \frac{1}{3}\sqrt{(\varepsilon_1 - \varepsilon_2)^2 + (\varepsilon_2 - \varepsilon_3)^2 + (\varepsilon_3 - \varepsilon_1)^2} \quad 3.12$$

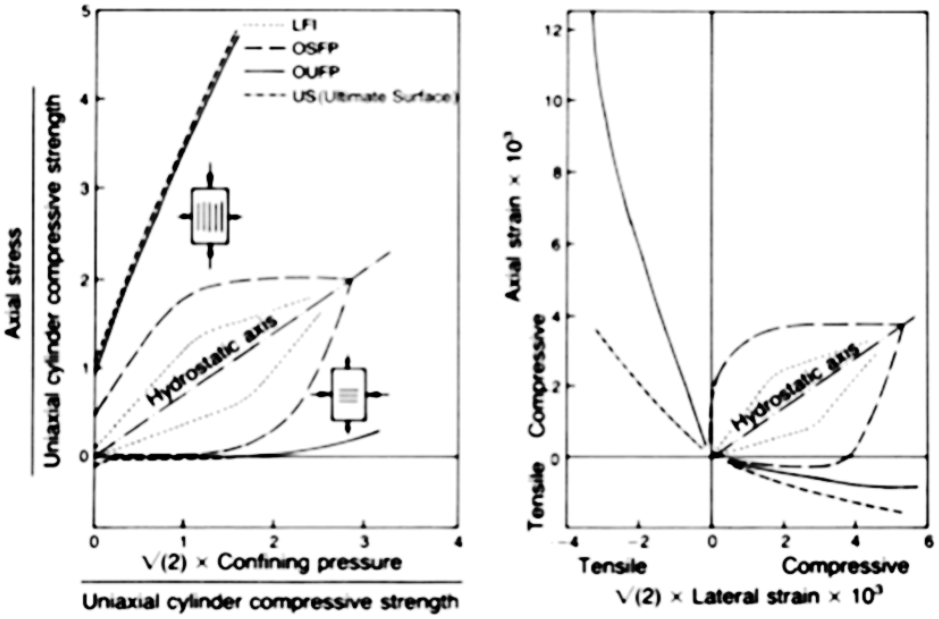

FIGURE 3.28 TYPICAL LFI, OSFP, AND US ENVELOPES IN STRESS SPACE AND STRAIN SPACE[185].

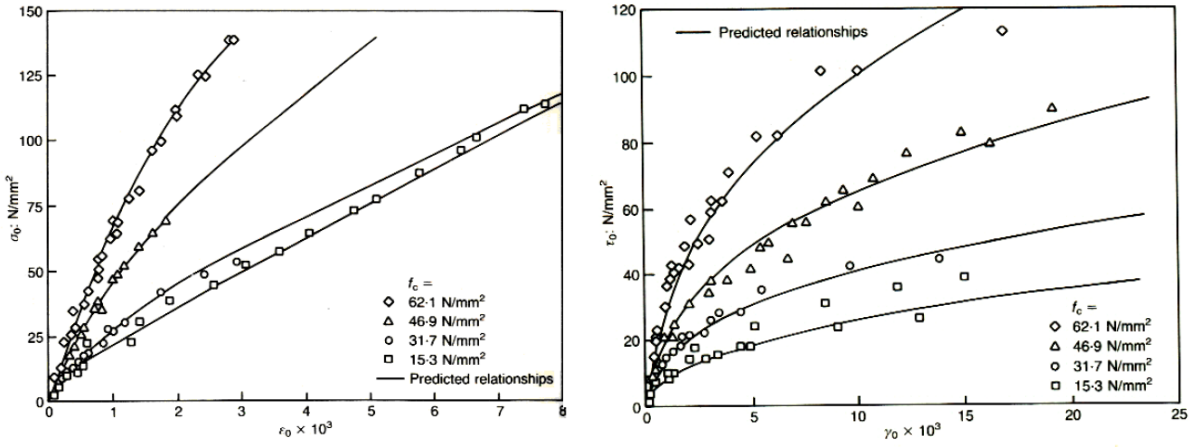

(A) (B)

FIGURE 3.29 TYPICAL EXPERIMENTAL (A) σ_o-$\varepsilon_{o(h)}$ AND (B) τ_o-$\gamma_{o(d)}$ CURVES FOR VARIOUS CONCRETES[95].

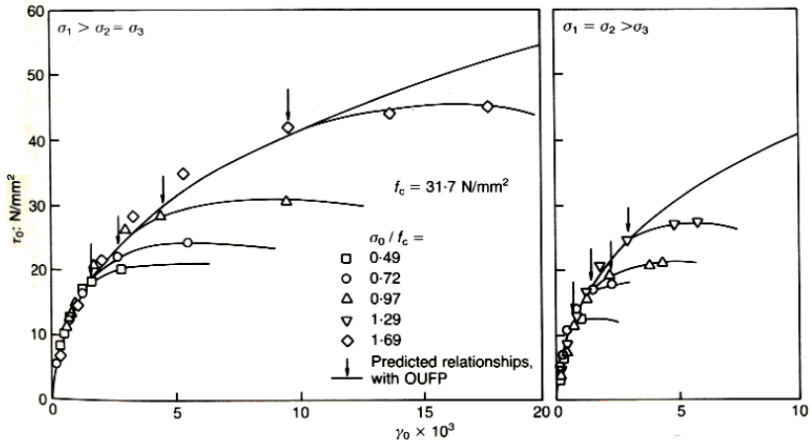

(A) (B)

FIGURE 3.30 TYPICAL EXPERIMENTAL τ_o-$\gamma_{o(d)}$ CURVES FOR CONCRETE WITH $f_c = 31.7MPa$, FOR TWO POSSIBLE STRESS PATHS. (A) $\sigma_1 > \sigma_2 = \sigma_3$ AND (B) $\sigma_1 = \sigma_2 > \sigma_3$[95].

The results of these tests, indicated that the deformational behavior of concrete material under hydrostatic stress σ_o can be described completely by the hydrostatic (volumetric) strain $\varepsilon_{o(h)}$, since the corresponding deviatoric strain $\gamma_{o(h)}$ has been found to be insignificant[185]. By using the subscript *h* it is denoted that the octahedral strains result from the application of pure hydrostatic stress state. These relationships $\sigma_o - \varepsilon_{o(h)}$ depend only on the uniaxial strength f_c of the concrete (Fig. 3.29a).

If the specimen is deformed through the application of an external deviatoric stress τ_0 then both volumetric and deviatoric strains are affected. Therefore, the deformation response of concrete under increasing deviatoric stress is defined by both $\tau_o - \gamma_{o(d)}$ and $\tau_o - \varepsilon_{o(d)}$ relationships. In this case, the subscript *d* denotes that the octahedral strains are due to a pure deviatoric stress state. Typical deviatoric results are shown in Fig. 3.29b and data points for both $\tau_o - \gamma_{o(d)}$ and $\tau_o - \varepsilon_{o(d)}$ characteristics are given in Figs. 3.31 and 3.32 respectively.

It is evident that both sets of curves are essentially independent of the stress path, indicating that the influence of the direction of τ_o on the octahedral planes is negligible and that any stress-induced anisotropy is insignificant and can be ignored for practical purposes. In addition to that, the stress path independency was also illustrated by Gerstle et al.[95] (1980) and it is shown in Fig. 3.32. The stress paths denoted as *1* and *3* correspond to the triaxial loading, while stress path *2* refers to the additional case of constant principal stress. It is obvious that these three paths coincide sufficiently thus it is safe to say that their differences are attributed to random effects.

It is important to annotate at this point that the volumetric deformation due to deviatoric stress is attributed to the normal octahedral internal stress σ_{id}, which is considered to be the result of cracking within the concrete specimen. In the next subsection, the procedure of computing this internal stress from the corresponding $\tau_o - \varepsilon_{o(d)}$ relationship will be shown.

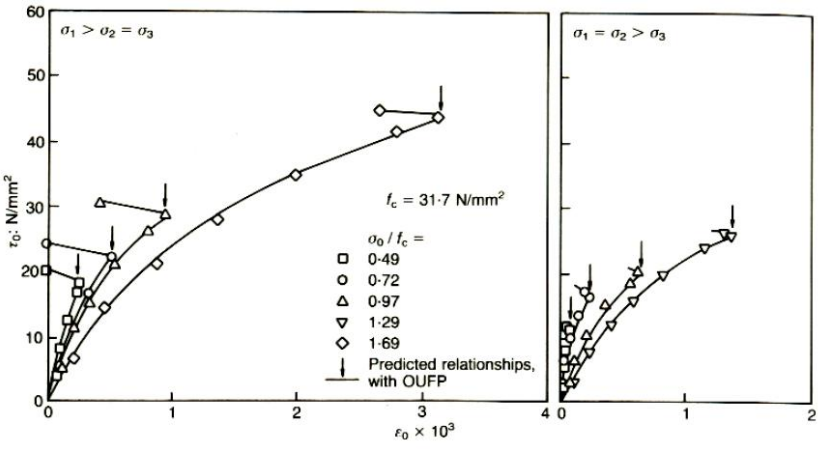

(A) (B)

FIGURE 3.31 TYPICAL EXPERIMENTAL τ_o-$\varepsilon_{o(d)}$ CURVES FOR CONCRETE WITH $f_c = 31.7MPa$, FOR TWO POSSIBLE STRESS PATHS. (A) $\sigma_1 > \sigma_2 = \sigma_3$ AND (B) $\sigma_1 = \sigma_2 > \sigma_3$[95].

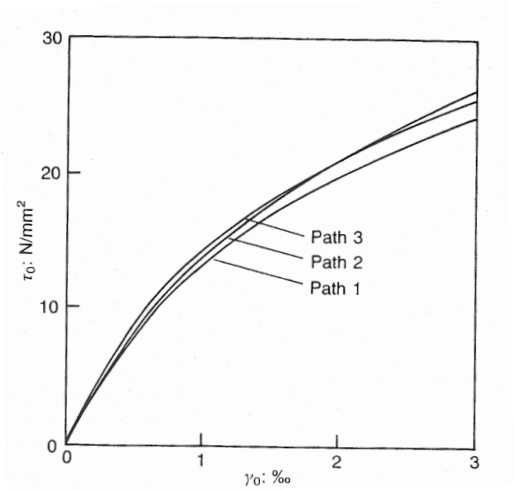

FIGURE 3.32 DEVIATORIC STRESS-STRAIN CURVES OBTAINED FROM TRIAXIAL TESTS BY USING DIFFERENT LOADING PATHS[95].

3.3.3 The Kotsovos and Pavlovic Concrete Material Model

Three different approaches were described by Kotsovos and Pavlovic[8] for the incorporation of the phenomenological features and corresponding experimental findings that were presented in the previous subsection.

Approach 1. Three Moduli
Approach 2. Internal Stress
Approach 3. Combined

The third approach is the material model used in this work and it is a combination of the first two. Given the detailed description of these approaches in the literature, specific features of the first two approaches will be given as they will be needed in the combined approach.

The *three moduli approach* adopts the octahedral representation of stresses and strains, and permits the decoupling of volume and distortional changes, with two natural material constants named bulk modulus *K* and shear modulus *G*, given by the following expressions:

$$K = \frac{\sigma_0}{3\varepsilon_0} = \frac{E}{3(1-2\nu)} \qquad 3.13a$$

$$G = \frac{\tau_0}{3\gamma_0} = \frac{E}{2(1+\nu)} \qquad 3.13b$$

The third material modulus proposed in this approach, is the coupling modulus *H* (Eq. 3.14), which was presented for the first time by Gerstle et al.[95] and modified in the combined approach by an equivalent superimposed stress state (σ_{id}) based on the internal stress concept.

$$H = \frac{\tau_0}{\varepsilon_{0(d)}} \qquad 3.14$$

Through the use of these three material moduli, the concrete behavior is described and the octahedral stress-strain relations can be computed for any given stress state (Eqs. 3.15).

$$\varepsilon_0 = \varepsilon_{0(h)} + \varepsilon_{0(d)} = \frac{\sigma_0}{3K_s} + \frac{\tau_0}{H_s} \qquad 3.15a$$

$$\gamma_0 = \gamma_{0(d)} = \frac{\tau_0}{2G_s} \qquad 3.15b$$

The internal stress concept is described through a typical ascending branch of the stress-strain relations of concrete, depicted in Fig. 3.33. It is assumed that the use of this internal stress state in conjunction with the initial moduli K_e, G_e or E_e, ν_e is sufficient to describe the nonlinear constitutive behavior.

When the material moduli are considered to be constant, the generalized form of Hooke's law for a stress state σ_{ij} may be written as:

$$\varepsilon_{ij} = -\frac{\nu_e}{E_e}\sigma_{kk}\delta_{ij} + \frac{(1+\nu_e)}{E_e}\sigma_{ij} \qquad 3.16$$

or equivalently

$$\varepsilon_{ij} = -\frac{3K_e - 2G_e}{18K_eG_e}\sigma_{kk}\delta_{ij} + \frac{1}{2G_e}\sigma_{ij} \qquad 3.17$$

where K_e, G_e the bulk and shear moduli, respectively. By decomposing the total strains ε_{ij} and stresses σ_{ij} into their hydrostatic components:

$$\varepsilon_0 = \varepsilon_{kk}/3, \quad \sigma_0 = \sigma_{kk}/3 \qquad 3.18$$

and deviatoric components:

$$e_{ij} = \varepsilon_{ij} - \varepsilon_0\delta_{ij}, \quad s_{ij} = \sigma_{ij} - \sigma_0\delta_{ij} \qquad 3.19$$

the following generalized form of Hooke's law is obtained:

$$\varepsilon_{ij} = \varepsilon_0\delta_{ij} + e_{ij} = \frac{\sigma_0}{3K_e}\delta_{ij} + \frac{s_{ij}}{2G_e} \qquad 3.20$$

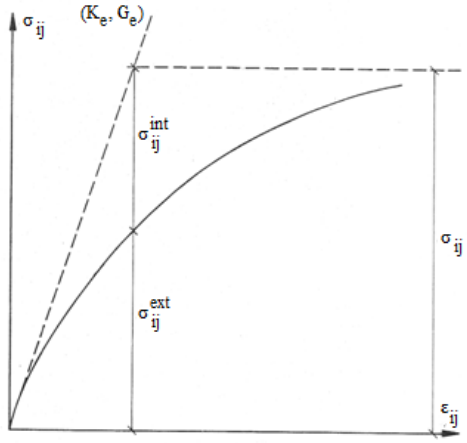

FIGURE 3.33 THE INTERNAL STRESS CONCEPT USED TO ACCOUNT FOR NONLINEAR CONSTITUTIVE RELATIONS OF CONCRETE MATERIALS[8].

In order for the above equations to be valid, the following expression must be satisfied:

$$\sigma_{ij} = \sigma_{ij}^{ext} + \sigma_{ij}^{\text{int}} \tag{3.21}$$

where the subscripts *ext* and *int* denote the external applied and the internal microcracking stress states, respectively. By decomposing each state of stress and strain into a hydrostatic and a deviatoric component, the internal stress state may be quantified through the use of experimental data shown in Figs. 3.29-3.31. After a regression analysis of $\sigma_o - \varepsilon_{o(h)}$ data, the relation between external stress and resulting strain was found to be:

$$\varepsilon_{0(h)} = \frac{\sigma_0 + 3\alpha K_e \sigma_0^b}{3K_e} \quad \text{for } \sigma_0/f_c \le 2 \tag{3.22a}$$

$$\varepsilon_{0(h)} = \frac{\sigma_0 + 3\alpha b K_e (2f_c)^{b-1}\sigma_0 + 3\alpha(1-b)K_e(2f_c)^b}{3K_e} \quad \text{for } \sigma_0/f_c > 2 \tag{3.22b}$$

$$\gamma_0 = \frac{\tau_0 + 2cG_e\tau_0^d}{2G_e} \tag{3.23}$$

where K_e and G_e are the initial bulk and shear moduli, respectively. The expressions that describe these moduli are given through the following relations:

$$K_e = 11000 + 3.2 \cdot f_c^2 \tag{3.24}$$

$$G_e = 9224 + 136 \cdot f_c + 3296 \cdot 10^{-15} \cdot f_c^{8.273} \tag{3.25}$$

where f_c is the uniaxial cylinder compressive strength expressed in *MPa*. Parameters *a, b, c, d* depend on the material characteristics and are described through the following equations:

$$b = 2.0 + 1.81 \cdot 10^{-8} \cdot f_c^{4.461} \tag{3.26}$$

$$d = 2.12 + 0.0183 \cdot f_c \quad \text{for } f_c \le 31.7MPa \tag{3.27a}$$

$$d = 2.70 \quad \text{for } f_c > 31.7MPa \tag{3.27b}$$

while parameters *a* and *b* are absorbed by parameters *A* and *B* which will be described below.

For Eq. 3.21 to be compatible with the first term on the right-hand side of Eq. 3.20, the hydrostatic component of the internal state of stress must be:

$$\frac{\sigma_{ih}}{f_c} = A \cdot \left(\frac{\sigma_0}{f_c}\right)^b \quad \text{for } \sigma_0/f_c \le 2 \tag{3.28a}$$

$$\frac{\sigma_{ih}}{f_c} = 2^{b-1}Ab \cdot \left(\frac{\sigma_0}{f_c}\right) + 2^b \mathrm{A}(1-b) \quad \text{for } \sigma_0/f_c > 2 \tag{3.28b}$$

where *A* is given by:

$$A = 3aK_e f_c^{b-1} \tag{3.29}$$

and with the regression analysis of the experimental data the following expressions for parameter *A* are obtained, thereby incorporating parameter *a*:

$$A = 0.516 \qquad \text{for } f_c \le 31.7MPa \tag{3.30a}$$

$$A = \frac{0.516}{1+0.0027\left(f_c - 31.7\right)^{2.389}} \qquad \text{for } f_c \le 31.7MPa \tag{3.30b}$$

Moreover, for Eq. 3.23 to be compatible with the second term of the right-hand side of Eq. 3.20, the shear stress τ_{id} must be expressed as:

$$\frac{\tau_{id}}{f_c} = C \cdot \left(\frac{\tau_0}{f_c}\right)^d \tag{3.31}$$

where

$$C = 2cG_e f_c^{d-1} \tag{3.32}$$

Parameter *C* incorporates and defines the parameter *c*, through the following expressions that yield after the regression analysis on the experimental data for the $\tau_o - \gamma_{o(d)}$ relations.

$$C = 3.573 \qquad \text{for } f_c \le 31.7MPa \tag{3.33a}$$

$$C = \frac{3.573}{1+0.0134\left(f_c - 31.7\right)^{1.414}} \qquad \text{for } f_c \le 31.7MPa \tag{3.33b}$$

The above relations are valid only for concrete materials with cylinder compressive strength ranging between$15\ MPa \le f_c \le 65\ MPa$. Outside this range, K_e and G_e remain constant and equal to the corresponding values obtained when $f_c = 15\ MPa$ or $f_c = 65\ MPa$, depending on the case at hand.

In order to classify the above stresses that are obtained from the corresponding loading type, the following three loading types were presented:

i. Hydrostatic Loading. This occurs when the current external stress σ_0^i exceeds any previous external stress $\sigma_0^{j<i}$, resulting in an increase of σ_{ih}.
ii. Deviatoric loading. This occurs when the current external stress τ_0^i exceeds any previous external stress $\tau_0^{j<i}$, resulting in an increase of τ_{id}.
iii. Combined loading. This occurs when the current combination of external stresses σ_0^i, τ_0^i exceeds any previous combination of external stresses $\sigma_0^{j<i}$, $\tau_0^{j<i}$, resulting in an increase of σ_{id}.

It is implied that various combinations of loading and unloading may take place simultaneously, thus the above formulation will be able to predict the correct material behavior.

The next step is to choose whether the nonlinearities of *K* and *G* moduli should be accounted for in the $\sigma_o - \varepsilon_{o(h)}$ and $\tau_o - \gamma_{o(d)}$ relations. The combined approach assumes that this numerical

feature can be accounted for through the use of the σ_{id} variable which takes into consideration the coupling effect $\tau_o - \varepsilon_{o(d)}$. In order to achieve this, Eqs. 3.15 must be rewritten to:

$$\varepsilon_0 = \varepsilon_{0(h)} + \varepsilon_{0(d)} = \frac{\sigma_0 + \sigma_{id}}{3K_s} \quad 3.34a$$

$$\gamma_0 = \gamma_{0(d)} = \frac{\tau_0}{2G_s} \quad 3.34b$$

where K_s and G_s are the secant bulk and shear moduli, respectively. Once more, a regression analysis of the experimental data similar to the one that led to expressions of Eqs 3.22 and 3.23 is performed giving

$$K_s = \frac{1}{3}\frac{\sigma_0}{\varepsilon_0}, \quad G_s = \frac{1}{2}\frac{\tau_0}{\gamma_0} \quad 3.35$$

The expressions that describe the relation between the secant bulk modulus and the initial bulk modulus write as:

$$\frac{K_s}{K_e} = \frac{1}{1 + A\left(\frac{\sigma_0}{f_c}\right)^{b-1}} \quad \text{for } \sigma_0/f_c \le 2 \quad 3.36a$$

$$\frac{K_s}{K_e} = \frac{1}{1 + 2^{b-1}Ab - 2^b A\left(\frac{\sigma_0}{f_c}\right)^{-1}} \quad \text{for } \sigma_0/f_c \le 2 \quad 3.36b$$

$$\frac{G_s}{G_e} = \frac{1}{1 + C\left(\frac{\tau_0}{f_c}\right)^{d-1}} \quad 3.37$$

Similarly, the tangent bulk and shear moduli, which relate stress and strain increments, may be obtained by differentiating the expressions in Eqs. 3.22 and 3.23, respectively. It is worth noting at this point that, even for very small stress values, the moduli are affected, meaning that the constitutive matrix $\boldsymbol{C}$ (Eq. 3.4) is changed. During the nonlinear solution procedure, this results into unbalanced forces very early in the iterative procedure requiring additional iterations until convergence is achieved. This feature applies also for the case of the tangent moduli which are computed from:

$$\frac{K_T}{K_e} = \frac{1}{1 + bA\left(\frac{\sigma_0}{f_c}\right)^{b-1}} \quad \text{for } \sigma_0/f_c \le 2 \quad 3.38a$$

$$\frac{K_T}{K_e} = \frac{1}{1 + 2^{b-1}Ab} \quad \text{for } \sigma_0/f_c \le 2 \quad 3.38b$$

$$\frac{G_T}{G_e} = \frac{1}{1 + dC\left(\frac{\tau_0}{f_c}\right)^{d-1}} \qquad 3.39$$

The above formulation for the secant and tangent moduli is schematically illustrated in Figs. 3.34. These figures refer to a particular concrete which has a cylindrical compressive strength $f_c = 31.7\,MPa$.

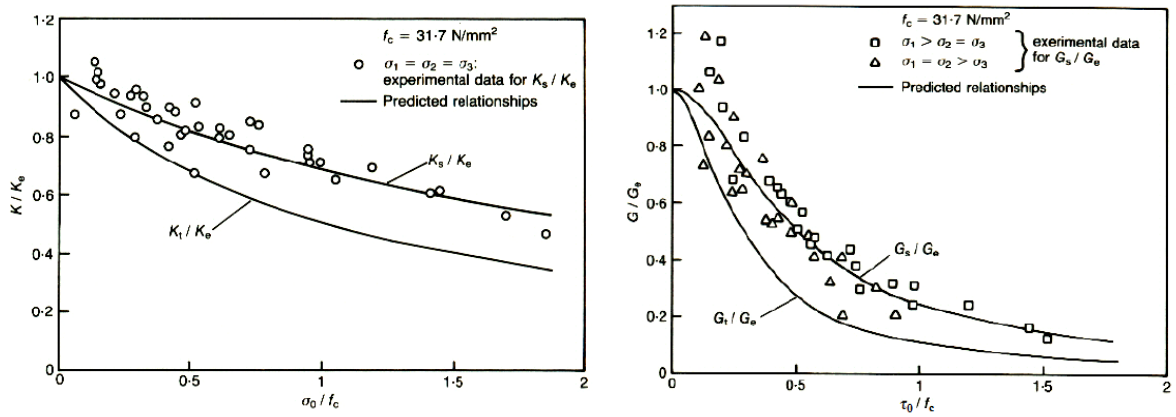

(A) (B)

FIGURE 3.34 TYPICAL VARIATION OF THE (A) BULK MODULI K_S, K_T WITH σ_0 AND (B) SHEAR MODULI G_S, G_T WITH τ_0 FOR A SPECIFIC CONCRETE ($f_c = 31.7MPa$)[101].

At this point, the computation of the stress σ_{id} is required. A regression analysis of the experimental data similar to those shown in Fig. 3.35 led to the following analytical expression that describes the stress σ_{id}:

$$\frac{\sigma_{id}}{f_c} = M\left(\frac{\tau_0}{f_c}\right)^n \qquad 3.40$$

where

$$M = \frac{k}{1 + l\left(\frac{\sigma_0}{f_c}\right)^m} \qquad 3.41$$

and parameters *k, l, m, n* are the material parameters which are expressed as:

$$k = \frac{4.0}{1 + 1.087 \cdot \left(f_c - 15.0\right)^{0.23}} \qquad 3.42a$$

$$l = 0.222 + 0.01086 \cdot f_c - 0.000122 \cdot f_c^2 \qquad 3.42b$$

$$m = -2.414 \qquad \text{for } f_c \le 31.7MPa \qquad 3.42c$$

$$m = -3.532 + 0.0352 \cdot f_c \qquad \text{for } f_c > 31.7MPa \qquad 3.42d$$

$$n = 1.0 \quad \text{for } f_c \le 31.7MPa \tag{3.42e}$$

$$n = 0.3124 + 0.0217 \cdot f_c \quad \text{for } f_c > 31.7MPa \tag{3.42f}$$

Since the stress σ_{id} is a pure hydrostatic correction, expressions in Eqs. 3.34 are equivalent to Eq. 3.43, which is expressed in the global coordinate directions.

Eq. 3.43 is obtained by noting that the two terms of the strain tensor of Eq. 3.20 must be handled separately when the constitutive relations are introduced in this tensor relation. Given that the second term of this equation does not impose any deviation from nonlinear elasticity, the first term does involve the correction σ_{id} to the applied σ_0.

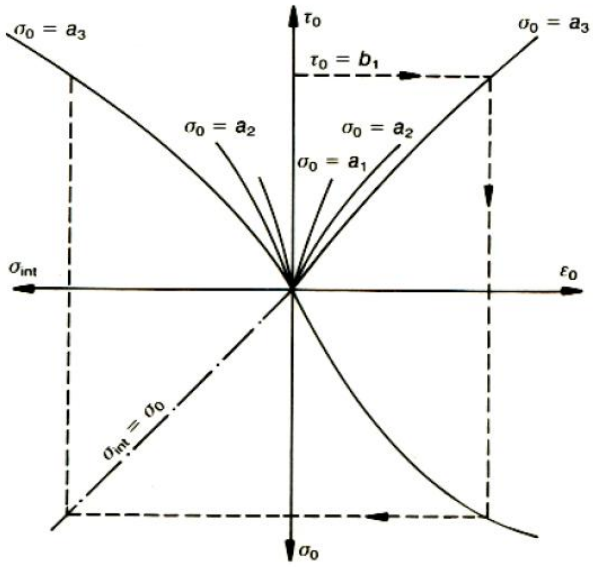

FIGURE 3.35 SCHEMATIC REPRESENTATION OF THE APPROACH USED TO EVALUATE σ_{id} FOR A GIVEN σ_0 AND τ_0 COMBINATION[8].

$$\varepsilon_{ij} = \frac{\sigma_0 + \sigma_{id}\delta_{ij}}{2G_s} - \frac{3\nu_s}{E_s}\left(\sigma_0 + \sigma_{id}\right)\delta_{ij} \tag{3.43}$$

where E_s and ν_s are the secant Young modulus and Poison ratio, respectively. These two material parameters derive from K_s and G_s by the following expressions:

$$E = \frac{9KG}{3K + G} \tag{3.44}$$

$$\nu = \frac{3K - 2G}{6K + 2G} \tag{3.45}$$

Eq. 3.43 describes the expression which forms the basis for calculating global strains from global stresses according to the following procedure:

- The octahedral stresses (σ_0, τ_0) are calculated either from the principal stresses (σ_1, σ_2, σ_3) - computed previously on the basis of the global stresses σ_{ij}, i.e. (σ_x, σ_y, σ_z, τ_{xy}, τ_{yz}, τ_{zx}) – or directly from the first and second stress invariants expressed in terms of σ_{ij} (Appendix A).
- K_s, G_s and E_s, ν_s are calculated.
- The hydrostatic correction σ_{id} is calculated.
- Global strains ε_{ij} are calculated.

The computation of global strain increments from global stress increments follows the same procedure, with the material constants being defined in terms of the tangent values K_T, G_T and E_T, ν_T.

3.3.4 The Failure Surface

The octahedral stresses are also used to describe the failure surface of concrete, which may be represented in the three-dimensional principal stress space as an open and convex failure surface. The form of such a failure surface can be seen in Fig. 3.36, indicating the very small strength of concrete under tensile stresses (positive axes refer to compressive stresses). The projection of the failure surface on the deviatoric plane, which is normal to σ_0, results in a curve that represents the geometrical locus of the ultimate deviatoric stress τ_{0u}[8]. This ultimate stress may be calculated from σ_0 and θ, where θ is the rotational angle that the deviatoric stress vector forms with one of the projected stress principal axes on the deviatoric plane.

$$\tau_{0u}=\frac{2\tau_{0c}\left(\tau_{0c}^2-\tau_{0e}^2\right)cos\theta+\tau_{0c}\left(2\tau_{0e}-\tau_{0c}\right)\sqrt{\left[4\left(\tau_{0c}^2-\tau_{0e}^2\right)cos^2\theta+5\tau_{0e}^2-4\tau_{0c}\tau_{0e}\right]}}{4\left(\tau_{0c}^2-\tau_{0e}^2\right)cos^2\theta+\left(\tau_{0c}-2\tau_{0e}\right)^2} \qquad 3.46$$

This expression describes a smooth convex curve with tangents perpendicular to the directions of τ_{0e} and τ_{0c} at $\theta = 0^o$ and $\theta = 60^o$ respectively (Figs. 3.37). Therefore, a full description of the strength surface can be established when the variants of τ_{0e} and τ_{0c} with σ_0 are determined. Once more, a mathematical description of the two strength envelopes may be obtained by fitting curves to the experimental data. Such an approach leads to the following expressions

$$\frac{\tau_{0c}}{f_c}=0.944\left(\frac{\sigma_0}{f_c}+0.05\right)^{0.724} \qquad 3.47a$$

$$\frac{\tau_{0e}}{f_c}=0.633\left(\frac{\sigma_0}{f_c}+0.05\right)^{0.857} \qquad 3.47b$$

When the state of stress is known, then the quantities σ_0, τ_0, θ may be calculated from

$$\sigma_0=\frac{1}{3}\mathrm{I}_1, \qquad \tau_0=\sqrt{\left(2\sigma_0^2-\frac{2}{3}\mathrm{I}_2\right)}, \qquad \cos 3\theta=-\frac{\sqrt{2}}{\tau_0^3}J_3 \qquad 3.48$$

where I_1 and I_2 are the first and second invariants of the stress tensor, whereas J_3 is the third invariant of the deviatoric stress tensor $s_{ij} = \sigma_{ij} - \sigma_0 \delta_{ij}$.

It is an experimentally documented fact that when the compressive stresses reach certain values, concrete starts to increase its volume. As a result of concrete's in-homogeneity, such a localized region under compression tends to expand against the surrounding material. The confining concrete therefore introduces in the localized region lateral compressive stresses, which, in turn, for equilibrium to be maintained, make the surrounding regions develop tensile stresses. This has an effect of increasing the strength of the localized region while the tensile stresses in the surrounding region eventually turn this state of stress into having one of its principal components tensile, thus leads to the reduction of the strength of the surrounding region where macrocracking takes place.

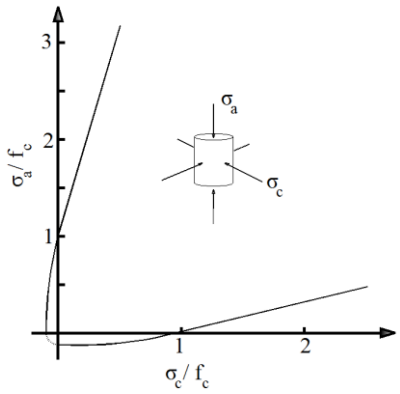

FIGURE 3.36 INTERSECTION OF FAILURE SURFACE FOR CONCRETE WITH PLANE INCLUDING SPACE DIAGONAL AND ONE OF PRINCIPAL AXES[8].

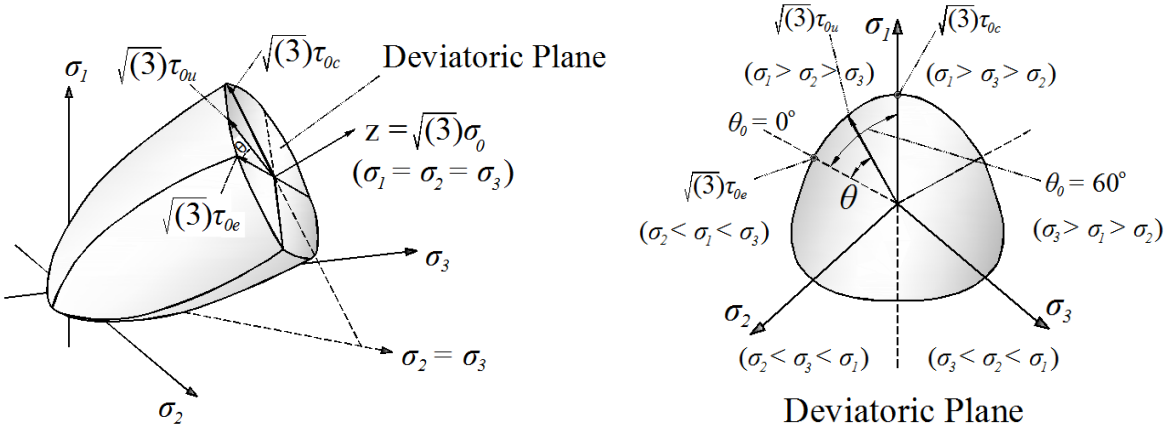

(A) (B)

FIGURE 3.37 SCHEMATIC REPRESENTATION OF THE ULTIMATE-STRENGTH SURFACE. (A) GENERAL VIEW IN STRESS SPACE (B) TYPICAL CROSS-SECTION OF THE STRENGTH ENVELOPE COINCIDING WITH A DEVIATORIC PLANE.

3.3.5 The Numerically Modified Kotsovos and Pavlovic Concrete Material Model

3D concrete material models combined with the smeared crack approach, produce ill-posed matrices, especially when the RC structure's rebars begin to yield. In some cases convergence problems rise sooner when cracking appears locally before the structure enters the high nonlinearity zone. This results mainly from the discontinuities that are introduced through the modification of the constitutive matrix ***C*** (Eq. 3.4) where eventually several diagonal terms of the elemental stiffness matrix will have near to zero or zero values. Additionally, when the opening of cracks occurs, the internal stresses are converted into unbalanced forces which are redistributed through the calculation of the internal forces of the corresponding nonlinear solution procedure (NR algorithm). This numerical process induces instability especially when large loading steps are applied, resulting in convergence problems.

Even though Kotsovos and Pavlovic[8] used 20- and 27-noded hexahedral elements with higher order integration rules, they had serious convergence problems which led them to introduce a restriction to the maximum number of cracks that were allowed to open (within each internal iteration). This constraint was studied numerically and the proposed number was set to *2 or 3*

cracks per internal iteration. By implementing such a constraint, the opening of cracks was restrained, thus overcoming the convergence problem. As a result of this restriction, the material model becomes non-objective as different values for the restriction parameter led to different numerical results.

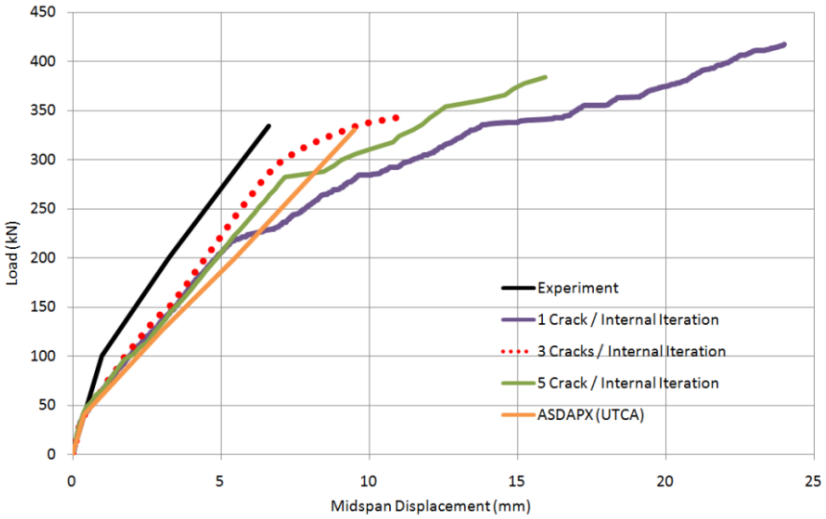

FIGURE 3.38 PREDICTED AND EXPERIMENTAL LOAD-DEFLECTION CURVES WITH THE USE OF DIFFERENT RESTRICTION PARAMETERS WITH THE KOTSOVOS AND PAVLOVIC[8] MATERIAL MODEL AND ROD ELEMENTS AS EMBEDDED REBAR ELEMENTS.

This numerical problem is depicted in Fig. 3.38 where the load-deflection curve is shown for the numerical prediction of a simply supported beam without stirrups[186]. Three different values for the allowed number of cracks per iteration were used (*1*, *3* and *5* respectively); the resulting curves had different inelastic branches, underlying the lack of objectivity of the proposed restriction. As it is going to be illustrated through this research work, the proposed material model by Kotsovos and Pavlovic[8] combined with the smeared crack model works without the need of numerical restrictions and can become objective after some numerical modifications are introduced.

Spiliopoulos and Lykidis[138], proposed a unified treatment of the crack opening (UTCA) where no crack opening restrictions were implemented in the Kotsovos and Pavlovic[8]. This implies that no restrictions are enforced on the number of cracks and all Gauss points could crack if their deviatoric stress strength was reached. They implemented the proposed model with 27-noded hexahedral elements with a corresponding *3*x*3*x*3* integration rule which led to high computational times.

Our proposed modeling method for the simulation of concrete uses the isoparametric 8-noded hexahedral element with a *2*x*2*x*2* integration rule, the numerically modified Kotsovos and Pavlovic material model and a unified treatment for the crack openings. As we are going to see through the numerical experiments that were contacted in this work, the proposed modeling method proves to be objective and computationally efficient. *ReConAn* FEA code architecture and programming techniques manage to further avoid the introduction of numerical errors that are usually induced due to the programming style of the code as will be illustrated through several numerical tests.

The Numerically Modified Concrete Material Model

The Kotsovos and Pavlovic[8] material model, assumes that the moduli K_s and G_s (Eqs. 3.36 and 3.37) change even when the stress state is much smaller than the concrete's compressive strength ($\tau_{0u} << max\ \tau$) because their values depend nonlinearly on the hydrostatic and deviatoric stresses (σ_0, τ_0). The updating of the hexahedral stiffness matrices at the early stages of loading demands extra computational effort with no measured effect on the linear and nonlinear structural behavior.

Additionally, numerical instability is induced to the nonlinear solution procedure, as a result of the unbalanced forces produced due to the update of the material constitutive matrix of the uncracked elements. According to the Kotsovos and Pavlovic[8] material model formulation, it is necessary to update the material constitutive matrix of each hexahedral Gauss point according to the change of K_s and G_s moduli. Having to solve an ill-posed numerical problem when cracking occurs, the uncracked hexahedral elements induce additional numerical instability and increase the computational cost through their material model formulation and the requirement of continuously updating of their stiffness matrices. It is important to note here that the assemblage of the global stiffness matrix does not demand as much computational time as the global structural stiffness matrix triangularization process which is the most time consuming procedure during a FE analysis process.

Taking into consideration these numerical difficulties, a modification to the numerical handling of the Kotsovos and Pavlovic[8] material model is proposed. Following an extensive parametric investigation and according to the experimental findings of the concrete material behavior that were discussed in the previous sections, it was concluded that if the ultimate deviatoric stress τ_{0u} at any Gauss point is less than *50%* of the corresponding ultimate strength (Eq. 3.46), then the elastic constitutive matrix $\boldsymbol{C}_{ij}$ (Eq. 3.49) can be used. It is only when the computed deviatoric stress τ_{0u} exceeds the *50%* of the corresponding ultimate strength, then the nonlinear material law is activated and the constitutive matrix is computed by updating the K_T and G_T moduli according to Eqs. 3.36 and 3.37. Fig. 3.39 illustrates the flow chart of the proposed numerical handling of the material model.

$$\boldsymbol{C}_{ij} = \begin{bmatrix} C & B & B & . & . & . \\ B & C & B & . & . & . \\ B & B & C & . & . & . \\ . & . & . & A/2 & . & . \\ . & . & . & . & A/2 & . \\ . & . & . & . & . & A/2 \end{bmatrix},\ A = \frac{E}{(1+\nu)},\ B = \frac{A \cdot \nu}{(1-2\nu)},\ C = A + B \qquad 3.49$$

where E is the concrete's Young modulus and ν its Poisson ratio.

Eq. 3.49 describes the relation of the elastic constitutive matrix $\boldsymbol{C}_{ij}$ that is used when the elasticity criteria is satisfied.

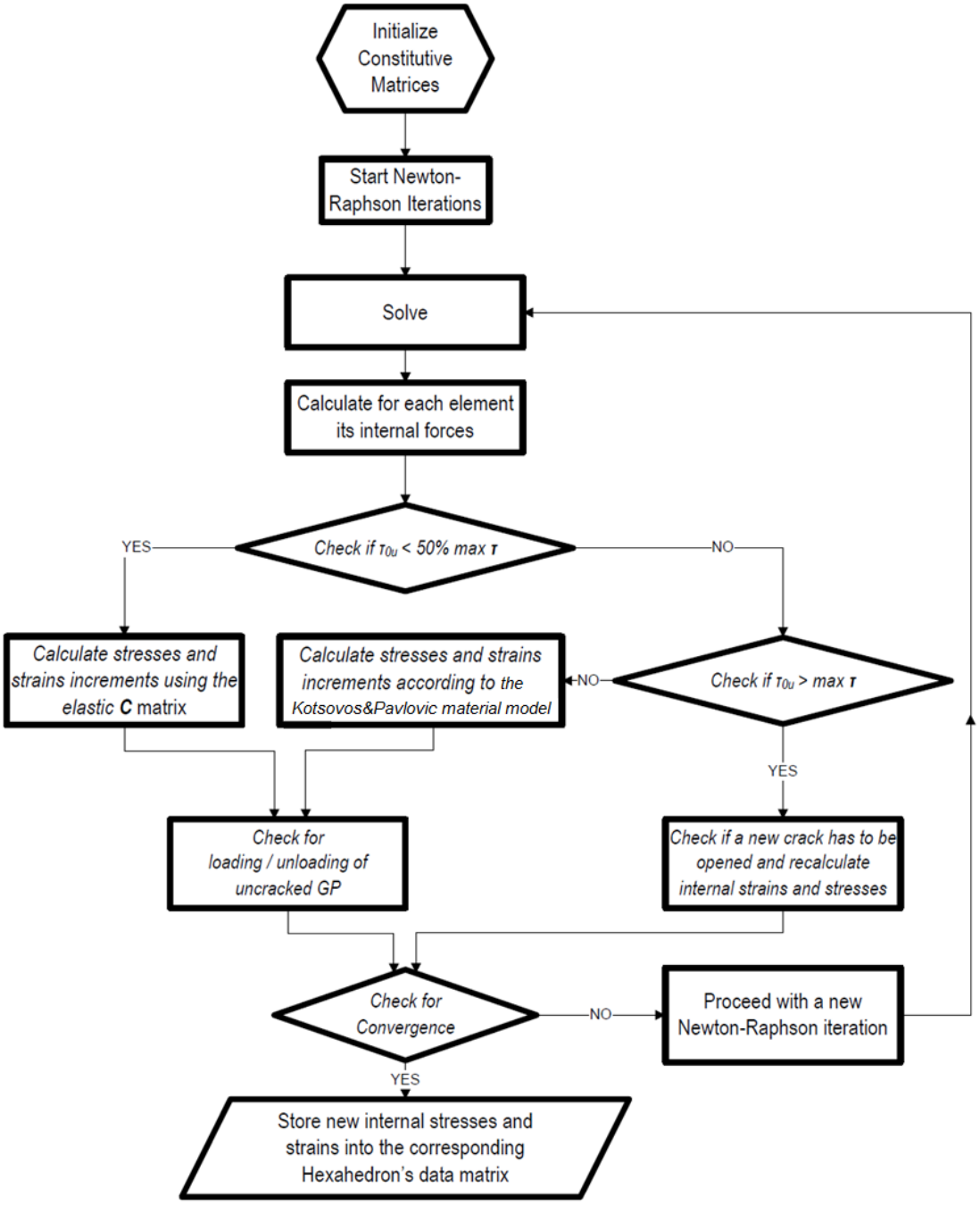

FIGURE 3.39 FLOW CHART OF THE MODIFIED CONCRETE MATERIAL MODEL.

3.4 Numerical Implementation

The constitutive relations of the Kotsovos and Pavlovic[8] concrete material model, have been verified through several numerical tests, thus the aim of this section is to illustrate the ability of the numerically modified material model to predict the behavior of a uniaxial compression test without any significant numerical instabilities when combined with the 8-noded isoparametric hexahedral element, which treats the phenomenon of cracking with the smeared crack approach. It is going to be illustrated that, despite the fact that the 8-noded isoparametric hexahedral

element uses a lower order integration scheme (*2x2x2* Gauss points), the model manages to predict the stress-strain paths without any significant numerical problems.

Being impartial on the selection process of the experimental test which will be analyzed, a uniaxial compression test was chosen that was presented in Kim et al.[187] (2009). The main reason for choosing this particular experimental test was to avoid modeling an experiment that was conducted by Kotsovos and Pavlovic[8] in the framework of their attempt to extrapolate the constitutive relations of the concrete material behavior, thus a confirmation of the experimental findings would have resulted. Moreover, through this test the numerical robustness and computational efficiency of the developed code when modeling plain concrete will be presented. It must be pointed here that, this test was analyzed extensively by Karakitsios[188] (2009) in his Diploma Thesis, with the use of *ReConAn* FEA.

The experimental setup is shown in Fig. 3.40a and the corresponding obtained stress-strain curves from the compressive strength test, in Fig. 3.40b. In addition, the maximum observed stresses and strains are given in Table 3.1.

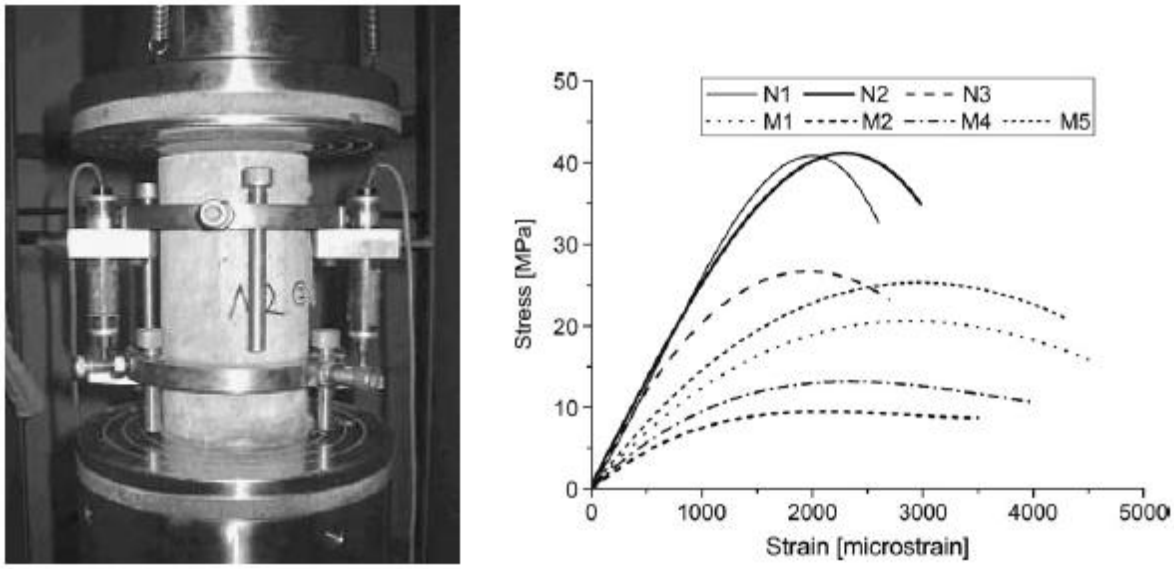

FIGURE 3.40 LEFT: EXPERIMENTAL SETUP OF A UNIAXIAL COMPRESSIVE TEST. RIGHT: OBTAINED STRESS-STRAIN CURVES[187].

Specimen	*Stress (MPa)*	*Strain (x10^6)*
N1	40.8	2,100
N2	40.0	2,240
N3	26.7	1,960

TABLE 3.1 CYLINDRICAL SPECIMENS. MAXIMUM MEASURED STRESSES AND STRAINS.

In their investigation, Kim et al.[187] tested two types of specimen with different concrete strengths in order to derive the phase similitude law for pseudodynamic test on small scale reinforced concrete models. The aim of their study was to simulate a small scale reinforced concrete structure. As it can be seen in Fig. 3.40, three normal size specimens (*10 cm* diameter x *20 cm* height) were tested and their stress-strain curves measured (N1, N2 and N3).

For the purpose of this work, the N2 specimen is selected and modeled using four different discretizations as shown in Figs. 3.41. The specimen is discretized with 8-noded hexahedral elements with *1*, *2*, *3* and *10 cm* height. In order to simulate the steel plates through which the external load was applied, two layers of steel hexahedral elements are positioned at the base and at the top of the concrete model (Fig. 3.41).

The concrete material parameters used for the four FE models are given in Table 3.2. The external load was divided into *50* load steps and the convergence energy criteria tolerance was set to 10^{-4}.

Parameter	*Value*
Compressive Strength f_c (MPa)	40.0
Young Modulus E_0 (GPa)	30.0
Tensile Strength (MPa)	2.0

TABLE 3.2 CYLINDRICAL SPECIMEN N2. CONCRETE MATERIAL PARAMETERS.

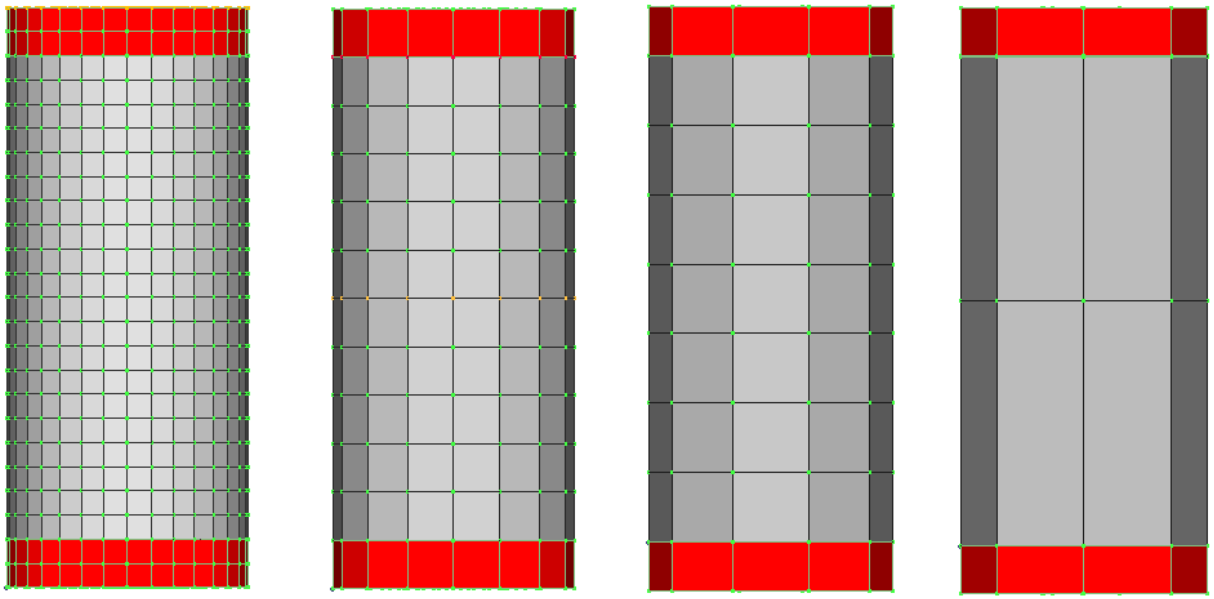

(A) (B) (C) (D)

FIGURE 3.41 FE HEXAHEDRAL MESHES OF THE CYLINDRICAL SPECIMEN N2. (A) *1*, (B) *2*, (C) *3* AND (D) *10 CM* HEIGHT OF EACH FE LAYER.

Fig. 3.42 shows the correlation between the experimental and the numerically predicted stress-strain paths for the case of specimen N2 for different discretizations. It is evident that, the concrete material model manages to predict with an acceptable accuracy the experimental results. The predicted curves are linear up to the point where elastic degradation of the concrete material begins to be significant, introducing nonlinear behavior to the ascending branches. As it can be seen, the predicted branches increase up to a certain load where due to excessive cracking, the analysis process terminates since the force-control NR procedure fails to converge. The obtained curves manage to predict the ultimate failure load with a *5%* accuracy which is an acceptable result. In addition to that, the scatter between the curves predicted by the four FE meshes is located inside an acceptable range (< *5%*). These results illustrate the

accuracy of the material model in predicting realistic concrete behaviors and the numerical robustness of the developed nonlinear FEA code.

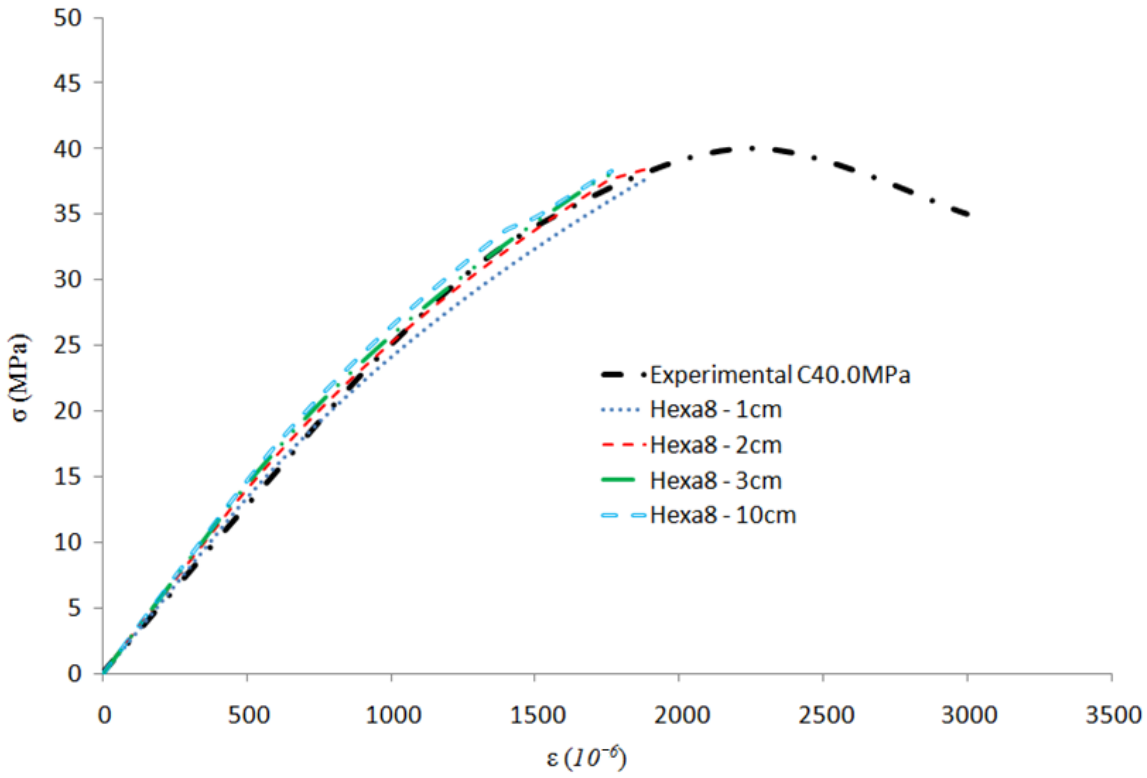

FIGURE 3.42 CYLINDRICAL SPECIMEN N2. STRESS-STRAIN PATHS FOR DIFFERENT FE MESHES.

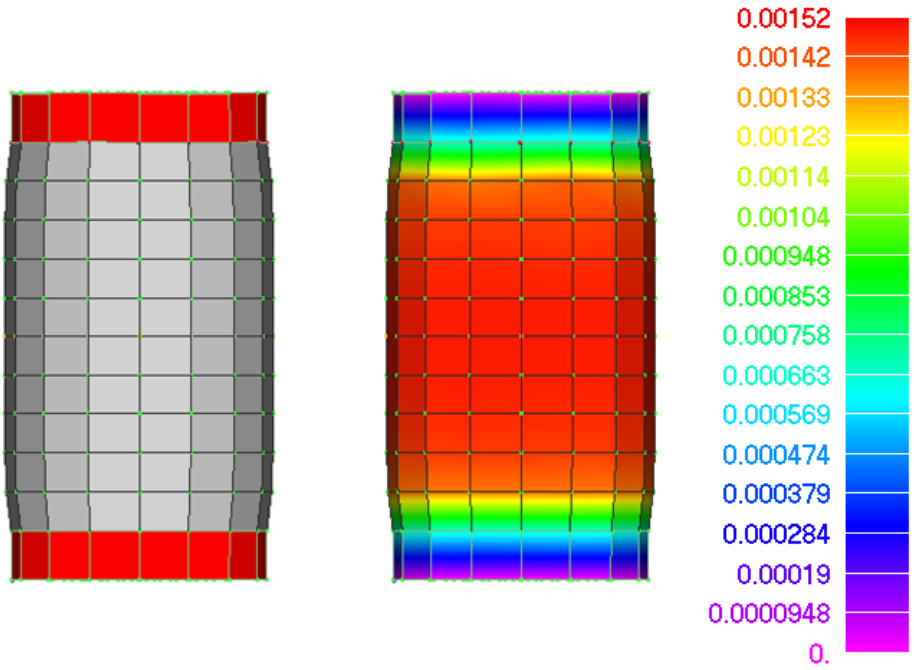

FIGURE 3.43 CYLINDRICAL SPECIMEN N2. DEFORMED SHAPE AND VON MISES STRAIN CONTOUR.

It is worth noting that when modeling experimental setups with three-dimensional models several secondary phenomena can be simulated since the accuracy of the numerical models enables the user to simulate with detail the experimental configuration. One of these

phenomena is the interaction between the steel plates and the concrete specimen as illustrated in Fig. 3.43. If the deformed shape figure is scaled *100* times then the outcome of the deformed shape will be that of Fig. 3.43. As it can be seen, the upper and lower interaction surfaces between the steel plates and the concrete specimen create triaxial stress states due to the stiffer steel plates, thus the specimen takes a shape similar to that of a barrel. The section of the cylinder located in the center of the specimen expands laterally and the sections located at the two ends of the specimen retain their initial shape.

Finally, the computational times for the nonlinear analysis procedure for the different FE meshes are given in Table 3.3. The computational efficiency of the proposed model is demonstrated since the prediction of the nonlinear response of a FE model that combines a nonlinear concrete material model with the smeared crack approach, was carried out in the minimal time.

FE mesh	*Number of Elements*	*Number of Nodes*	*Time (sec)*
A (1cm)	2,592	3,125	330
B (2cm)	384	533	6
C (3cm)	54	120	0.5
D (10cm)	28	60	0.3

TABLE 3.3 CYLINDRICAL SPECIMEN N2. REQUIRED COMPUTATIONAL TIMES FOR THE NONLINEAR SOLUTION PROCEDURE.

Chapter 4 Generating Embedded Reinforcement

Contents of Chapter 4

4.1 Overview

When modeling three-dimensional RC structures with the FE method, three main approaches are available for the simulation of the reinforcement: (i) smeared, (ii) discrete, and (iii) embedded[189-191]. The smeared formulation is more suitable for surface-type structures and for sparsely located reinforcing bars, either the discrete or embedded formulation are usually implemented. In the case of the discrete formulation, the rebars are modeled with uniaxial elements, which are positioned at the boundaries of the concrete elements connecting adjacent nodes. This approach has the obvious restriction of having to use a concrete element mesh based on the rebar geometry and location. Alternatively, in order to alleviate this type of problem, some researchers have altered the actual arrangement of rebars to conform with the FE modeling[192, 193].

The most noteworthy method for the generation of reinforcement rebar elements in FE modeling of concrete structures is proposed by Barzegar and Maddipudi[189] (1994), which is an extension of the work of Elwi and Hrudey[190] (1989). This approach has the advantage of allowing arbitrary positions for the rebars inside the concrete elements and a free geometry for each hexahedron element. However, a nonlinear search procedure based on the Newton-Raphson method is required in order to calculate the natural coordinates of each steel bar node. Despite the fact that the convergence rate of the nonlinear search is rather high, the computational demand for relatively large-scale structures with thousands of steel rebars becomes excessive. In addition to that, the method that was proposed in[189] for the generation of reinforcement rebars assumes no geometrical constraints during the rebar search process making its numerical implementation computationally demanding, especially when dealing with large-scale structures. Nevertheless, several researchers[8, 6, 9, 194] adopted this method in order to compute the natural coordinates of embedded rebars.

4.2 Generating Reinforcement

The method proposed in this work considers arbitrary positioning of the rebars inside the concrete elements, as shown in Fig. 4.1, while avoiding a nonlinear search procedure for the calculation of the natural coordinates of the embedded reinforcement nodes in the corresponding hexahedral elements that are orthogonal parallepiped.

Femap software[91] is used as the pre- and post-processing FE program, through which the initial mesh generation is performed. Thus, *ReConAn* uses the initial rebar node coordinates that were created with Femap software and generates the numerical model of the embedded rebar elements. The generation of embedded rebar elements is performed for each rebar element separately. This means that for each initial rebar, an independent search is conducted with the aim to detect all intersections of its straight part with the surrounding solid elements. The outcome of this arithmetic procedure is the placement of the embedded rebar elements in the corresponding hexahedral elements.

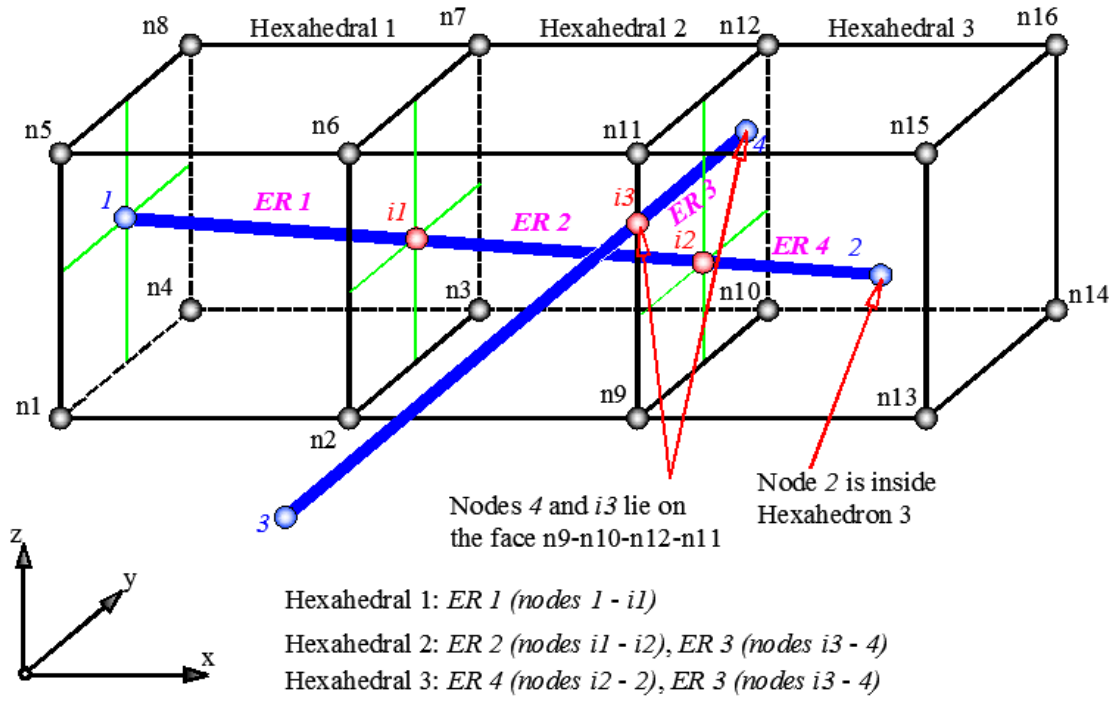

FIGURE 4.1 EMBEDDED REINFORCEMENT REBARS INSIDE HEXAHEDRAL ELEMENTS.

4.2.1 Generation of Embedded Virtual Nodes

The virtual nodes correspond to the intersections of the rebars with hexahedral faces or edges as shown in Fig. 4.1 (nodes *i1*, *i2* and *i3*). This procedure becomes cumbersome when the FE model consists of a large number of hexahedral and initial rebar elements. It is obvious that if we attempt to compute these possible intersection points without implementing any constraint on the search space, the computational cost of the search algorithm will be significant. The problem arises from the fact that it is required to locate all possible intersections that may exist between hexahedral faces and initial rebar elements (Figs. 4.2 and 4.3).

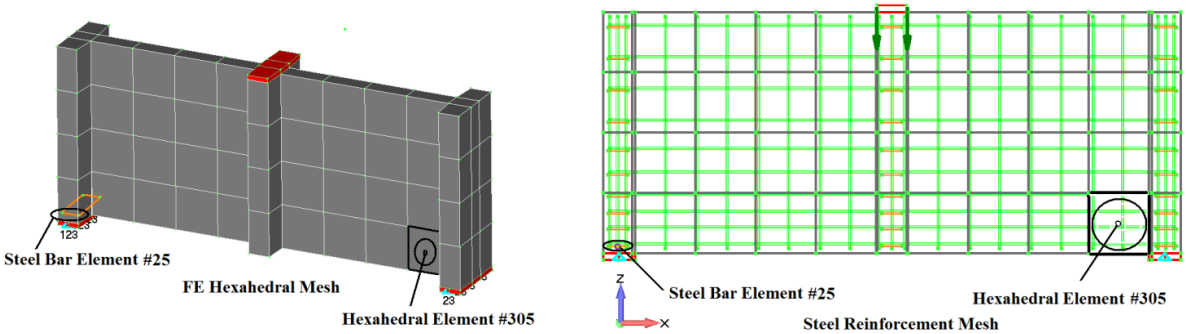

FIGURE 4.2 CONCRETE FE MESH AND STEEL REINFORCEMENT REBARS OF A SHEAR WALL.

To avoid unnecessary calculations, a geometric constraint was introduced in order to restrict the search in the vicinity of the corresponding steel reinforcement. The geometric constraint is implemented with the definition of an active sphere with radius R_c:

$$R_c = c \cdot L, \tag{4.1}$$

where

$$L = \sqrt{s_x^2 + s_y^2 + s_z^2} \tag{4.2}$$

and

$$s_x = \frac{\left(\sum_{n=1}^{8}\left(s_x^{cen} - s_x^n\right)\right)}{8}, \quad s_y = \frac{\left(\sum_{n=1}^{8}\left(s_y^{cen} - s_y^n\right)\right)}{8}, \quad s_x = \frac{\left(\sum_{n=1}^{8}\left(s_z^{cen} - s_z^n\right)\right)}{8} \tag{4.3}$$

with $\boldsymbol{s}^n$ and $\boldsymbol{s}^{cen}$ being the coordinates of the node *n* and the centroid of the hexahedron under consideration, respectively and parameter *c* defines the active volume around each hexahedron where the constraint is implemented. If the below relation is satisfied

$$d_{n1}^i \text{ or } d_{n2}^i < R_c \tag{4.4}$$

where $d_{n1}^i = \left|\boldsymbol{s}^{cen} - \boldsymbol{s}_{rebar}^{n1}\right|$, $d_{n2}^i = \left|\boldsymbol{s}^{cen} - \boldsymbol{s}_{rebar}^{n2}\right|$ are the distances of the initial rebar end nodes *1* and *2* from the hexahedral centroid *i* under consideration as it is illustrated in Fig. 4.3, then the search is performed.

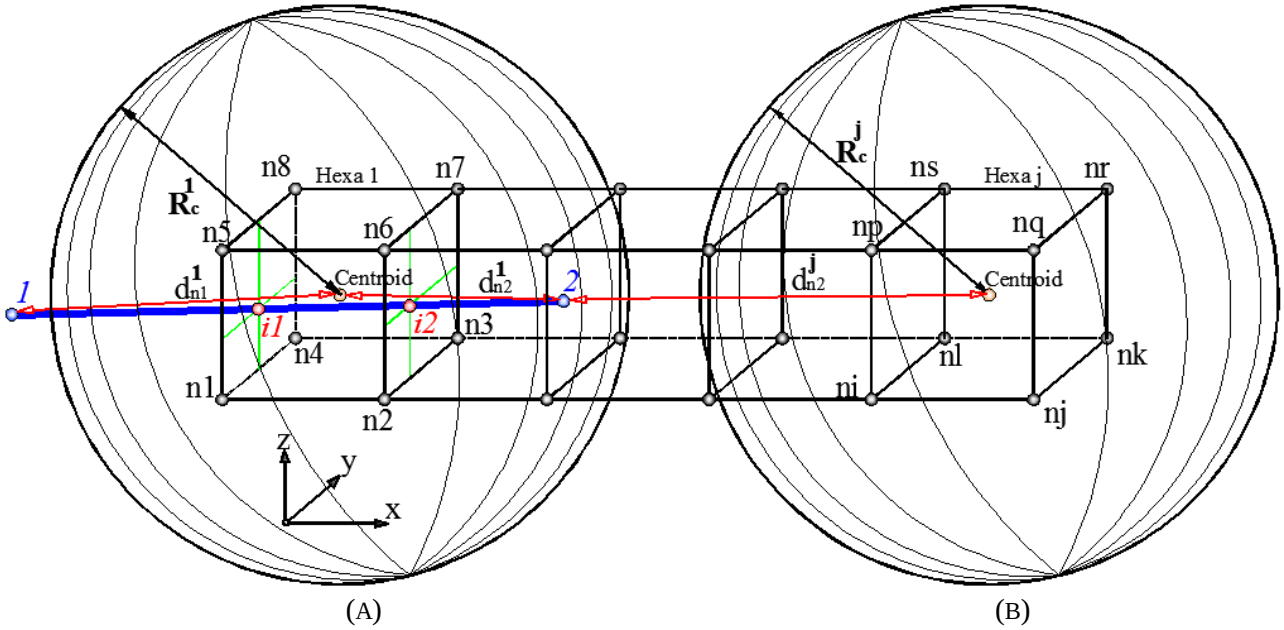

FIGURE 4.3 GEOMETRIC CONSTRAINT FOR THE SEARCH OF EMBEDDED REBAR NODES: (A) $R_e^1 > d_{n2}^1$ GEOMETRIC CONSTRAINT IS SATISFIED, (B) $R_e^1 < d_{n2}^j < d_{n1}^j$ GEOMETRIC CONSTRAINT IS NOT SATISFIED.

After a thorough parametric investigation the recommended value for the incremental parameter *c* is found to be *5*, which is also the value that was used in our numerical implementations. Larger values for *c* would lead to unnecessary computations for the location of possible rebar-hexahedral face intersections, while smaller values would make the generation of the initial rebar mesh through the pre-processing software more complicated and time consuming. This means, that the maximum penetrated hexahedral elements by an initial rebar member should not exceed that of *5* in order to assure that at least one initial rebar node will be located inside the hexahedral active volume, as Fig. 4.3 illustrates. The proposed constraint reduces the computational effort because it allows less neighboring hexahedral elements to be checked during this allocation process, especially when dealing with large-scale problems.

After the satisfaction of the constraint equation (Eq. 4.4), the generation of the reinforcement rebar elements proceeds according to the following three cases.

4.2.2 Virtual Node Allocation Cases

Case 1

In this case, a check is performed to detect whether one or both initial rebar nodes (*1*, *2*) are located on the hexahedral face(s) (Fig. 4.4a). If this is the case, then the corresponding node(s) are being stored. In order to locate the position of the corresponding node local coordinates, the distances *dX*, *dY* and *dZ* between the hexahedral centroid and its first node's coordinates located in the corresponding hexahedral connectivity matrix, need to be computed. By using Eqs. 4.5, we can calculated the required distances *dX*, *dY* and *dZ*.

$$d_X^{Hexa} = s_x^{Hn1} - s_x^{cen},\ \ d_Y^{Hexa} = s_y^{Hn1} - s_y^{cen},\ \ d_Z^{Hexa} = s_z^{Hn1} - s_z^{cen} \tag{4.5}$$

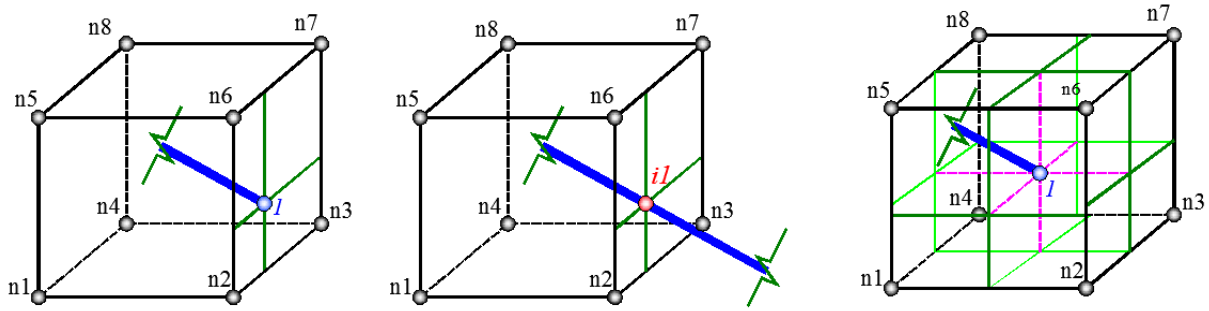

(A) (B) (C)

FIGURE 4.4 GEOMETRIC CONFIGURATION OF THE THREE CASES. (A) CASE 1: REBAR NODE ON HEXAHEDRAL FACE, (B) CASE 2: REBAR-HEXAHEDRAL FACE INTERSECTION, (C) REBAR NODE INSIDE HEXAHEDRAL VOLUME.

Finally the natural coordinates of any given point *P* inside a hexahedral, are given from the following expressions:

$$\xi_P = \frac{s_x^P - s_x^{cen}}{d_X^{Hexa}},\ \ \eta_P = \frac{s_y^P - s_y^{cen}}{d_Y^{Hexa}},\ \ \zeta_P = \frac{s_z^P - s_z^{cen}}{d_Z^{Hexa}} \tag{4.6}$$

given that the hexahedral has an orthogonal parallepiped shape. For the case where the hexahedral element shape is irregular, then the standard Barzegar and Maddipudi[189] method is performed in order to allocate the natural coordinates of the corresponding virtual node.

The Barzegar and Maddipudi[189] procedure for computing the natural coordinates of a virtual embedded rebar element node inside hexahedral concrete elements is described bellow.

A point P_1 with global coordinates $(x, y, z)_{P1}$ on the initial rebar mesh (Fig. 4.5), is contained in a given concrete element if its natural coordinates ξ_{P1}, η_{P1}, ζ_{P1} satisfy the constraint

$$\left|\xi_{P_1}, \eta_{P_1}, \zeta_{P_1}\right| \le 1 \tag{4.7}$$

associated with this particular hexahedral element.

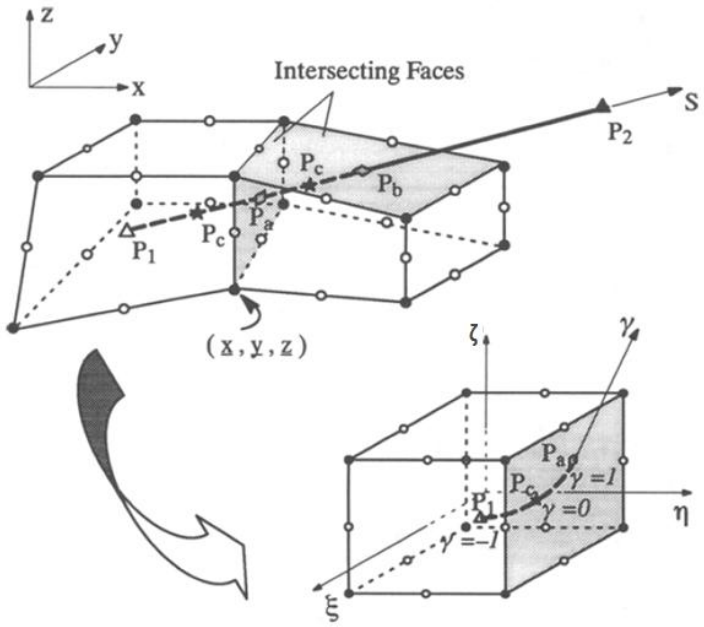

FIGURE 4.5 EMBEDDED REINFORCEMENT IN HEXAHEDRAL CONCRETE ELEMENT[189].

In the isoparametric formulation the global coordinates (x, y, z) of a generic point within a solid element are expressed as

$$\begin{Bmatrix} x \\ y \\ z \end{Bmatrix} = \begin{bmatrix} \boldsymbol{N} & \boldsymbol{0} & \boldsymbol{0} \\ \boldsymbol{0} & \boldsymbol{N} & \boldsymbol{0} \\ \boldsymbol{0} & \boldsymbol{0} & \boldsymbol{N} \end{bmatrix} \begin{Bmatrix} \boldsymbol{x}_i \\ \boldsymbol{y}_i \\ \boldsymbol{z}_i \end{Bmatrix} \tag{4.8}$$

where $\boldsymbol{x_i}$, $\boldsymbol{y_i}$, $\boldsymbol{z_i}$ are the global coordinate vectors of the hexahedral nodes and $\boldsymbol{N}$ represents the row vector of the displacement-shape functions.

Given that the natural coordinates $(\xi, \eta, \zeta)_{P1}$ are the roots of

$$\begin{Bmatrix} x \\ y \\ z \end{Bmatrix}_{P_1} - \begin{bmatrix} \boldsymbol{N} & \boldsymbol{0} & \boldsymbol{0} \\ \boldsymbol{0} & \boldsymbol{N} & \boldsymbol{0} \\ \boldsymbol{0} & \boldsymbol{0} & \boldsymbol{N} \end{bmatrix} \begin{Bmatrix} \boldsymbol{x} \\ \boldsymbol{y} \\ \boldsymbol{z} \end{Bmatrix} = \boldsymbol{0} \tag{4.9}$$

a NR iterative procedure is required in order to compute the solution of the above equation as follows:

$$\begin{Bmatrix} \xi \\ \eta \\ \zeta \end{Bmatrix}^{n+1}_{P_1} = \begin{Bmatrix} \xi \\ \eta \\ \zeta \end{Bmatrix}^{n}_{P_1} + \begin{Bmatrix} \Delta\xi \\ \Delta\eta \\ \Delta\zeta \end{Bmatrix}^{n+1}_{P_1} \tag{4.10}$$

Since

$$\begin{Bmatrix} d\xi \\ d\eta \\ d\zeta \end{Bmatrix} = \left(\boldsymbol{J}^T\right)^{-1} \begin{Bmatrix} dx \\ dy \\ dz \end{Bmatrix} \tag{4.11}$$

where $\boldsymbol{J}$ is the Jacobian matrix ($\boldsymbol{J}_{ij} = \partial N_i / \partial x_j$), the incremental natural coordinates are computed from

$$\begin{Bmatrix} \Delta\xi \\ \Delta\eta \\ \Delta\zeta \end{Bmatrix}_{P_1}^{n+1} = \left(\boldsymbol{J}^{n^T}\right)^{-1} \left[\begin{Bmatrix} x \\ y \\ z \end{Bmatrix}_{P1} - \begin{bmatrix} \boldsymbol{N}^n & \boldsymbol{0} & \boldsymbol{0} \\ \boldsymbol{0} & \boldsymbol{N}^n & \boldsymbol{0} \\ \boldsymbol{0} & \boldsymbol{0} & \boldsymbol{N}^n \end{bmatrix} \begin{Bmatrix} \boldsymbol{x} \\ \boldsymbol{y} \\ \boldsymbol{z} \end{Bmatrix} \right] \qquad 4.12$$

with $\boldsymbol{J}^n = \boldsymbol{J}\left(\xi^n, \eta^n, \zeta^n\right); \quad \boldsymbol{N}^n = \boldsymbol{N}\left(\xi^n, \eta^n, \zeta^n\right).$

Barzegar and Maddipudi[189] found that the preceding solution scheme has a high convergence ratio which was also confirmed in this study. If the converged values do not satisfy (Eq. 4.7), the procedure proceeds to the next hexahedral element until the geometric constraint is satisfied (Eq. 4.4).

For the case where both initial rebar nodes are located on the same plane of a hexahedral face, then the proposed algorithm searches for intersections with the hexahedral face edges and creates the corresponding virtual nodes. For this subcase, the stiffness matrix of the embedded rebar element (element *ER 3* in Fig. 4.1) is distributed between the two neighboring hexahedral elements (Hexahedral *2* and *3* in Fig. 4.1).

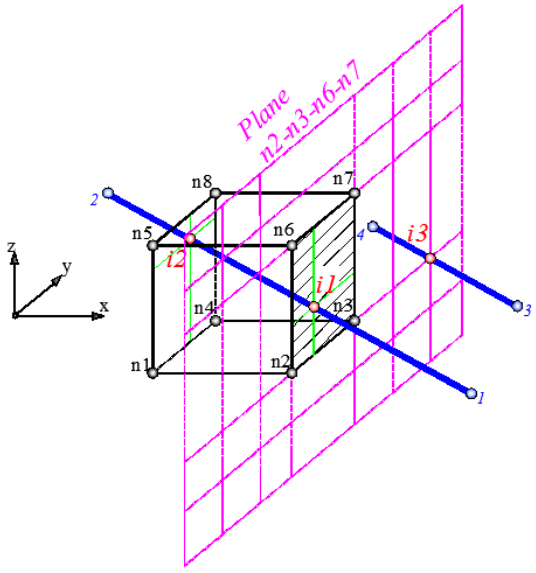

FIGURE 4.6 REBAR ELEMENT INTERSECTIONS WITH HEXAHEDRON FACES. NODES *i1* AND *i2* ARE RETAINED, NODE *i3* IS NOT ACCEPTABLE.

Case 2

In the second case a rebar element intersects with one or two hexahedral faces (Fig. 4.4b, 4.6). In order to find a potential line-plane intersection the corresponding algebraic equation has to be solved (see Appendix B). Then, if an intersection exists, the following constraint is checked, which guaranties that the nodal intersection is located inside the face of the hexahedral under consideration:

$$\left|\xi_P,\ \eta_P,\ \zeta_P\right| \le 1 \qquad 4.13$$

where ξ_P, η_P, ζ_P are the natural coordinates of the intersection point. If this constraint is not satisfied, the intersection point is not retained and the algorithm proceeds with the computation of the next intersection point.

Case 3

When cases *1* and *2* are not applicable then a check is performed for the satisfaction of the following constraint:

$$\left|\xi_R,\ \eta_R,\ \zeta_R\right| < 1 \qquad 4.14$$

where ξ_R, η_R, ζ_R are the natural coordinates of the initial rebar node. If the above inequality is satisfied, it means that the rebar node is located inside the volume of the hexahedral (Fig. 4.4c), otherwise the node is located outside the hexahedral volume and no action is taken. After the computation of the virtual nodes for each of the initial reinforcement rebars, the mesh generation of the embedded rebar elements is performed.

Following the described generation algorithm, all necessary data of each hexahedral element is determined regarding the corresponding virtual rebar nodes that were located inside the volume or on its faces. At this point, the main features of the embedded rebar element are calculated and stored: The type of element (*Beam* or *Rod*), nodal coordinates, the type of nodes (if a node is virtual or a physical node of the initial mesh) and the material properties. Fig. 4.7 illustrates the flow chart of the proposed embedded rebar element mesh generation algorithm. It has to be mentioned that, in order for the nodal natural coordinate's computations to be applicable, hexahedral elements must be orthogonal parallepiped. If the hexahedral shape is irregular then the Barzegar and Maddipudi[189] method is used instead of Eq. 4.6.

4.3 Numerical Implementation

In this section, a numerical verification of the efficiency of the proposed embedded reinforcement generation method will be presented. For this reason, four different FE models have been tested. Different reinforcement properties and geometries are considered in order to demonstrate the capability of the proposed method to allocate and generate embedded reinforcement elements with numerical robustness and computational efficiency when dealing with large-scale models. All numerical tests were performed with a *1.9 GHz* processor (personal laptop) with a *2GB* DDR2 Ram.

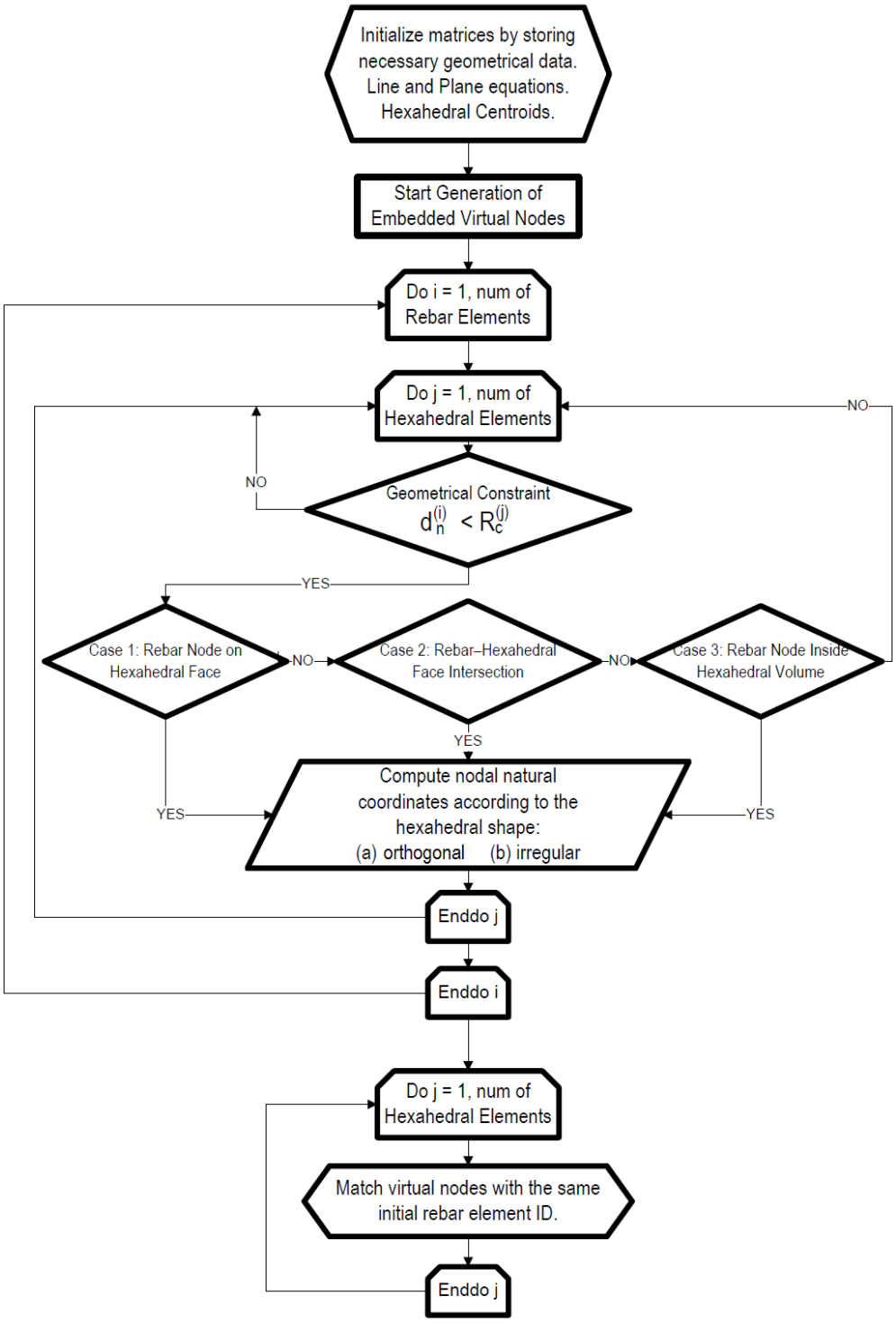

FIGURE 4.7 FLOW CHART OF THE PROPOSED EMBEDDED REBAR ELEMENT MESH GENERATION METHOD.

4.3.1 RC Shear Wall

The first model is a RC shear wall which consists of *1,680* hexahedral elements (*0.125 m* x *0.10 m* x *0.0767 m*) and *1,320* initial rebars (vertical reinforcement *Ø12/10* and horizontal reinforcement *Ø8/15*). As can be seen in Fig. 4.8, the RC shear wall has a total length of *2.80 m*, a height equal to *2.30 m* and a *0.25 m* thickness. The embedded rebar mesh generation terminates the generation with the allocation of *3,080* rebar elements in *1.1 sec*.

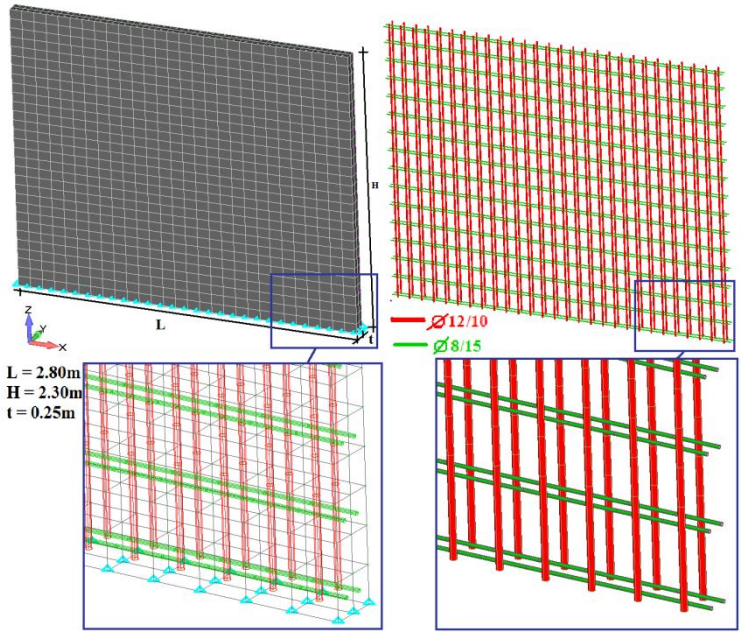

FIGURE 4.8 RC SHEAR WALL WITH *1,680* HEXAHEDRAL ELEMENTS AND *1,320* INITIAL REBAR ELEMENTS.

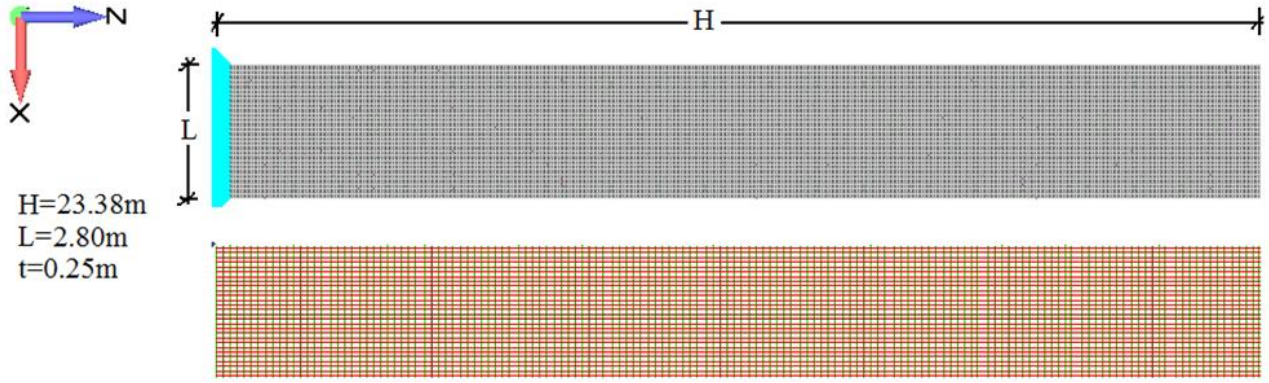

FIGURE 4.9 RC SHEAR WALL WITH *17,080* HEXAHEDRAL ELEMENTS AND *13,192* INITIAL STEEL BAR ELEMENTS.

With the intention of testing the proposed generation framework for larger topological space to be discretized a tenfold increase of the initial model is considered. The new FE model consists of *17,080* hexahedral elements and *13,192* initial rebar elements (Fig. 4.9). After the completion of the embedded rebar element mesh generation process, the total number of generated embedded rebar elements becomes *34,327* and the corresponding required computational time is *85 sec*. The proposed algorithm managed to scan and generate all the embedded reinforcement elements within an affordable computational time. This is mainly attributed to the implementation of the geometric constraint of Eq. 4.4. The corresponding computational time for the embedded rebar element mesh generation process, when the geometrical constraint is not used, was 7 min. This shows the importance of the proposed constraint during the mesh generation process particularly for large-scale models. Since the required CPU time for the embedded mesh generation procedure cannot be explicitly measured when ATENA software is used, the comparison cannot be made for this case. Nevertheless, the required initiation CPU time, for these two numerical tests, were 3 and 25 min, respectively. The corresponding CPU times of ReConAn are 2 and 160 sec (including the embedded rebar mesh generation

procedure). This differences are to a certain extend attributed to I/O procedures that ATENA performs during the initialization of the models.

4.3.2 RC Frame

This model was created in order to illustrate the ability of the proposed algorithm to generate embedded reinforcement for more complicated reinforcement layouts. The rebar layout for each structural member is depicted in Fig. 4.10. The RC frame has a *5 m* span and consists of a shear wall, a beam, a column and two foundation footings in order to make the geometry more complex.

Fig. 4.11 illustrates the initial discretization with hexahedral and reinforcement rebar elements. The initial FE model consists of *840* hexahedral elements and *3,046* rebar elements.

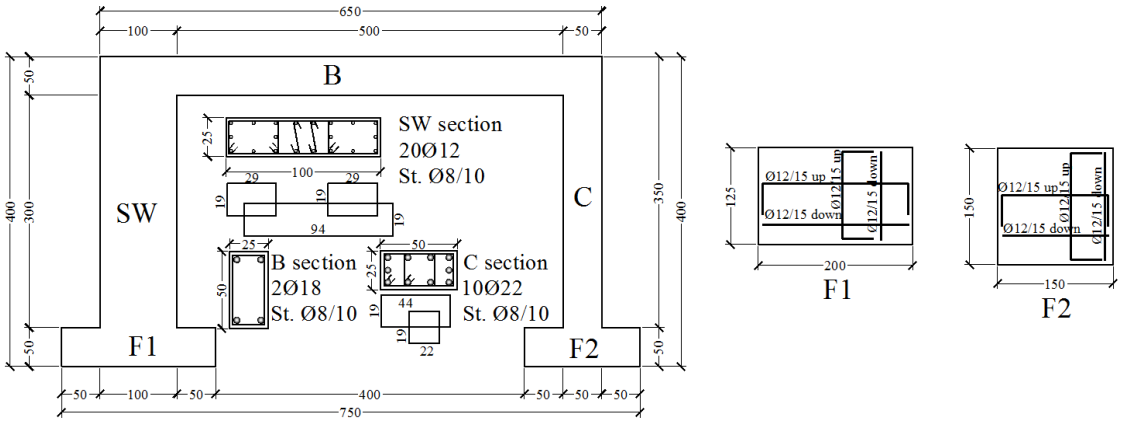

FIGURE 4.10 RC FRAME. GEOMETRY AND REINFORCEMENT DETAILS.

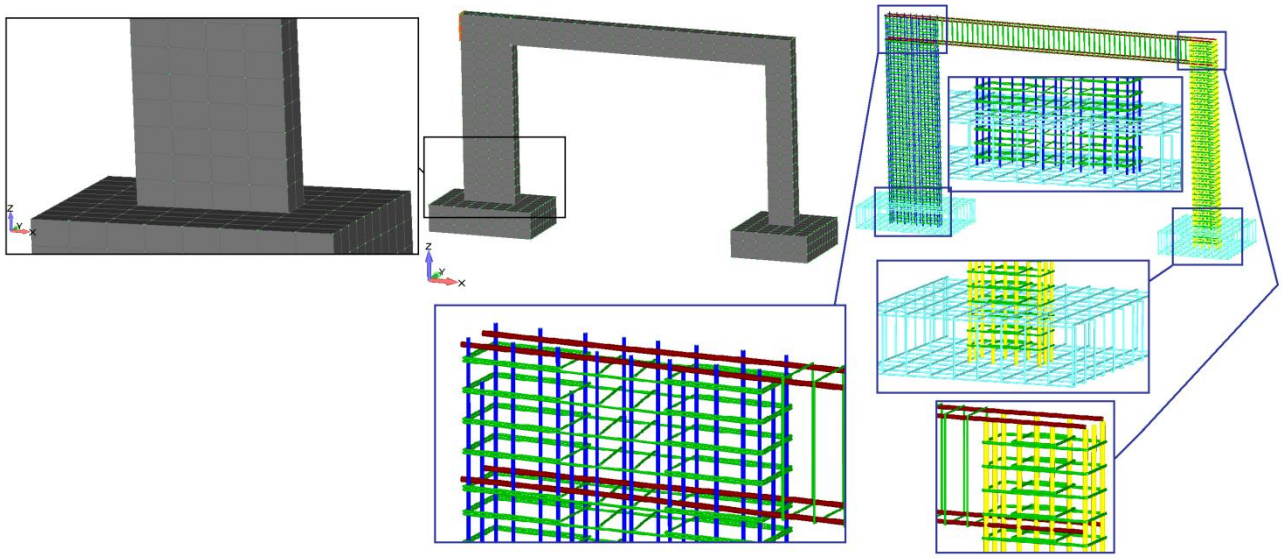

FIGURE 4.11 RC FRAME. INITIAL FE MESH (HEXAHEDRAL ELEMENTS – INITIAL REINFORCEMENT MESH).

The total number of embedded rebar elements created after the execution of the rebar element mesh generation process was *4,434* and the corresponding required time was *5 sec*. It can be seen that the mesh generation is completed in a minimal computational time despite the fact

that the mesh of the hexahedral elements was relatively dense, especially in the foundation footings.

4.3.3 Arch-Shaped RC Frame

This numerical test was constructed with the purpose of creating a base for the computational assessment of the proposed mesh generation method, when irregular hexahedral mesh geometries are presented. The geometry of this benchmark problem is shown in Fig. 4.12, where it can be seen that it consists of a circular arch rectangular in section and *3.40 m* internal diameter. The corresponding hexahedral and rebar element mesh is shown in Fig. 4.13 and the corresponding mesh details in Table 4.1. The basic feature of this FE model is the correlation between the number of the irregular shaped hexahedral elements and the orthogonal parallepiped hexahedral elements. The total number of hexahedrons is *592* and the corresponding number of irregular hexahedral elements (located in the volume of the arch) is *384* which comprise *64.86%* of the total hexahedral mesh.

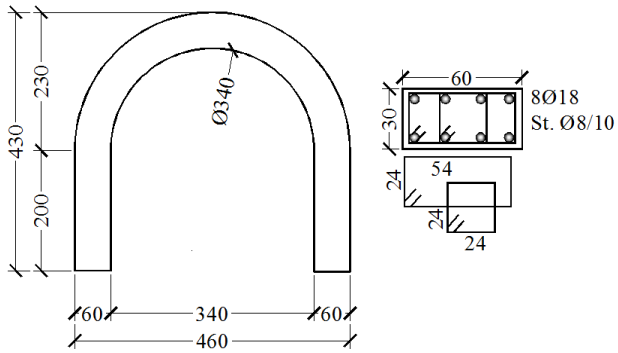

FIGURE 4.12 ARCH-SHAPED RC FRAME. GEOMETRICAL AND REINFORCEMENT DETAILS.

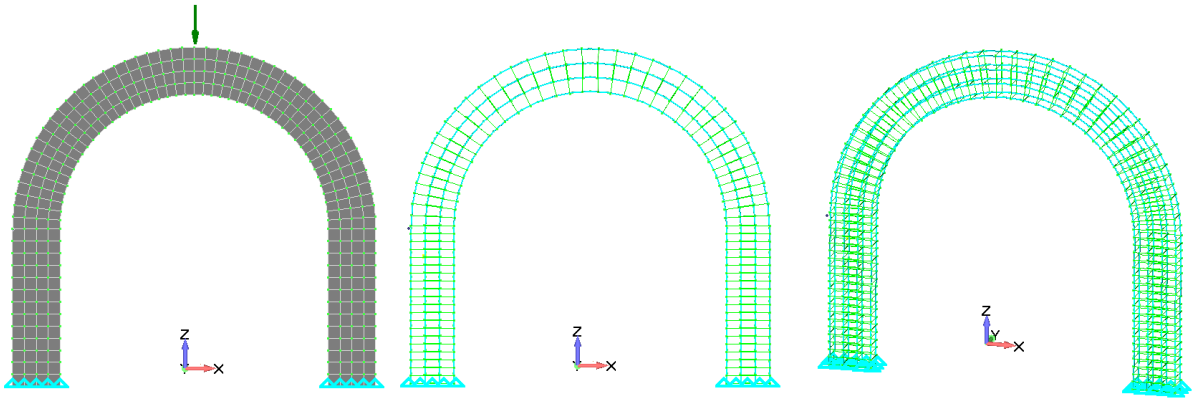

(A) (B) (C)

FIGURE 4.13 ARCH-SHAPED RC FRAME. MESH DETAILS OF (A) HEXAHEDRAL AND (B-C) INITIAL REBAR ELEMENTS.

The embedded rebar mesh generation procedure terminates with the allocation of *2,244* rebar elements in *0.25 sec*. For illustrational purposes, the predicted crack pattern is shown in Fig 4.14a when a nonlinear concentrated vertical load is applied on the center of the RC arch. In addition to that, the corresponding deformed shape of the rebar elements' mesh is given in Fig. 4.14b where the displacements are magnified x*50*.

a/a	*Element Type*	*Number of Elements*
1	Initial Rebar Elements	1040
2	Irregular Hexahedral Elements	384
3	Orthogonal Parallepiped Hexahedral Elements	208
4	Total Hexahedral Elements	592

TABLE 4.1 ARCH-SHAPED RC FRAME. FE MESH DETAILS.

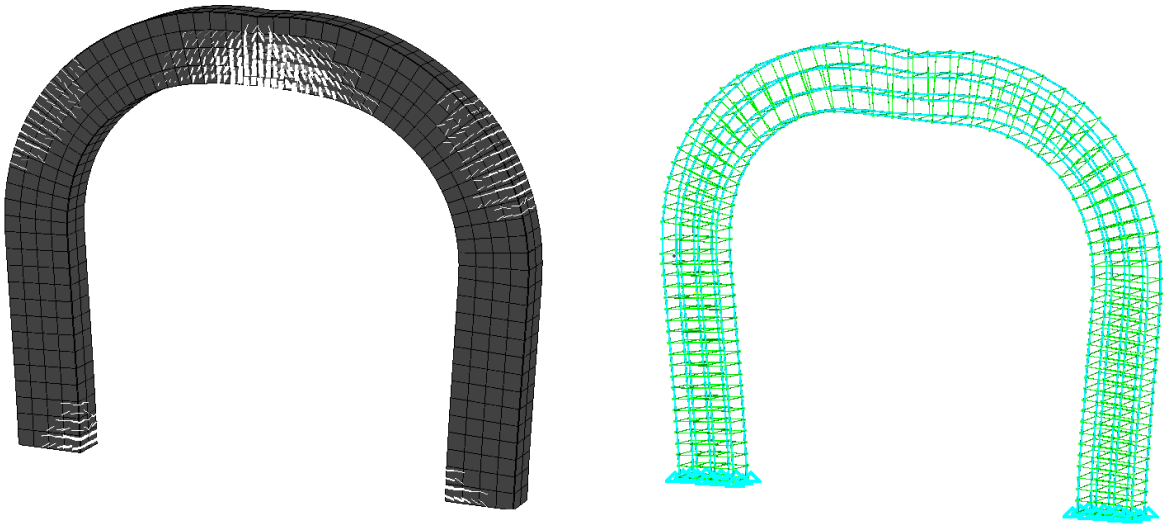

(A) (B)

FIGURE 4.14 ARCH-SHAPED RC FRAME. CRACK PATTERN AND DEFORMATION SHAPES OF THE (A) HEXAHEDRAL AND (B) REBAR ELEMENTS' MESHES.

To test the proposed generation framework for larger discretizations with irregular hexahedral shaped elements we considered a tenfold increase of the initial model. The new FE model consists of *5,920* hexahedral elements and *10,400* initial reinforcement rebar elements (Fig. 4.15).

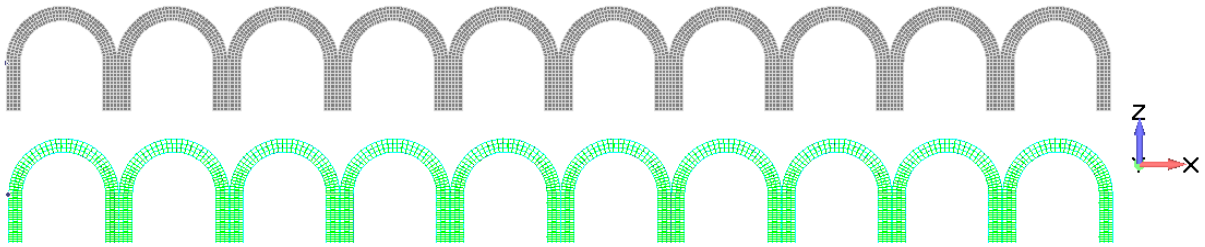

FIGURE 4.15 ARCH-SHAPED RC FRAME. MESH DETAILS OF THE HEXAHEDRAL (UP) AND INITIAL REBAR (DOWN) ELEMENTS.

After the completion of the embedded rebar element mesh generation process, the total number of generated embedded rebar elements becomes *22,440* and the corresponding required computational time is *26 sec*.

4.3.4 2-Storey RC Building

This numerical test was created for investigating the computational effort required by the proposed mesh generation method for the allocation of the embedded rebar elements for the case of a full-scale RC structure.

The rebar layout for this numerical test is given in Chapter 6 where the details of the FE model are given. Fig. 4.16 shows the FE mesh of the RC building which consists of *4,382* hexahedral elements and *26,959* initial rebar elements. After the completion of the embedded rebar mesh generation procedure, the proposed method managed to allocate *51,064* embedded rebar elements in *69 sec*. The corresponding computational time for the generation procedure when the geometrical constraint is not activated, is *400 sec*.

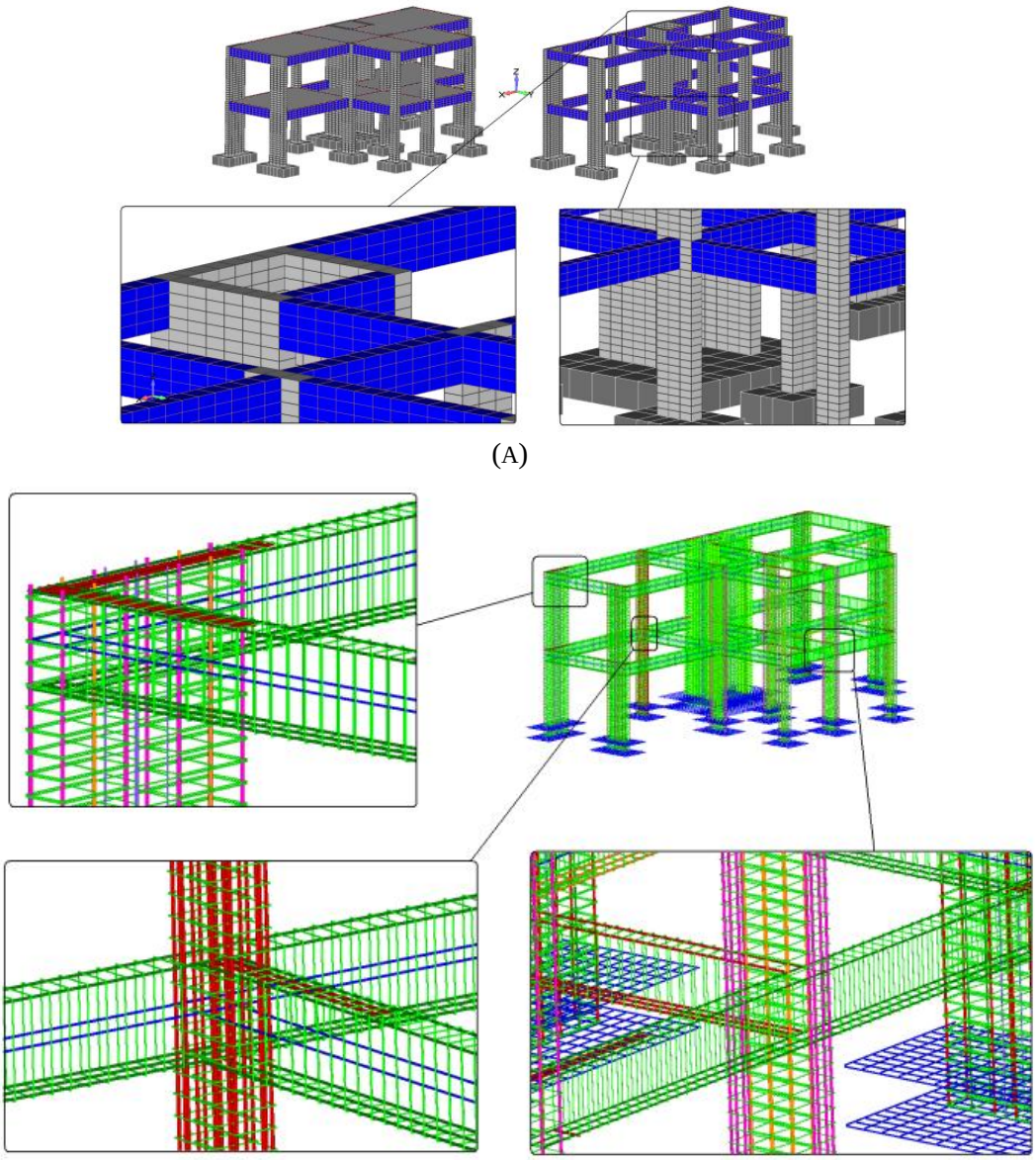

(A)

(B)

FIGURE 4.16 2-STOREY RC BUILDING. (A) HEXAHEDRAL AND (B) INITIAL REBAR ELEMENT MESH.

Chapter 5 3D Detailed Modeling of Reinforced Concrete Structures

Contents of Chapter 5

5.1 Brief Overview

Many numerical models have been developed for the analysis of RC structures but none of them has managed to provide the desired combination at an acceptable level of accuracy, robustness and computational efficiency in predicting the nonlinear inelastic behavior of different types of RC structural members when combined with the FEM. As it was mentioned in the first Chapter, 1D beam-column models, based on either concentrated plasticity models or distributed plasticity (fiber models), have difficulties in predicting the mechanical behavior of 3D RC framed structures due to their inability in capturing shear behavior and local phenomena that influence the global response of the structures.

On the contrary, the use of 2D plane-stress FE models[195-198] can avoid some simplification assumptions that are inherent in 1D beam-column models, like the influence of shear stresses, but their inability of capturing the out of plane response made them inadequate for 3D full-scale RC analysis. Three-dimensional simulation with solid finite elements, based on triaxial stress-strain relationships and embedded rebars[6, 8, 9, 139, 199-205] provides the highest quality of approximation but it is hindered with high computational cost and in several cases lack of robustness.

The computational complexity of such detailed models makes their use impractical for full-scale simulations. Furthermore, with the use of numerically unstable material models (i.e. concrete material model combined with the smeared crack approach), the sensitivity of such models to various user-defined parameters, becomes more pronounced[140]. These difficulties led a number of researchers[6, 8, 138, 199, 200, 205] to use higher order elements (20-noded and 27-noded hexahedral elements) in connection with high integration rules (*3*x*3*x*3*). The use of this type of 3D elements and numerically unstable material models has a direct consequence on the efficiency of the numerical simulations, requiring many NR iterations per load step and thus considerable computational effort, even for small-scale FE models.

8-noded hexahedral elements were used by Sato and Naganuma[139] (2007), where the stiffness matrix was computed only at the element centroid in the interest of reducing computational load, while in[202] the ATENA software code[140] was used with the 8-noded hexahedral isoparametric element combined with the 2-noded rod element for the reinforcement.

In this work, a 3D 8-noded hexahedral isoparametric element is used for the simulation of concrete based on an improved concrete material model originally proposed by Kotsovos and Pavlovic[8], as was presented in the previous Chapter. The reinforcement is modeled with an embedded steel bar simulated with the NBCFB element. The geometric treatment of the embedded reinforcement presented in Chapter 4 is adopted, which allows the arbitrary rebar elements orientation inside the concrete solid elements and a free hexahedral mesh.

The above features of the detailed 3D FE discretization of RC structures are incorporated into the proposed numerical model and the validation of the obtained numerical results is performed with experimental data and numerical results of different types of RC structural members, which are published in the literature[186, 206, 207]. The best-known commercial software that can simulate RC structures with the use of three-dimensional solid FE combined with the smeared

crack approach are the ATENA[140] and the DIANA[208]. In this work the ATENA software was used as a comparative tool for testing the accuracy and computational efficiency of the proposed formulation.

5.2 Proposed Modeling Method

When modeling RC structures with detailed 3D FE four basic numerical stages have to be considered:

i. FE type for concrete modeling.
ii. 3D concrete material constitutive model.
iii. FE type for embedded rebar modeling.
iv. Steel material constitutive model.

These stages will be discussed in detail in the following sections.

5.2.1 FE Type for Concrete Modeling

The hexahedral element is a 3D solid hexahedron, also known in the literature as "brick element". This type of element is used in modeling not only three-dimensional solids but also plates and shells as well as beam elements. The construction of the hexahedral shape functions and the computation of its stiffness matrix depend on the isoparametric description and numerical integration schemes adopted.

The natural coordinate system ξ, η, ζ is positioned in the barycenter of the hexahedron and the corresponding nodal coordinates are given in Table 5.1. In Fig. 5.1 the positioning of each node corresponding to the natural coordinate system ξ, η, ζ can be seen, for the case of the 8-noded hexahedral elements. This element has a total of *24* dof and therefore the size of its stiffness matrix is *24*x*24*. The 8-noded hexahedral finite element (hexa8) has the simplest formulation regarding the hexahedron finite element family, leading to a fast computation of the stiffness matrix.

The general matrix equation which describes the hexa8 formulation can be written as:

$$\begin{bmatrix} 1 \\ x \\ y \\ z \\ v_x \\ v_y \\ v_z \end{bmatrix} = \begin{bmatrix} 1 & 1 & 1 & 1 & 1 & 1 & 1 & 1 \\ x_1 & x_2 & x_3 & x_4 & x_5 & x_6 & x_7 & x_8 \\ y_1 & y_2 & y_3 & y_4 & y_5 & y_6 & y_7 & y_8 \\ z_1 & z_2 & z_3 & z_4 & z_5 & z_6 & z_7 & z_8 \\ v_{x1} & v_{x2} & v_{x3} & v_{x4} & v_{x5} & v_{x6} & v_{x7} & v_{x8} \\ v_{y1} & v_{y2} & v_{y3} & v_{y4} & v_{y5} & v_{y6} & v_{y7} & v_{y8} \\ v_{z1} & v_{z2} & v_{z3} & v_{z4} & v_{z5} & v_{z6} & v_{z7} & v_{z8} \end{bmatrix} \begin{bmatrix} N_1^{(e)} \\ N_2^{(e)} \\ \\ \vdots \\ \\ N_8^{(e)} \end{bmatrix} \quad 5.1$$

where

$$\begin{aligned} N_1^{(e)} &= \tfrac{1}{8}(1-\xi)(1-\eta)(1-\zeta), & N_2^{(e)} &= \tfrac{1}{8}(1+\xi)(1-\eta)(1-\zeta) \\ N_3^{(e)} &= \tfrac{1}{8}(1+\xi)(1+\eta)(1-\zeta), & N_4^{(e)} &= \tfrac{1}{8}(1-\xi)(1+\eta)(1-\zeta) \\ N_5^{(e)} &= \tfrac{1}{8}(1-\xi)(1-\eta)(1+\zeta), & N_6^{(e)} &= \tfrac{1}{8}(1+\xi)(1-\eta)(1+\zeta) \\ N_7^{(e)} &= \tfrac{1}{8}(1+\xi)(1+\eta)(1+\zeta), & N_8^{(e)} &= \tfrac{1}{8}(1-\xi)(1+\eta)(1+\zeta) \end{aligned} \quad 5.2$$

$N_i^{(e)}$ are the shape functions. These eight formulas can be summarized in a single expression:

$$N_i^{(e)} = \frac{1}{8}(1+\xi\xi_i)(1+\eta\eta_i)(1+\zeta\zeta_i) \quad 5.3$$

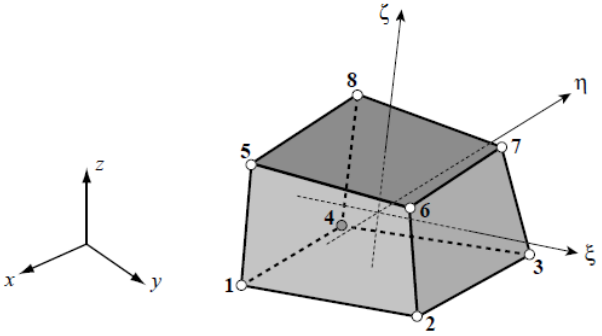

FIGURE 5.1 NATURAL COORDINATE SYSTEM OF THE 8-NODED HEXAHEDRAL ELEMENT.

More complex hexahedral elements can be seen in Figs. 5.2 with higher order shape functions and which have more dof thus requiring more computational effort for the formulation of the stiffness matrix. In this work the hexa8 element is adopted, for its simplicity and computational efficiency.

Node	ξ	η	ζ
1	-1	-1	-1
2	1	-1	-1
3	1	1	-1
4	-1	1	-1
5	-1	-1	1
6	1	-1	1
7	1	1	1
8	-1	1	1

TABLE 5.1 NATURAL COORDINATES OF THE HEXAHEDRAL NODES.

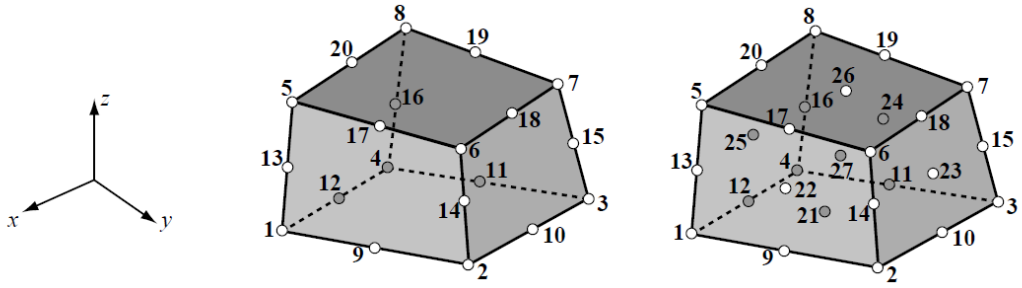

FIGURE 5.2 HEXAHEDRAL ELEMENTS WITH *20* AND *27* NODES.

5.2.2 3D Concrete Material Constitutive Model

As it was discussed in this Dissertation , several material models were proposed for the modeling of concrete[128, 142, 210-220]. The 3D material model for concrete implemented in this work was based on the Kotsovos and Pavlovic[8] model after a modification of its numerical implementation in order to improve its numerical robustness. The proposed modifications, which were presented in Chapter 3, ensure that the material model when combined with the

smeared crack approach, manage to predict the 3D nonlinear behavior of concrete material under any stress state conditions with computational accuracy and efficiency.

5.2.3 FE Type for Embedded Rebar Modeling

Previous simulations with the embedded rebar reinforcement used 2-noded or 3-noded rod elements. Hence, the reinforcement is considered to act as uniaxial element, without taking into consideration shear and bending stiffness. Although it is generally believed that shear and bending resistance of reinforcement is not significant, there are cases where the shear and bending resistance are important in capturing the nonlinear response of RC structural members. The discretization of the reinforcement is therefore performed with NBCFB element which in addition to the consideration of shear and bending it was found to increase the numerical stability of the NR iteration procedure due to its special formulation features. However, the choice of using 3D beam elements instead of uniaxial rod elements introduces some implementation issues.

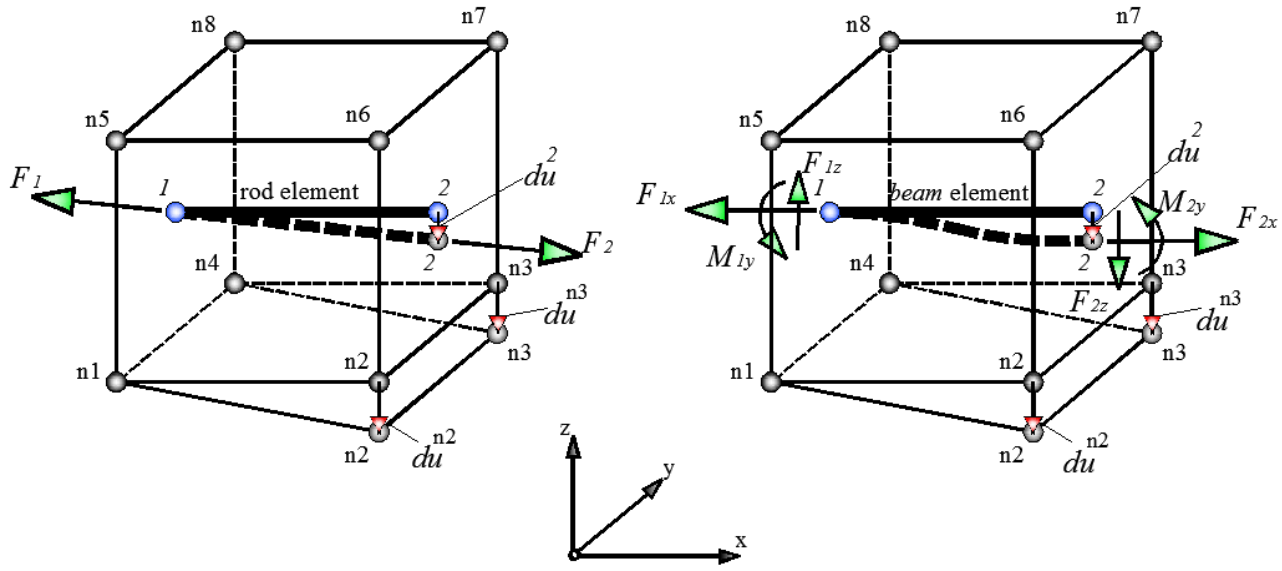

(A) (B)

FIGURE 5.3 EMBEDDED REBAR ELEMENTS UNDER IMPOSED TRANSVERSE DEFORMATION: (A) ROD ELEMENT AND (B) BEAM ELEMENT.

When 2-noded or 3-noded rod elements are used, the compatibility conditions between the nodes (*1* and *2*) of the rod and the corresponding hexahedral nodes (*n1-n8*) is enforced through the translational dof (Fig. 5.3a) since the rotation of the rod nodes is neglected. When beam elements are used, the compatibility of rotation between the hexahedral nodal displacements and the rotation of the rebar nodes that are located on the corresponding hexahedral faces must be enforced. The compatibility is achieved by computing the hexahedral face rotation and imposing it to the corresponding rotational dof of the rebar node.

Assuming that the angle $\bar{\theta}$ between the longitudinal axis of the rebar and the normal $\bar{\mathbf{n}}$ on the master triangle of the hexahedral face (Fig. 5.4) remains fixed before and after deformation, the required rotation can be derived through kinematic constraints. The assignment of a master triangle at each rebar node is performed prior to the analysis by detecting the three nearest

hexahedral nodes of the corresponding face containing the rebar node. These three nodes *n2, n3, n6* in Fig. 5.4 represent the master triangle of the rebar node *2* which controls the rotation of the corresponding rebar node.

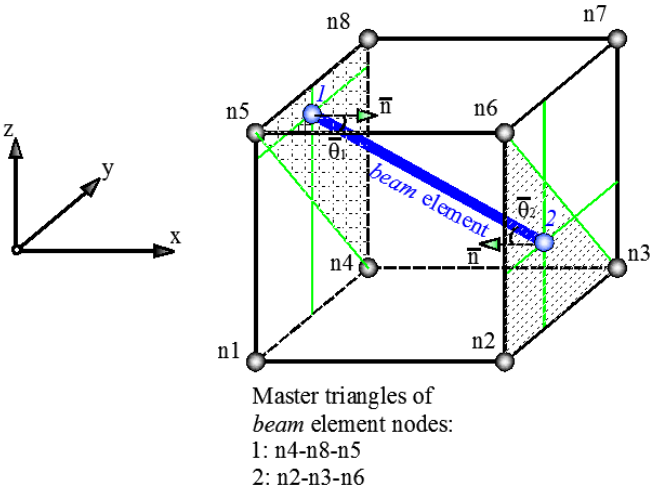

FIGURE 5.4 MASTER TRIANGLES OF BEAM ELEMENT NODES *1* AND *2*.

5.2.3.1 Kinematics

Most researchers[6, 8, 138, 189, 190, 225] use standard kinematic relations in order to connect the rod nodal displacements with the corresponding hexahedral displacements. A more recent approach was proposed by Jendele and Červenka[194] (2009) where the solution of a multi-point constraint conditions problem called Complex Boundary Conditions is performed. This procedure requires the solution of a system of non-symmetric constraint equations, which appears to be computationally demanding.

In this work, the kinematic relations that connect the beam nodal displacements with the nodal displacements of the corresponding hexahedral face, are given from the following expressions

$$\underset{(12x1)}{\boldsymbol{u}^B} = \underset{(12x24)}{\boldsymbol{T}} \cdot \underset{(24x1)}{\boldsymbol{U}^H} \quad , \quad \underset{(24x1)}{\boldsymbol{F}^H} = \underset{(24x12)}{\boldsymbol{T}^T} \cdot \underset{(12x1)}{\boldsymbol{F}^B} \tag{5.4}$$

where $\boldsymbol{u}^B$ and $\boldsymbol{U}^H$ are the displacement vectors of the beam and hexahedral elements, respectively, while $\boldsymbol{F}^B$ and $\boldsymbol{F}^H$ are the corresponding internal force vectors. The transformation matrix $\boldsymbol{T}$ is composed of 32 (3x3) submatrices which are computed from the natural coordinates of the hexahedral, the beam element and the master triangle nodes

$$\underset{12x24}{\boldsymbol{T}} = \begin{bmatrix} \boldsymbol{T}_1^1 & \boldsymbol{T}_2^1 & \boldsymbol{T}_3^1 & \boldsymbol{T}_4^1 & \boldsymbol{T}_5^1 & \boldsymbol{T}_6^1 & \boldsymbol{T}_7^1 & \boldsymbol{T}_8^1 \\ 0 & 0 & 0 & \boldsymbol{R}_4^1 & \boldsymbol{R}_5^1 & 0 & 0 & \boldsymbol{R}_8^1 \\ \boldsymbol{T}_1^2 & \boldsymbol{T}_2^2 & \boldsymbol{T}_3^2 & \boldsymbol{T}_4^2 & \boldsymbol{T}_5^2 & \boldsymbol{T}_6^2 & \boldsymbol{T}_7^2 & \boldsymbol{T}_8^2 \\ 0 & \boldsymbol{R}_2^2 & \boldsymbol{R}_3^2 & 0 & 0 & \boldsymbol{R}_6^2 & 0 & 0 \end{bmatrix}, \tag{5.5}$$

The submatrices located in rows *1* and *3* of $\boldsymbol{T}$ correspond to the translational rebar displacements T_i^j and those in rows *2* and *4* correspond to the rotational rebar displacements $\boldsymbol{R}_m^j$. Eq. 5.5 refers to the case illustrated in Fig. 5.4 where the nodes *1* and *2* of the rebar correspond to (*n4-n8-n5*) and (*n2-n3-n6*) master triangles, respectively.

Each transformation matrix $\boldsymbol{T}$ (Eq. 5.5) consists of *32* submatrices with dimension *3*x*3*. From Eq. 5.5 it can be seen that the translational dof of each beam element node are transformed through the use of $\boldsymbol{T}_i^j$ matrices

$$\underset{3x3}{\boldsymbol{T}_i^j} = \begin{bmatrix} N_i^j & 0 & 0 \\ 0 & N_i^j & 0 \\ 0 & 0 & N_i^j \end{bmatrix}, \tag{5.6}$$

where N_i^j (i = *1, 8*) correspond to the 8 hexahedral shape functions and j = *1, 2* denote the embedded rebar nodes. After the computation of the value of each shape function N_i^j at the natural coordinates of each beam node the corresponding matrices are assembled. As it can be seen from Eq. 5.6, submatrix $\boldsymbol{T}_i^j$ contains the shape function value N_i computed at the rebar node j.

In order to handle the rotational dof of the embedded rebar beam element, the definition of a master triangle is necessary with the purpose of computing the rotation along the three global axεs. This master triangle is formed with the three nearest to the rebar beam element node on the corresponding hexahedral face (Fig. 5.4). The computation of each master triangle body rotations are calculated with the natural mode theory of Argyris et al.[209] (1997). So as to estimate the translational modes ρ as functions of the displacements and rotations at vertices *1*, *2* and *3* of a triangle, it is assumed that the linear displacement field with respect to the local elemental coordinate can be described as:

$$u = p_o + p_1 x + p_2 y, \quad \upsilon = q_o + q_1 x + q_2 y, \quad \mathrm{w} = r_o \tag{5.7}$$

where p_i, q_i, r_i are the displacements referred to the local coordinate system. If the origin of the local coordinate system is placed at the element's barycenter, Eqs. 5.7 may be written in the form

$$u_1 + u_2 + u_3 = 3p_o, \quad \upsilon_1 + \upsilon_2 + \upsilon_3 = 3q_o, \quad w_1 + w_2 + w_3 = 3r_o \tag{5.8}$$

The rigid body drilling rotation ρ_{06} is given by

$$\rho_{06} = \frac{1}{2}\left(\frac{\partial \upsilon}{\partial x} - \frac{\partial u}{\partial y} \right) = \frac{1}{2}\left(q_1 - p_2 \right) \tag{5.9}$$

If we write Eqs. 5.7 for every vertex, the quantity in Eq. 5.9 becomes

$$\rho_{06} = -\frac{1}{2\Omega}\left(x_a u_1 + y_a \upsilon_1 + x_\beta u_2 + y_\beta \upsilon_1 + x_\gamma u_3 + y_\gamma \upsilon_3 \right) \tag{5.10}$$

where

$$x_\alpha = x_3 - x_2, \quad x_\beta = x_1 - x_3, \quad x_\gamma = x_2 - x_1, \quad y_\alpha = y_3 - y_2, \quad y_\beta = y_1 - y_3, \quad y_\gamma = y_2 - y_1 \tag{5.11}$$

and x_i, y_i (i=*1, 3* master triangle nodes) are the local Cartesian nodal coordinates of the triangle (Fig. 5.5) while Ω is the area of the triangle. Then the relation between the rigid body rotations ρ_{04}, ρ_{05} and the Cartesian coordinates of the triangle vertices need to be defined. For this purpose the rotation θ_1 of the triangle along the side *23*, as depicted in Fig. 5.5, is given by

$$\theta_1 = \frac{w_1}{h_a} = \frac{w_1 l_a}{2\Omega} \tag{5.12}$$

and its two projections on the local Cartesian axes, are given by

$$\theta_{1x} = \theta_1 \cos a_x = \theta_1 \frac{x_a}{l_a} = \frac{x_a}{2\Omega} w_1, \quad \theta_{1y} = \theta_1 \sin a_y = \theta_1 \frac{y_a}{l_a} = \frac{y_a}{2\Omega} w_1 \tag{5.13}$$

Similarly,

$$\theta_{2x} = \frac{x_\beta}{2\Omega} w_2, \quad \theta_{3x} = \frac{x_\gamma}{2\Omega} w_3, \quad \theta_{2y} = \frac{y_\beta}{2\Omega} w_2, \quad \theta_{3y} = \frac{y_\gamma}{2\Omega} w_3 \tag{5.14}$$

Therefore, the rigid-body rotations ρ_{04}, ρ_{05} are simply:

$$\rho_{04} = \theta_{1x} + \theta_{2x} + \theta_{3x}, \quad \rho_{05} = \theta_{1y} + \theta_{2y} + \theta_{3y} \tag{5.15}$$

$$\rho_{04} = \frac{x_a}{2\Omega} w_1 + \frac{x_\beta}{2\Omega} w_2 + \frac{x_\gamma}{2\Omega} w_3, \quad \rho_{05} = \frac{y_a}{2\Omega} w_1 + \frac{y_\beta}{2\Omega} w_2 + \frac{y_\gamma}{2\Omega} w_3 \tag{5.16}$$

The above equations can be expressed in matrix form

$$\underset{(3x1)}{\begin{Bmatrix} \rho_{04} \\ \rho_{05} \\ \rho_{06} \end{Bmatrix}} = \begin{bmatrix} \underset{(3x3)}{\bar{\boldsymbol{R}}_1^j} & \underset{(3x3)}{\bar{\boldsymbol{R}}_2^j} & \underset{(3x3)}{\bar{\boldsymbol{R}}_3^j} \end{bmatrix} \underset{(9x1)}{\begin{Bmatrix} \boldsymbol{x} \\ \boldsymbol{y} \\ \boldsymbol{z} \end{Bmatrix}} \tag{5.17}$$

where

$$\underset{(3x3)}{\bar{\boldsymbol{R}}_1^j} = \begin{bmatrix} 0 & 0 & \frac{x_a}{2\Omega} \\ 0 & 0 & \frac{y_a}{2\Omega} \\ -\frac{x_a}{2\Omega} & -\frac{y_a}{2\Omega} & 0 \end{bmatrix}, \underset{(3x3)}{\bar{\boldsymbol{R}}_2^j} = \begin{bmatrix} 0 & 0 & \frac{x_\beta}{2\Omega} \\ 0 & 0 & \frac{y_\beta}{2\Omega} \\ -\frac{x_\beta}{2\Omega} & -\frac{y_\beta}{2\Omega} & 0 \end{bmatrix}, \underset{(3x3)}{\bar{\boldsymbol{R}}_3^j} = \begin{bmatrix} 0 & 0 & \frac{x_\gamma}{2\Omega} \\ 0 & 0 & \frac{y_\gamma}{2\Omega} \\ -\frac{x_\gamma}{2\Omega} & -\frac{y_\gamma}{2\Omega} & 0 \end{bmatrix} \tag{5.18}$$

and $j = 1, 2$ corresponds to the embedded rebar beam nodes and Ω is the area of the corresponding master triangle. $\boldsymbol{x}$, $\boldsymbol{y}$, $\boldsymbol{z}$ are the translational displacement vectors of the master triangle.

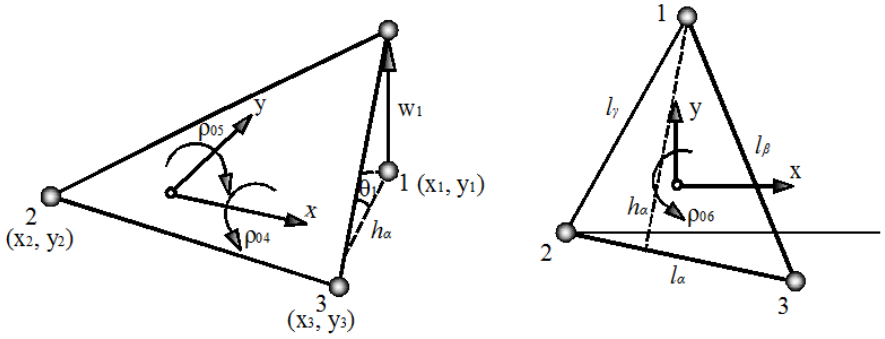

FIGURE 5.5 ROTATION θ_1.

Therefore, after the computation of the three transformation matrices $\boldsymbol{R}_m^j$ in the global coordinate system (Eq. 5.19) for each master triangle the computation of the transformation matrix $\boldsymbol{T}$ (*12*x*24*) of Eq. 5.5 is completed.

$$\underset{(3x3)}{\boldsymbol{R}_m^j} = \underset{(3x3)}{\boldsymbol{T}_o^T}\ \underset{(3x3)}{\bar{\boldsymbol{R}}_m^j}\ \underset{(3x3)}{\boldsymbol{T}_o} \qquad 5.19$$

where $\boldsymbol{T}_o$ is the known cosine matrix that transforms the local into global coordinate system (Eq. 2.80).

5.2.3.2 Transformation of the Stiffness Matrix of the Embedded NBCFB Element

The contribution of the rebar stiffness to the stiffness matrix of the parent hexahedral element is given by:

$$\underset{(24x24)}{\widehat{\boldsymbol{K}}_{Hexa}} = \underset{(24x24)}{\boldsymbol{K}_{Hexa}} + \sum_{i=1}^{nr} \underset{(24x12)}{\left(\boldsymbol{T}_i\right)^T} \cdot \underset{(12x12)}{\boldsymbol{K}_i^{rebar}} \cdot \underset{(12x24)}{\boldsymbol{T}_i} \qquad 5.20$$

where $\boldsymbol{T}_i$ is the transformation matrix given in Eq. 5.5 for imposing the compatibility condition between the rebar and the corresponding hexahedral nodal displacements, $\boldsymbol{K}_{Hexa}$ is the stiffness matrix of the hexahedral element and *nr* is the number of the embedded rebars in the element.

5.2.3.3 Idealization of the Rebar Element

As can be seen in Figs. 5.6, the section of any rebar may be transformed into an equivalent square section which is subdivided into a number of fibers in *x* and *y* directions. The idealization of the rebar's section into square is performed in order to simplify the discretization procedure. Given the diameter of the rebar, the dimensions of the square cross section are given by

$$b = h = \sqrt{\frac{\pi d^2}{4}} \qquad 5.21$$

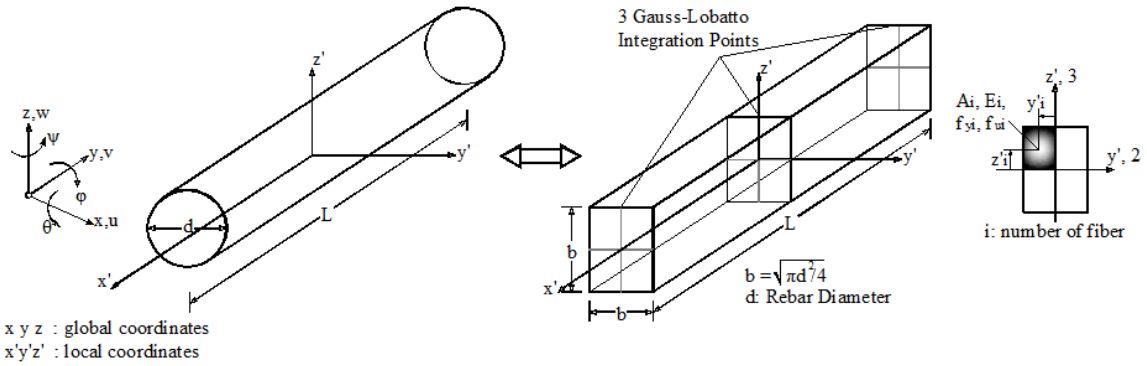

(A)

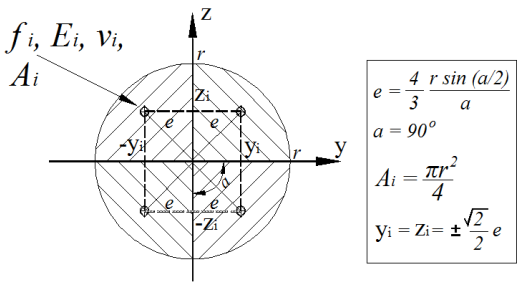

(B)

FIGURE 5.6 DISCRETIZATION OF (A) A SQUARE AND (B) A CIRCULAR SECTION WITH FIBERS.

Numerical tests performed for both cross sections produced identical results since the stiffness coefficients that are mainly affected through the sectional simplification correspond to the bending coefficient which is by nature much smaller than the corresponding axial and shear coefficients of the rebar.

5.2.4 Steel Material Constitutive Model

As described in Chapter 2, the constitutive material models that are available for predicting the steel behavior of reinforcement are the Menegotto and Pinto[86] material model, enhanced with the Filippou et al.[88] isotropic hardening, and the standard bilinear steel material model. It is widely accepted that the Menegotto and Pinto material model through its simple numerical formulation provides the necessary tools in predicting the behavior of rebar-type steel elements with an acceptable accuracy. Consequently, in this work, the Menegotto and Pinto[86] material model is adopted for all the numerical implementations.

5.3 Numerical Experiments

Many researchers have used the experimental results of Bresler and Scordelis[186] (1963) on a series of beams, the results of Lefas[206] (1988) on a series of shear walls and the experimental findings of Červenka[207] (1970) shear panel to verify their numerical models. In general, this task is demanding when attempting to reproduce numerically experimental results with different structural characteristics. In this work, the pre-mentioned experiments have been examined and their numerical response is compared with the corresponding experimental data. The aim is to illustrate the accuracy, robustness and the computational efficiency of the proposed modeling.

It has to be mentioned that, full bond between concrete and reinforcement rebars was considered in the numerical studies. For all the numerical simulations that were conducted in this work, the tensilε strength of concrete was assumed to be equal to *5%* of the corresponding cylindrical compressive strength, the remaining shear capacity parameter β was equal to *0.05* and the NR energy convergence criterion was set to 10^{-4}. It must be also noted that, the crack openings can occur only at the Gauss-Points of the hexahedral elements, thus the cracks are ploted the same way.

5.3.1 RC Beams with and without Stirrups

With these two numerical experiments, we will try to illustrate the importance of taking under consideration the stiffness of reinforcement by treating the rebars as beam elements instead of rod elements. The computational efficiency of the numerical treatment of the proposed formulation will also be demonstrated through the following numerical tests.

5.3.1.1 RC Beam without Stirrups under Central Point Load

The first numerical experiment consists of a simply supported beam with no stirrups[186]. Its geometrical features are depicted in Fig. 5.7. The experimental failure load was reported to be equal to *334 kN* with a corresponding central deflection of *6.6 mm*. Fig. 5.8 shows the first FE model which consists of *132* hexahedral elements for concrete and *88* NBCFB elements for the embedded reinforcement. Furthermore, two additional denser meshes were created, containing *264* and *528* hexahedral concrete elements (Fig. 5.9) in order to investigate the mesh sensitivity of the proposed method.

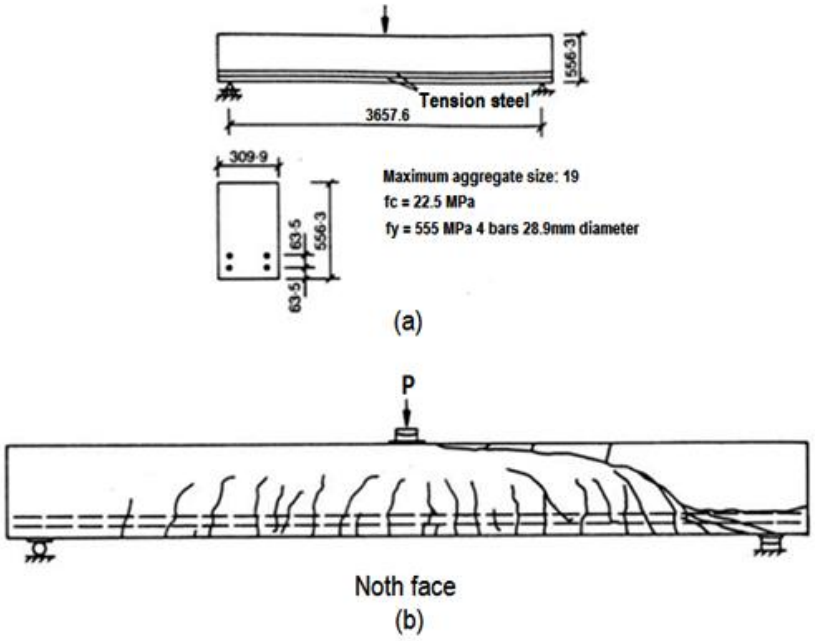

FIGURE 5.7 RC BEAM WITHOUT STIRRUPS UNDER CENTRAL POINT LOAD. (A) MEMBER CHARACTERISTICS, (B) EXPERIMENTALLY OBSERVED CRACK PATTERN AT ULTIMATE LOAD[186].

The four longitudinal bars have a diameter of *28.9 mm* which represents a large reinforcement ratio (*1.52%*) corresponding to the beam sectional dimensions (*309.9 mm* width and *556.3 mm* height). The results obtained for different simulations are shown in Fig. 5.10.

Curves 8 and 9 in Fig. 5.10 were reproduced using 27-noded and 8-noded hexahedral elements, respectively, the rod element as embedded reinforcement and the Kotsovos and Pavlovic[8] concrete material model. As it can be seen, the ultimate loads reached by lateral deflections of these curves are much larger than the ultimate loads computed by ATENA software (Curves 2-4), even though the embedded reinforcement bars are modeled by rod elements. These differences can be attributed to the different concrete material models based on the cubic compressive strength instead in the cylindrical embedded in 8-noded hexahedral elements used

in ATENA, since the bearing capacity is well under estimated corresponding to the experimental results. Curves 5, 6 and 7 were obtained with the present formulation.

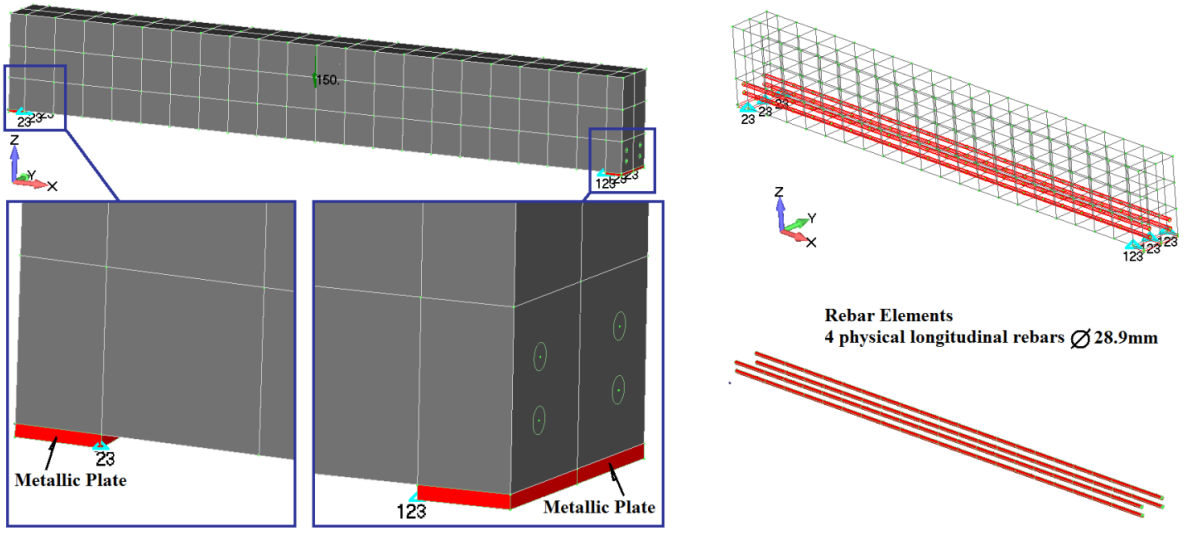

FIGURE 5.8 BEAM WITHOUT STIRRUPS UNDER CENTRAL LOADING. FE MESH.

The predicted failure loads with the corresponding mid-span deflections are shown in Table 5.2 and are in good agreement compared to the experimental ones. The predicted values illustrate the numerical accuracy of the proposed method and its robustness with respect to the mesh sensitivity. The failure of the beam was initiated due to cracking of the beam compressive zone, as can be seen in Fig. 5.11, where the deformed shape and crack pattern of the beam prior to failure are illustrated.

An analysis of the required computational effort for the *132* hexa8 elements model is shown in Table 5.3, where it can be seen that the required CPU time for solving this nonlinear problem with *30* load increments was *7 sec*.

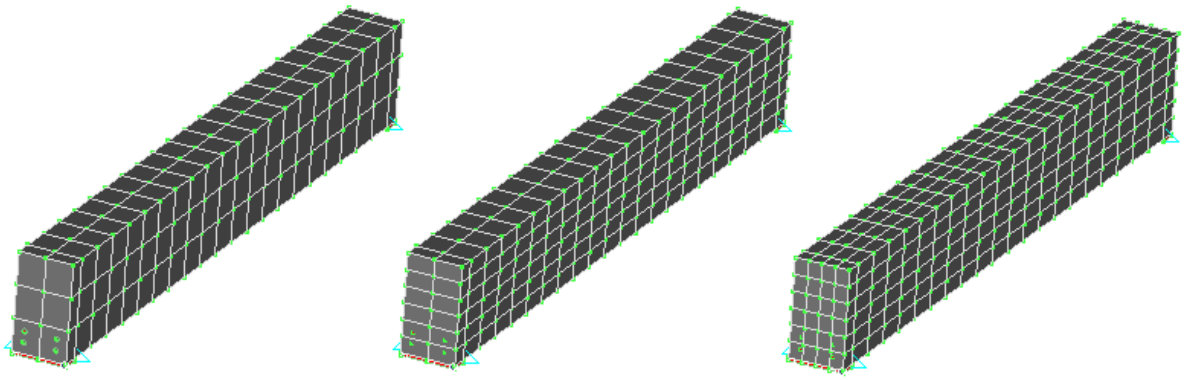

(A) (B) (C)

FIGURE 5.9 BEAM WITHOUT STIRRUPS UNDER CENTRAL LOADING. FE MESHES WITH (A) *132*, (B) *264* AND (C) *528* HEXA8 CONCRETE ELEMENTS.

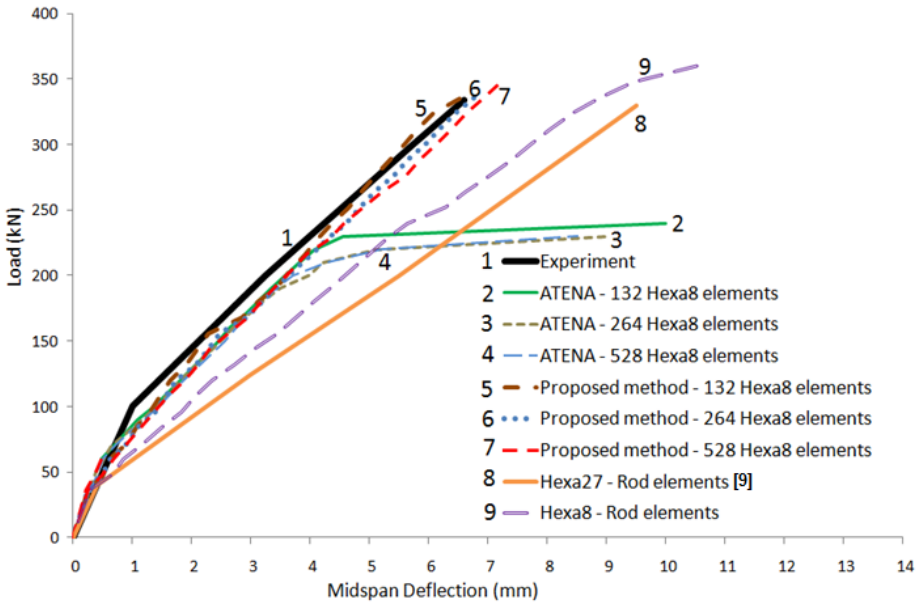

FIGURE 5.10 RC BEAM WITHOUT STIRRUPS UNDER CENTRAL POINT LOAD. PREDICTED AND EXPERIMENTAL LOAD-MIDSPAN DEFLECTION CURVES FOR DIFFERENT FE MODELS.

The required computational effort of *ATENA* software was approximately *9 min* for the solution process when using *132* hexa8 elements, *24 min* for the case of *264* hexa8 elements and *50 min* for the case of *528* hexa8 elements (Table 5.2). It has to be mentioned that ATENA performs several graphical representation procedures during execution, which increase the required CPU time for the solution. Furthermore, the same problem was solved in Lykidis[9], requiring approximately *10 min* with the use of a Pentium *4* extreme processor (*3.73 GHz*). The increased computational effort is attributed to the use of higher order hexahedral elements (27-noded hexahedral elements).

Model	*Failure Load (kN)*	*Deflection (mm)*	*CPU time (sec)*
Proposed method – 132 Hexa8 elements	338	6.7	7
Proposed method – 264 Hexa8 elements	348	7.0	18
Proposed method – 528 Hexa8 elements	348	7.2	55
ATENA – 132 Hexa8 elements	240	>8	540
ATENA – 264 Hexa8 elements	230	>8	1440
ATENA – 528 Hexa8 elements	230	>8	3000

TABLE 5.2 RC BEAM WITHOUT STIRRUPS UNDER CENTRAL POINT LOAD. PREDICTED FAILURE LOAD, MID-SPAN DEFLECTIONS AND CPU SOLUTION TIME FOR DIFFERENT MESHES.

Task	*CPU Time (sec)*
Embedded Rebar Element Mesh Generation	0.02
Newton-Raphson Nonlinear Solution	7.00
Writing Output Data	12.00
Other	0.08
Total Time	20.0

TABLE 5.3 RC BEAM WITHOUT STIRRUPS UNDER CENTRAL POINT LOAD. CPU TIME FOR DIFFERENT TASKS OF THE NONLINEAR ANALYSIS. PROPOSED METHOD WITH *132* HEXA8 ELEMENTS.

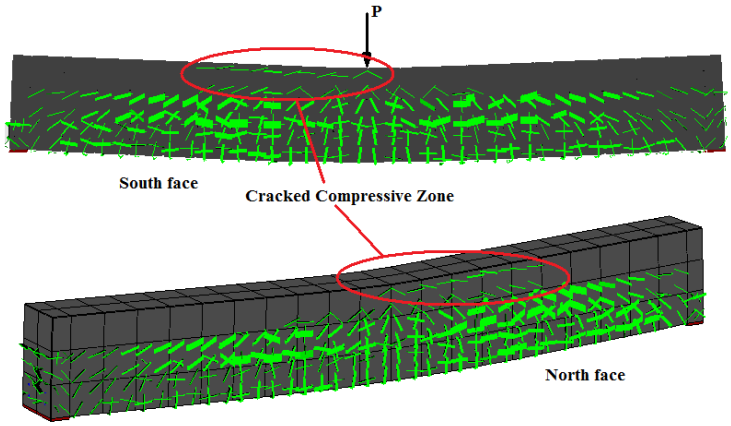

FIGURE 5.11 RC BEAM WITHOUT STIRRUPS UNDER CENTRAL POINT LOAD. CRACK PATTERN AND DEFORMED SHAPE PRIOR TO FAILURE. PROPOSED METHOD WITH *132* HEXA8 ELEMENTS.

Table 5.4 shows the required number of NR iterations during the solution procedure for the beam without stirrups for the case of *132* hexa8 concrete elements. It can be seen that most of the load steps when using the proposed modeling method, require less than *6-8* NR iterations which confirms the numerical robustness of the proposed method. However, in some load steps, like the 10^{th} load step, a significant number of internal iterations is required due to the large number of crack openings. In Fig. 5.12 the crack patterns at load steps *9* and *10* are depicted illustrating the additional cracks that were created in just a single load step which explains the increased number of iteration at this step.

In order to illustrate the computational efficiency of the proposed modeling method, different loading increments are applied for the case of *264* hexa8 elements and the corresponding load-deflection curves are depicted in Fig. 5.13. It can be seen that the variation of the predicted curves is negligible and it can therefore be concluded that the accuracy of the solution procedure is not sensitive to the size of load increment, which is a crucial numerical property when dealing with large scale problems. The corresponding required CPU time until failure for different load increments is given in Table 5.5.

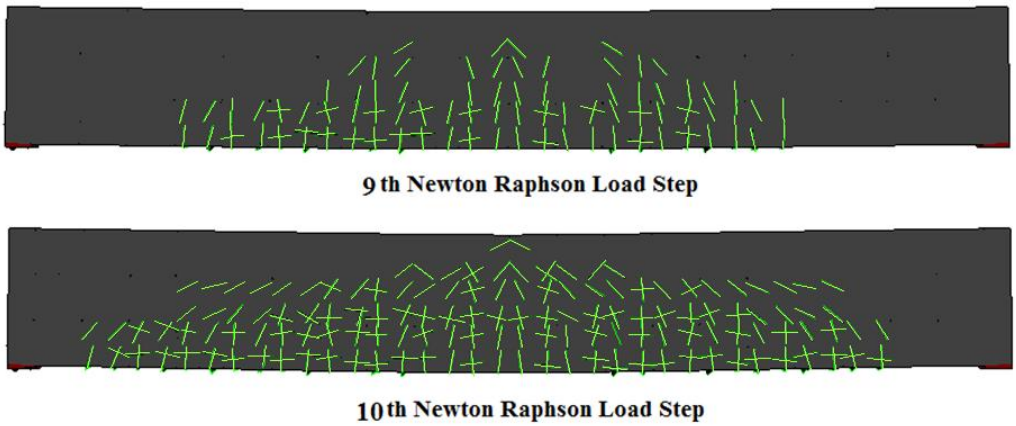

FIGURE 5.12 RC BEAM WITHOUT STIRRUPS UNDER CENTRAL POINT LOAD. CRACK PATTERN AT THE 9^{TH} AND 10^{TH} LOAD INCREMENTS. PROPOSED METHOD WITH *132* HEXA8 ELEMENTS.

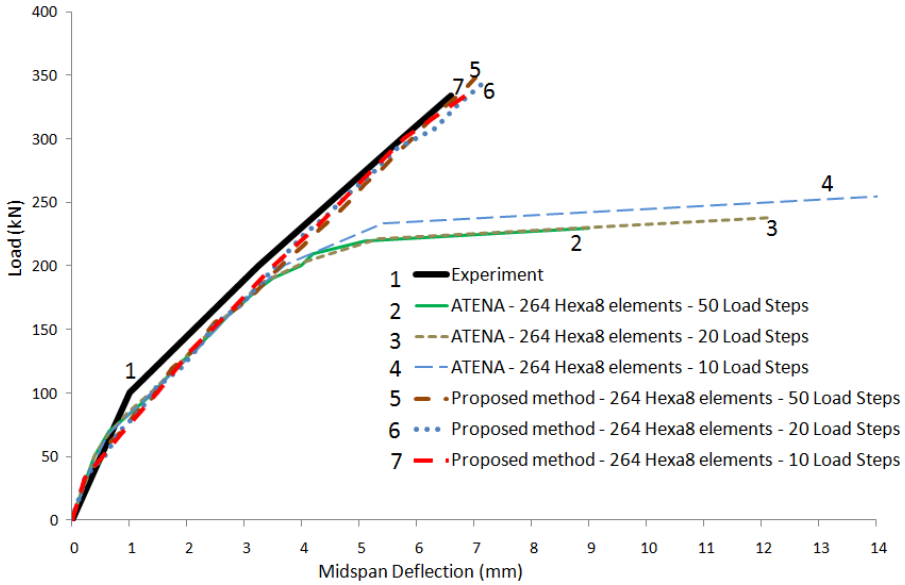

FIGURE 5.13 RC BEAM WITHOUT STIRRUPS UNDER CENTRAL POINT LOAD. LOAD-DEFLECTION CURVES FOR DIFFERENT LOAD INCREMENTS. PROPOSED METHOD WITH *264* HEXA8 ELEMENTS.

	Newton-Raphson Iterations per load step																													
Load Incr.	1	2	3	4	5	6	7	8	9	10	11	12	13	14	15	16	17	18	19	20	21	22	23	24	25	26	27	28	29	30
ATENA	1	1	1	1	8	12	23	21	18	8	17	14	8	14	9	17	40	12	15	40										
ReConAn	1	1	1	4	6	3	8	3	1	14	1	2	11	15	2	6	5	4	3	2	6	2	2	4	3	6	4	3	2	18

TABLE 5.4 RC BEAM WITHOUT STIRRUPS UNDER CENTRAL POINT LOAD. NEWTON-RAPHSON ITERATIONS PER LOAD STEP. PROPOSED METHOD WITH *132* HEXA8 ELEMENTS.

Load Increments	*CPU Time (sec)*
50	25
20	17
10	11

TABLE 5.5 RC BEAM WITHOUT STIRRUPS UNDER CENTRAL POINT LOAD. CPU TIMES UNTIL FAILURE FOR DIFFERENT LOAD INCREMENTS. PROPOSED METHOD WITH *264* HEXA8 ELEMENTS.

5.3.1.2 RC Beam with Stirrups under Central Point Load

The second numerical test refers to the same beam specimen with stirrups and compression reinforcement, as shown in Fig. 5.14. It must be mentioned that local stiffening is applied in the experimental set-up in the region of the central point load and at the support regions. The collapse of this beam member occurred when the central point load reached *467 kN* with a corresponding midspan deflection of *13.8 mm*[186]. The south face crack pattern is also depicted in Fig. 5.14, which was observed at the ultimate load level.

The failure of the beam was brittle without yielding of the tension bars. Diagonal cracking began at the same load level as for the beam without stirrups (*267 kN*), but did not lead to failure due to the presence of stirrups and compression reinforcement. Fig. 5.15 shows the FE model that was used for this numerical experiment, which consists of *102* hexahedral elements for concrete and *354* NBCFB elements for the embedded reinforcement.

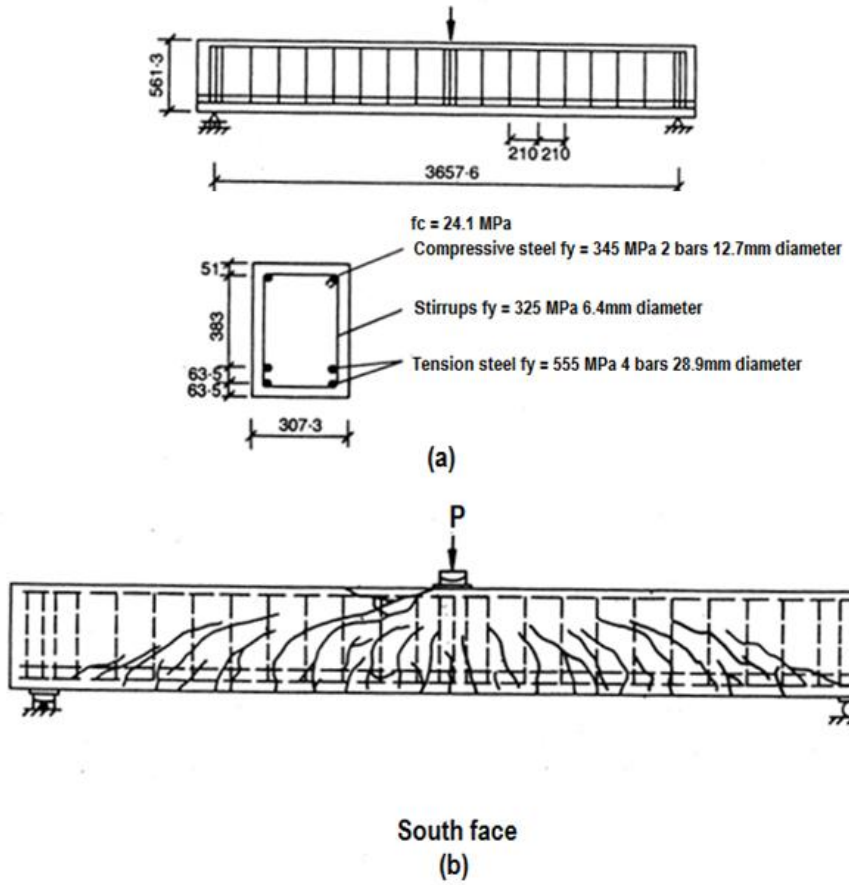

FIGURE 5.14 RC BEAM WITH STIRRUPS UNDER CENTRAL POINT LOAD. (A) MEMBER'S CHARACTERISTICS AND (B) EXPERIMENTALLY OBSERVED CRACK PATTERN AT ULTIMATE LOAD[186].

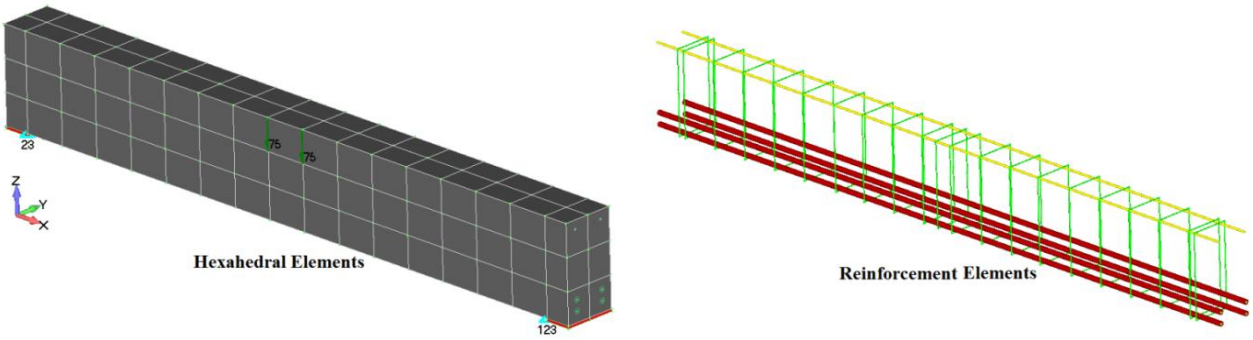

FIGURE 5.15 RC BEAM WITH STIRRUPS UNDER CENTRAL LOADING. FE MODEL.

As can be seen from Fig. 5.16, the predicted failure load of the proposed modeling is equal to *448 kN* with a corresponding midspan deflection of *13.5 mm* for the case where the external load is divided into *50* load steps (Curve 4). Similar failure loads were also obtained for *100* and *20* load step increments (Curves 3, 4 and 5). Curve 7 shows that ATENA with rod elements for the reinforcement failed prematurely due to extensive cracking.

Fig. 5.17 shows the crack pattern for several load levels up to failure. Cracking in the beam's compressive zone starts for an applied load of *300 kN*, but does not lead to failure of the beam due to stirrups confinement and the compressive contribution of the upper reinforcement. The

numerical solution terminates when failure of the compressive bars is manifested which is in good agreement with the experimental mode of failure.

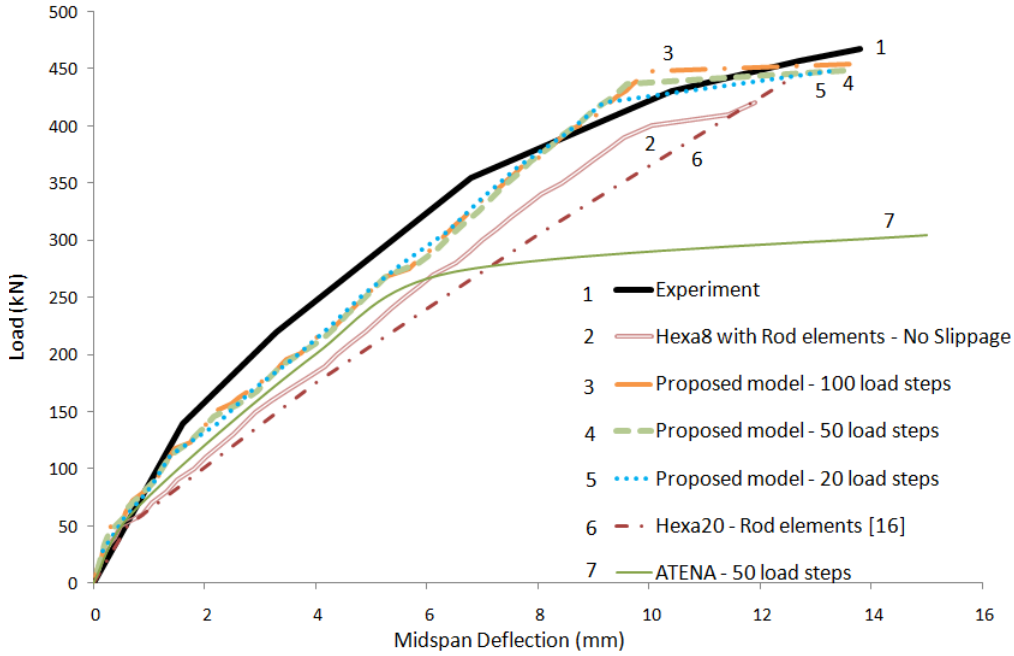

FIGURE 5.16 RC BEAM WITH STIRRUPS UNDER CENTRAL LOADING. LOAD-DEFLECTION CURVES FOR DIFFERENT LOAD INCREMENTS AND FE MODELS.

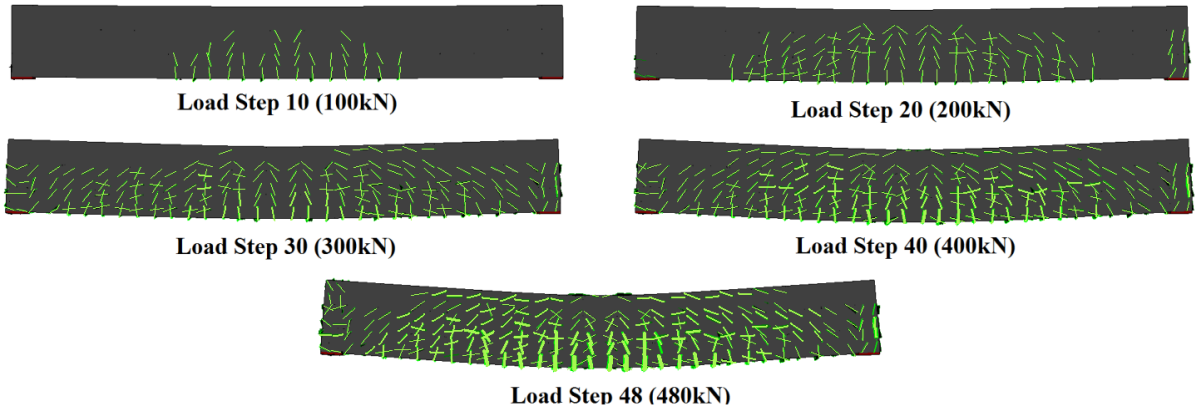

FIGURE 5.17 RC BEAM WITH STIRRUPS UNDER CENTRAL POINT LOAD. CRACK PATTERNS AND CORRESPONDING DEFORMED SHAPES AT DIFFERENT LOAD LEVELS.

The required NR iterations for this numerical experiment are depicted in the graph of Fig. 5.18 for *48* load steps. The maximum required number of NR iterations occurs at load step *31* where the initiation of the compressive zone cracking takes place and crack opening is extensive due to the excessive stress redistribution.

The required computational time for the nonlinear solution procedure is depicted in Table 5.6 which refers to *48* incremental load steps. It can be seen that the average CPU time per load increment is *0.354 sec* compared to *0.177 sec* for the corresponding problem without stirrups. This is attributed to the fourfold increase of the number of rebar beam elements used for this discretization. The corresponding computational time when analyzing this model with ATENA software for *25* steps was *15 min*.

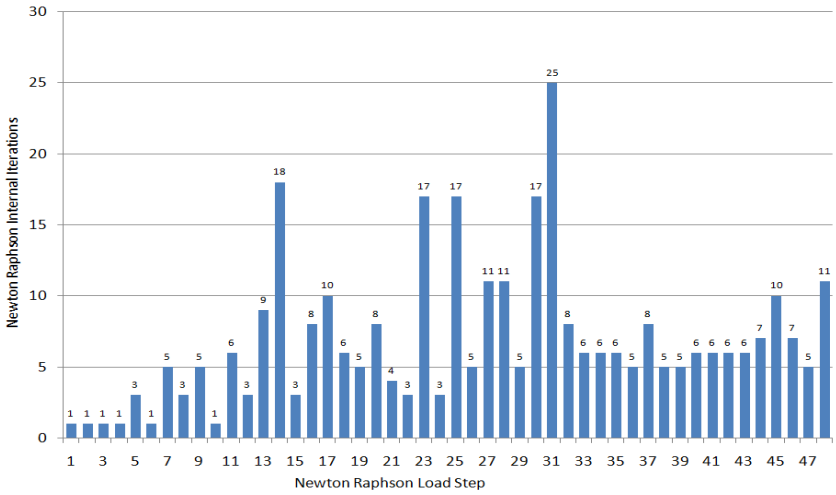

FIGURE 5.18 RC BEAM WITH STIRRUPS UNDER CENTRAL POINT LOAD. REQUIRED NEWTON-RAPHSON ITERATIONS PER LOAD STEP.

Task	*CPU Time (sec)*
Embedded rebar element mesh generation	0.03
Nonlinear incremental-iterative solution	17.00
Writing output data	25.00
Other	0.43
Total Time	42.46

TABLE 5.6 RC BEAM WITH STIRRUPS UNDER CENTRAL POINT LOAD. CPU TIME FOR DIFFERENT TASKS OF THE NONLINEAR ANALYSIS.

5.3.2 RC Shear Walls

Lefas[206] dealt with the experimental study of RC shear walls in monotonic and cyclic loading. Two types of reinforced structural shear walls were tested. Type I and Type II with different geometric characteristics given in Fig. 5.19. In all cases, the walls were monolithically connected at their ends to two beams. The lower beam was utilized to clamp down the specimens to the laboratory test floor.

The reinforcement used in these RC shear wall types consisted of two different diameters with different yield stress (Table 5.7). The first was high tensile rebars of *8 mm* diameter and the second was high tensile rebars of *6.25 mm* diameter. In addition to the previously mentioned reinforcement, horizontal stirrups were placed at the edges of the walls (concealed columns) providing confinement. Mild rebars of *4 mm* diameter were used for this purpose.

The shear wall specimens were clamped to the floor by means of two transverse long steel box girders *10 mm* thick and *4* holding-down post tensioned bolts. As it can be seen from Fig. 5.20, the vertical constant load was applied through a two point loading system. Taking into account that the proposed modeling is based on 3D material models that consider triaxial phenomena and have the ability to simulate the interaction between different structural members (i.e. interaction of steel plates and concrete), the boundary conditions and the application of the loads must be chosen in such a way that will realistically represent the experimental conditions.

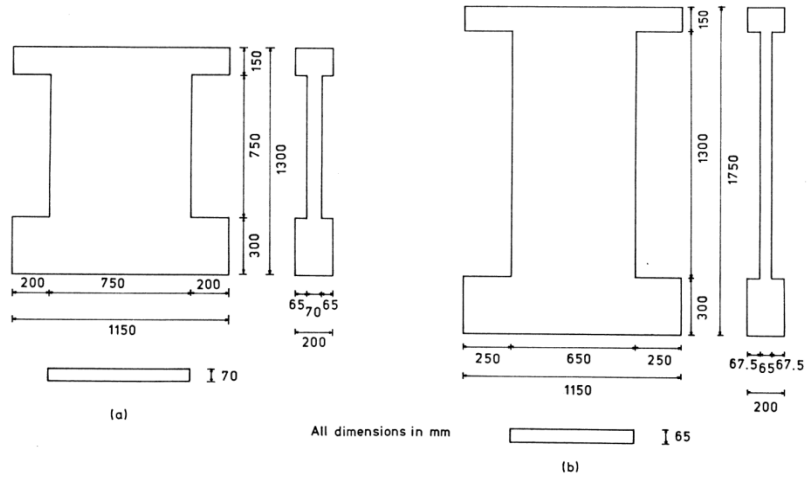

FIGURE 5.19 STRUCTURAL SHEAR WALL SPECIMENS (A) TYPE I AND (B) TYPE II[206].

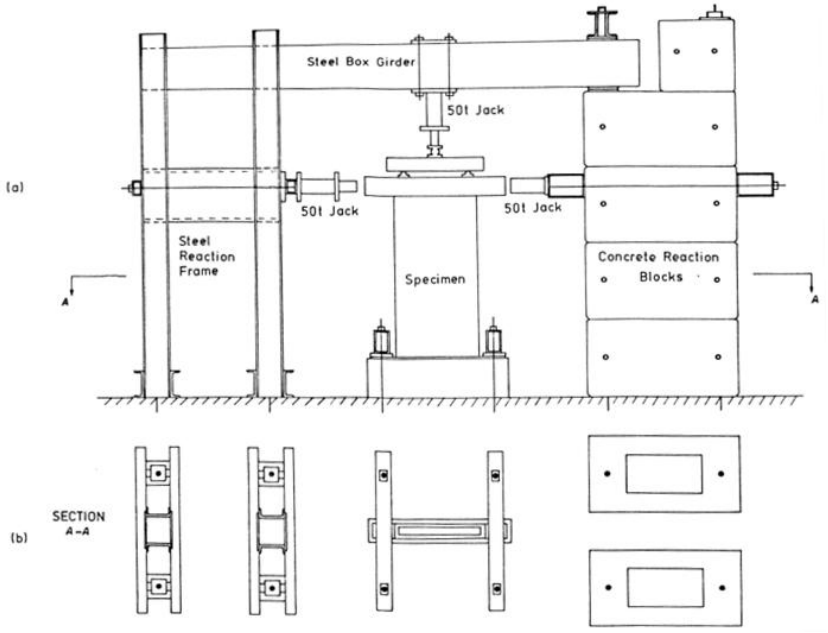

FIGURE 5.20 SCHEMATIC REPRESENTATION OF THE TEST RIG (A) ELEVATION, (B) PLAN VIEW[206].

In this work, the boundary conditions were simulated by constraining the hexahedral nodes located on the lower beam of the corresponding FE models at their base. Accumulating to that, the upper hexahedral nodes of the lower beam were also considered to be fixed in order to realistically simulate the experimental setup. The horizontal and vertical loads were applied through steel plates (Fig. 5.22) avoiding local node detachments and to assure that the loads were transferred to the upper beam uniformly.

Steel Bar Type	*Yield Strength f_{sy} (MPa)*	*Ultimate Strength f_{su} (MPa)*	*Modulus of Elasticity E_s (GPa)*
8 mm - high tensile bar	470	565	159
6.25 mm - high tensile bar	520	610	150
4 mm - mild steel bar	420	490	-

TABLE 5.7 MATERIAL PROPERTIES OF THE REINFORCEMENT USED FOR THE TWO TYPES OF RC SHEAR WALLS[206].

In order to illustrate the objectivity and robustness of the proposed modeling method in simulating RC structures, six different RC shear wall models were analyzed, three for each RC shear wall type. The main criterion for making this choice was to simulate all three loading types that were used in the experimental tests for each RC shear wall type.

5.3.2.1 Type I RC Shear Wall

Six specimens (SW11-SW16) were designed[206] based on the 1983 edition of the ACI code. All six specimens had the same reinforcement but were loaded with a different load combination. Three different vertical loads were used: *0, 0.1Af$_c$* and *0.2Af$_c$*, where *A* and *f$_c$* are the shear wall sectional area and cylindrical concrete compressive strength, respectively. Table 5.8 and Fig. 5.21 contain information associated with the reinforcement detailing and the level of constant vertical load applied on the three specimens SW14, SW15 and SW16, respectively, as well as with the level of maximum horizontal load attained during the experimental testing.

Specimen	*Reinforcement Percentage*				*Vertical Load*		*Ultimate Horizontal Load*	*Concrete Cylinder Strength*
	P_{hor} *(%)*	P_{ver} *(%)*	P_{fl} *(%)*	P_S *(%)*	F_v *(kN)*	$\frac{F_v}{blf_c}$	F_H *(kN)*	f_c *(MPa)*
SW14	1.1	2.4	3.1	1.2	0	0	265	34.0
SW15	1.1	2.4	3.1	1.2	185	0.10	320	30.5
SW16	1.1	2.4	3.1	1.2	460	0.20	355	43.6

TABLE 5.8 TYPE I RC SHEAR WALL. REINFORCEMENT PERCENTAGES, LOAD DATA AND CONCRETE STRENGTH FOR THE THREE SPECIMENS[206].

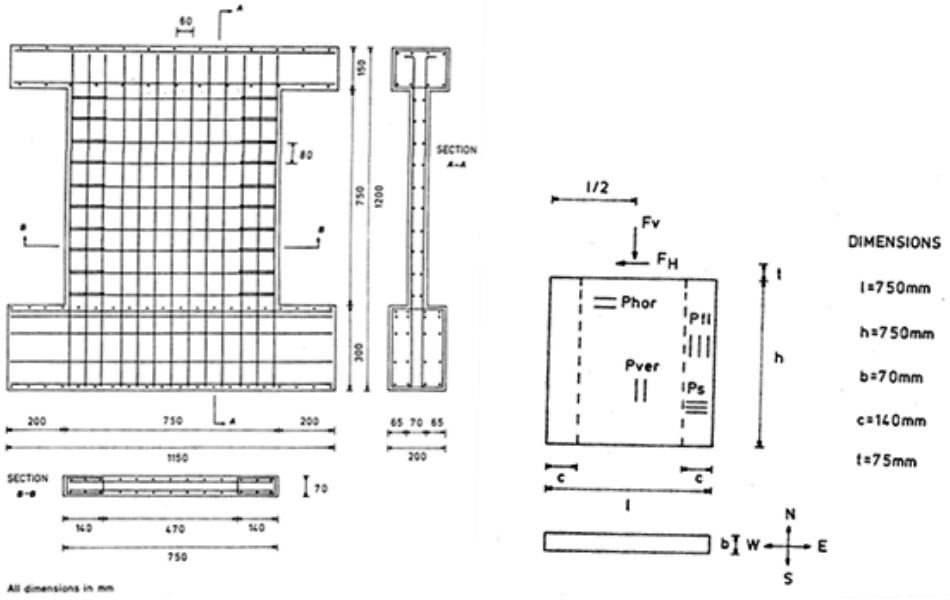

(A) (B)

FIGURE 5.21 TYPE I RC SHEAR WALL. (A) REINFORCEMENT DETAILS, (B) REINFORCEMENT PERCENTAGES[206].

As can be seen from Table 5.8, the three specimens had the same reinforcement and geometry but different concrete compressive strength and loading history, thus the same FE mesh (Fig.

5.22) can be used for the three numerical simulations following each time the material properties of the concrete and the loading history according to the experimental data.

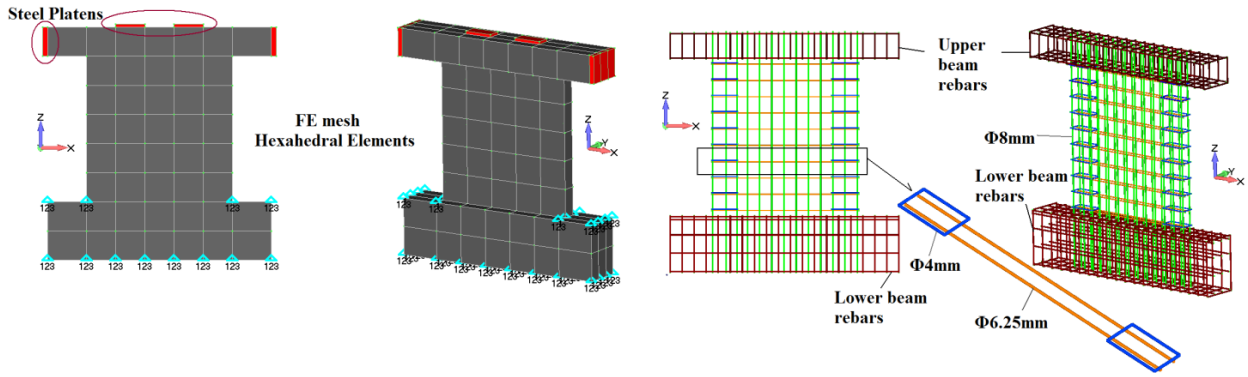

FIGURE 5.22 TYPE I RC SHEAR WALL. FE MESH.

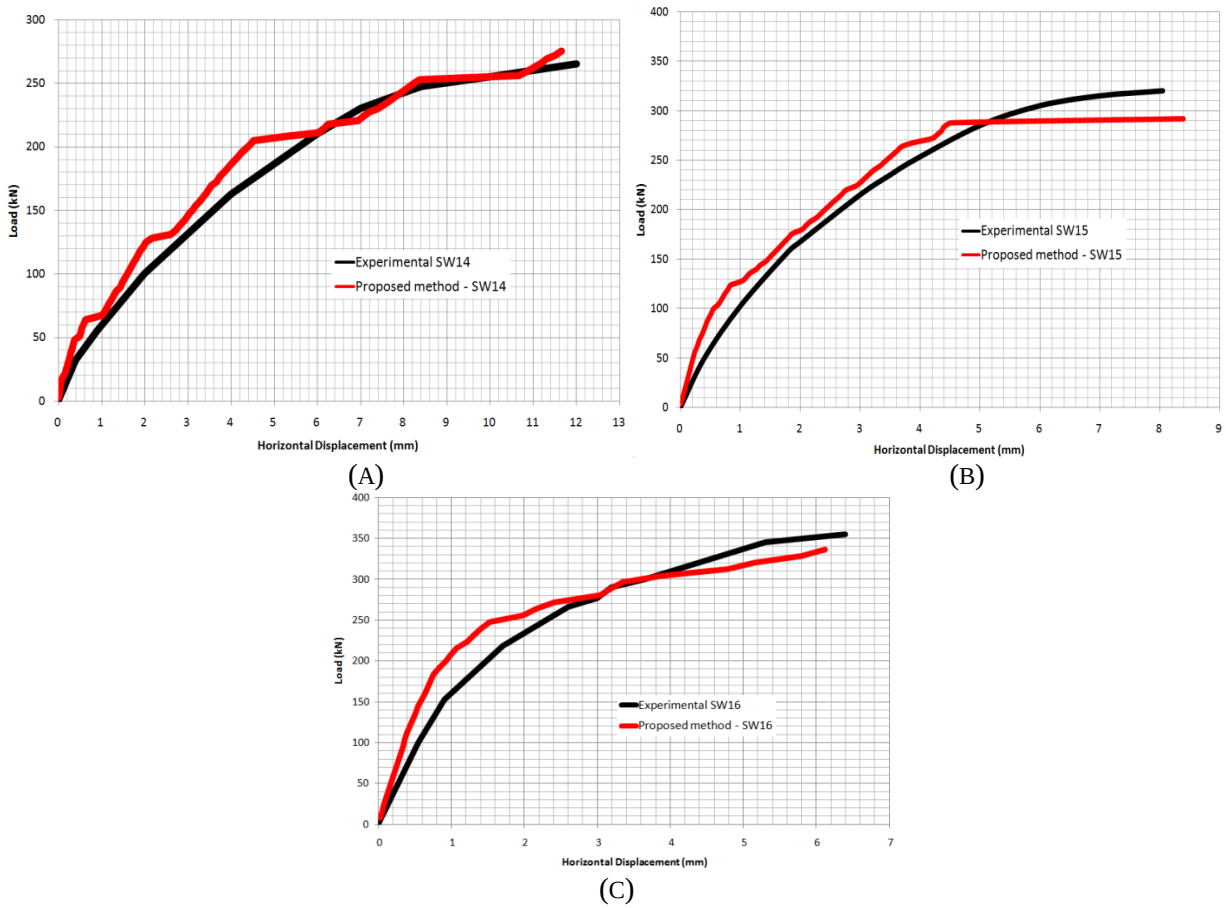

(A) (B)

(C)

FIGURE 5.23 TYPE I RC SHEAR WALL. EXPERIMENTAL AND PREDICTED CURVES FOR SPECIMEN (A) SW14, (B) SW15 AND (C) SW16.

Fig. 5.22 shows the FE mesh for the simulations of this type of RC shear walls and its boundary conditions as described above. The FE mesh for this type of RC shear walls consists of *96* hexahedral elements and *949* embedded rebar elements. The predicted numerical load-displacement characteristics by the proposed modeling are compared with the corresponding experimental results in Figs. 5.23, where a satisfactory correlation can be observed.

It is worth mentioning here that with the smeared crack approach abrupt loss of stiffness occurs during the analysis due to crack openings, which induces sudden increase of displacements, as

can be seen in Fig. 5.23a. We must also note, that due to the small global horizontal displacements occurring (less than *1 cm*) the experimental results are sensitive to uncertainties that inherently exist in the experimental setup.

Specimen	*Initiation of Cracking – Predicted Data*		*Initiation of Cracking – Experimental Data*		*Ultimate Horizontal Load - Predicted*	*Ultimate Horizontal Load - Experimental*
	F_H *(kN)*	δ *(mm)*	F_H *(kN)*	δ *(mm)*	F_U *(kN)*	F_U *(kN)*
SW14	35	0.34	25	0.25	275.5	265
SW15	45	0.27	59	0.22	304.5	320
SW16	80	0.40	80	0.31	336	355

TABLE 5.9 TYPE I RC WALL. PREDICTED INITIATION OF CRACKING AND ULTIMATE HORIZONTAL LOADING.

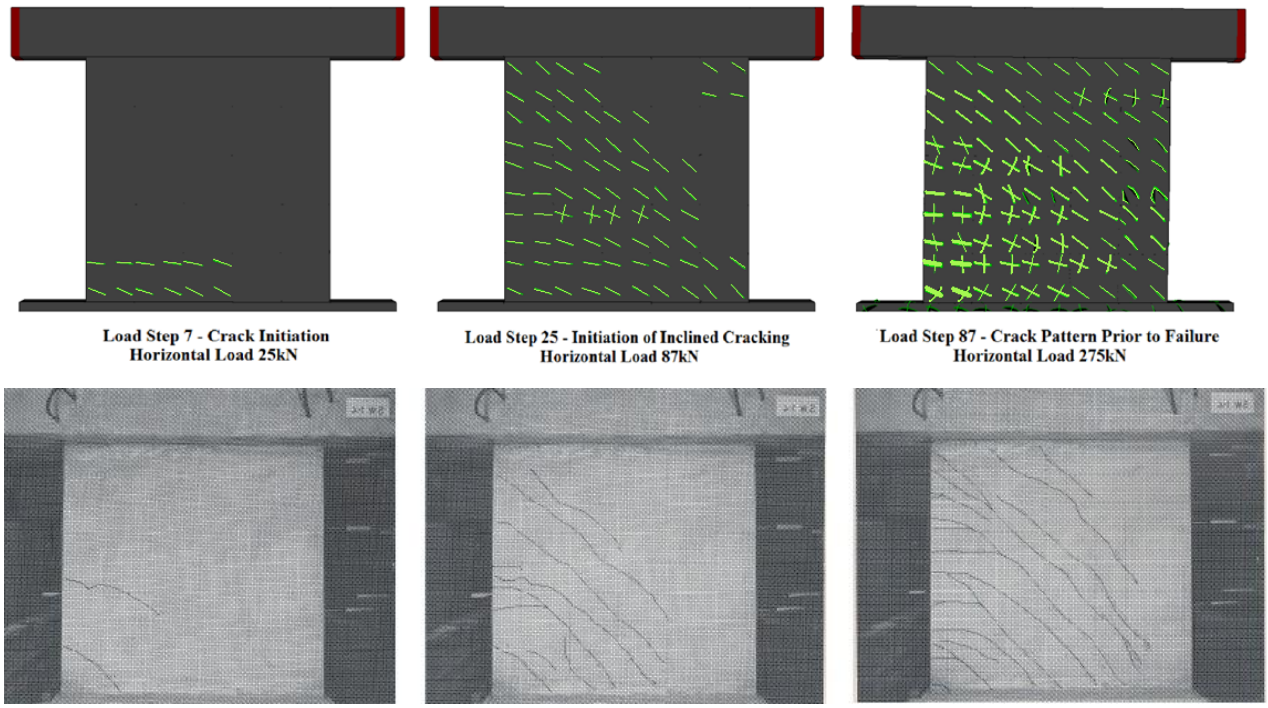

FIGURE 5.24 TYPE I RC SHEAR WALL. PREDICTED AND EXPERIMENTALLY OBSERVED CRACK PATTERN FOR DIFFERENT LOAD LEVELS OF SPECIMEN SW14.

The obtained crack patterns at the failure load are depicted in Figs 5.24 and 5.25. The largest cracks appear to be the flexural cracks that are located at the base of the three specimens where the RC shear walls are connected to the lower beam. Fig. 5.24 shows the three characteristic crack patterns that were predicted with the proposed method and were also mapped in[206] for the case of SW14. The corresponding experimental values for the three specimens are given in Table 5.9 where the good agreement between experimental and analytical data can be verified. The initiation of inclined cracking for SW14 was found experimentally to occur at a corresponding load of *100 kN*, which is reasonably close to the numerically obtained value (*87 kN*). The CPU time required for the solution of the three numerical models are given in Table

5.10 where it can be seen that the required CPU time for the case of SW15 specimen is larger than the time required for the specimen SW14 due to the increased number of NR iterations required for each load increment.

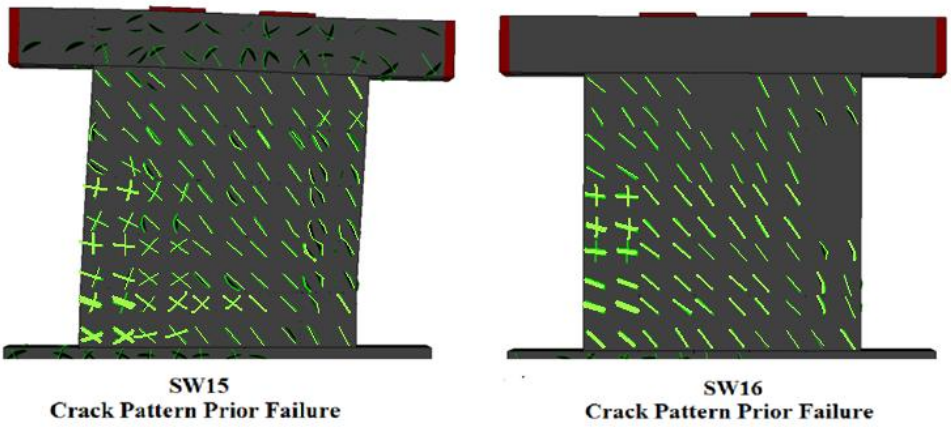

FIGURE 5.25 TYPE I RC SHEAR WALL. PREDICTED CRACK PATTERNS OF SPECIMENS SW15 AND SW16 AT ULTIMATE LOADS.

a/a	*Specimen*	*Newton Raphson Load Step*	*CPU Time (sec)*
1	SW14	86	50
2	SW15	87	60
3	SW16	88	35

TABLE 5.10 TYPE I RC SHEAR WALL. CPU TIMES FOR THE NONLINEAR SOLUTION PROCEDURE (NEWTON-RAPHSON LOAD STEPS).

5.3.2.2 Type II RC Shear Wall

Table 5.11 and Fig. 5.26 include information associated with the percentages of reinforcement and the level of constant vertical load applied for the three selected specimens (SW21, SW22 and SW25) of type II shear wall as well as the level of maximum horizontal load attained during the experimental testing[206]. Fig. 5.27 shows the FE mesh, which consists of *131* hexahedral elements and *1,118* embedded rebar elements.

It is important to stress that the same parameters were used for all numerical models, concerning the nonlinear solution process, where the horizontal load was divided into *100* load increments. The predicted load-capacity curves and crack distributions were compared with the corresponding experimental curves in Fig. 5.28 and the crack pattern in Figs. 5.29 and 5.30, where the close agreement between experimental results and the analysis can be verified. From Fig. 5.29, it can be seen that macrocracking initiates at the lower tensile edge of the wall and spreads progressively towards the lower compressive zone with increasing load. It is worth pointing out that the virtually vertical cracking observed near the failure load is in accordance with the corresponding patterns observed experimentally. Eventually, in this numerical model, the adjacent compressive state stress is transformed into a triaxial state of stress with a tensile component, which resulted in an immediate loss of the load-carrying capacity at the corresponding Gauss point.

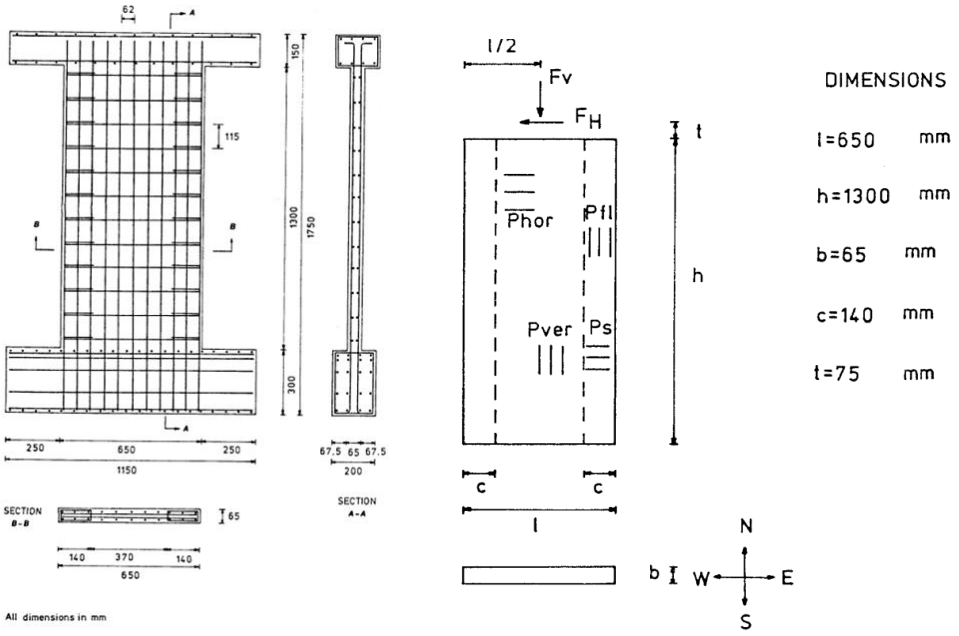

(A) (B)

FIGURE 5.26 TYPE II RC SHEAR WALL. (A) REINFORCEMENT DETAILS, (B) REINFORCEMENT PERCENTAGES[206].

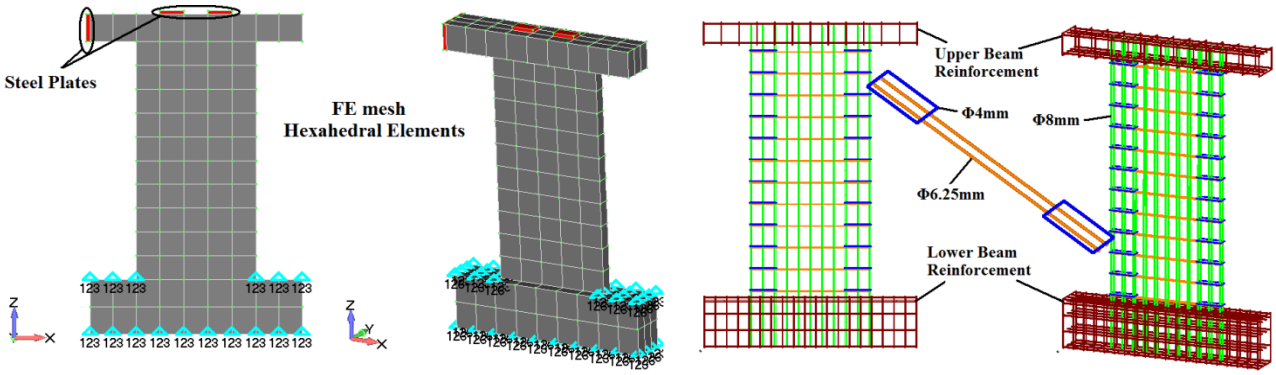

FIGURE 5.27 TYPE II RC SHEAR WALL. FE MESH.

In the case of specimen SW22 the predicted curve departs from the corresponding experimental curve when the horizontal load reaches the value of *60 kN* and the predicted stiffness becomes smaller than the corresponding experimental one. However, the ultimate load and the corresponding horizontal displacement were predicted with a relatively good accuracy (Table 5.13). Important observations can be derived from Fig. 5.28c, where the capacity load of specimen SW25 seems to be overestimated. This has to do with a premature failure of the experimental test, as was reported by Lefas[206]. Thus the numerical prediction of this simulation verifies the experimental findings. We must comment here that it is inevitable that some numerically predicted load-displacement characteristics will not fully comply with the experimental curves due to uncertainties involved in the experimental setups which could not be accurately simulated. The required CPU time is given in Table 5.13, which illustrates the computational efficiency of the developed FEA code.

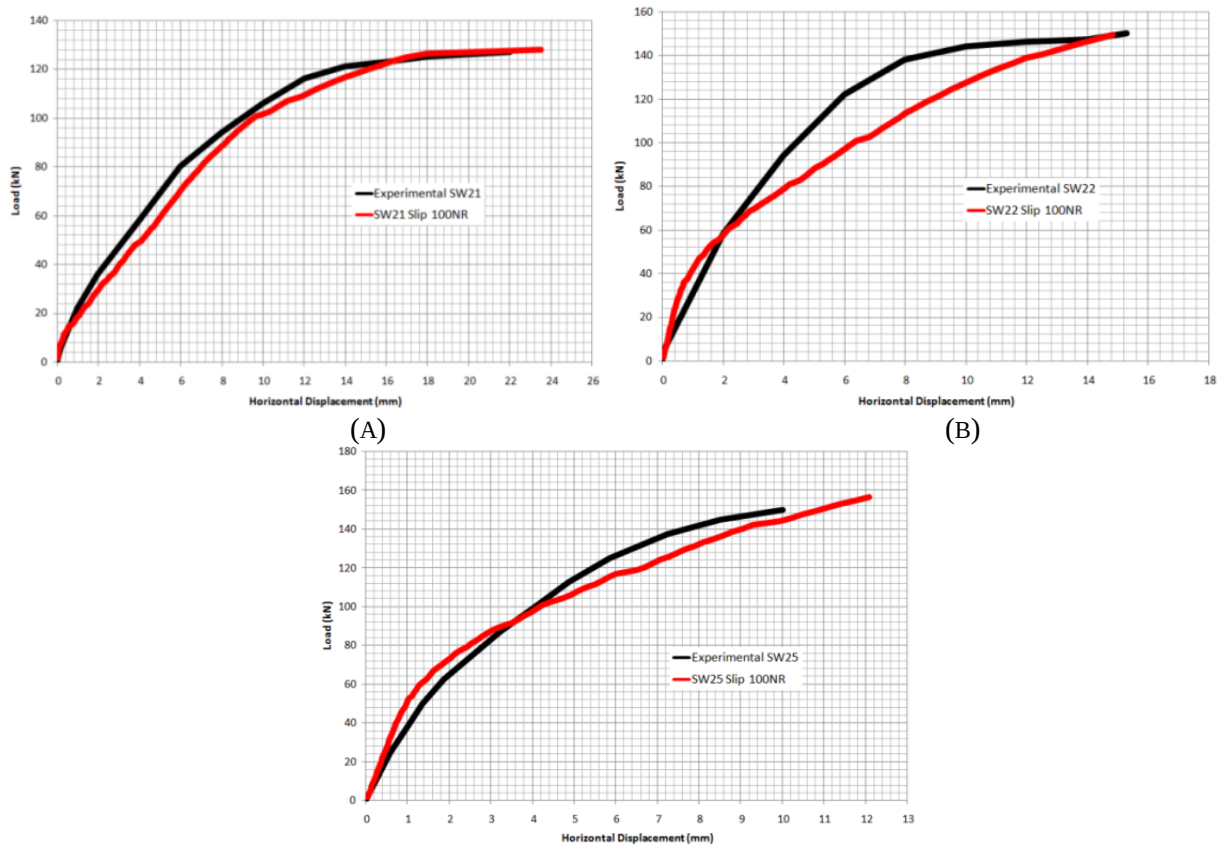

FIGURE 5.28 TYPE II RC SHEAR WALL. EXPERIMENTAL AND PREDICTED CURVES FOR SPECIMEN (A) SW21, (B) SW22 AND (C) SW25.

Specimen	*Reinforcement Percentage*				*Vertical Load*		*Ultimate Horizontal Load*	*Concrete's Cylinder Strength*
	P_{hor} (%)	P_{ver} (%)	P_{fl} (%)	P_S (%)	F_v (kN)	$\frac{F_v}{blf_c}$	F_H (kN)	f_c (MPa)
SW21	0.8	2.5	3.3	0.9	0	0	127	34.3
SW22	0.8	2.5	3.3	0.9	182.0	0.10	150	34.8
SW25	0.8	2.5	3.3	0.9	324.8	0.20	150	36.6

TABLE 5.11 TYPE II RC SHEAR WALL. REINFORCEMENT PERCENTAGES, LOAD DATA AND CONCRETE STRENGTH FOR SPECIMENS SW21, SW22 AND SW25[206].

Specimen	*Initiation of Cracking – Predicted Data*		*Initiation of Cracking – Experimental Data*		*Ultimate Horizontal Load - Predicted*	*Ultimate Horizontal Load - Experimental*
	F_H (kN)	δ (mm)	F_H (kN)	δ (mm)	F_U (kN)	F_U (kN)
SW21	8	0.20	10	0.32	128	127
SW22	27	0.48	14	0.39	148	150
SW25	45	0.24	25	0.60	157	150

TABLE 5.12 TYPE II RC SHEAR WALL. PREDICTED INITIATION OF CRACKING AND ULTIMATE HORIZONTAL LOADING.

a/a	*Specimen*	*Newton Raphson Load Steps*	*CPU Time (sec)*
1	SW21	80	60
2	SW22	83	50
3	SW25	87	48

TABLE 5.13 TYPE II RC SHEAR WALL. CPU TIMES FOR THE NONLINEAR SOLUTION PROCEDURE.

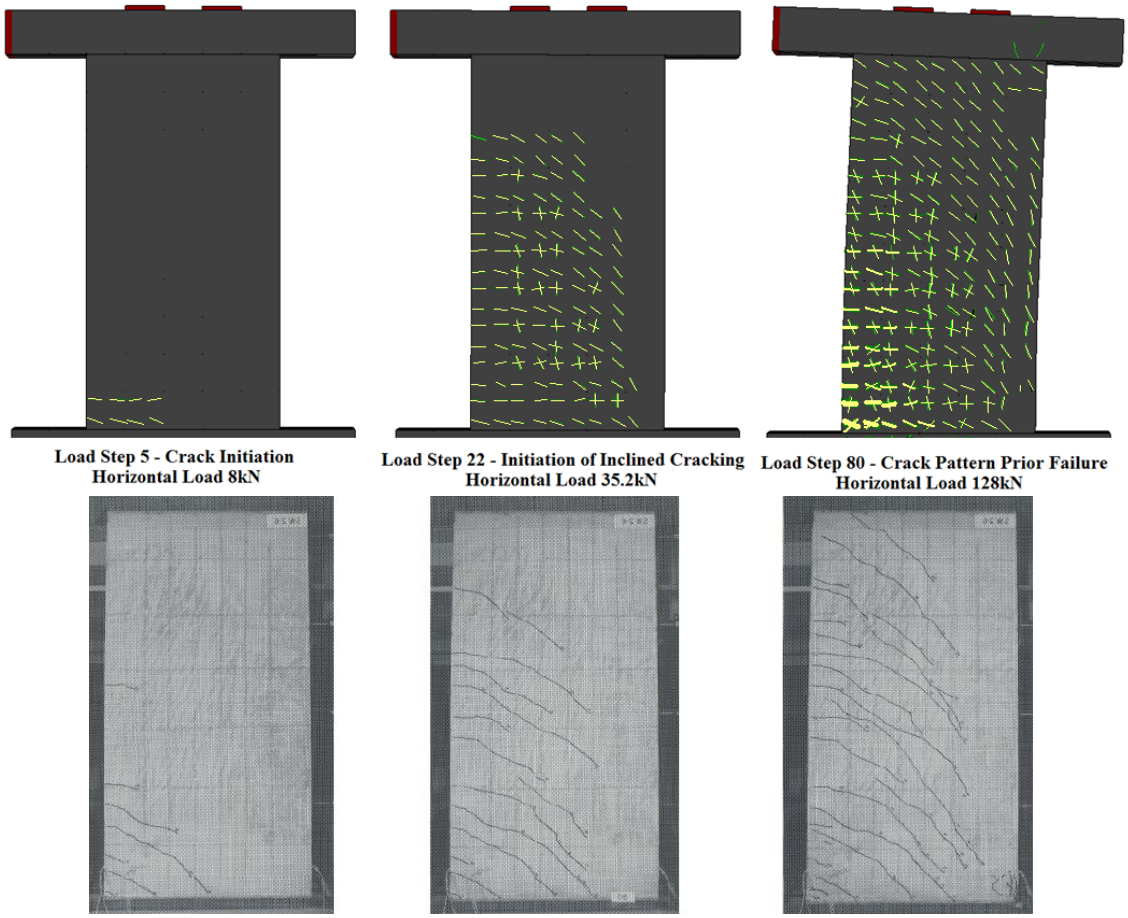

FIGURE 5.29 TYPE II RC SHEAR WALL. PREDICTED CRACK PATTERN FOR DIFFERENT LOAD LEVELS OF SPECIMEN SW21 AND EXPERIMENTALLY OBSERVED CRACK PATTERN OF SPECIMEN SW26.

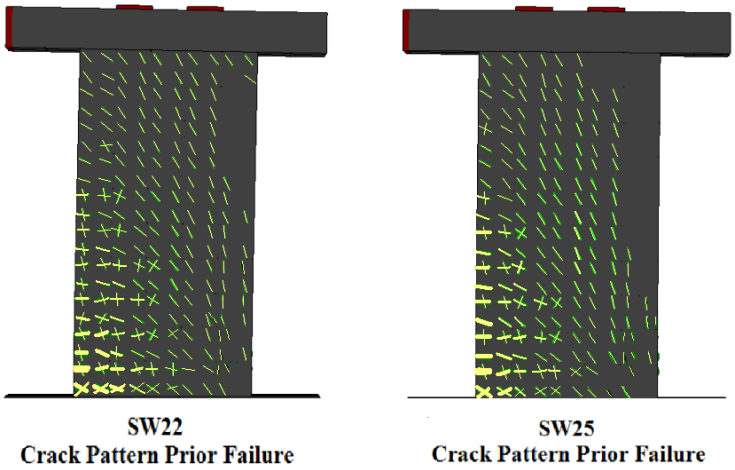

FIGURE 5.30 TYPE II RC SHEAR WALL. PATTERNS OF SPECIMENS SW22 AND SW25 AT ULTIMATE LOADS.

5.3.3 RC Shear Panel Beam

Shear panel beam W-2 tested by Červenka[207] has been frequently used by many researchers[196, 221-223] with the aim of verifying their numerical models. The panel beam consists of two orthogonally reinforced panels, *762 mm* wide, *762 mm* high and *76.2 mm* thick, separated by three ribs (Fig. 5.31). The concrete's compressive strength was f_c = *26.8 MPa* and the reinforcement steel material properties were E_s = *190 GPa* and f_y = *353 MPa*. The experimental findings showed that the ultimate load capacity of this panel beam is governed by yielding of the reinforcing steel following initial tensile cracking of concrete. Ultimately, the panel beam failed by local concrete crushing and splitting in the compressive zone of the panel.

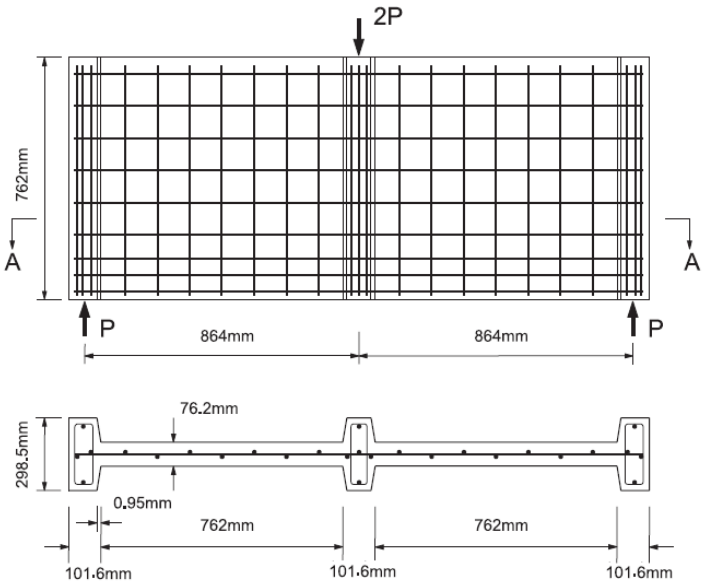

FIGURE 5.31 RC SHEAR PANEL BEAM W-2. GEOMETRY AND REINFORCEMENT DETAILS.

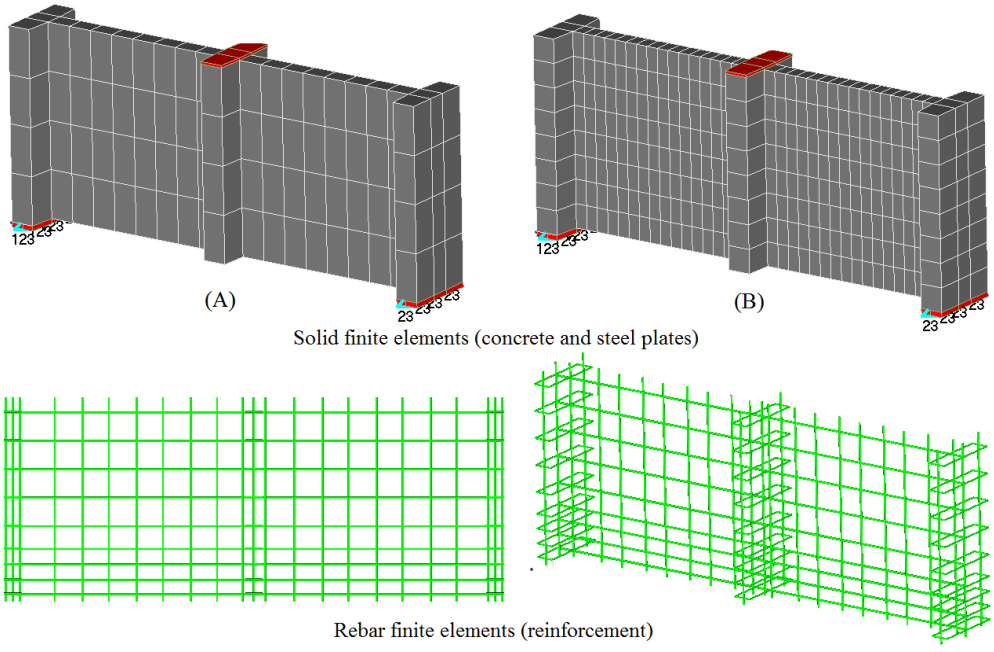

FIGURE 5.32 RC SHEAR PANEL BEAM W-2. FE MESH WITH (A) *100* AND (B) *328* CONCRETE HEXAHEDRAL ELEMENTS.

The finite element discretization and the corresponding reinforcement ratios are shown in Figs. 5.32 and Table 5.14, respectively. Two different models were considered, one that uses *100* solid elements and one that uses *328* solid elements for the modeling of concrete. In both FE models the reinforcement geometry remains the same (Fig. 5.32).

The experimental and predicted curves can be seen in Fig. 5.33, where good agreement between the results can be depicted. It can be seen that the proposed model manages to predict the ultimate failure load (*118 kN*) with an acceptable accuracy and at the same time the elastic and inelastic predicted branches are in a good correlation with the experimental curve. When the externally applied load reaches approximately *70%* (*80 kN*), the prediction of the RC member stiffness is slightly overestimated as a result of the stiffness introduced through the use of the β parameter when excessive cracking occurs (Fig. 5.34b).

Figs. 5.34 shows the crack patterns for both FE meshes at different load levels. It can be seen that the predicted failure mode is governed by flexural cracking which occurred at the load level of *40 kN* and *35 kN* for the coarse and fine FE models, respectively. As it was expected, the initiation of cracking occurred at a slightly lower load level for the case of the fine mesh FE model. Nevertheless, for both cases, the crack patterns were flexure dominated and the failure mechanism was initiated when the longitudinal reinforcement located at the basis of the specimen yielded, followed by the failure of the shear panel compressive zone.

The computational performance of the proposed model for the required computational time for the nonlinear solution procedure is depicted in Table 5.15, where the computational efficiency of the proposed model can also be observed for this test case.

Region	*Direction*	*Reinforcement Ratio ρ*	
		Panel	*Ribs*
A	x	0.0092	0.0023
A	y	0.0092	0.0047
B	x	0.0183	0.0047
B	y	0.0092	0.0047

TABLE 5.14 RC SHEAR PANEL BEAM W-2. REINFORCEMENT RATIOS.

Fig. 5.37 shows the magnified deformed shapes prior to failure and the von Mises strain contour predicted by the two FE models. The strain concentration is located on the base of the specimen, where the flexural cracks occur. It is clear that the differences between the fine and sparse models are insignificant thus the computational robustness and efficiency of the proposed model is verified.

a/a	*Num. of Elements*	*Newton-Raphson Load Steps*	*CPU Time (sec)*
1	100 Hexa8	20	10
2	100 Hexa8	50	15
3	328 Hexa8	20	40
4	328 Hexa8	50	60

TABLE 5.15 RC SHEAR PANEL BEAM W-2. CPU TIMES FOR THE NONLINEAR SOLUTION PROCEDURE.

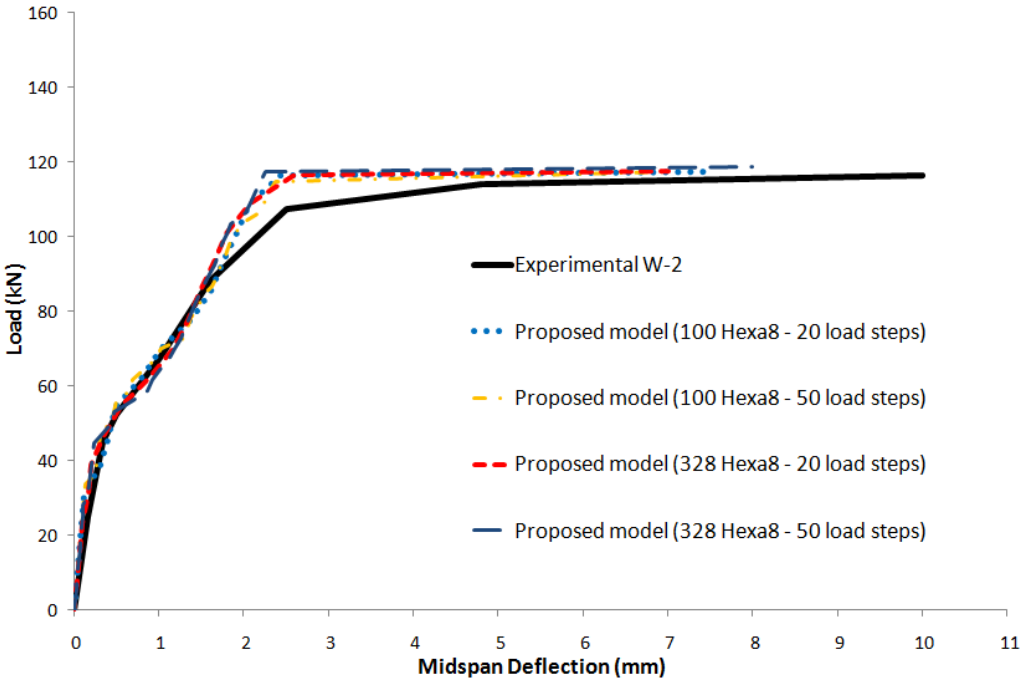

FIGURE 5.33 RC SHEAR PANEL BEAM W-2. EXPERIMENTAL AND PREDICTED CURVES.

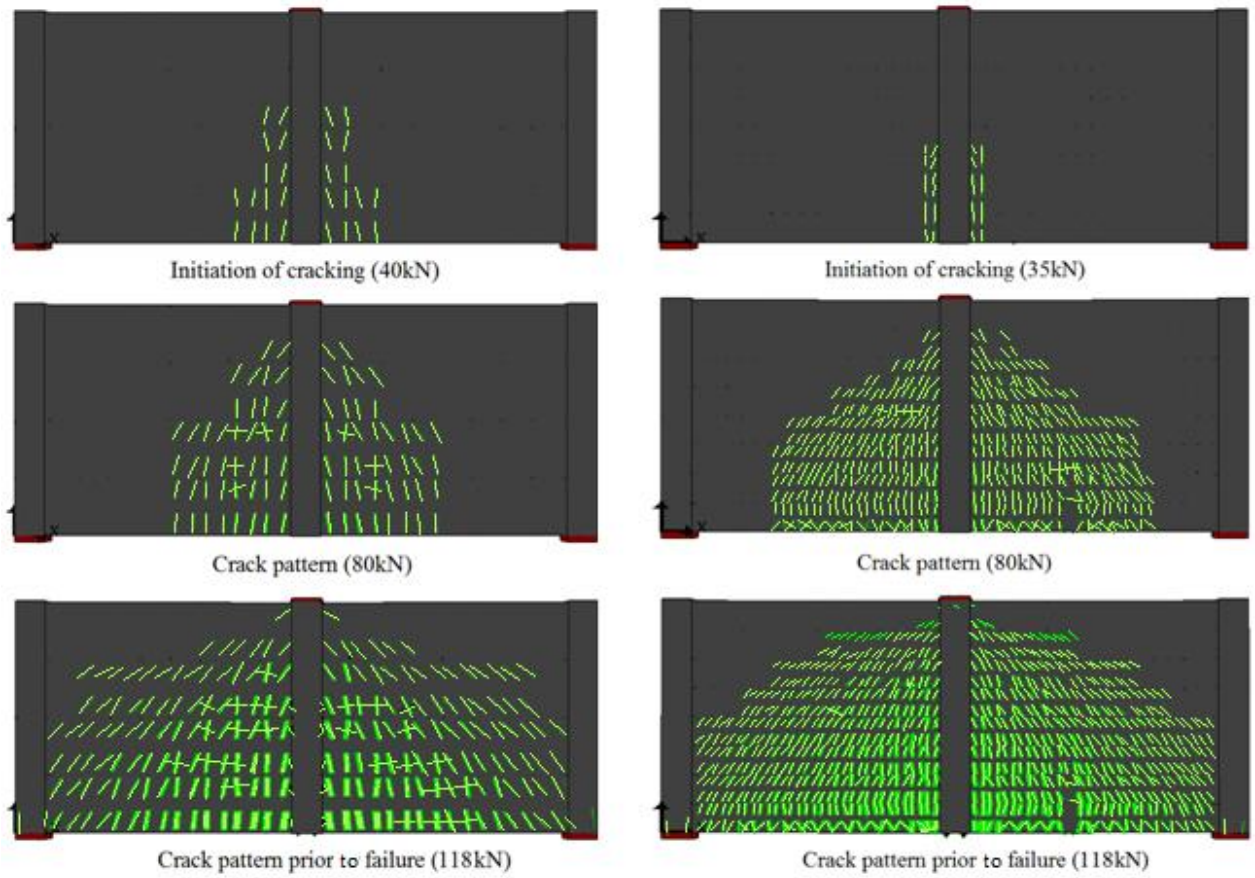

(A) (B)

FIGURE 5.34 RC SHEAR PANEL BEAM W-2. CRACK PATTERNS FOR VARIOUS LOAD LEVELS. (A) *100* AND (B) *328* HEXA8 CONCRETE ELEMENTS.

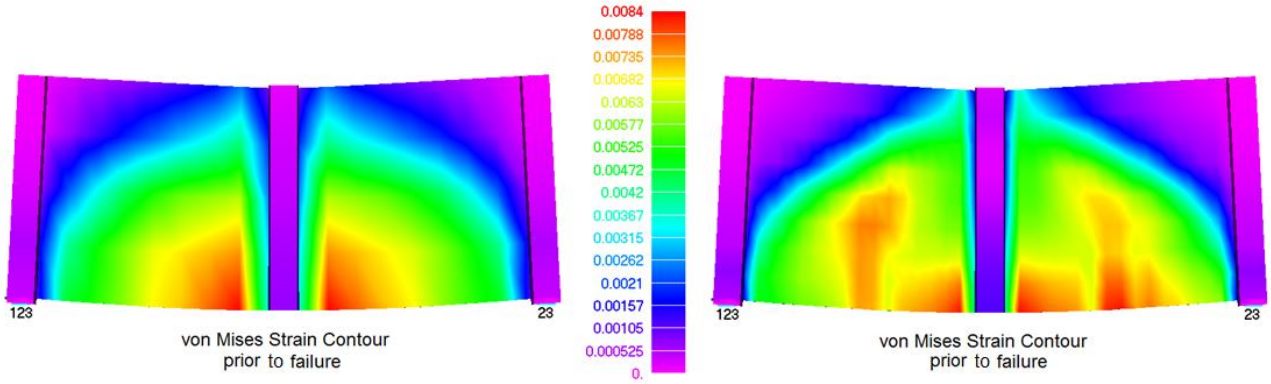

(A) (B)

FIGURE 5.35 RC SHEAR PANEL BEAM W-2. VON MISES STRAIN CONTOUR PRIOR TO FAILURE. (A) *100* AND (B) *328* HEXA8 CONCRETE ELEMENTS.

5.4. Limitations of the Proposed Modeling Method

The proposed modeling method uses the Kotsovos and Pavlovic material model which is presented in detail in[8]. It is well known that this material model is not based on a thermodynamic framework in order to dissipate energy with a proper loading-reloading behavior[227]. Nevertheless, its simplicity proved to be sufficient in predicting the nonlinear behavior of RC structural members[8, 9, 138, 225, 226] and promising, as illustrated in this research work, for the nonlinear analysis of full-scale RC structures. On the other hand, as Jiràsek and Rolshoven stated in[227], in nonlocal constitutive theories the local state of the material at a given point may not be sufficient to evaluate the stress at that point. This is physically justified by the fact that no real material is an ideal continuous medium, and on a sufficiently small scale the effects of heterogeneity and discontinuity at the microstructure level become non negligible, especially for the case of highly heterogeneous composite materials, like concrete. Moreover, convergence difficulties and failure of capturing experimental results when using relatively sparse meshes make this type of models prohibitive for the analysis of full-scale RC structures. This confirms that each numerical model has its advantages and disadvantages, thus their incorporation in FE algorithms requires special handling. For an overview and discussion of various non-local plasticity formats, see[227].

A second limitation of the proposed modeling method is the lack of taking into account the stiffening effect and the bond-slip phenomenon. The reason for this omission is that tension stiffening effect is not usually considered with detailed 3D modeling (see all relative references[6, 8, 138, 139, 199-203, 205, 225, 226]) and since the inclusion of a bond-slip model has an opposite effect to the tension stiffening, it was decided not to consider these phenomena at this stage. In addition to that, regarding the accuracy of the proposed modeling method, the bond-slip phenomenon, plays an important role for cases where the anchorage length of the reinforcement is insufficient. When slippage occurs, near and after the yielding of the reinforcement[224], it affects the elongation of the cracks' widths and the internal strain redistribution at the local regions where slippage takes place. It does not however affect the crack distribution, since crack formation takes place when reinforcement is still located in the

elastic range. Nevertheless, at local level the internal redistribution of stress and strains is significantly affected near the ultimate state of the structure.

As it was illustrated above, modeling of cracking with the smeared crack approach has the disadvantage the inaccurate modeling of the physical gap of the crack and the corresponding proper stress redistribution when cracking occurs. This is attributed to the fact that the same FE mesh is used throughout the analysis procedure thus the redistribution of the released internal forces is not performed in a physically correct manner. The outcome of this numerical feature is depicted in Figs. 5.34a and 5.34b where the predicted crack patterns differ in terms of their density thus the corresponding crack widths cannot be compared. Due to the nature of the smeared crack approach, cracks appear throughout the shear panel (Fig. 5.34b), failing to capture the uncracked areas in between the main flexural cracks as observed in the real experiment setup. A detailed discussion on the disadvantages of the smeared crack approach can be found in[126, 228]. It is important to note that the smeared crack method appears to be for the moment the only feasible approach[229] in modeling RC full-scale structures.

Finally, the use of parameter β after a crack opening introduces an additional stiffness in the FE model, especially in cases of flexural dominated RC structural members. Early work presented by Cedolin and Dei[230] concluded that the shear retention factor has to be computed through an objective manner thus they proposed its connection with the crack's width. In this research work it was concluded that the crack width is not the main factor that should be considered for the activation of the shear retention stiffness. It is obvious that when a RC structural member is dominated by flexural cracks, the shear stiffness along the crack's planes should not be activated since no shear deformations develop. Therefore, a formulation based on the stress-strain field is more appropriate for assessing whether this parameter will be activated or not and for computing its corresponding value.

Chapter 6 Hybrid Modeling of RC Structures

Contents of Chapter 6

6.1 Overview

A Hybrid Modeling approach is presented for the 3D inelastic analysis of full-scale RC structures which achieves accuracy, numerical robustness and computational efficiency. The proposed modeling approach combines two different modeling conventions in order to predict the nonlinear behavior of RC structures up to ultimate loading conditions.

Each structural component of RC buildings like foundation footings, beams, columns, monolithic connections, shear walls and slabs, exhibit different mechanical behavior due to their geometrical properties and is considerably affected by their reinforcement details. Modeling and simulating each type of structural component requires special consideration of their nonlinear behavior.

As it was presented in Chapters 2 and 5, the level of discretization of the structural members controls the resulting accuracy of the numerical simulation. The NBCFB element can be selected for modeling beam-like structural members, achieving maximum computational efficiency albeit with reduced accuracy in certain cases. The ability in predicting objectively the nonlinear response of any RC structural member is limited, since it cannot model members which are shear dominated or have 3D complex geometries (dams, retaining walls, tunnels, etc.), while slabs can only be assumed as diaphragms that are model with rigid elements or kinematic constraints that control the relative displacements between the nodes located on the diaphragm and, moreover, monolithic connections are disregarded since beam elements are unable to account for local effects that take place in these critical regions.

On the contrary, when using refined models, increased accuracy is achieved, thus any type of structural member can be analyzed nonlinearly, overcoming the discretization and modeling problems. The main issue when using this type of modeling was, is and "will be" the computational demand which rises because of the large number of elements that are required for the discretization of just a single structural member. Furthermore, the more sophisticated 3D material formulation of concrete combined with the numerically ill-posed smeared crack approach that aggravates the computational demand excessively, make the solution of such nonlinear system of equations impractical.

It is evident that both FE modeling methods have their numerical advantages and disadvantages which cannot be overcome just by improving their numerical features and formulations. For this reason, the concept of Hybrid Modeling methods (HYMOD) is introduced, in an attempt to overcome the computational demands of the detailed modeling and improve the numerical accuracy of the beam-column type models.

Research oriented to this field was initially conducted in the 1980s in research works that dealt with the problem of connection between plates and 3D solid elastic bodies[231-233]. This research was extended to the simulation of junctions between shells and the intersections of solid bodies and plates, as they were presented by Bernadou and Cubier[234] (1998) and Huang[235] (2004). In addition, Nazarov[236, 237] (1996, 1999) and Kozlov and Mazya[238] (2001) in their work covered the asymptotic analysis for the coupling between a 3D elastic body and a dimensionally reduced structure.

It is worth noting that, to the authors' knowledge, the previous studies which involved coupling between different structural models are limited to a few attempts that are mainly concerned with the kinematic connection of elastic bodies of a different dimensionality. Previous ideas regarding the coupling of models of different dimensionality from a purely kinematical point of view were explored in[239-243]. Blanco et al.[244] (2008) presented a generalized approach on the kinematical coupling of incompatible models. The numerical implementations were limited to two numerical tests dealing with the kinematical coupling of three-dimensional and two-dimensional models. It is worth noting that, in all these studies, material nonlinearities were neglected.

The most notable research work using hybrid models for modeling the monolithic joints of RC structures simulated with two different FE models (3D solid and 1D beam like elements) was presented by Mata et al.[245] (2008). In that work the structure was initially discretized with beam elements and when predefined regions entered the nonlinear state, they were assumed prismatic and discretized with 3D solid elements instead of beam finite elements. Complex kinematic compatibility and force equilibrium conditions were enforced in order to transfer displacements and forces to the prismatic part of the structure. Furthermore, a transformation of the stiffness matrix was required when a critical region entered the nonlinear range where the updated stiffness matrix of the prismatic part, at local level, was reduced back to the simple beam stiffness matrix at the global level. This approach has several disadvantages; the main one is that the actual local tangent stiffness matrix plays only a correctional role since its contribution during the solution procedure is indirect. Moreover, significant stiffness-related data is lost during the displacement computations since the transformation procedure simplifies the tangential stiffness matrix of the prismatic part into the simple beam stiffness matrix that is eventually used for the displacement computations. The authors reported computational times around *2.40 sec* for each load step for the solution of a model discretized with *202* elements (*192* linear hexahedral elements and 10 quadratic beams). This computational performance is considered poor compared to the detailed modeling of structures with similar size (Chapter 5). This will also be shown in the numerical results section of this Chapter.

In continuation of their research work, Bournival et al.[246, 247] (2010) used mixed-dimensional FEA models for the simulation of steel structures, combining beam, shell and 3D solid finite elements. They managed to reduce the computational effort at the expense of losing accuracy across the interface of different finite elements.

In this study a hybrid formulation is proposed combining beam and 3D solid elements. The proposed HYMOD method for modeling RC structures requires minimal transformations for achieving the coupling between different elements, while maintaining adequate accuracy in predicting the nonlinearities at the critical regions of the structure.

6.2 Hybrid Modeling Formulation

The proposed HYMOD combines hexahedral and beam finite elements where the coupling between them is achieved with kinematic constraints. Thus, the structural members that are shear dominated, such as shear walls and joints are discretized with 8-node hexahedral elements

while the rest of the structure is discretized with beam RC elements (Chapter 2). In the proposed modeling method the hexahedral elements treat the opening of cracks with the smeared crack approach, while steel reinforcement is modeled with beam elements (Chapter 5). The beam elements in both cases, incorporate the so called natural method and fiber approach that proved to be an excellent choice for the simulation of steel reinforcement embedded into the 8-noded hexahedral elements for the detailed simulation of RC structures (Chapter 4).

6.2.1 Kinematic Coupling of 1D and 3D FEs

The incorporation of the Hybrid Modeling approach within the framework of the *ReConAn* FEA code, developed for the purpose of this study, requires special attention at the pre- and post-processing phase where the Femap[91] software is implemented. When generating a hybrid model by using a CAD system, the node compatibility conditions must be enforced between deformations of the nodes at the interface through kinematic constraints. As it was described previously, several researchers proposed techniques in order to achieve mesh coupling of different type of elements. In this work the coupling between the two types of elements is treated as a kinematic constraint which considers that each hexahedral node, located at the interface between the beam and the solid elements, will displace according to the following kinematic relationship

$$\underset{(3x1)}{\boldsymbol{u}_i^{HEXA}} = \underset{(3x6)}{\boldsymbol{T}_{im}} \cdot \underset{(6x1)}{\boldsymbol{u}_m^{NBCFB}}, \tag{6.1}$$

with

$$\underset{(3x6)}{\boldsymbol{T}_{im}} = \begin{bmatrix} 1 & 0 & 0 & 0 & z_i - z_m & y_m - y_i \\ 0 & 1 & 0 & z_m - z_i & 0 & x_i - x_m \\ 0 & 0 & 1 & y_i - y_m & x_m - x_i & 0 \end{bmatrix} \tag{6.2}$$

where $\boldsymbol{u}_m^{NBCFB}$ and $\boldsymbol{u}_i^{HEXA}$ are the displacement vectors of the NBCFB node and hexahedral nodes at the interface, respectively. The subscript *i* of the global coordinates *x, y, z* refers to the hexahedral node ID located at the interface section Ω_j, while subscript *m* refers to the NBCFB elemental node ID that controls the displacements (master node) of the interface section Ω_j (Fig. 6.1). The connection matrix $\boldsymbol{T}_{im}$ is computed by using the corresponding NBCFB and hexahedral nodal coordinates. The compatibility between the *6* dof of the end node of the NBCFB element and the *3* translational dof of the nodes at the interface Ω_j is maintained through the kinematic constraint which applies for all hexahedral nodes that are located at the interface. Assuming that any hexahedral node located at the interface follows the body movements of section Ω_j, which are enforced by the NBCFB element nodal translational and rotational displacements (Fig. 6.1), the computation of the new position for any point on the interface section Ω_j is obtained through a linear transformation.

If we assume that the 8-noded hexahedral element has *n1-n8* nodes as shown in Fig. 6.1, then the coupled kinematic constraint is expressed as follows:

$$\underset{(24x1)}{\boldsymbol{U}^{\mathrm{HEXA}}} = \underset{(24x18)}{\boldsymbol{T}_H} \cdot \underset{(18x1)}{\boldsymbol{U}^{hybrid}} \tag{6.3}$$

$$\begin{Bmatrix} u_1 \\ v_1 \\ w_1 \\ u_2 \\ v_2 \\ w_2 \\ u_3 \\ v_3 \\ w_3 \\ u_4 \\ v_4 \\ w_4 \\ u_5 \\ v_5 \\ w_5 \\ u_6 \\ v_6 \\ w_6 \\ u_7 \\ v_7 \\ w_7 \\ u_8 \\ v_8 \\ w_8 \end{Bmatrix} = \begin{bmatrix} 1 & . & . & . & . & . & . & . & . & . & . & . & . & . & . & . & . & . & . & . & . & . \\ . & 1 & . & . & . & . & . & . & . & . & . & . & . & . & . & . & . & . & . & . & . & . \\ . & . & 1 & . & . & . & . & . & . & . & . & . & . & . & . & . & . & . & . & . & . & . \\ . & . & . & . & . & . & . & . & . & . & . & . & 1 & . & . & . & z_2 - z_{m1} & y_{m1} - y_2 \\ . & . & . & . & . & . & . & . & . & . & . & . & . & 1 & . & z_{m1} - z_2 & . & x_2 - x_{m1} \\ . & . & . & . & . & . & . & . & . & . & . & . & . & . & 1 & y_2 - y_{m1} & x_{m1} - x_2 & . \\ . & . & . & . & . & . & . & . & . & . & . & . & 1 & . & . & . & z_3 - z_{m1} & y_{m1} - y_3 \\ . & . & . & . & . & . & . & . & . & . & . & . & . & 1 & . & z_{m1} - z_3 & . & x_3 - x_{m1} \\ . & . & . & . & . & . & . & . & . & . & . & . & . & . & 1 & y_3 - y_{m1} & x_{m1} - x_3 & . \\ . & . & . & 1 & . & . & . & . & . & . & . & . & . & . & . & . & . & . \\ . & . & . & . & 1 & . & . & . & . & . & . & . & . & . & . & . & . & . \\ . & . & . & . & . & 1 & . & . & . & . & . & . & . & . & . & . & . & . \\ . & . & . & . & . & . & 1 & . & . & . & . & . & . & . & . & . & . & . \\ . & . & . & . & . & . & . & 1 & . & . & . & . & . & . & . & . & . & . \\ . & . & . & . & . & . & . & . & 1 & . & . & . & . & . & . & . & . & . \\ . & . & . & . & . & . & . & . & . & 1 & . & . & . & . & . & . & . & . \\ . & . & . & . & . & . & . & . & . & . & 1 & . & . & . & . & . & . & . \\ . & . & . & . & . & . & . & . & . & . & . & 1 & . & . & . & . & . & . \\ . & . & . & . & . & . & . & . & . & . & . & . & 1 & . & . & . & z_6 - z_{m1} & y_{m1} - y_6 \\ . & . & . & . & . & . & . & . & . & . & . & . & . & 1 & . & z_{m1} - z_6 & . & x_6 - x_{m1} \\ . & . & . & . & . & . & . & . & . & . & . & . & . & . & 1 & y_6 - y_{m1} & x_{m1} - x_6 & . \\ . & . & . & . & . & . & . & . & . & . & . & . & 1 & . & . & . & z_7 - z_{m1} & y_{m1} - y_7 \\ . & . & . & . & . & . & . & . & . & . & . & . & . & 1 & . & z_{m1} - z_7 & . & x_7 - x_{m1} \\ . & . & . & . & . & . & . & . & . & . & . & . & . & . & 1 & y_7 - y_{m1} & x_{m1} - x_7 & . \\ . & . & . & . & . & . & . & . & . & . & 1 & . & . & . & . & . & . & . \\ . & . & . & . & . & . & . & . & . & . & . & 1 & . & . & . & . & . & . \\ . & . & . & . & . & . & . & . & . & . & . & . & 1 & . & . & . & . & . \end{bmatrix} \begin{Bmatrix} u_1 \\ v_1 \\ w_1 \\ u_4 \\ v_4 \\ w_4 \\ u_8 \\ v_8 \\ w_8 \\ u_1^{NBCFB} \\ v_1^{NBCFB} \\ w_1^{NBCFB} \\ \theta_1^{NBCFB} \\ \varphi_1^{NBCFB} \\ \psi_1^{NBCFB} \end{Bmatrix} \tag{6.4}$$

The only required data in order to compute the connection matrix $\boldsymbol{T}_H$ are the coordinates x_i, y_i, z_i of the slave nodes that are controlled by the kinematic constraint and the x_m, y_m, z_m coordinates of the corresponding master node. The resulting hybrid hexahedral element has *18* dof, *12* corresponding to the *4* unconstraint hexahedral nodes and *6* corresponding to the master node dof.

The connection matrix $\boldsymbol{T}_H$ is used with the purpose of obtaining the *18*x*18* hybrid stiffness matrix according to Eq. 6.5 and is used once again to compute the hexahedral nodal displacements of the slave nodes from the hybrid element displacements after the solution of the equilibrium equations of the structure, according to Eq. 6.3. During the global stiffness computation, the corresponding dof of the hexahedral nodes that are located on the interface section, are eliminated according to

$$\underset{(18x18)}{\boldsymbol{K}_H^{\text{HEXA}}} = \underset{(18x24)}{\boldsymbol{T}_H^T} \cdot \underset{(24x24)}{\boldsymbol{K}^{\text{HEXA}}} \underset{(24x18)}{\boldsymbol{T}_H} \qquad 6.5$$

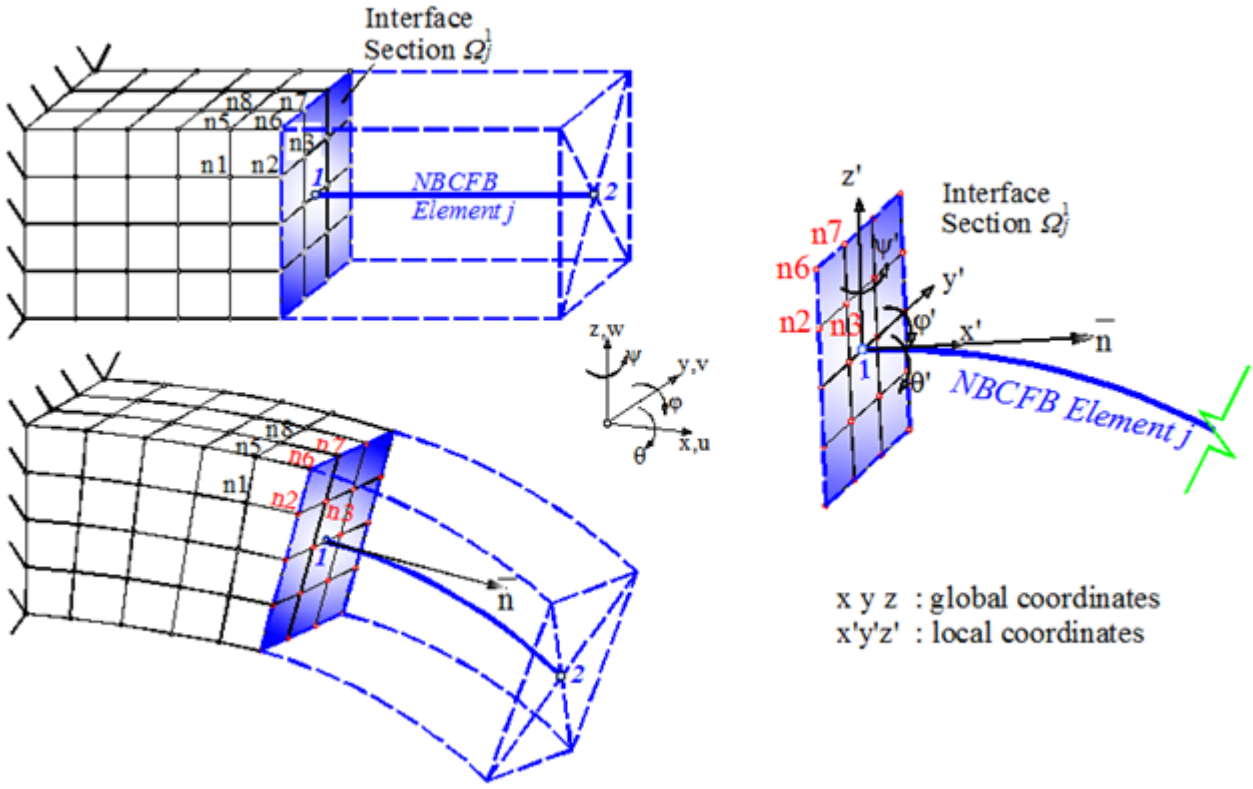

FIGURE 6.1 KINEMATIC CONSTRAINT IMPOSED BY THE 1D MODEL ON THE INTERFACE SECTION Ω_j.

The calculation of the internal forces of the hybrid hexahedral elements is performed with

$$\underset{(18x1)}{\boldsymbol{F}_H} = \underset{(18x24)}{\boldsymbol{T}_H^T} \cdot \underset{(24x1)}{\boldsymbol{F}^{\text{HEXA}}} \qquad 6.6$$

where $\boldsymbol{F}_H$ is the internal force vector of the hybrid hexahedral element, which is added to the global internal force vector during the nonlinear incremental iterative solution procedure.

With the above kinematic constraint, the interface section remains undeformed throughout the solution process as it is controlled by the master node of the corresponding NBCFB element. As it is going to be illustrated through a number of numerical experiments, this local effect has an insignificant influence on the overall numerical behavior of the structure. In addition to that, as it is going to be presented in the following sections, the degree of the reduced model is governing the numerical behavior of the HYMOD thus the overall accuracy is not affected by the assumed kinematic constraints.

One of the main issues that require further investigation and development is the automatic generation of hybrid models through 3D parametric and feature-based CAD models. At this stage, this process still remains rather cumbersome and not automatic. The required modifications are made directly on the 3D CAD model and the modification concerning parameters associated with the beam sections and interfaces are performed manually. The automatic generation of hybrid idealized models with the use of a 3D CAD environment would allow design changes directly on the 3D model and this would result into a considerable acceleration of the design process. This problem has been investigated by some researchers[248,

[249] who foresee an automation of this procedure. Despite the difficulty of automatically constructing parts of the mesh for hybrid FE models given the geometry of the RC structures, in this study *PRG* files (Programming files) were used with the aim of automatically reproducing specific joint types. The latter will be presented at the next Chapter of the Dissertation.

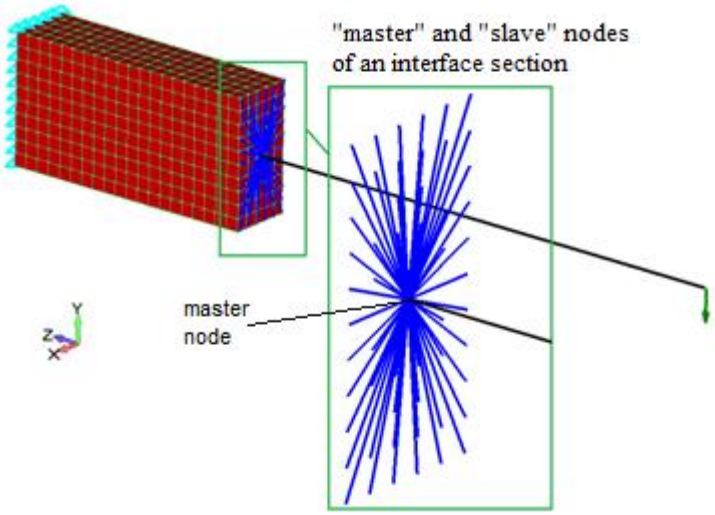

FIGURE 6.2 CANTILEVER BEAM. EXAMPLE OF 1D AND 3D FE DISCRETIZATION.

The model generation is performed with Femap[91] pre-processing software for constructing the necessary input data for the materials, element types and geometry of the structure. Then, rigid elements connect the master node of the interface with the corresponding slave nodes of the interface section. A schematic representation of the discretization concept with HYMOD is given in Fig. 6.2, where the hybrid model of a cantilever beam is presented.

6.2.2 Discretization with 1D and 3D FEs

The discretization scheme that can be chosen for the simulation of any RC structure is related to the desired accuracy and available computational resources. In Fig. 6.3, different Reduction Levels (RL) are depicted for the simulation of 3D RC frame structures. A description of the corresponding reduction models is given in Table 6.1.

The four main reduction models depicted in Fig. 6.3 and described in Table 6.1 represent four characteristic discretization schemes for a 3D RC structure with a shear wall. When using hybrid discretization schemes (RL 2-3 in Fig. 6.3), the selection of the proper length L_i of the solid part (Fig. 6.4) plays a crucial role in the efficiency of the model. In order to give an objective answer to this question, an extensive parametric investigation was conducted with the purpose of creating some general rules which could be followed depending on the geometrical features of the structure and structural members under consideration. The results of this parametric investigation will be presented in the next section where characteristic FE models were discretized by one element type or Hybrid Models and were subjected to different loading levels in order to investigate the most appropriate length of the prismatic part as shown in Figs. 6.3 and 6.4.

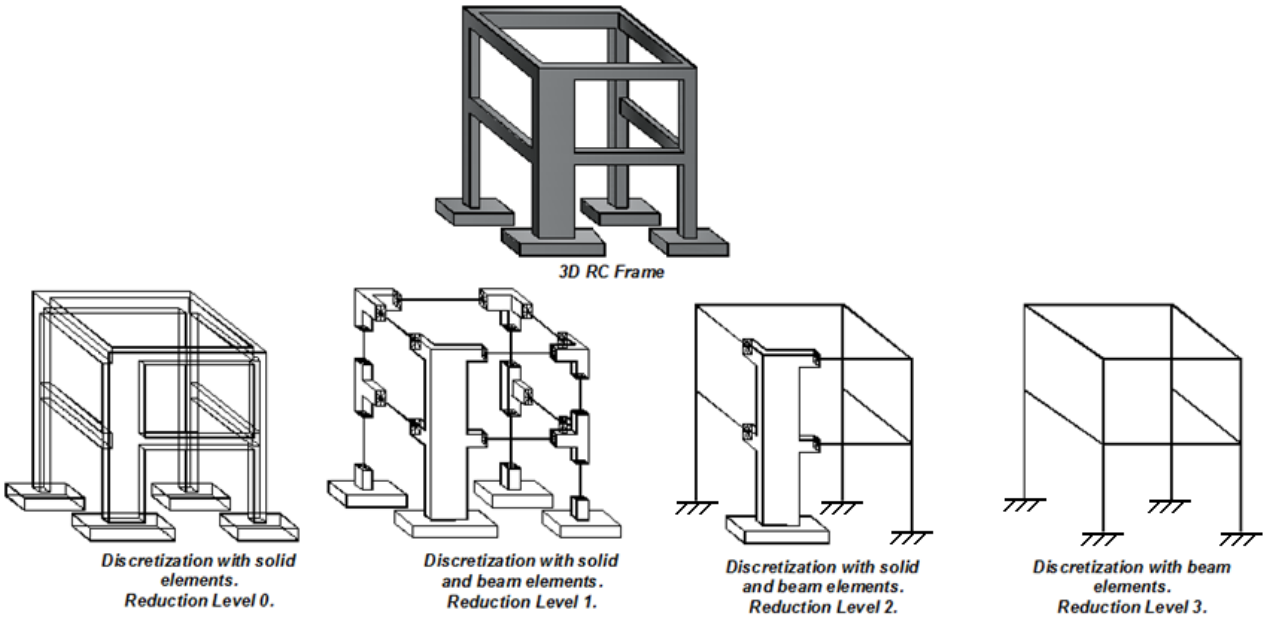

FIGURE 6.3 3D RC FRAME. DISCRETIZATION SCHEMES WITH DIFFERENT LEVELS OF MODEL REDUCTION.

Reduction Level of the Model	*Description*
0	The whole structure is discretized with 3D solid elements
1	Shear dominated structural members (shear walls, junctions etc.) are discretized with solid elements and the remaining parts of the structure with beam elements.
2	Shear walls are discretized with solid elements and the rest of the structure with beam elements.
3	The whole structure is discretized with beam elements.

TABLE 6.1 DISCRETIZATION WITH BEAM AND SOLID ELEMENTS. DESCRIPTION OF THE REDUCTION LEVELS.

6.3 Numerical Investigation on Length "L_i"

As it was mentioned above, the main reason for using the HYMOD is to reduce significantly the number of dof in order to be able to simulate full-scale structures with the required accuracy at an affordable computational time. In the case of RC structures, the FE model reduction requires the determination of the length L_i so that the derived model will meet the objectives stated previously.

In this section, a numerical investigation is performed on a series of cantilever and clamped beams for the determination of the proper length L_i (Fig. 6.4) when discretizing framed structures with HYMOD. The rationale behind this parametric study is to investigate the influence of the adopted assumptions for the simulation of the inelastic phenomena of RC joints using simple benchmark problems. Furthermore, to estimate the minimum length L_i for the adequate modeling of RC joints with solid finite elements. Accounting for the fact that cracking is directly determined from the stress-state of a critical region, a set of beams with homogenous materials are considered to illustrate the plastic hinge propagation by considering the stress distribution. Subsequently, the investigation of the behavior of the corresponding hybrid models

that derive from the modeling of these plastic hinges will be discussed. Following, the nonlinear behavior of RC benchmark problems will be presented verifying the investigation's numerical findings.

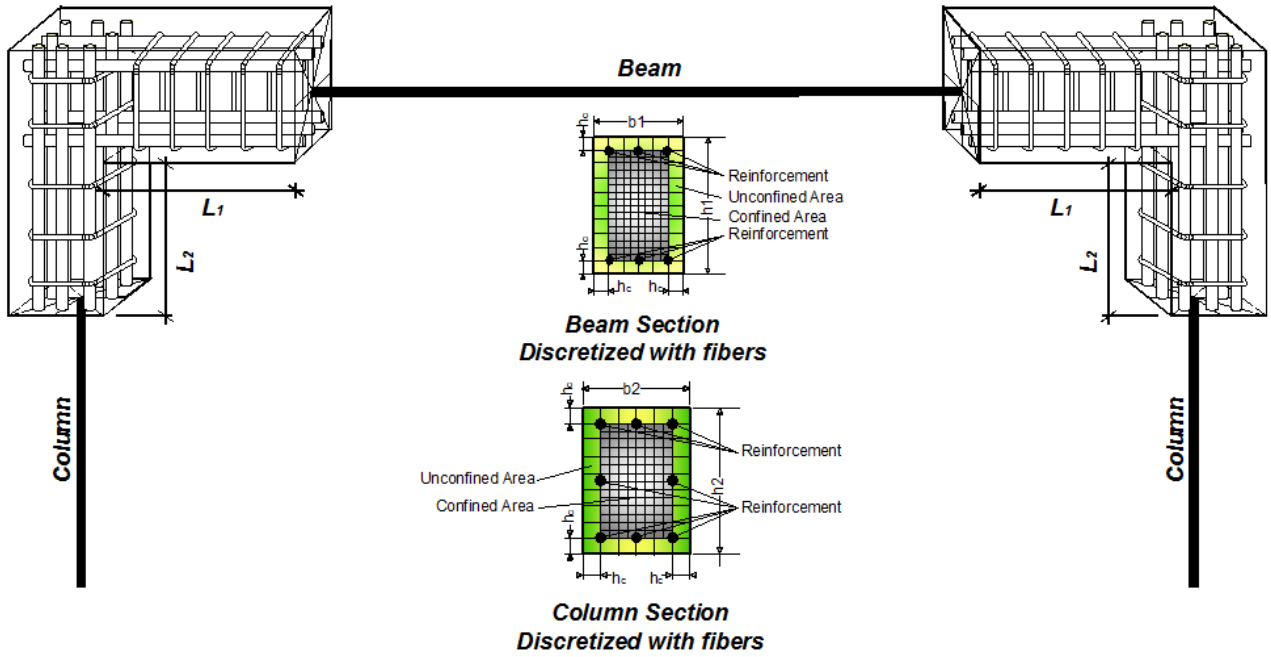

FIGURE 6.4 DISCRETIZATION OF JOINTS WITH DETAILED SOLID AND BEAM ELEMENTS. REINFORCEMENT DETAILS AND FIBER DISCRETIZATION OF THE BEAM-COLUMN SECTIONS.

6.3.1 Cantilever Beams

Five different models are considered based on Fig. 6.5 and the cross-sectional properties of Table 6.2. The concrete material characteristics of the cantilever beams are $f_c = 30\ MPa$, $E_c = 30\ GPa$, $E_T = 0$, $\nu = 0.2$ where f_c, E_c, E_T and ν correspond to the crushing stress, the Young modulus, the hardening modulus and the Poisson ratio, respectively. The material model used to simulate the nonlinear behavior of the cantilevers is the isotropic von Mises material which uses the von Mises yielding criterion without accounting for cracking. For each FE model (Figs. 6.6) a vertical load was placed at the end tip of the cantilevers and was applied incrementally until failure.

Due to the loading type and the geometry of the cantilever beam (Fig. 6.5), a plastic hinge will appear at the fixed end of the cantilever, which corresponds to the critical region of the beam that will control the nonlinear behavior of the structural member. The length of this critical region will be measured and thereafter a parametric investigation based on these lengths will be performed in order to conclude which is the minimum required hinge length to be discretized with solid elements in order to maintain an acceptable accuracy in relation to the detailed model.

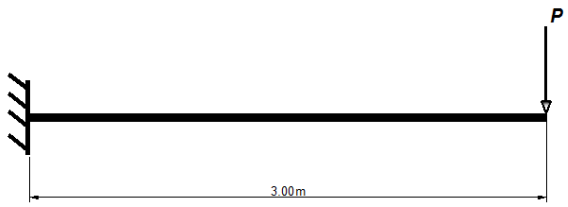

FIGURE 6.5 GEOMETRY OF THE CANTILEVER BEAM.

Beam	b_i *(cm)*	h_i *(cm)*	h_i/b_i
A	25	25	1
B	25	37.5	1.5
C	25	50	2
D	25	62.5	2.5
E	25	75	3

TABLE 6.2 GEOMETRY OF SECTIONS.

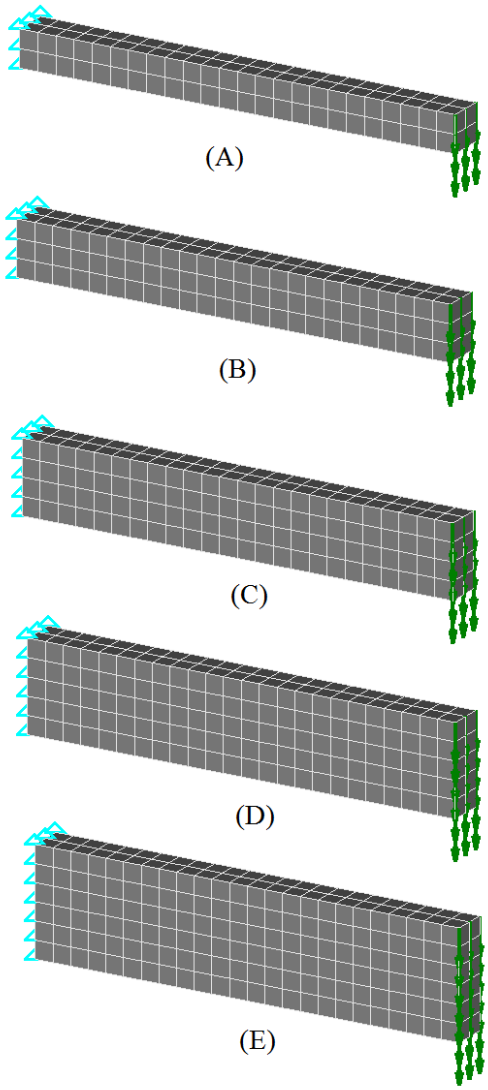

FIGURE 6.6 CANTILEVER BEAMS. FIVE FE MESHES (A-E).

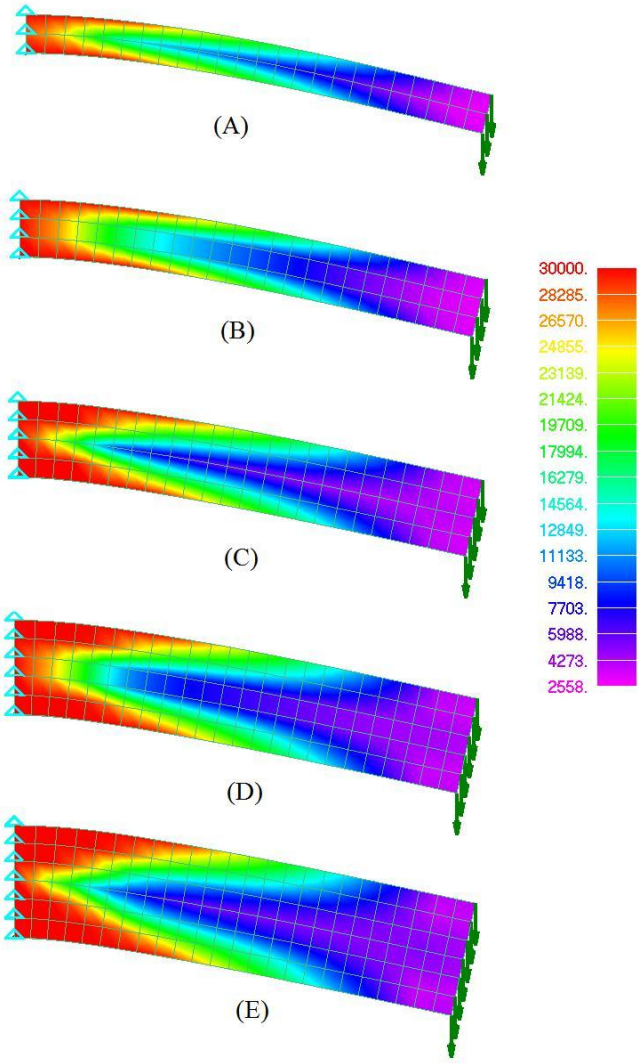

FIGURE 6.7 CANTILEVER BEAMS. VON MISES STRESS CONTOURS (*KPA*). SCHEMATIC REPRESENTATION OF PLASTIC HINGES.

In Figs. 6.7 the von Mises stress contour is shown for each cantilever beam model discretized with 3D solid elements. As it can be observed, the grid lines of the hexahedral elements are shown, having a constant distance between them (*12.5cm*) providing the ability of measuring any vertical or longitudinal distance manually. The shape of each plastic hinge has a similar geometry and it can be observed that for all cases, the plastic hinge has a *V* shaped geometry (red color). As the vertical load increases, the upper and lower regions of the fixed section enter the plastic range thus the initiation of the stiffness degradation begins. With a further load

increase, the plastic hinge spreads to the center of the section and at the same time it increases along the longitudinal axis of the beam until failure. Fig. 6.8 shows the *P-δ* curves that were computed through the analysis procedure.

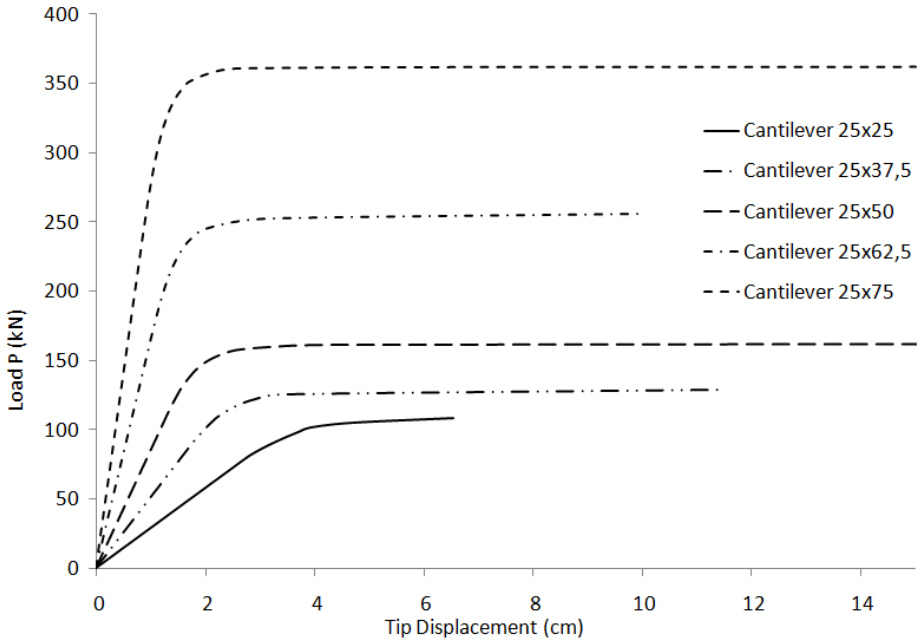

FIGURE 6.8 CANTILEVER BEAMS. *P-δ* CURVES FOR DIFFERENT GEOMETRIES.

One question that rises when observing Figs. 6.7 and 6.9 is how can a plastic hinge length be defined in the three dimensional space, taking into account the three dimensional behavior. The answer to this question is not direct because many assumptions can be made on just observing this type of figures. For this reason, an objective way of answering this question is through a parametric investigation on the required hinge length that has to be discretized with solid elements and will be able to predict the overall nonlinear behavior of the beam. For this purpose, a set of hybrid models were created, assuming different hinge lengths discretized with solid elements (Figs. 6.12). The beam with *25x50 cm* section was used in order to serve this purpose and the numerical findings are given in Fig. 6.10 where the *P-δ* curves are shown.

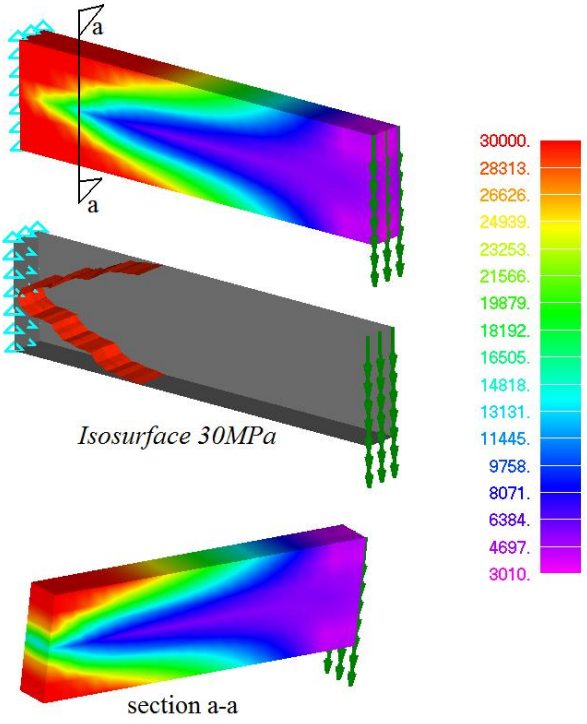

FIGURE 6.9 CANTILEVER BEAM. 3D REPRESENTATION OF A PLASTIC HINGE. VON MISES CONTOUR. BEAM MODEL E (*25x75*).

As it can be seen in Fig. 6.10, the elastic branches of the *7* models which were solved with the use of *ReConAn* (first six curves) and Femap NXNastran (red curve), are identical concerning the solid FE models. Even though it is not clear from the graph, the elastic branch of the curve predicted with the use of NBCFB element is slightly stiffer. This event was expected since solid elements are more flexible than the corresponding beam.

When the two model types (solid and beam) enter the nonlinear range (approximately at the same load level), it is evident that the beam FE model shows a softer response than the corresponding unreduced solid FE model. The main question is, which is the correct *P-δ* curve and subsequently, which is the correct ultimate load capacity for this structural member. So as to resolve this numerical phenomenon, the analytical solution when using the Euler-Bernoulli theory is computed.

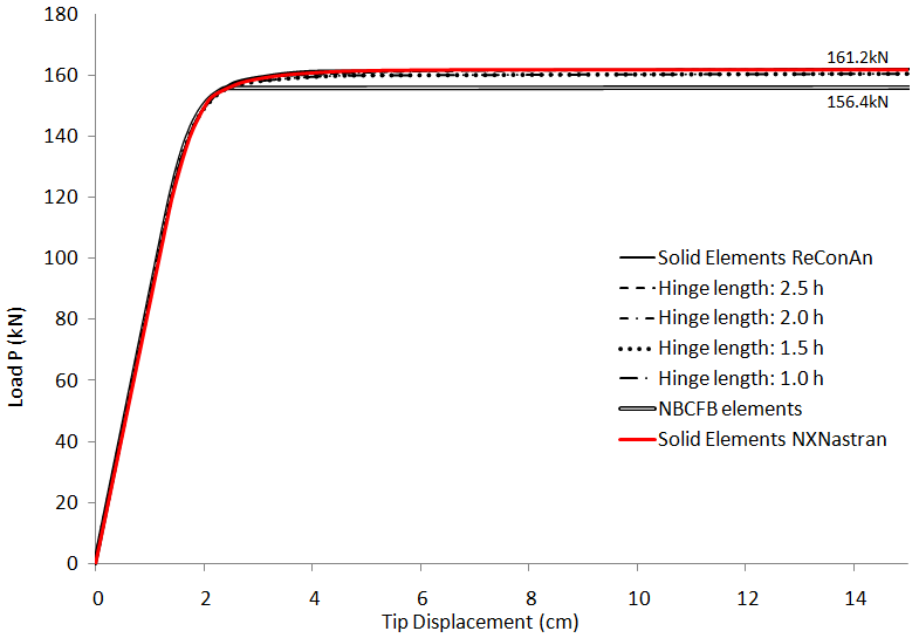

FIGURE 6.10 CANTILEVER BEAM. *P-δ* CURVES FOR DIFFERENT PLASTIC HINGE LENGTH ASSUMPTIONS.

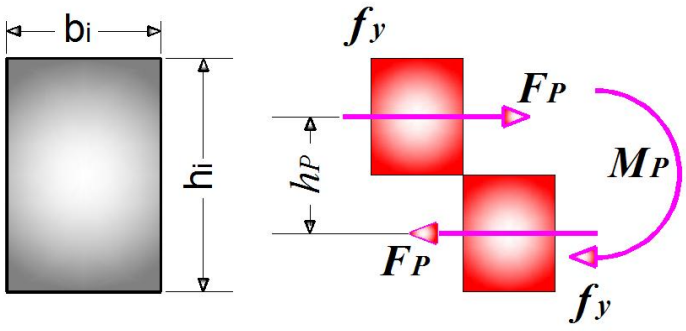

FIGURE 6.11 COMPLETE PLASTIFICATION OF A RECTANGULAR SECTION.

Using the Euler-Bernoulli theory and with the help of Fig. 6.11, the ultimate moment of the corresponding section when complete plastification occurs, is given by Eq. 6.7 and the ultimate capacity load which corresponds to this moment is given by Eq. 6.8. The analytical failure load is $P_P = 156.4\ kN$ which coincides with the load predicted by the FE model with the NBCFB elements. Since the formulation of this element adopts the Euler-Bernoulli theory of the undeformed section, the analytical solution coincides with the numerical which results from the combination of the FE method and the fiber approach.

$$M_P = F_P \cdot h_P, \text{ where } F_P = f_y \cdot \frac{h_i}{2} \cdot b_i \qquad 6.7$$

$$P_P = {}^{M_P}\!/_{L} \qquad 6.8$$

where P_P and L are the plastification load and the beam's length, respectively. These formulae, are valid only when the hardening modulus is equal to zero ($E_T = 0$), meaning that the sectional internal stress tensor remains constant when the value of yielding stress is reached, for any further load increase.

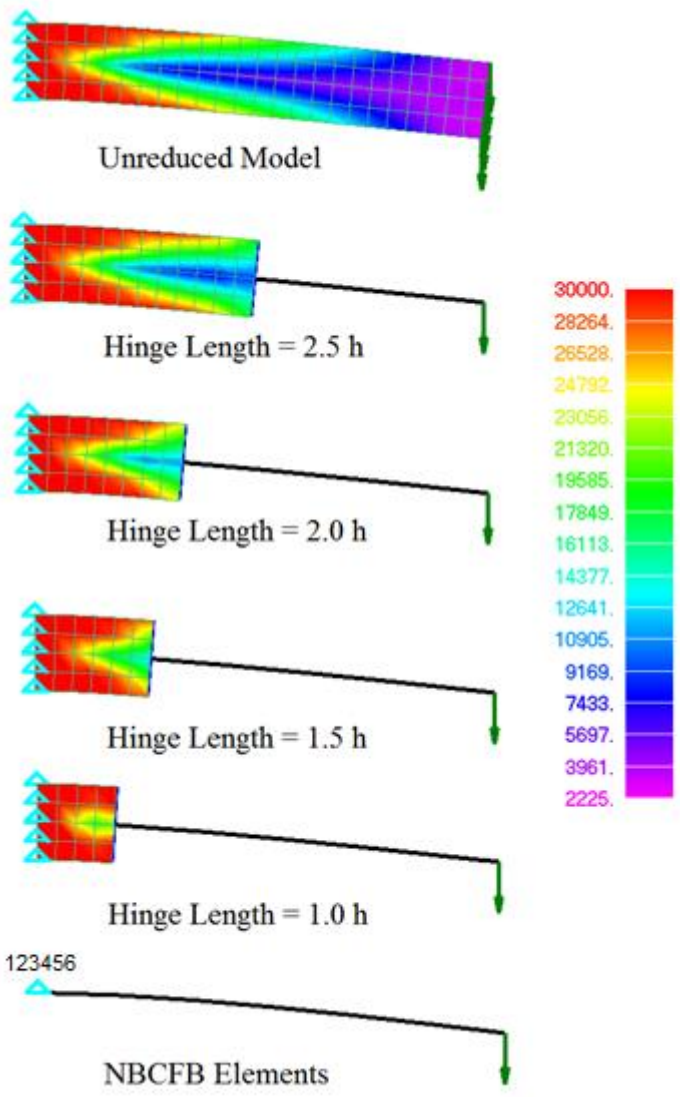

FIGURE 6.12 CANTILEVER BEAM *25X50*. VON MISES CONTOUR AND DEFORMED SHAPES FOR DIFFERENT MESHES.

Another observation that can be made, concerning the hybrid discretization, is that for all hybrid models the predicted inelastic branches are slightly below the corresponding inelastic branch predicted by the unreduced FE models. This numerical finding confirms that the kinematic constraints do not affect the overall response for this type of structural members with

the corresponding loading, since the predicted curves almost coincide with those produced by the unreduced FE models.

This type of problem was bending dominated and shear strains had no effect on the ultimate numerical response of the computed results. To illustrate that 3D solid FE models is the most appropriate approximation of capturing realistically the response of any structural member, the same numerical experimental investigation was conducted for the case of a shear dominated beam.

6.3.2 Clamped Beam

Fig. 6.13 shows the geometrical details of a clamped deep beam which has a rectangular section of *25x100 cm* and a total span of *3 m*. The material characteristics are f_c = *30 MPa*, E_c = *30 GPa*, E_T = *0*, ν = *0.2* where f_c, E_c, E_T and ν correspond to the crashing stress, the Young modulus, the hardening modulus and the Poisson ratio, respectively. A vertical load is applied on the midspan of the beam and is applied incrementally until failure.

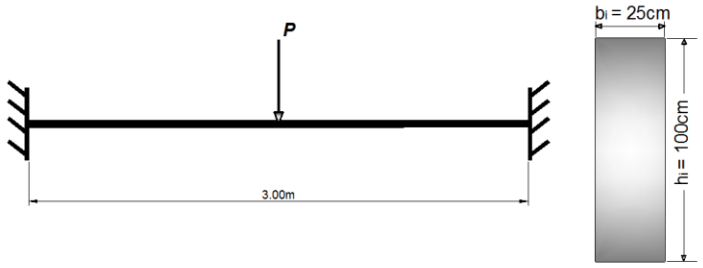

FIGURE 6.13 CLAMPED BEAM. GEOMETRIC AND SECTION DETAILS.

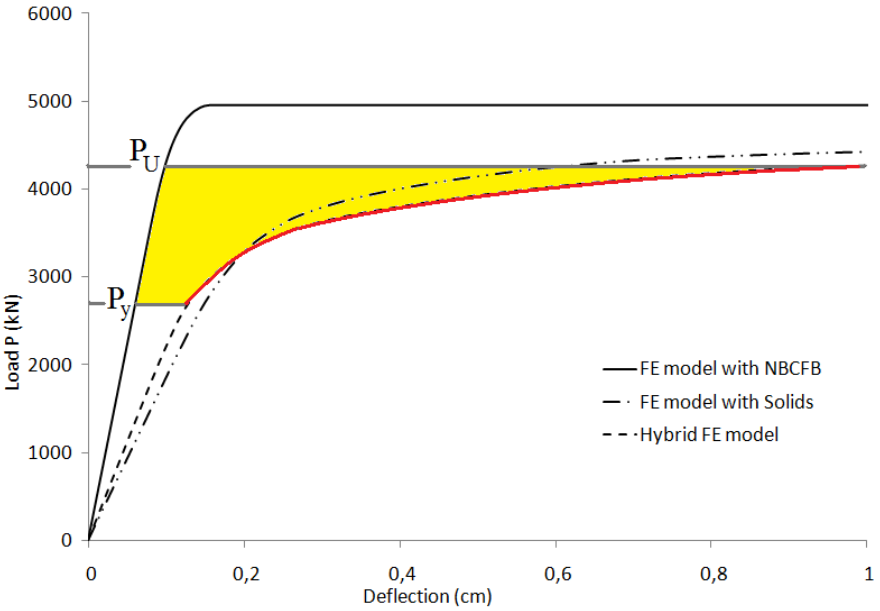

FIGURE 6.14 CLAMPED BEAM. *P-δ* CURVES FOR DIFFERENT FE MODELS.

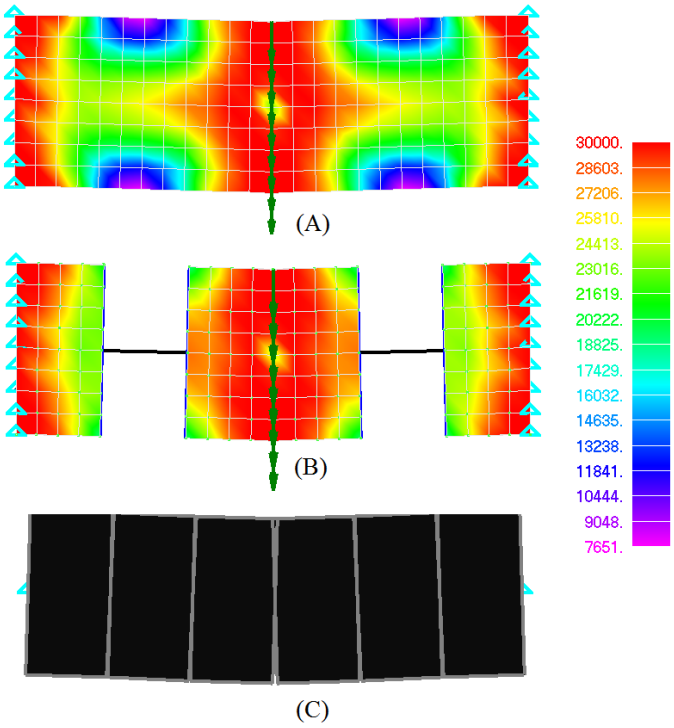

FIGURE 6.15 CLAMPED BEAM. DEFORMATION SHAPES AND STRESS VON MISES CONTOURS OF (A) FULL SOLID FE, (B) HYBRID FE AND (C) NBCFB FE MODELS.

Fig. 6.14 shows the computed *P-δ* curves for three different FE models illustrated in Figs. 6.15. The first model is the full FE model with solid elements (Fig. 6.15a), the second is the hybrid FE model which considers a characteristic length $L_i = h$ (section height) in the middle of the clamped beam and *h/2* at the fixed ends Fig. 6.15b) and finally the third FE model assumes that the clamped beam is discretized with 6 NBCFB elements (Fig. 6.15c). In order to evaluate the analytical failure loads, the bending moment capacity is computed using the Eq. 6.7 and assuming that the section obeys the Euler-Bernoulli assumption. After the necessary calculations, $M_P = 1{,}875\ kNm$ and considering that the moment at the end of a clamped beam due to a concentrated load at the midspan is given by *PL/8* then the capacity load of this beam is equal to *5,000 kN*. This failure load coincides with the computed failure load of the NBCFB FE model.

Since the adopted NBCFB model does not account for shear strains, the expected response when using the hexahedral elements should be softer, a numerical finding that can be seen in Fig. 6.14. It can be easily observed that the computed *P-δ* curves of the clamped beam when modeled with hexahedral elements (Fig. 6.15a) is much softer than the corresponding curve computed by the beam model, illustrating the shear effect in the stiffness degradation.

The most noteworthy numerical finding in this parametric investigation is illustrated in Fig. 6.14, where the hybrid model initially shows a slightly stiffer elastic response than the unreduced model while, following the initiation of yielding, its inelastic behavior appears to be softer than the unreduced model. This numerical phenomenon is attributed to the introduction of the two beam elements between the three plastic hinges. This results to a stiffer FE model, therefore a stiffer elastic branch occurs which leads to an earlier manifestation of yielding as depicted in Fig. 6.14 (P_y). Moreover, when yielding occurs a redistribution of the internal strains is performed and due to the inability of the beam elements to accommodate for shear strains (between load levels P_y - P_U) they maintain their elastic stiffness while the rate of deformation is increased at the critical regions which are discretized with hexahedral elements. As Fig. 6.14 shows, the yellow hatched area that represents the initiation of yielding up to complete failure is located on the elastic branch of the beam model curve, verifying the above observation. Additionally, Fig. 6.15b shows a larger concentration of von Mises stresses at the

clamped ends of the beam confirming the above numerical phenomenon. Despite this slight deviation of the predicted curve, it is evident that the kinematic constraints do not affect the overall nonlinear response of this type of structures as well, exhibiting a robust numerical behavior. It is also evident that the nonlinear response when modeling the structures with hybrid models is mainly controlled by the formulation of each FE type and, as is shown in this case, the predicted ultimate load is in favor of safety.

A basic conclusion that can be derived from this study is that shear dominated structural members should be modeled with hexahedral FE models thus beam elements must only be used for bending dominated structural members (beams and columns).

6.3.3 Computational Efficiency

One of the main reasons for using Hybrid Modeling methods, is to significantly reduce the computational cost of an unreduced hexahedral FE model maintaining at the same time the required accuracy. For this reason, the computational performance of the proposed modeling method is presented for the case of a clamped beam which is discretized with *5,000* hexahedral elements and *6,666* nodes (Fig. 6.17a). The second model corresponds to a reduced scheme with hexahedral elements in the midspan and the ends of the beam while the rest of the beam is modeled with *6* NBCFB elements (Fig. 6.17b).

Fig. 6.16 shows the geometrical details of a simply supported beam which has a rectangular section of *20x40 cm* and a total span of *4 m*. The material characteristics are $f_c = 25\ MPa$, $E_c = 28\ GPa$, $E_T = 0$, $\nu = 0.2$ where f_c, E_c, E_T and ν correspond to the crashing stress, the Young modulus, the hardening modulus and the Poisson ratio, respectively. A vertical load is applied on the midspan of the beam which is implemented incrementally (*50* load steps). It must be noted that the computed analytical ultimate vertical load is $P_P = 400\ kN$ when the effect of shear strains is neglected.

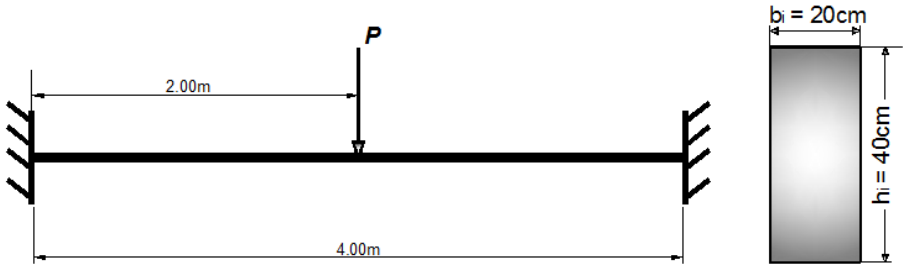

FIGURE 6.16 CLAMPED BEAM. GEOMETRIC AND SECTION DETAILS.

Model	*Hexahedral Elements*	*NBCFB Elements*	*Total Nodes*
A	5,000	-	6,666
B	2,000	6	2,846
C	-	10	11

TABLE 6.3 CLAMPED BEAM. DETAILS OF FE MODELS.

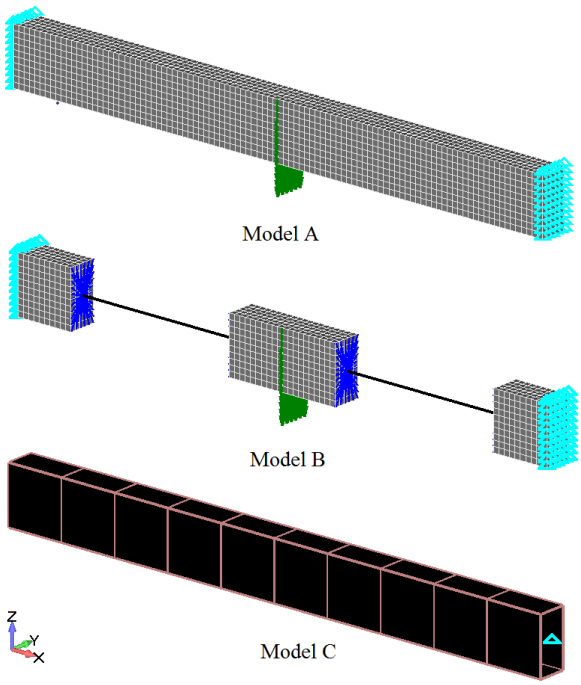

FIGURE 6.17 CLAMPED BEAM. DIFFERENT FE MODELS.

As it was mentioned, the aim of this numerical test is to illustrate the computational efficiency of the proposed modeling method and the corresponding decrease of the computational demands when the reduction of a hexahedral model is adopted. Figs. 6.17 show the three models used in this numerical test and the corresponding details of each FE model are given in Table 6.3. The first FE model is the unreduced hexahedral model which consists of *5,000* hexahedral elements and *6,666* nodes (Fig. 6.17a). The second FE model was derived from the unreduced model by assuming that the clamped ends are discretized with hexahedral elements over a length *h* (height of section) and the middle part of the beam over a length of *2h*. The rest of the beam is modeled with NBCFB elements as shown in Fig. 6.17b. The last FE model is the one given in Fig. 6.17c, which consists of *10* NBCFB elements.

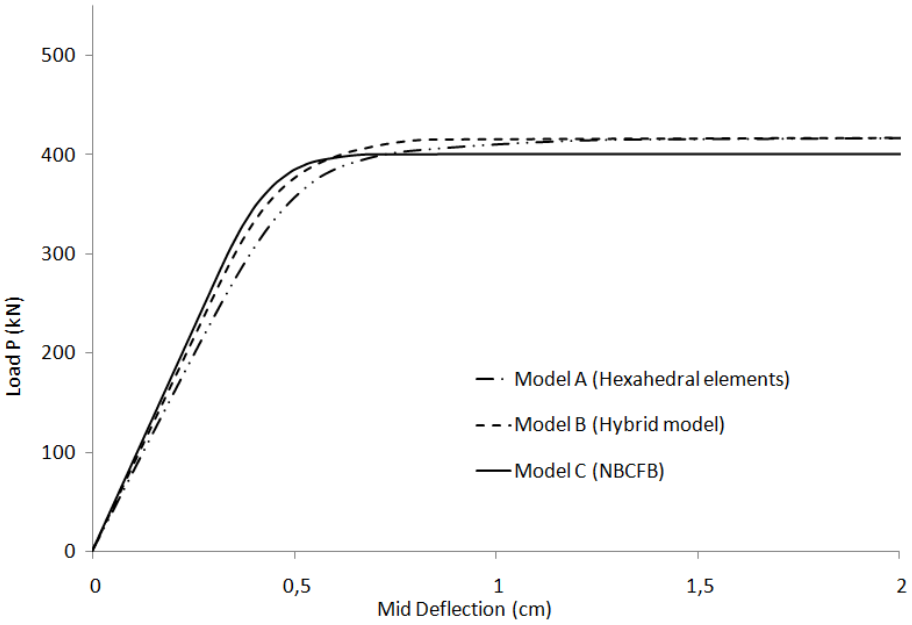

FIGURE 6.18 CLAMPED BEAM. *P-δ* CURVES FOR DIFFERENT FE MODELS.

Fig. 6.18 shows the computed *P-δ* curves for the three FE models. As it can be observed, model C appears to have the stiffer response since the NBCFB element does not account for shear strains. The predicted ultimate load is approximately *400 kN* verifying the analytical calculations which derived from the Euler-Bernoulli assumption. The elastic branch computed by the unreduced hexahedral model A is below the elastic branch of the beam model. On the

contrary, the predicted failure load for the case of the full model is higher than the beam's model, highlighting the numerical phenomenon described in section 6.3.1.

It is indisputable that independently from the geometry and the boundary conditions applied, the 3D formulation manages to predict accurately the nonlinear behavior of any structure. The von Mises contours and deformed shapes are shown in Figs. 6.19 where the computed plastic hinges can be seen. It is evident that the 3D representation of the final plastic hinge stress distribution describes the evolution of the phenomenon as the plasticity is spreading inside the volume of the structure (Fig. 6.19a). It can also be observed that the main critical regions of the clamped beam are its two ends and its middle "section".

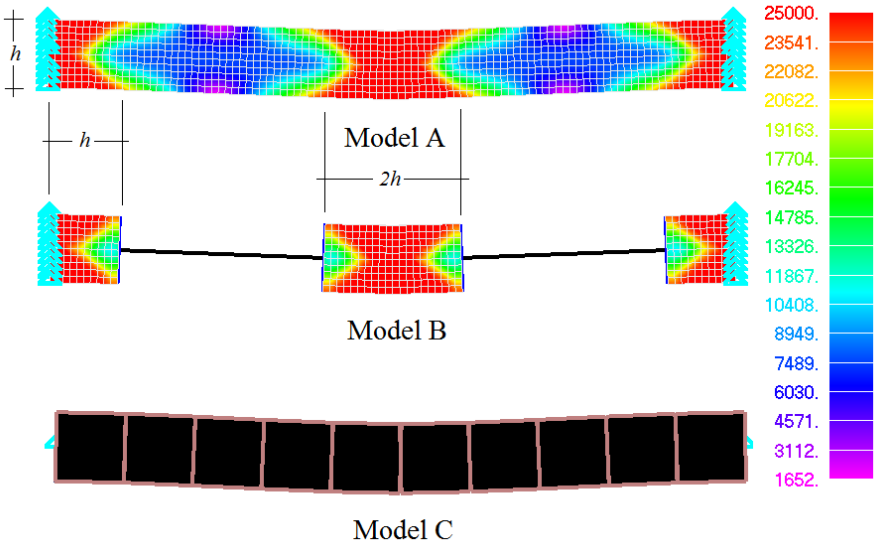

FIGURE 6.19 CLAMPED BEAM. VON MISES CONTOURS AND DEFORMED SHAPES OF MODELS A, B AND C.

Model	*Ultimate load (kN)*	*Time (sec)*
A	427.35	150.0
B	425.04	60.0
C	399.84	0.7

TABLE 6.4 CLAMPED BEAM. PREDICTED LOADS AND CPU TIMES FOR SOLUTION OF *49* LOAD STEPS.

The lengths L_i that were used in model B for the detailed discretization of its critical regions derive from the von Mises contour of model A in Fig. 6.19a. It is obvious that the main nonlinearities appear at a length *h* at the two ends of the beam and for a length *2h* in the middle critical region. As can be observed form Fig. 6.18, the computed *P-δ* curve of the hybrid model lying between the corresponding two curves computed by models A and C. This confirms that the hybrid model inherent additional stiffness which is attributed to the beam element's formulation. The ultimate computed loads are the same for both models (A, B) thus the reduction of the computational cost is indisputably a major gain when using this approach as is illustrated in Table 6.4.

Table 6.4 shows the computational time required for the solution of *49* load steps for each model. It is evident that the beam model is the most computationally efficient from the three model types thus the required CPU time for the execution of the nonlinear solution procedure was less than *1 sec*. Model A is the most computationally demanding FE model and requires

150 sec for the nonlinear solution process. On the other hand, the hybrid model requires only *60 sec* for the completion of the nonlinear solution process which is *60%* less than the required computational time by the detailed model. This is attributed to the decrease of elements which is also *60%* (*2,000/5,000* elemets) thus the computational time is reduced proportionally.

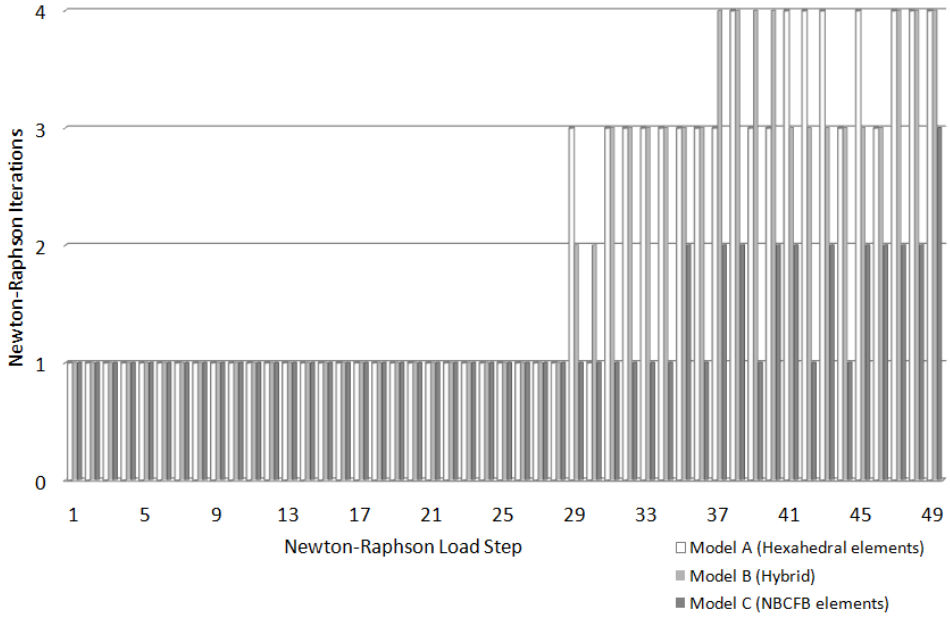

FIGURE 6.20 CLAMPED BEAM. INTERNAL ITERATIONS PER LOAD STEP.

As it was mentioned above, numerical robustness is also a main issue when implementing connection interface between the two domains. Fig. 6.20 shows the required NR iterations per load step for the three models where the robustness of the proposed modeling method can be verified. Instead of inducing numerical instability through the hybrid implementation, additional stability is observed which is attributed to the simplicity of the proposed kinematic constraints. Moreover, the numerical behavior of model B manages to predict the nonlinear response of the structure but accurately and computationally efficient.

Closing this numerical investigation, concerning the length of the plastic hinge that should be considered for each potential plastic hinge evidently depends on the geometry of the structural member. Nevertheless, a general rule may derive from these numerical tests and their numerical behavior. Assuming that the main structural member types that will be discretized using the hybrid concept are beam- or column-like members, the minimum proposed length of the potential plastic hinge at the ends of the members that should be considered is h (the height of the member's section) and $2h$ for the case of a potential symmetric plastic hinge that is expected to appear in the middle of a member. It is apparent that the larger the assumed lengths L_i, the closer the nonlinear responses to the unreduced model but the more computationally demanding the hybrid models will be.

6.4 Numerical Implementation

In this section a numerical investigation will be performed on different RC structural components and 3D structures in order to illustrate the efficiency of the proposed hybrid simulation. The 3D prismatic parts of these test examples are modeled with the 8-noded

hexahedral elements that treat cracking with the smeared crack approach and the steel reinforcement with the embedded NBCFB and rod elements (Chapter 5). The 1D parts of the HYMOD mesh are modeled with the RC NBCFB element (Chapter 2).

6.4.1 RC Beam Supported on two Shear Walls

This numerical test consists of a RC beam which is supported on two shear walls (Fig. 6.21). In order to study the nonlinear responses resulting from different simulations, three reduced models were considered corresponding to RL *0*, *1* and *3*, respectively, as indicated in Table 6.5. The geometrical and reinforcement details for the unreduced model are given in Fig. 6.21, where it can be seen that the *25x60 cm* rectangular beam section is reinforced with *3Ø18 mm* rebars placed at its upper and lower region of the beam. The diameter of the stirrups is *8 mm* and the spacing between stirrups is considered to be constant (*10 cm*) throughout the structure. The reinforcement details of the shear walls are also given in Fig. 6.21. The walls are reinforced with *12 mm* and *8 mm* diameter rebars and considered to be fixed at their ends. The span of the beam is *6 m* and the concrete cover was set equal to *3 cm* for both structural member types.

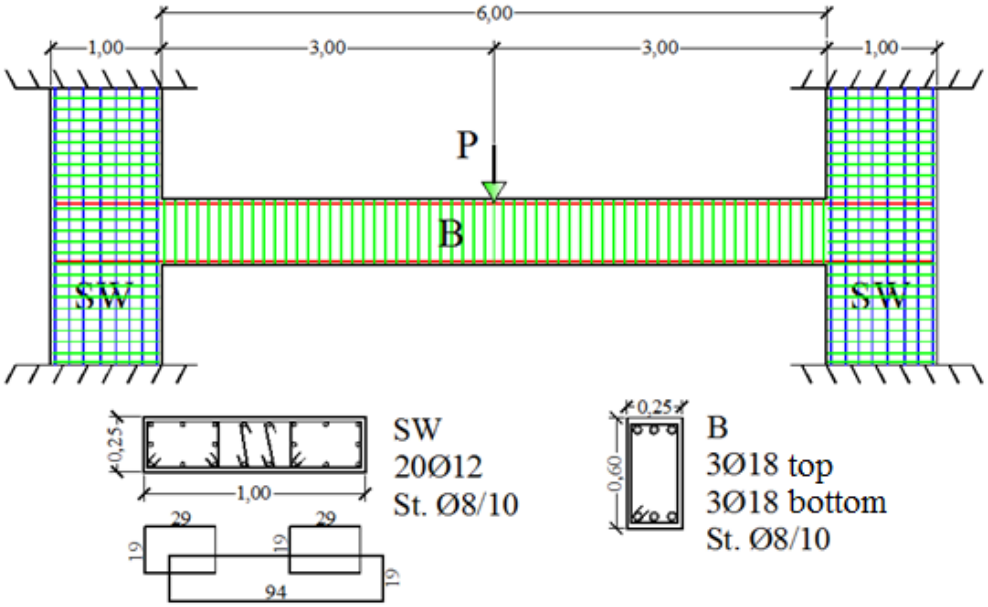

FIGURE 6.21 RC BEAM SUPPORTED ON TWO SHEAR WALLS. GEOMETRIC AND REINFORCEMENT DETAILS.

α/α	*Model*	*Hexahedral Elements*	*Embedded Rebar Elements*	*RC NBCFB Elements*	*Total Number of Dof*
A	Reduction Level 0	432	3256	-	2295
B	Reduction Level 1	368	2904	2	1869
C	Reduction Level 3	-	-	22	114

TABLE 6.5 RC BEAM SUPPORTED ON TWO SHEAR WALLS. DETAILS OF THE FOUR FE MODELS.

The material properties considered for this numerical test are given in Table 6.6. The external load is applied in the midspan of the beam and is implemented incrementally until failure. The number of load increments was set to *50* and the convergence tolerance of the NR iterative solution to 10^{-4}. For all FE models considered in the following numerical implementations of

this Chapter, concrete is assumed to have a tensional strength equal to the *5%* of its compressive cylindrical strength.

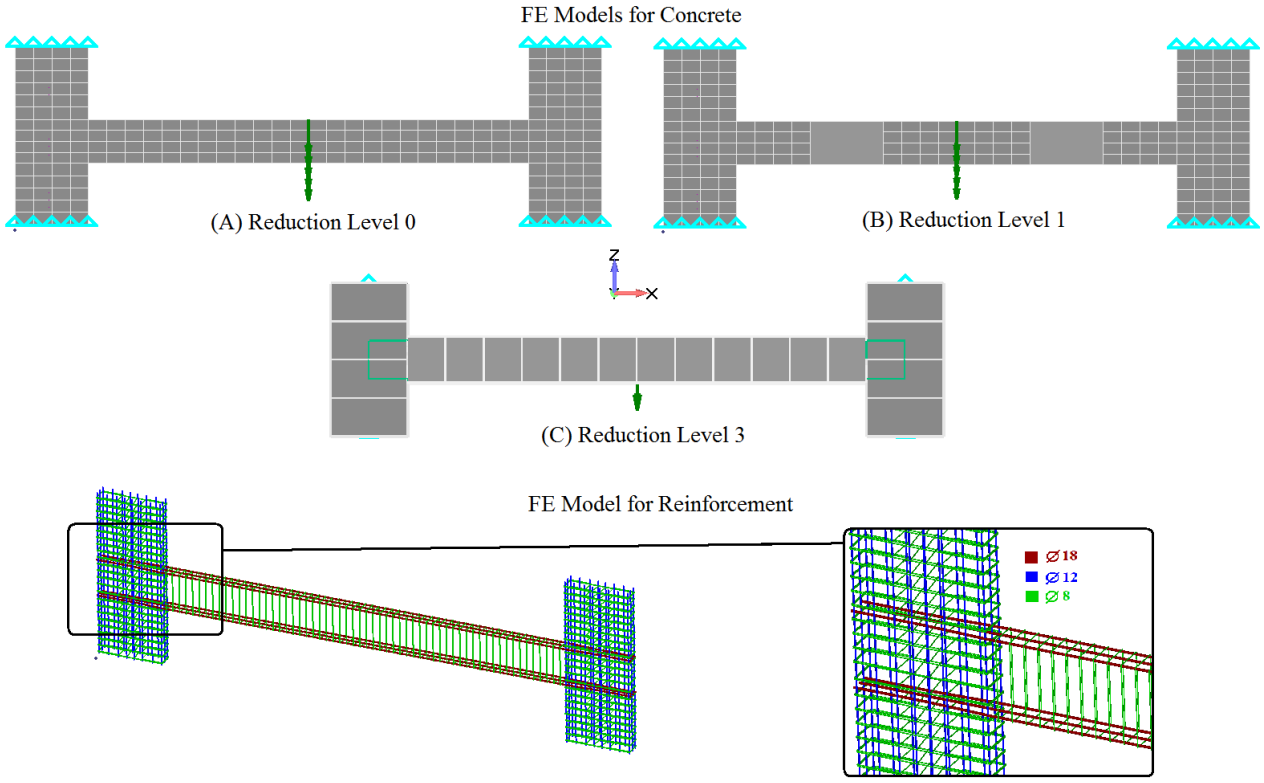

FIGURE 6.22 RC BEAM SUPPORTED ON TWO SHEAR WALLS. FE MODELS OF CONCRETE AND REINFORCEMENT.

Material	*Young Modulus (GPa)*	*Hardening Modulus (GPa)*	*Yielding Stress (MPa)*	*Compressive Strength (MPa)*	*Poisson Ratio*
Concrete	30	-	-	30	0,2
Steel	210	2,1	500	-	0,3

TABLE 6.6 RC BEAM SUPPORTED ON TWO SHEAR WALLS. MATERIAL DETAILS.

Fig. 6.23 shows the computed *P-δ* curves for the three FE models and as it can be seen for all cases the computed curves consists of three branches. The first branch of each curve corresponds to the elastic range of the beam where the structural member behaves completely elastically. After crack initiation, degradation of stiffness is manifested in the second branch corresponding to the nonlinear behavior of the cracked beam whose reinforcement behaves elastically. The third branch corresponds to the yielding of the longitudinal reinforcement and the occurrence of extensive cracking until failure. The elastic response of the beam model coincides with the 3D detailed model up to the total vertical load of *250 kN*. This is explained by the fact that shear strains do not have an important influence on the overall behavior of the structure and thus, the beam model appears to give a realistic numerical prediction. Following an increase in the crack pattern and the appearance of inclined cracks (Fig. 6.24), shear strains start to affect significantly the nonlinear behavior of the beam (Fig. 6.23), resulting into larger deformations. Figs. 6.24 show the computed crack pattern when the cracking is initiated (*60*

kN) and the corresponding crack pattern when inclined cracks appear due to increased shear strains (*300 kN*).

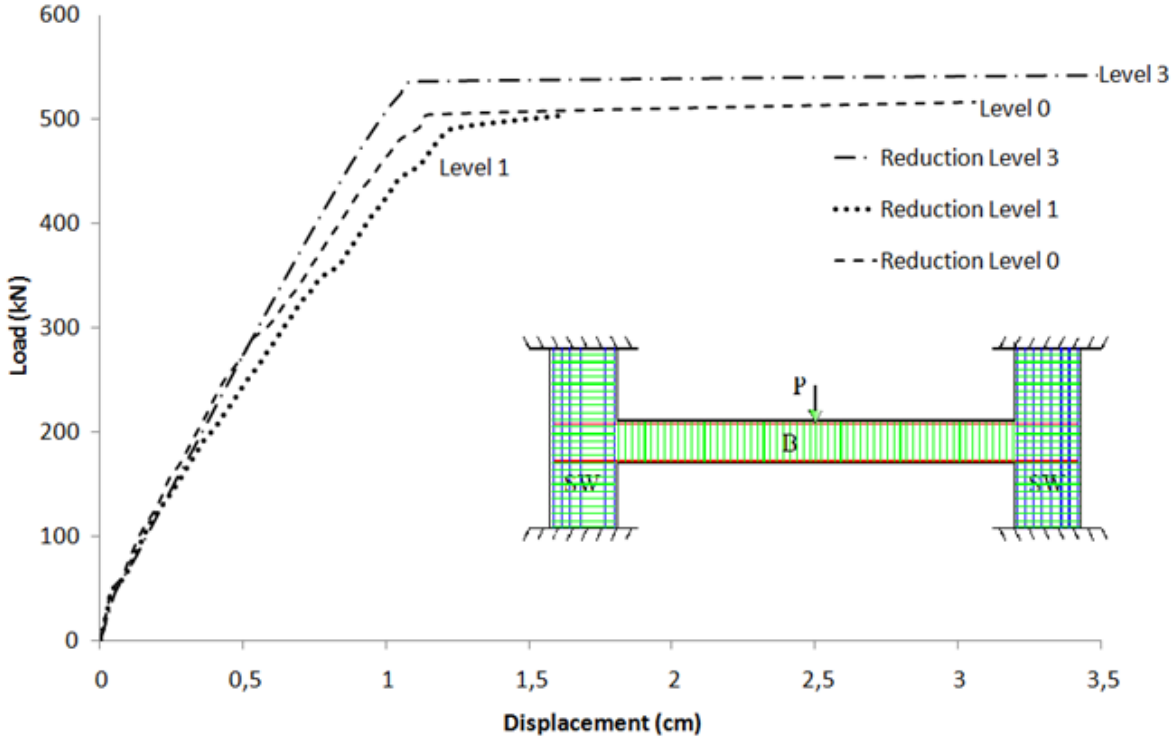

FIGURE 6.23 RC BEAM SUPPORTED ON TWO SHEAR WALLS. *P-δ* CURVES.

The predicted crack patterns (Figs. 6.24a and 6.24c) show that the tensile strength at the midspan of the beam and at the upper area of its clamped ends, is exceeded resulting to vertical flexural cracking. The correlation between the RL *1* is also shown and it can be seen that the reduced model maintains the desired accuracy, predicting the exact initiation crack load and the corresponding crack pattern.

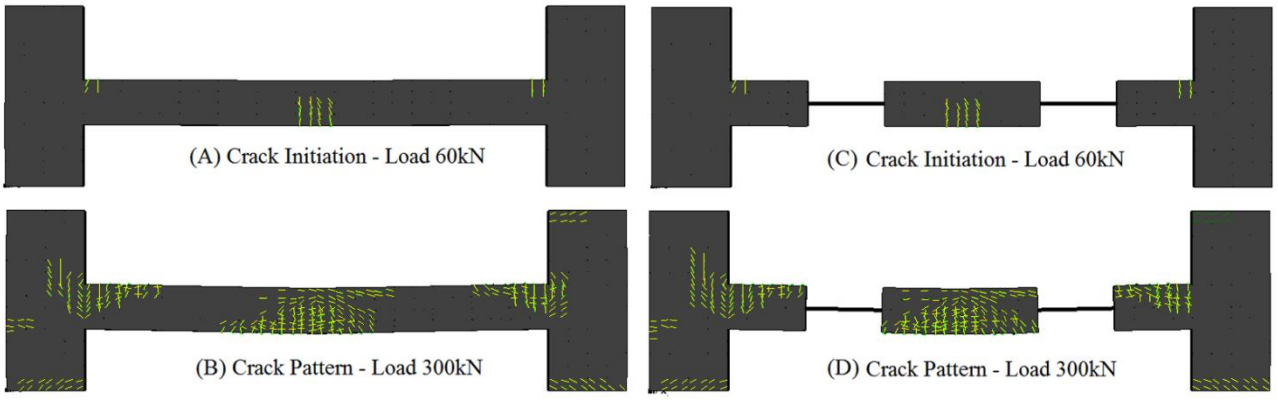

FIGURE 6.24 RC BEAM SUPPORTED ON TWO SHEAR WALLS. CRACK PATTERNS FOR DIFFERENT LOAD LEVELS.

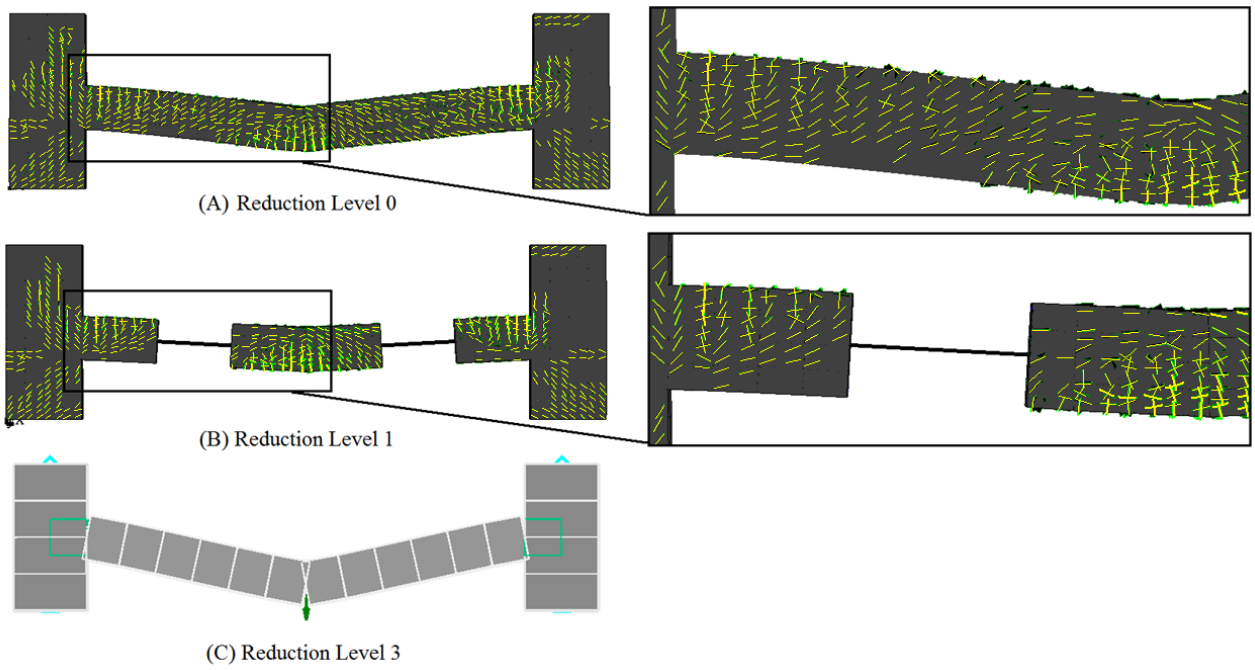

FIGURE 6.25 RC BEAM SUPPORTED ON TWO SHEAR WALLS. CRACK PATTERNS AND DEFORMED SHAPES PRIOR TO FAILURE.

The computed crack patterns and the corresponding deformed shapes prior to failure are illustrated in Figs. 6.25. Following the excessive cracking, the yielding of the longitudinal rebar elements at the midspan of the beam initiated the failure mechanism. The correlation between the crack patterns for the first two models is satisfactory where the different orientation cracking is observed. The deformed shape of the beam model and the computed *P-δ* curve underlines the inability of the beam element to account for shear strains and inclined cracking, thus the predicted ultimate load is higher than those predicted by the 3D detailed and hybrid models.

The numerical phenomenon depicted in Fig. 6.14 can also be used in order to explain why the RL *1* model appears to be slightly softer than the corresponding unreduced model when shear stains begin to play an important role. As it was explained previously, the combination of two different FE types affect the strain redistribution when shear strains play a significant role in the overall response of the structure, resulting to larger strain concentrations at the domain where shear strains are accounted for. Nevertheless, the hybrid model manages to predict a satisfactory ultimate load (*504 kN*) in relation to the unreduced model (*516 kN*), whereas the predicted nonlinear response of the beam being in favor of safety.

Finally, the required CPU time for the solution of *50* load steps for the three models is given in Table 6.7. It can be seen that the beam model requires negligible computational time in relation to the unreduced model completing the nonlinear analysis in only *5 sec* compared to *140 sec* for the RL *0* model and *103 sec* for the RL *1* model.

Model	*Time (sec)*
A	140.0
B	103.0
C	5.0

TABLE 6.7 RC BEAM SUPPORTED ON TWO SHEAR WALLS. COMPUTATIONAL TIMES FOR *50* LOAD STEPS.

6.4.2 RC Frame with Shear Wall

In order to have a more clear idea on the nonlinear behavior of hybrid models and conclude on the simulation of RC framed structures, a 3D RC frame is considered, where by using the four reduction levels the corresponding FE mesh models are derived. Fig. 6.26 shows the geometrical features of the frame, which has a net span of *5 m* and it consists of a shear wall (*200*x*25 cm*), a beam (*25*x*50 cm*) and a column (*50*x*25 cm*). The frame has a total height of *3.5 m* and its reinforcement details are given in Fig. 6.26. The material properties considered for this numerical test are given in Table 6.8. Two types of external loads are being applied: a) A vertical static linear concentrated load placed at the top of the shear wall and column, respectively; b) a horizontal static nonlinear load on the upper left region of the frame (Fig. 6.26).

The vertical loads V_1 and V_2 were assumed to be equal to the *20%* of the axial capacity of each structural member (*SW* and *C* in Fig. 6.26). These two vertical loads and the loads that derive from the self-weight of the structure are applied entirely at the first load step. The horizontal load H_1 is divided into *25* load steps and it is applied incrementally until failure.

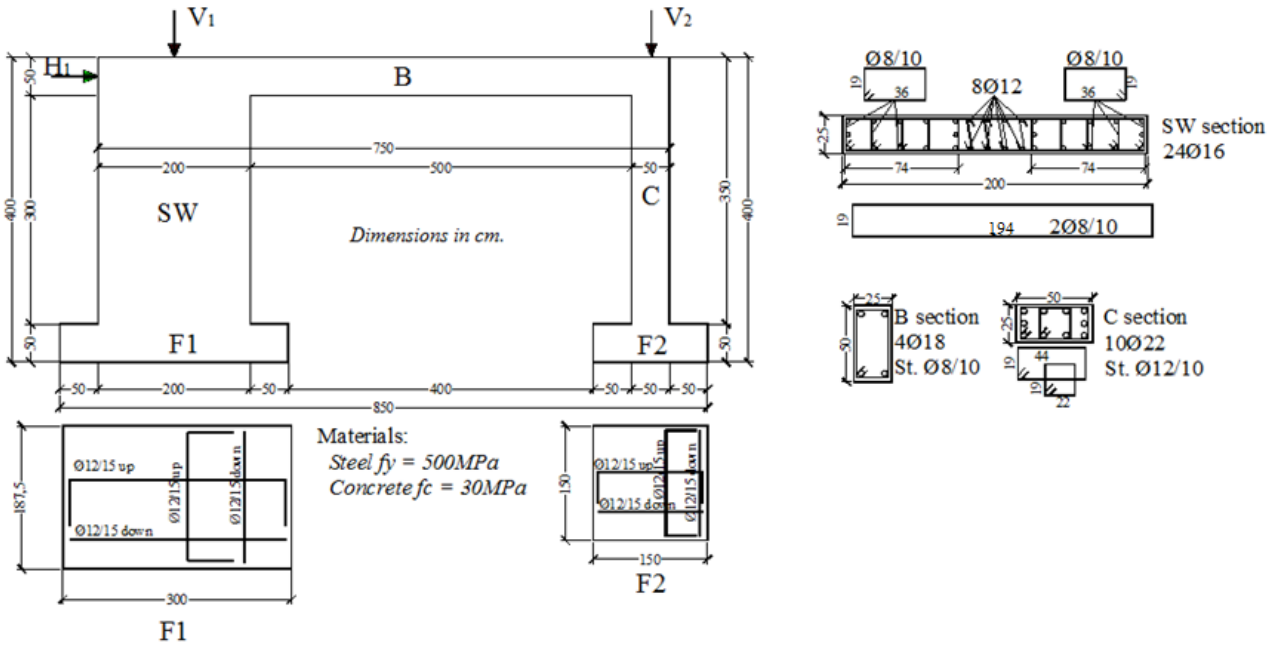

FIGURE 6.26 RC FRAME. GEOMETRIC FEATURES AND REINFORCEMENT DETAILS.

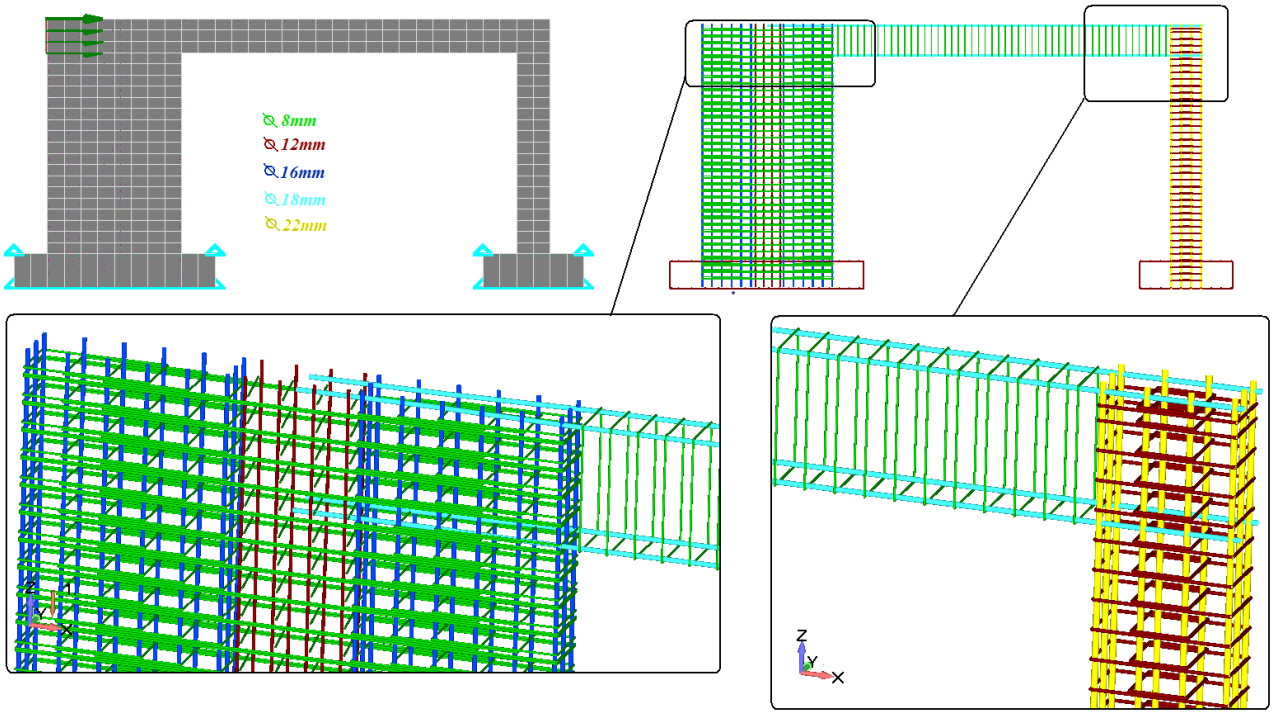

FIGURE 6.27 RC FRAME. FE MESH DETAILS.

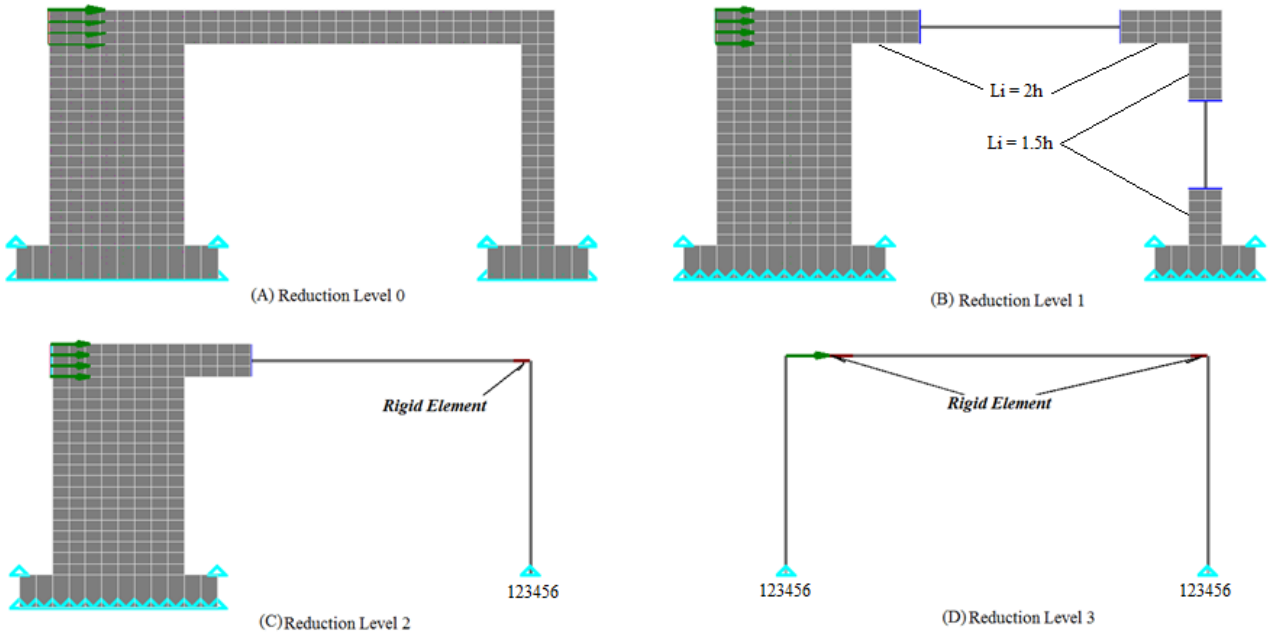

FIGURE 6.28 RC FRAME. FE MESHES.

The unreduced FE mesh is shown in Fig. 6.27, where the hexahedral brick elements and the initial reinforcement rebar elements are schematically presented. By performing the reduction process (RLs *1*, *2* and *3*), three additional FE meshes derive as illustrated in Fig. 6.28. As it can be seen from Figs. 6.27 and 6.28, the footing foundation of the RC frame was also modeled for the cases of RL *0*, *1* and *2* to make the analysis more realistic. The four FE model details concerning the number of each element type and dof are given in Table 6.9.

It is worth mentioning that the geometrical features of this frame requires a large number of hexahedral elements for the discretization of the shear wall. Thus the dof of RL *1* and *2* correspond to a decrease of *22.52%* and *37.52%*, respectively, compared to the initial unreduced model.

Material	*Young Modulus (GPa)*	*Hardening Modulus (GPa)*	*Yielding Stress (MPa)*	*Compressive Strength (MPa)*	*Poisson Ratio*
Concrete	28	-	-	30	0,17
Steel	190	1,9	500	-	0,3

TABLE 6.8 RC FRAME. MATERIAL DETAILS.

a/a	*Model*	*Hexahedral Elements*	*Embedded Rebar Elements*	*RC NBCFB Elements*	*Total Number of Dof*	*Dof Reduction (%)*
A	Reduction Level 0	576	6,608	-	3,150	-
B	Reduction Level 1	472	5,892	2	2,436	22.67
C	Reduction Level 2	384	5,104	2	1,968	37.52
D	Reduction Level 3	-	-	30	186	94.09

TABLE 6.9 RC FRAME. FE MESH DETAILS.

Fig. 6.29 compares the four load-displacement curves computed from the four different RL models. As can be seen, the obtained curve when using only beam elements is much stiffer than the other three, a nonlinear response attributed to the beam's formulation which neglects shear effects. It is evident that the beam model fails to predict the response as well as the inelastic branch of the curve compared to the computed response by the 3D detailed unreduced model. The inability of modeling the shear strains, 3D crack propagation and the three-dimensional internal stress state of the structure makes the beam model inadequate to model realistically this type of structures.

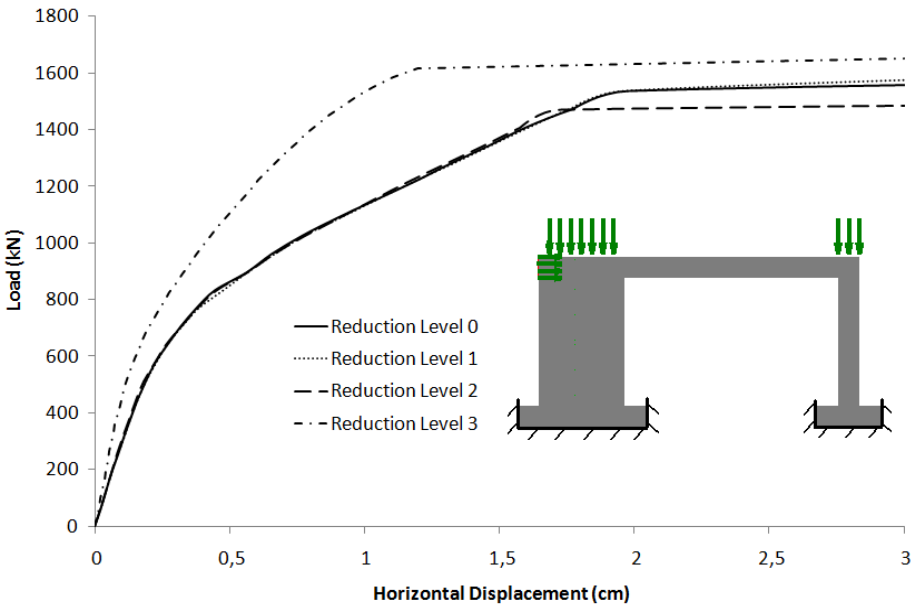

FIGURE 6.29 RC FRAME. *P-δ* CURVES.

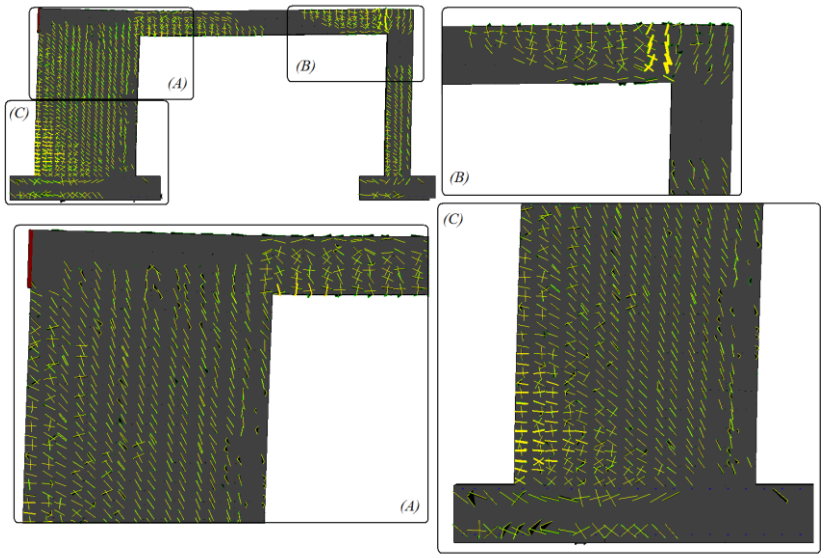

FIGURE 6.30 RC FRAME. CRACK PATTERN PRIOR TO FAILURE. REDUCTION LEVEL *0*.

On the contrary, the unreduced model shows a softer numerical behavior which results form the ability to account for shear strains and the accurate internal stress redistribution due to 3D cracking. Figs. 6.30 show the crack pattern of the RL *0* model prior to failure. As can be seen, the crack orientation is inclined especially at the shear wall region where shear strains are significant. Flexural cracks are observed at the lower left region of the base of the shear wall (Fig. 6.30c) and at the lower and upper regions of the left and right end sections of the beam, respectively (Figs 6.30a and 6.30b).

These critical regions are governed from tensile stresses which lead to flexural cracking, thus decreasing the stiffness of the structure. The failure mechanism was initiated when longitudinal reinforcement located at the end sections of the beam reached their maximum strain capacity (*8%*). After the tensile failure of the longitudinal reinforcement, the redistribution of the internal stresses caused excessive cracking which eventually led to the frame failure.

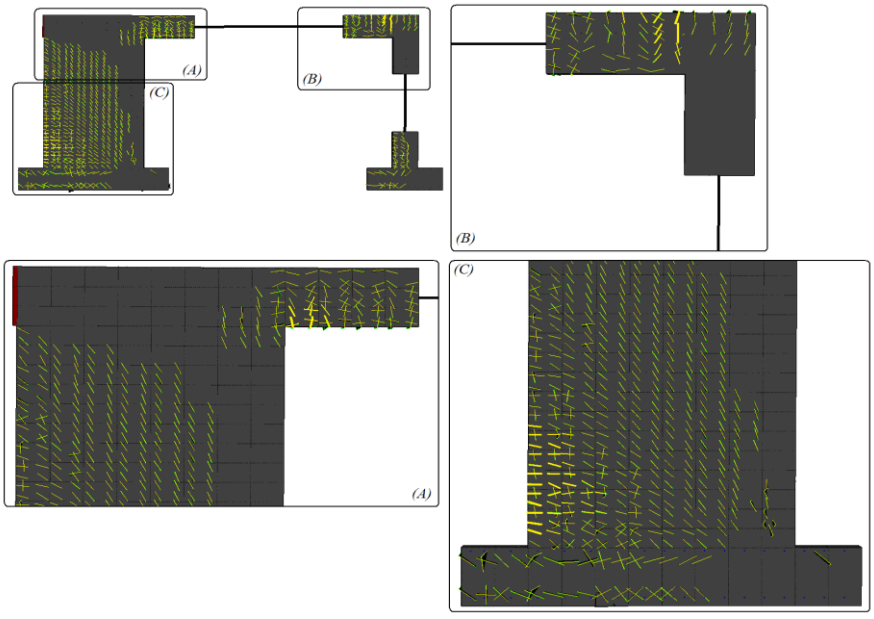

FIGURE 6.31 RC FRAME. CRACK PATTERN PRIOR TO FAILUERE. REDUCTION LEVEL *1*.

RL *1* model manages to predict an acceptable nonlinear response of the frame, without any significant deviations with regard to the unreduced model. As can be seen in Fig. 6.29, the two curves are in an almost absolute correlation, except a slight deviation at the final stage of loading where the hybrid model appears to have a slightly stiffer behavior. This numerical behavior is attributed to the inability of the beam model to account for shear strains, thus they are unable to capture the stiffness degradation due to the inclined cracks

observed at the mid-span of the column and beam which can be seen in Fig. 6.30 for the RL *0* model. On the other hand, RL *2* model, appears to have a premature failure which is attributed to the numerical phenomenon described in the previous section. Thus the stiffer beam model fails to capture the stiffness degradation retaining its initial stiffness, leading to a strain concentration at the domain modeled with the 3D detailed elements. This strain concentration led to the increased crack openings at the left end region of the beam when the loading level reached the ultimate capacity of RC frame where the shear strains are significant, resulting to a premature failure. The corresponding predicted failure loads and computational times for the solution of the four models are given in Table 6.10.

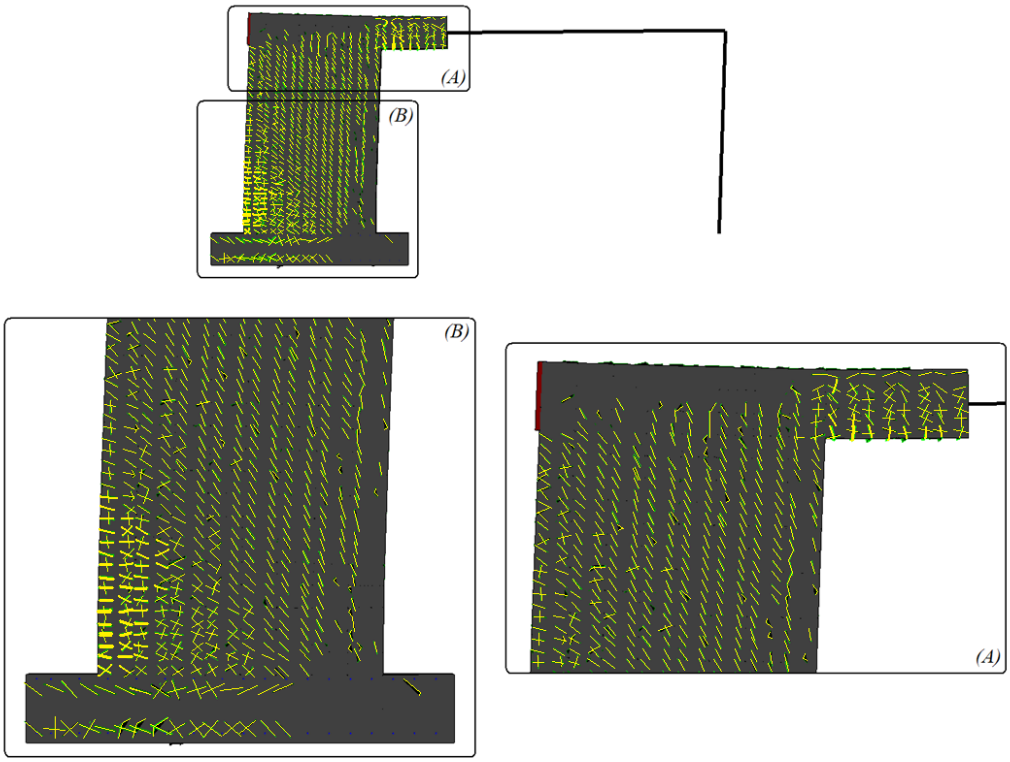

FIGURE 6.32 RC FRAME. CRACK PATTERN PRIOR TO FAILUERE. REDUCTION LEVEL *2*.

	Model	*Predicted Ultimate Horizontal Load (kN)*	*Horizontal Displacement (cm)*	*Number of Load Increments*	*CPU Time (sec)*	*Reduction in CPU Time (%)*
A	Reduction Level 0	1,600	5.94	25	167	-
B	Reduction Level 1	1,600	3.87	25	110	34.1
C	Reduction Level 2	1,536	9.74	24	76	54.5
D	Reduction Level 3	1,650	3.10	25	4	> 98

TABLE 6.10 RC FRAME. PREDICTED ULTIMATE LOADS, HORIZONTAL DISPLACEMENT AND REQUIRED CPU TIME FOR DIFFERENT RL MODELS.

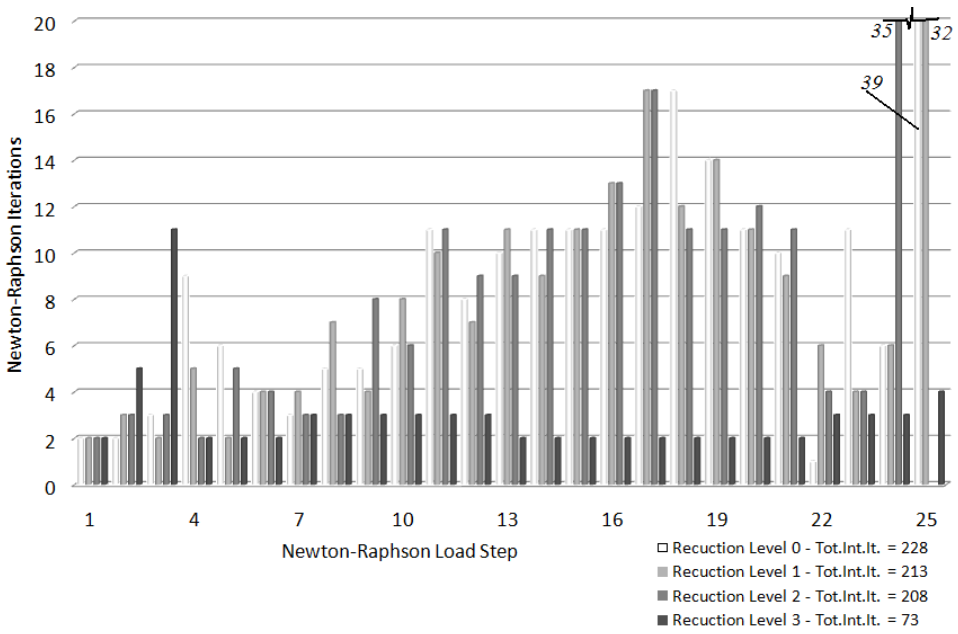

FIGURE 6.33 RC FRAME. NR ITERATIONS PER LOAD STEP FOR THE UNREDUCED AND HYBRID FE MODELS.

The required CPU time for the solution of *25* load increments was *167 sec* for the case of the unreduced FE model, which demonstrates the computational efficiency of the developed FEA code. The corresponding computational times for the case of the RL *1* and *2* models were *110 and 75 sec*, respectively. As depicted in Table 6.10, the reduction in CPU time was greater than the corresponding reduction of the models' dof. This is attributed to the required NR iterations for each model, thus implying the corresponding numerical stability of the reduction schemes.

Fig. 6.33 shows the required NR iteration per load increment for the different FE models. It is not very clear which model display the more stable behavior. For this reason, the total NR iterations were counted in order to have a better perspective of the numerical overall behavior. As can be seen in Fig. 6.33, as the RL increases, the required NR iterations are decreased. It can be observed that minimum NR iterations are required when the NBCFB elements are used exhibiting maximum numerical stability, attributed to the internal state formulation described in Chapter 2.

The von Mises strain contours between the different FE models are illustrated in Figs. 6.34 for two different load levels (*40%* and *92%*, respectively). As can be seen from this Fig. 6.34, the different FE models are in a good agreement between them verifying the observation made through their computed load-displacement curves. It is noteworthy to say that, the schematic representation of the resulted crack patterns and deformed rebar elements as shown in Fig. 6.35 is significant for the verification of the correctness of the output data. Dealing with thousands of nodes, a simple load-displacement curve may not give the proper insight into the correctness of the computed simulation. The corresponding deformations were increased *50* times in order to facilitate the detection of any inconsistency in the deformed mesh.

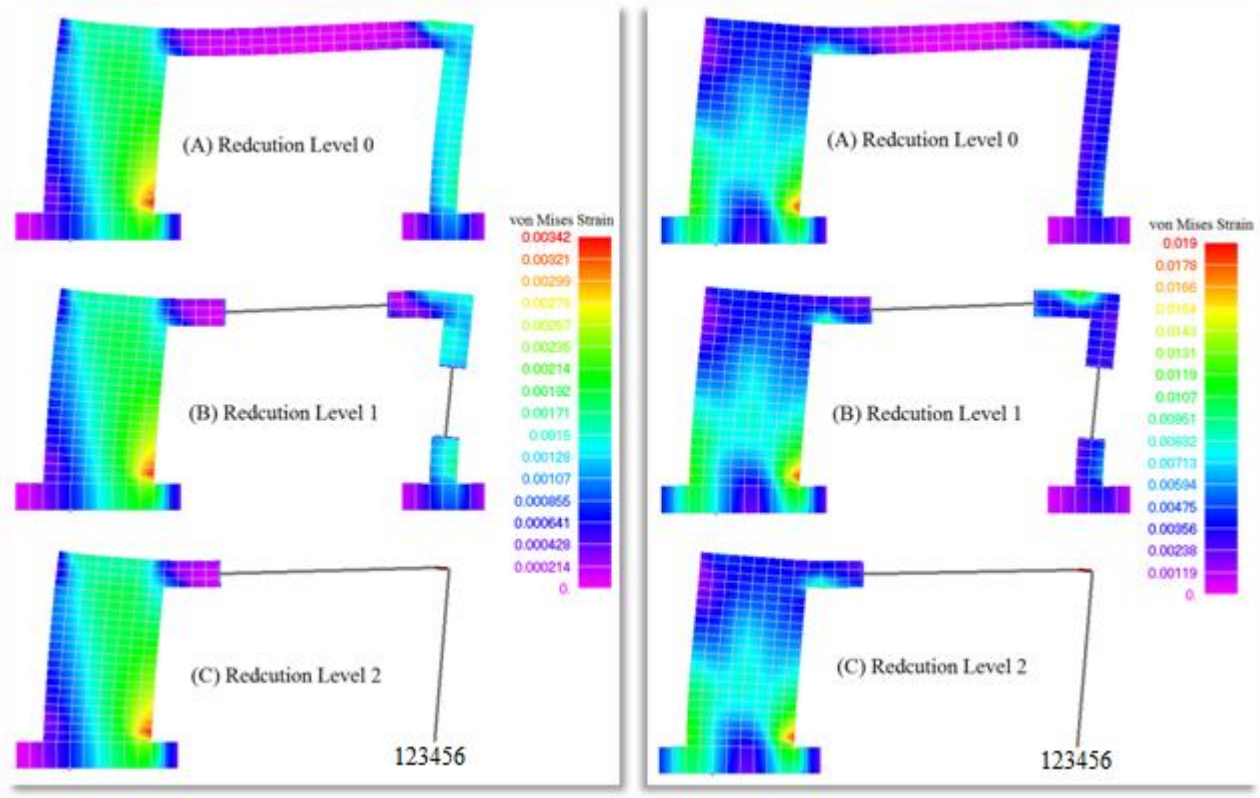

FIGURE 6.34 RC FRAME. VON MISES STRAIN CONTOURS AND DEFORMED SHAPES FOR DIFFERENT FE MODELS. LEFT: *40%* (STEP *10*) AND RIGHT: *92%* (STEP *23*) OF THE ULTIMATE LOAD CAPACITY.

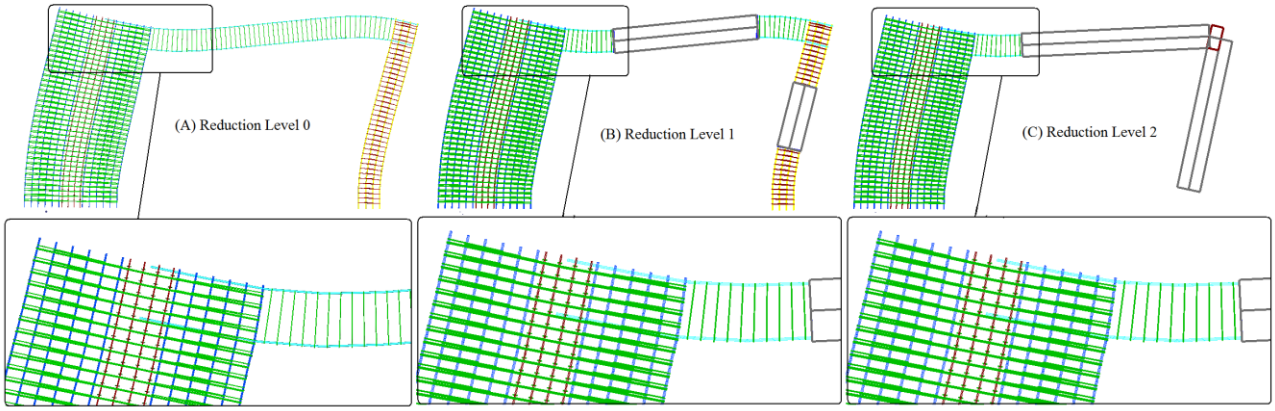

FIGURE 6.35 RC FAME. DEFORMED SHAPES OF REINFORCED REBAR ELEMENTS FOR DIFFERENT FE MODELS (STEP *23*). DEFORMATIONS ARE SCALED X*50*.

6.4.3 3-Storey RC Frame

This numerical test results from an approximate fourfold increase of the RC frame described in section 6.4.2. As illustrated in Fig. 3.36, the RC frame has *3* stories of *3.5 m* height and two openings with a constant span of *5 m*. The material characteristics and the reinforcement details are shown in Fig. 3.36 and the loading conditions are considered to be as in the previous numerical test, a vertical fixed and a horizontal varying load sets that are distributed at each storey according to EC8. The horizontal loading is divided in *20* load increments which are implemented using the force-control NR solution scheme with the energy criterion tolerance set

to 10^{-4}. It is important to note that the force-control NR scheme is less stable, regarding its convergence features. Thus, the ability of solving ill-posed numerical problems, to capture their nonlinear response, illustrates the numerical robustness of the proposed modeling method and of the developed FEA code.

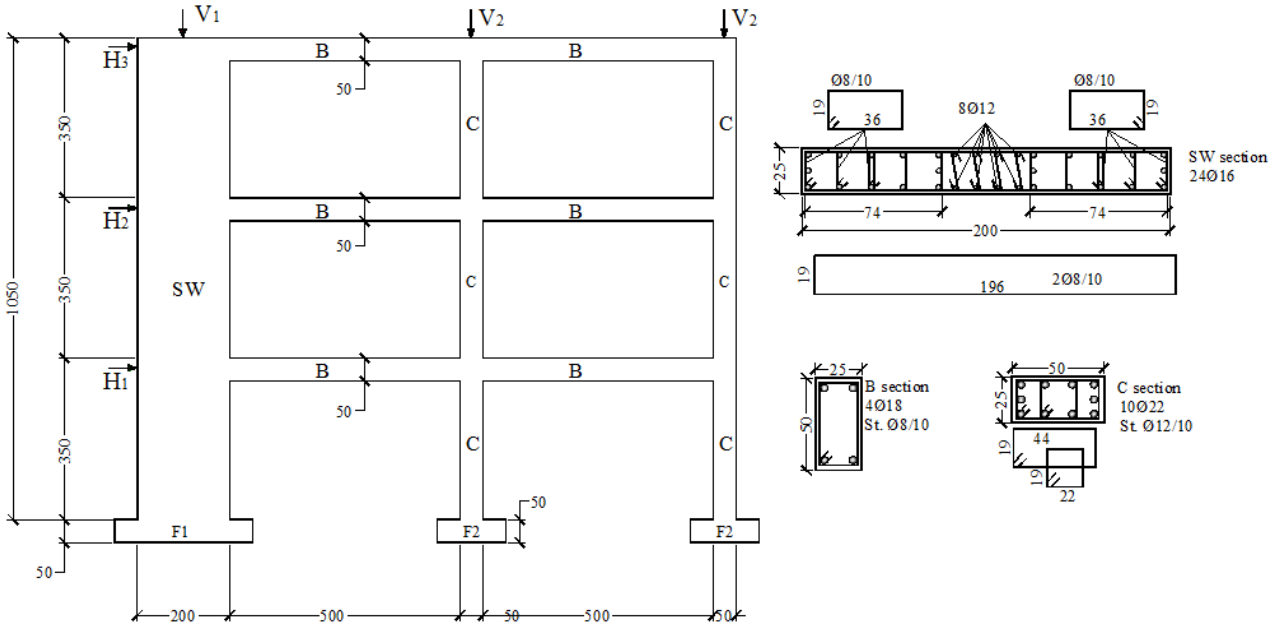

FIGURE 6.36 3-STOREY RC FRAME. GEOMETRIC FEATURES AND REINFORCEMENT DETAILS.

Details concerning the FE mesh are given in Table 6.11, where it can be seen that the unreduced model consists of *2,298* hexahedral and *23,264* embedded elements which result into a total of *12,938* dof. It must be mentioned that, as a result of the embedded rebar elements' formulation, no additional dof are induced due to the rebar elements. By performing the reduction procedure, three additional reduced FE models RL *1*, RL *2*, RL *3* are derived which are shown in Figs. 6.37. If we compare the reduction of the dof with the previous numerical test, it can be observed that by applying the same reduction schemes the resulting reduction is larger. This is attributed to the number of columns and beams which is larger corresponding to the number of shear walls for this FE model. Therefore, the reduction is performed to a larger number of structural members leading to a significant reduction of the size of the corresponding FE models (*31.9* and *55.6%* less dof for the RL *1* and *2* respectively).

a/a	*Model*	*Hexahedral Elements*	*Embedded Rebar Elements*	*RC NBCFB Elements*	*Total Number of Dof*	*Dof Reduction (%)*
A	Reduction Level 0	2,298	23,264	-	12,938	-
B	Reduction Level 1	1,674	18,946	12	8,816	31.9
C	Reduction Level 2	1,122	14,372	12	5,748	55.6
D	Reduction Level 3	-	-	162	936	92.8

TABLE 6.11 3-STOREY RC FRAME. FE MESH DETAILS.

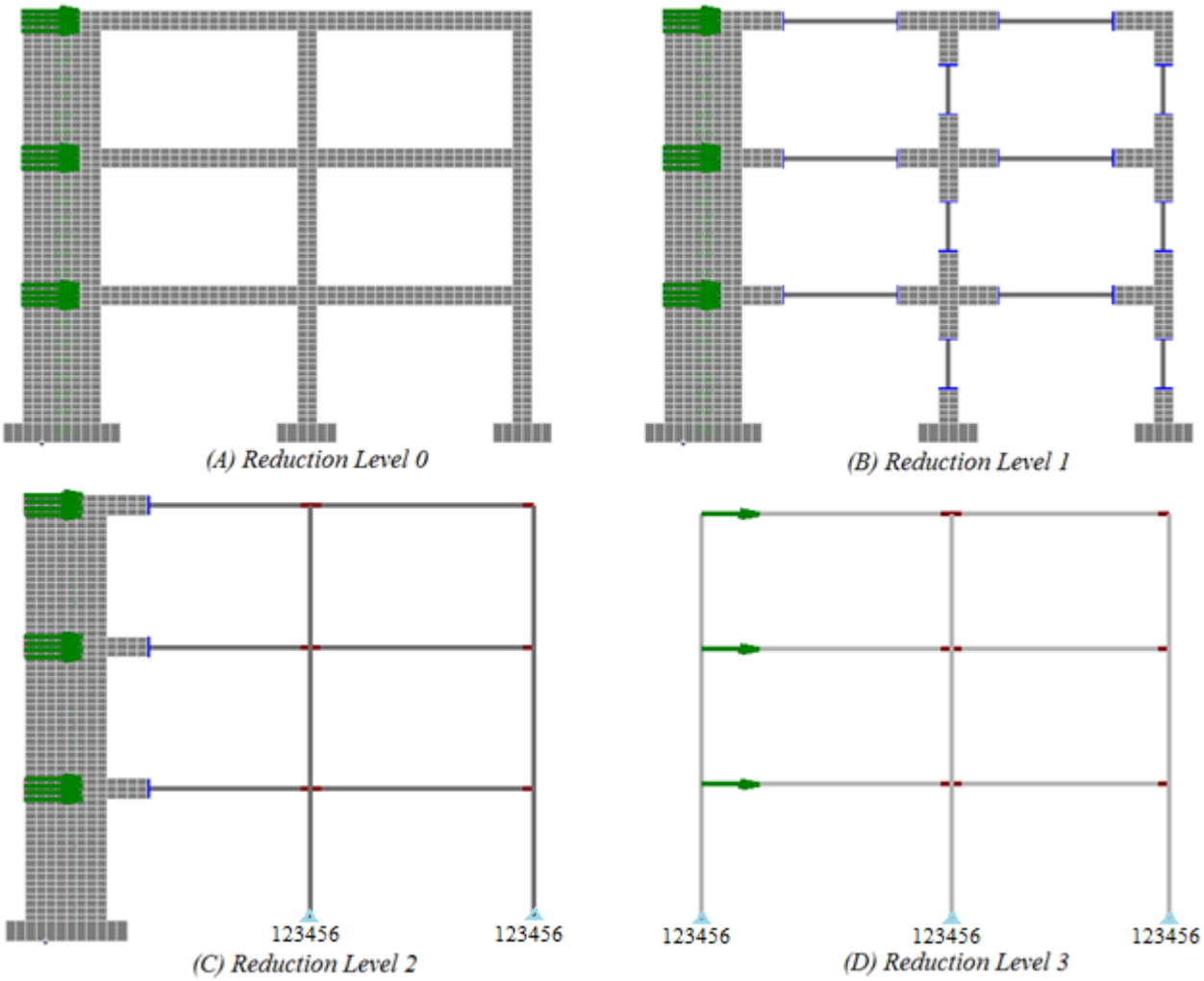

FIGURE 6.37 3-STOREY RC FRAME. FE MODELS.

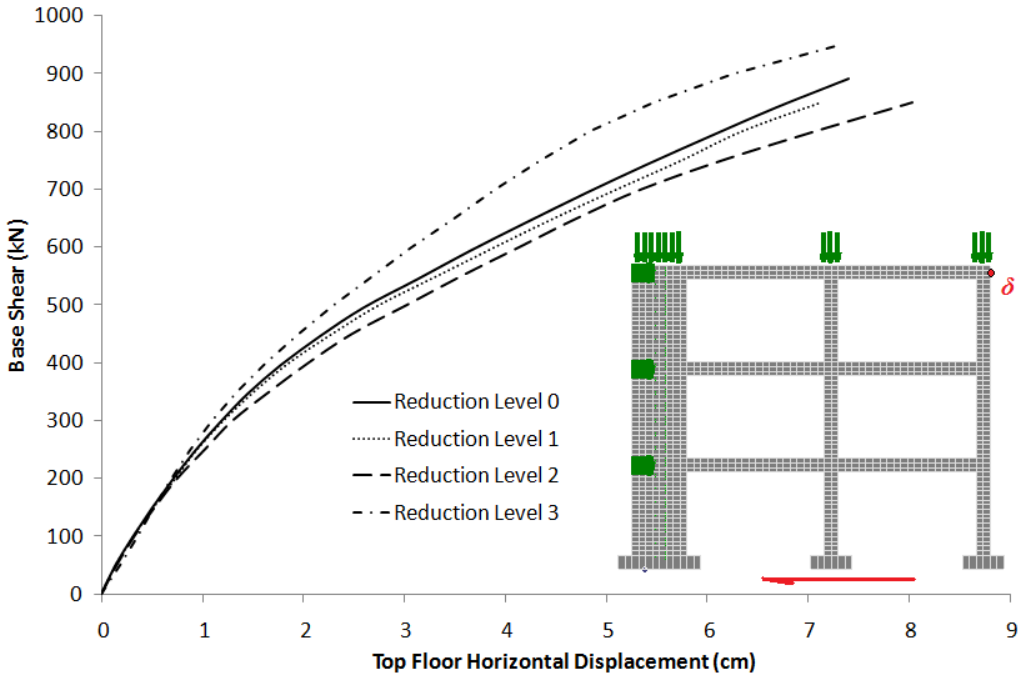

FIGURE 6.38 3-STOREY RC FRAME. *P-δ* CURVES.

Fig. 6.38 shows the computed equilibrium paths predicted from each FE model. The computed curves correspond to the top floor horizontal displacements (Fig. 6.38) and the corresponding total base shear force. As it can be observed, the beam model overestimates the initial stiffness of the RC frame exhibiting a stiffer behavior throughout the analysis procedure. This is attributed to the formulation of the beam element which does not account for the shear strain effects and 3D cracking of concrete, thus important features that reduce the stiffness of RC during its loading history are neglected.

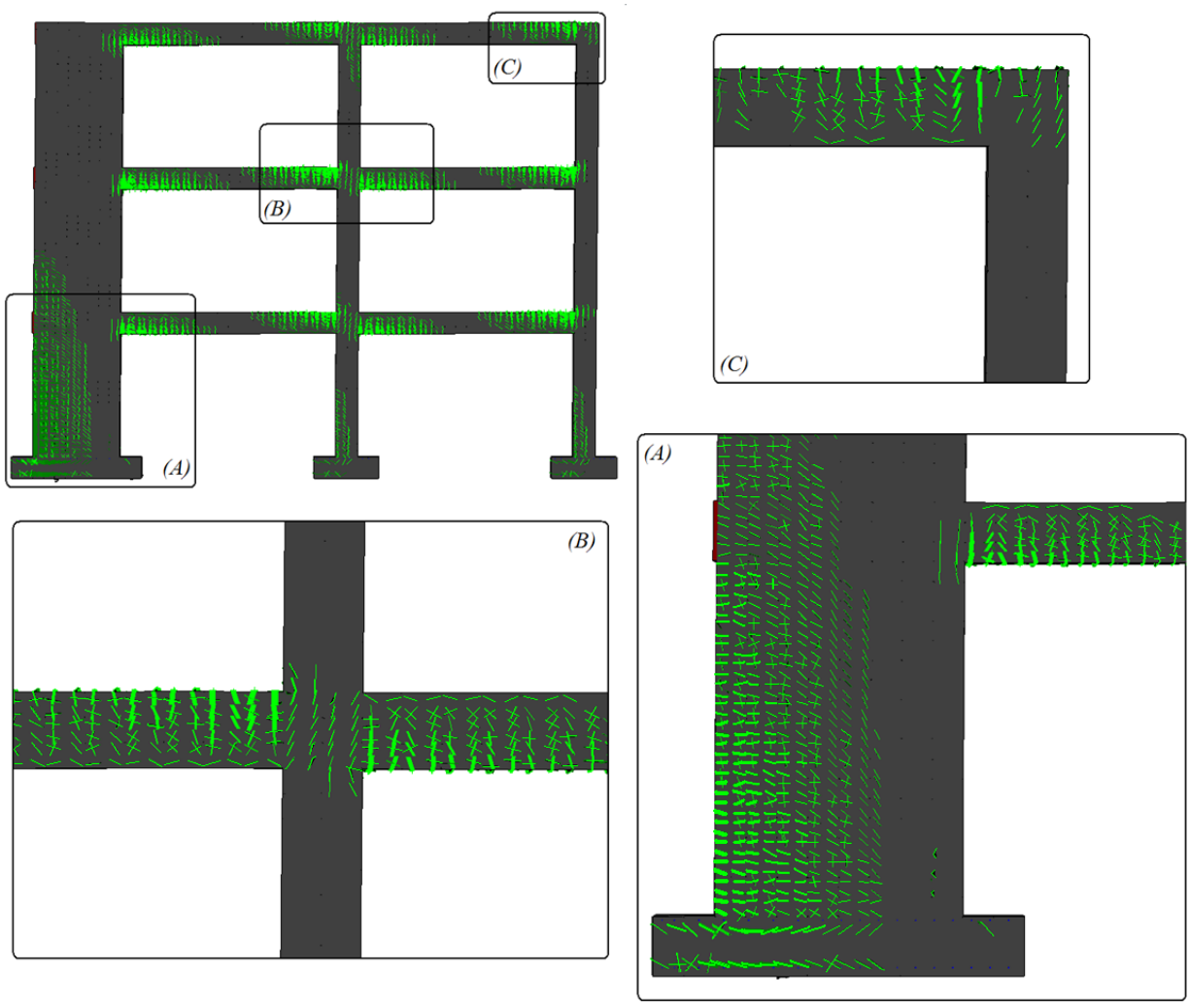

FIGURE 6.39 3-STOREY RC FRAME. CRACK PATTERN PRIOR TO FAILURE. REDUCTION LEVEL *0*.

This deficiency results from the loss of important local phenomenon which take place in critical regions of the structure such as cross joints. When shear stresses increase significantly at these regions, inclined crack patterns occur resulting in significant stiffness degradation of the overall structure. Even though the fiber beam takes into account cracking of concrete by setting equal to zero the corresponding Young modulus of the cracked fiber which is always vertical to the longitudinal axis of the beam, it fails to capture the local phenomena which take place in shear dominated critical regions (Figs. 6.39b and 6.39c) and are affected by 3D stress and strain states.

Fig. 6.39c shows the crack pattern of the shear wall and the left end of the beam which is supported on the shear wall. As it can be seen, the crack pattern of the beam member is vertical to its longitudinal axis characterizing the flexural nature of the crack evolution attributed to the bending moment acting on this region. A similar observation can be seen for the case of the shear wall which is dominated by horizontal cracks. This changes as the cracks propagate toward the compressive region of the shear wall section where inclined cracks can be observed. This local phenomenon characterizes the shear strain effect and the ability of 3D crack modeling which plays a significant role in modeling the nonlinear behavior of RC structures.

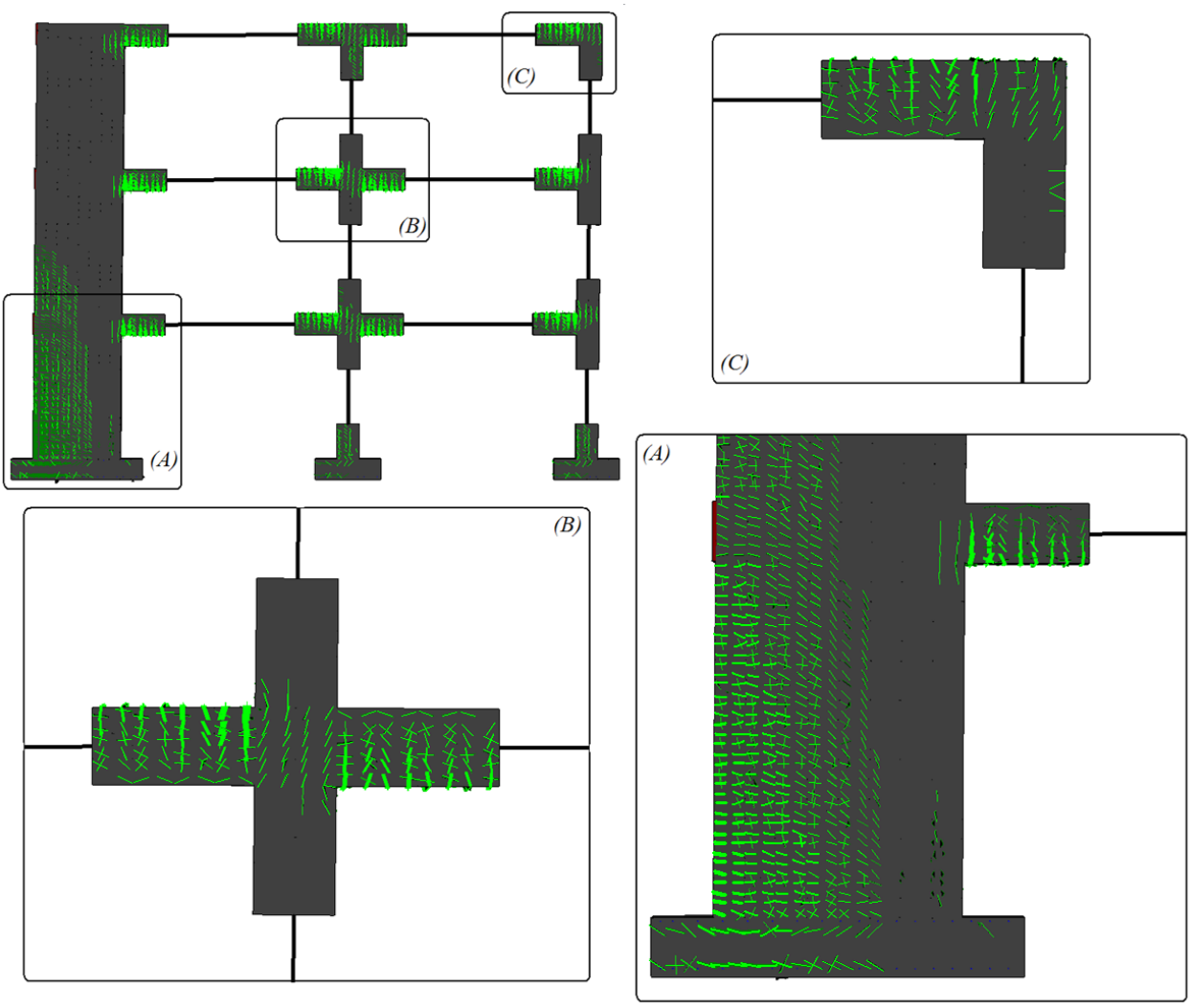

FIGURE 6.40 3-STOREY RC FRAME. CRACK PATTERN PRIOR TO FAILURE. REDUCTION LEVEL *1*.

The horizontal cracks which initiate at the base of the shear wall spread along the shear wall's height (Figs. 6.39, 6.40 and 6.41). Furthermore, a very important observation regarding local phenomenon that take place between steel plate-concrete interfaces can be made from Figs. 6.39a, 6.40a and 6.41a. It can be observed that the cracks pass through the region located at the steel plate which was used for applying the horizontal loads at the first storey. It is evident that the crack openings at this region are restrained from the steel plate which induces additional confinement at this specific region.

Figs. 6.40 and 6.41 illustrate the crack patterns prior to failure, as predicted by the RL *1* and *2* models. A good correlation is observed between the crack patterns in relation to the unreduced model, managing to capture the different type of local phenomenon (flexural and inclined cracks, crack restraint due to the steel plate).

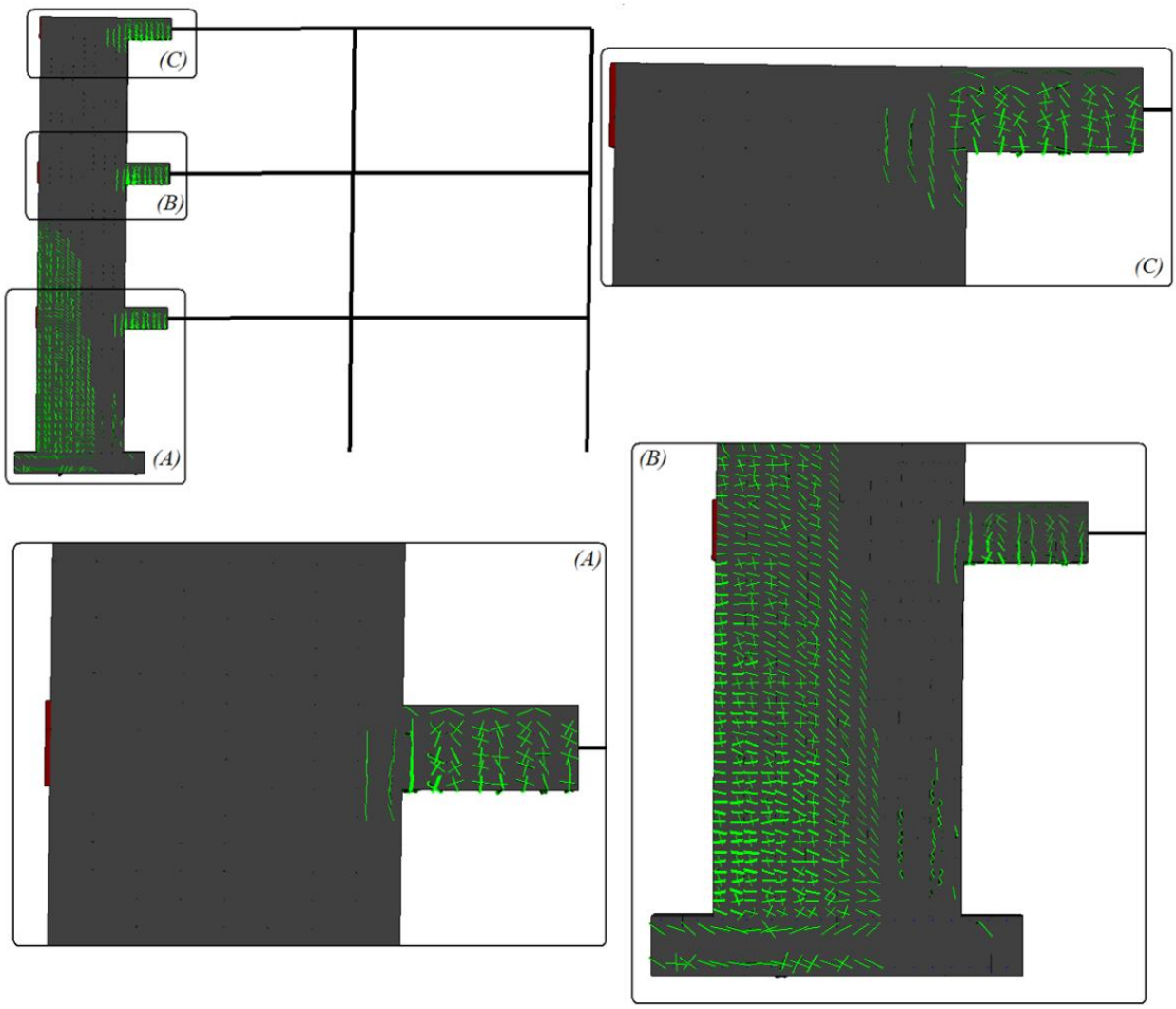

FIGURE 6.41 3-STOREY RC FRAME. CRACK PATTERN PRIOR TO FAILURE. REDUCTION LEVEL *2*.

The final observation regarding the computed nonlinear response of the 3-storey RC frame with the four different FE models concerns the correlation between the curves shown in Fig. 6.38. The FE models which derive from the implementation of the reduction schemes appear to be softer than the corresponding unreduced model. This is attributed to the numerical phenomenon observed for the clamped beam (Fig. 6.15) which is a result of the strain concentration at the softer domains of the FE model when the hybrid models are considered (Fig. 6.42c). The numerical results of this test verify the above observation and as it was stated previously are in favor of safety.

The computational times for the solution procedures are given in Table 6.12, where it can be seen that the unreduced model requires *38 min* to perform *18* load increments. It must be noted that a total horizontal load of *1,000 kN* was applied in *20* load increments until failure. It is indisputable that the beam model is much faster than any type of hybrid model. In addition to

that, the reduction in CPU time is once more greater than the corresponding dof reduction, illustrating the robustness induced when the HYMOD schemes are implemented. The reduction in CPU time given in Table 6.12 refers to the CPU time per load increment, since the second and third FE models managed to reach *17* load increments instead of *18*.

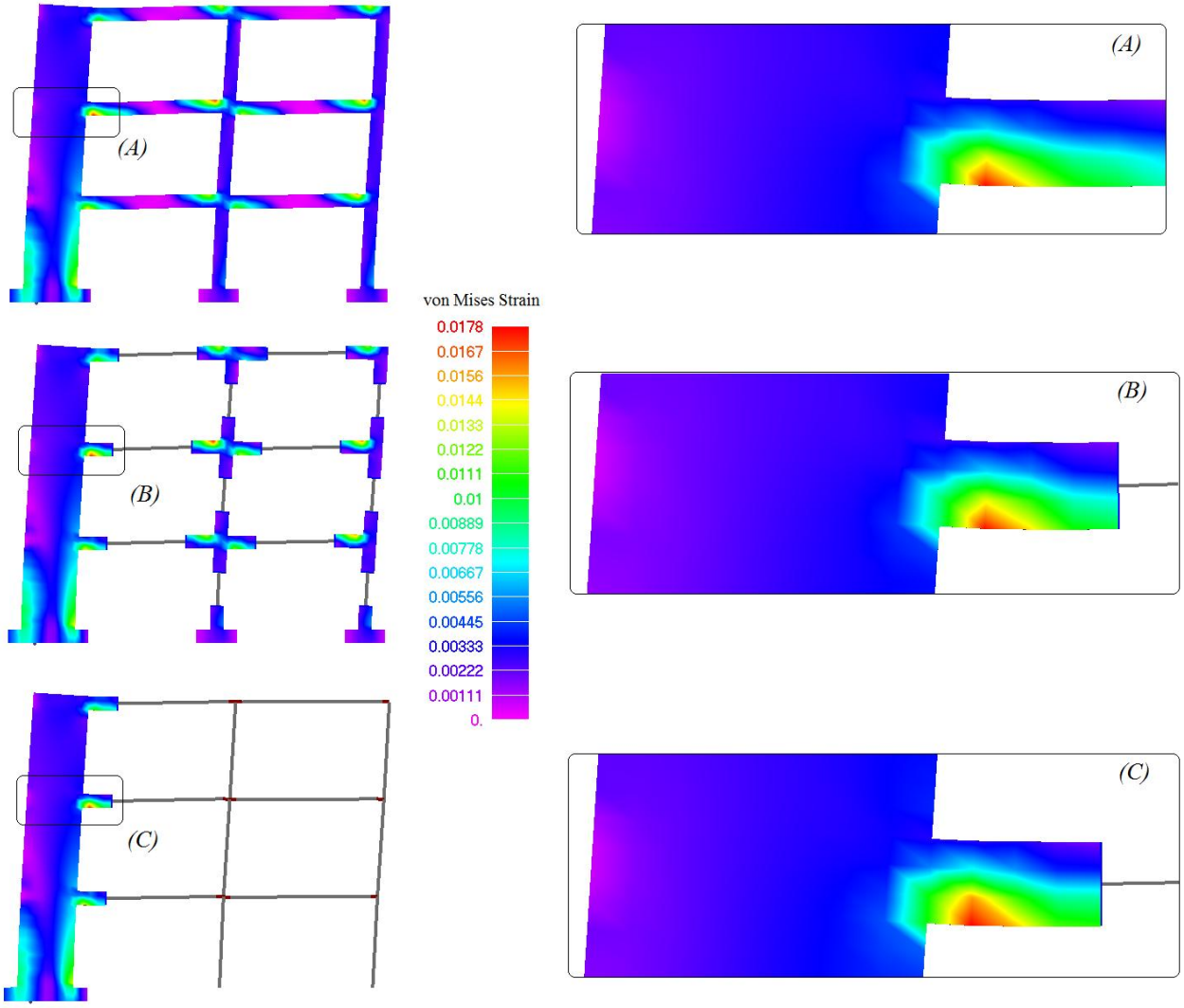

FIGURE 6.42 3-STOREY RC FRAME. VON MISES STRAIN CONTOUR AT LOAD INCREMENT *17*.

a/a	*Model*	*Number of Load Increments*	*CPU Time (min)*	*CPU Time per Load Increment (sec)*	*Reduction in CPU Time (%)*
A	Reduction Level 0	18	38	127	-
B	Reduction Level 1	17	17	60	52.6
C	Reduction Level 2	17	7	25	80.3
D	Reduction Level 3	19	10sec	-	>99

TABLE 6.12 3-STOREY RC FRAME. CPU TIME FOR THE SOLUTION PROCEDURE.

6.4.4 Full-Scale 2-Storey RC Building

The aim of this final numerical test is to demonstrate the ability of the proposed modeling method to analyze the nonlinear behavior of full-scale RC structures. A full-scale 2-storey RC building (Fig. 6.43) is seismically assessed after it was designed with the use of a commercial Civil Engineering software. The design code used by the software for the reinforcement computations was the Greek Seismic Code[250]. After the completion of the structure's design process with the commercial software, the resulted reinforcement details shown in Table 6.13 were used for the construction of four FE models shown in Figs. 6.45, 6.46 and 6.47, which are derived from the implementation of the four RL schemes. The details on the reinforcement of the beams and columns are given in Tables 6.13, 6.14 and Fig. 6.44.

a/a	*Dimensions (cm)*	*Rebars*		*Additional Left*		*Additional Right*		*Rebars for Torsion*	*Stirrups*		
		Up	*Down*	*Up*	*Down*	*Up*	*Down*		*Left*	*Middle*	*Right*
1	25x50	2 Ø14	3Ø14	2Ø18	-	-	-	-	Ø8/10	Ø8/10	Ø8/10
2	25x50	2 Ø14	3Ø14	-	-	2Ø18	-	-	Ø8/10	Ø8/10	Ø8/10
3	25x50	2 Ø14	3Ø16	2Ø18	-	-	-	2Ø12	Ø8/10	Ø8/10	Ø8/10
4	25x50	2 Ø14	3Ø14	-	-	-	-	2Ø12	Ø8/10	Ø8/10	Ø8/10
5	25x50	2 Ø14	3Ø14	-	-	2Ø18	-	2Ø12	Ø8/10	Ø8/10	Ø8/10
6	25x50	2 Ø14	3Ø14	2Ø18	-	2Ø18	-	-	Ø8/10	Ø8/10	Ø8/10
7	25x50	2 Ø14	3Ø14	2Ø20	-	2Ø20	-	2Ø12	Ø8/10	Ø8/10	Ø8/10
8	25x50	2 Ø14	3Ø14	2Ø18	-	-	-	2Ø12	Ø8/10	Ø8/10	Ø8/10
9	25x50	2 Ø14	3Ø14	-	-	2Ø18	-	-	Ø8/10	Ø8/10	Ø8/10
10	25x50	2 Ø14	3Ø14	2Ø18	-	2Ø18	-	2Ø12	Ø8/10	Ø8/10	Ø8/10
11	25x50	2 Ø14	3Ø14	2Ø18	-	2Ø18	-	2Ø12	Ø8/10	Ø8/10	Ø8/10
12	25x50	2 Ø16	3Ø16	3Ø20	-	-	-	-	Ø8/10	Ø8/10	Ø8/10
13	25x50	2 Ø14	3Ø14	-	-	2Ø18	-	2Ø12	Ø8/10	Ø8/10	Ø8/10
14	25x50	2 Ø14	3Ø14	2Ø18	-	-	-	2Ø12	Ø8/10	Ø8/10	Ø8/10
15	25x50	2 Ø14	3Ø14	-	-	2Ø18	-	2Ø12	Ø8/10	Ø8/10	Ø8/10
16	25x50	2 Ø14	3Ø14	2Ø18	-	2Ø20	1Ø14	2Ø12	Ø8/10	Ø8/10	Ø8/10

TABLE 6.13 2-STOREY RC BUILDING. REINFORCEMENT DETAILS OF THE BEAMS. STOREY *1* AND *2*.

Footing ID	*Dimensions (cm)*	*Height (cm)*	*Rebars X-axis*	*Rebars Y-axis*
1	125x150	50	Ø12/15	Ø12/15
2	125x150	50	Ø12/15	Ø12/15
3	125x150	50	Ø12/15	Ø12/15
4	125x200	50	Ø12/15	Ø12/15
5	175x125	50	Ø12/15	Ø12/15
6	125x175	50	Ø12/15	Ø12/15
7	125x200	50	Ø12/15	Ø12/15
8	200x125	50	Ø12/15	Ø12/15
9	300x275	50	Ø12/15	Ø12/15
10	125x150	50	Ø12/15	Ø12/15
11	225x125	50	Ø12/15	Ø12/15

TABLE 6.14 2-STOREY RC BUILDING. REINFORCEMENT DETAILS OF THE FOOTING FOUNDATION.

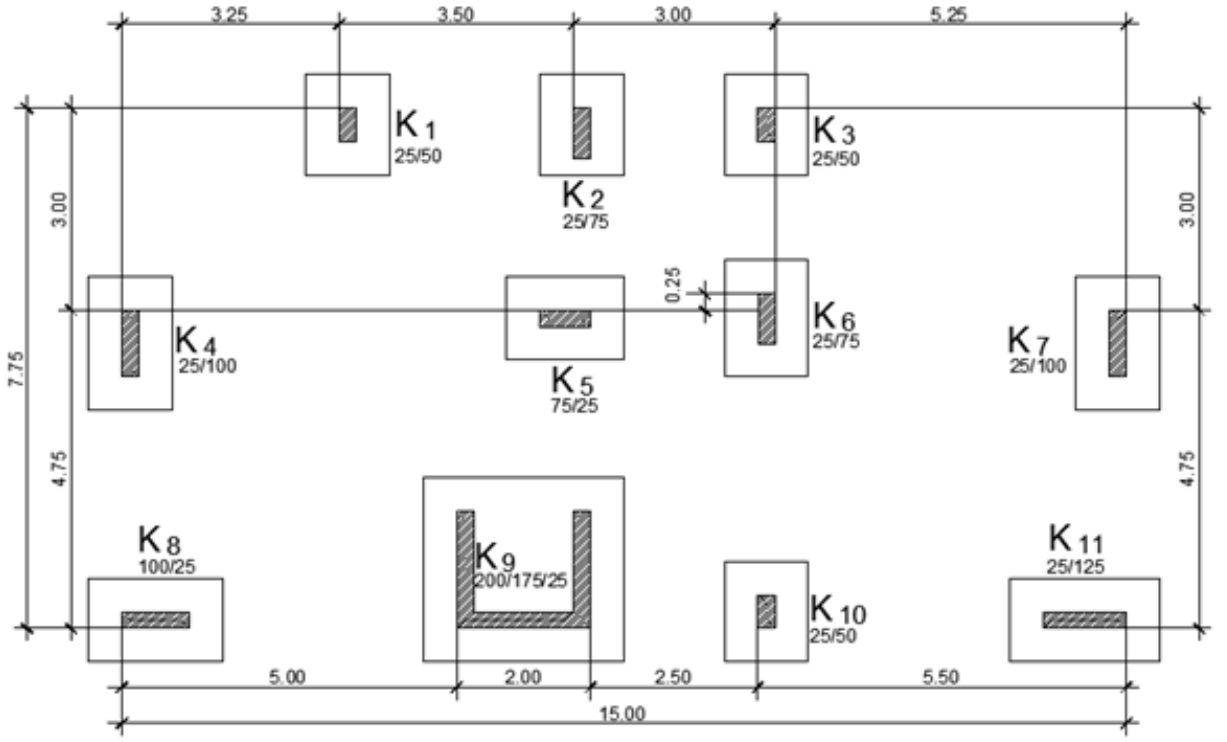

Plan View 0 - Footing Foundation

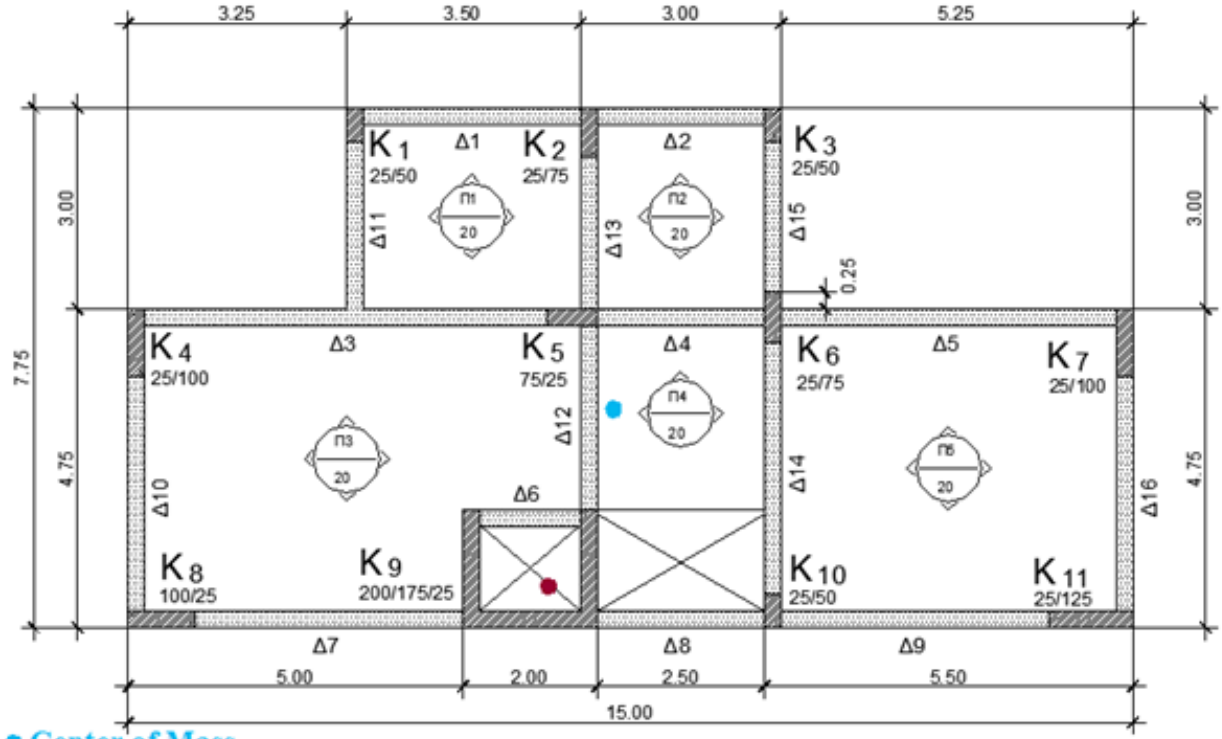

Plan View 1

FIGURE 6.43 2-STOREY RC BUILDING. FRAMING PLANS.

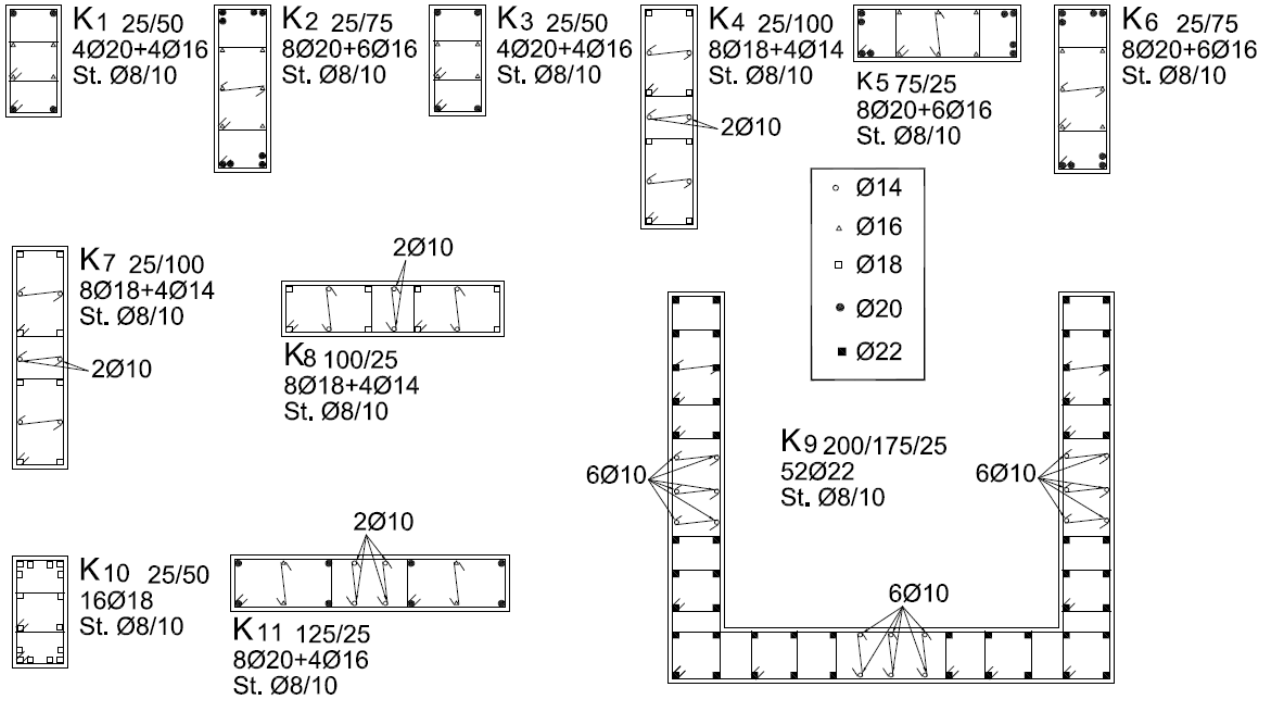

FIGURE 6.44 2-STOREY RC BUILDING. REINFORCEMENT DETAILS OF THE COLUMNS AND SHEAR WALLS.

As it can be seen in Fig. 6.43, the building has an irregular shape and stiffness distribution resulting to a considerable deviation between the center of mass and the corresponding stiffness center along the *Y* axis. The position of the center of elastic rotation is governed by the shear wall core which is positioned at the lower boundary of the architectural plan view of the building, resulting to a considerable abnormality on the stiffness distribution. Shear walls K_4, K_7, K_8 and K_{11} are positioned at the four boundary corners of the structure whereas the rest of the vertical structural members are considered to have standard column sections (Fig. 6.44). The height of both storeys is *3 m*. Material details used in the design and analysis process are given in Table 6.15.

Material	*Young Modulus (GPa)*	*Hardening Modulus (GPa)*	*Yielding Stress (MPa)*	*Compressive Strength (MPa)*	*Poisson Ratio*
Concrete	30	-	-	30	0,2
Steel	210	2.1	500	-	0,3

TABLE 6.15 2-STOREY RC BUILDING. MATERIAL DETAILS.

α/α	*Model*	*Hexahedral Elements*	*Embedded Rebar Elements*	*RC NBCFB Elements*	*Total Number of Dof*	*Dof Reduction (%)*
A	Reduction Level 0	4,382	51,064	-	30,036	-
B	Reduction Level 1	3,398	41,235	44	21,762	27.55
C	Reduction Level 2	2,312	29,042	92	15,282	49.12
D	Reduction Level 3	-	-	298	1,416	95.29

TABLE 6.16 2-STROREY RC BUILDING. FE MESH DETAILS.

Table 6.16 contains the FE mesh details of the four FE models shown in Figs. 6.45 and 6.47. The unreduced model consists of *4,382* hexahedral elements and *51,064* embedded rebar elements. When the RL *1* and *2* correspond to a reduction of *27.55%* and *49.12%*, respectively, in the dof compared to the detailed model. It must be noted that all footing foundations are considered to be fixed. This is achieved by restraining all the nodes located at the external boundary of each footing (Fig. 6.48).

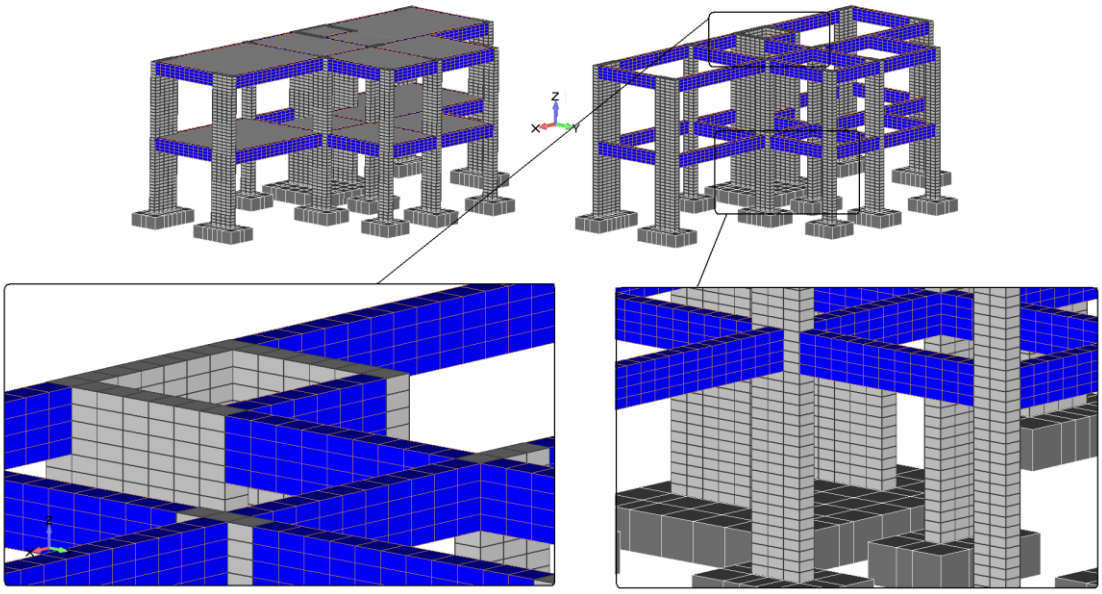

FIGURE 6.45 2-STOREY RC BUILDING. HEXAHEDRAL FE MESH OF THE RL *0* MODEL.

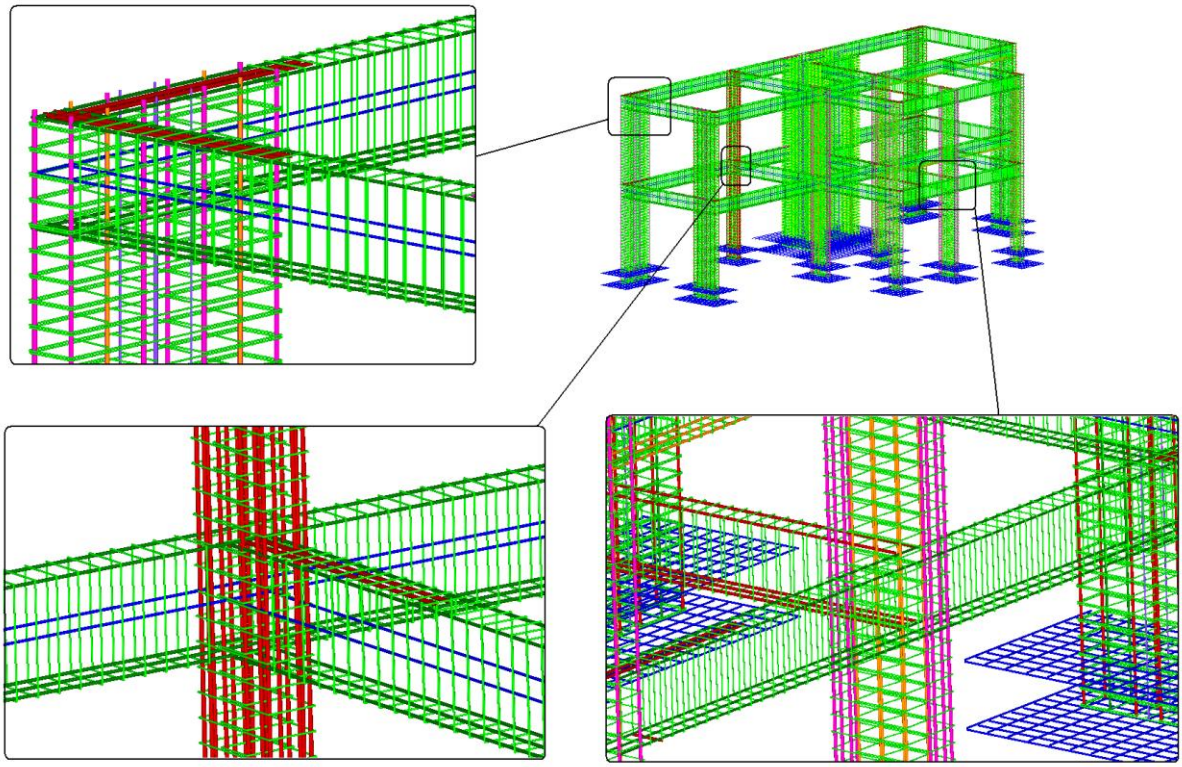

FIGURE 6.46 2-STOREY RC BUILDING. FE MESH OF THE REINFORCEMENT REBAR ELEMENTS. REDUCTION LEVEL *0*.

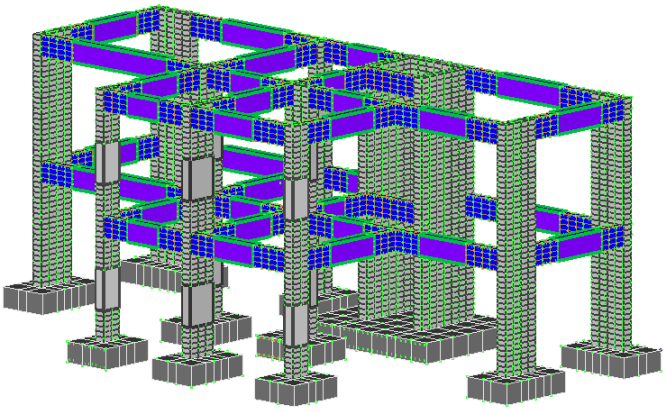

(A) Reduction Level 1

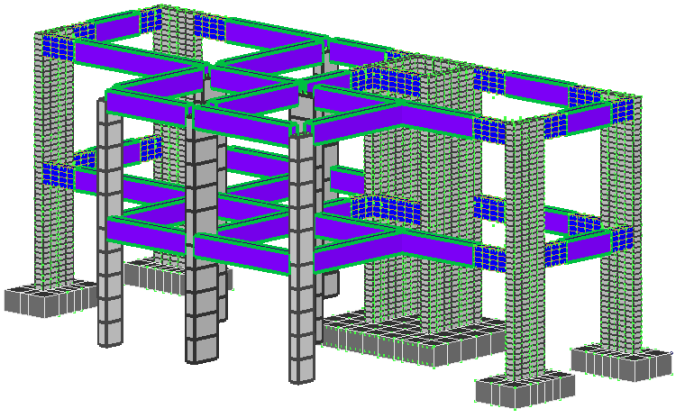

(B) Reduction Level 2

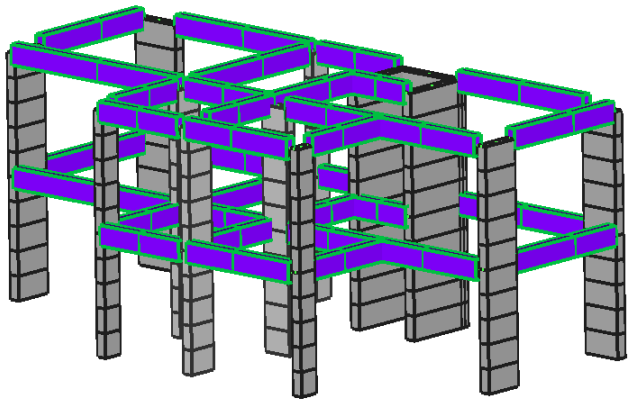

(C) Reduction Level 3

FIGURE 6.47 2-STOREY RC BUILDING. FE MESH FOR DIFFERENT REDUCTION LEVELS.

Since the aim of this work is to illustrate the numerical behavior of the proposed modeling method under static loading, it was decided to compute the distribution of the horizontal load at each storey with the EC8 code[251] and apply them along the *Y* axis direction of the structure through metallic plates that can be seen in Fig. 6.49. The assumptions made for the computation of the horizontal loads are given in Table 6.17, where it is assumed that the Type 1 response spectra is used, which corresponds to an anticipated surface-wave magnitude M_s which is greater than *5.5* (high seismicity areas).

As can be seen in Fig. 6.49, the horizontal load is applied through metallic plates which are positioned at the heads of the four structural members namely K_8, K_9, K_{10} and K_{11}. The distribution of the horizontal load is performed according to the mass distribution of the structure along the *Y* axis direction in *10* load increments.

The vertical distributed loads were assumed to be equal to *2* and *2.5* kN/m^2 for the dead and live loads, respectively. The self-weight of the structure was also taken into account by activating the self-weight command. It must be noted that the assumed concrete nominal weight was *25* kN/m^3. For simplification reasons the difference between the reinforcement and concrete weights which derives from the volume that is occupied from the rebars is neglected. Nevertheless, it is evident that this numerical simplification does not alter the mass redistribution since the two stories of the RC building are of similar shapes. Their only

difference is located at the stair case opening beside the east side of the shear wall of the lift (Fig. 6.43).

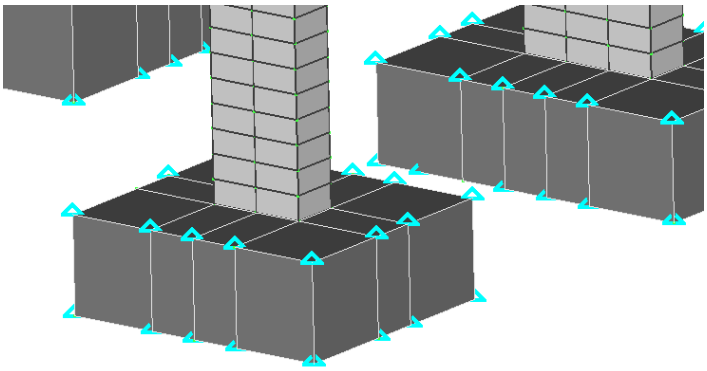

FIGURE 6.48 2-STOREY RC BUILDING. BOUNDARY CONDITIONS. FIXED NODES ARE MARKED WITH A CYAN TRIANGLE.

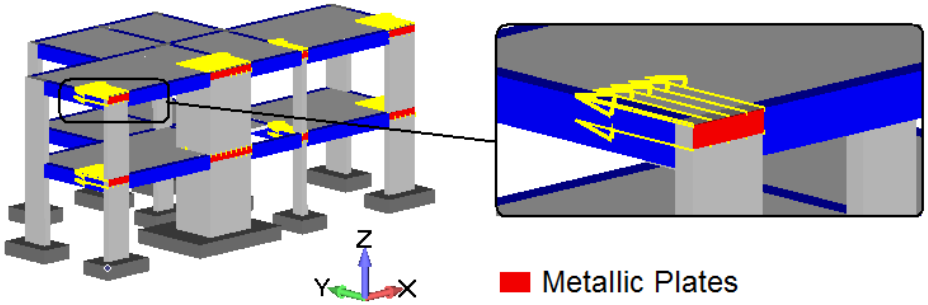

FIGURE 6.49 2-STOREY RC BUILDING. METALLIC PLATES FOR HORIZONTAL LOADING.

Parameters of EC8	*Value*
Ground Type	D
T_B	0.2 sec
T_C	0.8 sec
S	1.35
q	3.3
Acceleration a_g	0.24g
Importance Class	II
Importance Factor γ_I	1

TABLE 6.17 2-STOREY RC BUILDING. EC8 PARAMETERS.

In Fig. 6.50 the horizontal displacement of the top floor is plotted at each load increment as it is shown in the corresponding figure. For all model cases, the horizontal displacement along the *Y* direction is plotted (a node located on the head of the column K_2). It is obvious that all FE models appear to have almost identical stiffness at the first loading increment, thus the building is governed by bending deformations.

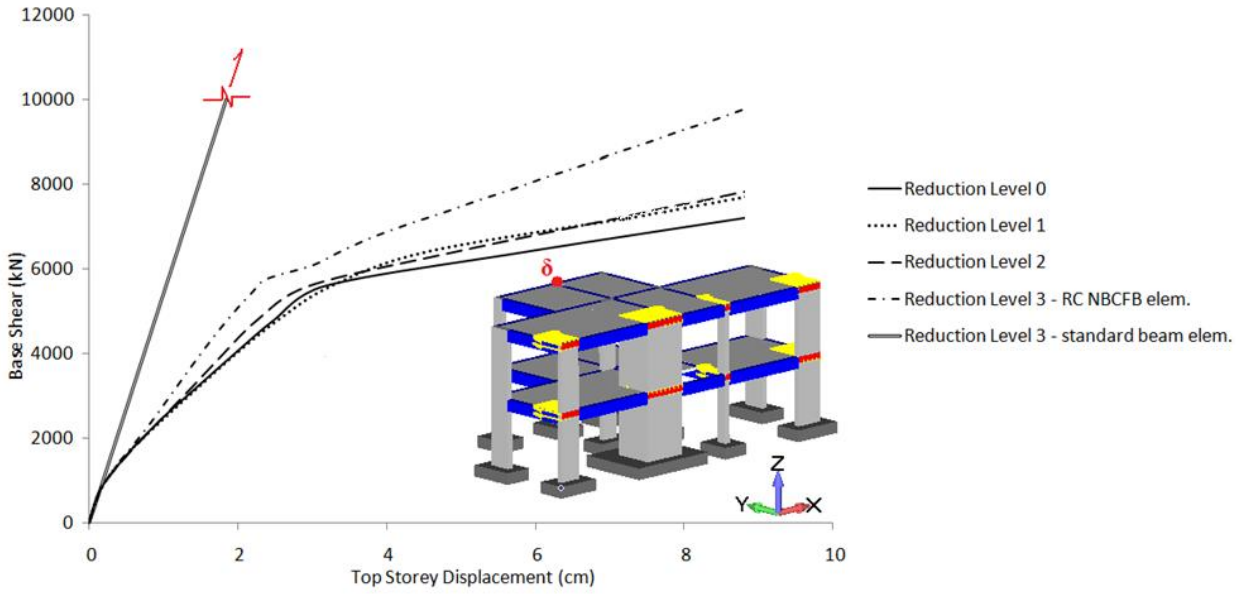

FIGURE 6.50 2-STOREY RC BUILDING. PREDICTED *P-δ* CURVES.

As it is shown in Fig. 6.51, the first cracks appear at several structural members of the building which have a horizontal orientation confirming their flexural nature. The first cracks appear at the base of shear walls (K_7, K_4, K_9) that have an orientation parallel to the *Y* axis which bear a significant part of the seismic forces. Due to their structural form, they attract larger values of the applied load and therefore they are the first to enter the nonlinear state. It is worth noting that columns K_2 and K_6, which have an orthogonal section of *25x75 cm* and their orientation is also parallel to the *Y* axis, appear to deform at their base and develop similar cracks to the corresponding shear walls (Fig. 6.51). In addition to that, beams that are connected to these shear walls appear to crack near their end-sections. This is attributed to the deformations that are induced at the softer beam sectional areas of the joint since the corresponding stiffness of the shear wall is greater. This illustrates the importance of 3D detailed modeling since the realistic crack pattern and nonlinear behavior of RC structures can be predicted for a given loading set, thus providing the necessary data for the seismic assessment of this type of structures and the required information in order to guide the designing process into seismic resistant structures.

The computed *P-δ* curves indicate that for a load level of *4,800 kN* the initiation of rebar yielding occurs since the slope of the inelastic branch decreases significantly. The same load level was predicted by all three FE models which use the detailed modeling in order to discretize and model the shear dominated structural members and sections of the structure (RL *0*, *1* and *2*). It is evident that shear dominated structural members and sections control the overall nonlinear behavior of this particular RC building. Fig. 6.52 shows the predicted crack pattern for this load level, where it can be observed that the cracking is excessive especially in the shear walls and the joints of the structure. Furthermore, it can be seen that many cracks located in the shear walls are inclined, underling the shear deformation effect on the 3D stress state of concrete.

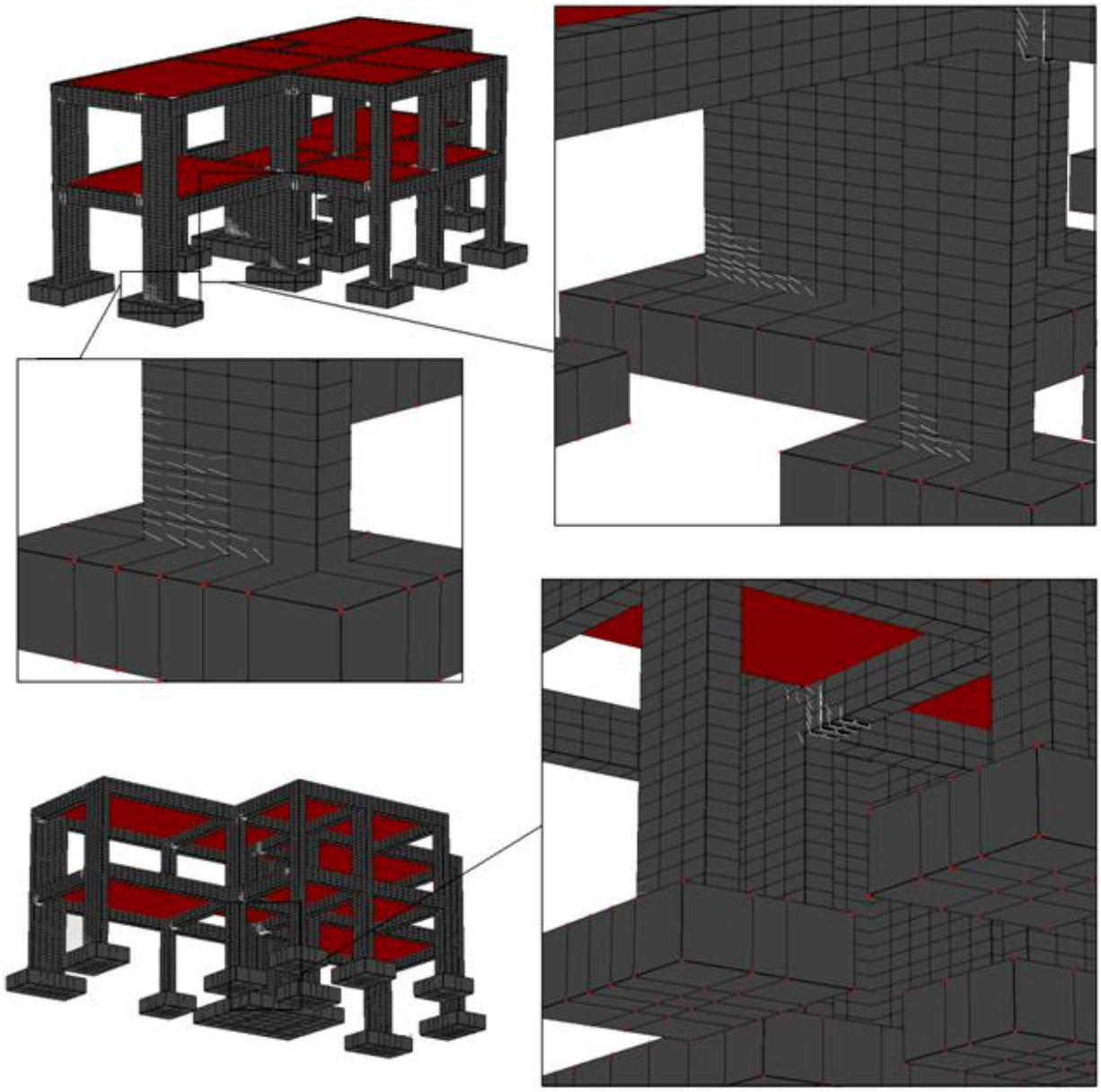

FIGURE 6.51 2-STOREY RC BUILDING. CRACK INITIATION OF THE UNREDUCED FE MODEL.

The failure of the 2-storey RC building is initiated when the load level exceeds the shear base load of *7,200 kN* where the tension rebars, located at the shear wall of the lift, failed initializing significant internal force redistributions leading to additional reinforcement failures where eventually the structure was unable to bear the additional external horizontal load. Fig. 6.53 shows the predicted crack pattern of the structure prior to failure, where it can be observed that the number of crack openings did not increase significantly corresponding to the crack pattern given in Fig. 6.52 (initiation of rebar yielding) where the elongation of the cracks can be observed.

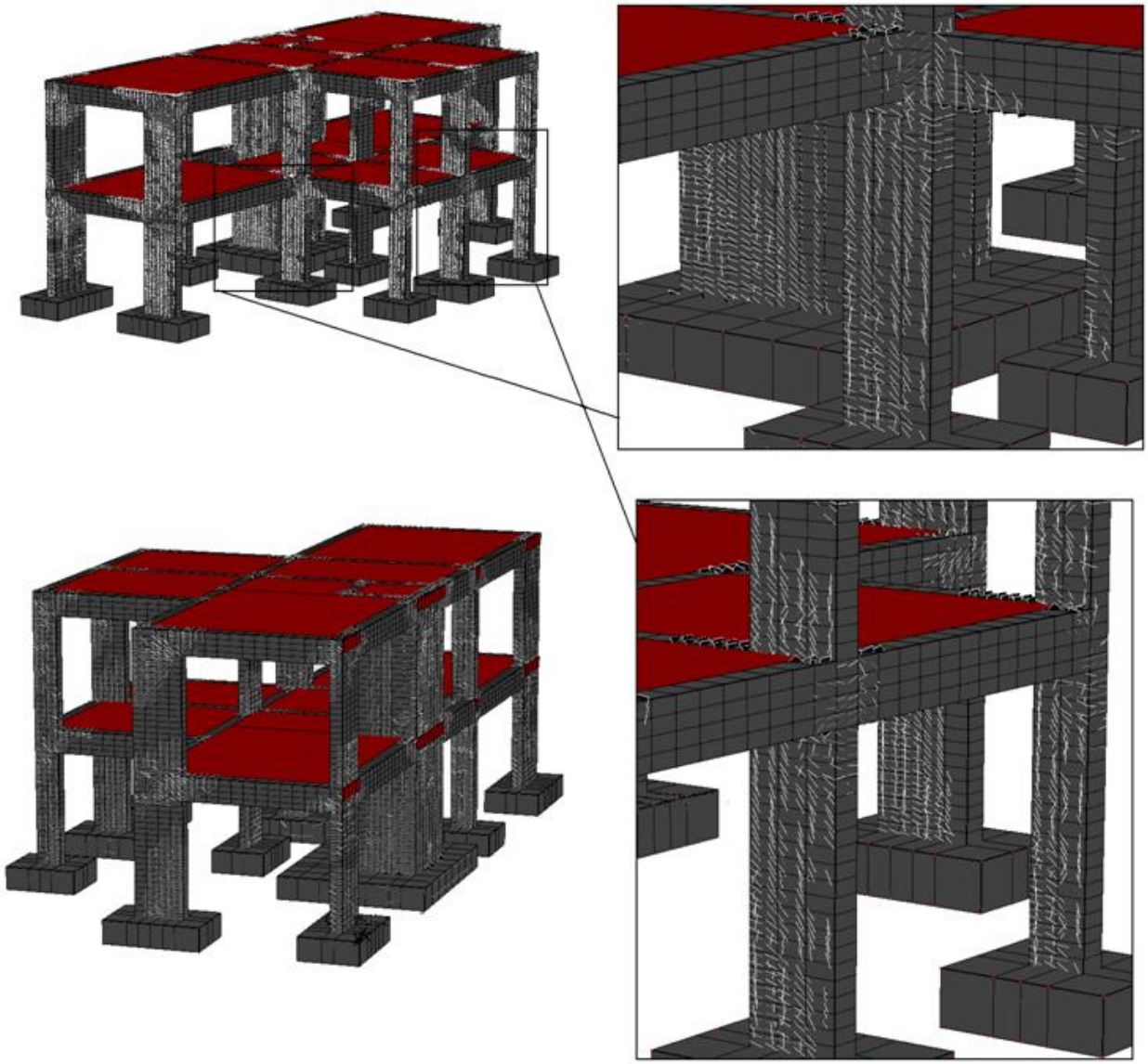

FIGURE 6.52 2-STOREY RC BUILDING. PREDICTED CRACK PATTERN OF THE UNREDUCED FE MODEL. SHEAR BASE *4,800 KN*.

A correlation of the predicted crack patterns between the RL *0*, *1* and *2* models, is shown in Figs. 6.54 and 6.55 where the crack patterns for different load levels are shown. As can be seen, there is a good agreement between the predicted crack patterns illustrating that hybrid models have the ability of retaining the required accuracy and at the same time reducing significantly the computational cost. The von Mises strain contours in the hexahedral elements are given in Fig. 6.56 prior to failure. It is evident that both hybrid and unreduced FE models lead to similar predictions of the structure nonlinear behavior thus underlining the superiority of hybrid modeling compared to the beam model in capturing significant local phenomena that affect the overall response of the structure.

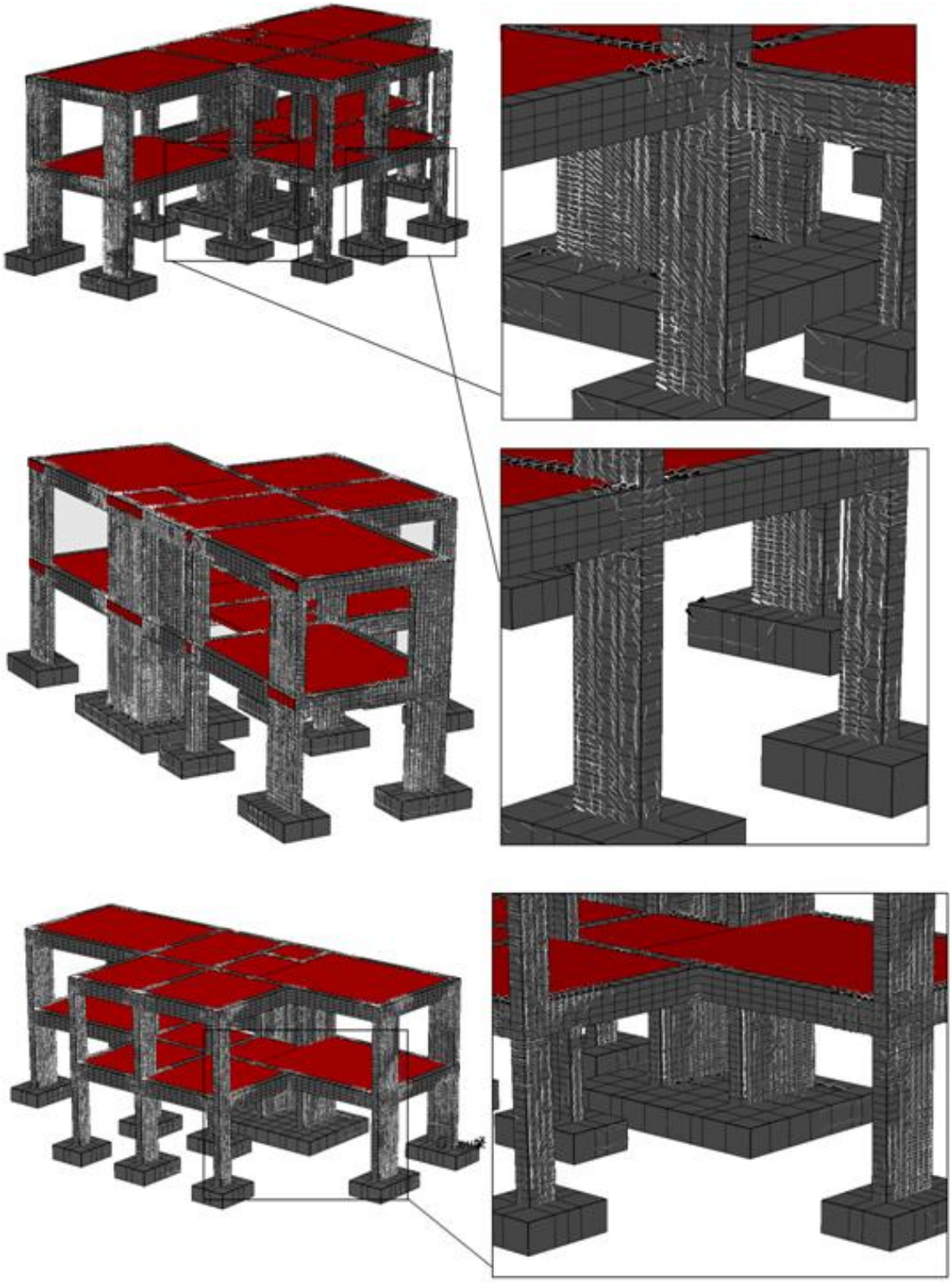

FIGURE 6.53 2-STOREY RC BUILDING. PREDICTED CRACK PATTERN OF THE UNREDUCED FE MODEL PRIOR TO FAILURE.

The CPU times required by the four FE models are given in Table 6.18 where the computational efficiency of the developed FEA code can be seen. The solution time for *9* load increments for the unreduced model is *95 min* and the corresponding reduction in CPU times, when using HYMOD models, verifies the previous findings.

a/a	*Model*	*Number of Load Increments*	*CPU Time (min)*	*Reduction in CPU Time (%)*	*Rebar Yield at (kN)*
A	Reduction Level 0	9	95	-	4,800
B	Reduction Level 1	9	65	31.57	4,800
C	Reduction Level 2	9	30	66.67	4,800
D	Reduction Level 3	25	-	-	5,760

TABLE 6.18 2-STOREY RC BUILDING. CPU TIMES FOR THE SOLUTION PROCEDURE.

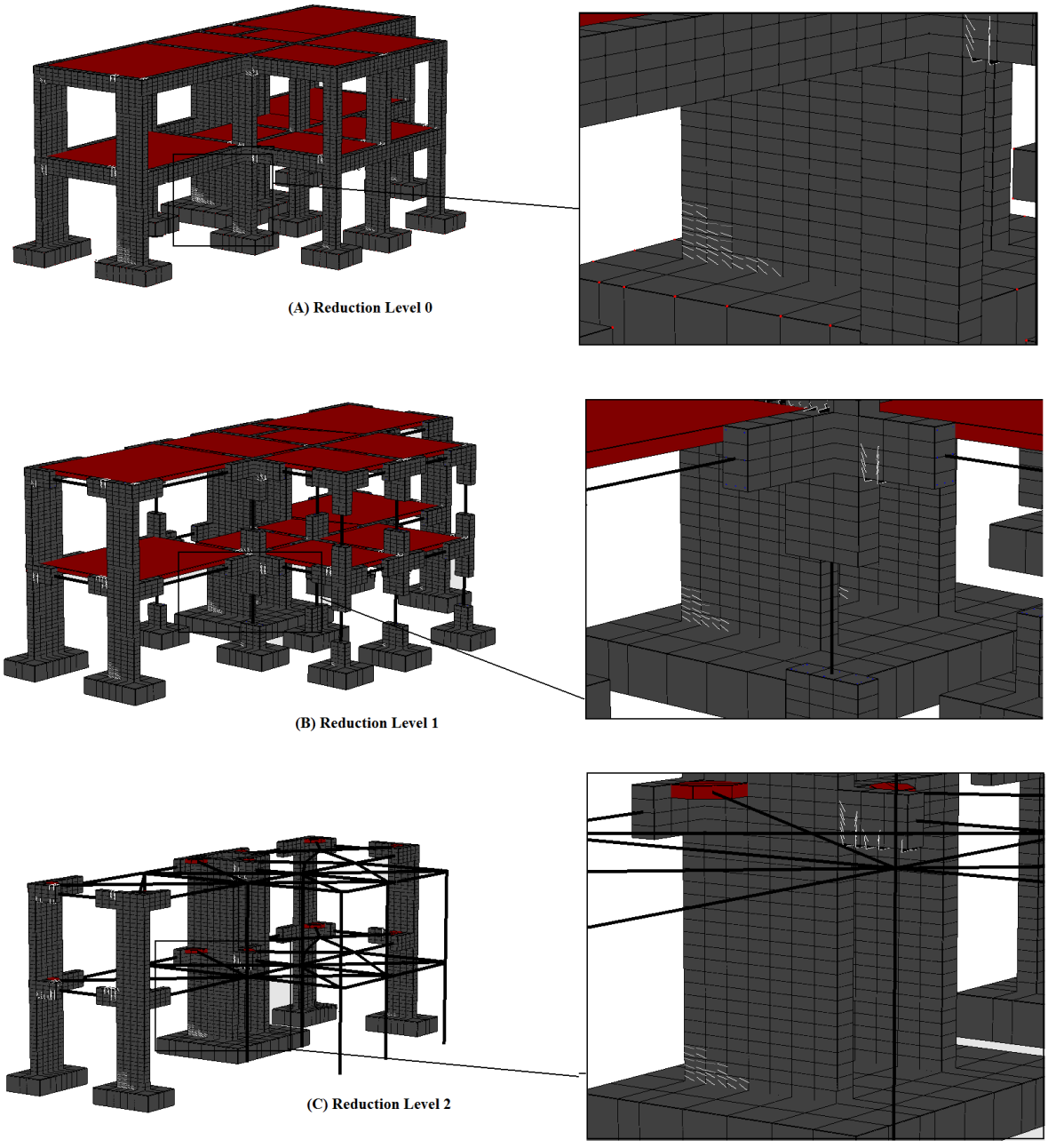

FIGURE 6.54 2-STOREY RC BUILDING. INITIATION OF CRACK FOR DIFFERENT FE MODELS.

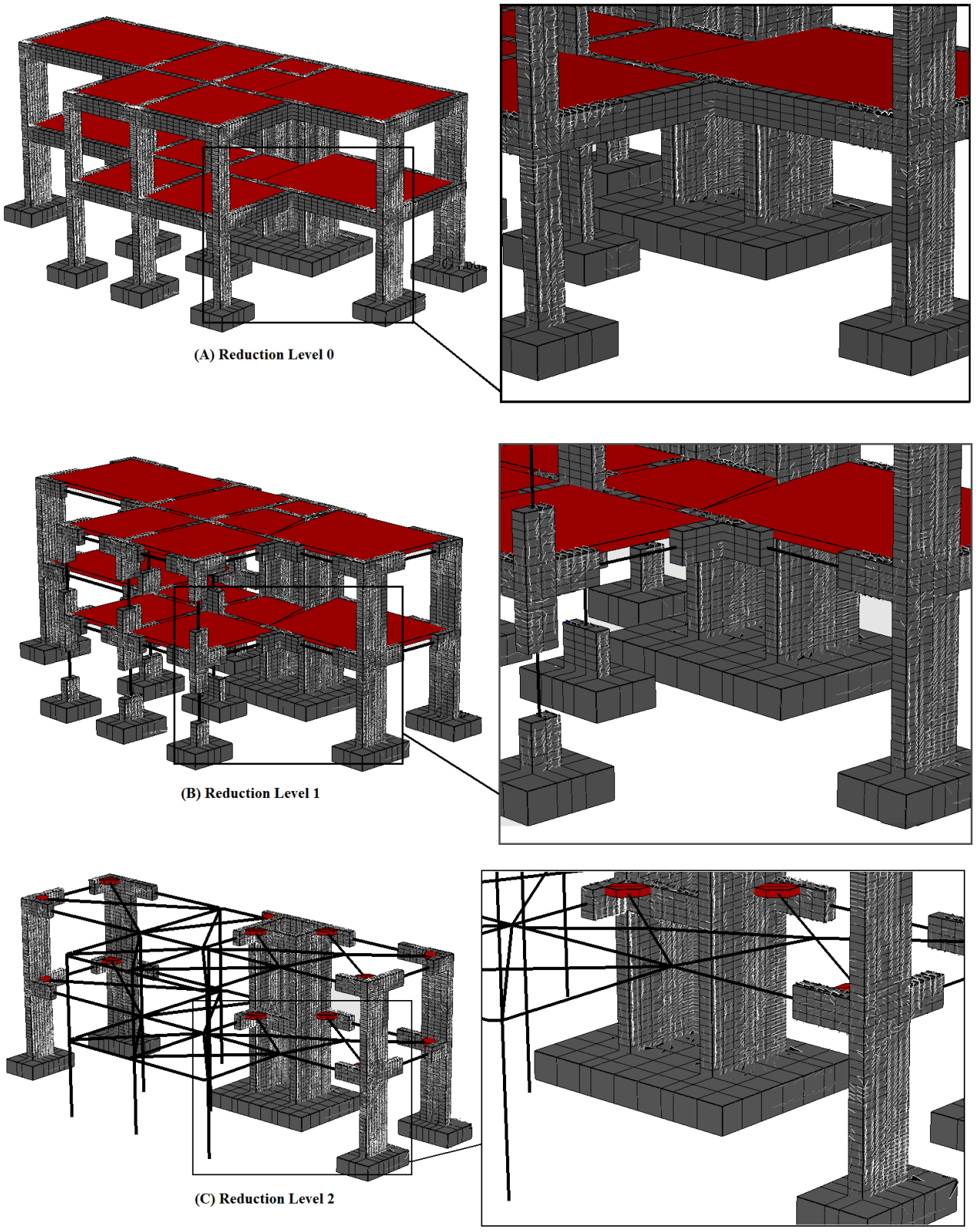

FIGURE 6.55 2-STOREY RC BUILDING. CRACK PATTERN PRIOR TO FAILURE FOR DIFFERENT FE MODELS.

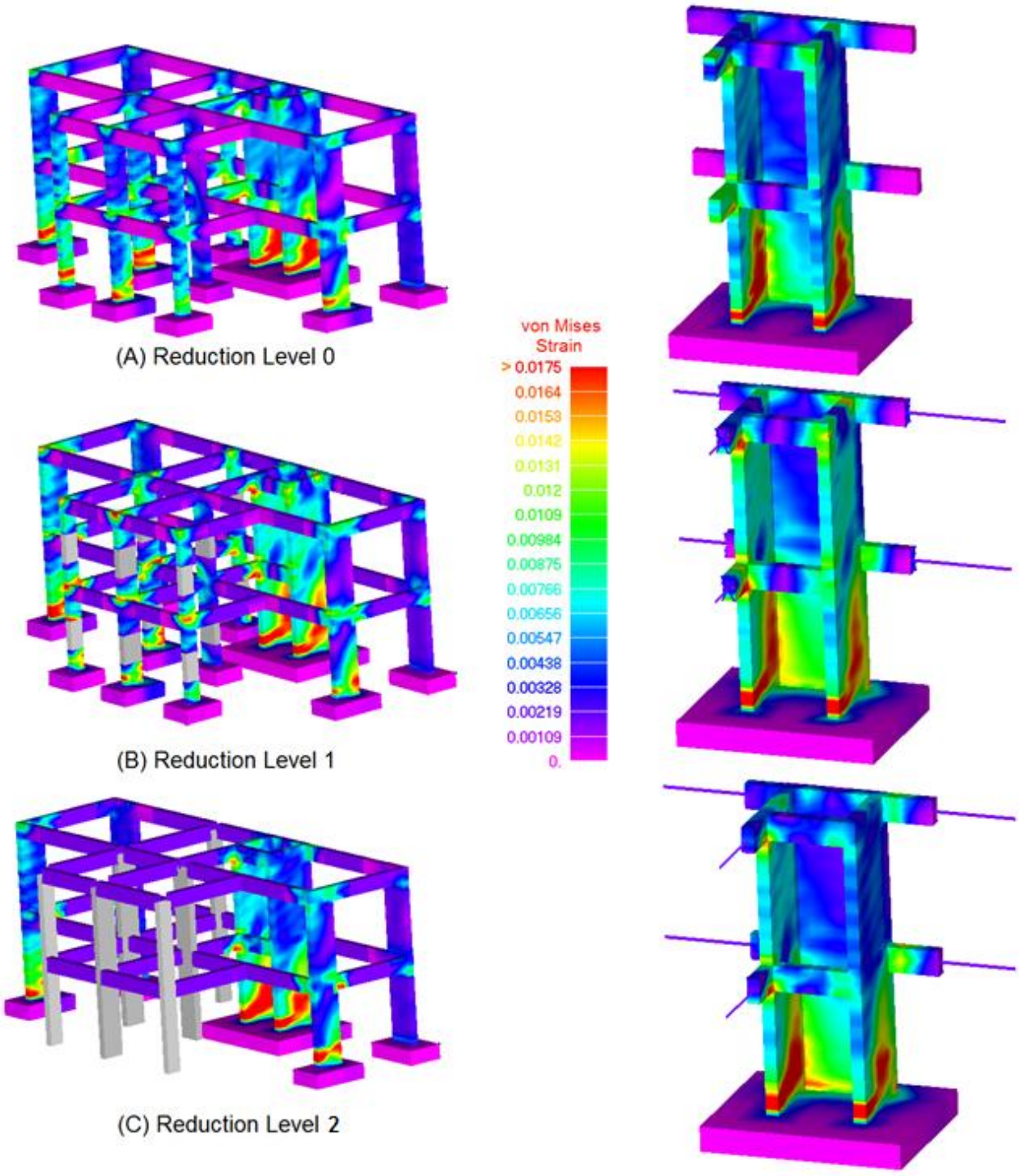

FIGURE 6.56 2-STOREY RC BUILDING. VON MISES STRAIN CONTOUR PRIOR TO FAILURE FOR DIFFERENT FE MODELS.

Chapter 7 Overview of the *ReConAn* FEA Software

Contents of Chapter 7

7.1 Overview and Programming Language

During the development of *ReConAn* FEA software (***Re***inforced ***Con***crete ***An***alysis), the necessity for the creation of a more general in-core object-oriented analysis code emerged. This necessity was emerged from the fact that FEA codes should be easily extendable and maintained (reusability). In addition to that, from the developers' point of view, in order to be able to control the numerical procedures and to have the ability to check the results produced during the analysis phase, the structure of the code must have object oriented architecture.

Object-Oriented Programming (OOP) can trace its roots to the 1960s. As hardware and software became increasingly complex, the quality was often overlooked. Researchers studied ways in which software quality could be maintained. OOP was deployed in part as an attempt to address this problem by strongly emphasizing discrete units of programming logic and re-usability in software. Computer programming methodology focuses on data rather than processes, with programs composed of self-sufficient modules (objects) containing all the information needed within its own data structure for manipulation. OOP may be seen as a collection of cooperating objects, as opposed to a traditional view in which a program may be seen as a group of tasks to compute ("subroutines"). In OOP, each object is capable of receiving messages, processing data, and sending messages to other objects. Each object can be viewed as an independent little machine with a distinct role or responsibility. The actions or "operators" on the objects are closely associated with the object. For example, in OOP, the data structures tend to carry their own operators with them (or at least "inherit" them from a similar object or "class"). The traditional approach tends to view and consider data and behavior separately.

The development of an OOP type FEA code has many advantages such as the control of the arithmetic flow which is a rather difficult task as the code is growing and the enrichment of the code with new Finite Elements, Analysis Procedures, Solvers and other numerical tools that can be encapsulated very fast (extendibility). Taking under consideration the above code development strategy, *ReConAn* adopted this philosophy and has all the previously mentioned abilities. The outcome from the adoption of this code architectural type is the evolution of *ReConAn* into a general FEA program that is able to use several Finite Elements, Material Models and Solution Procedures.

Object oriented format requires the use of Data Types where, for every element, material, property, solution variables, etc., we create a different Data Type. With this approach, each FE has its own property type that tells us which material model will be used during the solution procedure and its characteristics. Therefore, two different types of elements can use the same material model or vice-versa. Material variables have their own data types which are used to store data that refer to material characteristics like the Young's Modulus, Poisson Ratio, etc. Property data type contain information about each element and its characteristics concerning the material model that an element is going to use during the analysis procedure, the Integration Method that the stiffness procedure will use for the stiffness matrix creation etc. Taking this philosophy of code format under consideration, the input data file must be also grouped into data blocks.

Programming the FE method may be considered by many users as a straight forward job and it does not require any sophisticated code language. In reality this is partially true. Even the smallest in size FE simulations require a certain number of arithmetic operations between two dimensional matrices and arrays. These matrix operations require a certain amount of time in order to be carried out, depending on the number of unknowns at hand. This means, the bigger a FEM model is the more CPU time and virtual memory is required to be solved. Since commercial software use finite element modeling and there is the need, during the designing process, for more accurate models, more refined FE models are frequently used. CPU hardware limitations in performing large scale calculations were the main barriers for limitations on the size of the FE models. This need for large-scale simulations created advances in parallel processing and in optimum dynamic usage of CPU hardware abilities through optimum code programming. Which advance should be adopted in the FEM case? The answer is not straight forward. The optimum choice is a combination of these two advances in order to have optimum code structure and architecture which will lead to optimum performance.

To have an optimum code programming structure, first of all we must choose an appropriate programming language which will provide us the necessary tools in order to create an optimally designed code for the problems at hand. Taking under consideration the above remarks (about the FEM arithmetical nature), one could easily say that we need a programming language which will be able to dynamically redistribute CPU virtual memory and handle optimally large arithmetic matrix operations.

In computer science, dynamic memory allocation is the allocation of memory storage for use in a computer program during its runtime. It can be seen also as a way of distributing ownership of limited memory resources among many pieces of data and code. Dynamically allocated memory exists until it is released either explicitly by the programmer, exiting a block, or by the garbage collector. This is in contrast to static memory allocation, which has a fixed duration. It is said that an object that is allocated has a dynamic lifetime (allocate - deallocate). Programming languages like Java, Visual Basic, Pascal, Matlab, Apple etc. have the ability of memory dynamic allocation and OOP but they are deficient in speed due to their inability in handling large arithmetic operations. This problem immersed from the fact that the creators of these programming languages in order to make them more user friendly they included many invisible intermediate operations that reduced significantly the operations speed during the runtime. The best choices for our problem at hand are C++ (or C#) and Fortran 90/95.

C++ and C# are widely used by many developers but Fortran 77 and the new Fortran 90/95 due to its simpler language style always dominated in the scientific research field in terms of preference. Fortran 77 is considered to be rather “old” and antiquated since the new features of Fortran 90/95 language were introduced.

The much delayed successor to FORTRAN 77, informally known as Fortran 90, was finally released as an ISO standard in 1991 and an ANSI Standard in 1992. This major revision added many new features to reflect the significant changes in programming practice that had evolved since the 1978 standard:

- Free-form source input, also with lowercase Fortran keywords

- Identifiers up to 31 characters in length
- Inline comments
- Ability to operate on arrays (or array sections) as a whole, thus greatly simplifying math and engineering computations.
    - whole, partial and masked array assignment statements and array expressions, such as X(1:N)=R(1:N)*COS(A(1:N)))
    - WHERE statement for selective array assignment
    - array-valued constants and expressions,
    - user-defined array-valued functions and array constructors.
- RECURSIVE procedures
- Modules, to group related procedures and data together making them available to other program units, including the capability to limit the accessibility only to specific parts of the module.
- A vastly improved argument-passing mechanism, allowing interfaces to be checked at compile time
- User-written interfaces for generic procedures
- Operator overloading
- Derived/abstract data types
- New data type declaration syntax, to specify the data type and other attributes of variables
- Dynamic memory allocation by means of the ALLOCATABLE attribute and the ALLOCATE and DEALLOCATE statements
- POINTER attribute, pointer assignment and NULLIFY statement to facilitate the creation and manipulation of dynamic data structures
- Structured looping constructs, with an END DO statement for loop termination, and EXIT and CYCLE statements for "breaking out" of normal DO loop iterations in an orderly way
- SELECT . . . CASE construct for multi-way selection
- Portable specification of numerical precision under the user's control
- New and enhanced intrinsic procedures.

Unlike the previous revision, Fortran 90 did not delete any features. Any standard-conforming FORTRAN 77 program is also standard-conforming under Fortran 90 and either standard should be usable to define its behavior.

A small set of features were identified as "obsolescent" and expected to be removed in a future standard (Table 7.1).

Fortran 95 was a minor revision, mostly to resolve some outstanding issues from the Fortran 90 standard. Nevertheless, Fortran 95 also added a number of extensions, notably from the High Performance Fortran specification:

- FORALL and nested WHERE constructs to aid vectorization,
- User-defined PURE and ELEMENTAL procedures,
- Pointer initialization and structure default initialization.

Obsolescent feature	*Example*	*Status / 95*
Arithmetic IF-statement	`IF (X) 10, 20, 30`	
Non-integer DO parameters or control variables	`DO 9 X= 1.7, 1.6, -0.1`	Deleted

Shared DO-loop termination or termination with a statement other than END DO or CONTINUE	`DO 9 J= 1, 10`
	
	`DO 9 K= 1, 10`
	`9 L= J + K`	

Branching to END IF
 	
from outside a block
	`66 GO TO 77 ; . . .`
	
	`IF (E) THEN ; . . .`
	`77 END IF`
		Deleted

Alternate return	`CALL SUBR( X, Y *100, *200 )`	
PAUSE statement	`PAUSE 600`	Deleted

ASSIGN statement and assigned GO TO statement	`100 . . .`
	
	`ASSIGN 100 TO H`
	`. . .`
	`GO TO H . . .`
		Deleted

Assigned FORMAT specifiers	`ASSIGN F TO 606`	Deleted
H edit descriptors	`606 FORMAT ( 9H1GOODBYE. )`	Deleted
Computed GO TO statement	`GO TO (10, 20, 30, 40), index`	(Obso.)
Statement functions	`FOIL( X, Y )= X**2 + 2*X*Y + Y**2`	(Obso.)

DATA statements among executable statements	`X= 27.3`
	
	`DATA A, B, C / 5.0, 12.0. 13.0 /. . .`
		(Obso.)

CHARACTER* form of CHARACTER declaration	`CHARACTER*8 STRING ! Use CHARACTER(8)`	(Obso.)
Assumed character length functions		
Fixed form source code	* Column 1 contains * or ! or C for comments. C Column 6 for continuation.	

TABLE 7.1 FORTRAN 77 OBSOLESCENT FEATURES.

A number of intrinsic functions were extended (i.e. a dim argument was added to the maxloc intrinsic). Several features noted in Fortran 90 to be deprecated were removed from Fortran 95:

- REAL and DOUBLE PRECISION DO variables,
- Branching to an END IF statement from outside its block,
- PAUSE statement,
- ASSIGN and assigned GOTO statement and assigned format specifiers,
- H edit descriptor.

An important supplement to Fortran 95 was the ISO technical report TR-15581: Enhanced Data Type Facilities, informally known as the Allocatable TR. This specification defined enhanced the use of ALLOCATABLE arrays, prior to the availability of fully Fortran 2003-compliant Fortran compilers. Such uses include ALLOCATABLE arrays as derived type components, in procedure dummy argument lists and as function return values. ALLOCATABLE arrays are preferable to POINTER-based arrays because ALLOCATABLE arrays are guaranteed by Fortran 95 to be deallocated automatically when they go out of scope, eliminating the possibility of memory leakage. In addition, aliasing is not an issue for optimization of array references, allowing compilers to generate faster code than in the case of pointers. Another important supplement to Fortran 95 was the ISO technical report TR-15580: Floating-point exception handling, informally known as the IEEE TR. This specification defined support for IEEE floating-point arithmetic and floating point exception handling.

do…enddo command	*Assignments and Pure Procedures*
do I = 1, iSize *raArray (I) = 2.d0* *raArray (I) = raArray (I)+ abs(raArray (I) -* *(raArray (I) * (-16.d0))) + 4.d0 * raArray (I)* *– (raArray (I) **(1.d0/3.d0))* *enddo*	*raArray (1:iSize) = 2.d0* *raArray = raArray + abs(raArray - (raArray* ** (-16.d0))) + 4.d0 * raArray –* *(raArray**(1.d0/3.d0))*

TABLE 7.2 EXAMPLE OF COMPACTING OUR SOURCE CODE.

One of the most significant features that Fortran 90/95 introduced was the ability to use pure procedures and array assignments. For example if someone wants to allocate, initialize and contact some arithmetical operation with a real double precision array that has a size of *iSize*, then there are two ways of implementing this. The first way is by using the standard do … enddo format and the second is by using assignments and pure procedures (Table 7.2).

The first thing that comes to our attention just by looking at these two code formats is that when assignments and pure procedures are used the code becomes automatically more compact and it requires half of the lines than the do…enddo format. The second thing that we achieve by using these new features is that the array elements assignment utilizes the compiler for optimum compilation during the build procedure a feature not available when the standard do…enddo programming format is used. The third advantage when using this programming format is that there is no need for creating additional subroutines for initializing matrices (set to zero any type of matrix or array).

Another choice that the developer has to make is that of choosing the appropriate Compiler that will be used in order to convert the text written code into machine language. Since we chose as our programming language Fortran 90/95, the choices reduce to the latest and more advanced Fortran Compiler.

Intel® Fortran Compiler Professional Edition offers the best support for creating multi-threaded applications. Only the Professional Edition offers the breadth of advanced optimization, multi-threading, and processor support that includes automatic processor dispatch, vectorization, auto-parallelization, OpenMP, data prefetching, loop unrolling, substantial Fortran 2003 support and an optimized math processing library. The Professional Edition combines a high performance compiler, which now includes support for Debian and Ubuntu, with Intel® Math Kernel Library (Intel® MKL). While this library is available separately, the Professional Edition creates a strong foundation for building robust, high performance parallel code.

Finally, since we've made all the choices concerning the programming language and compile/build procedures, we need to choose a suitable developing program which will provide the necessary developing and debugging tools to make the developing task easier and as controllable as possible. The most advanced developing studio that uses .NET technology is considered to be Visual Studio 2008 Professional Edition.

Visual Studio 2008 Professional Edition is a comprehensive set of tools that accelerates the process of turning the developer's code into numerically robust programs. Visual Studio 2008 Professional Edition was engineered to support development projects that target the Web (including ASP.NET AJAX), Windows Vista, Windows Server 2008, 2007 Microsoft Office system, SQL Server 2008 and Windows Mobile devices. Visual Studio 2008 Professional Edition provides the integrated toolset for addressing all the developer's needs by providing a superset of the functionality available in Visual Studio 2008 Standard Edition. In addition to that, Visual Studio 2008 Professional Edition can create Fortran console applications. This is done by simply installing the Intel® Fortran Compiler Professional Edition after the installation of Visual Studio 2008 Professional Edition. By doing so, Visual Studio 2008 Professional Edition adds in its Project Types an additional one named Intel(R) Fortran.

Summarizing the above features, the developmental tools of *ReConAn* FEA code are:

- Programming Language: ***Fortran 90/95***
- Compiler: ***Intel® Fortran Compiler Professional Edition v11***
- Development Studio: ***Visual Studio 2008 Professional Edition***

7.2 Graphical Environment

Visual illustration of the FE model and the corresponding results after the completion of an analysis, is one of the most essential features of a FEA code for the following basic reasons:

1. Create and check the geometry of the FE model.
2. Set or modify the material and analysis parameters.
3. Represent visually the output data in order to verify the correctness of the computed results during the analysis procedure.

When dealing with relatively large models, the use of user friendly post-processing software is imperative for assessing the quality of the FE models. Many researchers use text type input file to provide the necessary information regarding the FE geometry, material properties and analysis details. Furthermore, the usual output that results from this type of analysis is restrained to monitoring the displacement along a specific direction of a node. It is obvious that this leads to many uncertainties which increase as the FE increases in terms of the dof number.

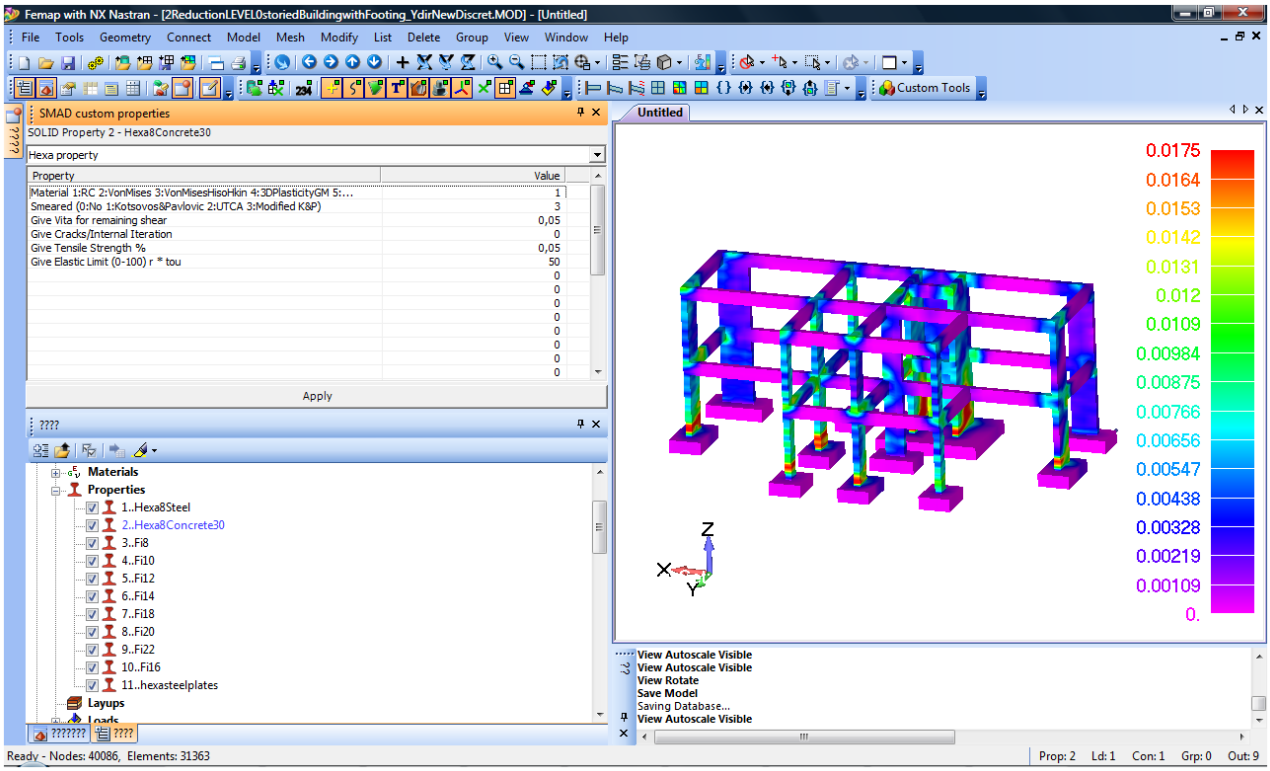

FIGURE 7.1 MAIN WINDOW OF FEMAP[91] FEA WITH SMAD CUSTOM PROPERTIES.

For the above reasons, *ReConAn* FEA has been supplemented with the ability of reading the required FE geometry and features from a Femap[91] neutral file and exporting its output data in a text file which can be imported in Femap[91] post-processing software utilizing the user with the ability of illustrating visually the deformations and several contour options of the resulted stresses and strains. Additionally, *ReConAn* Eye post-processing software was developed during this Dissertation so as to visualize the predicted crack patterns when the smeared modeling command was activated. This software is OpenGL based and has the ability of animating the evolution of cracking during the load history analysis of a RC structure. The necessity of developing such a tool emerges from the fact that Femap[91] post-processing software does not provide the ability of crack representation, thus all figures of this research work containing crack patterns were taken from *ReConAn* Eye post-processing software.

Since Femap pre-processing software does not provide the user with the necessary tools for entering custom made properties regarding several features of the FE models (like the number of fibers per control section in the case of the NBCFB element), the SMAD Custom properties software (Fig. 7.1) was used for providing any additional parameters required by the *ReConAn* solver for the assemblage and solution of the numerical problem at hand. The SMAD Custom

properties software was developed by G. Stavroulakis during his Ph.D. thesis, which deals with soil-structure interaction problems under seismic loading with the use of the FEM.

7.3 Automation Tools

Civil engineering commercial software usually provides user-friendly pre-processing environment that enables the user to create the geometry of their structures and thereafter automatically identify the nature of each structural member given its geometry and its position inside the model where the discretization is performed. This ability derives from the fact that civil engineering commercial softwares use beam elements in order to model the structural members of the structures where the discretization process is performed without the need of the implementation of any sophisticated numerical techniques.

In the case of HYMOD, this task cannot be implemented in a straightforward manner since the requirement of recognizing the geometrical features of each structural member of a RC structure and choosing the proper FE model to discretize it, is a rather computationally complicated CAD procedure. Achieving such a task, it is necessary to use advanced programming techniques and given the fact that this was not a goal of this work, standard CAD tools were used during the creation of each hybrid model. Nevertheless, in order to save significant amount of time in the process of the creation of the FE mesh of a structure, program file (prg) was used with the aim of developing simple scripts in Femap, which create the solid volumes of different types of joints given their geometrical characteristics. These joint volumes are shown in Fig. 7.2, where the required geometrical features are given. Since one of the most complex geometries to mesh in a building is the areas where columns and beams intersect, the three types of joints corresponding to different cases of beam-column connections are constructed.

The Program File Dockable Pane (Fig. 7.3) allows you to dynamically record any number of FEMAP menu, toolbar, and keyboard commands in sequence to create "macros". Once a program file has been recorded, it can be "played back" as a "macro" inside FEMAP to perform a customized series of commands to perform a specific action or achieve a particular goal.

When the Record button in the Program File Dockable Pane is on, the commands will be recorded in the main text window of the Program File Pane in the order they are chosen in FEMAP user interface. Once completed, the record button is toggled to off and the text in the window can be saved as a Program File (either a *.prg file or a *.pro file which saves the text in Rich Text Format).

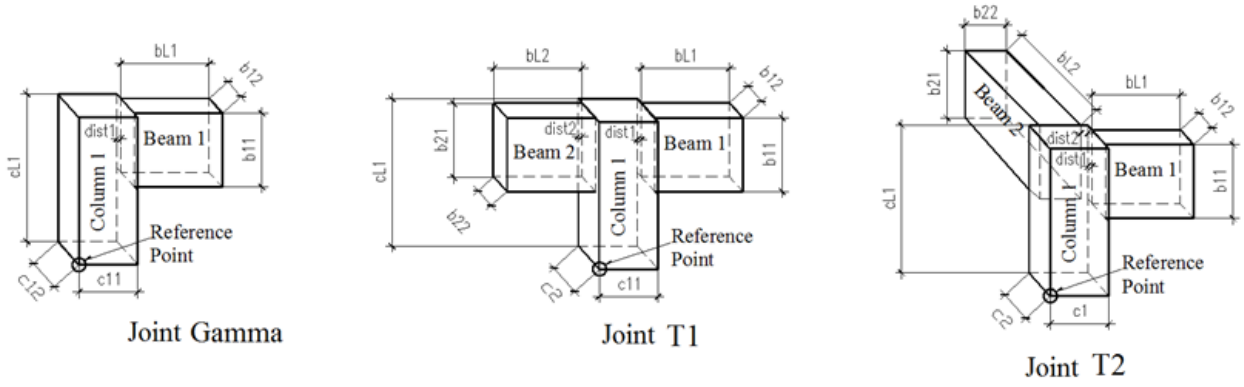

FIGURE 7.2 DIFFERENT TYPES OF 3D CROSS SECTIONS.

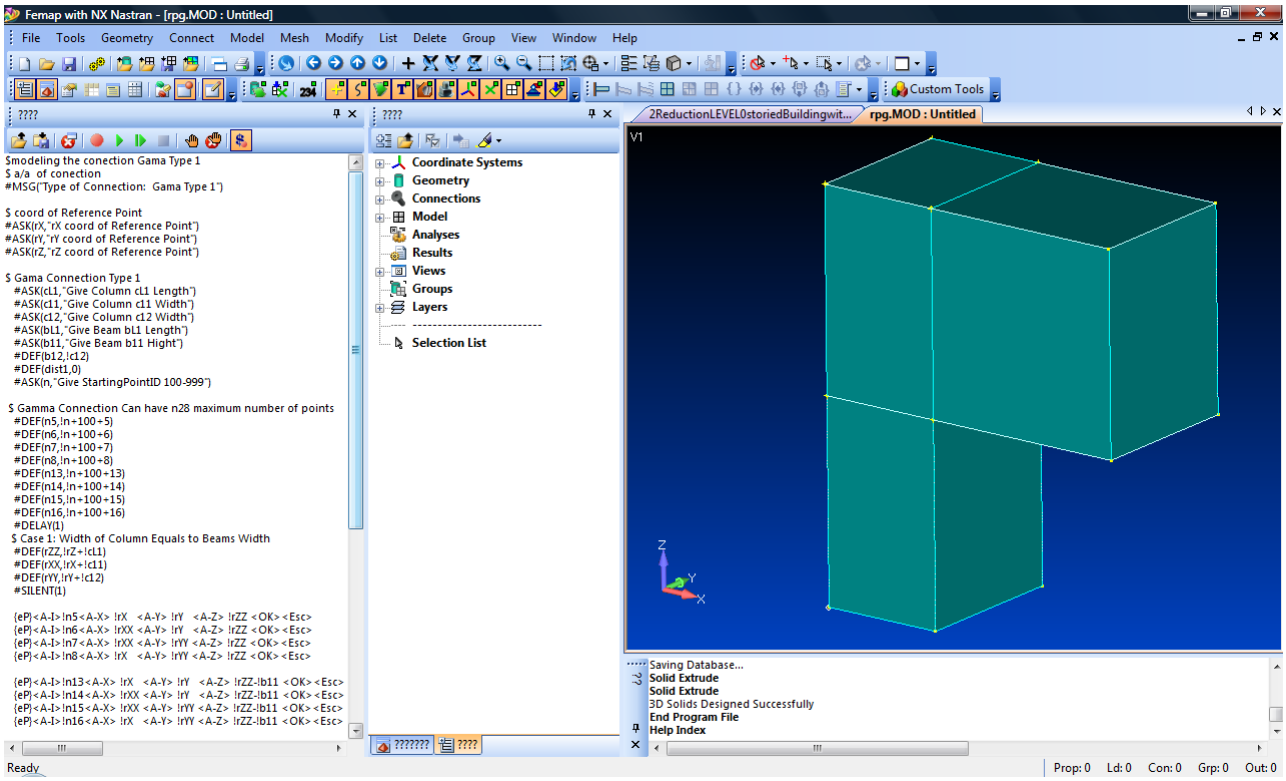

FIGURE 7.3 PROGRAM FILE DOCKABLE PANE.

In their simplest form, FEMAP Program Files are essentially ASCII text files which instruct FEMAP to perform certain commands based on the syntax of the ASCII file. This FEMAP specific syntax includes unique numbered identifiers representing every FEMAP command, normal keystrokes (for typing values and text), and special keystrokes used to perform different tasks in specific dialog boxes (such as pushing buttons, choosing selection methods, and designating specific fields to activate). You can add logic commands, define and manipulate variables, stop and prompt a user for input, or send messages to the Messages Pane.

There are three basic types of data that will be placed in program files created with the Program File Pane. The first type is unique numbered identifiers representing every FEMAP command. These identifiers tell FEMAP which menu, toolbar, or keyboard shortcut commands to use while the program file is running. The second is keystroke information that mimics what you

would type from the keyboard if you were performing the operation manually (this is how FEMAP knows which buttons to push, methods to select, and fields to activate). When you run a program file, this text essentially "pushes the keys" in dialog boxes for you to run FEMAP commands. You may also want to add other program file commands. These commands do not execute FEMAP commands, rather, they are commands themselves which control the flow of the program file, work with variables, print messages, or ask for input.

Following, the program file for the case of Joint Gama is given, where the geometric features of the joints are requested in order to create the points, surfaces and volumes of this Joint type.

PRG file for the case of Joint Gamma

```
$ Joint Gamma    c12 > b12     dist1 <= c12 - b12

$ a/a  of connection

#MSG("Type of Joint:  Gamma")


$ coord of Reference Point

#ASK(rX,"rX coord of Reference Point")

#ASK(rY,"rY coord of Reference Point")

#ASK(rZ,"rZ coord of Reference Point")


$ Gamma Connection Type 2

  #ASK(cL1,"Give Column cL1 Length")

  #ASK(c11,"Give Column c11 Width")

  #ASK(c12,"Give Column c12 Width")

  #ASK(bL1,"Give Beam bL1 Length")

  #ASK(b11,"Give Beam b11 Height")

  #ASK(b12,"Give Beam b12 Width")

  #ASK(dist1,"Give dist1")

  #ASK(n,"Give StartingPointID 100-999")


 $ Gamma Connection Can have n28 maximum number of points)

  #DEF(n6,!n+100+6)
```

```
#DEF(n7,!n+100+7)
#DEF(n13,!n+100+13)
#DEF(n14,!n+100+14)
#DEF(n15,!n+100+15)
#DEF(n16,!n+100+16)
#DEF(n21,!n+100+21)
#DEF(n22,!n+100+22)
#DEF(n23,!n+100+23)
#DEF(n24,!n+100+24)
#DEF(n26,!n+100+26)
#DEF(n27,!n+100+27)

#DELAY(1)
$ Case 1: Width of Column Equals to Beams Width
#DEF(rZZ,!rZ+!cL1)
#DEF(rXX,!rX+!c11)
#DEF(rYY,!rY+!c12)
#SILENT(1)

{eP}<A-I>!n6<A-X> !rXX <A-Y> !rY   <A-Z> !rZZ <OK><Esc>
{eP}<A-I>!n7<A-X> !rXX <A-Y> !rYY <A-Z> !rZZ <OK><Esc>

{eP}<A-I>!n13<A-X> !rX   <A-Y> !rY   <A-Z> !rZZ-!b11 <OK><Esc>
{eP}<A-I>!n14<A-X> !rXX <A-Y> !rY   <A-Z> !rZZ-!b11 <OK><Esc>
{eP}<A-I>!n15<A-X> !rXX <A-Y> !rYY <A-Z> !rZZ-!b11 <OK><Esc>
{eP}<A-I>!n16<A-X> !rX   <A-Y> !rYY <A-Z> !rZZ-!b11 <OK><Esc>

{eP}<A-I>!n21<A-X> !rX  <A-Y> !rYY-!b12-!dist1 <A-Z> !rZZ-!b11 <OK><Esc>
{eP}<A-I>!n22<A-X> !rXX <A-Y> !rYY-!b12-!dist1 <A-Z> !rZZ-!b11 <OK><Esc>
```

```
{eP}<A-I>!n23<A-X> !rXX <A-Y> !rYY-!dist1 <A-Z> !rZZ-!b11       <OK><Esc>

{eP}<A-I>!n24<A-X> !rX  <A-Y> !rYY-!dist1 <A-Z> !rZZ-!b11       <OK><Esc>


{eP}<A-I>!n26<A-X> !rXX <A-Y> !rYY-!b12-!dist1 <A-Z> !rZZ       <OK><Esc>

{eP}<A-I>!n27<A-X> !rXX <A-Y> !rYY-!dist1     <A-Z> !rZZ       <OK><Esc>


#DEF(ns1,!n*500-500+1)

#DEF(ns2,!n*500-500+2)

#DEF(ns3,!n*500-500+3)

#DEF(ns4,!n*500-500+4)

$ Draw Surface

{efC}          <A-Y>YPT(!n13)<A-Z>ZPT(!n13)<A-X>XPT(!n13)<A-P><@11003>!ns1<OK>          <OK><A-
Y>YPT(!n14)<A-Z>ZPT(!n14)<A-X>XPT(!n14)<OK>          <A-Y>YPT(!n22)<A-Z>ZPT(!n22)<A-X>XPT(!n22)
<OK><A-Y>YPT(!n21)<A-Z>ZPT(!n21)<A-X>XPT(!n21)<OK><Esc>

{efC}          <A-Y>YPT(!n21)<A-Z>ZPT(!n21)<A-X>XPT(!n21)<A-P><@11003>!ns2<OK>          <OK><A-
Y>YPT(!n22)<A-Z>ZPT(!n22)<A-X>XPT(!n22)<OK>          <A-Y>YPT(!n23)<A-Z>ZPT(!n23)<A-X>XPT(!n23)
<OK><A-Y>YPT(!n24)<A-Z>ZPT(!n24)<A-X>XPT(!n24)<OK><Esc>

{efC}          <A-Y>YPT(!n23)<A-Z>ZPT(!n23)<A-X>XPT(!n23)<A-P><@11003>!ns3<OK>          <OK><A-
Y>YPT(!n15)<A-Z>ZPT(!n15)<A-X>XPT(!n15)<OK>          <A-Y>YPT(!n16)<A-Z>ZPT(!n16)<A-X>XPT(!n16)
<OK><A-Y>YPT(!n24)<A-Z>ZPT(!n24)<A-X>XPT(!n24)<OK><Esc>

{efC}          <A-Y>YPT(!n22)<A-Z>ZPT(!n22)<A-X>XPT(!n22)<A-P><@11003>!ns4<OK>          <OK><A-
Y>YPT(!n23)<A-Z>ZPT(!n23)<A-X>XPT(!n23)<OK>          <A-Y>YPT(!n27)<A-Z>ZPT(!n27)<A-X>XPT(!n27)
<OK><A-Y>YPT(!n26)<A-Z>ZPT(!n26)<A-X>XPT(!n26)<OK><Esc>

$ Create Solids ..... Geometry Solid Extrude

#SILENT(1)

#DEF(len1,!cL1-!b11)

#DEF(len2,!b11)

#DEF(len3,!bL1)

{eSu}<@14001><PUSH><@12004><PUSH>!ns1<OK><@14101><PUSH><@12002><PUSH><A-
M>L<@10011>0<@10012>0<@10013>0<@10021>0<@10022>0<@10023>-
1<OK><@10501>!len1<OK><Esc>

{eSu}<@14001><PUSH><@12004><PUSH>!ns2<OK><@14101><PUSH><@12002><PUSH><A-
M>L<@10011>0<@10012>0<@10013>0<@10021>0<@10022>0<@10023>-
1<OK><@10501>!len1<OK><Esc>
```

```
  {eSu}<@14001><PUSH><@12004><PUSH>!ns3<OK><@14101><PUSH><@12002><PUSH><A-
M>L<@10011>0<@10012>0<@10013>0<@10021>0<@10022>0<@10023>-
1<OK><@10501>!len1<OK><Esc>

  {eSu}<@14001><PUSH><@12004><PUSH>!ns1<OK><@14101><PUSH><@12002><PUSH><A-
M>L<@10011>0<@10012>0<@10013>0<@10021>0<@10022>0<@10023>1<OK><@10501>!len2<OK><
Esc>

  {eSu}<@14001><PUSH><@12004><PUSH>!ns2<OK><@14101><PUSH><@12002><PUSH><A-
M>L<@10011>0<@10012>0<@10013>0<@10021>0<@10022>0<@10023>1<OK><@10501>!len2<OK><
Esc>

  {eSu}<@14001><PUSH><@12004><PUSH>!ns3<OK><@14101><PUSH><@12002><PUSH><A-
M>L<@10011>0<@10012>0<@10013>0<@10021>0<@10022>0<@10023>1<OK><@10501>!len2<OK><
Esc>

  {eSu}<@14001><PUSH><@12004><PUSH>!ns4<OK><@14101><PUSH><@12002><PUSH><A-
M>L<@10011>-
1<@10012>0<@10013>0<@10021>0<@10022>0<@10023>0<OK><@10501>!len3<OK><Esc>

 $ View Autoscale

  {VA}



#MSG("3D Solids Designed Successfully")

#EXIT()

# (6969)



$ File Program Stop
```

By entering the following parameters (*rX = rY = rZ = 0, cL1 = 1.5, c11 = 0.5, c12 = 0.5, bL1 = 1, b11 = 0.5, b12 = 0.3, dist1 = 0.1*) when executing the above code, the resulted geometry of the corresponding joint volume is that shown of Fig. 7.4a.

It is obvious that automation tools are significant when dealing with full-scale RC structures, which consists of large numbers of structural members and joints. The procedure of creating the geometry and generating the mesh of a FE model is a time consuming task that undermines the risk of possible omissions since it's performed manually. This task becomes even more complicated when the FE model consists of embedded rebar elements for the reinforcement modeling. Therefore, the need of a fully automated CAD tool for generating 3D complex meshing for *HYMOD* models through the use of simple geometrical features and standard reinforcement configuration is essential.

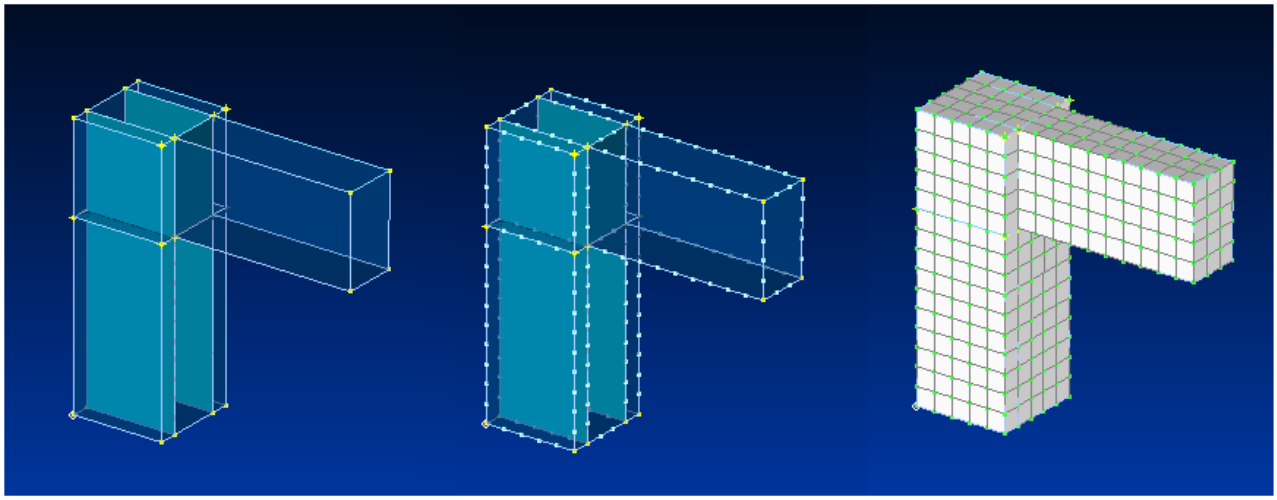

(A) (B) (C)

FIGURE 7.4 JOINT GAMMA. (A) SOLID GEOMETRY; (B) MESH ATTRIBUTE ON SOLIDS; (C) HEXAHEDRAL MESH.

Chapter 8 Conclusions and Future Work

Contents of Chapter 8

8.1 Original Contribution

In this section the original contributions of this research work are summarized in the following Table.

a/a	*Description*
1	A computationally efficient flexibility-based fiber element was developed (NBCFB element). The originality of this element lies in the computational implementation, which exhibits remarkable computational efficiency when modeling RC and Steel structures. It is also proved that the natural method of J. Argyris improves the computational efficiency of the high performance beam-column fiber FE.
2	A general computationally robust and efficient mesh generation procedure was proposed for the allocation of embedded rebar elements inside the hexahedral elements used for modeling 3D concrete structures. The proposed method overcomes computational problems, thus it can be applied in the mesh generation procedure for the allocation of the embedded rebar elements for any structural geometry and scale. Even for real-scale structures with thousands of embedded rebar elements, the proposed method manages to allocate in a minimal CPU time the embedded rebar elements.
3	A numerically improved concrete material model is proposed, which treats the concrete cracking with the smeared crack approach and manages to minimize the numerical instabilities induced due to the unbalanced forces released in the numerical system during the structural state determination. For the first time, 3D smeared crack concrete material model was successfully incorporated in an 8-noded isoparametric hexahedral element.
4	A new modeling approach was proposed for the embedded rebar elements. A high performance beam-column fiber element was used for modeling the embedded rebar element, which is force-based, incorporates the natural method and is kinematically connected to the embedding hexahedral element. The proposed modeling method for the embedded rebar elements proved to be numerically robust, computationally efficient and induces, through its numerical formulation, additional stability in the nonlinear solution procedure.
5	A new 3D detailed modeling method is proposed which uses the isoparametric 8-noded hexahedral element which treats cracking with the smeared crack approach and models the embedded rebar elements with the NBCFB element. The verification of the proposed modeling method was performed through computations with a set of experimental data found in the literature.

6	A hybrid FE model which use 1D and 3D elements for the nonlinear modeling of RC structures was presented. The shear dominated structural members, that are characterized as critical regions, are modeled with 3D detailed models (hexahedral elements with embedded rebar elements where the smeared crack approach is adopted) and the rest of the structure is modeled with the RC NBCFB fiber element. This method was named as HYMOD and appears to be numerically robust and computationally efficient when implemented in real-scale RC structures. Moreover, different levels of reduction models to the initial 3D detailed model, were presented. Depending on the reduction demands that a FE model requires for the sufficient decrease of its dof, an appropriate reduced model may be implemented for the analysis of a RC structure.
7	*ReConAn* is an object-oriented FEA software, which was developed during this research work and incorporates all the previously mentioned numerical features, techniques and methods. Its computational superiority, especially when dealing with 3D detailed FE modeling of RC structures, is verified through a number of demanding test examples.

TABLE 8.1 LIST OF ORIGINAL CONTRIBUTIONS.

8.2 Conclusions

8.2.1 Natural Beam-Column Flexibility-Based Element

A computationally robust and efficient fiber NBCFB element was developed which exhibits both accuracy and numerical stability. The numerical tests revealed that the natural method proposed by J. Argyris endows the element with additional computational efficiency attributed to the properties of the natural formulation. After the numerical comparison of the NBCFB element with the standard flexibility-based element incorporated in OpenSees, it was shown that the proposed element appeared to be more robust and computationally efficient. The numerical robustness of the element is attributed to both the natural method and the nonlinear iterative procedure which is performed for the determination of its internal stress-state equilibrium.

The assessment of the numerical behavior of the NBCFB element was investigated in both RC and steel structures, illustrating the ability in capturing the overall nonlinear response with adequate accuracy. As it was described in Chapter 2, the natural method decomposes the deformed shape of a member into rigid body modes and strain modes, making easier the determination of the element's stress-strain state.

The computational efficiency that *ReConAn* FEA code was demonstrated in a number of test examples exhibiting its ability in predicting the ultimate load capacity of any type of structure in a minimal CPU time. This enables the user in performing nonlinear analysis for large-scale structures with thousands of structural members with the use of standard CPU systems. In

addition to that, it was shown that, through the formulation of the NBCFB element, it is feasible to discretize each structural member with only one element, thus reducing significantly the numerical model. This improved performance of the element derives from the state determination procedure of the element and the adopted Gauss-Lobato integration scheme which uses specific sections along the element to determine the stiffness matrix degradation during the loading history.

A nonlinear analysis of a 37-storey RC building was performed for demonstrating the capability of the developed software code to perform nonlinear analysis of large-scale RC structures. Moreover, the computational efficiency of the code was demonstrated with the nonlinear solution this large-scale structure through the use of a standard CPU system (personal laptop).

8.2.2 Embedded Rebar Mesh Generation Procedure

Previous work on detailed three-dimensional models for the analysis of RC structures limit their numerical implementations to experimental setups that consist of simple structural members. Thus the need for a computationally efficient mesh generation method of the embedded rebar elements inside the concrete domain, has not attracted the appropriate attention.

In this work, an embedded reinforcement mesh generation method is proposed, which can effectively allocate and generate embedded reinforcement elements inside hexahedral elements with an arbitrary positioning of the reinforcement and allowing a free geometric shape of the hexahedrons. The computational robustness and efficiency of the proposed mesh generation method, when dealing with relatively large-scale problems with arbitrary reinforcement geometry, were illustrated through numerical experiments.

8.2.3 Concrete Material Model and Smeared Crack Approach

An improved numerical handling of the Kotsovos and Pavlovic 3D material concrete model for monotonic loading combined with a smeared crack model was implemented. The material model was applied to an 8-noded hexahedral element with no restriction on the number of crack openings inside the load increment.

The numerical behavior of the improved material model was illustrated through several numerical tests of plain and reinforced concrete experiments. It is worth noting that the ability of incorporating this fully brittle material model in an 8-noded isoparametric hexahedral element with a *2*x*2*x*2* Gauss integration scheme, illustrates the computational superiority of the developed FEA code and its numerical robustness when dealing with highly ill-posed numerical problems.

Furthermore, the numerical handling of the smear crack approach appears to minimize the numerical instabilities induced when crack openings occur and significant unbalanced forces are released during the NR incremental iterative solution procedure. If the algorithmic implementation is not optimally applied, this numerical phenomenon can create numerical instabilities that could lead to the divergence of the iterative solution procedure. This is attributed to the additional crack openings that occur as a result of the unbalanced forces produced by the previous crack openings. It is evident that this numerical problem requires

special handling and the use of advanced programming techniques in order to control the numerical stability of the problem.

8.2.4 Reinforced Concrete Modeling

A detailed FE modeling of reinforced concrete structures is proposed with the following characteristics:

(i) A mesh generation technique for the embedded reinforcement is implemented which can effectively allocate and generate embedded reinforcement elements inside hexahedral elements with an arbitrary positioning of the reinforcement and a free geometry of the hexahedral mesh.

(ii) An improved numerical handling of a 3D material concrete model for monotonic loading combined with a smeared crack model. The material model was applied to an 8-noded hexahedral element with no restriction on the number of crack openings inside the load increment.

(iii) The modeling of the reinforcement is performed with the use of a 2-noded flexibility-based beam element, formulated with natural modes and the fiber approach. It was shown that the results obtained with rod elements for modeling the reinforcement does not lead to accurate numerical simulations especially for heavily RC members.

The proposed NBCFB element increases the stability of the nonlinear solution procedure through its physical characteristics. The numerical robustness exhibited by the proposed modeling methodology is attributed to the following features:

- The nonlinear procedure for the calculation of the internal forces of the NBCFB element.
- The stability induced by the consideration of shear and bending stiffness of the NBCFB elements.
- The modification of the concrete material model and the handling of the stress redistribution due to cracking.

The proposed modeling method managed to predict with an adequate precision a number of experimental test results reported in the literature, illustrating its ability to predict failure loads, failure mechanisms and crack patterns with a high computational efficiency up to failure. This is an important component when dealing with large-scale structures where the sensitivity on the required number of load increments applied during the analysis plays a crucial role in the feasibility of any detailed FE simulation of real-scale RC structures.

One of the most interesting conclusions that result from this research work is the ability of capturing, through the use of detailed FE models, the nonlinear response of real-world RC structures and furthermore, acquire a relatively detailed overview of their nonlinear behavior in terms of stress-strain distribution. With this ability of predicting the stress-strain distribution inside the concrete domain, significant conclusion can be drawn for several mechanical features of the RC studies. Specifically, in a series of beams (Bresler and Scordelis[186]) that was numerically investigated in this work, it was found that both type of beams (with and without

stirrups) exhibited high shear behavior near the limit loading state which affected significantly their overall behavior. As it was observed in the computed crack pattern for both beam types, inclined cracking was excessive, especially when the load level was near the ultimate capacity of the beams. This behavior was not foreseen when the experimental setup was designed, since the general belief that beam like structural members are flexural dominated was acceptable. Through this study, it is shown that shear strains and 3D crack simulation play a significant role in the overall behavior of RC structural members when the load level is near the ultimate state limit load, even for cases of simple beam-like RC structural members.

8.2.5 Hybrid Modeling (HYMOD) Method

The HYMOD method was presented in an attempt of using detailed FE modeling in the simulation of real-world RC structures. The basic objective for this type of modeling is the decrease of the dof of the FE model by using a detailed approach (hexahedral and embedded rebar elements) when necessary and at the same time retain an acceptable accuracy on the predicted displacements.

In the scope of creating a generalized procedure when reducing the fully detailed FE model, the introduction of four Reduction Levels was presented. The first and last Reduction Levels (RL *0* and *3*) correspond to the unreduced and the FE model with only beam type elements, respectively. The RL *1* and RL *2* Reduction Levels correspond to a specific decrease in the number of hexahedral elements and their replacement with beam-column elements in non-shear-dominated structural members areas of the structure.

The basic idea behind the reduction of a detailed FE model relies on the assumption that shear dominated structural members should be modeled with the detailed approach, whereas the rest of the structure and modeled with beam-column elements. When performing this type of reduction scheme, the resulted model consists of elements with different dimensionality which requires special numerical handling at their interface. In this work, the compatibility at the interface is performed through kinematic constraints that are implemented at the interface of the detailed domain and the beam node which controls the translational and rotational displacements of the coupled elements. The proposed formulation was found to be computationally robust since it does not require any special iterative procedure for its implementation.

A parametric investigation was performed for defining the required joint length which is adequate enough for capturing the nonlinear behavior of the hand critical region requiring detailed simulation. It was concluded that the corresponding length of a joint should be between *h-2h*, where *h* is the sectional height of the corresponding structural member (beam or column). It was shown through a number of numerical tests that the proposed geometric constraint manages to provide the adequate length for capturing the nonlinearities that occur in a critical region while simultaneously maximizing the reduction of the resulting dof.

The HYMOD was applied in the case of a real-scale 2-storey RC building which was initially designed with the use of a Greek civil engineering software package. The geometry of the structure was discretized with the use of hexahedral solid elements and the resulted

reinforcement was modeled with embedded rebar elements. The previously mentioned four Reduction Levels were implemented and the resulted FE models where analyzed for comparing the results and their corresponding numerical performance. As it was illustrated, the predicted curves when using the RL *0*, *1* and *2* FE models are in a good agreement in between them thus the reduction of the initial FE model does not affect the accuracy of the predicted behavior of the structure.

A second observation that was made through the resulted curves is that the simulation with the NBCFB Euler-Bernoulli fiber element overestimates the ultimate load of the structure and underestimates the corresponding interstory drift demand. This would provide an unconservative estimation of the demand if it is used for the seismic damage assessment of RC buildings that consist of shear dominated structural members.

A third very important observation is the inability of the beam-column element formulation to capture the numerous local effects which play a significant role in the overall behavior of a RC structure. Even if the beam element is equipped with a shear material model, the ability to predict the influence of local effects is highly questionable.

Concluding with a general remark: It is evident that 3D detailed modeling is the most numerically sufficient method for predicting the nonlinear behavior of any type of RC structure, especially when dealing with highly nonlinear behaviors, where the prediction of the 3D stress state is the only adequate way for capturing the numerical behavior of physical phenomena such as yielding, cracking, stiffness degradation, etc. It is also evident that through the outcome of this research work, the seismic assessment of RC structures should be performed using 3D detailed FE models which account for most of the basic concrete material features that govern the overall nonlinear behavior of the structures. This can be done through the implementation of performance-based design procedures. The main restriction for this type of implementations is the automation of the whole process and moreover, the numerical handling of the different structural members in a 3D detailed model and particularly the enforcement of the compatibility constant at the interface when the Hybrid Modeling approach is implemented. It is a complicated task which requires extensive research work.

8.2.6 *ReConAn* FEA Software

As a final remark in this work, an object-oriented software package was developed to incorporate the previously mentioned state of the art numerical methods and techniques for modeling and analysing of RC and steel structures. The outcome of this attempt was named *ReConAn* FEA software and it was demonstrated that it can predict accurately the nonlinear behavior of RC and steel structures with computational efficiency and robustness. The computational superiority of the developed software was demonstrated though numerous numerical tests and computational comparison between commercial and research software codes.

ReConAn is a practical proof that through the implementation of an intelligent programming technique, the future prospects in FE modeling can widen even more, providing the common

user with almost endless abilities in modeling complicated physical phenomena through the use of standard CPU systems.

8.3 Future Work

In this research work, the nonlinear behavior of RC structures under monotonic loading was investigated. It was shown that the developed software code constitutes an objective and accurate modeling method for the realistic prediction of the nonlinear behavior of RC structures under monotonic loading. Given the results presented in the present Dissertation, this task has been accomplished and therefore the cyclic loading solution procedure has to be implemented and numerically investigated in order to conduct any type of static and dynamic-cyclic analysis. For accomplishing such a task the following numerical features have to be incorporated in *ReConAn* FEA software:

1. Opening and closing of cracks for the cyclic concrete material model.
2. Displacement-control NR iterative solution procedure.
3. Dynamic solution algorithm.

The most important part when dealing with cyclic loading conditions is to manage the numerical implementation regarding the material model of concrete. Since the monotonic loading problem is ill-posed especially when cracking initiates, the closing and opening of cracks will introduce additional implementation issues which require special attention. The main algorithmic integrations towards this aim have been made, thus further development is required in order to accomplish this task.

The numerical feature that has to do with the displacement-control solution strategy is already under development and numerical tests remain to be carried out in order to verify the correctness of the algorithmic implementation. Finally, the dynamic solution algorithm is under development.

An important feature that is considered to play a significant role in RC structure modeling is the bond-slip mechanism between the concrete and reinforcement. This feature was taken into account through an indirect method with the consideration of three additional dof per embedded rebar element and by considering that the bond-slip mechanism is triggered near the yielding of the rebar elements, a phenomenon proved by several experimental research projects. However, by adding *3* additional dof per rebar element the computational demand of such a modeling method would have led to higher computational demands with no particular gain in terms of accuracy. This is attributed to the fact that slip initiates near the rebar yielding where the concrete at this stage is excessively cracked. In addition to that, in order for the bond-slip to play an important role, the anchorage length has to be small enough for the mechanism to be activated during the loading procedure, a geometric constraint that does not characterize real structures. Nevertheless, incorporating an efficient bond-slip model is in the future task list, which will be developed.

Regarding the NBCFB element, it was shown that the Euler-Bernoulli formulation appears to have serious disadvantages when modeling structural members that are shear dominated. To

improve the numerical accuracy of the predicted behavior of RC and Steel structures, the extension of the element to incorporate shear effects can improve its numerical performance.

At this point let us draw the attention back to the forest instead of looking at the trees thus missing the whole picture. Assuming that the ability of realistic simulations of the nonlinear behavior of RC structures is established, it is the author's belief that the basic feature that was neglected, throughout this research work, is the interaction of the RC structure foundation with the soil (Fig. 8.1) which is the media that plays the most significant role for bearing the superstructure loads.

Given the object-oriented code structure of *ReConAn* FEA, it is rather easy to incorporate new material models in the code without the need of radical alterations in the code. Therefore, the integration of *ReConAn* with a soil material model for monotonic and cyclic loading will be performed in the immediate future in order to investigate Soil-Structure Interaction problems for the prediction of the static and dynamic nonlinear behavior of these coupled systems.

It is evident that when referring to algorithmic implementations in terms of possible future tasks, it is impossible to cover all the subjects that a FE program can incorporate. Nevertheless, when referring to algorithmic implementations the parallel solution of the numerical problem cannot be neglected, thus it is one of the main future tasks of this research work.

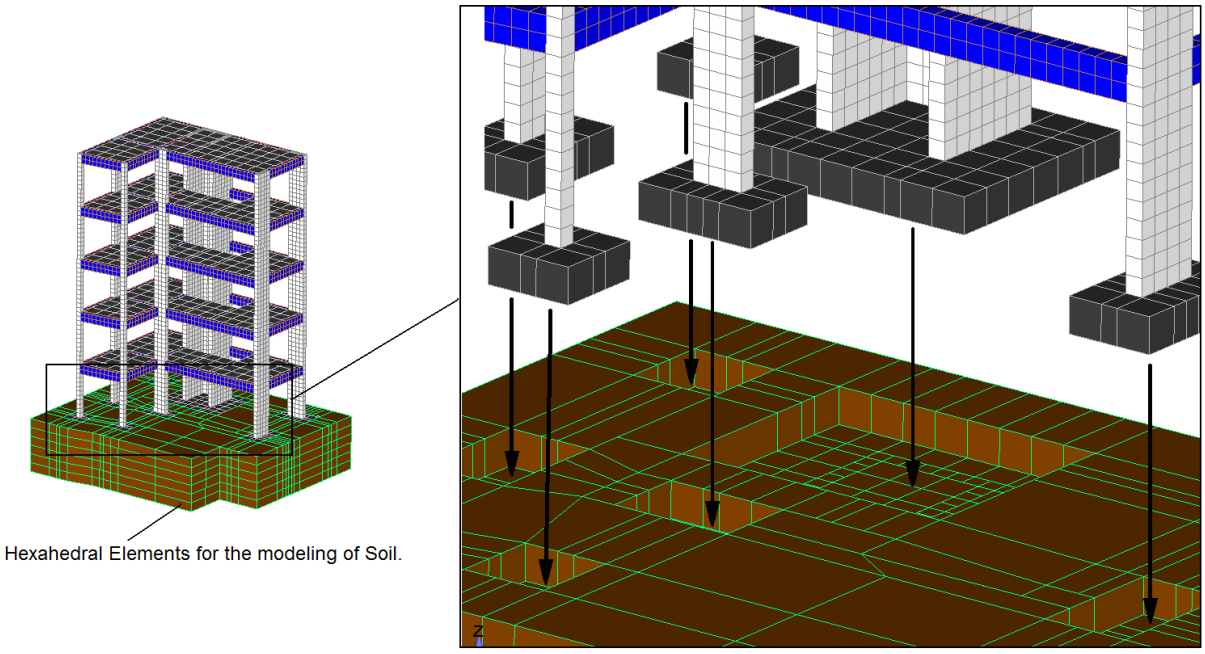

FIGURE 8.1 5-STOREY RC BUILDING. HEXAHEDRAL FINITE ELEMENT MESH OF THE CONCRETE AND SOIL DOMAINS.

References

[1] Argyris J. (1954 & 1955), "Energy theorems and structural analysis", Aircraft Engrg, 26, 347-356; 383-387; 394 & 27, 42-58; 80-94; 125-134; 145-158.

[2] Clough R.W. (1960), "The finite element method in plane stress analysis", Proceedings of the Second ASCE Conference on Electronic Computation, Pittsburgh, PA.

[3] Turner M.J., Clough R.W., Martin H.C. and Topp L.J. (1956), "Stiffness and deflection analysis of complex structures", J. Aero. Sci., Vol. 23, pp. 805-824.

[4] Zienkiewicz O.C. (1977), "The Finite Element Method (3rd edn)", McGraw-Hill, New York.

[5] Beer G. (2001), "BEFE user's reference and verification manual", CSS, Graz.

[6] Hartl H. (2002), "Development of a Continuum-Mechanics-Based Tool for 3D Finite Element Analysis of Reinforced Concrete Structures and Application to Problems of Soil-Structure Interaction", Ph.D. Thesis, Graz University of Technology, Institute of. Structural Concrete.

[7] Hitchings D. (1972), "FINEL user's manual", Imperial College, London.

[8] Kotsovos M.D. and Pavlovic M.N. (1995), "Structural Concrete – Finite-element analysis for limit-state design", Thomas Telford Publications.

[9] Lykidis G. (2007), "Static and Dynamic Analysis of Reinforced Concrete structures with 3D Finite Elements and the smeared crack approach", Ph.D. Thesis, NTUA, Greece, 2007. [In Greek]

[10] Clough R.W. Benuska, K.L. and Wilson E.L. (1965), "Inelastic Earthquake Response of Tall Buildings, Proceedings", Third World Conference on Earthquake Engineering, New Zealand, Vol. 11, New Zealand National Committee on Earthquake Engineering.

[11] Giberson M. (1967), "The Response of Nonlinear Multi-Storey Structures Subjected to Earthquake Excitations", Earthquake Engineering Research Laboratory, Pasadena.

[12] Otani S. (1974), "Inelastic Analysis of R/C Frame Structures", Journal of the Structural Division, ASCE, Vol. 100, No. ST7.

[13] Mahin S.A. and Bertero V.V. (1976), "Problems in Establishing and Predicting Ductility in Seismic Design", International Symposium on Earthquake Structural Engineering, St. Louis, Missouri, USA.

[14] Anderson J.C. and Townsend W.H. (1977), "Models for RC Frames with Degrading Stiffness", Journal of the Structural Division, ASCE, Vol. 103, No. ST12.

[15] Soleimani D. (1979), "Reinforced Concrete Ductile Frames Under Earthquake Loading with Stiffness Degradation", Ph.D. Dissertation , University of California, Berkeley.

[16] Takayanagi T. and Schnobrich W.C. (1979), "Non-Linear Analysis of Coupled Wall Systems", Earthquake Engineering and Structural Dynamics, Vol. 7, pp. 1-22.

[17] Emori, K. and Schnobrich, W.C. (1981), "Inelastic Behavior of Concrete Frame-Wall Structures", Journal of the Structural Division, ASCE, Vol. 107, No. ST1.

[18] Anagnostopoulos S.A. (1981), "Inelastic Beams for Seismic Analyses of Structures", Journal of the Structural Division, ASCE, Vol. 107, No. ST7.

[19] Banon H., Biggs J.M. and Irvine M.H. (1981), "Seismic Damage in Reinforced Concrete Frames", Journal of the Structural Division, ASCE, Vol. 107, No. ST9.

[20] Takeda T., Sozen M.A. and Nielsen N.N. (1970), "Reinforced Concrete Response to Simulated Earthquakes", Journal of the Structural Division, ASCE, Vol. 96, ST12.

[21] Park Y.J. and Ang A.H.S. (1985), "Mechanistic Seismic Damage Model for Reinforced Concrete", Journal of Structural Engineering, ASCE, Vol. 111, No. 4.

[22] Keshavarzian M. and Schnobrich W.C. (1984), "Computed Nonlinear Seismic Response of R/C Frame-Wall Structures", Civil Engineering Studies, Structural Research Series No. 515, University of Illinois at Urbana-Champaign, Urbana, Ill.

[23] Vecchio F.J. and Collins M.P. (1986), "Modified Compression-Field Theory For Reinforced Concrete Elements Subjected To Shear", Journal of the American Concrete Institute, Vol. 83, pp. 219-231.

[24] Ozcebe G. and Saatcioglu M. (1989), "Hysteretic Shear Model for Reinforced Concrete Members", Journal of Structural Engineering, ASCE, Vol. 115, No. 1.

[25] Roufaiel M.S.L. and Meyer C. (1987), "Analytical Modeling of Hysteretic Behavior of R/C Frames", Journal of Structural Engineering, ASCE, Vol. 113, No. 3.

[26] Meyer C., Roufaiel M.S. and Arzoumanidis S.G. (1983), "Analysis of Damaged Concrete Frames for Cyclic Loads", Earthquake Engineering and Structural Dynamics, Vol. 11, pp. 207-228.

[27] Pantazopoulou S.J. and Moehle J.P. (1987), "The effect of slabs on the flexural behavior of beams", UCB/EERC-87/17, Earthquake Engineering Research Center, University of California, Berkeley, 1987-10.

[28] Mahasuverachai M. and Powell G.H. (1982), "Inelastic Analysis of Piping and Tubular Structures", EERC Report 82/27, Earthquake Engineering Research Center, University of California, Berkeley.

[29] Kaba S. and Mahin S.A. (1984), "Refined Modeling of Reinforced Concrete Columns for Seismic Analysis", EERC Report 84/03, Earthquake Engineering Research Center, University of California, Berkeley.

[30] Zeris C.A. (1986), "Three Dimensional Nonlinear Response of Reinforced Concrete Buildings", Ph.D. Thesis, University of California, Department of Civil Engineering, Berkeley.

[31] Zeris C.A. and Mahin S.A. (1988), "Analysis of Reinforced Concrete Beam-Columns under Uniaxial Excitation", Journal of Structural Engineering, ASCE, 114(ST4), pp. 804-820, pp.2640-2656.

[32] Zeris C.A. and Mahin S.A. (1991), "Behavior of Reinforced Concrete Structures under Biaxial Excitation", Journal of Structural Engineering, ASCE, 117(ST9), pp. 2657-2673.

[33] Spacone E., Ciampi V. and Filippou F.C. (1992), "A beam element for seismic damage analysis", Report No. UCB/EERC-92/07, College of Engineering, University of California.

[34] Spacone E., Ciampi V. and Filippou F.C. (1996), "Mixed formulation of nonlinear beam element", Computers and Structures, Vol. 58(1), pp. 71-83.

[35] Spacone E., Filippou F.C. and Taucer F.F. (1996), "Fibre beam-column model for non-linear analysis of R/C frames: Part I. Formulation", Earthquake Engineering and Structural Dynamics, Vol. 25, pp. 711-725.

[36] Petrangeli M. and Ciampi V. (1997), "Equilibrium based iterative solutions for the non-linear beam problem", International Journal for Numerical Methods in Engineering, Vol. 40, pp. 423-437.

[37] Petrangeli M., Pinto P.E. and Ciampi V. (1999), "A Fibre Element for cyclic bending and Shear. I: Theory", Journal of Engineering Mechanics, ASCE, Vol. 125(9), pp. 994-1001.

[38] Petrangeli M. (1999), "A Fibre Element for cyclic bending and Shear. II: Verification", Journal of Engineering Mechanics, ASCE, Vol. 125(9), pp. 1002-1009.

[39] Mohammad R.S. and Spacone E. (2001), "Finite element formulations of one-dimensional elements with bond-slip", Engineering Structures, Vol. 23, pp. 815-826.

[40] Neuenhofer A. and Filippou F.C. (1997), "Evaluation of Nonlinear Frame Finite Element Models", Journal of Structural Engineering, American Society of Civil Engineers, Vol. 123(7), pp. 958-966.

[41] Neuenhofer A. and Filippou F.C. (1998), "A Geometrically Nonlinear Flexibility-Based Frame Finite Element", Journal of Structural Engineering, American Society of Civil Engineers, Vol. 124(6), pp. 704-711.

[42] Ayoub A. and Filippou F.C. (1999), "Mixed Formulation of Bond-Slip Problems under Cyclic Loads", Journal of Structural Engineering, American Society of Civil Engineers, Vol. 125(6), pp. 661-671.

[43] Schulz M. and Filippou F.C. (2001), "Non-linear spatial Timoshenko beam element with curvature interpolation", Int. J. Numer. Meth. Engng, Vol.50, pp. 761-785 .

[44] Limkatanyu1 S. and Spacone E. (2002), "Reinforced Concrete Frame Element with Bond Interfaces. I: Displacement-Based, Force-Based and Mixed Formulations", Journal of Structural Engineering, Vol. 128, No. 3, pp. 346-355.

[45] Limkatanyu1 S. and Spacone E. (2002), "Reinforced Concrete Frame Element with Bond Interfaces. II: State Determinations and Numerical Validation", Journal of Structural Engineering, Vol. 128, No. 3, pp. 356-364.

[46] Battini J.M. and Pacoste C. (2002), "Co-rotational beam elements with warping effects in instability problems", Computer Methods in Applied Mechanics and Engineering, Vol. 191, pp. 1755-1789.

[47] Battini J.M. and Pacoste C. (2002), "Plastic instability of beam structures using co-rotational elements", Computer Methods in Applied Mechanics and Engineering, Vol. 191 (51-52), pp. 5811-5831.

[48] Klinkel S. and Govindjee S. (2002), "Using finite strain 3D-material models in beam and shell elements", Engineering Computations, Vol. 19, pp. 902-921.

[49] Saritas A. and Filippou F.C. (2004), "Modeling of Shear Yielding Members for Seismic Energy Dissipation", Proceedings of the 13th World Conference on Earthquake Engineering, Vancouver, BC, Canada.

[50] Papaioannou I., Fragiadakis M. and Papadrakakis M. (2005), "Inelastic analysis of framed structures using the fiber approach", Proceedings of the 5th International Congress on Computational Mechanics (GRACM 05), Limassol, Cyprus, 29 June-1 July 2005, Vol. 1, pp. 231-238.

[51] Argyris J.H., Balmer H., Doltsinis J.S., Dunne P.C., Haase M., Kleiber M., Malejannakis G.A., Mlejnek H.P., Muller M. and Scharf D.W. (1979), "Finite element method - the natural approach", Computer Methods in Applied Mechanics and Engineering, Vol. 17(18), pp. 1-106.

[52] Mazars J., Kotronis P., Ragueneau F. and Casaux G. (2006), "Using multifiber beams to account for shear and torsion Applications to concrete structural elements", Computer Methods Applied Mechanics Engineering, Vol. 195, pp. 7264-7281.

[53] Marini A. and Spacone E. (2006), "Analysis of reinforced concrete elements including shear effects", ACI Structural Journal, Vol. 103, pp. 645-655.

[54] Navarro G.J., Miguel S.P., Fernandez P.M.A and Filippou F.C. (2007), "A 3D numerical model for reinforced and prestressed concrete elements subjected to combined axial, bending, shear and torsion loading", Engineering Structures, Vol. 29, pp. 3404-3419.

[55] Filippou F.C. and Constantinides M. (2004), "FEDEASLab. Getting started guide and simulations examples", Technical report NEESgrid-2004-22.

[56] Addessi A. and Ciampi V. (2007), "A regularized force-based beam element with a damage–plastic section constitutive law", Int. J. Numer. Meth. Engng, Vol.(70), pp. 610-629.

[57] Mata P.A., Oller S.M and Barbat A.H. (2007), "Static analysis of beam structures under nonlinear geometric and constitutive behavior", Computer Methods in Applied Mechanics and Engineering, Vol. 196 (45-48), pp. 4458-4478.

[58] Simo J.C. and Vu-Quoc L. (1986), "A three-dimensional finite-strain rod model. Part II: Computational aspects", Computer Methods in Applied Mechanics and Engineering, Vol. 58, pp. 79-116.

[59] Simo J.C. and Vu-Quoc L. (1988), "On the dynamics in space of rods undergoing large motions - A geometrically exact approach", Computer Methods in Applied Mechanics and Engineering, Vol. 66, 125-161.

[60] Ghosh S. and Roy D. (2008), "Consistent quaternion interpolation for objective finite element approximation of geometrically exact beam", Computer Methods in Applied Mechanics and Engineering, Vol. 198 (3-4), pp. 555-571.

[61] Fardis N. (2008), "Practical Modeling and Nonlinear Seismic Response Analysis of Concrete Buildings", 3rd Conference on Earthquake Engng & Engng Seismol., Greece, 5-7 November, 2008. [in Greek]

[62] Papachristidis A., Fragkiadakis M. and Papadrakakis M. (2008), "Seismic Assessment of Structures with a Beam-Column Element Based on the Natural Mode Method", 6th GRACM International Congress on Computational Mechanics Thessaloniki, 19-21 June 2008.

[63] Papachristidis A., Fragkiadakis M. and Papadrakakis M. (2009), "Modeling of the inelastic response of RC structures accounting for shear strains", [In Greek: "Προσομοίωση ανελαστικής συμπεριφοράς κατασκευών από Οπλισμένο Σκυρόδεμα με θεώρηση διατμητικών Παραμορφώσεων"], 16th Conference of Concrete, Paphos, Cyprus, 21-23 Oct 2009.

[64] Kwak H.G. and Kim S.P. (2010), "Simplified monotonic moment-curvature relation considering fixed-end rotation and axial force effect", Engineering Structures, Vol. 32, pp. 69-79.

[65] Landesmann A. (2010), "Plastic-hinge approach for inelastic analysis of steel-concrete framed structures", Journal of Constructional Steel Research, Vol. 66(3), pp. 323-334.

[66] Valipour H.R. and Foster S.J. (2010), "Nonlinear reinforced concrete frame element with torsion", Engineering Structures, Vol. 32(4), pp. 988-1002.

[67] Oden J.T. (1972), "Finite Element of Nonlinear Continua", McGraw-Hill Book Company, New York, N.Y.

[68] Stricklin J.A., Heisler W.E. and von Riesemann W.A. (1973), "Evaluation of Solution Procedures for Material and/or Geometrically Nonlinear Structural Analysis", A.I.A.A. Journal, Vol. 11, pp. 292-299.

[69] Fellipa C.A. (1976), "Procedures for Computer Analysis of Large Nonlinear Structural Systems", Proceedings, Int. Symp. On Large Engineering Systems, Manitoba, Winnipeg, Canada, Aug 1976.

[70] Argyris J.H., Vaz L.E. and Willam K.J. (1978), "Improved Solution Methods for Inelastic Rate Problems", Computer Methods in Applied Mechanics and Engineering, Vol. 16, pp. 231-277.

[71] Bathe K.J. and Cimento A.P. (1980), "Some Partial Procedures for the Solution of Nonlinear Finite Element Equations", Computer Methods in Applied Mechanics and Engineering, Vol. 22, pp. 59-85.

[72] Wempner G.A. (1971), "Discrete approximation related to nonlinear theories of solids", International Journal of Solids and Structures, Vol. 7, pp. 1581-1599.

[73] Riks E., (1972), "The application of Newton's method to the problem of elastic stability", Journal of Applied Mechanics, Vol. 39, pp. 1060-1065.

[74] Riks E. (1979), "An incremental approach to the solution of snapping and buckling problems", International Journal of Solids and Structures, Vol. 15, 529-551.

[75] Baltoz J.L., Dhatt, G. (1979), "Incremental displacement algorithms for nonlinear problems", International Journal for Numerical Methods in Engineering, Vol. 14, pp. 1262-1266.

[76] Crisfield M.A. (1981), "A fast incremental/iterative solution procedure that handles snap-through", Computer and Structures, Vol. 13, pp. 55-62.

[77] Lam W.F. and Morley C.T. (1992), "Arc-length method for passing limit points in structural calculation", Journal of Structural Engineering, Vol. 118(1), pp. 169-185.

[78] Carrera E. (1994), "A study on arc-length type methods and their operation failures illustrated by a simple model", Computer and Structures, Vol. 50(2), pp. 217-229.

[79] Memon B.-A. and Su X.-Z. (2004), "Arc-length technique for nonlinear finite element analysis", Journal of Zhejiang University, SCI, Vol. 5 (5), pp. 618-628.

[80] Hellweg H.B. and Crisfield M.A. (1998), "A new arc-length method for handling sharp snap-backs", Computer and Structures, Vol. 66(5), pp. 705-709.

[81] Alfano G. and Crisfield M.A. (2003), "Solution strategies for the delamination analysis based on a combination of local-control arc-length and line searches", Int. J. Numer. Meth. Engng, Vol. 58, pp. 999-1048.

[82] Manuel R.C. and Dinar C. (2008), "On the arc-length and other quadratic control methods: Established, less known and new implementation procedures", Computers and Structures, Vol. 86, pp. 1353-1368.

[83] Argyris J., Tenek L. and Mattsson A. (1998), "BEC: A 2-node fast converging shear-deformable isotropic and composite beam element based on 6 rigid-body and 6 straining modes", Computer Methods in Applied Mechanics and Engineering, Vol. 152, pp. 281-336.

[84] Zienkiewicz O.C. and Taylor R.L. (1989), "The Finite Element Method", Volume 1, Basic Formulation and Linear Problems, Fourth Edition, McGraw Hill, London.

[85] Zienkiewicz O.C. and Taylor R.L. (1991), "The Finite Element Method", Volume 2, Solid and Fluid Mechanics, Dynamics and Non-Linearity, Fourth Edition, McGraw Hill, London.

[86] Menegotto M. and Pinto P.E. (1973), "Method of Analysis for Cyclically Loaded Reinforced Concrete Plane Frames Including Changes in Geometry and Non-Elastic Behavior of Elements under Combined Normal Force and Bending", Proceedings, IABSE Symposium on Resistance and Ultimate Deformability of Structures Acted on by Well Defined Repeated Loads, Lisbon, pp.15-22.

[87] Kent D.C. and Park R. (1971), "Flexural Members with Confined Concrete", Journal of the Structural Division, ASCE, Vol. 97(ST7).

[88] Filippou F.C., Popov E.P. and Bertero V.V. (1983), "Effects on Bond Deterioration on Hysteretic Behavior of Reinforced Concrete Joints", EERC Report 83-19, Earthquake Engineering, Research Center, Berkeley.

[89] Scott B.D., Park R. and Priestley M.J.N. (1982), "Stress-Strain Behavior of Concrete Confined by Overlapping Hoops at Low and High Strain Rates", ACI Journal, Vol. 79, No 1, pp. 13-27.

[90] Mazzoni S., McKenna F. and Fenves G.L. (2000), "OpenSees Command Language Manual", Pacific Earthquake Engineering Research Center University of California, Berkeley.

[91] Siemens PLM Software (2009), "World-class finite element analysis (FEA) solution for theWindows desktop", Siemens Product Lifecycle Management Software Inc.

[92] Vasilomichelaki S. (2008), "ΑΝΕΛΑΣΤΙΚΗ ΣΤΑΤΙΚΗ ΑΝΑΛΥΣΗ ΠΛΑΙΣΙΑΚΩΝ ΦΟΡΕΩΝ ΜΕ ΤΗΝ ΜΕΘΟΔΟ ΤΩΝ ΠΕΠΕΡΑΣΜΕΝΩΝ ΣΤΟΙΧΕΙΩΝ", Diploma Thesis, National Technical University of Athens, Department of Civil engineering. [In Greek]

[93] Vasilomichelaki S. (2010), "ΠΑΡΑΜΕΤΡΙΚΗ ΔΙΕΡΕΥΝΗΣΗ ΠΛΑΙΣΙΑΚΩΝ ΦΟΡΕΩΝ ΑΠΟ ΟΠΛΙΣΜΕΝΟ ΣΚΥΡΟΔΕΜΑ ΜΕ ΤΗΝ ΜΕΘΟΔΟ ΤΩΝ ΠΕΠΕΡΑΣΜΕΝΩΝ ΣΤΟΙΧΕΩΝ ", Master's Thesis, National Technical University of Athens. [In Greek]

[94] Gerstle K.H, Linse D., Bertacchi P., Kotsovos M.D., Ko H-Y., Newman J.B., Rossi P., Schickert G., Taylor M.A., Traina L.A., Zimmerman R.M. and Bellotti R. (1978), "Strength of concrete under multiaxial stress states", Proc. Douglas McHenry International Symposium on concrete and Concrete Structures, SP-55, American Concrete Institute, Detroit, pp. 103-131.

[95] Gerstle K.H, Aschl H., Bellotti R., Bertacchi P., Kotsovos M.D., Ko H-Y., Linse D., Newman J.B., Rossi P., Schickert G., Taylor M.A., Traina L.A., Winkler H. and Zimmerman R.M. (1980), "Behavior of concrete under multiaxial stress states", Journal of Engineering Mechanics Div., Proc. ASCE, Vol. 106, pp. 1383-1403.

[96] van Mier J.G.M., Shah S.P., Arnaud M., Balayssac J.P., Bassoul A., Choi S., Dasenbrock D., Ferrara G., French C., Gobbi M.E., Karihaloo B.L., Konig G., Kotsovos M.D., Labnz J., Lange-Kornbak D., Markeset G., Pavlovic M.N., Simsch G., Thienel K.C., Turatsinze A., Ulmer M., van Vliet M.R.A., and Zissopoulos D. (1997), "TC 148-SSC: Test methods for the strain-softening of concrete. Strain-softening of concrete in uniaxial compression", Materials & Structures RILEM, Vol. 30(198), pp. 195-209.

[97] Zisopoulos P.M., Kotsovos M.D. and Pavlovic M.N, (2000), "Deformational behavior of concrete specimens in uniaxial compression under different boundary conditions", Cem. Concr. Res., Pergamon, Vol. 30, pp. 153-159.

[98] Schickert G. (1981), "Formfaktoren der Betondruckfestigkeit", Die Bautechnik, Vol. 58, pp. 52-57.

[99] Wesche K. (1996), "Baustoffe für tragende Bauteile Band 2 Beton", 3rd ed., Bauverlag, Wiesbaden.

[100] Grübl P., Weigler H. and Sieghart K. (2001), "Beton Arten, Herstellung und Eigenschaften", Ernst & Sohn, Berlin.

[101] Kotsovos M.D. and Newman J.B. (1977), "Behavior of concrete under multiaxial stresses", ACI J., Vol. 74(9), pp. 443-446.

[102] Kotsovos M.D. and Newman J.B. (1978), "Generalized stress – strain relations for concrete", J. Engng Mech. Div. Proc., ASCE, Vol. 104, pp. 845-856.

[103] Kotsovos M.D. and Newman J.B. (1979), "A mathematical description of the deformational behavior of concrete under complex loading", Mag. Conc. Res., Vol. 31(107), pp. 77-90.

[104] Kotsovos M.D. (1983), "Effect of testing techniques on the post-ultimate behavior of concrete in compression", Mat. Struct., RILEM, Vol. 16, pp. 3-12.

[105] CEB (1996), "RC Elements under cyclic loading", Thomas Telford.

[106] Bažant Z.P. and Cedolin L. (1991), "Stability of Structures", Oxford University Press.

[107] Duda H. (1991), "Bruchmechanisches Verhalten von Beton unter monotoner und zyklischer Zugbeanspruchung", Deutscher Ausschuß für Stahlbeton, Heft 419, Beuth, Berlin.

[108] Cotterel B. and Mai Y.W. (1996), "Fracture mechanics of cementitious materials", Chapman & Hall.

[109] Shah S.P., Swartz S.E. and Ouyang C. (1995), "Fracture mechanics of concrete. Applications of fracture mechanics to concrete, rock and other quasi-brittle materials", John Wiley & sons.

[110] Wittmann F.H. (1977), "Grundlagen eines Modells zur Beschreibung charakteristischer Eigenschaften des Betons", Deutscher Ausschuß für Stahlbeton, Heft 290, Ernst & Sohn, Berlin.

[111] fib bulletin No 1 (1999), "Structural concrete", Vol. 1, International Federation for Structural Concrete (fib), Lausanne.

[112] Ross A.D., England G.L. and Suan R.H. (1965), "Prestressed Concrete Beams under a Sustained Temperature Crossfall", Mag. Concr. Res., Vol. 17(52), pp. 117-126.

[113] England G.L. (1966), "Steady-state stresses in concrete structures subjected to sustained temperatures and loads", Nucl. Eng. Des., Vol. 4(1), pp. 54-65; Vol. 3(2), pp. 246-255.

[114] Browne R.D. (1967), "Properties of concrete in reactor vessels, Conference on prestressed concrete pressure vessels at Church House", Westminster SW1, 13-17 March 1967, The institution of civil engineers, London.

[115] Lykidis G.Ch. (2001), "Time dependent analysis of prestressed concrete structures under a change of statically indeterminate form", MSc Dissertation , Imperial College, London.
[116] Wittmann F.H. (1985), "Deformation of concrete at variable moisture content", in Bažant Z.P. (ed.), Mechanics of Geomaterials, John Wiley & Sons, New York, 1985, pp. 425-459.
[117] Mahin S.A., Bertero V.V., Atalya M.B. and Rea. D. (1972), "Rate of Loading Effects on Uncracked and Repaired Reinforced Concrete Members", Report UCB/EERC-72/09. Berkeley: EERC, University of California.
[118] Lowes L.N. (1999), "Finite Element Modeling of Reinforced Concrete Beam – Column Bridge Connections", Ph.D. Thesis, University of California, Berkeley.
[119] Kotsovos M.D. and Pavlovic M.N. (2001), "The 7/9/99 Athens earthquake: Causes of damage not predicted by structural-concrete design methods", The Structural Engineer, IStructE, Vol. 79(15), pp. 23-29.
[120] van Mier J.G.M. (1986), "Multiaxial strain-softening of concrete", Materials & Structures, RILEM. Vol. 19, No. 111, pp. 179-200.
[121] Newman J.B. (1973), "Deformational behavior, failure mechanisms and design criteria for concretes under combinations of stress", University of London, Ph.D. Thesis.
[122] Ottosen N.S. (1977), "A failure criterion for concrete", Journal of the Engineering Mechanics Division, Vol. 103, pp. 527-535.
[123] Rashid Y.R. (1968), "Ultimate Strength Analysis of Pre-stressed Concrete Pressure Vessels," Nuclear Engineering and Design, Vol. 7, pp. 334-344.
[124] Červenka V. and Gerstle K. (1972), "Inelastic Analysis of Reinforced Concrete Panels: (1) Theory, (2) Experimental Verification and application", Publications IABSE, Zürich, V.31-00, 1971, pp. 32-45, and V.32-II, 1972, pp. 26-39.
[125] Owen J.M., Figueiras J.A. and Damjanic F. (1983), "Finite Element Analysis of Reinforced and Pre-stressed concrete structures including thermal loading", Comp. Meth. Appl. Mech. Eng., Vol. 41, pp. 323-366.
[126] Bažant Z.P and Oh B.H. (1983), "Crack Band Theory for Fracture of Concrete", Materials and Structures, RILEM, Vol. 16, pp. 155-177.
[127] De Borst R. (1986), "Non-linear analysis of frictional materials", Ph.D. Thesis, Delft University of Technology.
[128] Simo J.C. and Ju J.W. (1987), "Strain and Stress-based Continuum Damage Models-I. Formulations, II Computational Aspects", Int. J. Solids Structures, Vol. 23(7), pp. 821-869.
[129] Rots J.G. and Blaauwendraad J. (1989), "Crack models for concrete: discrete or smeared? Fixed, multi-directional or rotating?", HERON, Vol. 34(1).
[130] Pramono E. and Willam K.J. (1989), "Fracture Energy-Based Plasticity Formulation of Plain Concrete", ASCE-JEM, Vol. 115, pp. 1183-1204.
[131] Etse G. (1992), "Theoretische und numerische Untersuchung zum diffusen und lokalisierten Versagen in Beton", Ph.D. Thesis, University of Karlsruhe.
[132] Feenstra P.H. (1993)," Computational Aspects of Bi-axial Stress in Plain and Reinforced Concrete", Ph.D. Thesis, Delft University of Technology.
[133] Feenstra P.H., Rots J.G., Amesen A., Teigen J.G. and Hoiseth K.V. (1998), "A 3D Constitutive Model for Concrete Based on Co-rotational concept", Proc. EURO-C, Vol. 1, pp. 13-22.
[134] Menetrey Ph., Walther R., Zimmerman Th., Willam K.J. and Regan P.E. (1997), "Simulation of punching failure in reinforced concrete structures", Journal of Structural Engineering, Vol. 123(5), pp. 652-659.

[135] Bažant Z.P, Caner F.C., Carol I., Adley M.D. and Akers S.A. (2000), "Microplane Model M4 for Concrete I: Formulation with Work - Conjugate Deviatoric Stress", J. Engng Mech., ASCE, Vol. 126, pp. 944-953.

[136] Bažant Z.P. and Caner F.C. (2005), "Microplane model M5 with kinematic and static constraints for concrete fracture and anelasticity I: Theory", J. Engng Mech., ASCE, Vol. 131(1), pp. 31-40.

[137] Bažant Z.P. and Caner F.C., (2005), "Microplane model M5 with kinematic and static constraints for concrete fracture and anelasticity II: Computation", J. Engng Mech., ASCE, Vol. 131(1), pp. 41-47.

[138] Spiliopoulos K.V. and Lykidis G.Ch. (2006), "An efficient three-dimensional solid finite element dynamic analysis of reinforced concrete structures", Earthquake Engng Struct. Dyn., Vol. 35, pp. 137-157.

[139] Sato Y. and Naganuma K. (2007), "Discrete-like crack simulation by smeared crack-based FEM for reinforced concrete", Earthquake Engng Struct. Dyn., Vol. 36, pp. 2137-2152.

[140] Červenka V., Jendele L. and Červenka J. (2008), "ATENA Program Documentation, Part 1: Theory", Prague, November 21.

[141] Kotsovos M.D. (1979), "Fracture processes of concrete under generalized stress state", Mat. & Struct., RILEM, Vol. 12, pp. 431-437.

[142] Lubliner J., Oliver J., Oller S. and Onate E. (1989), "A plastic-damage model for concrete", Int. J. Sol. Struct., Vol. 25(3), pp. 299-326.

[143] Lubliner J. (1990), "Plasticity Theory", Macmillan, New York.

[144] Valanis K.C. (1971), "A theory of viscoplasticity without a yield surface, part I: general theory", Archives of Mechanics, Vol. 23, pp. 517-534

[145] Bažant Z.P. and Kim S.S. (1979), "Plastic-fracturing theory for concrete", J. Engng Mech. Div., ASCE, Vol. 105(3), pp. 407-428.

[146] Mazars J. (1986), "A description of micro- and macro-scale damage of concrete structures", Journal of Engineering Fracture Mechanics, Vol. 25, pp. 729-737.

[147] Lemaitre J. (1986), "Local approach of fracture", Engineering Fracture Mechanics, Vol. 25, pp. 523-537.

[148] Chaboche J.L. (1988), "Continuum damage mechanics: part I – general concepts", Journal of Applied Mechanics, Vol. 55, pp. 59-64.

[149] Chaboche J.L. (1988), "Continuum damage mechanics: part II – damage growth, crack initiation and crack growth", Journal of Applied Mechanics, Vol. 55, pp. 65-72.

[150] Lemaitre J. (1996), "A course on damage mechanics", 2nd ed., Springer, Berlin.

[151] Meschke G., Lackner R. and Mang H.A. (1998), "An anisotropic elastoplastic-damage model for plain concrete", International Journal for Numerical Methods in Engineering, Vol. 42, pp. 703-727.

[152] Ragueneau F., La Borderie Ch. and Mazars J. (2000), "Damage model for concrete-like materials coupling cracking and friction, contribution towards structural damping: first uniaxial applications", Mechanics of Cohesive-frictional Materials, Vol. 5(8), pp. 607-625.

[153] Kattan P.I. and Voyiadjis G.Z (2002), "Damage mechanics with finite elements", Springer, Berlin.

[154] Cusatis G., Beghini A. and Bažant Z.P. (2008), "Spectral stiffness microplane model for quasibrittle composite laminates - Part I: Theory", Journal of Applied Mechanics, Transactions ASME, Vol. 75 (2), pp. 0210091-0210099.

[155] Benzarti K., Freddi F. and Frémond M. (2009), "Construction and Building Materials. A damage model to predict the durability of bonded assemblies. Part I: Debonding behavior of FRP strengthened concrete structures", Construction and Building Materials, Article in Press.

[156] Yu T., Teng J.G., Wong Y.L. and Dong S.L. (2010), "Finite element modeling of confined concrete-II: Plastic-damage model", Engineering Structures, Vol. 32(3), pp. 680-691.
[157] Bažant Z.P. and Gambarova P.G. (1984), "Crack shear in concrete: crack band microplane model", Journal of Structural Engineering, Vol. 110, pp. 2015-2036.
[158] Bažant Z.P. and Prat P.C. (1988), "Microplane model for brittle plastic material I. Theory, II Verification", J. Engng Mech., Vol. 114, pp. 1672-1702.
[159] Bažant Z.P., Červenka J., and Wierer M. (2001), "Equivalent localization element for crack band approach to mesh-size sensitivity in microplane model", Int. J. Numer. Methods Eng., Vol. 62 (5), pp. 700-726.
[160] Bažant Z.P. and Ozbolt J. (1990), "Nonlocal Microplane model for fracture, damage and size effect in Structures", J. Engng. Mech., ASCE, Vol. 116(11), pp. 2845-2505.
[161] Ngo D. and Scordelis A.C. (1967), "Finite element analysis of reinforced concrete beams", ACI J., Vol. 64(3), pp. 152-163.
[162] Nilson A.H., (1968), "Nonlinear analysis of reinforced concrete by the finite element method", ACI Journal, pp. 757-766.
[163] Grootenboer H.J., Leijten S.F.C.H. and Blaauwendraad J. (1981), "Numerical models for concrete structures in plane stress", Heron, 26, No. 1c, Delft.
[164] Feenstra P.H., de Borst R. and Rots J.G. (1991), "Numerical study on crack dilatancy I: Models and Stability analysis II: Applications", J. Engng Mech., ASCE, Vol. 117, pp. 733-769
[165] Rots J.G. (1991), "Smeared and discrete representations of localized fracture", Int. J. Fract., Vol. 51(1), pp. 45-59.
[166] Xie M. and Gerstle W. (1995), "Energy based cohesive crack propagation modeling", J. Engng Mech., Vol. 121, pp. 1349-1358.
[167] Bittencourt T. and Ingraffea A.R. (1995), "Three-Dimensional Cohesive Crack Analysis of Short-Rod Specimens", Erdogan F., Hartranft R.J. (ed.), ASTM STP 1220, Fracture Mechanics, Philadelphia, Vol. 25, pp. 46-60.
[168] Riddell W.T., Ingraffea A.R. and Warwrzynek P.A. (1997), "Experimental Observations and Numerical Predictions of Three-Dimensional Fatigue Crack Propagation", Engineering Fracture Mechanics, Vol. 58, pp. 293-310
[169] Ruiz G., Pandolfi A. and Ortiz. M. (2001), "Three dimensional cohesive modeling of dynamic mixed - mode fracture", Int. J. Num. Meth. Engng, Vol. 52, pp. 97-120.
[170] Galvez J.C., Červenka J., Cendon D.A. and Saouma V. (2002), "A discrete crack approach to normal/shear cracking of concrete", Cem. Concr. Res., Pergamon, Vol. 32(10), pp. 1567-1585.
[171] Prasad M.V. and Krishnamoorthy C.S. (2002), "Computational model for discrete crack growth in plain and reinforced concrete", Computer Methods in Applied Mechanics and Engineering, Vol. 191, pp. 2699-2725.
[172] Dias-da-Costa D., Alfaiate J., Sluys L.J. and J̈ulio E. (2009), "Towards a generalization of a discrete strong discontinuity approach", Computer Methods in Applied Mechanics and Engineering, Vol.198, pp. 3670-3681.
[173] Gonzalez-Vidosa F., Kotsovos M.D. and Pavlovic M.N. (1991), "Three-dimensional non-linear finite-element model for structural concrete. Part 1: main features and objectivity study; and Part 2: generality study", Proceedings of the Institution of Civil Engineers, Part 2, Research and Theory, Vol. 91, pp. 517-544; pp. 545-560.
[174] Gonzalez-Vidosa F., Kotsovos M.D. and Pavlovic M.N. (1988), "On the numerical instability of the smeared-crack approach in the non-linear modeling of concrete structures", Commun. Appl. Num. Meth. Engng, Vol. 4, pp. 799-806.

[175] Hentz S., Daudeville L. and Donze F.V. (2004), "Identification and validation of a discrete element model for concrete", J Eng Mech, Vol. 130, pp.709-719.
[176] Rousseau J., Frangin E., Marin P. and Daudeville L. (2009), "Multidomain finite and discrete elements method for impact analysis of a concrete structure", Engineering Structures, Vol. 31(11), pp. 2735-2743.
[177] Rousseau J., Frangin E., Marin P. and Daudeville L. (2007), "Some aspects of DE/FE combined method: Model identification and combined method", In: Proceedings of 9th international conference on computational plasticity, COMPLAS.
[178] Rabczuk T. and Belytschko T. (2007), "A Three Dimensional Large Deformation Meshfree Method for Arbitrary Evolving Cracks", Computer Methods in Applied Mechanics and Engineering, Vol. 196(29-30), pp. 2777-2799.
[179] Camacho G.T. and Ortiz M. (1996), "Computational modeling of impact damage in brittle materials", International Journal of Solids and Structures, Vol. 33, pp. 2899-2938.
[180] Ortiz M. and Pandolfi A. (1999), "Finite-deformation irreversible cohesive elements for three-dimensional crack-propagation analysis", International Journal for Numerical Methods in Engineering, Vol. 44, pp. 1267-1282.
[181] Zhou F. and Molinari J.F. (2004), "Dynamic crack propagation with cohesive elements: a methodology to address mesh dependence", International Journal for Numerical Methods in Engineering, Vol. 59(1), pp. 1-24.
[182] Belytschko T. and Gracie R. (2007), "On XFEM applications to dislocations and interfaces", International Journal of Plasticity, Vol. 23 (10-11), pp. 1721-1738.
[183] Belytschko T. and Lu Y.Y. (1995), "Element-free galerkin methods for static and dynamic fracture", International Journal of Solids and Structures, Vol. 32, pp. 2547-2570.
[184] Liu G.R. (2003), "Mesh Free Methods. Moving beyond the Finite Element Method", CRC Press, LLC.
[185] Kotsovos M.D. and Newman J.B. (1981), "Plain concrete under load – a new interpretation", Proceedings IABSE Colloquium on Advanced Mechanics of Reinforced Concrete, Delft, pp. 143-158.
[186] Bresler B. and Scordelis A.C. (1963), "Shear strength of reinforced concrete beams", ACI Journal, Vol. 60, pp.51-74.
[187] Kim N.-S., Lee J.-H. and Chang S.-P. (2009), "Equivalent multi-phase similitude law for pseudodynamic test on small scale reinforced concrete models", Engineering Structures, Vol. 31, pp. 834-846.
[188] Karakitsios P. (2009), "ΑΝΕΛΑΣΤΙΚΗ ΣΤΑΤΙΚΗ ΑΝΑΛΥΣΗ ΠΛΑΙΣΙΑΚΩΝ ΦΟΡΕΩΝ ΑΠΟ ΟΠΛΙΣΜΕΝΟ ΣΚΥΡΟΔΕΜΑ ΜΕ ΤΗ ΜΕΘΟΔΟ ΤΩΝ ΜΗ ΓΡΑΜΜΙΚΩΝ ΠΕΠΕΡΑΣΜΕΝΩΝ", Diploma Thesis, National Technical University of Athens, Department of Civil Engineering, Athens. [In Greek]
[189] Barzegar F. and Maddipudi S. (1994), "Generating reinforcement in FE modeling of concrete structures", Journal of Structural Engineering, Vol. 120, pp.1656-1662.
[190] Elwi A.E. and Hrudey T.M. (1989), "Finite element model for curved embedded reinforcement", Journal of Engineering Mechanics, Vol. 115, pp.740-754.
[191] ASCE Task Committee on Concrete and Masonry Structures (1982), "Finite element analysis of reinforced concrete", ASCE.
[192] Abdel-Halim M.A.H., and Abu-Lebdeh T.M. (1989), "Analytical study of concrete confinement in tied columns", J. Struct. Engrg., ASCE, Vol. 115(11), pp. 2810-2828.
[193] Gonzalez-Vidosa F., Kotsovos M.D. and Pavlovic M.N. (1990), "Three-dimensional finite element analysis of structural concrete", Proc., Second Int. Conf. on Computer Aided Anal. and

Des. of Concrete Struct., N. Bicanic, and H. Mang, eds., Pineridge Press, Swansea, Wales, Vol. II, pp. 1029-1040.

[194] Jendele L. and Červenka J. (2009), "On the solution of multi-point constraints – Application to FE analysis of reinforced concrete structures", Computers and Structures, Vol. 87, pp. 970-980.

[195] Kwan W.P. and Billington S.L. (2001), "Simulation of structural concrete under cyclic load", Journal of Structural Engineering,Vol.127, pp. 1391-1401.

[196] Kwak H.-G. and Kim D.-Y. (2001), "Nonlinear analysis of RC shear walls considering tension-stiffening effect", Computers and Structures, Vol. 79, pp. 499-517.

[197] Mazars J., Ragueneau F., Casaux G., Colombo A. and Kotronis P. (2004), "Numerical modeling for earthquake engineering: the case of lightly RC structural walls", International Journal for Numerical and Analytical Methods in Geomechanics, Vol. 28, pp. 857-874.

[198] Kwak H.-G. and Kim D.-Y. (2006), "Cracking behavior of RC panels subject to biaxial tensile stresses", Computers and Structures, Vol. 84, pp. 305-317.

[199] Girard C. and Bastien J. (2002), "Finite Element bond slip model for concrete columns under cyclic loads", J. Struct. Engng, ASCE, Vol. 128(12), pp. 1502-1510.

[200] Mirzabozorg H. and Ghaemian M. (2005), "Nonlinear behavior of mass concrete in 3d problems using a smeared crack approach", Earthquake Engineering and Structural Dynamics, Vol. 34, pp. 247-269.

[201] Červenka J. and Papanikolaou V.K. (2008), "Three dimensional combined fracture-plastic material model for concrete", International Journal of Plasticity, Vol. 24(12), pp. 2192-2220.

[202] Papanikolaou V.K. and Kappos A.J. (2009), "Numerical study of confinement effectiveness in solid and hollow reinforced concrete bridge piers: Part 1: Methodology and Part 2: Analysis results and discussion", Engineering Structures, Vol. 87 (21-22), pp. 1427-1439; pp.1440-1450.

[203] Ozbolt J. and Li Y.J. (2001), "Three dimensional cyclic analysis of compressive diagonal shear failure", Finite Element Analysis of RC Structures, Eds: Willam K, Tanabe T.; ACISP-205-4, pp. 61-79.

[204] Jendele L., Červenka J., Saouma V. and Pukl R., "On the choice between discrete or smeared approach in practical structural FE analyses of concrete structures". ČERVENKA CONSULTING, Predvoje 22, 16200 Prague 6, Czech Republic and CEAE Dep., University of Colorado at Boulder, U.S.A.

[205] Cervera M., Hinton E. and Hassan O. (1987), "Nonlinear Analysis of RC plate and shell structures using 20-noded isoparametric brick elements", Computers and Structures, Vol. 25, pp. 845-869.

[206] Lefas I. (1988), "Behavior of reinforced concrete walls and its implication for ultimate limit state design", Ph.D., University of London.

[207] Červenka V. (1970), "Inelastic finite element analysis of reinforced concrete panels under plane loads", Ph.D., University of Colorado, University Microfilms, Inc., Michigan.

[208] DIANA-9.4 (2009), "User's Manual - Release Notes", Copyright (c) 2009 by TNO DIANA BV.

[209] Argyris J., Tenekb L. and Olofssond L. (1997), "TRIC: a simple but sophisticated 3-node triangular element based on 6 rigid-body and 12 straining modes for fast computational simulations of arbitrary isotropic and laminated composite shells", Computer Methods in Applied Mechanics and Engineering, Vol. 145, pp. 11-85

[210] Fardis M.N., Alibe B. and Tasoulas J.L. (1983), "Monotonic and cyclic constitutive law for concrete", J. Engng Mech., Proc. ASCE, Vol. 109, pp. 516-536.

[211] Kolleger J. and Mehlhorn G. (1987), "Material model for cracked reinforced concrete", Proc. IABSE Colloquium on Computational Mechanics of Concrete Structures – Advances and Applications, Delft, August, pp. 63-74.

[212] Armero F. and Oller S. (2000), "A general framework for continuum damage models I. Infinitesimal plastic damage models in stress space", Int J Solids Struct, Vol. 37(48-50), pp. 7409-7436.

[213] Balan T.A., Spacone E. and Kwon M. (2001), "A 3d hypoplastic model for cyclic analysis of concrete structures. Eng Struct, Vol. 23(4), pp. 333-342.

[214] Lee J. and Fenves G.L. (2001), "A return-mapping algorithm for plastic-damage models: 3-D and plane stress formulation", Int. J. Numer. Methods Eng., Vol. 50(2), pp. 487-506.

[215] Nechnech W., Meftah F. and Reynouard J.M. (2002) "An elasto-plastic damage model for plain concrete subjected to high temperatures", Eng. Struct., Vol. 24(5), pp. 597-611.

[216] Borja R.I., Sama K.M. and Sanz P.F. (2003), "On the numerical integration of three-invariant elastoplastic constitutive models", Computer Methods in Applied Mechanics and Engineering, Vol. 192, pp. 1227-1258.

[217] Park H. and Kim J.Y. (2005), "Hybrid plasticity model for reinforced concrete in shear", Eng. Struct., Vol. 27, pp. 35-48.

[218] Jason L., Huerta A., Pijaudier-Cabot G. and Ghavamian S. (2006), "An elastic plastic damage formulation for concrete: Application to elementary tests and comparison with an isotropic damage model", Computer Methods in Applied Mechanics and Engineering, Vol. 195(52), pp. 7077-7092.

[219] Desmorat R., Gatuingt F. and Ragueneau F. (2007), "Nonlocal anisotropic damage model and related computational aspects for quasi-brittle materials", Eng. Fracture Mech., Vol. 74(10), pp. 1539-1560.

[220] Oliver J., Linero D.L., Huespe A.E., Manzoli O.L. (2008) "Two-dimensional modeling of material failure in reinforced concrete by means of a continuum strong discontinuity approach", Computer Methods in Applied Mechanics and Engineering, Vol. 197, pp. 332-348.

[221] Ile N. and Reynouard J.M. (2000), "Nonlinear analysis of reinforced concrete shear wall under earthquake loading", Journal of Earthquake Engineering, Vol.4(2), pp. 183-213.

[222] Kwak H.-G. and Kim D.-Y. (2004), "Material nonlinear analysis of RC shear walls subject to cyclic loadings", Engineering Structures, Vol. 26, pp. 1423-1436.

[223] Darwin D. and Pecknold D.A. (1976), "Analysis of RC shear panels under cyclic loading", J. Struct. Div. ASCE, Vol. 102(2), pp. 355-369.

[224] Viwathenatepa S., Popov E.P. and Bertero V.V. (1979), "Effects of generalized loadings on bond of reinforcing bars embedded in confined concrete blocks", Report to National Science Foundation, University of California Berkeley, California.

[225] Cotsovos D.M., Zeris Ch.A. and Abas A.A. (2009), "Finite Element Modeling of Structural Concrete", ECCOMAS Thematic Conference on Computational Methods in Structural Dynamics and Earthquake Engineering, COMPDYN 2009, Rhodes, Greece, 22–24 June 2009.

[226] Papanikolopoulos K. (2003), "Investigation of the non-linear behavior of reinforced concrete members with finite elements", Postgraduate Thesis, National Technical University of Athens.

[227] Jiràsek M. and Rolshoven S. (2003), "Comparison of integral-type nonlocal plasticity models for strain-softening materials", International Journal of Engineering Science, Vol. 41, pp. 1553–1602.

[228] Bažant Z.P. and Zdenek P. (1983), "Comment on orthotropic models for concrete and Geomaterials", Journal of Engineering Mechanics, Vol. 109(3), pp. 849-865.

[229] Oliver, J. (1989), "Consistent characteristic length for smeared cracking models", International Journal for Numerical Methods in Engineering, Vol. 28 (2), pp. 461-474.

[230] Cedolin L. and Dei.P.S. (1977), "Finite Element studies of shear-Critical R/C Beams", ASCE, Journal of Engineering Mechanics Div, Vol. 103(3), pp. 395-410.

[231] Aufranc M. (1989), "Numerical study of a junction between a three-dimensional elastic structure and a plate", Computer Methods in Applied Mechanics and Engineering, Vol. 74, pp. 207-222.
[232] Bernadou M., Fayolle S. and Lenei F. (1989), "Numerical analysis of junctions between plates", Computer Methods in Applied Mechanics and Engineering, Vol. 74, pp. 307-326.
[233] Ciarlet P.G., Le Dret H. and Nzengwa R. (1989), "Junctions between three-dimensional and two-dimensional linearly elastic structures", J. Math. Pure Appl., Vol. 68, pp. 261-295.
[234] Bernadou M. and Cubier A. (1998), "Numerical analysis of junctions between thin shells. Part 1: continuous problems, Part 2: approximation by finite element methods", Computer Methods in Applied Mechanics and Engineering, Vol. 161 pp. 349-363, pp. 365-387,
[235] Huang J. (2004), "Numerical solution of the elastic body-plate problem by nonoverlapping domain decomposition type techniques", Math. Comput., Vol. 73 pp. 19-34.
[236] Nazarov S.A. (1996), "Junctions of singularly degenerating domains with different limit dimensions I", J. Math. Sci. Vol. 80, pp. 1989-2034.
[237] Nazarov S.A. (1999), "Junctions of singularly degenerating domains with different limit dimensions II", J. Math. Sci. Vol. 97, pp. 4085-4108.
[238] Kozlov V.A. and Mazya V.A. (2001), "Fields in non-degenerate 1D–3D elastic multi-structures", Quart. J. Mech. Appl. Math., Vol. 54, pp. 177-212.
[239] Park K.C. and Felippa C.A. (2000), "A variational principle for the formulation of partitioned structural systems", Int. J. Numer. Methods Engrg., Vol. 47, pp. 395-418.
[240] Park K.C., Felippa C.A. and Ohayon R. (2001), "Partitioned formulation of internal fluid–structure interaction problems by localized Lagrange multipliers", Computer Methods in Applied Mechanics and Engineering., Vol. 190, pp. 2989-3007.
[241] Formaggia L., Gerbeau J.F., Nobile F. and Quarteroni A. (2001), "On the coupling of 3D and 1D Navier–Stokes equations for flow problems in compliant vessels", Computer Methods in Applied Mechanics and Engineering, Vol. 191, pp. 561-582.
[242] Urquiza S.A., Blanco P.J., Venere M.J. and Feijoo R.A. (2006), "Multidimensional modeling for the carotid artery blood flow", Computer Methods in Applied Mechanics and Engineering, Vol. 195, pp. 4002-4017.
[243] Blanco P.J., Feijoo R.A. and Urquiza S.A. (2007), "A unified variational approach for coupling 3D–1D models and its blood flow applications", Computer Methods in Applied Mechanics and Engineering, Vol. 196, pp. 4391-4410.
[244] Blanco P.J., Feijoo R.A. and Urquiza S.A. (2008), "A variational approach for coupling kinematically incompatible structural models", Computer Methods in Applied Mechanics and Engineering, Vol. 197, pp. 1577-1602.
[245] Mata P., Barbat A.H. and Oller S. (2008), "Two-scale approach for the nonlinear dynamic analysis of RC structures with local non-prismatic parts", Engineering Structures, Vol. 30(12), pp. 3667-3680.
[246] Bournival S., Cuillière J.-C. and François V. (2010), "A mesh-based method for coupling 1D and 3D elements." Advances in Engineering Software, Vol. 41, pp. 838-858.
[247] Bournival S., Cuillière J.-C. and François V. (2010), "A mesh-geometry-based solution to mixed-dimensional coupling", Computer-Aided Design, Vol. 42, pp. 509-522.
[248] Suresh K. (2003), "Generalization of the Kantorovich method of dimensional reduction", In: International meshing roundtable, Santa Fe (NM).
[249] Robinson T. et al. (2008), "Automated mixed dimensional modeling with the medial object", In: Proceedings of the 17th international meshing roundtable, Pittsburgh (USA), Sandia National Laboratory.
[250] ΕΑΚ2000, "Ελληνικός Αντισεισμικός Κανονισμός", Greek Earthquake Resistant Code.

[251] EN1998, Eurocode 8, "Design of structures for earthquake resistance".

Author's References

[gm1] Mouroutis Z.S., Markou G., Charmpis D.C., Koubogiannis D.G. and Papadrakakis M. (2005), "An efficient mesh updating technique for fluid structure interaction problems", Int. Conf. on Computational Methods for Coupled Problems in Science and Engineering, COUPLED PROBLEMS, Santorini, May 2005.

[gm2] Markou G. and Papadrakakis M. (2006), "Numerical study of four mesh update techniques", First South-East European Conference on Computational Mechanics SEECCM-06, June 28-30, 2006, Kragujevac, Serbia and Montenegro.

[gm3] Markou G., Mouroutis Z.S., Charmpis D.C. and Papadrakakis M. (2007), "The ortho-Semi-Torsional (OST) spring analogy method for 3D mesh moving boundary problems", Computer Methods in Applied Mechanics and Engineering, Vol. 196, pp. 747-765.

[gm4] Mouroutis Z.S., Markou G., Charmpis D.C. and Papadrakakis M. (2007), "An efficient mesh updating technique for fluid structure interaction problems", International Journal of Computational Methods, Vol. 4(2), pp. 249-263.

[gm5] Markou G. and Papadrakakis M. (2007), "MESH UPDATE TECHNIQUES: ROBUSTNESS AND EFFICIENSY", Int. Conf. on Computational Methods for Coupled Problems in Science and Engineering, COUPLED PROBLEMS 2007, Santa Eulalia, Ibiza, Spain.

[gm6] Markou G. and Papadrakakis M. (2010), "3D Mesh Update Techniques in Fluid-Structure Interaction Problems", 9th HSTAM International Congress on Mechanics Limassol, Cyprus, 12-14 July, 2010.

[gm7] Markou G. and Papadrakakis M. (2010), "Generating Embedded Reinforcement in Hexahedral Elements for Concrete Simulation", 9th HSTAM International Congress on Mechanics, Limassol, Cyprus, 12-14 July.

[gm8] Markou G. and Papadrakakis M. (2010), "Detailed Three-Dimensional Modeling of Reinforced Concrete Structures", 9th HSTAM International Congress on Mechanics, Limassol, Cyprus, 12-14 July.

[gm9] Markou G. and Papadrakakis M., "Generating Embedded Reinforcement in Hexahedral Concrete Elements", Submitted for Publication, 2011.

[gm10] Markou G. and Papadrakakis M., "ACCURATE AND COMPUTATIONALLY EFFICIENT THREE-DIMENSIONAL FINITE ELEMENT MODELING OF REINFORCED CONCRETE STRUCTURES", Submitted for Publication, 2011.

[gm11] Markou G. and Papadrakakis M., "MODELING OF FULL-SCALE RC STRUCTURES FOR INELASTIC ANALYSIS WITH HYBRID MODELS (HYMOD)", Submitted for Publication, 2011.

Appendix A: Formulation of the Octahedral Stresses and Strains

In order to describe the octahedral formulation of the corresponding stresses and strains, the representation of the Cartesian stress space has to be defined. Considering a Cartesian space, as shown in Fig. A.1a, the principal stresses (σ_1, σ_2, σ_3) which correspond to the coordinate axes, are used to define any given state of stress at any point P. The octahedral coordinates (z, r, θ'), refer to a cylindrical coordinate system having its z axis coincide with the space diagonal ($\sigma_1 = \sigma_2 = \sigma_3$), while r and θ' represent the radius and rotational variables, respectively. Fig. A.1a represents schematically this type of system. Furthermore, the cylindrical system may be transformed along the space diagonal or z axis, as illustrated in Fig. A.1b, which lies in the plane normal to z (known as the deviatoric plane). The following relations results from standard algebra computations, thus the octahedral and Cartesian coordinates are connected through:

$$z = \frac{1}{\sqrt{3}}(\sigma_1 + \sigma_2 + \sigma_3) \quad \text{A1}$$

$$\rho = \frac{1}{\sqrt{3}}\sqrt{\left[(\sigma_1 - \sigma_2)^2 + (\sigma_2 - \sigma_3)^2 + (\sigma_3 - \sigma_1)^2\right]} \quad \text{A2}$$

$$cos\theta' = \frac{1}{\sqrt{6}\cdot r}(\sigma_1 + \sigma_2 - 2\sigma_3) \quad \text{A3}$$

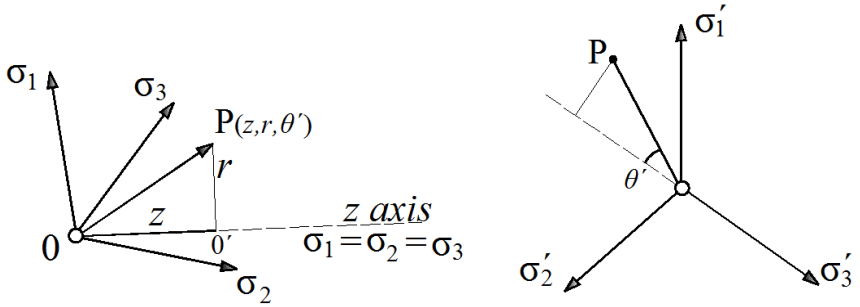

FIGURE A.1 STRESS (A) CARTESIAN AND CYLINDRICAL COORDINATES; (B) TRANSFORMED IN THE DEVIATORIC PLANE.

The octahedral stress, σ_{oct}, acts on a plane orthogonal to the line that equally trisects the sets of axes defined by principal stress directions. Such a plane is known as the deviatoric plane (Fig. A.2), which is shown as a triangle. Given that u_z is the unit vector along the z axis that is given by $1/\sqrt{3}\,(1,1,1)$, the octahedral stress is obtained through the following formula:

$$\sigma_{oct} = \begin{bmatrix} \sigma_1 & . & . \\ . & \sigma_2 & . \\ . & . & \sigma_3 \end{bmatrix} \frac{1}{\sqrt{3}} \begin{bmatrix} 1 \\ 1 \\ 1 \end{bmatrix} = \frac{1}{\sqrt{3}} \begin{bmatrix} \sigma_1 \\ \sigma_2 \\ \sigma_3 \end{bmatrix} \quad \text{A4}$$

The octahedral stress is fully defined by its direct and shear components, σ_0 and τ_0 as well as the angle θ that the shear octahedral stress vector forms with the projection of any given principal direction on the deviatoric plane (Fig. A.2b). the magnitudes of these parameters are denoted by σ_0, τ_0 and θ which are known as hydrostatic stress, deviatoric stress and the rotational angle, respectively. The relation of the octahedral and quantities and the principal stresses through the

use of the octahedral coordinate system derives from standard vector operations and has the form:

$$\sigma = \frac{1}{3}(\sigma_1 + \sigma_2 + \sigma_3) = \frac{1}{\sqrt{3}} z \quad \text{A5}$$

$$\tau_0 = \frac{1}{3}\sqrt{\left[(\sigma_1 - \sigma_2)^2 + (\sigma_2 - \sigma_3)^2 + (\sigma_3 - \sigma_1)^2\right]} = \frac{1}{\sqrt{3}} r \quad \text{A6}$$

$$cos\theta = \frac{1}{\sqrt{2} \cdot \tau_0}(\sigma_0 - \sigma_3) = cos\theta' \quad \text{A7}$$

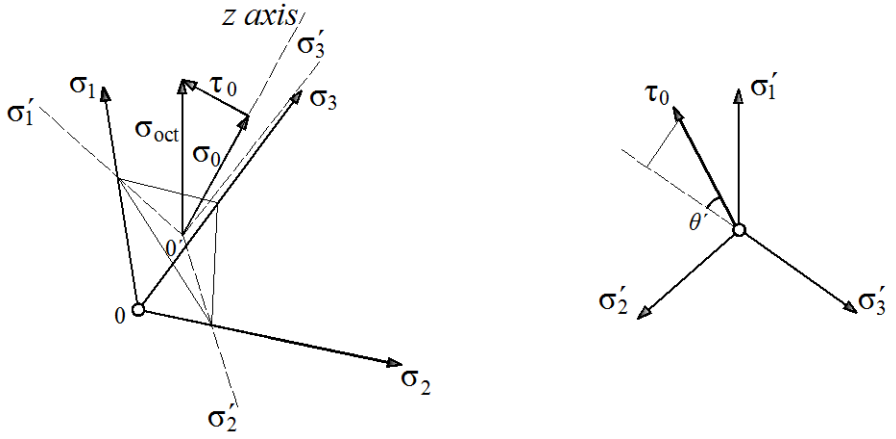

(A) (B)

FIGURE A.2 OCTAHEDRAL STRESS (A) $\sigma_{oct} = \sigma_0 + \tau_0$; (B) TRANSFORMED IN THE DEVIATORIC PLANE.

The search for the principal stresses (σ_1, σ_2, σ_3) and the associated principal directions corresponding to an arbitrary stress state (σ_x, σ_y, σ_z, τ_{xy}, τ_{yz}, τ_{zx}) is performed by solving the standard eigenvalue problem which can be written in the cubic equation format as follows:

$$\sigma^3 - I_1\sigma^2 + I_2\sigma - I_3 = 0 \quad \text{A8}$$

Eq. A8 always gives three real roots (σ_1, σ_2, σ_3). Given that these three quantities represent the corresponding principal stresses, they are independent from the coordinate system orientation which was assumed originally (x, y, z) thus it follows that the coefficients I_1, I_2 and I_3 must be also independent from the coordinate system orientation. This is the reason why these three quantities are known as the first, second and third invariants of the stress tensor. In order to connect the two coordinate systems defined by the arbitrary orientation of the arbitrary (x, y, z) axes and the principal directions, the following formula are provided:

$$I_1 = (\sigma_x + \sigma_y + \sigma_z) = (\sigma_1 + \sigma_2 + \sigma_3) \quad \text{A9}$$

$$I_2 = (\sigma_x\sigma_y + \sigma_y\sigma_z + \sigma_z\sigma_x) - (\tau_{xy}^2 + \tau_{yz}^2 + \tau_{zx}^2) = \sigma_1\sigma_2 + \sigma_2\sigma_3 + \sigma_3\sigma_1 \quad \text{A10}$$

$$I_3 = (\sigma_x\sigma_y\sigma_z + 2\tau_{xy}\tau_{yz}\tau_{zx}) - (\sigma_x\tau_{yz}^2 + \sigma_y\tau_{zx}^2 + \sigma_z\tau_{xy}^2) = \sigma_1\sigma_2\sigma_3 \quad \text{A11}$$

The relations that connect the principal invariants the octahedral stresses can be verified that they are given from the following expressions:

$$\sigma_0 = \frac{1}{3} I_1 \quad \text{A12}$$

$$\tau_0 = \sqrt{2\sigma_0^2 - \frac{2}{3} I_2} \quad \text{A13}$$

$$\cos 3\theta = -\frac{\sqrt{2}}{\tau_0^3} J_3 \quad \text{A14}$$

where J_3 is the third invariant of the deviatoric stress tensor $s_{ij} = \sigma_{ij} - \sigma_0 \delta_{ij}$.

Since all octahedral stress variables were defined in the component quantities of (σ_0, τ_0, θ) the corresponding strain counterparts need to be expressed in an identical mathematical nature. Therefore, denoting the three principal strains by (ε_1, ε_2, ε_3), the following definitions for the hydrostatic and deviatoric strains ε_0 and γ_0, respectively, as well as the angle (δ) between the vector γ_0 and the projection of the ε_3 axis, hold:

$$\varepsilon_0 = \frac{1}{3}(\varepsilon_1 + \varepsilon_2 + \varepsilon_3) \quad \text{A15}$$

$$\gamma_0 = \frac{1}{3}\sqrt{\left[(\varepsilon_1 - \varepsilon_2)^2 + (\varepsilon_2 - \varepsilon_3)^2 + (\varepsilon_3 - \varepsilon_1)^2\right]} \quad \text{A16}$$

$$cos\delta = \frac{1}{\sqrt{2} \cdot \gamma_0}(\varepsilon_0 - \varepsilon_3) \quad \text{A17}$$

What remains is to define the elastic constitutive relations in terms of octahedral stresses and strains which derive from the standard elastic constitutive principal elastic relations:

$$\varepsilon_1 = \frac{1}{\mathrm{E}}\left[\sigma_1 - \nu(\sigma_2 + \sigma_3)\right] \quad \text{A18}$$

$$\varepsilon_2 = \frac{1}{\mathrm{E}}\left[\sigma_2 - \nu(\sigma_3 + \sigma_1)\right] \quad \text{A19}$$

$$\varepsilon_3 = \frac{1}{\mathrm{E}}\left[\sigma_3 - \nu(\sigma_1 + \sigma_2)\right] \quad \text{A20}$$

therefore

$$\varepsilon_0 = \frac{1-2\nu}{E}\sigma_0 = \frac{\sigma_0}{K} \quad \text{A21}$$

$$\gamma_0 = \frac{1+\nu}{E}\tau_0 = \frac{\tau_0}{2G} \quad \text{A22}$$

where K and G are the bulk and shear moduli, respectively and they are defined as:

$$K = \frac{E}{3(1-2\nu)} \quad \text{A23}$$

$$G = \frac{E}{2(1+\nu)} \quad \text{A24}$$

Appendix B: Algebraic Algorithm for the Computation of a Line-Plane Intersection

The algebraic algorithm for the computation of a line-plane intersection will be presented. A plane can be represented by the equation:

$$Ax + By + Cz + D = 0 \quad \text{B1}$$

where (x, y, z) represent the coordinates of any point that lies on the plane.

Assuming that point P1 and P2 with coordinates ($x1$, $y1$, $z1$) and ($x2$, $y2$, $z2$), are two points defining the line, then the equation of the line can be written as:

$$P = P1 + \lambda\left(P2 - P1\right) \quad \text{B2}$$

By substituting Eq. B2 into Eq. B1 results:

$$A\left(x1 + \lambda\left(x2 - x1\right)\right) + B\left(y1 + \lambda\left(y2 - y1\right)\right) + C\left(z1 + \lambda\left(z2 - z1\right)\right) + D = 0 \quad \text{B3}$$

and by solving for λ:

$$\lambda = \frac{A \cdot x1 + B \cdot y1 + C \cdot z1 + D}{A\left(x1 - x2\right) + B\left(y1 - y2\right) + C\left(z1 - z2\right)} \quad \text{B4}$$

There are two cases that we have to take under consideration regarding the value of λ. The first case is when this value is equal to zero which means that the normal of the plane is perpendicular to the line, therefore there is no intersection between them (Fig. B1b). If λ is not equal to zero then there is an intersection between the line and the plane which is computed by substituting the expression of λ into Eq. B2 (Fig. B.1a).

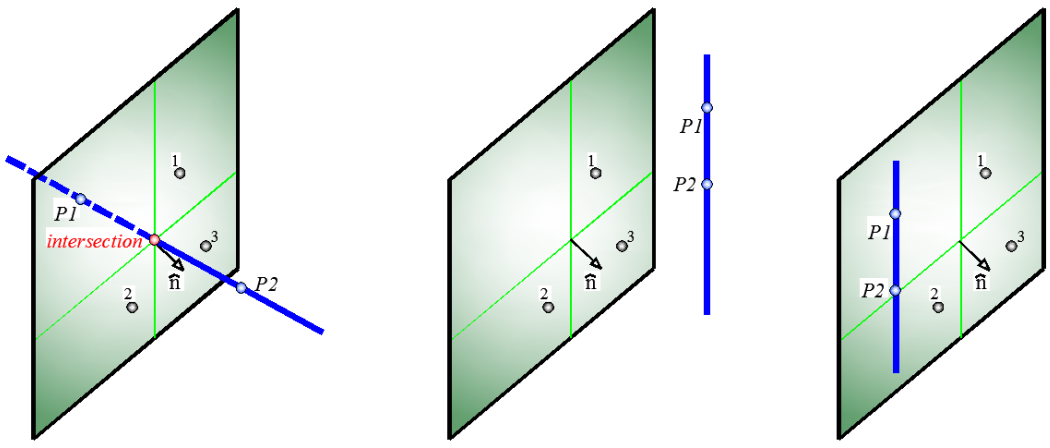

(A) (B) (C)

FIGURE B.1 LINE-PLANE HAVE (A) AN INTERSECTION, (B) NO INTERSECTION AND (C) LINE IS LOCATED ON THE PLANE.

In addition to that, we have to check if the line is located on the plane. This can be easily performed by substituting the coordinates of the two points of the line into the equation of the plane (Eq. B1). If both coordinates satisfy the equation of the plane it means that the line is located on the plane (Fig. B1c).

Επίλογος

"Μια εκτενής παρουσίαση πολύχρωμων διαγραμμάτων και πανέμορφων σχημάτων, με απώτερο σκοπό την σύνδεση του αριθμητικού αποτελέσματος που προκύπτει μέσα από αναρίθμητες υπολογιστικές πράξεις, με την αντίστοιχη μηχανική συμπεριφορά μίας κατασκευής η οποία προκύπτει από την τελειότερη οντότητα που υπήρξε ποτέ, τη «φύση»."

Είναι γενικώς αποδεκτό ότι η φύση δεν μπορεί να αναπαραχθεί από κανέναν άλλο πάρα μόνο από την ίδια τη φύση. Συνεπώς, είναι αδιαμφισβήτητο ότι η σύνδεση των αριθμητικών αποτελεσμάτων τα οποία προκύπτουν μέσα από κάποιες αριθμητικές πράξεις με την αντίστοιχη απόκριση των φυσικών φαινομένων που προκύπτουν μέσω της πραγματικής συμπεριφοράς των κατασκευών στη φύση, είναι εγγενώς άτοπη και συνυφασμένη με την έννοια της προσεγγιστικής λύσης.

Πάρα ταύτα, έχει διαπιστωθεί ότι η ανάπτυξη λογισμικών προγραμμάτων έχει αλλάξει τον τρόπο με τον οποίο σκεφτόμαστε αλλά και κατ' επέκταση τον τρόπο με τον οποίο αφομοιώνουμε νέα γνώση. Εάν αναλογιστεί κανείς ότι οι υπολογιστές αποτελούν το νούμερο ένα εργαλείο το οποίο χρησιμοποιούν σήμερα οι επιστήμονες για να παράγουν νέα γνώση και θεωρίες, τότε είναι αδιαμφισβήτητο ότι η μεγαλύτερη ανακάλυψη του 20ου αιώνα έχει εισβάλει για τα καλά στις ζωές μας επηρεάζοντας άμεσα την ίδια την κοινωνία. Μέσα από τη διατριβή αυτή και κυρίως μέσα από την εμπειρία που είχα με επαγγελματίες Πολιτικούς Μηχανικούς, η έννοια "Computer Educated Civil Engineer (CECE)" είναι πλέον πραγματικότητα.

Όσο υπάρχει αναβάθμιση και εξέλιξη των λογισμικών πακέτων Πολιτικού Μηχανικού, σε μία προσπάθεια υλοποίησης της λογικής που προσπαθούν να προωθήσουν τα Windows: "Anyone can use it!", τότε όλο ένα και περισσότερο θα αυξάνονται οι CECE, με αποτέλεσμα να ακούγονται με μεγαλύτερη συχνότητα σχόλια του τύπου:

«*Μα το έβγαλε το πρόγραμμα… Τότε πρέπει να είναι σωστό!!!*»

Το πιο πάνω φαινόμενο πρέπει να σταματήσει μέσω της σωστής εκπαίδευσης και ενημέρωσης των νέων φοιτητών και εν δυνάμει Πολιτικών Μηχανικών, για το πόσο επικίνδυνοι είναι οι υπολογιστές όταν χρησιμοποιούνται ως υπολογιστικά μέσα κατά τη διάρκεια εκτέλεσης μίας στατικής μελέτης.

Υπάρχουν αναρίθμητα γνωμικά για το τι είναι ένα *computer* ή για το πώς αυτό επηρεάζει τη ζωή των ανθρώπων όπως:

"*Computers are useless. They can only give you answers.*" Pablo Picasso

"*Computers have enabled people to make more mistakes faster than almost any invention in history, with the possible exception of tequila and hand guns.*" Mitch Ratcliffe

"*A computer will do what you tell it to do, but that may be much different from what you had in mind.*" Joseph Weizenbaum

και στην αντίπερα όχθη:

"*I do not fear computers. I fear the lack of them.*" Isaac Asimov

"*Computing is not about computers any more. It is about living*." Nicholas Negroponte

και το τελευταίο αλλά όχι έσχατο

"*Computers shape the theory*." John Argyris

Συνοψίζοντας τα πιο πάνω μέσα από το βλέμμα του Πολιτικού Μηχανικού, αποδεχόμαστε την αναγκαιότητα της χρήσης των υπολογιστών στην επιστήμη μας, αλλά ποτέ δεν αποδεχόμαστε τα αποτελέσματα που μας δίνουν χωρίς την αντιπαράθεση αυτών με την επιστημονική γνώση και την αντίληψη που έχουμε η οποία περιγράφεται σχεδόν απόλυτα από την ακόλουθη «λαϊκή παραβολή»:

«Καθόντουσαν σε μία καφετέρια τρεις κύριοι οι οποίοι ασκούσαν τα εξής επαγγέλματα: Μαθηματικός, Φυσικός και Πολιτικός Μηχανικός. Καθώς απολάμβαναν τον καφέ τους, προσπαθούσαν παράλληλα να λύσουν το εξής θεμελιώδες μαθηματικό πρόβλημα: Δεδομένης της ύπαρξης μίας καλλίγραμμης και συνάμα πανέμορφης ξανθιάς γυναίκας και του γεγονότος ότι τους χώριζε μία απόσταση 10 μέτρων, θα κατάφερνε κάποιος από τους τρεις να φτάσει σε αυτή, με την υπόθεση ότι κάθε φορά ο καθένας τους θα προχωρούσε διανύοντας την μισή απόσταση από αυτή που τους χώριζε από την γυναίκα? Όπως είναι κοινώς γνωστό, ο μαθηματικός άρχισε να περιγράφει το μαθηματικό πρόβλημα μέσω πολύπλοκων μαθηματικών συναρτήσεων όπου κατέληξε στην απόδειξη του μαθηματικού θεωρήματος το οποίο προέβλεπε ότι πάντα θα υπήρχε μία απόσταση μεταξύ αυτού και της γυναίκας, άρα ποτέ δεν θα μπορούσε να την φτάσει. Στη συνέχεια ο Φυσικός άρχισε να περιγράφει τη φύση του προβλήματος μέσω της παράθεσης της μαθηματικής διατύπωσης με βαρυτικά πεδία και μαγνητικές δυναμικές γραμμές, όπου εν τέλη κατέληξε στο συμπέρασμα ότι θα υπήρχε μία μικρή πιθανότητα δεδομένων εξωγενών παραγόντων και στρέβλωσης της παραλληλίας, να φτάσει τελικά στη γυναίκα. Τέλος, μετά από σοβαρό περί-συλλογισμό και σκέψη, ο Πολιτικός Μηχανικός έδωσε την εξής απάντηση: Ξεκινώντας την πορεία μου προς τον ποθητό στόχο, η απόσταση θα μειώνετε με σταθερό ρυθμό, όπου σε κάποια χρονική στιγμή αυτή θα είναι μικρότερη των 10 εκατοστών, απόσταση επαρκής μέσα στην οποία θα εφαρμόσω την γνωστή κίνηση πιασίματος, αγκαλιάζοντας τον ποθητό στόχο!»